APPLIED COMPUTATIONAL ELECTROMAGNETICS SOCIETY JOURNAL

September 2019
Vol. 34 No. 9
ISSN 1054-4887

The ACES Journal is abstracted in INSPEC, in Engineering Index, DTIC, Science Citation Index Expanded, the Research Alert, and to Current Contents/Engineering, Computing & Technology.

The illustrations on the front cover have been obtained from the research groups at the Department of Electrical Engineering, The University of Mississippi.

SEPTEMBER 2019 REVIEWERS: REGULAR PAPERS

Danial Abdorahimi
Iftikhar Ahmed
Mohamed Ahmed
Mohammad Alibakhshikenari
Stamatios Amanatiadis
Marco Arjona
Ercument Arvas
Seyed Hesam Asgari
Wendell Brokaw
William Coburn
Danesh Daroui
Pasquale Dottorato
Alistair Duffy
Sidra Farhat
Krishnaveni G.
Andrey Grigoryev
Tianqi Jiao
Ming Jin
Zhu Jun
Anan Kruesubthaworn
Wang-Sang Lee
Xiuping Li
Yue Li
Chia-Hsien Lin
Xingnan Liu
Shengyuan Luo
Peyman Mahouti
Zahéra Mekkioui
Anton Menshov
Antonino Musolino
Turgut Ozturk
John J. Pantoja
Balachandra Pattanaik
Mohammd Pourbagher
Oscar Quevedo-Teruel
James Quinlan
Hassan Ragheb
Leonardo Ranzani
Hatem Rmili
Vince Rodriguez
Imaculate Rosaline
Sivaprakash S.C.
Suganthi Santhanam
Khalil Sayidmarie
Stefano Selleri
Meriah Sidi Mohammed
Vitawat Sittakul
Wanchun Tang
Xuezhe Tian
Praveen N. Vummadisetty
Julia Wolff
Binbin Yang
Fan Yang
Xiaokang Yin
Tara Yousefi

SEPTEMBER 2019 REVIEWERS: EXPRESS PAPERS

Ali Foudazi
Amin Gorji
George Kyriacou

THE APPLIED COMPUTATIONAL ELECTROMAGNETICS SOCIETY JOURNAL

Vol. 34 No. 9 September 2019

TABLE OF CONTENTS – REGULAR PAPERS

TABLE OF CONTENTS – EXPRESS PAPERS

Pattern Synthesis for Array Antennas based on Interpolation Gravitational Search Algorithm

Cuizhen Sun [1,2], Jun Ding [1], Chenjiang Guo [1], and Jian Liu [2]

[1] School of Electronics and Information
Northwestern Polytechnical University, Xi'an 710072, China
scz@xust.edu.cn

[2] School of Communication and Information Engineering
Xi'an University of Science and Technology, Xi'an 710054, China

Abstract ─ A new algorithm known as interpolation gravitational search algorithm (IGSA) is proposed in this paper when be used to synthesize pattern for array with complicated side lobe and notch. First, a novel and adjustable coefficient q for inertia mass is introduced, which can render the particle large in inertia mass get larger and more attractive to other particles to access to more optimal location, so the convergence can be accelerated through varying the discrepancy of inertia mass $M_i(t)$ of particles in a specific population. Second, a simplified quadratic approximation algorithm (SQA) is interpolated that can make the algorithm perform better in the aspect of optimum seeking, so the computational accuracy can be increased through utilizing the stronger local search ability of SQA. To verify the validation of the algorithm, the proposed IGSA is applied to commit pattern synthesis in terms of different targets. Simulation results show that the IGSA, as a whole, is better than the other algorithms the same kind, mainly because the IGSA can be possessed of faster speed in convergence and perform more accurate in optimization.

Index Terms ─ Inertia mass coefficient, interpolation gravitational search algorithm, notches, side-lobe reduction, simplified quadratic approximation.

I. INTRODUCTION

The pattern synthesis for array antenna is a procedure with deliverables of antenna's relevant parameters upon the required radiation. Since the pattern synthesis can greatly simplify design complexity and reduce design cost, it has increasingly become a hot research topic in the field of antenna design and study. The pattern synthesis belongs to the optimization problems. To solve the optimization problem, various meta-heuristic (M-HS) algorithms such as honey bee mating optimization (HBMO) [1], the sailfish optimizer (SFO) [2], the differential evolution algorithm (DE) [3] and the moth-flame optimization algorithm (MFO) [4] have been proposed recently. The genetic algorithm (GA) [5,6], the particle swarm optimization algorithm (PSO) [7,8] have been verified to be able to satisfy in the requirement of the pattern synthesis of array antennas.

The gravitational search algorithm (GSA) [9] is one of the recent M-HS algorithms inspired by the law of gravity. In GSA, a particle is guided by the sum of gravitational force exerted on it by other particles. To search the optimum efficiently, various improvement versions for the original GSA algorithms have been presented, which can be classified into two categories. One focuses on improving the variable parameters [10]; The other is to combine other state-of-the-art algorithms with GSA to enhance GSA [11].While these efforts ameliorate the performance of GSA, GSA is easier to fall into local optimal and become quite lower in the speed of convergence whenever dealing with the problems in the application of pattern synthesis such as the lower side lobe's level and the notches in specific location. Because the specified objective functions which are usually nonlinear, nondifferentiable and even discontinuous with multiple parameters, how to balance the exploration and exploitation according to evolutionary states is challenging.

In this paper, an interpolation gravitational search algorithm (IGSA) is proposed. First, a novel and adjustable inertia mass coefficient q is configured which changes the distribution of inertial masses to improve the searching speed to the optimum; Subsequently, to overcome the drawback that GSA is easier falling into local optimal, the simplified quadratic approximation (SQA) is used as a local search operator and embedded into GSA to enhance the entire ability of optimal seeking. Based on different simulation examples, the IGSA can be verified to be better than the traditional GSA both in the convergence rate and in the solution accuracy, which can be proved that the proposed algorithm is more suitable for solving the issue of the complicated synthesis of array antenna such as ultra side

Submitted On: November 12, 2018
Accepted On: May 4, 2019

lobe and notches.

The remainder of this paper is arranged as follows. Section II briefly describes the pattern synthesis framework. In Section III, a detailed introduction of the proposed IGSA is presented. The IGSA is used to simulate standard benchmark functions and design pattern synthesis in Section IV. Finally, Section V concludes this paper.

II. PATTERN SYNTHESIS FOR LINEAR ARRAY ANTENNAS

In terms of an equispaced linear array with N elements, the principle of pattern multiplication governs that the radiation pattern of this array will be equal to the multiplication of the pattern of element with the array factor, therefore, the pattern function normalized is:

$$F(\theta) = 20\log\left[F_e(\theta)^* \mid \sum_{n=1}^{N} I_n e^{jk(n-1)d\sin\theta} \mid / F_{\max} \right], \quad (1)$$

where N is the number of elements, d is the distance between neighboring elements, $k = 2\pi/\lambda$ is the wave number, I_n is the complex excitation of the *nth* element (amplitude and phase); θ is the included angle between the direction of radiation and the axis of array, $F_{\max}$ is the maximum of the pattern function, $F_e(\theta)$ is the pattern of element that represents the radiation feature of the element own, the current excitation amplitude is described as I_n $n=1,2,...,N$,N is the number of elements.

The increasing traffic in the electromagnetic environment prompts to design the antenna array with a lower side lobe level (SLL). A lower SLL is required to avoid the interference with the other systems operating in the same frequency band. In this article, the design target of antenna synthesis is to make the side lobe level become lower than a specified value and create a deep notch in a designated location. The design of fitness function is determined by the design target. Therefore, the fitness function will be set by taking the following two aspects into consideration:

1) The level of side lobe is lower than the expected target about the peak level of side lobe L_{ESL}.
2) Given m directions $\theta_i (i = 1, 2, ..., m)$ in a region of side-lobe, forming notches which is deep in L_{ENL}.

So the fitness function is designed as:

$$f_{fit} = \alpha|L_{MSL} - L_{ESL}| + \beta|L_{MNL} - L_{ENL}|,$$

$$L_{MSL} = \underset{\theta \in P}{MAX}\left\{ F(\theta) \right\}, \quad (2)$$

$$L_{MNL} = \underset{\theta_i \in P, i=1,2,\cdots,m}{MAX}\left\{ F(\theta_i) \right\},$$

the optimization objective is described as:

$$\min\ f_{fit} = \alpha\left|L_{MSL} - L_{ESL}\right| + \beta\left|L_{MNL} - L_{ENL}\right|,$$
$$\text{subject to } I_{\min} < I_n < I_{\max}, \quad (3)$$

where L_{MSL} is the maximum level of the side lobe in a real pattern; L_{MNL} is the one within m direction in the side lobe domain, the level of which is the maximum notch; P is the domain of side lobe; α and β are the weights of error, $\alpha + \beta = 1$. The range of excitation current amplitude is $[I_{\min}, I_{\max}]$, the penalty function method is used to deal with the constraint conditions, when the value of I_n exceeds the range, the corresponding objective value is set to the maximum, so that the individual can't be selected into the next generation. To prevent the happening of the fitness value to be null, the issue about minimum specified by the equation closely above is going to be that of the maximum:

$$f_{fit} = \frac{100}{1 + f_{fit}}. \quad (4)$$

III. DESCRIPTION OF INTERPOLATION GRAVITATIONAL SEARCH ALGORITHM

A. The basic principle of GSA

Different from these clustering algorithms like PSO, the particle in GSA is unnecessary to perceive situation in ambient through the factor of environment. On the contrary, the particle can share information through the gravitation applied each other. Therefore, when be influenced without the factor of environment, the particle can commence a search in terms of the environment perceived by overall situation.

In GSA, the initial location of the particle is randomly produced. Given that there are N particles in a space for D dimensional search, the exact location for the i_{th} particle is $x_i = \left\{ x_i^1, x_i^2, \cdots x_i^d, \cdots x_i^D \right\}$ $i = 1, 2, \cdots N$, where, x_i^D representing the location of the i_{th} particle in D dimension.

At the moment of t, F_{ij}^d is the gravitation of the *ith* particle exerted by the *jth* counterpart, that is:

$$F_{ij}^d(t) = G(t)\frac{M_{pi}(t) \times M_{aj}(t)}{R_{ij}(t) + \varepsilon}\left(x_j^d(t) - x_i^d(t)\right), \quad (5)$$

where, $M_{pi}(t)$ and $M_{aj}(t)$ are the inertia mass of the *ith* and the *jth* particles, respectively. ε is a quite small constant; $G(t)$ is a gravitation constant at the moment t: $G(t) = G_0 e^{-\alpha_0 \frac{t}{T}}$, $R_{ij}(t)$ is the 2-norm between the *ith* and *jth* particles:

$$R_{ij}(t) = \left\| x_i(t), x_j(t) \right\|_2.$$

According to the Newton's second law, the velocity of the *ith* particle at *t* on the *dth* dimension is:

$$v_i^d(t+1) = rand_i \times v_i^d(t) + a_i^d(t), \quad (6)$$

where, the acceleration is:

$$a_i^d(t) = \frac{\sum_{j=1, j\neq i}^{N} rand_j F_{ij}^d(t)}{M_i(t)}, \quad (7)$$

$M_i(t)$ is the inertia mass of the *ith* particle. The inertia mass and the value of the fitness will be tough related each other. The inertia mass, as a measure used to scale the value of fitness, is involved into the movement of the particle, it can be revised by following:

$$M_i = \frac{m_i(t)}{\sum_{j=1}^{N} m_j(t)}, \quad (8)$$

where, $M_{ai} = M_{pi} = M_{ii} = M_i, i = 1, 2, \cdots, N$,

$m_i(t) = \frac{fit_i(t) - worst(t)}{best(t) - worst(t)}$, $fit_i(t)$ denotes the value of fitness of the *ith* particle at the moment *t*. Upon the issue of maximum, *best(t)* and *worst(t)* represent the fitness's maximum and minimum value at the moment *t*.

In the process of iteration, the fitness value will be calculated through updating the location of particles. Result will be output subsequently (the location of particle) if either the calculation accuracy is satisfied or the maximal iteration time is reached, otherwise, the iteration should be started again:

$$x_i^d(t+1) = x_i^d(t) + v_i^d(t+1), \quad (9)$$

B. The adjustable coefficient of inertia mass

In GSA, the particle's inertia mass is closely related to the value of fitness. Inertia mass, as a measure for scaling the value of fitness, involve the movement of location. If inertia mass is updated by the value of the function of fitness, it can be seen that the larger the inertia mass, the easier the attraction to other particles will be, which, as a result, will move to more optimal location. Therefore, in this paper, a novel and adjustable coefficient of inertia mass *q* is designed to change the discrepancy of particle's inertia mass, which can make particle with large inertia mass larger, while particle with small inertia mass smaller. As a result, the velocity for the algorithm to converge to the maximum can be absolutely improved. When (8) is updated to (10):

$$M_{qi}(t) = \begin{cases} (1+q)^{\beta_0} M_i(t) & fit_i(t) > f_{AVG}(t) \\ (1-q)^{\beta_0} M_i(t) & fit_i(t) < f_{AVG}(t) \end{cases}, \quad (10)$$

$$q = \begin{cases} (\gamma_{\max} - \gamma_{\min}) \dfrac{fit_i(t) - f_{AVG}(t)}{best(t) - f_{AVG}(t)} & fit_i(t) > f_{AVG}(t) \\ (\gamma_{\max} + \gamma_{\min}) \dfrac{f_{AVG}(t) - fit_i(t)}{f_{AVG}(t) - worst(t)} & fit_i(t) < f_{AVG}(t) \end{cases}, \quad (11)$$

where, $M_{qi}(t)$ is the inertia mass of the *ith* particle at the *t* moment after adjustment, *q* is the adjustment factor of the inertia mass, $f_{AVG}(t)$ represents the mean value of the fitness at the moment *t*. $\gamma_{\min}$ and $\gamma_{\max}$ are the zoom factors, controlling the size and the change of the adjustable factor of inertia mass that is usually set by one just between 1 and 0. The value of the exponential weight β_0 can be changed further to adjust the distribution of inertia mass. In this paper, $\gamma_{\min} = 0.1$, $\gamma_{\max} = 0.7$, $\beta_0 = 3$. When $fit_i(t)$, the value of the inertia mass of the *ith* particle is equal to $f_{AVG}(t)$, the average value of all the particles at the time *t*, the inertia mass is unchanged, $M_{qi}(t) = M_i(t)$. Compared with the basic GSA, the size of *q* can be used to change the inertia mass of particle, making the discrepancy of particle's inertia mass increase, which, as a result, will accelerate the speed to approach the optimal location, the velocity of convergence can thus be increased.

C. The SQA algorithm

As a simplified three point quadratic approximation, SQA is a simple, directive and efficient method for searching. It needn't the message of derivative anymore, three points are enough for model delivery. Since the message of the objective function solved can be effectively utilized, the amount of calculation is quite small to bring more convenient to solve the issue of optimization. A combination method between SQA and DE is reported in terms of the problem of constraint optimization [12].After being optimized with respect to test function, it can be concluded that, compared with the original DE, this algorithm is more superior. This paper attempts to interpolate SQA into GSA for improving the algorithm's overall performance.

In terms of the issue of maximization, three optimal individuals x_a, x_b, x_c are provided. In which,

$$x_a = [x_a^1, x_a^2, \cdots, x_a^D]^T, \; x_b = [x_b^1, x_b^2, \cdots, x_b^D]^T,$$
$$x_c = [x_c^1, x_c^2, \cdots, x_c^D]^T.$$

The fitness function are $f^a = f_{fit}(x_a)$, $f^b = f_{fit}(x_b)$, $f^c = f_{fit}(x_c)$, where $f^a > f^b > f^c$. The approximation points achieved by SQA are:

$$x_w = [x_w^1, x_w^2, \cdots, x_w^D]^T,$$
$$x_w^i = \frac{1}{2}\frac{M_i}{N_i} \quad i = 1, 2, ..., D, \tag{12}$$
$$M_i = [(x_a^i)^2 - (x_c^i)^2]f^b + [(x_c^i)^2 - (x_b^i)^2]f^a + [(x_b^i)^2 - (x_a^i)^2]f^c,$$
$$N_i = (x_a^i - x_c^i)f^b + (x_c^i - x_b^i)f^a + (x_b^i - x_a^i)f^c.$$

The interpolation of SQA into basic GSA can improve the problem that the algorithm is easy to fall into local optimal and can increase the velocity for particle to approximate the best.

D. The procedure of IGSA

The IGSA can be realized by following procedures:

Step 1: Population Initiation

Step 2: Gravitation calculation

(1) Particle's fitness value is calculated by equation (4), updated by *G(t)*, $f_{AVG}(t)$, *best(t)*, *worst(t)*, simultaneously.

(2) Updating particle's inertia mass by utilizing well-designed inertia mass coefficient *q* according to equation (11). Updating the total gravitation from all directions by equation (5).

Step 3: Updating particle's velocity by equation (6).

Step 4: Updating particle's location, the location is calculated by equation (9), updating the value of fitness. The result will be output (the location of particle) if either the calculation accuracy is satisfied or the maximal iteration times are reached, otherwise, turn to Step 2.

Step 5: Interpolation into SQA

(1) Calculating f^a, f^b, f^c, selecting three optimal particles x_a, x_b, x_c to calculate fitness from Step 4.

(2) Approximation point determination. If $N_i = 0$, the Step 5 is omitted, otherwise the approximating point x_w is calculated according to (12). In the meanwhile, fitness $f_{fit}(x_w)$ is calculated.

(3) Substitution. If $f_{fit}(x_w) > f^a$, x_w is used to replace the optimal x_a in old population. If $f^a > f_{fit}(x_w) > f^b$, x_w is used to replace the worst case there; otherwise Step 5 is omitted.

Step 6: Stop Judgment. If meeting stop criteria, the algorithm is terminated, the optimal result is output, otherwise turn to Step 2.

IV. RESULT ANALYSIS

A. Standard benchmark functions

In this section, IGSA is compared with the MFO [4], PSOGSA [11], GSA, PSO, GA algorithms. The parameters of GSA and IGSA are set by the same as these in [9]. In benchmark functions, dimension is 30(n=30) and maximal iteration is 1000(T=1000). The minimum value (f_{opt}) of the benchmark functions are zero, except for *F4* which has a minimum value of -12569.487 (-418.9829*n, n=30).

The results are averaged over 30 runs and the average best-so-far solution and median of the best solution in the last iteration are given in Table 1:

(1) $F_1(X) = \sum_{i=1}^{n} x_i^2 \qquad x_i \in [-100, 100]^n$,

(2) $F_2(X) = \max_i\{|x_i|, 1 \le i \le n\} \qquad x_i \in [-100, 100]^n$,

(3) $F_3(X) = \sum_{i=1}^{n}([x_i + 0.5])^2 \qquad x_i \in [-100, 100]^n$,

(4) $F_4(X) = \sum_{i=1}^{n} -x_i \sin(\sqrt{|x_i|}) \qquad x_i \in [-500, 500]^n$,

(5) $F_5(X) = -20\exp(-0.2\sqrt{\frac{1}{n}\sum_{i=1}^{n} x_i^2}) - \exp(\frac{1}{n}\sum_{i=1}^{n}\cos(2\pi x_i)) + 20 + e$

$x_i \in [-32, 32]^n$,

(6) $F_6(X) = \frac{\pi}{n}\{10\sin(\pi y_1) + \sum_{i=1}^{n-1}(y_i - 1)^2[1 + 10\sin^2(\pi y_{i+1})]$

$+(y_n - 1)^2\} + \sum_{i=1}^{n} u(x_i, 10, 100, 4), \quad y_i = 1 + \frac{x_i + 1}{4}$

$$u(x_i, a, k, m) = \begin{cases} k(x_i - a)^m & x_i > a \\ 0 & -a < x_i < a \\ k(-x_i - a)^m & x_i < -a \end{cases} \qquad x_i \in [-50, 50]^n.$$

Table 1: Minimization results of benchmark functions with the average best-so-far solution and median of the best solution

	IGSA	PSOGSA	MFO	RGA	PSO	GSA
F_1	1.69×10^{-18}	5.31×10^{-16}	1.49×10^{-15}	23.13	$1.8*10^{-3}$	7.3×10^{-11}
	1.68×10^{-18}	5.04×10^{-16}	1.32×10^{-15}	21.87	$1.2*10^{-3}$	7.1×10^{-11}
F_2	7.38×10^{-10}	3.65×10^{-8}	2.05×10^{-11}	11.78	8.1	3.7×10^{-6}
	9.30×10^{-10}	3.57×10^{-8}	1.97×10^{-11}	11.94	7.4	3.7×10^{-6}
F_3	2.78×10^{-18}	4.39×10^{-15}	6.23×10^{-12}	24.01	$1.0*10^{-3}$	8.3×10^{-11}
	4.18×10^{-18}	3.86×10^{-15}	5.72×10^{-12}	24.55	6.6×10^{-3}	$7.7*10^{-11}$
F_4	$-1.04\times10^{+4}$	$-6.83\times10^{+4}$	$-7.68\times10^{+4}$	$-1.2\times10^{+4}$	$-9.8*10^{+3}$	$-2.8\times10^{+3}$
	$-1.45\times10^{+4}$	$-6.95\times10^{+4}$	$-7.41\times10^{+4}$	$-1.2\times10^{+4}$	$-9.8*10^{+3}$	$-2.6\times10^{+3}$
F_5	1.023×10^{-9}	2.145×10^{-9}	7.1780×10^{-7}	2.13	9.0×10^{-3}	6.9×10^{-6}
	1.023×10^{-9}	2.150×10^{-9}	7.1780×10^{-7}	2.16	6.0×10^{-3}	6.9×10^{-6}
F_6	2.72×10^{-19}	6.59×10^{-9}	1.49×10^{-7}	0.051	0.29	0.01
	1.89×10^{-19}	4.98×10^{-9}	1.36×10^{-7}	0.039	0.11	$4.2*10^{-13}$

Statistically speaking, for the average value of 30 runs, IGSA reaches best in all of the benchmark functions except F_2 for which the average best-so-far solution and median of the best solution based on MFO is better. The number of functions which the MFO performs better is inferior to PSOGSA and superior to GSA. The MFO and PSOGSA can balance the exploration and exploration well than the GA and PSO algorithms. From the Table 1, it can be concluded that IGSA performs best on the test functions.

Table 2: Results comparison of ultra low side lobe synthesis for the six algorithms

Results of Ultra Low Side Lobe Synthesis			
Algorithms	Directivity	Peak Side-Lobe Level (dB)	Width of Main-Lobe (°)
GA	15.1579	-37.8756	0.8
PSO	15.2763	-39.1364	0.8
GSA	15.3204	-40.5069	0.6
MFO	15.2987	-40.7952	0.6
PSOGSA	15.3462	-41.0551	0.6
IGSA	15.4543	-42.0317	0.6

The linear antenna arrays (LAA) are widely used in many high-performance radio systems like radar, sonar, air and space navigation, underground propagation etc. In this paper, we consider a central symmetry linear array with N=20, $d = \lambda/2$. The current excitation amplitudes are optimized for the synthesis of LAA keeping the excitation phase as zero. So the optimization parameters are 10 amplitudes, the amplitude range of I_n is [0.1,1], $n=1,2,...,N,N$ is the number of elements.

B. The pattern synthesis for ultra low side lobe

In this section, the design objective is that beam width of the main lobe is 20°, and the side lobe levels are lower than -42dB. So, in equations (1), (3), $F_e(\theta) = \sin\theta$, L_{ESL}=-42dB, $\alpha = 1$, $\beta = 0$.

The IGSA is used compared with the GA, PSO, standardized GSA, PSOGSA, MFO to conduct a specific optimization, the iterative times for them are 1000; the number of population for GSA and IGSA are 100, $G_0 = 10$ $\alpha_0 = 5$. Simulation results averaged over 30 runs are depicted in Figs. 1-4 and Table 2.

Figure 1 shows the patterns of ultra low side lobe for the six algorithms. It is clear that the pattern obtained by IGSA meets the desired objective very well. Figure 2 shows the average evolution curves of these six algorithms when they run 30 times. It can be seen that the IGSA performs better in convergence speed and computer accuracy. The best convergence profile, worst convergence profile, average profile for IGSA over 30 runs are depicted in Fig. 3. Figure 4 is the optimized current amplitude value. Table 2 is the detailed comparisons of the above algorithms. PSOGSA and MFO perform similar and only inferior to IGSA. The GA and PSO have no advantages. It can be noted that under the same width of main lobe, GSA is better than MFO dealing with directivity, while it is weak in peak side lobe level. When the width of main lobe is almost unchanged, the IGSA not only performs most low peak side lobe (-42.0317), but also has the best directivity value (15.4543). It can conclude that the IGSA outperforms other algorithms according to the directivity, the peak side lobe level and width of main lobe.

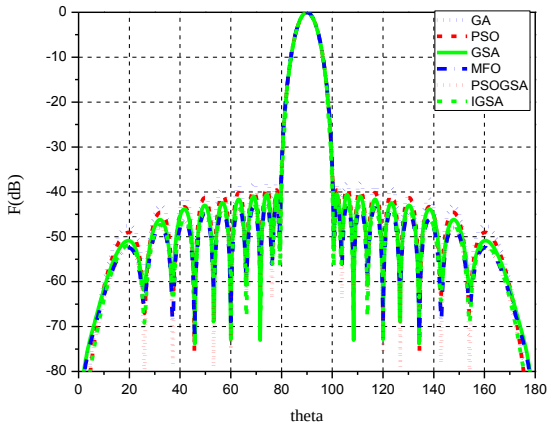

Fig. 1. Patterns of ultra low side lobe for the six algorithms.

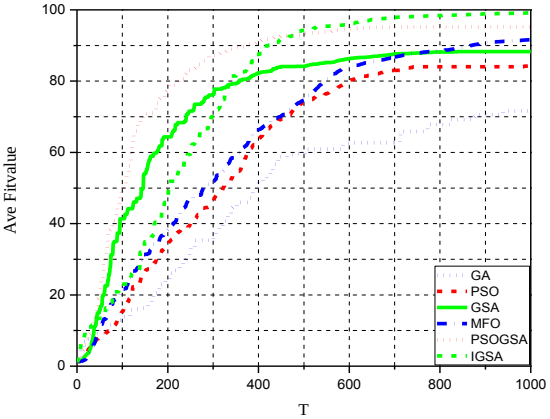

Fig. 2. Average convergence based on six algorithms for the pattern synthesis of ultra low side lobe.

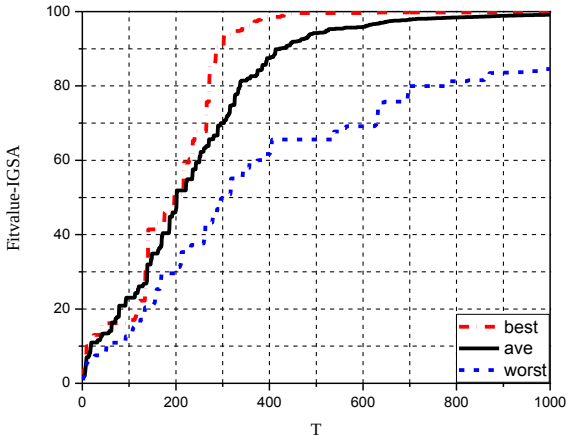

Fig. 3. Comparison of different convergence curves based on IGSA.

C. The pattern synthesis for low side lobe with notches

In this section, the optimizing objective is that the side lobe level is required not exceeding -29dB and between 50°and 60°, a notch with -70dB is required to be created. In equation (1), $F_e(\theta)=1$. In equation (3), $L_{ESL}=-29dB$, $L_{ENL}=-70dB$, $\alpha=0.65$, $\beta=0.35$. The parameters are same as that in Section B. The optimal results averaged over 30 runs are shown in Figs. 5-8 and Table 3.

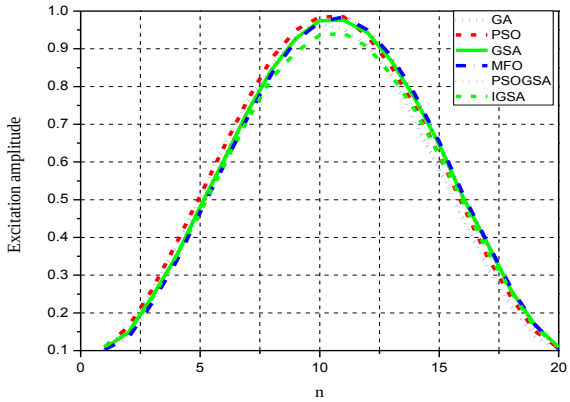

Fig. 4. The optimized current excitation amplitude for the pattern synthesis of ultra low side lobe.

Table 3: Results comparison of low side lobe and notches for the six algorithms

Results of Low Sidelobe and Notches			
Algorithms	Peak Side Lobe Level (dB)	Peak Level of Notch (dB)	Width of Main Lobe (°)
GA	-27.7897	-65.2736	1.4
PSO	-28.4271	-67.4101	1.6
GSA	-29.0359	-70.3720	1.4
PSOGSA	-29.1577	-70.3410	1.2
MFO	-29.6085	-71.0416	1.4
IGSA	-29.6170	-71.3873	1.2

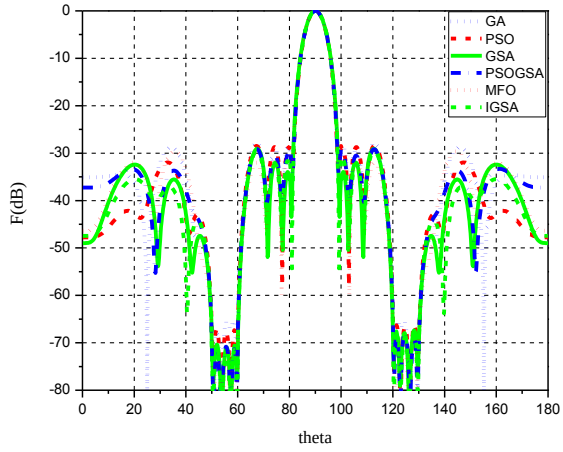

Fig. 5. Patterns of low side lobe with notches based on six algorithms.

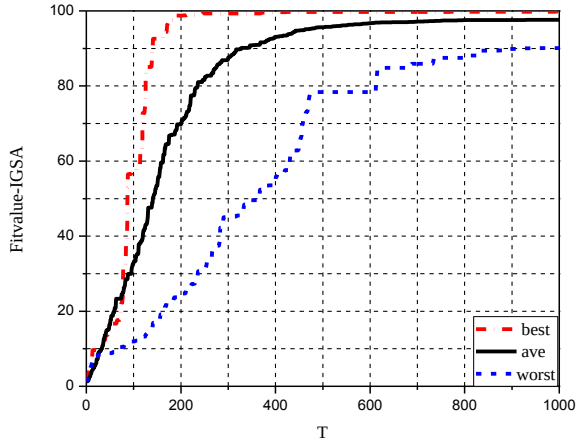

Fig. 6. Comparison of different convergence curves based on the IGSA algorithm.

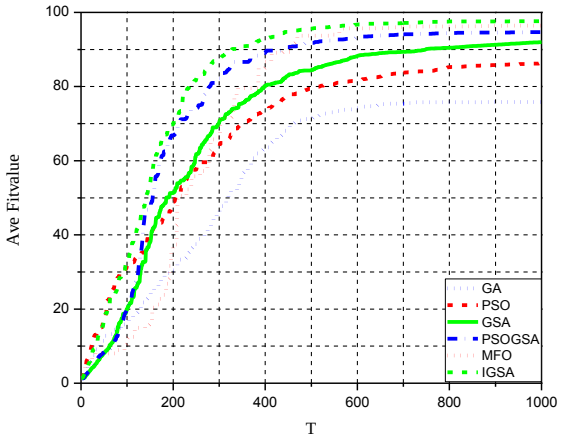

Fig. 7. Average convergence based on six algorithms for the pattern synthesis of low side lobe with notches.

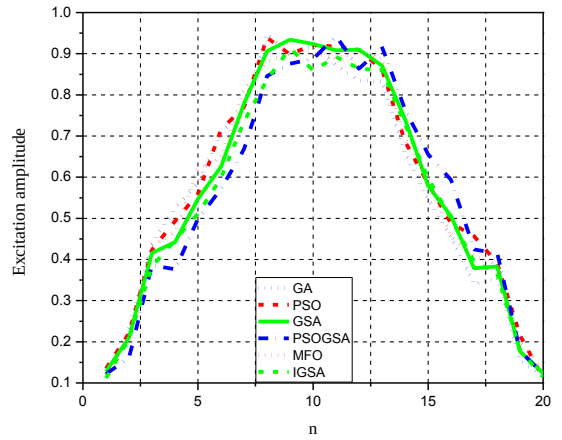

Fig. 8. The optimized current excitation amplitude for the pattern synthesis of low side-lobe with notches.

The patterns obtained by these six algorithms after 1000 iterations are shown in Fig. 5. The best convergence profile, worst convergence profile, average profile for IGSA over 30 runs are depicted in Fig. 6. It can be seen that the peak side lobe level and notches value obtained by IGSA is lower than the result obtained by GSA and other algorithms. Figure 7 shows the average evolution curves after 30 runs. It can be seen that IGSA outperforms other algorithms in evolutionary speed and accuracy. It is worth noting that the problem of trapping in local optimum of GSA is improved efficiently by using IGSA. The further comparison of IGSA with GSA and other four algorithms are shown in Table 3.

The notch depth of PSOGSA is relatively poor than that of GSA and MFO, but the peak side lobe level is better than GSA. It is worth noting that MFO performs better than GSA and PSOGSA, when dealing with the peak side lobe level, MFO is even comparable to that of IGSA. When the width of main lobe is narrower than other algorithms, the IGSA also performs better in peak side lobe and notch value. It can conclude that IGSA outperforms other algorithms. Figure 8 is the optimized current value. The optimization results meet the current amplitude requirements in the constraint conditions.

V. CONCLUSION

In terms of the drawbacks of the basic GSA that is slow in convergence and fall easily into local optimal when synthesizing patterns to the array with low side lobe and notch, IGSA is proposed in this paper. This algorithm can realize the balance between the overall convergence and the local convergence to improve convergence speed through introducing new inertia mass adjustable factor q. This algorithm can also be enhanced to foster local search through interpolating the SQA. In IGSA, the SQA is used as an algorithm with high power in local searching, and the GSA is used to commit search overall. The simulation results in the final show that the proposed IGSA, compared with the same kind of algorithm under the same situation, can be endorsed with faster convergence speed, while keeping the smaller width of the main lobe and the lower level of side lobe. As a conclusion, the proposed algorithm is really more suitable for the pattern synthesis of the complicated array antenna, IGSA can balance between the exploration and the exploitation to reach the optimum quickly and accurately.

REFERENCES

[1] F Günes, S. Demirel, and P. Mahouti, "A simple and efficient honey bee mating optimization approach to performance characterization of a microwave transistor for the maximum power delivery and required noise," *International Journal of Numerical Modelling-Electronic Networks Devices and Fields: Electronic Networks, Devices and Fields*, vol. 1, pp. 4-20, 2015.

[2] S. Shadravan, H. R. Naji, and V. K. Bardsiri, "The sailfish optimizer: A novel nature-inspired metaheuristic algorithm for solving constrained engineering optimization problems," *Engineering Applications of Artificial Intelligence*, vol. 80, pp. 20-34, 2019.

[3] F. Güne, M. A. Belen, and P. Mahouti. "Competitive evolutionary algorithms for building performance database of a microwave transistor," *International Journal of Circuit Theory and Applications*, vol. 4, pp. 1-15, 2017.

[4] A. Das, D. Mandal, S. P. Ghoshal, and R. Kar, "Moth flame optimization based design of linear and circular antenna array for side lobe reduction," *Int. J. Numer. Model*., 32:e2486, 2019.

[5] O.-B. Pinar, "GA optimization of the optical directional coupler," *ACES Journal*, vol. 32, pp. 1136-1139, 2017.

[6] G. Oliveri and A. Massa, "Genetic algorithm

(GA)-enhanced almost difference set (ADS)-based approach for array thinning," *IET Microwaves Antennas & Propagation*, vol. 5, no. 3, pp. 305-315, 2011.

[7] W. Wang and Q. Feng, "Application of PSO algorithm in pattern synthesis," *Journal of Xidian University*, vol. 38, no. 3, pp. 175-180, 2011.

[8] O. Kilic and Q. M. Nguyen. "Enhanced artificial immune system algorithm and its comparison to bio-inspired optimization techniques for electromagnetics applications," *ACES Journal*, vol. 33, no. 2, pp. 132-135, 2018.

[9] R. Esmat, N. Hossein, and S. Saeid, "GSA: A gravitational search algorithm," *Information Sciences*, vol. 179, no. 13, pp. 2232-2248, 2009.

[10] A. Z. Zhang, G. Y. Sun, J. C. Ren, X. D. Li, Z. J. Wang, and X. P. Jia, "A dynamic neighborhood learning based gravitational search algorithm," *IEEE Trans. on Cyb.*, vol. 48, no. 1, pp. 436-447, 2018.

[11] S. Mirjalili and S. Z. M. Hashim, "A new hybrid PSOGSA algorithm for function optimization," *International Conference on Computer and Information Application*, pp. 374-377, 2010.

[12] H. Li, Y. C. Jiao, and L. Zhang, "Hybrid differential evolution with a simplified quadratic approximation for constrained optimization problems," *Engineering Optimization*, vol. 43, no. 2, pp. 115-134, 2011.

Cuizhen Sun was born in 1981. She is a Ph.D. candidate in the Northwestern Polytechnical University. She is also a Teacher in Xi'an University of Science and Technology. Her current research interests are antenna arrays and optimization algorithms in antenna design.

CPW-fed UWB Antenna with Tri-band Frequency Notch Functionality

S. Irum Jafri [1], Rashid Saleem [2], and Khawar Khokhar [1]

[1] Electrical Engineering Department, School of Engineering
University of Management and Technology, UMT, Lahore, 54000, Pakistan
irum.jafri@umt.edu.pk, een.cod@umt.edu.pk

[2] Telecommunication Engineering Department
University of Engineering and Technology, UET, Taxila, 47050, Pakistan
rashid.saleem@uettaxila.edu.pk

Abstract ─ In this paper, a UWB antenna exhibiting frequency suppression characteristics for WiMAX and WLAN spectra is modeled and analyzed. The proposed geometry is composed of a circular radiating element. Impedance matching at higher frequencies is achieved by incorporating steps near the feedline. Introduction of arc-shaped slots in the radiator results in significant band rejection for 3.3-3.7 GHz, 5.15-5.25 GHz and 5.725-5.825 GHz. Designed antenna has an impedance bandwidth (VSWR < 2) of 9 GHz ranging 3-12 GHz. A prototype of the proposed model is fabricated on a low loss substrate. Comparative study of measured results to the simulated results depicts that the performance parameters of the antenna, e.g., impedance bandwidth, S-parameters and radiation characteristics meet the criteria for wideband applications.

Index Terms ─ Circular patch antenna, impedance bandwidth, multiband antenna, tri-band notch, UWB antenna.

I. INTRODUCTION

The advancements in the wireless technology focus primarily on high data rate transmission with minimum interference to the existing wireless standards. In 2002, ultra wide band (UWB) spectrum from 3.1-10.6 GHz is allocated for commercial use, resulting in extensive research in UWB system designing [1]. It is observed that when multiple wireless devices are operated in a close proximity, the UWB systems experience interference as the designated spectrum is simultaneously shared by various wireless standards like WiMAX and WLAN [2]. Therefore, to improve the performance, interference mitigation has become the prime task while designing UWB antennas.

The deployment of conventional RF filters in UWB systems is not feasible as this technique results in the increased size of the circuitry and complexity. Therefore, multiple band notch characteristics can be incorporated in antennas to eliminate narrowband interferences [3].

Various band stop techniques have been proposed to combat interference challenge, e.g., etching slots in the ground plane, feedline, or in the radiating element [4-6]. Parasitic elements, defected ground structures (DGS) and use of fractal geometry is also observed to obtain band notch characteristics [7-9]. The most common technique is to etch slots in the radiating element, which affects the current distribution of the radiating patch resulting in the elimination of undesired frequency ranges overlapping the operational frequency of antenna [1]. The commonly experimented slot shapes are C shape, U and inverted U, L shaped and meander line [1, 3]. Different approaches to introduce tri-band notch characteristics are presented in [10-12]. The reported UWB antennas deploy double layered metallization. However, it is indicated in [13] that single layered metallization can further reduce the fabrication cost of monopole antennas; therefore, the presented UWB antenna is based on this concept.

This manuscript introduces a planar UWB antenna with frequency rejection functionality to minimize the interference. The proposed design displays efficient elimination of WiMAX and WLAN bands. The paper is arranged as follows, Section-II comprises of the antenna modeling and optimization process, followed by the performance analysis of proposed design in Section-III. The fabricated prototype and comparison of results is presented in Section-IV. The conclusion drawn by the presented work is given in Section-V.

II. GEOMETRY OF PROPOSED DESIGN

A modified monopole antenna, printed on Roger RT Duroid 5880 of permittivity ε_r=2.2, is proposed for band notch design. Commercially available electromagnetic simulator Ansys HFSS is used to model and investigate the simulated results of proposed antenna.

Submitted On: November 6, 2018
Accepted On: May 12, 2019

The presented UWB antenna is compact in nature, with a size of 30 mm × 32.5 mm. The radiating structure is a circular antenna of radius **R**=9.2 mm, fed by a coplanar waveguide (CPW) transmission line of impedance 50Ω with dimensions $\mathbf{L_F}$=13 mm × $\mathbf{W_F}$=3 mm. Square shaped ground plane of dimensions $\mathbf{L_G}$=12.6 mm × $\mathbf{W_G}$=13 mm is placed on both sides of feedline, separated by a distance of 0.35mm on each side.

The criterion of VSWR less than 2 was limited to the spectrum 3-8 GHz as shown in Fig. 1. It is reported that the steps near the antenna's feedline contributes towards the reduction of impedance mismatch between the feedline and antenna [14, 15]. Therefore, three symmetrical steps were integrated within the radiating structure to enhance the bandwidth of designed antenna. It is evident from Fig. 1 that the addition of each step enhances the impedance bandwidth of the antenna.

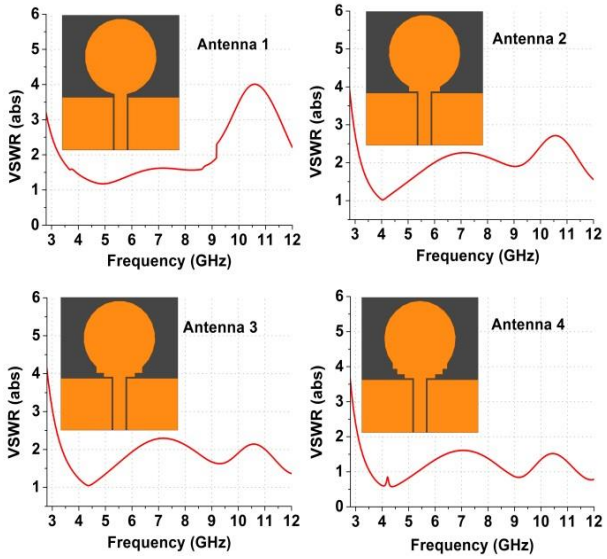

Fig. 1. Step by step optimization of simulated UWB antenna.

In Fig. 1 the simulated model Antenna 4, having three steps fused with the circular patch exhibits a VSWR < 2 for 3-12 GHz, making it operational for the ultrawide spectrum. The design is further optimized to remove electromagnetic interference caused by WLAN or WiMAX devices present in the same vicinity. For this purpose, three arcs are embedded in the radiating element to stop the reception of WiMAX and WLAN bands as shown in Fig. 2. The effective length ***Ls*** for each arc is computed using formulas [16]:

$$f_{notch} = \frac{c}{2L_s\sqrt{\epsilon_{eff}}}, \quad (1)$$

$$\epsilon_{eff} = \frac{\epsilon_r + 1}{2}. \quad (2)$$

where, $\boldsymbol{c}$ is representing the speed of light, $\boldsymbol{f_{notch}}$ corresponds to the central frequency of the desired spectrum to be eliminated, and ϵ_{eff} is the permittivity of the dielectric substrate, which is dependent on the dielectric contact ϵ_r of the substrate. The calculated lengths of etched slots along with the placement position of these structures, determine the frequencies to be filtered out.

Fig. 2. Placement of resonators, S_1, S_2 and S_3 in the simulated model.

The resonating structure **'S_1'** embedded near the edge of the antenna contributes towards the suppression of WiMAX band ranging from 3.3-3.7 GHz. The slot **'S_2'** placed in the mid-section, governs the rejection of lower WLAN band from 5.15-5.25 GHz. Slot **'S_3'** present near the feedline of antenna stops the WLAN band ranging from 5.725-5.825 GHz. These slots are embedded in the radiator separately and then optimized to achieve resonance at the require frequency. The resonance produced by the slot **'S_1'** is centered at the frequency $\mathbf{fc_1}$=3.55 GHz. Similarly **'S_2'** and **'S_3'** resonate at $\mathbf{fc_2}$ and $\mathbf{fc_3}$ respectively as shown in Fig. 3.

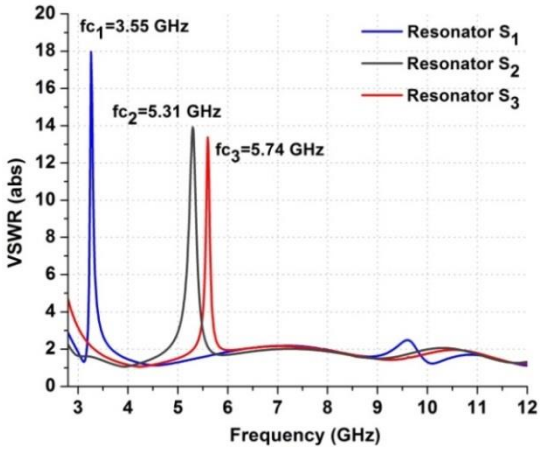

Fig. 3. Frequency response of the slots S_1, S_2 and S_3.

The three band notch structures are simultaneously deployed to suppress WiMaX and two WLAN bands. These slots are optimized to function for minimizing interference between UWB and narrowband systems. The placement distance of these slots is adjusted from the edges of antenna and the feedline [3]. The position of slots, separation between them and the arc width of each structure collectively controls the overall current

distribution of the radiating element. By carefully optimizing these parameters very narrowband frequency rejections are achieved. The simulated band-notch antenna model is presented in Fig. 4. The optimized dimensions are given in Table 1.

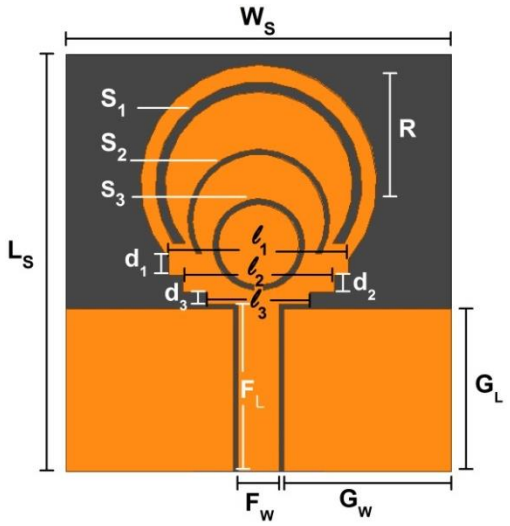

Fig. 4. Simulated UWB antenna model.

Table 1: Complete dimensions of band-notch design

Symbol	Dimension in mm	Symbol	Dimension in mm
L_S	32.5	l_1	14
W_S	30	l_2	11.8
G_L	12.6	l_3	8
G_W	13	d_1	1.28
F_L	13	d_2	1.25
F_W	3	d_3	1
S_1 Length	34.85	S_1 Width	0.93
S_2 Length	22.8	S_2 Width	0.45
S_3 Length	21.6	S_3 Width	0.4

III. PERFORMANCE EVALUATION OF THE PRESENTED DESIGN

The performance of the presented antenna is analysed on the basis of VSWR and return loss, surface current distribution and radiation characteristics.

A. VSWR and S-parameter

Figure 5 (a) shows the VSWR graph of the simulated antenna. The proposed geometry exhibits a VSWR below the value 2, except for the WiMAX and WLAN bands, where narrowband high magnitude notches are observed, as observed in Fig. 5 (a).

Similarly the return loss graph, S_{11} corresponding to the VSWR is presented in Fig. 5 (b). It is noticed that S_{11} remains below the value of -10 dB in the entire band except the band rejection frequency where it obtains a value higher than -5 dB.

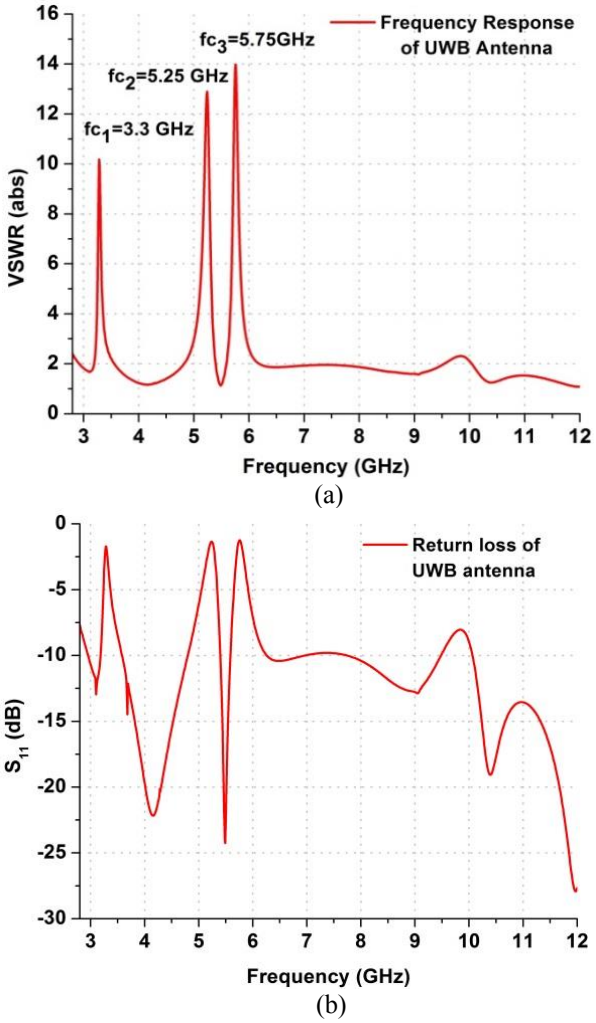

Fig. 5. Simulated results: (a) VSWR and (b) return loss.

B. Current distribution

The arc shaped slots are critically adjusted to obtain sharp rejection at the tuning frequencies. The surface current distribution plotted at the central frequency fc_1= 3.55 GHz (WiMAX), fc_2=5.25 GHz (lower WLAN) and fc_3=5.775 GHz (upper WLAN) is shown in Figs. 6 (a), (b), and (c).

It can be seen that the integration of etched slots induce band notch characteristics in the UWB antenna. The current is accumulated around the etched structure which prevents the antenna from radiating at these particular frequencies, resulting in effective band rejection. In Fig. 6 (a), the maximum current is distributed along the slot S1, which brings about the suppression of WiMAX frequencies. Similarly for the frequencies fc_2 and fc_3 the current distribution along S2 and S3 is responsible for the rejection WLAN bands.

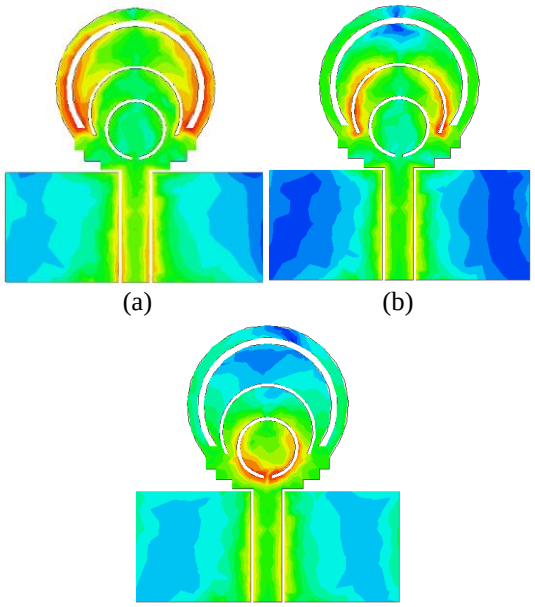

Fig. 6. Current distribution (J-surf) at frequencies (GHz): (a) 3.55, (b) 5.25, and (c) 5.77.

C. Radiation characteristics and gain

The gain of the antenna with reference to the operational frequency is presented in Fig. 7. The radiation patterns of the presented UWB antenna design are plotted in Figs. 8 (a) and (b). Due to the band notch properties, some degree of distortion is observed in the E-plane and H-plane radiation characteristics of the band-notch antenna.

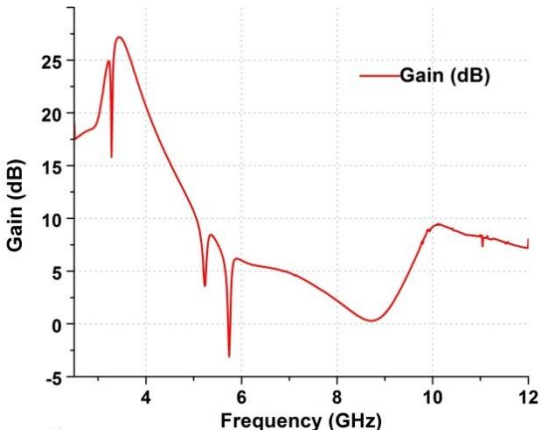

Fig. 7. Antenna gain corresponding to frequency.

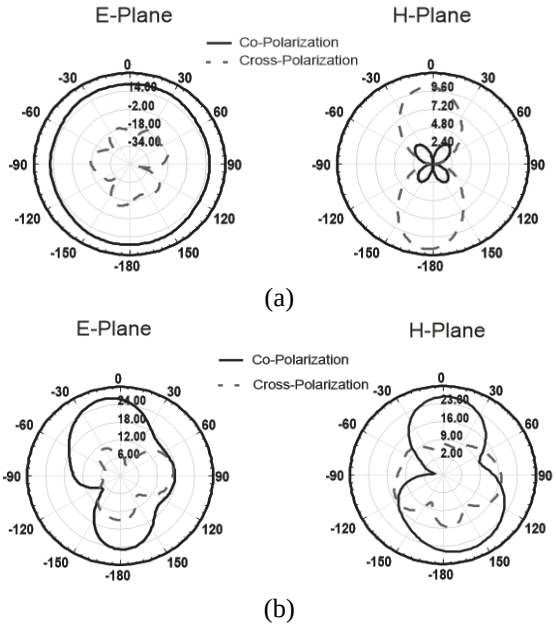

Fig. 8. E and H-field distribution: (a) 4 GHz and (b) 7 GHz.

IV. COMPARATIVE STUDY OF SIMULATED VS MEASURED PARAMETERS

A prototype of the simulated model is realized on low loss substrate Roger RT Duroid 5880 using the optimized dimensions. Single layer of substrate and one-sided metallization is deployed in the fabrication as the radiating element and ground plane is placed on the same plane. This further reduces the fabrication cost of the proposed antenna [13].

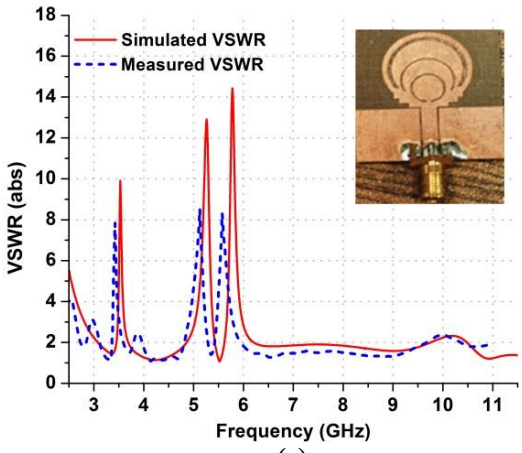

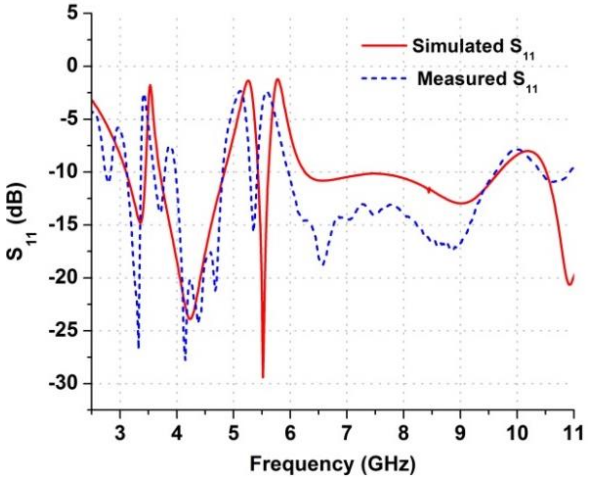

(b)

Fig. 9. Measured vs. simulated plots: (a) VSWR and (b) S_{11}.

It is evident from Figs. 9 (a) and (b) that the measured VSWR and return loss follows the same trend as observed in the simulated results. Minor deviation in central frequency of each notch is observed due to the manufacturing and calibration limitations.

V. CONCLUSION

A multiband notch antenna is modeled, realized and tested for its band rejection characteristics. The presented configuration exhibits well matched impedance characteristics, stable radiation pattern and sharp rejection capabilities in the required frequency spectrum. Investigation of the results shows that the proposed design is a feasible solution to eliminate electromagnetic interference for UWB applications.

ACKNOWLEDGMENT

The authors acknowledge the financial support of National ICT R&D fund.

REFERENCES

[1] K. Sultan, O. Dardeer, and H. Mohamed, "Design of compact dual notched self-complementary UWB antenna," *Open Journal of Antennas and Propagation*, vol. 5, pp. 99-109, 2017.

[2] J. Y. Zhang, F. Zhang, W. P. Tian, and Y. L. Luo, "ACS-fed UWB-MIMO antenna with shared radiator," *Electronics Letters*, vol. 51, no. 17, pp. 1301-1302, Aug. 2015.

[3] G. Srivastava, S. Dwari, B. K. Kanaujia, "A compact triple band notch circular ring antenna for UWB applications," *Microwave and Optical Technology Letters*, vol. 57, no. 3, pp. 668-72, Mar. 2015.

[4] W. Ali, A. A. Ibrahim, and J. Machac, "Compact size UWB monopole antenna with triple band notches," *Radioengineering*, vol. 26, no. 2, pp. 57-63, 2017.

[5] S. Naser and N. Dib, "Printed UWB pacman shaped antenna with two frequency rejection bands," *Applied Computational Electromagnetics Society Journal*, vol. 32, no. 3, pp. 186-192, 2017.

[6] H. Liu, Z. Xu, B. Wu, and J. Liao, "Compact UWB antenna with dual band-notches for WLAN and WiMAX applications," *IEICE Electronics Express*, vol. 10, no. 17, pp. 1-6, 2013.

[7] A. Boutejdar, A. A. Ibrahim, and E. Burte, "A compact multiple band-notched planer antenna with enhanced bandwidth using parasitic strip lumped capacitors and DGS-technique," *TELKOMNIKA Indonesian Journal of Electrical Engineering*, vol. 13, no. 2, pp. 203-208, 2015.

[8] T. Shabbir, R. Saleem, A. Akram, and M. F. Shafique, "UWB-MIMO quadruple with FSS-inspired decoupling structures and defected grounds,"*Applied Computational Electromagnetics Society Journal*, vol. 30, pp. 184-190, Feb. 2015.

[9] M. Sahoo and S. Sahu, "Design & amp, development of UWB notch antenna with fractal geometry," *2015 International Conference on Circuits, Power and Computing Technologies [ICCPCT-2015]*, Nagercoil, 2015.

[10] P. S. Bakariya, S. Dwari, and M. Sarkar, "Triple band notch UWB printed monopole antenna with enhanced bandwidth," *AEU - International Journal of Electronics and Communications*, pp. 26-30, 2015.

[11] S. K. Venkata, M. Rana, P. S. Bakariya, S. Dwari, and M. Sarkar, "Planar ultrawideband monopole antenna with tri-notch band characteristics," *Progress In Electromagnetics Research C*, vol. 46, pp. 163-170, 2014.

[12] Q. Wang and Y. Zhang, "Design of a compact UWB antenna with triple band-notched characteristics," *International Journal of Antennas and Propagations*, 2014.

[13] Y. Yang, Q. Chu, and J. Li, "Dual band-notched ultrawideband MIMO antenna array," *2013 IEEE International Wireless Symposium (IWS)*, Beijing, 2013.

[14] Z. Ahmed, G. Perwasha, S. Shahid, H. Zahra, I. Saleem, and S. M. Abbas, "Ultra wideband antenna with WLAN band-notch characteristic," *2013 3rd IEEE International Conference on Computer, Control and Communication (IC4)*, Karachi, 2013.

[15] W. Ali and A. A. Ibrahim, "Tunable band-notched UWB antenna from WLAN to WiMAX with open loop resonators using lumped capacitors," *Applied Computational Electromagnetics Society Journal*, 2018.

[16] Y. Jin and J. Choi, UWB antenna with quintuple

notch bands," *IEEE International Symposium on Antennas and Propagation & USNC/URSI National Radio Science Meeting*, Vancouver, BC, pp. 1950-1951, 2015.

Syeda Irum Jafri has completed her M.Sc. in Telecommunication Engineering from University of Engineering and Technology, UET, Taxila in 2014. She is a faculty member at the Electrical Engineering Department, University of Management and Technology, UMT Lahore. Her research interests include antenna design, MIMO antenna systems and chipless RFID technology.

Rashid Saleem received B.S. Electronic Engineering from Ghulam Ishaq Khan Institute of Engineering Sciences and Technology, Pakistan, in 1999. He pursued a career in the telecommunication industry for several years while continuing education. He received M.S. from UET Taxila through Center for Advanced Studies in Engineering, Pakistan, in 2006 and Ph.D. from The University of Manchester, United Kingdom in 2011. He worked on antennas, channel modeling and interference aspects of Ultra Wideband systems during his Ph.D. and was also member of a team designing and testing arrays for the Square Kilometer Array project. Currently, he is working as Assistant Professor at University of Engineering and Technology (UET), Taxila, Pakistan where he is supervising several postgraduate students and heading the MAP (Microwaves, Antennas and Propagation) research group. His research interests include antennas, mm-wave communication, microwave periodic structures and metamaterials.

Khawar Siddique Khokhar obtained his Ph.D. degree from Durham University in 2006 in Mobile Communications. He has served as a member technical in Pakistan Telecommunication Authority (PTA, Pakistan). Currently he is serving as a Chairman of the Electrical Engineering Department in University of Management & Technology Lahore. Area of his reach includes Wireless Communication and Performance Evaluation of Mobile Communication.

Ultra-wideband Planar Log-periodic Slot Antenna with Exponential Shapes on Slot Edges

Wei-Chung Weng and Min-Chi Chang

Department of Electrical Engineering, National Chi Nan University, 301, University Rd., Puli, Nantou 54561, Taiwan
wcweng@ncnu.edu.tw, s100323910@mail1.ncnu.edu.tw

Abstract ─ An improved method of using exponential curve shape on edges of log-periodic slots to decrease resonances and further reduce the antenna size is proposed. The proposed method is adopted to design a planar log-periodic slot antenna for ultra-wideband (UWB) applications. Numerical investigation shows that resonant frequencies can be decreased around 12.3% in low frequencies compared with the conventional planar log-periodic slot antenna with regular shape on edges of slots. Measured and simulated reflection coefficients and radiation patterns of the proposed antenna agree well with each other to demonstrate the validity. The measured |S11| shows that the operating frequency range (|S11| below -10 dB) is from 2.9 GHz to 11.36 GHz, covering the UWB spectrum (3.1 – 10.6 GHz). The proposed antenna has good radiation characteristics and antenna gains. The proposed antenna is a good candidate for the UWB applications.

Index Terms ─ Broadband antennas, log-periodic antennas, slot antennas, ultra-wideband antennas.

I. INTRODUCTION

Log-periodic structures have near frequency independent properties and are widely applied for wideband antennas. Metal poles or metal hollow cylinders are mainly used as radiators to design conventional log-periodic antennas [1]–[4] for television receiving/ broadcasting and wireless communication in VHF band. Antennas with log-periodic structures are usually designed by formulas to determine the dimensions of radiators [5], [6]. In addition, log-periodic structures can be also designed using Koch fractals [7] or using optimization techniques [8], [9]. These conventional log-periodic antennas are huge and heavy. To overcome the disadvantages, planar log-periodic structures [10]–[16] were applied for wideband antennas. Planar structures have advantages of low cost, low weight, portability, and easy fabrication.

The shape of radiators on conventional UWB antennas is usually regular or uniform. However, irregular shapes and curve shapes are less applied to radiators [9], [17] since they are difficult to design. Irregular shapes provide more flexibility to design the antenna with wideband specifications. In this study, the improved method of using exponential curve shape on edges of log-periodic slots was adopted to design the proposed planar UWB antenna. Numerical investigation in this study demonstrates that resonant frequencies of the proposed antenna with unique exponential shapes on top or bottom edge of slots can be further decreased as compared with those of the conventional planar log-periodic slot antenna [15] when its shapes of slot edges are trapezoidal. This merit of using the proposed exponential shapes on log-periodic slot edges provides a novel design method for designing compact antennas. Comprehensive analyses as well as the mechanism and design procedure of the proposed antenna are given and discussed. Results of the proposed UWB log-periodic slot antenna show that the proposed antenna has good characteristics of impedance bandwidth, radiation pattern, and gain in the UWB band.

II. ANTENNA DESIGN

The proposed antenna's log-periodic slot structure and antenna design procedures are described in this section. Figure 1 (a) shows the geometry of the planar proposed log-periodic slot UWB antenna. The proposed antenna was fabricated on a cheap FR4 substrate with the thickness of 0.8 mm, dielectric constant of 4.4, and loss tangent of 0.02. The enlargement near the center or the apex of the antenna geometry is shown in Fig. 1 (b). The slot structure's center is located at the origin of the coordinates. The log-periodic slot structure is symmetric to the origin of the coordinates. Namely, the portion of the slot structure in the negative x region mirrors and reverses that in the positive x region.

The proposed slot antenna is fed by a four-segment CPW line, which serves as a wideband impedance transformer to transfer from the antenna input impedance around 105 ohms to the input port characteristic impedance 50 ohms. Each segment of the CPW fed-line has the same gap of g whereas its width and length are different from others. By adjusting the strips' widths

Submitted On: February 21, 2019
Accepted On: July 16, 2019

(W1-W4) and lengths (L1-L4), the wideband impedance match (|S11| < -20 dB, 3 GHz < f < 11 GHz) of the four-segment CPW fed-line can be achieved. The CPW fed-line is terminated at the antenna's center. The small spacing between the slot terminals is W4. No balun is used to feed the proposed antenna. Detailed dimensions of the slot antenna are listed in Table 1. All metal patches are printed on the top surface of the substrate. The photo of the antenna prototype is shown in Fig. 1 (c).

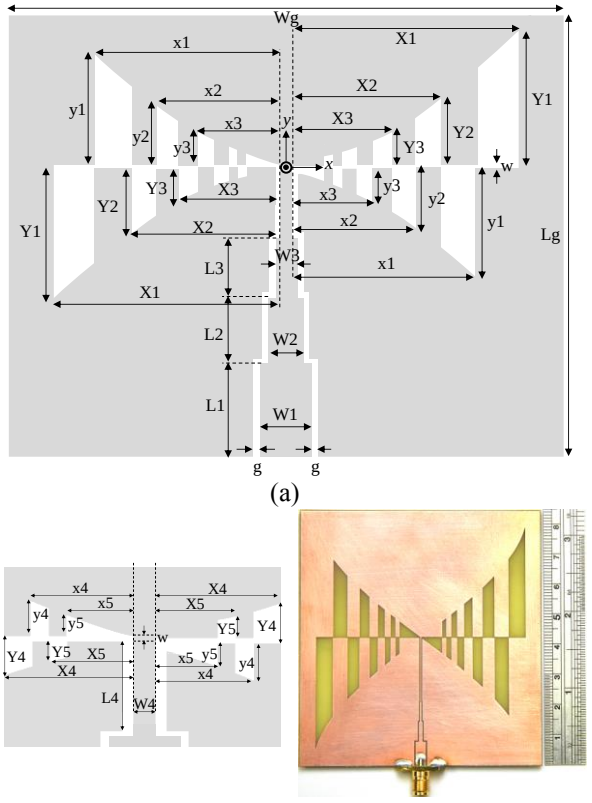

Fig. 1. The proposed log-periodic UWB slot antenna geometry and its prototype picture. (a) Geometry of antenna structure, (b) the enlargement around the center of the antenna, and (c) a photo of the antenna prototype.

The lowest frequency f_{min} in the working band is determined by the maximum physical dimension of the antenna [15]. The sum of X1 and Y1 is about half guided wavelength, $\lambda_{g,\,min}$ when frequency is at f_{min}. That is,

$$\lambda_{g,\,min} \cong 2(X1+Y1). \tag{1}$$

The dimensions of each slot can be determined using (2) and (3) [5], [6]:

$$\frac{Xn+1}{Xn} = \frac{Yn+1}{Yn} = \frac{xn+1}{xn} = \frac{yn+1}{yn} = \tau\ , \tag{2}$$

$$\frac{xn}{Xn} = \frac{yn}{Yn} = \sqrt{\tau}\ ,\ \ (n = 1-N), \tag{3}$$

where n is the n-th slot on a quarter portion of the antenna and τ is the geometric ratio of the slot and its adjacent slot; τ is a value between 0 and 1. The total number of slots used in the antenna is 4N. Each slot will excite its resonant frequencies. The more slots are, the more resonances. Therefore, wideband characteristics of the proposed slot antenna can be achieved by multi-resonances. If wideband characteristics of the antenna are desired, the N can be set to be larger. However, the drawbacks about large N are that the antenna configuration becomes complicated and a large size of the antenna is required. A compromise will be made for the advantages and disadvantages. τ can determine the distribution of resonant frequencies in the working band. Figure 2 shows different values of τ affecting the geometries and dimensions of slots when Y1 and X1 are fixed and N is 5. As the τ increases, the width of slots decreases and location of slots shifts towards to the outermost slot resulting in small spacing between slots; meanwhile, the slot located closest to the apex becomes larger. Hence, resonant frequencies are more concentrated each other. Nevertheless, if τ is a small value, the slot located closest to the apex becomes too small to implement. Therefore, τ is suggested to set to be the value between 0.6 and 0.9. In the proposed antenna design, τ is set to be 0.7; the X1 and Y1 are set to be 34 mm and 37 mm, respectively. Other parameters such as X2 to X5, Y2 to Y5, x1 to x5, and y1to y5 can be obtained using (2) and (3).

Table 1: Dimensions of the proposed log-periodic UWB slot antenna

Parameter	Size (mm)	Parameter	Size (mm)
X1	34.0	Y1	37.0
X2	23.8	Y2	25.9
X3	16.66	Y3	18.13
X4	11.66	Y4	12.69
X5	8.16	Y5	8.88
x1	28.45	y1	30.96
x2	19.91	y2	21.67
x3	13.94	y3	15.17
x4	9.76	y4	10.62
x5	6.83	y5	7.43
W1	3.3	L1	7.8
W2	1.19	L2	6.5
W3	0.4	L3	6.5
W4	0.2	L4	21.2
Wg	78.0	Lg	84.0
g	0.4	w	0.35

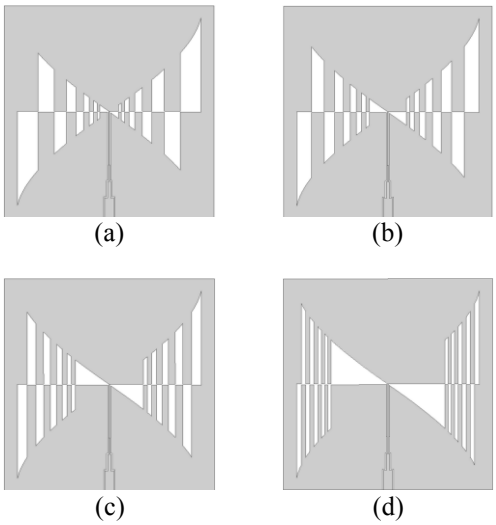

Fig. 2. The geometry variation of the proposed log-periodic slots with different values of τ when Y1 and X1 are fixed and N is 5. (a) $\tau = 0.6$, (b) $\tau = 0.7$, (c) $\tau = 0.8$, and (d) $\tau = 0.9$.

In this study, the edges of log-periodic slots are cut by exponential curves created by using (4) to further decrease resonant frequencies:

$$y = \frac{x}{\mathrm{X1}}\left(\frac{\mathrm{Y1}}{e^{p\,\mathrm{X1}}}\right)e^{px}\ , \quad x, y \geq 0\,. \tag{4}$$

Figure 3 shows the different exponential curves representing different curvatures by p. The curvature of exponential curve changes more when p is larger. A conventional planar log-periodic slot antenna configuration as shown in [15] is the trapezoidal slot teeth log-periodic structures when the edges of slots are linear; that is, when $p = 0$. In this design, p is set to be 0.025 and N is set to be 5.

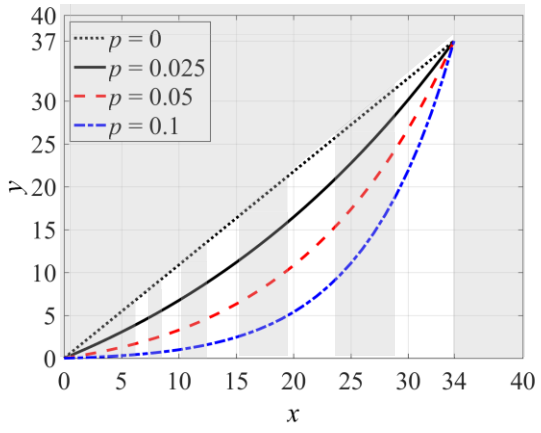

Fig. 3. Slot edges in the positive x and positive y region cut by different exponential curves representing different curvatures by p.

Parametric studies were performed to investigate effects of key parameters on reflection coefficients |S11|. Figure 4 to Fig. 6 reveal the parametric studies of Y1, X1, and w versus the |S11|, where Y1, X1, and w are varied respectively whereas the other parameters are fixed the same values as listed in Table 1. As shown in Fig. 4, a larger value of Y1 will result in lower resonant frequencies as indicated in the dotted blue arrow since it will increase the electrical length. However, a larger value of Y1 will result in larger antenna size. Increasing X1 will result in small effects in resonant frequencies as shown in Fig. 5. Hence, to obtain the lower $f_{\min}$, Y1 larger than X1 is desirable. Another reason for Y1 is larger than X1 is that more spaces can be available for slots in the y-direction since the CPW fed-line is already placed in the y-direction. To design a compact size of the antenna, the spaces in the y-direction can be effectively utilized. Parametric studies also show that the width of the horizontal narrow slot lines (w) does not significantly affect the |S11| of the proposed slot antenna as shown in Fig. 6. Hence, w is selected to be 0.35 mm in this design for easily feeding the smallest slot near the apex of the antenna. Numerical investigations have also shown that the X1, Y1, τ, and N are key parameters of the proposed log-periodic slot antenna to excite required resonances.

To design the proposed planar log-periodic UWB slot antenna, the design procedure is suggested and listed below.

Step 1: Determine the X1 and Y1 by (1).

Step 2: Choose the number of N and the geometric ratio τ, then determine the dimensions of each slot using (2) and (3).

Step 3: Determine the curvature of exponential curve using (4). Additionally, the value of τ can be slightly changed to adjust the resonant frequencies of each slot.

Step 4: Adjust the lengths and widths of the CPW fed-line for wideband impedance matching.

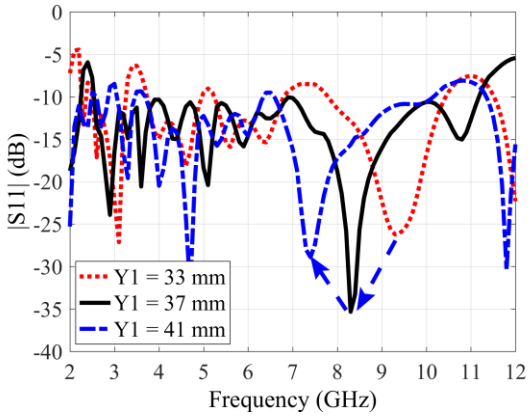

Fig. 4. Simulated |S11| with different dimensions of Y1. Other dimensions shown in Table 1 are fixed.

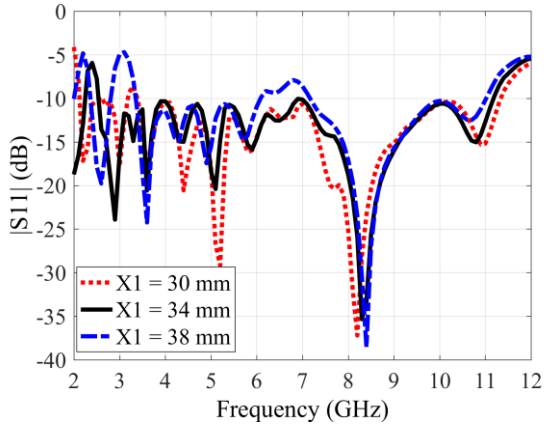

Fig. 5. Simulated |S11| with different dimensions of X1. Other dimensions shown in Table 1 are fixed.

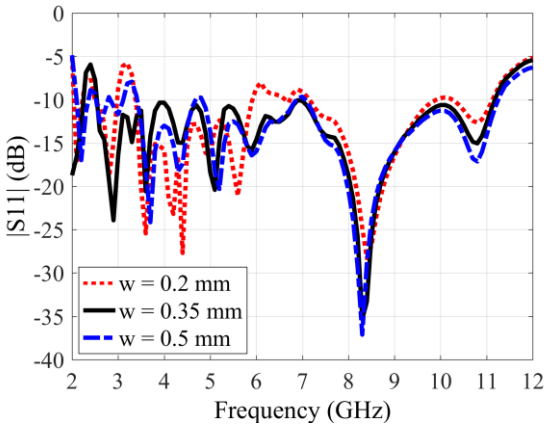

Fig. 6. Simulated |S11| with different dimensions of w. Other dimensions shown in Table 1 are fixed.

III. RESULTS AND DISCUSSIONS

A. Reflection coefficient

Simulated and measured reflection coefficients |S11| of the proposed antenna are obtained by using a full-wave electromagnetic simulator, Ansoft HFSS, and an Agilent N5230A network analyzer, respectively. |S11| results are shown together in Fig. 7 for comparison. Apparently the simulated results reasonably agree well with the measured ones, which validate the antenna design. The measured impedance bandwidth exhibits wideband performance from 2.9 to 11.36 GHz (118.7%) for |S11| < -10 dB, covering the entire UWB frequency band.

B. Log-periodic behavior

Figure 8 reveals the simulated magnitude of antenna input impedance $|Z_{in}|$ of the proposed antenna, where $Z_{in} = R_{in} + jX_{in}$; R_{in} and X_{in} are real part and imaginary part of $|Z_{in}|$, respectively. This plot is made against the logarithm of frequencies. It can be seen that the variation of $|Z_{in}|$ is near periodic in the working band. The three successive maxima of the impedance occur at 5.2 GHz ($f1$), 7.6 GHz ($f2$), and 10.3 GHz ($f3$). The three frequencies $f1$, $f2$ and $f3$ are related by [5]:

$$\frac{f1}{f2} \cong \frac{f2}{f3} \cong \tau \,. \tag{5}$$

The ratio for $f1$ and $f2$ and the ratio for $f2$ and $f3$ determined by (5) are 0.68 and 0.73, respectively, which is about the geometric ratio of τ (= 0.7) set in this study. This result shows that the proposed slot antenna does have near logarithmically periodic impedance properties; hence, the proposed antenna can be named *log-periodic antenna*.

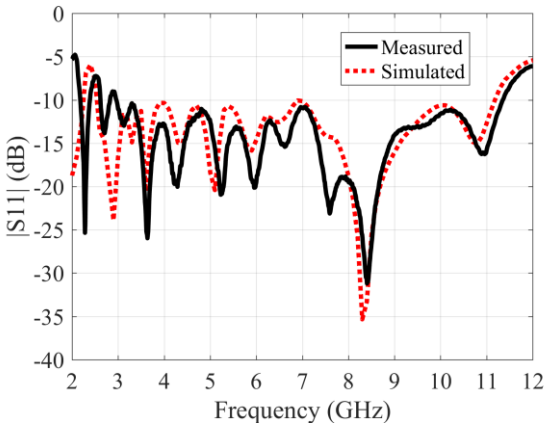

Fig. 7. Reflection coefficients |S11| of the proposed log-periodic UWB slot antenna.

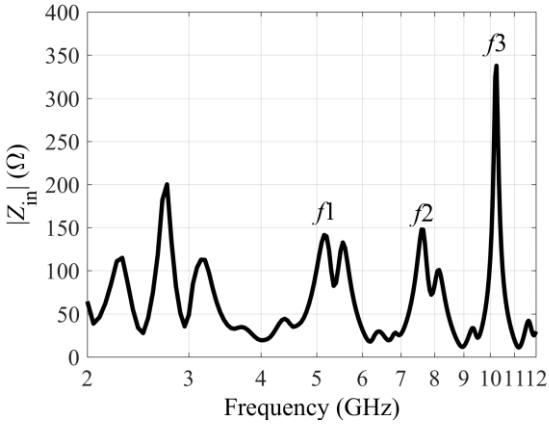

Fig. 8. Simulated magnitude of input impedance $|Z_{in}|$ of the proposed antenna against the logarithm of frequencies.

C. Benefit of exponential shape

Figure 9 shows the curves of simulated imaginary part (X_{in}) of antenna input impedance with cases of p = 0 and p = 0.025. The lowest resonant frequency $f_{r,\min}$

(at $X_{in} = 0$) of slot antenna without exponential curve cut ($p = 0$ case) on edges of slots is at 2.52 GHz, whereas the $f_{r,\min}$ with exponential curve cut on edges of slots ($p = 0.025$ case) decreases to 2.21 GHz. The $f_{r,\min}$ decreases 0.31 GHz (12.3%) as indicated by the dotted blue arrow. This frequency decrement demonstrates the fact that the required antenna size for the proposed antenna with exponential curve cut on edges of slots can be reduced 12.3% if the two antennas have the same $f_{r,\min}$. By the same token, the next resonant frequency also decreases from 2.95 GHz to 2.65 GHz (10.2%) as indicated by the dotted green arrow as also shown in Fig. 9. Hence, the obvious advantage of the exponential curve cut on edges of slots arises from the facts that resonant frequencies can be decreased. Meanwhile, more compact antenna size can be realized compared with the slot antenna with regular shapes on edges.

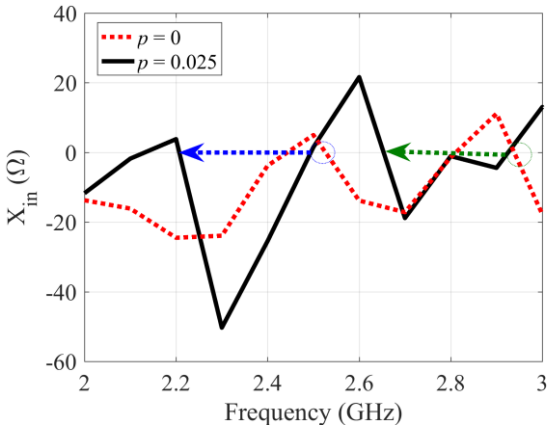

Fig. 9. The curves of simulated imaginary part (X_{in}) of antenna input impedance with cases of $p = 0$ and $p = 0.025$ near the lowest resonant frequency $f_{r,\min}$.

D. Surface current

Figure 10 (a) to Fig. 10 (d) reveal surface currents of the proposed antenna at 3.1, 5.5, 8.3, and 10.6 GHz, respectively. The region with more surface currents encompassing slots can be considered as radiating regions in which slots operate about half wavelength. The strong surface currents encompass the edges of both large and small slots in lower frequencies whereas surface currents encompass the edges of small slots onlyin higher frequencies. This phenomenon shows that large slots operate at both low and high frequencies while small slots operate only at high frequencies. Hence, ultra-wideband characteristics can be achieved by the proposed log-periodic slot structure. Although tiny slots can be used to extend the operating frequency to be higher, the highest frequency f_{max} in the working band is limited by the dimensions of the smallest slot near the apex of the antenna since it is required fine fabrication of the antenna structure. Moreover, a tiny slot is difficult to fit the CPW fed-line at the apex.

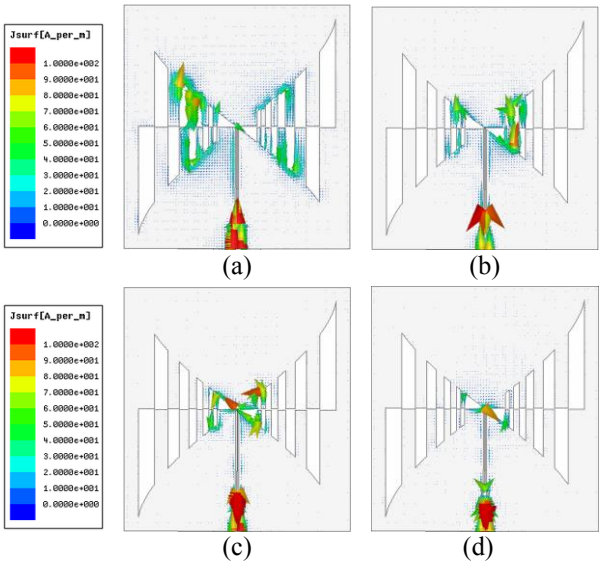

Fig. 10. Simulated surface currents of proposed antenna at: (a) 3.1 GHz, (b) 5.5 GHz, (c) 8.3 GHz, and (d) 10.6 GHz.

E. Radiation pattern

Radiation patterns were measured by using an MVG Satimo antenna measurement system. Figure 11 gives the normalized radiation gain patterns of the proposed log-periodic slot in two principal planes at 3.1, 5.5, 8.3, and 10.6 GHz. Good agreements between simulated and measured patterns are observed as well, which demonstrates the validity of the design. The antenna radiation gain patterns are bidirectional in the broadside direction. In addition, the proposed antenna maintains approximately constant radiation patterns in both principal planes from low to high frequencies, which reveals the characteristics of self-scaling at discrete log-periodically related frequencies [18] by using the proposed log-periodic slot structure. The measured antenna peak gains are 1.43, 4.49, 3.92, and 4.67 dBi at 3.1, 5.5, 8.3, and 10.6 GHz, respectively. The proposed antenna has satisfactory antenna gain and flat antenna efficiency around 78% in the UWB band.

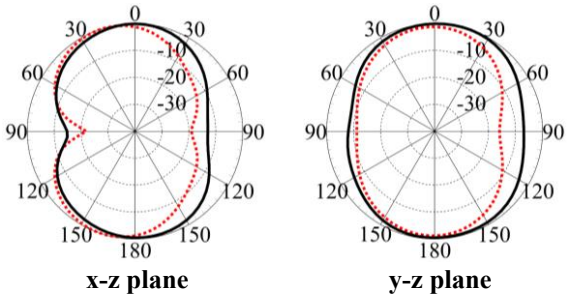

(a)

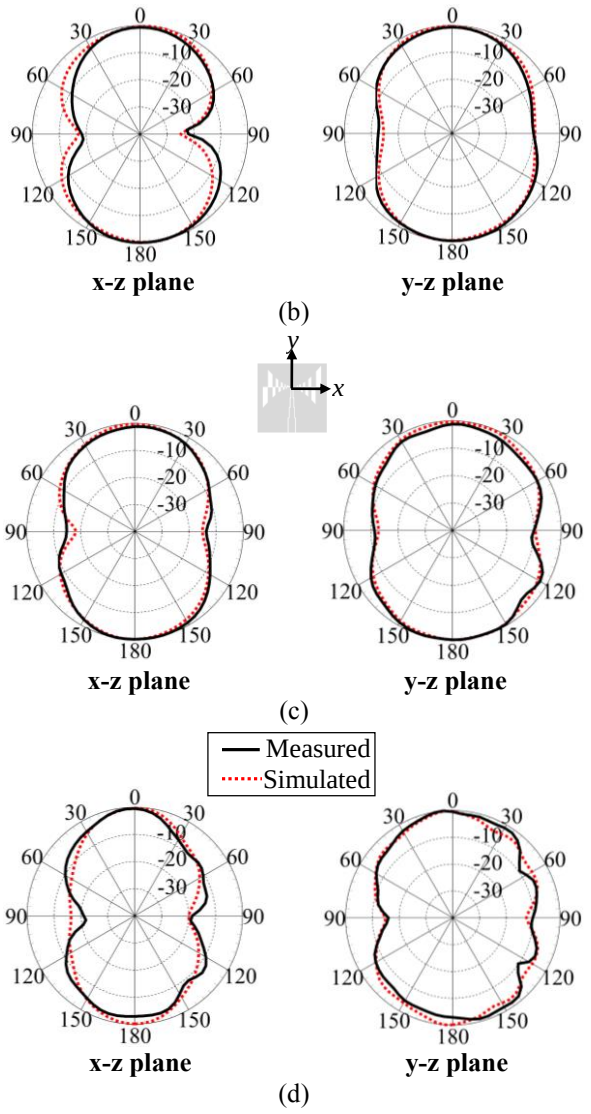

Fig. 11. Normalized radiation gain patterns of the proposed antenna in the x-z plane and y-z plane at: (a) 3.1 GHz, (b) 5.5 GHz, (c) 8.3 GHz, and (d) 10.6 GHz.

VI. CONCLUSION

This study presents a novel UWB log-periodic planar slot antenna design using exponential curves cut on edges of slots. The proposed antenna has a compact substrate size of 78 mm by 84 mm. Results have been verified by simulations and measurements. Mechanism and design procedures of the proposed antenna have been described. Numerical investigations have shown that the lowest resonant frequency can be decreased around 12.3% using the proposed exponential curve cut on edges of slots compared with the conventional planar log-periodic slot antenna with regular shapes on edges. This benefit provides a useful method to design an antenna with more compact size under the same lowest frequency f_{min} in the working band. Good properties of wideband impedance matching, radiation pattern, and antenna gain have been achieved in the band of interest. The proposed log-periodic slot antenna is promising for UWB applications.

ACKNOWLEDGMENT

The authors thank the National Center for High-performance Computing for providing software and facilities. This work was supported in part by the MOST under Grant 106-2918-I-260-002.

REFERENCES

[1] D. E. Isbell, "Log periodic dipole array," *IRE Trans. Antennas Propag.*, vol. 8, pp. 260-267, May 1960.

[2] N. Barbano, "Log periodic Yagi-Uda array," *IEEE Trans. Antennas Propag.*, vol. 14, pp. 235-238, Mar. 1966.

[3] S. A. Amanatiadis, A. X. Lalas, N. V. Kantartzis, and T. D. Tsiboukis, "Efficient volume reduction of optimally designed pyramidal log-periodic antennas via meander elements," *Applied Computational Electromagnetic Society Journal*, vol. 28, pp. 653-662, Aug. 2013.

[4] X. Gao, Z. X. Shen, and C. Z. Hua, "Conformal VHF log-periodic balloon antenna," *IEEE Trans. Antennas Propag.*, vol. 63, pp. 2756-2761, June 2015.

[5] C. A. Balanis, *Antenna Theory Analysis and Design*. 3rd ed., John Wiley & Sons Inc., pp. 619-628, 2005.

[6] L. V. Blake and M. W. Long, *Antennas: Fundamentals, Design, and Measurement*. 3rd ed., SciTech Publishing Inc., pp. 294-297, 2009.

[7] G. Liu, L. Xu, and Z. Wu, "Miniaturised wideband circularly-polarised log-periodic koch fractal antenna," *Electronics. Letter*, vol. 49, pp. 1315-1316, Oct. 2013.

[8] R. Lehmensiek and D. I. L. de Villiers, "Optimization of log-periodic dipole array antennas for wideband omnidirectional radiation," *IEEE Trans. Antennas Propag.*, vol. 63, pp. 3714-3718, Aug. 2015.

[9] W. C. Weng, "Optimal design of an ultra-wideband antenna with the irregular shape on radiator using particle swarm optimization," *Applied Computational Electromagnetic Society Journal*, vol. 27, pp. 427-434, May 2012.

[10] K. M. Keen, "A planar log-periodic antenna," *IEEE Trans. Antennas Propag.*, vol. 22, pp. 489-490, May 1974.

[11] R. Sammeta and D. S. Filipovic, "Reduced size planar dual-polarized log periodic antenna for bidirectional high power transmit and receive applications," *IEEE Trans. Antennas Propag.*, vol. 62, pp. 5453-5461, Nov. 2014.

[12] J. Ha and D. S. Filipovic, "Electrothermal design of bidirectional wide-boom log-periodic antennas," *IEEE Trans. Antennas Propag.*, vol. 65, no. 4, pp. 1661-1669, Apr. 2017.
[13] Y. Sun, G. Wen, H. Jin, P. Wang, Y. Huang, and J. Li, "Wide bandwidth endfire antenna with log-period directors," *Applied Computational Electromagnetic Society Journal*, vol. 30, pp. 1173-1179, Nov. 2015.
[14] M. I. Mirzapour, S. M. J. Razavi, and S. H. M. Armaki, "Ultra-wideband planar LPDA antenna with mode converter balun," *Electronics. Letter*, vol. 50, pp. 848-850, June 2014.
[15] S. Y. Chen, P. H. Wang, and P. W. Hsu, "Uniplanar log-periodic slot antenna fed by a CPW for UWB applications," *IEEE Antennas and Wireless Propagation Letters*, vol. 5, pp. 256-259, June 2006.
[16] A. U. Bhobe, C. L. Holloway, M. Piket-May, and R. Hall, "Wide-band slot antennas with CPW feed lines: hybrid and log-periodic designs," *IEEE Trans. Antennas Propag.*, vol. 52, pp. 2545-2554, Oct. 2004.
[17] M. Y. Ting and W. C. Weng, "Design of the crescent-shape planar ultra-wideband antenna with a band-notch structure," *IEEE AP-S Int. Symp. Dig.*, Canada, ON, July 2010.
[18] P. Ingerson and P. Mayes, "Log-periodic antennas with modulated impedance feeders," *IEEE Trans. Antennas Propag.*, vol. 16, no. 6, pp. 633-642, Nov. 1968.

Wei-Chung Weng received the B.S. degree in Electronic Engineering from National Changhua University of Education, Changhua, Taiwan, in 1993, the M.S. degree in Electrical Engineering from I-Shou University, Kaohsiung, Taiwan, in 2001, and the Ph.D. degree in Electrical Engineering from The University of Mississippi, MS, USA, in 2007.

In 2008, he joined the Department of Electrical Engineering, National Chi Nan University, Puli, Taiwan, where he is currently an Associate Professor. From 2017 to 2018, he was a Visiting Scholar at the Department of Electrical Engineering, Colorado School of Mines, Golden, CO, USA. From 2004 to 2007, he was a Graduate Research Assistant in the Department of Electrical Engineering, The University of Mississippi. He has authored or coauthored over 50 journal articles and conference papers and a book entitled *Electromagnetics and Antenna Optimization Using Taguchi's Method* (Morgan & Claypool, 2007). His research interests include antennas and microwave circuits design, computational electromagnetics, electromagnetic compatibility, and optimization techniques in electromagnetics.

Weng is the Associate Editor-in-Chief for *Applied Computational Electromagnetics Society (ACES) Journal*. He has served many journals as a reviewer for years. He is a Member of ACES, a Senior Member of IEEE, and a Life Member of the Institute of Antenna Engineers of Taiwan (IAET). He was the recipient of Outstanding Teaching Award of National Chi Nan University in 2013 and 2016, respectively.

Min-Chi Chang was born in Yunlin, Taiwan. He received the B.S. degree in Electrical Engineering from National United University, Miaoli, Taiwan, in 2009. He is currently working toward the Ph.D. degree in the Department of Electrical Engineering, National Chi Nan University, Puli, Taiwan. His research interests focus on antenna design, computational electromagnetics, and optimization techniques in electromagnetics.

Design of a Frequency Reconfigurable Notched-Band Ultra-Wideband Antenna for Cognitive Radio Applications

Muflih Alsulami [1], Hatem Rmili [1], Sondos Mehri [1], Bandar Hakim [1], Muntasir Sheikh [1], and Raj Mittra [1,2]

[1] Electrical and Computer Engineering Department, Faculty of Engineering, King Abdulaziz University
P.O. Box 80204, Jeddah 21589, Saudi Arabia
hmrmili@kau.edu.sa

[2] Electrical and Computer Engineering Department, University of Central Florida
EMC Lab, Orlando, FL 32816, USA
rajmittra@ieee.org

Abstract ─ This paper proposes a frequency reconfigurable notched-band UWB antenna design, which is capable of wide band rejection. We begin with a conventional reconfigurable modified-square monopole printed antenna and insert a U-shaped slot to create the rejection band. Next, we add two identical SMV1249 varactor diodes with variable capacitances in the created slots to tune the rejected band. We modify the capacitances, which, in turn, controls rejected band by controlling the reverse bias voltage applied across the varactor diodes. The proposed structure has been simulated, optimized, fabricated and experimentally tested. Good agreement has been achieved between the simulation and measurement results. Experimental results show that when the bias voltage is varied from 0 to 7 V, the antenna can be reconfigured to achieve various rejection frequency bands, and to maintain good impedance match as well as stable radiation patterns over the explored frequency band ranging from 1 to 6 GHz.

Index Terms ─ Frequency reconfigurability, notched band, varactor diode, ultrawide band.

I. INTRODUCTION

Recently, Ultra-Wideband (UWB) radio technology has drawn increasing attention of communication engineers, owning to its high data transmission rate, low cost and small size. In comparison to many other existing wireless communication standards, UWB has a very wide bandwidth, ranging from 3.1 to 10.6 GHz [1]. Additionally, the UWB can coexist with other narrowband communication standards that occupy the same spectrum. Of course, an overlap of the UWB and other bands may lead to a severe interference between them. To avoid this interference, UWB antennas with single or multiple notch frequencies techniques have been developed, and their band-notch characteristics have been achieved through two main techniques [2-4]. The first of these is based the addition of various slots, either in the radiating patch [5, 6] or in the ground plane [7, 8], while the second employ parasitic elements to achieve the desired goal [9-11].

To realize dynamically-controlled band-notches, UWB antennas integrated with reconfigurable band-notch characteristics have recently been proposed [4]. These antennas have the capability of dynamically altering the notch frequency by using electrical switching circuits [7] such as MEMS switches, PIN diodes, or varactor diodes. Generally speaking, varactor diode [12-14] are the most widely used for tuning technique because they are simple to integrate into antenna system and to achieve different notch frequencies.

In this paper, a reconfigurable band-notched UWB antenna is investigated to achieve wideband rejection. We begin by using the basic structure presented in [15, 16] to realize the UWB behavior. Next, we introduce a U-shaped slot within the patch to obtain two rejected bands. Finally, we insert a pair of varactor diodes into the vertical slots, optimize their positions, and study the effect of varying the capacitance on the frequency of rejection. Next, we numerically optimize the position of the lumped elements before varying their capacitance. The tuning of the rejection frequency was realized by varying the reverse-bias voltages that are applied across the two varactor diodes. Experimental results show that, by properly varying the bias voltage value from 1 to 7 V, the proposed antenna can achieve a wideband behavior from 2 to 6 GHz with a rejection band which ranges from 2 GHz to 2.12 GHz.

This paper is organized as follows: the design procedure for the reconfigurable antenna is described in detail in the next section. In section 3, the simulation and measurement results are presented, compared and

Submitted On: November 12, 2018
Accepted On: April 3, 2019

discussed. Concluding remarks are presented in the last section.

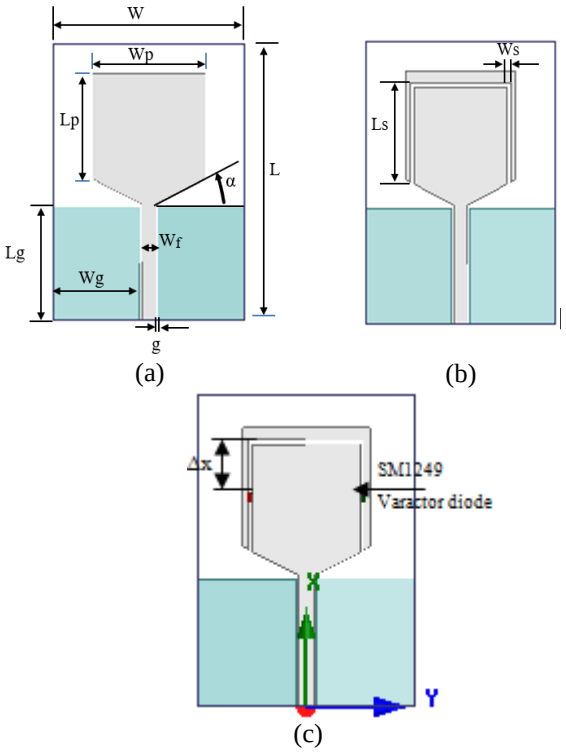

Fig. 1. Schemas of the studied antennas during the design procedure: (a) UWB basic structure, (b) UWB-antenna with slots only, and (c) UWB-antenna with slots and varactor diodes.

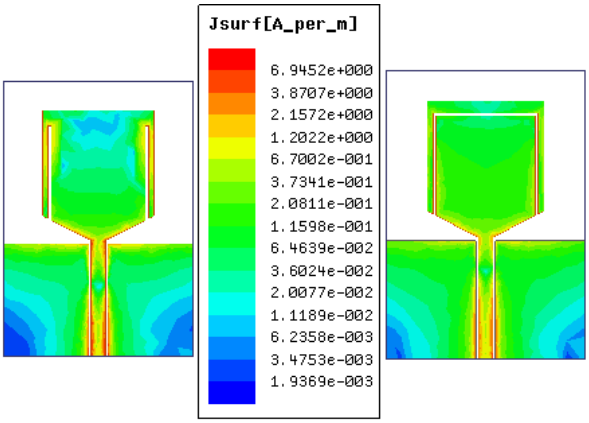

Fig. 2. Surface current distribution at 4 GHz for the basic UWB structure before (a) and after (b) addition of the horizontal part of the U-slot.

II. DESIGN PROCEDURE

The first step, we have designed the basic UWB antenna comprising of a planar CPW-fed structure, in which both the modified square monopole and the CPW ground plane are printed on one face of an Epoxy FR4 substrate whose loss tangent is 0.02 and 0.8 mm thickness. The geometrical parameters are first optimized to cover the UWB frequency band 3.1-10.3 GHz (Fig. 1 (a)). Next, two vertical slots were inserted into the radiating patch to generate a rejection frequency which is proportional to the length of the slot (Fig. 1 (b)). Then, a horizontal slot is inserted to split the patch into two parts in order to place the varactors (Fig. 1 (c)). The position of the horizontal slot was determined by analyzing the surface current distribution on the patch such that the radiation performance of the antenna is not affected (Fig. 2). Finally, we insert the two pin diodes within the two slots and we apply a reverse bias voltage across their electrodes to vary the varactor capacitance. Using the full-wave EM Simulator HFSS, the positions of the varactors are optimized to get high rejection level (mod (S_{11}) > -5 dB) with a wideband tuning capability of the rejected band, as shown in Fig. 3.

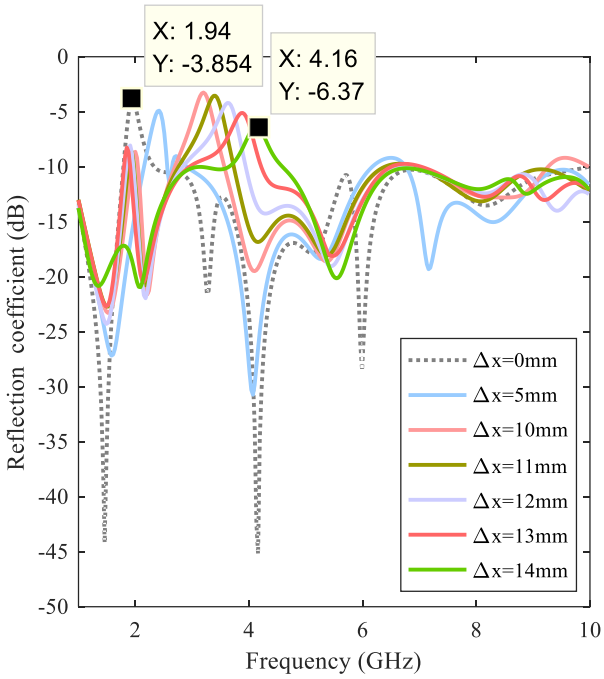

Fig. 3. Evolution of the simulated reflection coefficient of the designed antenna versus frequency, for different position Δx of the inserted varactors.

Table 1: Design parameters of the proposed antenna

Parameter (mm)			
L	76	Wf	4
W	52.5	g	0.75
Lp	36.8	α	27°
Wp	30.8	Ws	1
Lg	31	Ls	26.6
wg	23.6	Δx	11

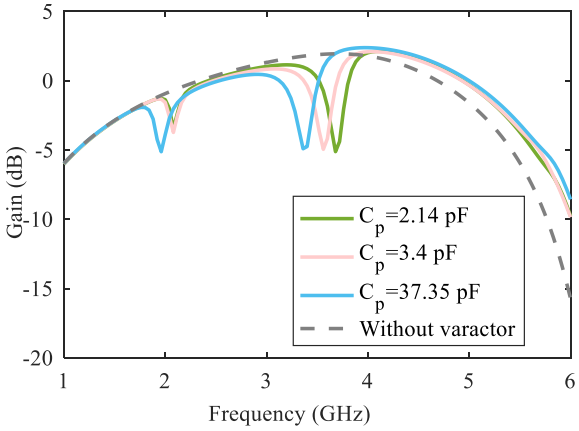

Fig. 4. Simulated gain of the UWB-antenna with slots and varactor diode (Fig.1c) versus frequency for different values of Cp and for Δx=11mm.

The gain variation according the frequency for different values of varactors has also been studied. During the performed simulations, we have modeled the varactor diode according to its equivalent electric circuit delivered by the manufacturer. This circuit consists on a parasitic inductance L in series with a capacitor Cp which is in parallel with an intrinsic resistance R_{ON}. When the varactor diode is active (ON sate), the values of L and R_{ON} for the used SMV 1249 diode are 0.45 nH and 1.7 Ω, respectively, according to the manufacturer's data sheet, whereas the capacitance may be changed. Figure 4 shows the gain variation when the lumped element capacitance is changed within the range 37.35 to 2.14 pF. The simulated results show that for each value of the capacitance 'Cp', a significant gain drop is observed at the rejected frequency. Such results attest that a frequency notch reconfiguration is clearly obtained using the varactor diode. More the capacitance decreases, more the narrow-notched frequency shifts to higher frequencies. Table 1 provides the values of the optimized design parameters for the reconfigurable notched-band antenna.

III. RESULTS AND DISCUSSIONS

A prototype of the reconfigurable notched-band antenna with the two inserted SMV 1249 diodes was fabricated and characterized (Fig. 5). Both the impedance characteristics and radiation patterns were measured. The impedance mismatch as a function of the source frequency was measured by using a vector Network analyzer (VNA), Agilent N5230A, over the frequency range of 1-6 GHz. The radiation pattern were measured were by using the "SATIMO Stargate32" anechoic chamber (IETR, INSA Rennes, France). As shown in Fig. 5, a low-pass filter was added to the antenna structure during the measurement procedure to eliminate the effect of the diode on the radiation pattern of the antenna. In Fig. 6 and Fig. 7, we present the simulated and measured results for S_{11} of the basic UWB structure with and without, slots, respectively. The investigated frequencies were limited to the operating range of 1-6 GHz of the anechoic chamber. It is worth to note that a small difference between simulated and measured results is observed, since in the simulation model the mismatch due to the connector used is not taken into consideration. In addition, the small discrepancy between the diodes and their equivalent circuits used in simulation affects the antenna performance. For the performed experimentation, the effect of the varactor diode capacitance has been investigated by varying the applied voltage across the lumped element. The results of this study, illustrated in Fig. 8, show that a continuous tuning of the notched frequency within the band 2-2.55 GHz has been achieved. For the antennas realized with varactor diodes of capacitances 37.35, 3.40, 2.38 and 2.14 pF, corresponding to the applied simulated and measured results is observed since in the voltages of 0, 3, 5 and 7 V, respectively, the rejected frequencies are 2, 2.05, 2.1 and 2.12 GHz, respectively. Table 2, summarizes all of these details and compares experimental and simulated results. Analysis of results given in Table 2 shows that we obtain a wideband reconfigurability of the rejected frequency (around 550 MHz which corresponds to a fractional bandwidth of 27.5%) by integration of SMV 1249 diodes within the antenna slots. The lumped element capacitance may be changed within the range 37.35 to 2.14 pF by increasing the reverse voltage from 0 to 7 V. This implies, that the capacitance of the loaded varactor is inversely proportional to the applied reverse voltage, and more the voltage increases, more the narrow-notched frequency band shifts to the higher frequencies. We note that a small difference between the simulated and experimental rejected frequency is observed however, for both results the wideband behavior of the antenna is maintained. To better characterize the designed antenna, we have measured its radiation patterns with and without the varactor diodes, at selected operating frequencies close to the rejected bands. Figure 9 compares the 3D radiation patterns for the basic structure without slots (Fig. 5 (a)) and the antenna with integrated SMV 1249 diodes (Fig. 5 (c)) under reverse voltages 0 and 5 V. We note that we have considered identical values for the capacitances of SMV 1249 diodes integrated in both sides of the radiating patch to realize symmetric radiation patterns. The patterns corresponding to the basic UWB structure without band rejection behavior showed maximum gains of 1.28 and 4.7 dB at frequencies 2.5 and 3.7 GHz, respectively against to the structures designed with capacitances 34.35 pF to reject the frequencies 2.0 and 2.3 GHz, have maximum gain values of 1.17 dB and 2.12 dB

respectively. Further maximum gain values realized for Cp=2.38 pF are -0.80 dB and -0.11 dB at 2.8 GHz 3.3 GHz, respectively. Analysis of the measured pattern shapes shows also that both the UWB basic structure and the reconfigurable one with diodes are omni-directional.

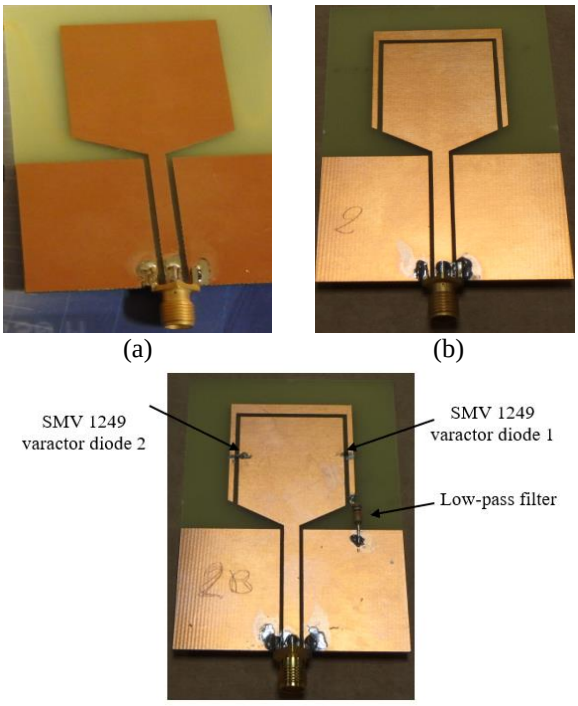

Fig. 5. Schemas of the studied antennas during the design procedure: (a) UWB basic structure, (b) UWB-antenna with slots only, and (c) UWB-antenna with slots and varactor diodes.

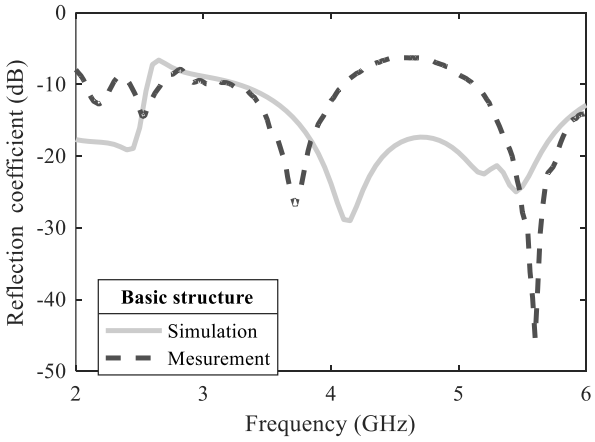

Fig. 6. Simulated and measured reflection coefficient for the basic structure (Fig. 2 (a)).

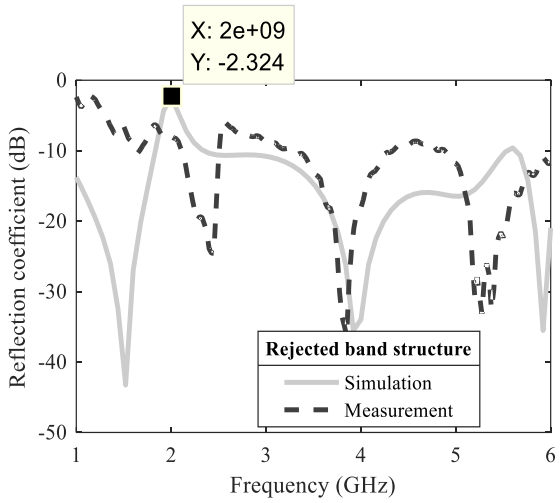

Fig. 7. Simulated and measured reflection coefficient for the rejected band structure (Fig. 2 (b)).

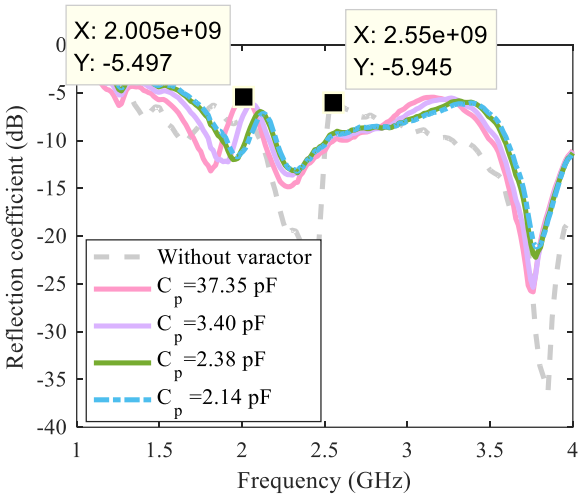

Fig. 8. Measured reflection coefficient S11 for 'Cp' varying from 37.35 pF to 2.14 pF (equivalent to the bias voltage variation from 0 V to 7 V).

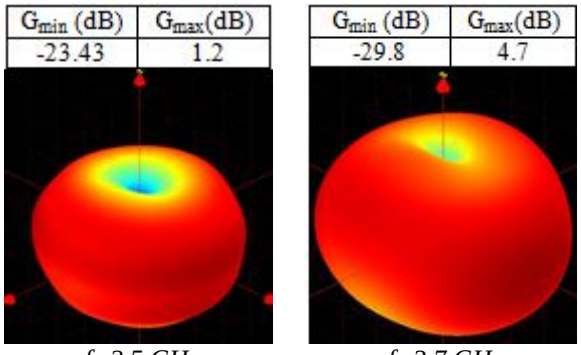

(a)

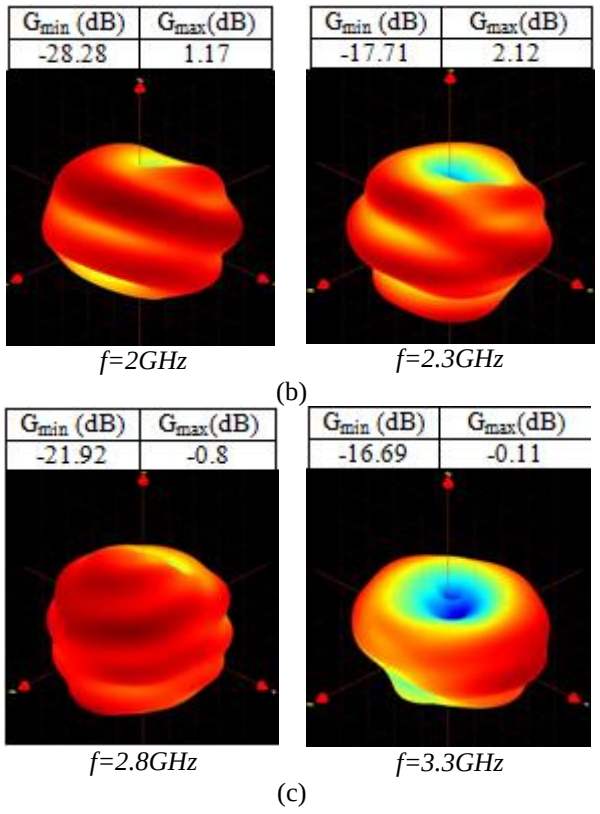

Fig. 9. 3D Measured radiation pattern at selected frequencies for: (a) the basic UWB structure, (b) rejected-band structure with varactor capacitance Cp=37.35 (reverse voltage equal to 0 V), and (c) rejected-band structure with varactor capacitance Cp=2.38 (reverse voltage equal to 5V).

Table 2: Rejected-frequency for different capacitance and reverse voltage values of realized antennas

Capacitance Value (pF)	Reverse Voltage (V)	Rejected Frequency (GHz)	
		Sim.	Meas.
Without varactor diode	--	2	2.55
37.35	0	3.4	2
3.40	3	3.6	2.05
2.38	5	3.62	2.1
2.14	7	3.72	2.12

IV. CONCLUSION

The paper has presented a procedure for designing procedure for a reconfigurable notched-band UWB antenna utilizing electrical switching circuits. The notched-band was dynamically tuned by inserting two identical varactor diodes with variable capacitance and varying the capacitance values from 37.35 pF to 2.14 pF (equivalent to the bias voltage variation from 0 V to 7 V). The rejection band range was tuned from 2 GHz to 2.12 GHz, corresponding to the fractional bandwidth of 27.5% was realized while maintaining good impedance matching.

The desirable attributes of the antenna namely its radiation pattern stability, wideband behavior, capability of the tuning rejection band over a wide range, and moderate gain values, renders it a potential candidate for use in wireless radio applications.

ACKNOWLEDGMENT

This project was funded by the Deanship of Scientific Research (DSR), King Abdulaziz University, Jeddah, Saudi Arabia under Grant No. (KEP-Msc-3-135-39). The authors therefore, acknowledge with thanks DSR technical and financial support.

The authors are grateful to the help of Dr. Jean-Marie Floch from the IETR Institute, INSA Rennes, France, for his help during experiments.

REFERENCES

[1] Y. Rahayu, T. Abd Rahman, R. Ngah, and P. Hall, "Ultra-wideband technology and its applications," *IFIP International Conference Wireless and Optical Communications Networks*, Surabaya, Indonesia, 2008.

[2] J. Costantine, Y. Tawk, and C. G. Christodoulou, "Reconfigurable antennas: Design and applications," *Proceedings of the IEEE*, vol. 103, no. 3, pp. 424-437, 2015.

[3] Y. J. Guo and P. Y Qin, *Handbook of Antenna Technologies*, S. Science, Editor, 2015.

[4] Y. J. Guo, P. Y. Qin, S. L. Chen, W. Lin, and R. W. Ziolkowski, "Advances in reconfigurable antenna systems facilitated by innovative technologies," *IEEE Access*, vol. 6, pp. 5780-5794, 2018.

[5] I. B. Trad, S. Dakhli, H. Rmili, J. M. Floch, W. Zouch, and M. Drissi, "Planar square multiband frequency reconfigurable micro-strip fed antenna with Koch-island fractal slot for wireless devices," *Microwave and Optical Technology Letters*, vol. 57, no. 1, pp. 207-212, 2015.

[6] M. Fakharian, P. Rezaei, and A. Orouji, "A novel slot antenna with reconfigurable meander-slot DGS for cognitive radio applications," *ACES Journal*, vol. 30, no. 7, 2015.

[7] G. Saini and P. K.chakravarti, "Design of reconfigurable notch band antenna for UWB application using P-I-N Diodes," *International Journal of Emerging Trends & Technology in Computer Science*, vol. 6, no. 5, pp. 245-252, 2017.

[8] H. A. Mohamed, A. S. Elkorany, S. A. Saad, and D. A. Saleeb, "New simple flower shaped reconfigurable band-notched UWB antenna using

single varactor diode," *Progress In Electromagnetics Research*, vol. 76, pp. 197-206, 2017.
[9] V. Bhushan, J. KadamaLucy, K. Gudinob, C. K. Rameshaa, and S. Nagaraju, "A band-notched ultra-wideband compact planar monopole antenna with U-shaped parasitic element," *Procedia Computer Science*, vol. 93, pp. 101-107, 2016.
[10] M. Mohammadifar and Y. Zehforoosh, "Designing four notched bands microstrip antenna for UWB applications, assessed by analytic hierarchy process method," *Journal of Microwaves, Optoelectronics and Electromagnetic Applications*, vol. 16, no. 3, pp. 1-12, 2017.
[11] W. Ali and A. Ibrahim, "Tunable band-notched UWB antenna from WLAN to WiMAX with open loop resonators using lumped capacitors," *ACES Journal*, vol. 33, no. 6, pp. 603-609, 2018.
[12] I. Rouissi, J. M. Floc'h, H. Rmili, and H. Trabelsi, "Design of a frequency reconfigurable patch antenna using capacitive loading and varactor diode," *European Conference on Antennas and Propagation*, 2015.
[13] S. Dakhli, H. Rmili, J. M. Floch, M. Sheikh, K. Mahdjoubi, F. Choubani, and R. Ziolkowski, "Capacitively loaded loop-based antennas with reconfigurable radiation patterns," *International Journal on Antennas and Propagation*, pp. 1-10, 2015.
[14] I. B. Trad, J. M. Floch, H. Rmili, L. Laadhar, and M. Drissi, "Planar elliptic broadband antenna with wide range reconfigurable narrow notched bands for multi-standard wireless communication devices," *Progress in Electromagnetic Research*, vol. 146, pp. 69-80, 2014.
[15] I. B. Trad, H. Rmili, J. M. Floch, and H. Zangar, "Design of planar mono-band rejected UWB CPW-fed antennas for wireless communications," *Mediterranean Microwave Symposium*, 2011.
[16] S. K. Singh, M. P. Sharma, and N. K. Kashyap, "A modified planar triangular monopole antenna for wide band applications," *International Conference on Industrial and Information Systems*, 2016.

Muflih Alsulami received the B.Sc. in Electronics and Communication Engineering, King Abdulaziz University, Saudi Arabia, 2012. Currently, he is pursuing his M.Sc. degree in Electronics and Communication Engineering at King Abdulaziz University, Jeddah, Saudi Arabia. He is currently associated with National Grid SA Company, Saudi Arabia. His research interests include designing of compact antennas and wireless communication networks.

Hatem Rmili received the B.S. degree in General Physics from the Science Faculty of Monastir, Tunisia in 1995, and the DEA diploma from the Science Faculty of Tunis, Tunisia, in Quantum Mechanics, in 1999. He received the Ph.D. degree in Physics (Electronics) from both the University of Tunis, Tunisia, and the University of Bordeaux 1, France, in 2004. From December 2004 to March 2005, he was a Research Assistant in the PIOM Laboratory at the University of Bordeaux 1. During March 2005 to March 2007, he was a Postdoctoral Fellow at the Rennes Institute of Electronics and Telecommunications, France. From March to September 2007, he was a Postdoctoral Fellow at the ESEO Engineering School, Angers, France. From September 2007 to August 2012, he was an Associate Professor with the Mahdia Institute of Applied Science and Technology (ISSAT), Department of Electronics and Telecommunications, Tunisia. Actually, he is Associate Professor with the Electrical and Computer Engineering Department, Faculty of Engineering, King Abdulaziz University, Jeddah, Saudi Arabia. His main research activities concern antennas, metamaterials and metasurfaces.

Sondos Mehri has received the Ph.D. degree in 2017 in Electrical Engineering, from the National School of Engineering in Tunis (ENIT), Tunisia and is currently working as a postdoctoral researcher under the supervision of Prof. Raj Mittra. Her research interests are focused on the design of a substrate integrated waveguide slot array for millimeter waves frequencies.

Mehri has been awarded the 2nd Prize of Students Paper Poster Competition of the IEEE Melecon in 2016.

Bandar Hakim is an Assistant Professor of Electrophysics at KAU. He received his Ph.D. degree in Electrophysics from the University of Maryland. He worked with the Medical Robotics Group at the École Polytechnique Fédérale de Lausanne in Switzerland, the Center for Devices and Radiological Health at the Food and Drug Administration in Washington, DC and the Neurology Department at Mount Sinai School of Medicine in the New York, NY. He served as an

industrial consultant in the US, Switzerland and Germany.

Muntasir Sheikh received his B.Sc. from King Abdulaziz University, Saudi Arabia, in Electronics and Communications Engineering, M.Sc. in RF Communications Engineering from the University of Bradford, U.K., and Ph.D. from the University of Arizona, U.S.A.

Since then he has been teaching in the Electrical and Computer Engineering Dept. in KAU. His research interests are Antenna Theory and Design, Radar applications, and electromagnetic metamaterials.

Raj Mittra is a Professor in the Department of Electrical & Computer Science of the University of Central Florida in Orlando, FL., where he is the Director of the Electromagnetic Communication Laboratory. Prior to joining the University of Central Florida, he worked at Penn State as a Professor in the Electrical and Computer Engineering from 1996 through June, 2015. He also worked as a Professor in the Electrical and Computer Engineering at the University of Illinois in Urbana Champaign from 1957 through 1996, when he moved to the Penn State University. Currently, he also holds the position of Hi-Ci Professor at King Abdulaziz University in Saudi Arabia,

He is a Life Fellow of the IEEE, a Past-President of AP-S, and he has served as the Editor of the Transactions of the Antennas and Propagation Society. He won the Guggenheim Fellowship Award in 1965, the IEEE Centennial Medal in 1984, and the IEEE Millennium medal in 2000. Other honors include the IEEE/AP-S Distinguished Achievement Award in 2002, the Chen-To Tai Education Award in 2004 and the IEEE Electromagnetics Award in 2006, and the IEEE James H. Mulligan Award in 2011.

Mittra is a Principal Scientist and President of RM Associates, a consulting company founded in 1980, which provides services to industrial and governmental organizations, both in the U.S. and abroad.

UWB MIMO Antenna for High Speed Wireless Applications

Ahmed A. Ibrahim [1], Jan Machac [2], and Raed M. Shubair [3]

[1] Faculty of Engineering, Minia University, Minia, Egypt
ahmedabdel_monem@mu.edu.eg

[2] Department of Electromagnetic Field, Czech Technical University in Prague
Technicka 2, 166 27 Prague, Czech Republic
machac@fel.cvut.cz

[3] Research Laboratory of Electronics, Department of Electrical Engineering and Computer Science
Massachusetts Institute of Technology, USA
rshubair@mit.edu

Abstract ─ The paper proposes a MIMO antenna composed of two elements in the form of UWB monopole antennas. Polarization diversity of the proposed antenna is obtained locating the two elements perpendicularly on a common substrate. Also the isolation between elements is accomplished without using any extra decoupling structures. The two monopoles antennas with half elliptical shape are fed with asymmetric coplanar strip (ACS). The presented antenna is located on substrate 48×28 mm^2 in total size. The distance between the two elements is 15 mm that is $0.15\lambda_0$ at 3GHz. The antenna was designed to work effectively from 3 to 11.5 GHz with reflection coefficient better than -10 dB and isolation lower than 18 dB. In addition, antenna with elements located in parallel was designed to show the advantage of the original design. Envelope correlation coefficient, diversity gain and channel capacity loss document the antennas behavior. The antenna was fabricated and measured. Measurement validated the simulation and showed that the designed antenna can be well applied in UWB MIMO systems.

Index Terms ─ MIMO antenna, omni-directional radiation pattern, polarization diversity, UWB antenna.

I. INTRODUCTION

Ultra wideband (UWB) communication systems are a hot topic in wireless communication systems. There are clear advantages of these systems as high data rates, and low power consumption [1]. The unlicensed band of UWB technology operating at frequency band from 3.1 to 10.6 GHz is realized by the Federal Communication Commission (FCC) [2]. Many efforts have been employed to design UWB antennas due to their advantages such as low profile, compact size, larger impedance bandwidth and stable radiation characteristics [3-5]. In order to enhance the channel capacity, to decrease multipath fading, and to raise the quality of the received signals, antennas with polarization diversity are used more often than antennas known as MIMO systems [6-10]. The integration of the UWB antenna and diversity technology is used in wireless systems to achieve the good performance of the MIMO systems. Many UWB diversity antennas have been presented, e.g., in [11-13]. In the MIMO system, multiple and uncorrelated antenna elements are used to transmit and receive signals. The reliability of the system can be enhanced by selecting the received signal from different antenna elements. The design of compact size MIMO antennas of low signal correlation is important for portable devices. The problem is that antenna elements must be located very closely to save space, and at the same time high isolation between their elements must be kept. A number of ways how to increase the isolation between antenna elements has been proposed. These are: application of electromagnetic band gap (EBG) structures [14], and application of defected ground structures (DGSs) [15]. However, these structures are of a very complex configuration and occupy large areas. The asymmetric coplanar strip (ACS) feeding structure is used in the design to reduce the size of the UWB MIMO antenna. The ACS feeding structure introduces size reduction about one half of the CPW-fed antennas [16]. This paper proposes an original compact MIMO antenna with polarization diversity suitable for ultra wideband applications. The UWB antenna has bandwidth allocated for UWB applications from 3.1 to 10.6 GHz. More than -18 dB transmission coefficient through the entire UWB frequency range is achieved by without using any extra structure. The proposed UWB MIMO antenna has size of 48×28 mm^2. The two antenna elements are separated by 15 mm that is $0.15\lambda_0$ at 3 GHz. For a verification

Submitted On: October 26, 2018
Accepted On: March 3, 2019

purpose, the antenna was fabricated and its impedance and radiation characteristics were measured. The performance of simulated and measured results confirms that the proposed MIMO UWB antenna is suitable for UWB applications. All simulations are performed by the CST microwave studio (CST MwS). Correctness of the design is verified by measurements.

II. UWB MIMO ANTENNA CONFIGURATION

In this section two different UWB MIMO arrangements are presented as illustrated in Fig. 1 together with corresponding dimensions. Figure 1 (a) shows side by side configuration (antenna 1) and Fig. 1 (b) illustrates the perpendicular configuration (antenna 2).

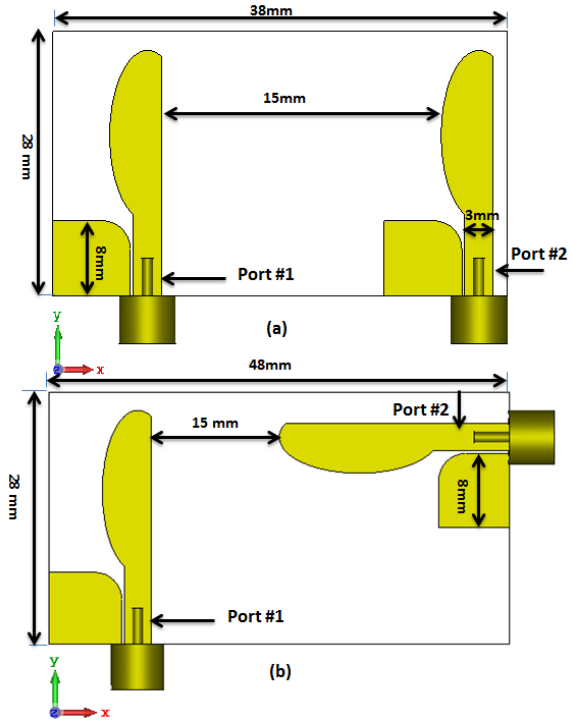

Fig. 1. Layout of the UWB MIMO antenna: (a) Antenna 1 (side by side arrangement), and (b) Antenna 2 (orthogonal arrangement).

The antennas are designed on FR4 substrate of permittivity 4.4 and 1.6 mm in thickness. The two antennas are fed by ACS with strip 3 mm in width and gap distance 0.3 mm to achieve 50 Ω characteristic impedance. The particular radiators are monopole antennas with semi elliptical shape. In order to improve the bandwidth of the UWB antenna, the ACS ground has a small curvature. ACS-fed is used to decrease the over size of the antennas. The distance between the two antenna edges in the two configurations has been succeeded to become 15 mm which equals $0.15\lambda_0$ at 3 GHz.

III. RESULTS AND DISCUSSION

A. Simulation

Figure 2 presents calculated scattering parameters of the two antenna versions. The antenna fed at port 2 shows similar values. The simulation results illustrate that the two antenna configurations have wide impedance bandwidth from 3 to 11.5 GHz with reflection coefficient lower than -10 dB. On the other hand, the mutual coupling in the antenna 2 (orthogonal arrangement) is better than the mutual coupling in the antenna 1 (side by side arrangement) as shown in Fig. 2 (b). There is more than -5 dB difference between the two antenna arrangements at different frequencies.

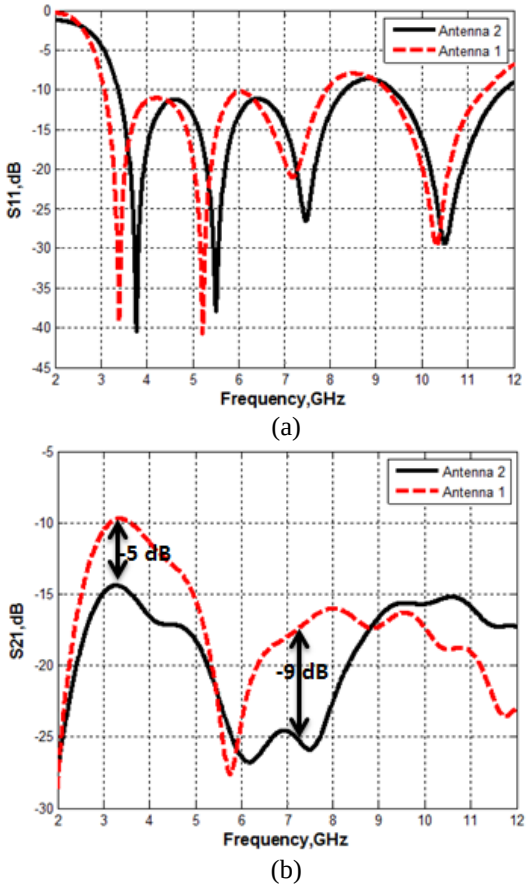

Fig. 2. Simulated S-parameters of the UWB MIMO antenna: (a) reflection coefficient, (b) transmission coefficient.

This presents the advantage the original configuration of antenna 2. The isolation coupling of antenna 2 is better than -18 dB at frequency bands from 4.5 to 9 GHz and around -15 dB from 3 to 4 GHz and from 9 to 11 GHz.

The simulated radiation patterns (3D) of the antenna 2 when one port 1 is excited and port 2 is matched with 50 Ω load and vice versa at 4 GHz, 6 GHz, and 10 GHz are presented in Fig. 3. Radiation patterns of the antenna excited by ports 1 and 2 are mutually orthogonal. Good polarization and pattern diversity between the two antenna elements follow from that. Peak gain and efficiency of antenna 2 calculated by the CST MwS supposing that port 1 is excited and port 2 is terminated by 50 Ω load are plotted in Fig. 4. The antenna has average gain around 3.5 dBi, and the efficiency has average value around 85% within the operating frequency band.

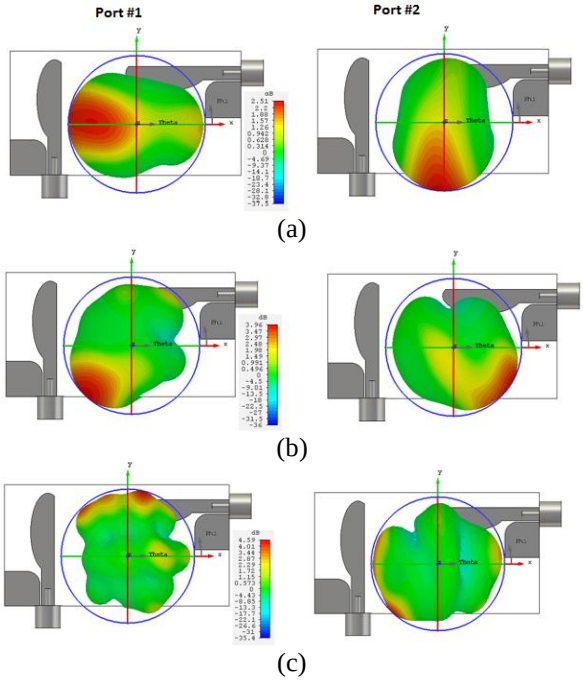

Fig. 3. Simulated 3D radiation patterns of the antenna 2: (a) at 4 GHz, (b) at 6 GHz, and (c) at 10 GHz.

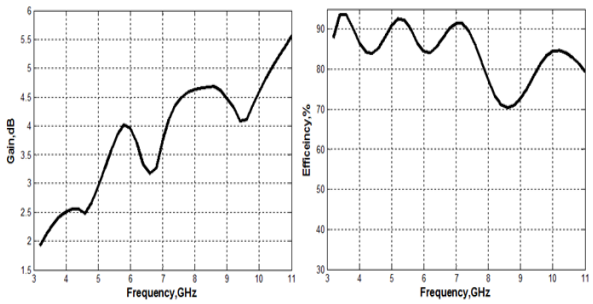

Fig. 4. Simulated results of UWB MIMO Antenna 2 (orthogonal arrangement): (a) peak gain and (b) total efficiency.

B. Measurement

The FR4 substrate with relative permittivity 4.4, 1.6 mm in thickness, and loss tangent equal to 0.025 was used in the fabrication of the proposed UWB MIMO antenna, see photograph in Fig. 5. Measured and simulated reflection and transmission coefficients are plotted in Fig. 6. Figure 6 (a) shows that the antenna operates at frequency band from 3 to 11.5 GHz with reflection coefficient lower than -10 dB. Mutual coupling is better than -18 dB within the frequency band from 4.5 to 11 GHz and from 4 to 4.5 GHz it reaches value better than -15 dB. A good consistency can also be noticed between the measured and simulated results. However, measured and calculated resonance frequencies are shifted. This is due to the mismatch of the feeding setup and the accuracy of fabrication process.

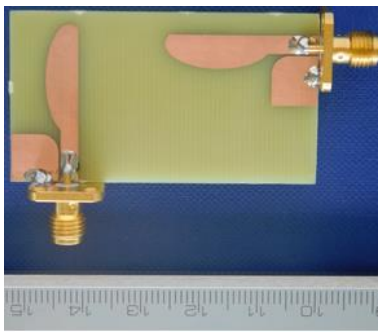

Fig. 5. Photograph of the fabricated UWB MIMO antenna.

Antenna radiation patterns were measured inside anechoic chamber using the NSI 800F-30 system at 4 GHz and 10 GHz for the three main planes, x-z plane, x-y plane, and y-z plane. They are plotted in Fig. 7 and Fig. 8. The measurement was done assuming the excitation at port 1 while port 2 was matched with 50 Ω load and vice versa. Radiation patterns in x-y and y-z planes of port 1 and port 2 are rotated by 90 degrees, and the radiation pattern in x-z plane of port 1 is almost similar to the radiation pattern in x-z plane of port 2. This is due to the fact that the two antenna elements are positioned on the substrate perpendicularly. The radiation patterns in x-z plane of port 1 and port 2 are omnidirectional, and are bidirectional in the x-y and y-z planes of port 1 and port 2. However, there are small differences between the measured and calculated radiation patterns. This is due to the asymmetric ground plane of the presented design fed through ACS and because the measured setup such as there is some radiated power doesn't take into account in the measurements due to the small size of the proposed antenna. Finally, it can be observed that there is reasonable agreement between the simulated and measured radiation patterns in all planes.

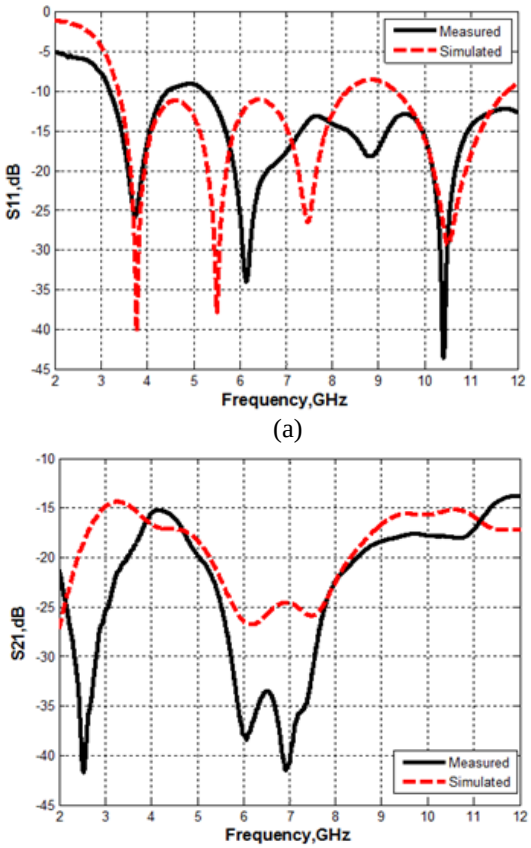

Fig. 6. Measured and simulated S-parameters of the UWB MIMO antenna: (a) reflection coefficient, and (b) transmission coefficient.

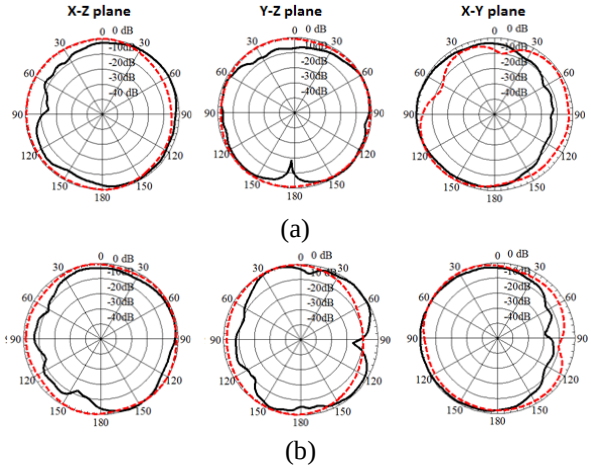

Fig. 7. Measured black (solid) and simulated red (dashed) results of the directive gain at 4 GHz: (a) port 1 and (b) port 2.

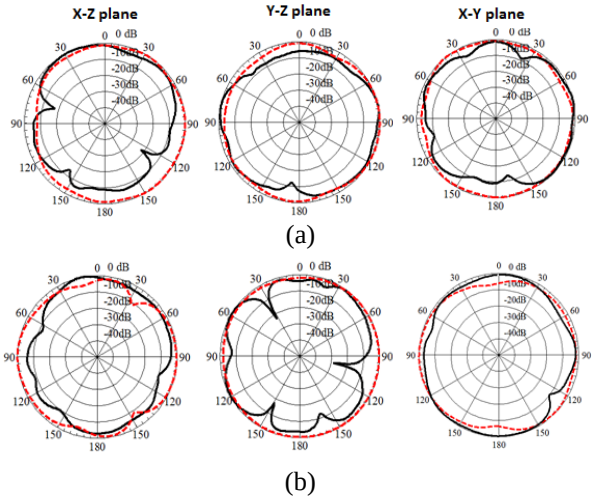

Fig. 8. Measured black (solid) and simulated red (dashed) results of the directive gain at 10 GHz: (a) port 1 and (b) port 2.

IV. MIMO PERFORMANCE

The diversity behaviour of the MIMO antenna can be confirmed by one of the three parameters: envelope correlation coefficient (ECC), by diversity gain, and/or by channel capacity loss (CCL).

A. Envelope correlation coefficient and diversity gain

ECC defines the correlation of antenna elements. The correlation coefficient between the antenna elements should to be with lower values for achieving a higher diversity between the MIMO antenna elements [17]:

$$ECC = \rho_e = \left|\rho_{ij}\right| = \frac{\left|S_{ii}^{*}S_{ij} + S_{ji}^{*}S_{jj}\right|^2}{\left(1-\left(\left|S_{ii}\right|^2+\left|S_{ji}\right|^2\right)\right)\left(1-\left(\left|S_{jj}\right|^2+\left|S_{ij}\right|^2\right)\right)}. \quad (1)$$

ECC of both antenna 1 and antenna 2 is plotted in Fig. 9. ECC of the proposed antenna 2 has value lower than -50 dB within the operating frequency band. However, ECC of the antenna 1 shows the same values except at the frequency band from 3.5 to 4.8 GHz where it increases to -40 dB. This means that the correlation between the elements of the proposed antenna 2 is better than the correlation of the antenna 1. Diversity gain (DG) relates to ECC [18]:

$$DG = 10 * \sqrt{1-\left|ECC\right|}. \quad (2)$$

The diversity gain of proposed antenna is plotted in Fig. 10. It is 10 dB within the operating frequency band. However, at frequency from 3.5 to 4.8 GHz it decreases to 9.8 dB in the case of the antenna 1.

B. Channel capacity loss (CCL)

CCL is an important parameter evaluating the MIMO performance. In any conventional system, CCL increases linearly with the number of used antenna elements without increasing the bandwidth or transmitted power and this occurred under a specified assumption [19]. The correlation between elements in MIMO channel systems produces capacity loss calculated by using [20]:

$$CCL = -\log_2 \det(\psi^R), \quad (3)$$

$$\psi^R = \begin{bmatrix} \rho 11 & \rho 12 \\ \rho 21 & \rho 22 \end{bmatrix}$$

where $\rho_{ii} = 1 - \left(|S_{ii}|^2 + |S_{ij}|^2 \right)$. (4)

$$\rho_{ij} = -\left(S_{ii}^{*} S_{ij} + S_{ji}^{*} S_{ij} \right) \text{ for } i, j = 1 \text{ or } 2$$

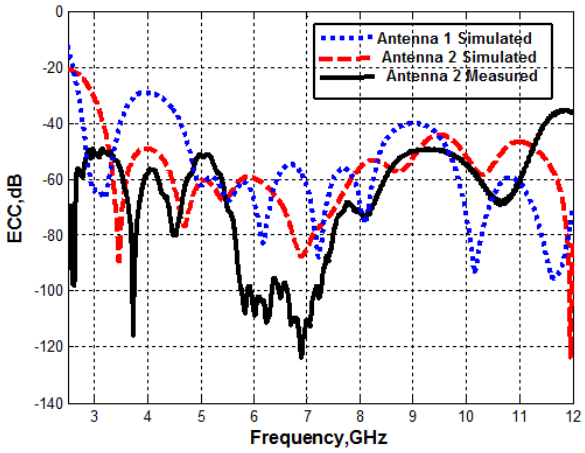

Fig. 9. Simulated and measured results of the envelope correlation coefficient of UWB MIMO antenna.

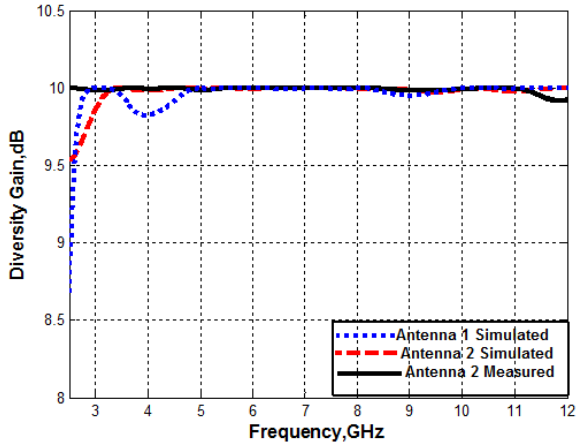

Fig. 10. Simulated and measured results of diversity gain of UWB MIMO antenna.

The simulated and measured CCL is plotted in Fig. 11. CCL value is lower than 0.4 bits/s/Hz within the operating frequency band. CCL of antenna 1 is higher than 0.4 bits/s/Hz as shown in Fig. 11. Finally, it follows from Fig. 9, Fig. 10, and Fig. 11, that the proposed MIMO UWB antenna achieves good MIMO performance, better than antenna 1. This confirms that the proposed antenna can be considered as a good choice to operate in UWB MIMO applications.

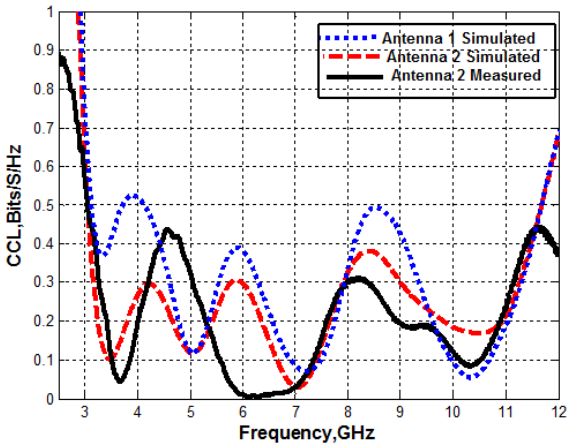

Fig. 11. Simulated and measured channel capacity loss of the UWB MIMO antenna.

V. CONCLUSION

A compact UWB MIMO antenna with polarization diversity has been presented. It consists of two elements in the form of monopoles of half elliptical shape. The elements are fed through asymmetric coplanar strip. The proposed antenna operates at frequency band from 3 to 11.5 GHz with reflection coefficient lower than -10 dB and isolation lower than 18 dB. Both simulations and measurements showed that the proposed configuration has polarization diversity features, low ECC through the operating frequency band, and has good MIMO performance. Due to this the designed antenna is a good candidate for UWB MIMO and polarization diversity applications. Theoretical design has been verified by experiments.

REFERENCES

[1] J. Ren, W. Hu, Y. Yin, and R. Fan, "Compact printed MIMO antenna for UWB applications," in *IEEE Antennas and Wireless Propagation Letters*, vol. 13, pp. 1517-1520, 2014.

[2] Federal Communications Commission, "Federal communications commission revision of Part 15 of the commission's rules regarding ultra-wideband transmission system from 3.1 to 10.6 GHz," *FCC*, Washington, DC, ET-Docket, 98-153, 2002.

[3] A. A. Ibrahim, M. A. Abdalla, and A. Boutejdar, "A printed compact band-notched antenna using octagonal radiating patch and meander slot technique for UWB applications," *Progress In Electromagnetics Research M*, vol. 54, pp. 153-162, 2017.

[4] A. A. Ibrahim, W. Ali, and J. Machac, "UWB monopole antenna with band notched characteristics mitigating interference with WiMAX," *Radio Engineering Journal*, vol. 26, no. 2, 2017.

[5] A. Boutejdar, A. A. Ibrahim, and E. P. Burte, "Novel microstrip antenna aims at UWB applications," *Microwave & RF*, 2015.

[6] W. Ali and A. A. Ibrahim, "A compact double-sided MIMO antenna with an improved isolation for UWB applications," *International Journal of Electronics and Communications*, vol. 82, pp. 7-13, 2017.

[7] A. A. Ibrahim, M. A. Abdalla, and Z. Hu, "Design of a compact MIMO antenna with asymmetric coplanar strip-fed for UWB applications," *Microwave and Optical Technology Letters*, vol. 59, no. 1, 2017.

[8] K. Yu, Y. Li, and X. Liu, "Mutual coupling reduction of a MIMO antenna array using 3-D novel meta-material structures," *Applied Computational Electromagnetics Society Journal*, vol. 33, no. 7, July 2018.

[9] T. Jiang, T. Jiao, Y. Li, and W. Yu, "A low mutual coupling MIMO antenna using periodic multi-layered electromagnetic band gap structures," *Applied Computational Electromagnetics Society Journal*, vol. 33, no. 3, pp. 305-311, 2018.

[10] Y. Li, W. Li, and W. Yu, "A multi-band/UWB MIMO/diversity antenna with an enhance isolation using radial stub loaded resonator," *Applied Computational Electromagnetics Society Journal*, vol. 28, no. 1, pp. 8-20, 2013.

[11] L. Liu, S. W. Cheung, and T. I. Yuk, "Compact MIMO antenna for portable devices in UWB applications," *IEEE Trans Antennas Propag*., vol. 61, pp. 4257-4264, 2013.

[12] M. A. Abdalla and A. A. Ibrahim "Design and performance evaluation of metamaterial inspired MIMO antennas for wireless applications" *Wireless Personal Communications*, vol. 95, pp. 1001-1017, 2016.

[13] X. -B. Sun and M. Y. Cao, "Mutual coupling reduction in an antenna array by using two parasitic microstrips," *AEU-International Journal of Electronics and Communications*, vol. 74, pp. 1-4, 2017.

[14] L. Zhang, J. A. Castaneda, and N. G. Alexopoulos, "Scan blindness free phased array design using PBG materials," *IEEE Trans. Antennas Propag.*, vol. 52, no. 8, pp. 2000-2007, 2004.

[15] A. A. Ibrahim, M. A. Abdalla, A. B. Abdel-Rahman, and H. F. A. Hamed, "Compact MIMO antenna with optimized mutual coupling reduction using DGS," *International Journal of Microwave and Wireless Technologies*, vol. 6, no. 2, 2014.

[16] X. Li, X. W. Shi, W. Hu, P. Fei, and J. F. Yu, "Compact triband ACS-fed monopole antenna employing open-ended slots for wireless communication," *IEEE Antennas Wireless Propag. Lett.*, vol. 12, pp. 104-107, 2013.

[17] S. Blanch, J. Romeu, and I. Corbella, "Exact representation of antenna system diversity performance from input parameter description," *Electron. Lett.*, vol. 39, no. 9, 2003.

[18] K. Rosengren and P. -S. Kildal, "Radiation efficiency, correlation, diversity gain and capacity of a six monopole antenna array for a MIMO system: Theory, simulation, and measurement in reverberation chamber," *IEE Proc. Microw. Antennas Propag.*, vol. 153, no. 6, 2006.

[19] C. Chuan, D. Tse, J. Kahn, and R. Valenzuela, "Capacity scaling in MIMO wireless systems under correlated fading," *IEEE trans. Inf. Theory*, vol. 48, pp. 637-650, 2002.

[20] H. Shin and J. H. Lee, "Capacity of multiple-antenna fading channels: Spatial fading correlation, double scattering, and keyhole," *IEEE Trans. Inform. Theory*, vol. 49, pp. 2636-2647, 2003.

Compact Design of Non-uniform Meta-surface for Patch Antenna Main Beam Steering

Hailiang Zhu [1], Yuwei Qiu [1], Jinliang Bai [2], and Gao Wei [1]

[1] Department of Electronic Engineering, School of Electronics and Information
Northwestern Polytechnical University, Xi'an, 710129, Shaanxi, China
zhuhl@nwpu.edu.cn, qiuyuwei@mail.nwpu.edu.cn, weigao@nwpu.edu.cn

[2] Beijing Institute of Space Long March Vehicle, Beijing, China
jinliangbai@163.com

Abstract ─ A compact design of non-uniform meta-surface for patch antenna main beam steering is presented in this paper. The proposed design is realized using printed circuit board technology. By adding the non-uniform meta-surface to a patch antenna, the main-beam direction of the patch antenna can be steered by an angle up to 30° from the boresight direction. The meta-surface together with the patch antenna here is called meta-surfaced antenna, which has a very compact structure since there is no air gap between the meta-surface and the patch antenna. The meta-surfaced antenna is studied and designed to operate around 2.45GHz. To verify the results of simulation, the meta-surfaced antenna is fabricated and measured. Measured results show that the antenna has an operating bandwidth from 2.35-2.5GHz and peak realized gain of 7.1dBi.

Index Terms ─ Beam steering, compact design, non-uniform meta-surface.

I. INTRODUCTION

As a transducer to transmit or receive electromagnetic (EM) wave, antenna has played an increasingly significant role in modern wireless communication systems [1-3]. In general, we need to make the main beam of an antenna point in a specific direction to achieve highly efficient transmission of EM energy into a given area. One straightforward solution to the beam pointing is adjusting the attitude of the antenna itself. This method is certainly the simplest but not feasible always, since the adjustment to antenna's attitude would require more mounting space in most cases. Moreover, if the antenna is conformally installed on the surface of aircrafts or some other mobile platforms [4-6], it would be impossible to change the antenna's attitude arbitrarily. For the reasons mentioned above, a solution with low cost and simple structure, which is capable of steering the antenna main beam without adjusting the attitude of the antenna itself, is highly desirable to modern wireless communication systems.

Adding meta-surface to antenna is a potential solution to beam steering [7-9]. Take the patch antenna for instance, of which the main beam is along the boresight direction, to steer the main beam direction without adjusting the attitude of the patch antenna, the meta-surface is supposed to work as a prism, which can deflect the EM wave radiated from patch antenna. However, because of the symmetric and uniform layout of the unit cells, most of current meta-surfaces are designed for gain enhancement or polarization conversion [10-12], where the main beam direction is still along the boresight after going through the meta-surface. Moreover, air gap between the meta-surface and antenna is usually required, leading to a bulky structure of the final antenna design. Surface of four parallel strips are fed through the slot-to-CPW transition in a very compact way in [13], composing a quasi-periodic radiating aperture. By optimizing the geometry of the quasi-periodic aperture and the slot-to-CPW transition, the fundamental TM_{10} mode and anti-phase TM_{20} mode can be efficiently excited, coupled, and matched over a broad bandwidth. However, the main-beam is still along the boresight direction after adding the quasi-periodic aperture. Similar design can also be seen in [14].

In this paper, a compact design of asymmetrical and non-uniform meta-surface for patch antenna main beam steering is proposed. The meta-surface is printed on one side of substrate and the other side (non-copper) of the substrate is placed in direct contact with the patch antenna. Therefore, on one hand, the total size of the antenna is barely changed after adding meta-surface, on the other hand, the main beam of the patch antenna can be deflected after going through the meta-surface. Moreover, the deflection angle can also be adjusted by properly designing the sizes and layout of the unit cells of meta-surface.

Submitted On: December 5, 2018
Accepted On: April 6, 2019

II. DESIGN OF META-SURFACE AND PATCH ANTENNA

The meta-surface and patch antenna are both designed using planar technology, as shown in Figs. 1. The patch antenna is designed on a double-sided substrate, with one side being the ground plane and the other side a patch as shown in Fig. 1. The meta-surface as shown in Fig. 2 is designed on a single-sided substrate, composing of a number of rectangular-strip unit cells with different lengths. The unit cells are placed periodically along the x-axis but non-uniformly along the y-axis directions on the substrate.

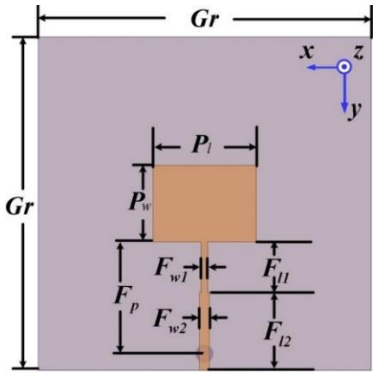

Fig. 1. Top view of patch antenna.

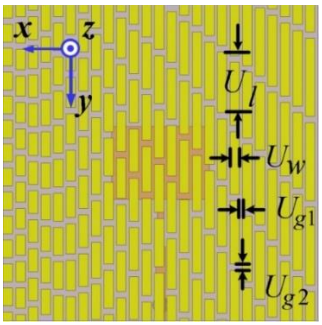

Fig. 2. Top view of non-uniform meta-surface.

The perspective view and assembly schematic are shown in Figs. 3 and 4. The non-copper side of the meta-surface is placed on the top of and in direct contact with the patch antenna. It will be shown later that the main beam of the patch antenna can be steered from +z-axis in x-z plane by adding the meta-surface. The deflection angle can be changed by adjusting the layout of the unit cells on meta-surface. The FR-4 substrate, with a thickness of 1.6 mm and a dielectric constant of ε_r = 4.4, is used for the designs of the patch antenna and the meta-surface. Optimized dimensions are listed in Table 1 and these dimensions are used to fabricate the prototypes of patch antenna and meta-surface as shown in Figs. 5 and 6.

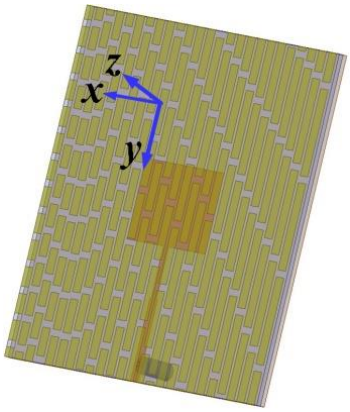

Fig. 3. Perspective view.

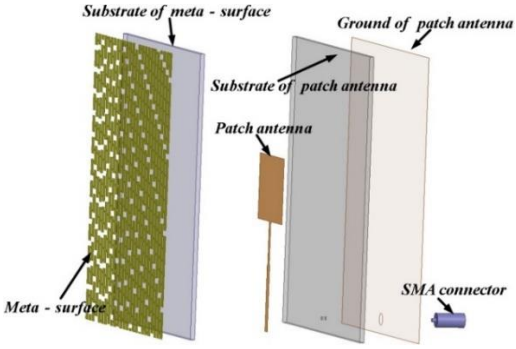

Fig. 4. Assembly schematic.

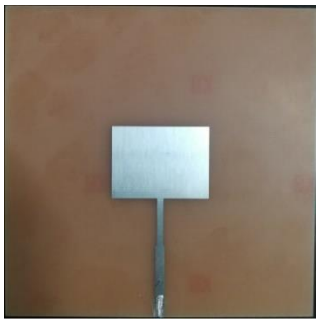

Fig. 5. Prototype of patch antenna (top view).

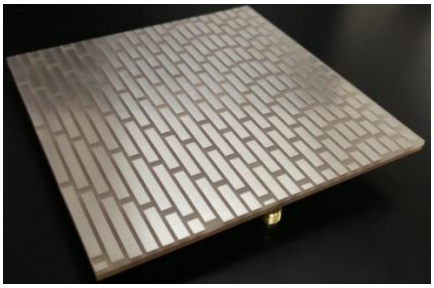

Fig. 6. Prototype of non-uniform meta-surface on patch antenna.

Table 1: Dimensions of meta-surface and patch antenna (mm)

P_l	P_w	F_{l1}	F_{l2}	F_{w1}	F_{w2}
31	23	15	23.5	2	3
U_w	U_{g1}	U_{g2}	G_r	F_p	U_l
3	1	2	100	33.5	4 - 25

III. WORKING PRINCIPLE OF NON-UNIFORM META-SURFACE

It was shown in [15] that the meta-surface placed atop of antenna would behave like a dielectric substrate and different lengths of unit cells along polarization direction would present different equivalent relative permittivity (ε_r) of the substrate. To be more specific, when strip is used as the unit cell, longer strip along polarization direction would present higher equivalent ε_r. Therefore, if we make the length of unit cells keep constant in one column and decrease gradually among different columns from right to left side as shown in Fig. 2, we are essentially placing unit cells with higher equivalent ε_r on one side (right side in Fig. 2) of the meta-surface and lay out unit cells with lower equivalent ε_r gradually to the other side. Such configuration makes the meta-surface an equivalent prism which is planar and placed very close to the patch antenna as shown in Fig. 7. Both simulated and measured results have shown that the main beam of the patch antenna is steered from +z-axis in x-z plane by a certain angle as expected.

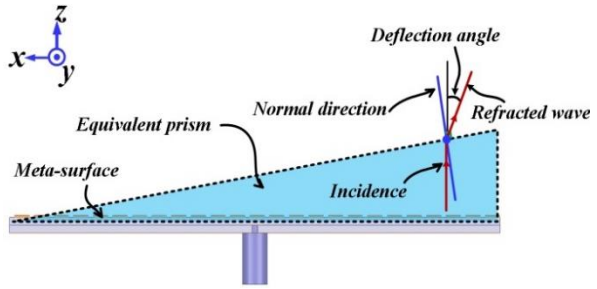

Fig. 7. Equivalent prism realized from non-uniform meta-surface.

By adjusting the variation range of the unit cell length, we can have different variation range of equivalent ε_r accordingly, the deflection angle is then changed. However, as it will be shown later, tradeoff must be made between deflection angle and overall performance of antenna, because excessive deflection angle will lead to lower peak gain and unacceptable side lobe. Moreover, the impedance matching will become more difficult when the variation range of the unit cell length is too wide. As compromise between deflection angle and other antenna performance in simulation, the main beam of the patch antenna can be steered by an angle up to 30° at operating frequencies around 2.45GHz.

IV. SIMULATED AND MEASURED RESULTS

Simulated and measured results of S11 are shown in Fig. 8. The antenna has a simulated impedance bandwidth from 2.35 to 2.5GHz, for S11 less than about -10dB. It should be noted that compared to a patch antenna working around 2.45GHz without meta-surface, the size of patch antenna in this paper is smaller, since adding the meta-surface atop of it generally shifts the operating frequency down. Besides fabrication error, the discrepancy between the simulated and measured S11s is mainly because that the relative permittivity (ε_r) of the FR4-substrate in fabrication is not exactly 4.4 as in simulation.

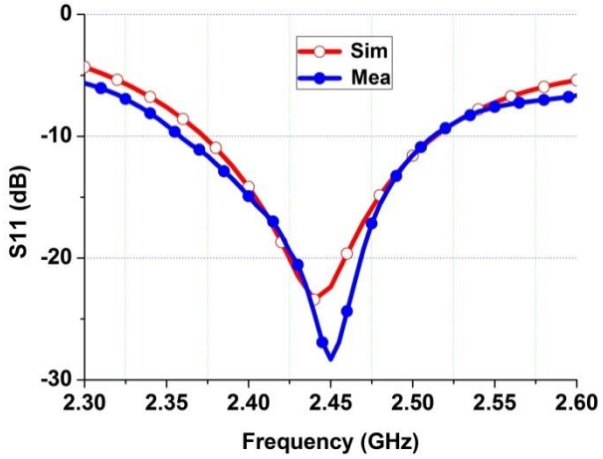

Fig. 8. Simulated and measured S11.

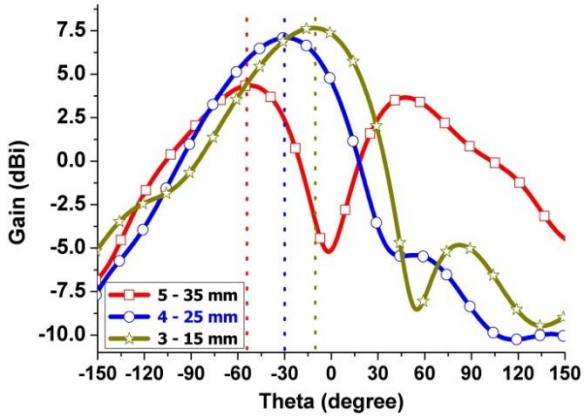

Fig. 9. Main beam directions in x-z plane for different variation range of the unit cell length.

As for radiation pattern, after adding the meta-surface, the antenna main beam is deflected from +z-axis in x-z plane as expected. As mentioned above, tradeoff must be made between deflection angle and overall performance of antenna. Therefore, here the variation

range of the unit cell length is chosen to be from 4mm-25mm, as a result, the deflection angle is -30° which can be seen in Fig. 9 indicated by blue line. To show the relationship between the deflection angle and the variation range of the unit cell length, simulated results for unit cells vary from 5mm to 35mm and from 3mm to 15mm are also shown in the same figure for comparison. It can be seen from Fig. 9 that when the variation range of unit cell length is set to be from 5mm to 35mm, the deflection angle can be further increased to -55° as indicated by red line, however, unacceptable side lobe will appear around +57°.

The polar plots of simulated and measured two-dimensional radiation patterns are shown in Fig. 10, where it can be seen that the measured realized gain reaches a peak of 7.1dBi at 2.45GHz. The half power beam-width (HPBW) is 66° (-2°to -64°). The cross-polarizations are too small to be shown in the same figure and so omitted. It should be pointed out that the co-polarization of the antenna in far-field is still linear. Result of simulated three-dimensional radiation plot is shown in Fig. 11.

The simulated and measured efficiencies are plot in Fig. 12, where it can be seen the proposed antenna has simulated and measured peak efficiencies of 95% and 91% respectively around 2.45GHz.

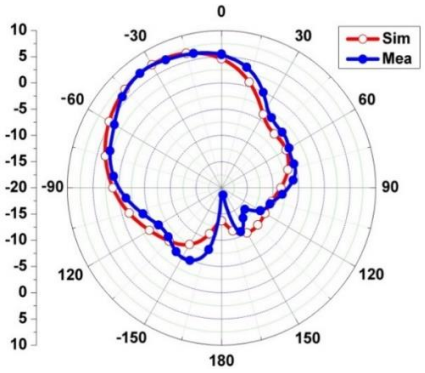

Fig. 10. Simulated and measured 2D radiation patterns.

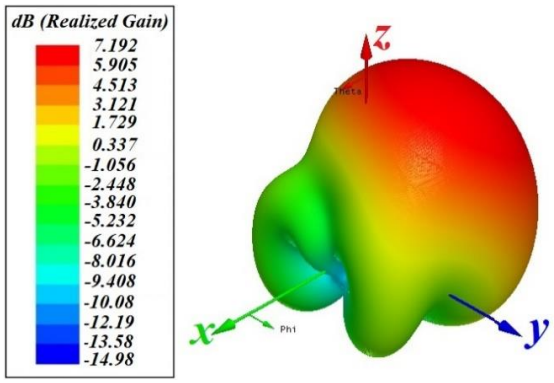

Fig. 11. 3D radiation pattern.

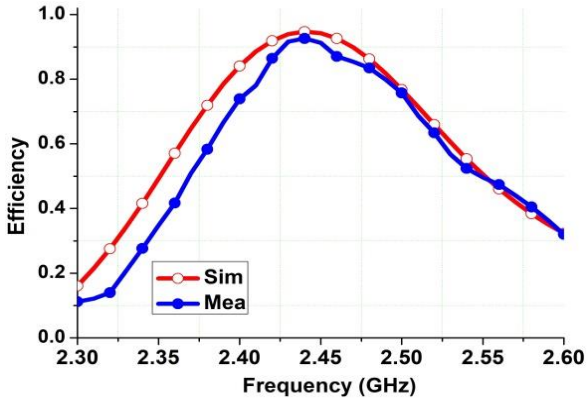

Fig. 12. Simulated and measured efficiencies.

V. CONCLUSION

Compact design of non-uniform meta-surface for patch antenna main beam steering has been proposed. Through adjusting the dimensions and layout of unit cells of meta-surface, the main beam of patch antenna can be steered by an angle up to 30°. Measured results have shown that the peak realized gain of the main beam can reach up 7.1dBi with a half power beam width of 66°, the final operating bandwidth is from 2.35 to 2.5GHz. Based on the meta-surface proposed in this paper, our future work will focus on the design of radiation-pattern-reconfigurable antenna using meta-surface, which is possible to be achieved if we use diodes or varactors to tune the electrical lengths of the unit cells on meta-surface.

ACKNOWLEDGMENT

The work was supported by the National Natural Science Foundation of China (Grant Number: 61601366), Study on the Application of Non-Uniform Meta-material in the Optimization of Antenna's Radiation Pattern.

REFERENCES

[1] B. Feng, J. Lai, Q. Zeng, and K. L. Chung, "A dual-wideband and high gain magneto-electric dipole antenna and its 3D MIMO system with metasurface for 5G/WiMAX/WLAN/X-band applications," in *IEEE Access*, vol. 6, pp. 33387-33398, 2018.

[2] W. An, Y. Li, H. Fu, J. Ma, W. Chen, and B. Feng, "Low-profile and wideband microstrip antenna with stable gain for 5G wireless applications," in *IEEE Antennas and Wireless Propagation Letters*, vol. 17, no. 4, pp. 621-624, Apr. 2018.

[3] C. Ding, H. Sun, Y. J. Guo, and R. W. Ziolkwoski, "A dual-layered loop array antenna for base station with enhanced cross-polarization discrimination (XPD)," in *IEEE Transaction on Antenna and Propagation*, vol. 66, no. 12, pp. 6975-6985, Sep. 2018.

[4] B. D. Braaten, S. Roy, I. Irfanullah, S. Nariyal, and

D. E. Anagnostou, "Phase-compensated conformal antennas for changing spherical surfaces," in *IEEE Transactions on Antennas and Propagation*, vol. 62, no. 4, pp. 1880-1887, Apr. 2014.

[5] D. Psychoudakis and J. L. Volakis, "Conformal Asymmetric Meandered Flare (AMF) antenna for body-worn applications," in *IEEE Antennas and Wireless Propagation Letters*, vol. 8, pp. 931-934, 2009.

[6] T. Yousefi, C. B. Daniel, D. T. Auckland, and R. E. Diaz, "A wideband multimode permeable conformal antenna thinner than λ/75 using advanced ferromagnetic laminate composite materials," in *IEEE Antennas and Wireless Propagation Letters*, vol. 15, pp. 1931-1934, 2016.

[7] G. Minatti, S. Maci, P. De Vita, A. Freni, and M. Sabbadini, "A metasurface isoflux antenna and potential beam reconfigurability," in *Antennas and Propagation (EUCAP)*, 2012 6th European Conference, pp. 2613-2617, 2012.

[8] C. L. Holloway, E. F. Kuester, J. A. Gordon, J. O'Hara, J. Booth, and D. R. Smith, "An overview of the theory and applications of metasurfaces: The two-dimensional equivalents of metamaterials," *Antennas and Propagation Magazine, IEEE*, vol. 54, pp. 10-35, 2012.

[9] C. L. Holloway, P. Kabos, M. A. Mohamed, E. F. Kuester, J. A. Gordon, M. D. Janezic, et al., "Realisation of a controllable metafilm/metasurface composed of resonant magnetodielectric particles: measurements and theory," *Microwaves, Antennas & Propagation, IET*, vol. 4, pp. 1111-1122, 2010.

[10] K. L. Chung and S. Chaimool, "Diamagnetic metasurfaces for performance enhancement of microstrip patch antennas," in *Antennas and Propagation (EUCAP), Proceedings of the 5th European Conference*, pp. 48-52, 2011.

[11] H. L. Zhu, S. W. Cheung, K. L. Chung, and T. I. Yuk, "Linear-to-circular polarization conversion using metasurface," in *IEEE Transactions on Antennas and Propagation*, vol. 61, pp. 4615-4623, 2013.

[12] M. E. Badawe, T. Almoneef, and O. M. Ramahi, "A true metasurface antenna," in *IEEE International Symposium on Antennas and Propagation (APSURSI)*, Fajardo, pp. 1903-1904, 2016.

[13] W. Sun, Y. Li, Z. Zhang, and P. Chen, "Low-profile and wideband microstrip antenna using quasi-periodic aperture and slot-to-CPW transition," in *IEEE Transactions on Antennas and Propagation*, 2018.

[14] W. Sun, Y. Li, Z. Zhang, and Z. Feng, "Broadband and low-profile microstrip antenna using strip-slot hybrid structure," in *IEEE Antennas and Wireless Propagation Letters*, vol. 16, pp. 3118-3121, 2017.

[15] H. L. Zhu, X. H. Liu, S. W. Cheung, and T. I. Yuk, "Frequency-reconfigurable antenna using meta-surface," in *IEEE Transactions on Antennas and Propagation*, vol. 62, pp. 80-85, 2014.

Hailiang Zhu received his B.Eng. and M.Eng. degrees from Beijing Institute of Technology, China, in 2009 and 2011, respectively, and his Ph.D. degree from The University of Hong Kong in 2015. He is currently working at the School of Electronics and Information of The Northwestern Polytechnical University, Xi'an, China. His research interests include antenna design and the study of meta-surface.

Yuwei Qiu is currently working toward the Bachelor's degree in School of Electronics and Information at the Northwestern Polytechnical University, Xi'an, Shaanxi, China. She has already been admitted by her school as a postgraduate student without taking its entrance examination and will work for her Master's degree next year. Her research interests include antenna design and application of meta-surface.

Jinliang Bai received his Bachelor's degree from Hebei University of Technology, China, in 2009, and his Ph.D. degree from Beijing Institute of Technology in 2011. He is currently a Senior Engineer at Beijing Institute of Space Long March Vehicle. His research interests include radar imaging and antenna design.

Gao Wei received his B.Eng., M.Eng. and Ph.D degrees from Northwestern Polytechnical University, Xi'an, Shaanxi, China. He is currently a full professor at the School of Electronics and Information of The Northwestern Polytechnical University, Xi'an, China. His research interests include antenna design and microwave measurement.

Design of the Tri-band UWB Microstrip Patch Antenna for WBAN Applications

Kefa G. Mkongwa, Qingling Liu, and Chaozhu Zhang

College of Information and Communication Engineering
Harbin Engineering University, Harbin, 451 150000, China
ggkefa@gmail.com, liuqingling@hrbeu.edu.cn, zhangchaozhu@hrbeu.edu.cn

Abstract ─ The increasing commercialization of the Wireless Body Area Networks (WBAN) in various healthcare facilities poises for the growing network resources competition in the Physical layer. In remote health monitoring, energy scarcity and limited bandwidth compromise demand for optimized network lifetime and high data rate of the multimedia information with reduced spectral noises. In this paper, we have designed a compact Tri-band antenna with three rejection bands for WBAN applications. The rectangular antenna patch is etched on RT/Duroid substrate. The patch consists of flat chamfers, semi-circular, and elliptical slots. The simulated antenna resonates at three distinct frequencies; 6.39 GHz, 7.15 GHz, and 9.89 GHz each operating at the ultrawideband (UWB) with a return loss ($|S_{11}|$) > 10 dBm. The antenna is designed using Computer Simulation Technology software (CST-2016) and analyzed for its return loss, field radiation, bandwidth (cumulative BW, 3473.8 MHz), and voltage standing wave ratio (VSWR<1.5). Simulation results show antenna performance characteristics which suit various WBAN applications.

Index Terms ─ Data rate, frequency bands, Quality of Service (QoS), radiation patterns, return loss (S_{11}), Ultra-wideband (UWB), Voltage Stand Wave Ratio (VSWR), Wireless Body Area Networks (WBAN).

I. INTRODUCTION

Advances in research for Wireless sensor networks (WSN) envisaged the development of Wireless body area networks (WBAN). Currently, WBAN uses biological sensors for real-time remote health monitoring of the human body vital signs. Monitored physiological signs may include heart rate, blood pressure, blood sugar, blood oxygen concentration, ECG, and EEG among others [1-2]. The primary element of the WBAN is the wireless body sensor embedded with a miniaturized radiating antenna [3]. Biological sensors usually positioned in the body as implants or a wearable device are used to acquire physiological parameters for noninvasive medical diagnosis from the remote health facilities.

In the remote health facility, the accurate prognosis of the health situation depends on the quality of the received data. Although in the transmission media, data packets are highly impeded by several factors including anomalies as a result of packet collision, latency, energy scarcity, intrusion, interference, transmission link drop out and tissue-specific absorption rate (SAR) [4-5].

WBAN sensors are battery powered and are reportedly consuming more energy during transmission and detection of the wireless signals. Therefore, deployment of low power transceivers and power budget consideration during network design is necessary [6]. Sometimes, energy requirement and network resources management in WBAN depends on the nature of the monitored body organ. Since various body organs generate data with different rates, so communicating data with varying data rates demand compatible transmitters.

In this view, a significant volume of data in the transmission channel affects successful data delivery and reduced throughput due to interference, power and bandwidth limitation of the network infrastructure [7-9]. As far as network resource competition in WBAN is increasing in parallel with its commercialization, in this work, we have proposed a multi-band UWB antenna which resonates at three distinct frequencies to support higher data rates with minimal spectral noises and operational power requirement.

The contribution of this work focus on the design of the compact and low cost Tri-band UWB microstrip patch antenna with a reduced size by ~25% of the analytical design, isolation of the rejection bands using slots and cuts which subsequently enhanced impedance matching and, bandwidth enhancement whereas distinct operational bands support bandwidth >500 MHz each.

The organization of this work consists of five sections; Section I gives the introduction about WBAN network requirement, Section II briefs about UWB antennas, Section III discusses the materials and antenna design methods, Section IV discusses simulation results,

Submitted On: October 12, 2018
Accepted On: April 6, 2019

findings, and Section V conclude our work.

II. ULTRA-WIDEBAND ANTENNAS

Rising demand for eHealth multimedia services and future generation communication inquires broader bandwidth in the transmission channel. Since IEEE 802.15.6 standard for WBAN supports UWB spectrum in its PHY layer, the enormous demand for higher data rates in the wireless channel influence UWB antenna design for various QoS aware healthcare applications [10-11]. One of the characteristics of the PHY layer channels includes the bandwidth of ~500MHz and a data rate between 971.4Kbps - 15.6 MHz. Antennas supporting channel bandwidth greater than 500MHz (BW>=0.5GHz) or with a percent bandwidth of more than 20% are said to operate in the UWB spectrum [12].

UWB antennas have merits including; low power consumption, support for higher data rates and low interference probabilities. These features make UWB suitable for both Personal area networks (PAN) and BAN [13-14]. The UWB spectrum (3.1 - 10.6 GHz) support a range of wireless applications (e.g., radars and satellites) which ease WBAN mobile ambulatory services depending on the country of implementation [15].

Microstrip patch, unlike conventional antenna, is conformal; it can be deformed into different shapes and geometries to meet UWB application flexibility using notches [16]. Antenna notches are implemented through bending or introducing slots on the patch and ground plane; this alters its radiation characteristics and impendence matching. Notched antennas limit radio frequency interference at specific frequency bands. The significance of using slots in Notched antennas is to isolate interfering frequencies from operational frequency bands [17]. Slotted patch has existed in different shapes like a spearhead, U, E, H, F, PIFA slots and spiral antennas with distinct mechanisms of feeding. Various slitting techniques, use of thick substrate, stacked patch and parasitic elements have proven to improve bandwidth, radiation efficiency, gain and minimize scattering parameters [18-21].

Numerous research findings propose different design materials and recommend a minimum requirement to ensure better gain and minimum return loss while meeting body compatibility [22]. Authors in [23-24], suggests that WBAN antenna must be durable and portable for body implants and wearables with lower Specific Absorption Rate (SAR) for personal radiation safety.

Single band UWB signals (3.1-10.6 GHz), can be interfered by Wireless Local Area Network (WLAN, 5.2 - 5.8 GHz), and X-Band (7.25 - 8.4 GHz) for satellite communications which exist within UWB spectrum hence threatening data security and quality of service [25]. To avoid such impeding issues implementation of the multi-band UWB is necessitated.

To achieve minimal spectrum noises and low power requirement in the transmission channel, this work, used similar design criteria as in ([9]) and ([12]) to design an antenna with hybrid characteristics. We have introduced flat chamfers and circular cuts on the patch and an aperture on the ground plane to design an ultra wideband (UWB) microstrip patch antenna using Finite Difference Time Domain (FDTD).

III. MATERIALS AND DESIGN METHODS

The proposed rectangular Microstrip patch antenna is designed using lossy RT/duroid® 5880LZ substrate with dielectric constant and loss tangent (Tanô) of 1.96 and 0.0019 respectively as shown in Fig. 1. We preferred RT/Duroid due to its low cost, low moisture absorption, wide operating temperature range (-55ºC - 260ºC), excellent chemical resistance and uniform electrical properties over the frequency band [26]. We use Annealed copper with a thickness of 0.035mm in both radiating surfaces (patch) and a background plane.

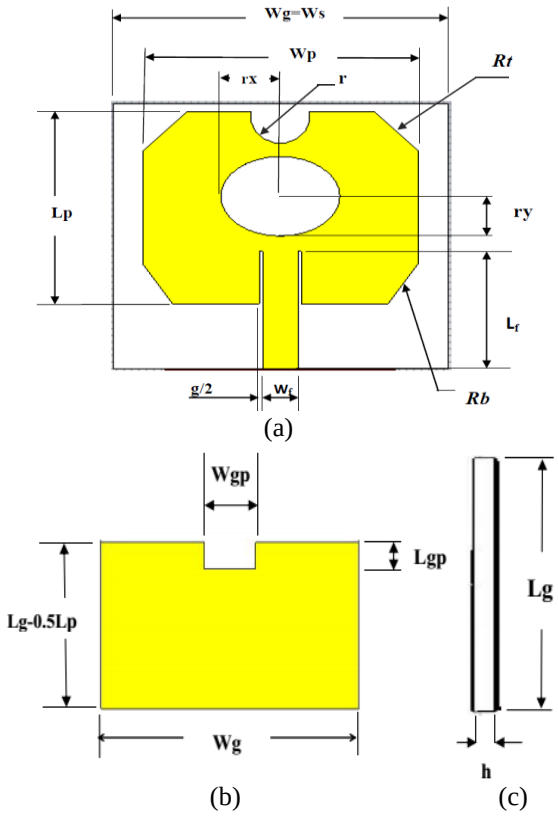

Fig. 1. Proposed antenna structure, (a) front view; consisting of patch and substrate dimensions. (b) Back view (ground plane); including the height of the ground plane and the narrow slot dimensions (c) side view.

Table 1: Antenna dimensions

Dimensions (mm)			Dimensions (mm)		
Parameter	**Calculated (initial)**	**Proposed**	**Parameter**	**Calculated (initial)**	**Proposed**
L_p	42.77	29	N_d	12.34	7.87
W_p	50.33	37	W_{gp}	-	9
L_s	52.73	40	L_{gp}	-	0.5
W_s	60.29	45	R_b	-	$4.7*45^0$
L_g	52.73	40	R_t	-	$6*45^0$
W_g	60.29	45	r_x	-	8
W_f	4.164	4.7	r_y	-	6
L_f	22.291	17.69	h	1.66	1.66
g	1	0.9	r		4

A. Mathematical modeling

An antenna was initially designed to resonate at 3.1 GHz, with a height of substrate (h=1.66). Other antenna dimensions were calculated using the following equations as stipulated in [27-28]. Patch width and length were obtained using equations (1) and (2):

$$W_P = \frac{c}{2 * f_r * \sqrt{\frac{\varepsilon_r + 1}{2}}}, \tag{1}$$

Where ***c*** is the speed of the electromagnetic wave in free space, $\boldsymbol{\varepsilon_r}$ is the permittivity in free space and $\boldsymbol{f_r}$ is the antenna resonant frequency.

Length of the patch is affected by fringing fields due to varying dielectric constant when electric fields propagate between air and substrate material along with radiating surfaces. Fringing fields results into the incremented length of the patch by 2*ôL; actual patch length is determined based on the effective length as follows:

$$L_p = L_{eff} - 2\partial L. \tag{2}$$

Where,

$$\varepsilon_{reff} = \frac{\varepsilon_r + 1}{2} + \frac{\varepsilon_r - 1}{2}\left[1 + 12\frac{h}{w_p}\right]^{-0.5}, \tag{3}$$

$$L_{eff} = \frac{c}{2 * f_r * \sqrt{\varepsilon_{reff}}}, \tag{4}$$

$$\partial L = 0.412 * h\left[\frac{\varepsilon_{reff} + 0.3}{\varepsilon_{reff} - 0.258}\right]\left[\frac{\frac{w_p}{h} + 0.264}{\frac{w_p}{h} + 0.8}\right]. \tag{5}$$

Equations (6) and (7) evaluates the length and width of the substrate:

$$L_s = L_p + 6h, \tag{6}$$

$$W_s = W_p + 6h, \tag{7}$$

Length of the microstrip feed line is obtained using equation (8):

$$L_f = \frac{c}{4 * f_r * \sqrt{\varepsilon_{reff}}}. \tag{8}$$

Table 1 shows calculated and proposed antenna dimensions respectively. Antenna dimensions were modified to meet minimum size requirements and operational frequency bands.

B. Design modification

In this work, we use hybrid design criteria as applied in the papers presented by Award et al. ([9]) and Turkmen et al. ([12]). In our design, we only considered methods used for bandwidth enhancement with some alteration of the design approach and materials. In [9], authors enhanced antenna bandwidth using round step cuts on the patch with similar dimensions while in our work, we introduced flat chamfer with different sizes on the edges of the radiating planes as illustrated in Table 1 ($\boldsymbol{R_t > R_b}$).

The implementation of the flat chamfers, round cut and the elliptical slot on the patch extended antenna radiation surface as shown in Fig. 2 (a), therefore apart from enhancing the bandwidth of the remaining frequency bands it also eliminated frequencies in the narrowband spectrum. The impact of slots and chamfers formed three notch bands between 0 - 6.12 GHz, 6.8 - 6.9 GHz and 8 - 9.47 GHz respectively.

Since the antenna could not resonate at UWB in all the frequency bands, we introduced a narrow slot on the ground plane as proposed by [12] to further extend operational antenna bandwidth and S_{11} far below -10dB. The antenna structure in Fig. 2 (b) shows the proposed antenna ground plane reduced by half the patch length (Lg-0.5Lp) with a narrow slot of dimensions Wgp*Lgp mm^2.

In practical application, WBAN requires smaller antenna size. Whereas, using lower permittivity substrate results into larger size antenna. This work focused on a well performing, compact and portable antenna. Therefore both substrate and patch dimensions were scaled down

by ~25% of the original design as demonstrated in Table 1. The proposed antenna dimensions were 40×45×1.66 mm^3 for the substrate.

IV. SIMULATION RESULTS

We ran simulations using Computer Simulation Technology (CST-2016) software. Simulation of the proposed antenna considered essential performance parameters including far-field radiation patterns, reflection coefficient and voltage standing wave ratio on free space.

After simulation, three sharp narrow troughs deep below -10dB at 6.39 GHz, 7.15 GHz, and 9.89 GHz were obtained. The three narrow, deep points of the S_{11} proves that the proposed antenna is a Tri-band resonating at three distinct frequencies.

A. Radiation patterns

Antenna E and H-field radiation patterns were simulated as shown in Fig. 2 and 3. Figure 2 (a) shows electric surface current on the patch, where higher field intensities (dB) indicated in yellow concentrates on the patch edges, notch gap, semicircular and elliptical slot.

During simulation, setting a narrow notch gap widened the operational bandwidth with gradual distortion on antenna return loss. Similarly, a thin slot at the middle of the ground plane was introduced. Figure 2 (b) demonstrates the impact of a narrow slot in the ground plane to the antenna field radiation patterns. A slight variation of the size of the aperture in the background plane highly contributed to the bandwidth enhancement of the antenna. 2D radiation patterns of the antenna are as shown in Fig. 3.

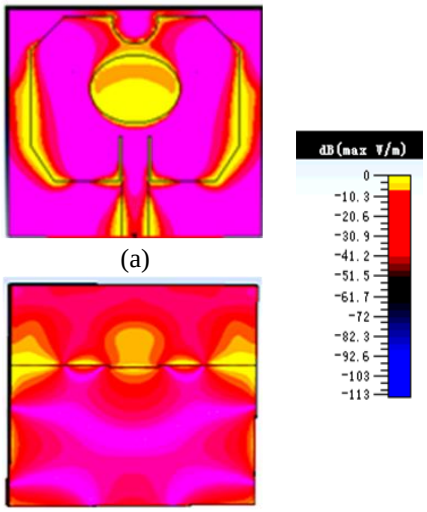

(a)

(b)

Fig. 2. E-Field distribution (a) on the patch, and (b) on the background plane respectively.

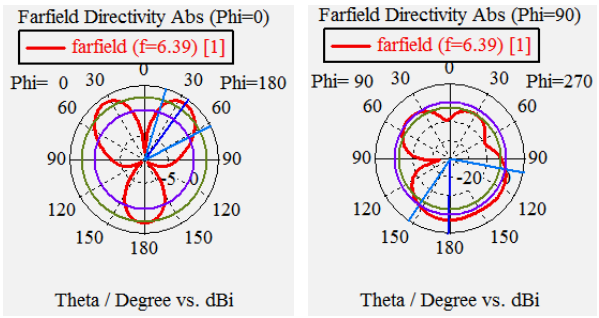

(a)

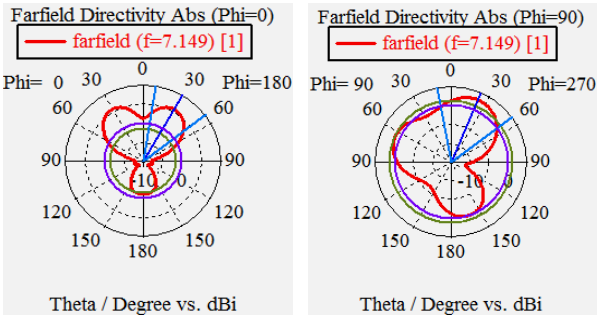

(b)

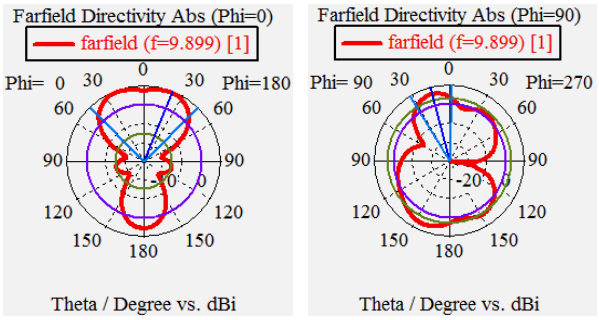

(c)

Fig. 3. Far-field radiation patterns for (a) 6.39 GHz, (b) 7.15 GHz, and (c) 9.89 GHz respectively.

B. Antenna bandwidth and return loss (S11)

Amount of power reflected from the antenna due to termination mismatch determines the performance of the designed antenna. As S_{11} become, much smaller antenna performance improves due to lower losses. In this paper, a microstrip patch with insert feed was intended. Before design modification, the notch gap, ***g*** was initially set to 1mm. An antenna bandwidth became very narrow despite good S_{11} values at some center frequencies as demonstrated in Fig. 4 (a).

In the proposed design, we reduced the size of the notch gap '***g'*** and widened the microstrip feed line (Table 1) which subsequently improved $|S_{11}|$ and antenna bandwidth as demonstrated in Fig. 4 (b).

Simulation results of the proposed design showed, free space return loss; -44.16 dB, -24.34 dB and -18.50 dB and the operational bandwidth of the antenna at the

resonant frequencies; 653.3 MHz (6.39 GHz), 1044.7 MHz (7.15 GHz) and 1775.8 MHz (9.89 GHz) respectively.

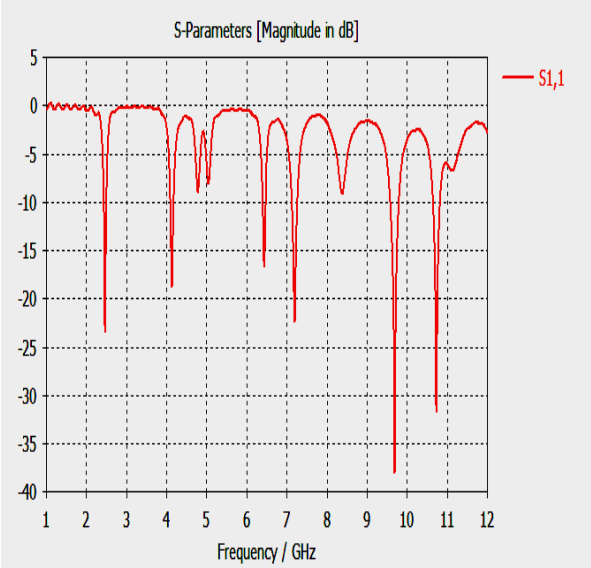

(a)

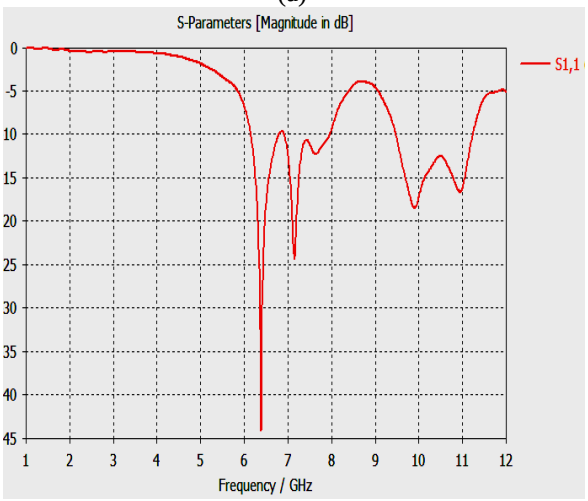

(b)

Fig. 4. Return loss (S_{11}) of the antenna: (a) based on calculation before modification, and (b) proposed antenna characteristics after modification.

C. Voltage Standing Wave Ratio (VSWR)

The quality of the antenna termination determines its reflection coefficient. Proper impedance matching at the antenna feed point (50Ω) results to lower reflection loss and subsequently the voltage standing wave ratio.

During simulation, the magnitude of the S_{11} improved proportionally with the voltage standing wave ratio. Lower VSWR shows how well the antenna impedance is matched to the transmission line characteristic impedance. Simulation results show that at the resonant frequencies the VSWR remained below standard limits (VSWR<1.5) as demonstrated in red dotted line Fig. 5.

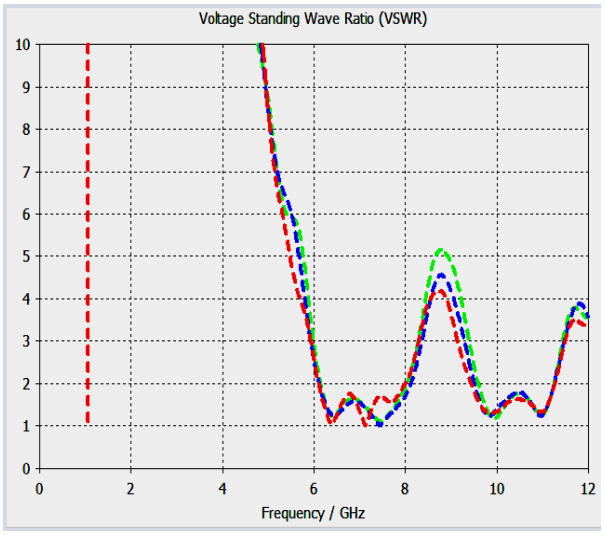

Fig. 5. VSWR values at the resonant frequencies.

Antenna dimensions, support bandwidth and return loss of the referenced design method are tabulated comparatively against the proposed model in Table 2. The antenna features varied from one another due to the type of the simulation software or slight variation of the substrate material, dielectric constant and overall antenna dimensions. Apart from the lowest dielectric constant, the thickness of the antenna remained nearly equal to those of the higher permittivity values without any performance constraints. Lower dielectric constant of the substrate material results into larger antenna size, tabulated results show that the antenna dimension remained smaller despite the analytical design requirement.

Table 2: Comparison of common antenna features

Ref. #	Substrate	Size mm^3	BW GHz	Highest S_{11} (dBm)
[9]	FR4, $\varepsilon_{r=4.4}$	30 x 35 x1.6	8.28	-47 (HFSS)
[12]	RT/duroid 5880, $\varepsilon_{r=2.2}$	38 x 50 x 1.57	4.171	-26.3 (CST)
Prop.	RT/duroid 5880, $\varepsilon_{r=1.96}$	40 x 45 x 1.66	3.474	-44.16 (CST)

V. CONCLUSIONS

In this work, we have designed a Triple Ultra Wide Band (Triple-UWB) patch antenna which resonates at 6.39 GHz, 7.15 GHz and 9.89 GHz. The entire cumulative bandwidth of the proposed antenna subdivides into three frequency bands (653.3 MHz, 1044.7 MHz, and 1775.8 MHz respectively) each operating at UWB. The design

approach by introducing chamfers, elliptical and circular slots on the patch with a minor rectangular aperture on the background plane has highly improved antenna radiation properties as well as the bandwidth and return loss. The three separate bands ease frequency planning and usage for various off-body WBAN applications. The notched frequency bands were under the influence of the thickness of the substrate and a very narrow notch gap. Using UWB antenna, WBAN applications can use uniform energy for signal communication which ensures reduced spectrum noises, longer network lifetime and better quality of service.

ACKNOWLEDGMENT

This research was funded by the National Key Research & Development Project, "Non-contact Noninvasive Cardiac Magnetic Resonance Imaging Diagnosis System," Project No. 2016YFC0101700.

REFERENCES

[1] M. Ghamari, B. Janko, R. S. Sherratt, W. Harwin, and R. Piechockic, "A survey on wireless body area networks for eHealthcare systems in residential environments," *Sensors*, vol. 16, no. 6, p. 831, 2016.

[2] M. Waheed, R. Ahmed, W. Ahmed, M. Drieberg and M. M. Alam, "Towards efficient wireless body area networks using two-way relay cooperation," *Sensors*, vol. 18, no. 2, p. 565, 2018.

[3] S. L. Cotton, R. D'Errico, and C. Oestges, "A review of radio channel models for Body-centric communications," *Radio Sci*., vol. 49, pp. 371-388, 2014.

[4] H. Sun, Z. Zhang, R. Q. Hu, and Y. Qian, "Wearable communications in 5G: Challenges and enabling technologies," *arXiv:*1708.05410v2 [cs.NI], 22 Dec. 2017.

[5] J. Lilja, P. Salonen, T. Kaija, and P. de Maagt, "Design and manufacturing of robust textile antennas for harsh environments," *IEEE Transactions on Antennas and Propagation*, vol. 60, no 9, Sep. 2012.

[6] M. Hamalainen, et al., "ETSI TC smart BAN: Overview of the wireless body area network standard," *15th International Symposium on Medical Information and Communication Technology (ISMICT)*, 2015.

[7] Y. Liao, M. S. Leeson, M. D. Higgins, and C. Bai, "Analysis of in-to-out wireless body area network systems: Towards QoS-aware health internet of things application," *Electronics*, vol. 5, no. 38, 2016.

[8] S. Hussain, "Current trends in antenna design for body-centric wireless communication," *International Journal of Science and Engineering Research*, ISSN 2229-5518, vol. 3, no. 6, June 2012.

[9] N. M. Award and M. K. Abdelazeez, "Multislot microstrip antenna for ultra-wideband applications," *Journal of King Saudi University of Engineering Sciences*, vol. 30, no. 1, pp. 38-45, Jan. 2018.

[10] S. Ullah, M. Ali, Md. A. Hussain, and K. Sup Kwek, "Applications of UWB Technology," *arXiv*:0911. 168v3 [cs: NI], 2 Apr. 2016.

[11] Md. S. Bin Alam and S. Moury, "Conversion of an ultra-wide band (UWB) antenna to dual band antenna for wireless body area network (WBAN) applications," *3rd International Conference on Informatics, Electronics, and Vision*, 2014.

[12] M. Turkmen and H. Yalduz, "Design and analysis of quad-band grid array microstrip antenna at UWB and ISM channel frequencies for WBAN operations," *IEEE-2017, 10th International Conference on Electrical and Electronics Engineering (ELECO)*, 2017.

[13] K. Shafique, B. A. Khawaja, M. A. Tarar, B. M. Khan, M. Mustafa, and A. Raza, "A wearable ultra-wideband antenna for wireless body area networks," *Microwave Application Technology Letters*, vol. 58, no.7, July 2016.

[14] I. Gill and F. Garcia, "Wearable PIFA antenna implemented on the jean substrate for wireless body area network," *Journal of Electromagnetic Waves and Application*s, 31:11-12, pp. 1194-1204.

[15] A. H. Bondok, A. M. El-Mohandes, A. Shalaby, and M. S. Sayed, "A low complexity UWB-PHY baseband transceiver for IEEE 802.15.6 WBAN," *IEEE-2017, 30th IEEE International System on Chip Conference (SOCC)*, 2017.

[16] A. W. Alshareefa, S. F. Amleb, N. M. Awadc, and M. K. Abdelazeezd, "UWB Antenna for WLAN band rejection," *Jordan Journal of Electrical Engineering*, vol. 4, no. 2, pp. 62-70, 2018.

[17] J. Dong, Q. Li, and L. Deng, "Compact planar ultra wide-band antenna with 3.5/5.2/5.8GHz triple band-notched characteristics for the internet of things applications," *Sensors*, vol. 17, no. 349, 2017.

[18] N. S. Reddy, K. S. Naidu, and S. A. Kumar, "Performance and design of spear-shaped antenna for UWB band applications," *Alexandria Engineering Journal*, 2017.

[19] C. Liu, Y. Guo, and S. Xiao, "review of implantable antennas for wireless biomedical devices," *Forum for Electromagnetic Research Methods and Application Technologies (FERMAT)*.

[20] A. A. Roy, J. M. Mom, and G. A Igwue, "Enhancing bandwidth of a microstrip patch antenna using slots shaped patch," *American Journal of Engineering Research (AJER)*, vol. 2, no. 9, pp. 23-30, 2013.

[21] S. Bhattacharjee, S. Maity, S. K. Metya, and H. T. Bhunia, "Performance enhancement of an implant-

able medical antenna using differential feed technique," *Engineering Science and Technology an International Journal*, vol. 19, pp. 642-650, 2016.

[22] M. Nachiappan and T. Azhagarsamy, "Design and development of dual-spiral antenna for implantable biomedical applications," *Biomedical Research*, vol. 20 no. 12, pp. 5237-5240, 2017.

[23] B. Ivsic, G. Golemac, and D. Bonefacic, "Performance of wearable antenna exposed to adverse environmental conditions," *IEEE 2013, 21st International Conference on Applied Electromagnetics and Communications (ICECom)* - Dubrovnik, Croatia (2013.10.14-2013.10.16) ICECom, 2013.

[24] P. Soontornpipit, "A dual-band compact microstrip patch antenna 403.5MHz and 2.45 GHz ISM for on-body communications," *2016 International Electrical Engineering Congress* (iEECON2016), Chiang Mai, Thailand, 2-4 Mar. 2016.

[25] M. Jahanbakht and A. A. Neyestanak, "A survey on recent approaches in the design of Band notching UWB antennas," *Journal of Electromagnetic Analysis and Applications*, 4, pp. 77-84, 2015.

[26] A. Khan and R. Nema, "Analysis of five different dielectric substrates on microstrip patch antenna," *International Journal of Computer Applications (0975-8887)*, vol. 55, no. 18, Oct. 2012.

[27] M. T. Ali, N. Ramli, M. K. M Salleh, and M. N. Md. Tan, "A design of reconfigurable rectangular microstrip patch antenna," *2011 IEEE International Conference on System Engineering and Technology (ICSET)*, 2011.

[28] S. Sharma, C. C. Tripathi, and R. Rishi, "Impedance matching techniques for microstrip patch antenna," *Indian Journal of Science and Technology*, vol. 10, no. 28, July 2017.

Kefa G. Mkongwa received his B.Eng. in Electronics and Communication Engineering and M.Eng. in Signal and Information Processing from St. Joseph University of Engineering and Technology in Tanzania and Tianjin University of Technology and Education in Tianjin, China in 2009 and 2013 respectively. He is currently pursuing Ph.D. research studies in Signal and Information Processing at Harbin Engineering University. His current area of research interests is the Internet of Things, Microstrip patch antennas, Wireless sensor networks and Wireless Body Area Networks (WBAN).

Qingling Liu received B.S. and M.S. degrees in Signals and Information Processing from the College of Information and Communication Engineering, Harbin Engineering University, Harbin, China in 2000 and 2004 respectively.

She completed her Ph.D. degree in Computer and Software Engineering, Kumoh National Institute of technology, Korea in 2012. Since 2018, she holds a Deputy Director of the Institute in the College of Information and Communication Engineering.

Her research interests include Wireless Network Technology, Internet Information Security, Artificial Intelligence, Information Technology, Routing in MANETs and Wireless Sensor Networks.

Chaozhu Zhang received his B.S. degree in Electronics and Information Engineering, M.S. degree in Communications and Information Systems and a Ph.D. degree in Signal and Information Processing from Harbin Engineering University in 1993, 2002 and 2006 respectively.

Since 2009, he has been a Professor with the Harbin Engineering University, where he now holds an Associate Dean in the College of Information and Communication Engineering. Also, he is an academician of Aerospace Society and a member of the Institute of biomedical, Heilongjiang Province.

His research interests include radar signal processing, biological signal processing, and communication engineering.

RF MEMS Switches Enabled H-Shaped Beam Reconfigurable Antenna

Wazie M. Abdulkawi [1], Abdel-Fattah A. Sheta [1], Waqar A. Malik [2], Sajjad U. Rehman [3], and Majeed S. Alkanhal [1]

[1] Department of Electrical Engineering, King Saud University, Riyadh, KSA
{walkadri, asheta, majeed}@ksu.edu.sa

[2] Department of Electrical Engineering, Abasyn University Islamabad, Pakistan
waqar.ahmad@abasynisb.edu.pk

[3] Department of Electrical Engineering, Qurtuba University, Dera Ismail Khan, Pakistan
sajjad.rehman@qurtuba.edu.pk

Abstract ─ This work presents a novel RF MEMS-based pattern reconfigurable antenna capable of steering beam in three different directions. The proposed H-shaped microstrip antenna is based on the basic structure of a dipole antenna and forms an 'H' shape by combining two dipoles in reverse fashion. The proposed antenna provides pattern reconfigurability at a single resonant frequency of 1.8 GHz, that lies in L-band. The optimized simple structure of the proposed antenna allows easy incorporation of single pole single throw (SPST-RSMW101) RF MEMS switches. The antenna is simulated using electromagnetic (EM) simulators (HFSS and IE3D). The proposed antenna is fabricated on RT Duroid substrate with 2.2 dielectric constant, and 1.75 mm thickness. The ON and OFF state of RF MEMS switches enables three different scenarios of operation with peak gains of 6.25 dBi, 6.28 dBi, and 4.01 dBi respectively. For validation of pattern reconfigurability the antenna is tested using time domain antenna measurement system and found to have a good agreement with the simulated results.

Index Terms ─ Beam steering, low profile, microstrip, reconfigurable antenna, RF MEMS switches.

I. INTRODUCTION

Recent advances in modern multi-directional radar systems and wireless applications demand high performance reconfigurable antennas. Reconfigurability in antennas can be achieved in frequency of operation, pattern, polarization and combinations of them [1]. Among the reconfigurability techniques, pattern reconfiguration devises the antenna beam in different axial directions for the same operating frequency. This ensures the pattern reconfigurability using the same antenna. The beam steering antennas are widely used in satellite, telemedicine, and radar communications [2-4].

Reconfigurability in antennas can be achieved by use of RF tunable components like radio frequency microelectromechanical system (RF MEMS) switches [1, 5, 6], Varactor diodes [7], and PIN diodes [8-10]. The RF MEMS have been proposed for incorporation into reconfigurable antennas for the last 2 decades. Since then many designs are reported [11-14] due to its profound advantages like electromechanical isolation and minimal power consumption, in comparison to conventional semiconductor devices.

The beam steering antennas can be classified into two broad categories: firstly, single antenna element configuration [15] and secondly the adaptive array antenna system [16, 17]. The size of a single antenna configuration is smaller in comparison to the array configuration. However, the gain achieved with the array configuration is higher than single antenna system [15].

In [18], radiation pattern reconfigurable antenna based on square spiral-microstrip is presented. The antenna is capable to reconfigure the radiation patterns between end-fire and broadside with the help of two Radant single-pole single throw RF MEMS switches. Another MEMS based reconfigurable Vee antenna was presented in [11], that steered the radiation beam in different directions at 3 GHz and 17.5 GHz.

In [12], two pattern reconfigurable antennas based on four RF MEMS switches is presented, operating at 6 GHz and 10 GHz. The gain of both the antennas reported is in the range of 3-6 dBi. The antenna composition is based on rectangular spiral microstrip along with the RF MEMS monolithically integrated and packaged in the same substrate. The physical length of the rectangular spiral is varied by activating the switches and thus achieving reconfigurability in radiation pattern for the same antenna. The authors in [19] presented an E-shaped frequency reconfigurable antenna operating at 1.9 GHz and 2.4 GHz with 30.3% bandwidth. The bandwidth was

Submitted On: November 8, 2018
Accepted On: April 3, 2019

increased by introducing slots that forms the E-shape of the final structure.

In this paper, a new beam steering H-shaped antenna is presented. RF-MEMS switches are used to change the physical arm length of the H-shaped antenna to achieve the reconfigurability in its radiation pattern. The proposed antenna is able to steer the beam in two different directions in the elevation plane. The simulation results are carried out by using two artificial switches (S_1 and S_2), while the RF-MEMS are placed instead in fabrication. The proposed H-shaped pattern reconfigurable antenna is compact in size and has good agreement in its simulation and measured results.

II. DESCRIPTION OF THE ANTENNA

The composition of antenna is based on basic dipole antenna structure. However, two radiating elements opposite to each other are incorporated for different axial direction coverage. The geometry of the antenna is shown in Fig. 1. The right dipole and left dipole forms an H-shape and are activated using two RF MEMS switches (S_1 and S_2). The proposed pattern reconfigurable antenna operates at 1.8 GHz that lies in L-band. The design specifications of the proposed H-shaped pattern reconfigurable antenna are summarized in Table 1.

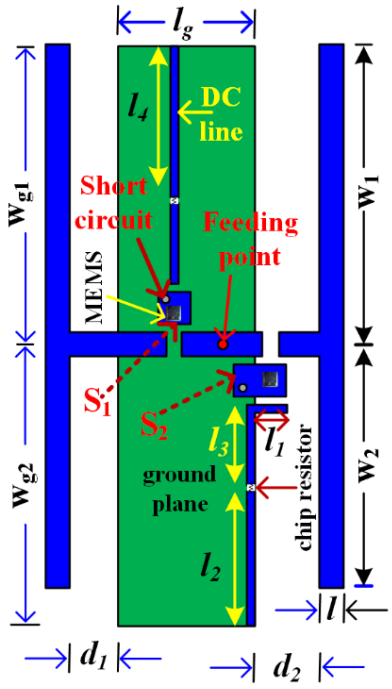

Fig. 1. The geometry of the proposed H-shaped antenna with MEMS.

The simulation of the proposed antenna is carried by Ansoft HFSS and Zeeland IE3D. The proposed antenna is fabricated on RT Duroid-5880 substrate with a dielectric constant of 2.2, loss tangent of 0.0009 and thickness of 1.57 mm. The width of the microstrip line is calculated using the Line Gauge of EM software IE3D. The resonant frequency of the proposed antenna depends on the total length of the microstrip line. The total length of the antenna (l_{tot}) can be calculated as:

$$l_{tot} = w_1 + w_2 . \quad (1)$$

In order to get accurate dimensions and accurate response of the proposed antenna, the ratio between w_1 and w_2 should be roughly 1.23. Keeping the ratio between w_1 and w_2 constant to about 1.23 and the width of the strip line (l) constant, the equation for the resonant frequency (f_0) of the antennas can be derived using the same procedure explained in [20, 21] as:

$$f_0 = \frac{c}{1.67 \times l_{tot} \sqrt{\varepsilon_e}}, \quad (2)$$

where ε_e is the effective dielectric constant, and c is the speed of light in free space.

Table 1: Proposed antenna parameters

Parameters	Value (mm)	Parameters	Value (mm)
l	3	d_1	6
w_1	37.25	d_2	8
w_2	30.25	l_1	4
l_g	17	l_2	10
w_{g1}	37	l_3	16.7
w_{g2}	35	l_4	18.7

The antenna consists of an optimized ground plane with dimensions of 17×72 mm². The H-shaped patch has dimensions of 37×67.5 mm², where the width of each side of the H-shaped patch is 3 mm. The overall dimensions of the proposed antenna including the ground plane are 37×72 mm².

Two Radant MEMS single pole single through (SPST) RF MEMS switches are used for integration with the H-shaped antenna. The RF MEMS switches are highlighted in the fabricated version of proposed antenna as shown in Fig. 2. The RF MEMS switches (SPST-RMSW101) has a frequency range up to 12 GHz.

Figure 3 shows the close-up photograph of the RF-MEMS switch placement. One RF MEMS switch is placed on the rectangular patch with dimensions of 6.5×4 mm², while the other switch is placed on a square patch of 4×4 mm² size. The DC lines of 1 mm width each, as shown in Fig. 2, are used to apply the DC voltage. The switches are activated by applying DC voltage of 90 volts, while the Gate, source and drain are connected to the antenna arms with three bonding wires as shown in Fig. 3. Each RF MEMS switch is also connected to the ground to activate it. In addition, a 220 kΩ chip resistor is placed in each DC line to limit the current flow for the RF MEMS switches.

The operation of the antennas is therefore based ON and OFF state of the switches (S1 and S2). Thus the RF MEMS switches are placed in such a way that the left arm, right arm or both arms of the H-shape antenna can be activated or de-activated accordingly. This enables the antenna to steer its beam in 3 different directions. In case 1 switch 1 is ON and switch 2 is OFF, in case 2 switch 1 is OFF and switch 2 is ON, and in case 3 both switches are ON.

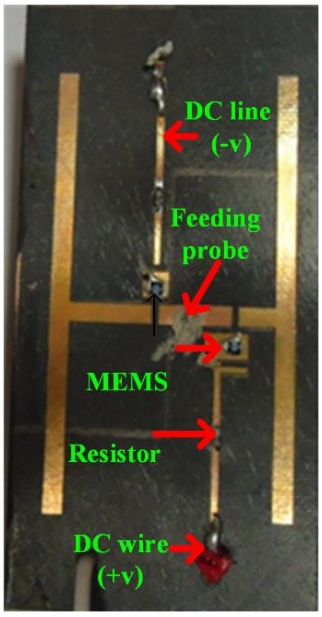

(a)

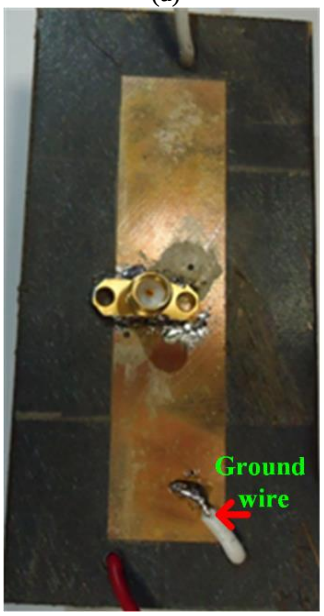

(b)

Fig. 2. The photograph of the fabricated H-shaped patch reconfigurable antenna with two artificial switches: (a) front side and (b) back side.

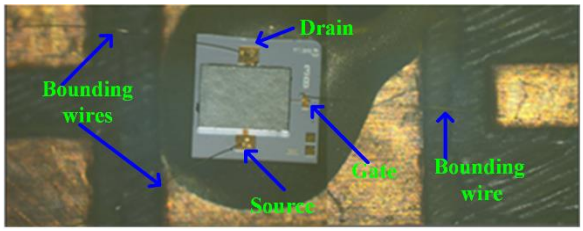

Fig. 3. The photograph of the RF MEMS switch placement.

III. SIMULATED AND MEASURED RESULTS

The H-shaped antenna was simulated using HFSS and IE3D for all the three cases. The fabricated antenna was also tested for all the three cases using Anritsu vector network analyzer 37369C. Figures 4-6 show the comparison of simulated and measured return loss (dB) for all the three cases, i.e. case 1 (ON-OFF), case 2 (OFF-ON), case 3 (ON-ON).

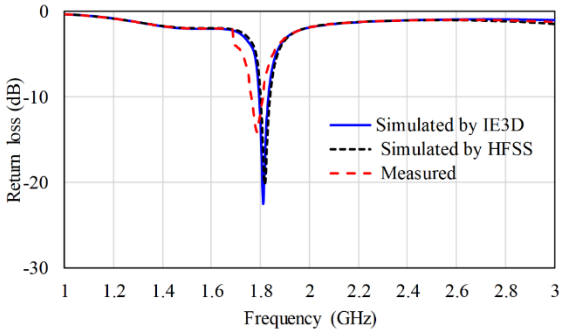

Fig. 4. Simulated and measured return loss for case 1 (ON-OFF).

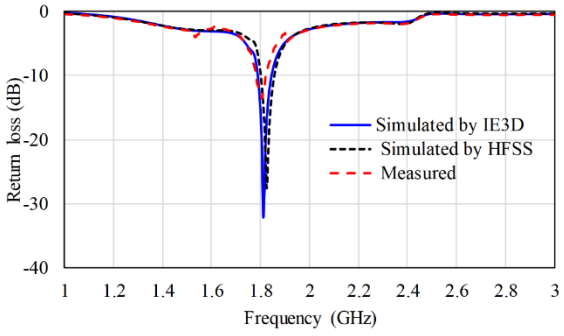

Fig. 5. Simulated and measured return loss for case 2 (OFF-ON).

As evident from Fig. 4, Fig. 5 and Fig. 6, a good agreement can be found in simulated and measured results. For all the three different cases the proposed H-shaped antenna has an operating frequency of 1.8 GHz

with good matching. The characteristics of the H-shaped microstrip antenna such as gain, maximum beam direction, and maximum electric current for all the three cases using IE3D and HFSS are listed in Table 2 and Table 3 respectively.

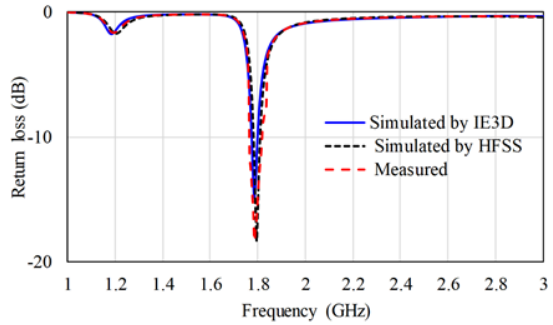

Fig. 6. Simulated and measured return loss for case 3 (ON-ON).

Table 2: Simulated characteristics of proposed antenna using IE3D simulator

Antenna State		Case 1	Case 2	Case 3
State of Artificial Switches	s_1	ON	OFF	ON
	s_2	OFF	ON	ON
Max. Beam Direction (degree)		-70	75	10
		0	0	90
Gain (dBi)		5.45	5.49	3.3

Table 3: Characteristics of H-shaped antenna in three cases by HFSS simulator

Antenna State		Case 1	Case 2	Case 3
State of Artificial Switches	s_1	ON	OFF	ON
	s_2	OFF	ON	ON
Max. Beam Direction (degree)		-75	80	10
		0	0	90
Gain (dBi)		6.25	6.28	4.01

Figure 7 illustrates the simulated 3D radiation patterns of the three cases of proposed antenna at 1.8 GHz using HFSS. A time domain antenna measurement system GEOZONDAS-AMS [22] is used to measure the radiation patterns for the proposed antenna. Figure 8 shows the normalized 2D simulated and measured radiation patterns of the proposed antenna on xz-plane are presented for case 1 (ON-OFF state), case 2 (OFF-ON state), and case 3 (ON-ON state) respectively. As seen in Fig. 8, the beam is steered in three different directions for the three cases. In case 1, the beam is directed at 270˚, while in case 2 the beam steers 180 degree apart from case 1, i.e., the maximum beam direction is at 90˚. However, for case 3, a multiplicative beam of case 1 and case 2 is observed with slightly reduced gain of 4 dB. The surface current distributions on the antenna arms for the three cases is presented in Fig. 9. The current distributions were carried out in IE3D simulator at 1.8 GHz.

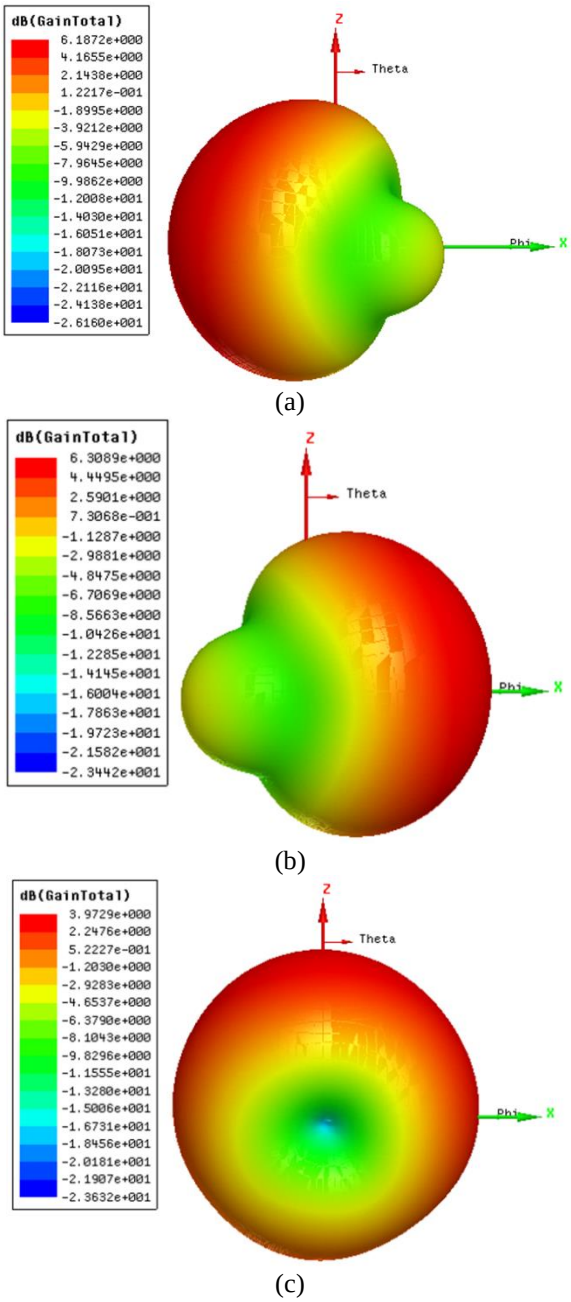

Fig. 7. The simulated 3D radiation patterns of the proposed antenna at 1.8GHz.

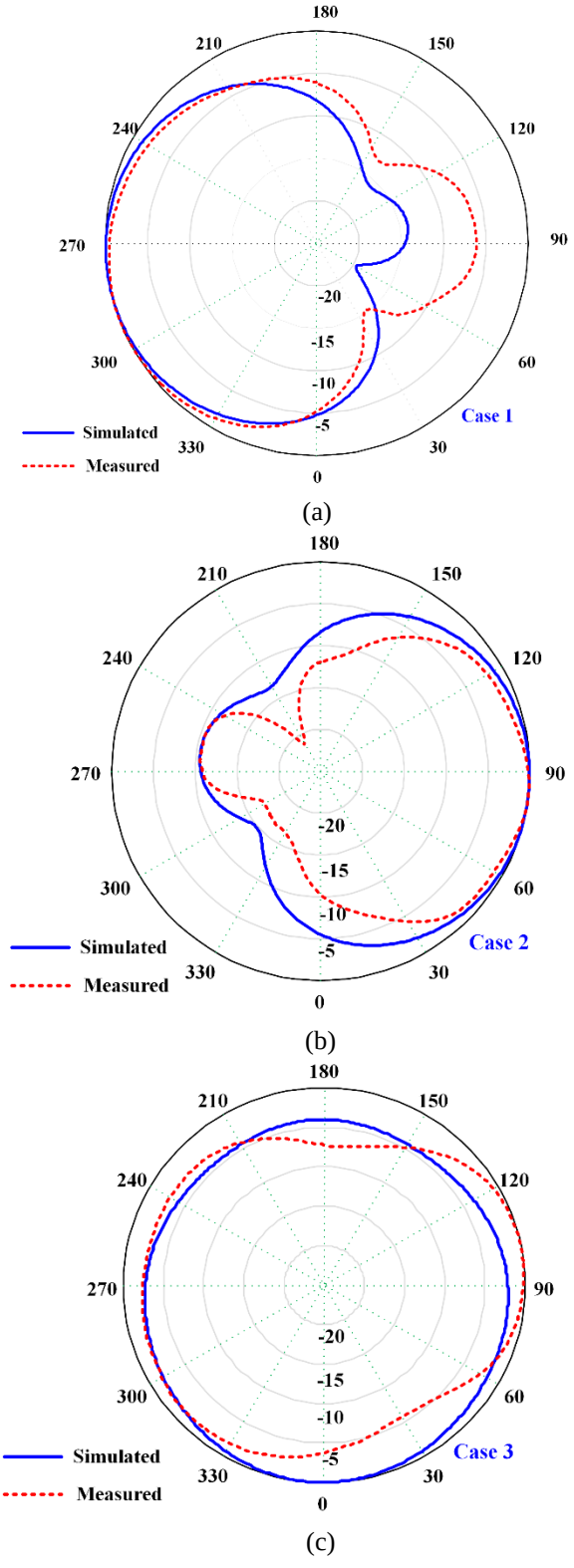

Fig. 8. The simulated and measured 2D normalized radiation patterns of the proposed antenna at 1.8GHz for: (a) case 1, (b) case 2, and (c) case 3 respectively.

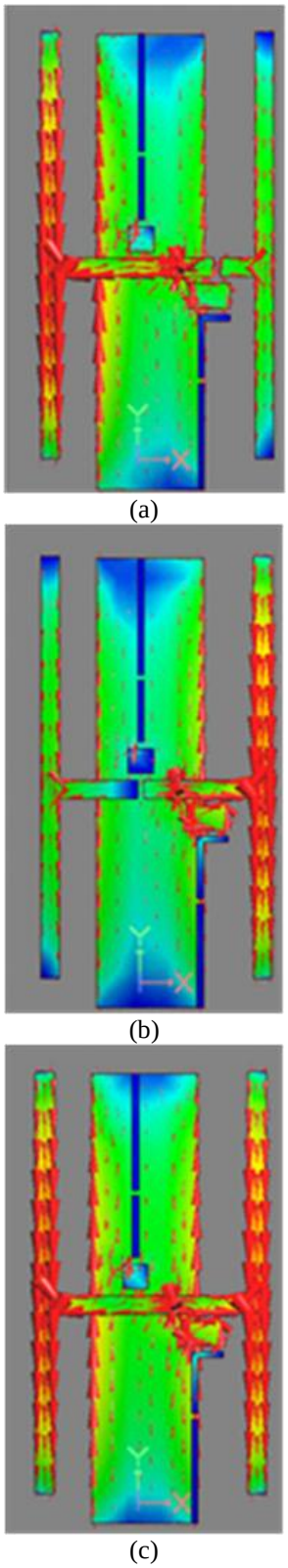

Fig. 9. Surface current distributions for: (a) case 1, (b) case 2, and (c) case 3 respectively.

The proposed reconfigurable antenna has more switchable directions than all MEMS reconfigurable antennas mentioned in Table 4. Additionally, our antenna has better gain among all the antennas listed in Table 4.

Table 4: Comparison Chart of reconfigurable antennas

Reference	No. of Beam Switchable Directions	Gain in All Directions (dBi)
[18]	2	NA
[11]	2	NA
[12]	2	3 ~ 6
Our proposed antenna	3	Case 1: 6.25 Case 2: 6.28 Case 3: 4.01

IV. CONCLUSION

A novel pattern reconfigurable H-shaped microstrip antenna has been designed, simulated, fabricated and tested. Two commercially available RF MEMS switches are utilized to steer the beam in three distinct directions. The proposed antenna has a simple structure, low profile, and has low manufacturing cost. The frequency of the proposed microstrip antenna is 1.8GHz with peak gains of 6.25 dBi, 6.28 dBi, and 4.01 dBi for case 1, case 2, and case 3 respectively. The different states of the MEMS switches make it possible to steer the beam in different prescribed directions without affecting the resonant frequency. This concept of reconfigurable antenna pattern is quite attractive as on antenna device can be utilized to steer the pattern in different desirable directions. The measured return loss and radiation patterns of the fabricated antenna shows a close agreement with the simulated results. Thus making the proposed antenna suitable for incorporation in pattern reconfigurable systems.

ACKNOWLEDGMENT

The authors would like to thank the Deanship of the Scientific Research and the Research Center at the College of Engineering, King Saud University, Riyadh, Saudi Arabia, for the financial support.

REFERENCES

[1] J. Costantine, Y. Tawk, S. E. Barbin, and C. G. Christodoulou, "Reconfigurable antennas: Design and applications," *Proceedings of the IEEE*, vol. 103, pp. 424-437, 2015.

[2] J. R. James, *Handbook of Microstrip Antennas*, vol. 1: IET, 1989.

[3] T. Huynh and K.-F. Lee, "Single-layer single-patch wideband microstrip antenna," *Electronics letters*, vol. 31, pp. 1310-1312, 1995.

[4] R. Garg, P. Bhartia, I. J. Bahl, and A. Ittipiboon, *Microstrip Antenna Design Handbook*, Artech House, 2001.

[5] M. Wright, M. Ali, W. Baron, J. Miller, J. Tuss, and D. Zeppettella, "Effect of bias traces and wires on a MEMS reconfigurable pixelated patch antenna," in *Antennas and Propagation (APSURSI)*, 2016 IEEE International Symposium, pp. 1429-1430, 2016.

[6] H. Mirzajani, M. Nasiri, and H. B. Ghavifekr, "A new design of MEMS-based wideband frequency reconfigurable microstrip patch antenna," in *Mechatronics and its Applications (ISMA)* 8th International Symposium, pp. 1-6, 2012.

[7] R. Jeanty and S.-Y. Chen, "A low-profile polarization-reconfigurable cavity antenna based on partially reflective surface," in *Radio-Frequency Integration Technology (RFIT)*, 2017 IEEE International Symposium, pp. 226-228, 2017.

[8] Y. Chen, L. Ye, J. Zhuo, Y. Liu, L. Zhang, M. Zhang, and Q. H. Liu, "Frequency reconfigurable circular patch antenna with an arc-shaped slot ground controlled by PIN diodes," *International Journal of Antennas and Propagation*, vol. 2017, 2017.

[9] W.-Q. Deng, X.-S. Yang, C.-S. Shen, J. Zhao, and B.-Z. Wang, "A dual-polarized pattern reconfigurable Yagi patch antenna for microbase stations," *IEEE transactions on antennas and propagation*, vol. 65, pp. 5095-5102, 2017.

[10] Y.-M. Cai, S. Gao, Y. Yin, W. Li, and Q. Luo, "Compact-size low-profile wideband circularly polarized omnidirectional patch antenna with reconfigurable polarizations," *IEEE transactions on antennas and propagation*, vol. 64, 2016.

[11] J.-C. Chiao, Y. Fu, I. M. Chio, M. DeLisio, and L.-Y. Lin, "MEMS reconfigurable Vee antenna," in *Microwave Symposium Digest*, 1999 IEEE MTT-S International, pp. 1515-1518, 1999.

[12] C. W. Jung, M.-J. Lee, G. Li, and F. D. Flaviis, "Reconfigurable scan-beam single-arm spiral antenna integrated with RF-MEMS switches," *IEEE transactions on antennas and propagation*, vol. 54, pp. 455-463, 2006.

[13] D. E. Anagnostou, G. Zheng, M. T. Chryssomallis, J. C. Lyke, G. E. Ponchak, J. Papapolymerou, and C. G. Christodoulou, "Design, fabrication, and measurements of an RF-MEMS-based self-similar reconfigurable antenna," *IEEE Transactions on Antennas and Propagation*, vol. 54, pp. 422-432, 2006.

[14] E. R. Brown, "RF-MEMS switches for reconfigurable integrated circuits," *IEEE Transactions on Microwave Theory and Techniques*, vol. 46, pp. 1868-1880, 1998.

[15] J.-Y. Kim, B. Lee, and C. W. Jung, "Reconfigurable beam-steering antenna using double loops," *Electronics Letters*, vol. 47, pp. 430-431, 2011.
[16] P. Parthiban, B.-C. Seet, and X. J. Li, "Low-cost low-profile UHF RFID reader antenna with reconfigurable beams and polarizations," in *IEEE International Conference on RFID (RFID)*, 2017.
[17] H. Tang and J.-X. Chen, "Microfluidically frequency-reconfigurable microstrip patch antenna and array," *IEEE Access*, vol. 5, pp. 20470-20476, 2017.
[18] G. H. Huff and J. T. Bernhard, "Integration of packaged RF MEMS switches with radiation pattern reconfigurable square spiral microstrip antennas," *IEEE Transactions on Antennas and Propagation*, vol. 54, pp. 464-469, 2006.
[19] F. Yang, X.-X. Zhang, X. Ye, and Y. Rahmat-Samii, "Wide-band E-shaped patch antennas for wireless communications," *IEEE Transactions on Antennas and Propagation*, vol. 49, pp. 1094-1100, 2001.
[20] R. Ghosh, K. Patra, B. Gupta, and S. Chowdhury, "Accurate formula to determine resonant frequency of double sided printed dipole antenna," *IETE Journal of Research*, vol. 64, pp. 331-336, 2018.
[21] M. Jamaluddin, M. Rahim, M. A. Aziz, and A. Asrokin, "Microstrip dipole antenna analysis with different width and length at 2.4 GHz," in *Applied Electromagnetics, APACE 2005, Asia-Pacific Conference on*, pp. 4, 2005.
[22] Geozandas.com, "Time Domain Antenna Measurement Systems," www.geozondas.com/main_page.php?pusl=12.

Engr. Wazie M. Abdulkawi is currently pursuing Ph.D. at Electrical Engineering Department in King Saud University. He received M.S. in Electrical Engineering degree from King Saud University in 2013 and B.Sc. in Communication Engineering degree from Ibb University, Ibb, Yemen in 2007. His research interest includes antenna theory, chipless RFID, electromagnetics, and microwave engineering.

Abdel-Fattah A. Sheta received B.S. degree in Communications and Electro-Physics from Alexandria University, Egypt in 1985. He obtained his M.S. degree in Electrical Engineering Department, Cairo University, in 1991. In 1996, he received the Ph.D degree in Microwave Circuits Analysis and Design from ENST, Université de Bretagne Occidentale, France. During 1996-1998, he worked as a Researcher in the National Telecommunication Institute, Cairo, Egypt. In 1998, he joined Electric Engineering Department, Cairo University, Fayoum Branch. Currently he is Prof. in Electrical Engineering at King Saud University, Saudi Arabia. His current research interests include microstrip antennas, planar, and uniplanar MIC's and MMIC's.

Waqar Ahmad Malik received his B.S degree in Electrical Engineering from NWFP University of Engineering & Technology Peshawar, Pakistan in 2004 and M.S in Radio Systems Engineering from The University of Hull, UK in 2006. He then joined academia as a Lecturer and taught for a total of 5 years at University of Engineering & Technology, Mardan Campus and National University of Computer and Emerging Sciences, Peshawar Campus, both situated at Pakistan. He resumed teaching at Abasyn University Islamabad, Pakistan after attaining his Ph.D. in Electrical Engineering from King Saud University, Riyadh, KSA. His research interest includes optimization of microwave circuits, broadband matching of RF and microwave circuits, and wideband high power amplifiers.

Sajjad Ur Rehman is currently Associate Professor at the Department of Electrical Engineering Qurtuba University, Dera Ismail Khan, Pakistan. He received his Ph.D in Electrical Engineering degree from King Saud University in January 2019. He was working as a Lecturer at the Department of Electronics Engineering in Iqra University Karachi (Peshawar Campus) from 2007 to 2008. He obtained M.Sc. Electrical Engineering degree from King Saud University in 2012.

Majeed A. S. Alkanhal is a Full Professor in the Department of Electrical Engineering at King Saud University, Riyadh, Saudi Arabia. He received his Ph.D. in Electrical Engineering from Syracuse University, Syracuse, New York in 1994. His research interests include wireless communications, radar systems, electromagnetic propagation and scattering in complex materials, microwave/millimeter-wave antenna design and optimization, modern optimization techniques, and computational electromagnetics. Professor Alkanhal has served as consultant, visiting scholar, editor, and referee for several institutes and scientific journals. He has published books, book chapters, research papers, technical reports, and patents in his fields of research interests.

A Reconfigurable Crossed Dipole Antenna for Polarization Diversity Using Characteristic Mode Theory

Amirreza Nikfal [1], Gholamreza Dadashzadeh [2], and Mohammad Naser-Moghadasi [1]

[1] Department of Electrical Engineering
Islamic Azad University - Science and Research Branch, Tehran, 1477893855, Iran
nikfal.amirreza@srbiau.ac.ir, mn.moghaddasi@srbiau.ac.ir

[2] Department of Electrical and Electronic Engineering
Shahed University, Tehran, 3319118651, Iran
gdadashzadeh@shahed.ac.ir

Abstract ─ A novel printed crossed dipole antenna with reconfigurable circular and linear polarization is proposed. This antenna consists of a pair of L-shape elements and a narrow gap on each arm for inserting a conductive metal tab as an ideal switch in the center of the gap to control its on-off status. The theory of characteristic modes has been used to design and analyze the proposed antenna. Based on the presented idea, a prototype of such antenna has been constructed with the center operating frequency at about 2500 MHz. The experimental results have been presented and compared with those obtained from the simulation showing a good agreement. The antenna is low cost and possesses simultaneous circular and linear polarization which has not been reported in the literature for single-feed crossed dipole antennas.

Index Terms ─ Characteristic modes, circular polarization, crossed dipole, diversity, linear polarization, reconfigurable.

I. INTRODUCTION

The crossed dipole is a common type of antenna used in a wide frequency range for generating circular polarization.

Brown developed the first crossed dipole antenna in the 1930s under the name of "Turnstile Antenna" [1]. In 1961 Bolster introduced a new type of crossed dipole antenna with a single feed for circular polarization radiation [2].

Based on this idea, numerous single-feed circularly polarized crossed dipole antennas have been designed [3-6]. For recent wireless communications, a circular polarization (CP) technique is popularly used because of its insensitivity to transmitter and receiver orientations [7]. In addition, antennas with a reconfigurable polarization have been studied to avoid the signal fading loss caused by multipath effects. Recent reconfigurable crossed dipole antennas only cover circular polarization [8] and having circular and linear polarization simultaneously can improve antenna applications.

The theory of characteristic modes is one of the useful methods which are widely used for analyzing the antennas [9-10]. The theory of CM was first developed by Garbacz [11] and was later refined by Harrington and Mautz in the seventies [12-13]. Recently the theory of CM reemerged in designing antennas for modern applications such as crossed dipole antenna [14].

In this paper first, we provide a brief description of the theory of CM and its applications. Second, we introduce and analyze crossed dipole antenna in linear and circular polarization with CM theory. Finally, with the combination of the antenna structure in two types of polarizations a reconfigurable crossed dipole antenna with a switchable circular and linear polarization is presented. After implementation, we compare simulation and measurement results.

II. THEORY OF CHARACTERISTIC MODES

The theory of characteristic modes is presented here in brief. The characteristic modes or characteristic currents can be obtained as the eigenfunctions of the following particular weighted eigenvalue equation:

$$X(\overrightarrow{J_n}) = \lambda_n R(\overrightarrow{J_n}), \quad (1)$$

where the λ_n are the eigenvalues, (J_n) are the eigenfunctions or the eigencurrents, and R and X are the real and imaginary parts of the impedance operator:

$$Z = R + jX. \quad (2)$$

Modal significance (3) and characteristic angle (4) are other antenna characteristics using the eigenvalue information to extract resonance information,

$$MS_n = \left|\frac{1}{1+j\lambda_n}\right|, \quad (3)$$

$$\alpha_n = 180^\circ - tan^{-1}\,\lambda_n. \quad (4)$$

Submitted On: October 27, 2018
Accepted On: April 1, 2019

The resonance of each mode can be identified by the maximum value of each modal significance curve corresponding to the characteristic angle that is equal to 180°. This means that the closer the modal significance to its maximum value or characteristic angle to 180°, the more effective the associated mode contributing to radiation.

If excitation is present the modal excitation and the modal weighting coefficient are calculated, giving an indication of how well the excitation will excite each mode and how presented in total current distribution.

III. ANTENNA DESIGN

The idea and the procedure for antenna design are presented in the following subsections. The crossed dipole antenna is analyzed in the forms of simple metal strip structures in linear and circular polarization according to CM theory. With the reference obtained from the above procedure, we propose a reconfigurable antenna with linear and circular polarization. This prototype antenna is simulated and constructed based on a dielectric substrate.

A. Linear polarization mode

Figure 1 shows the configuration of a simple crossed dipole antenna composed of two orthogonal L-shape metal strips with a vertical distance of 0.5 millimeters in air substrate and the length of each arm along x or y-direction is d1= d2 = 30 millimeters and the width of each arm is w = 1 millimeter.

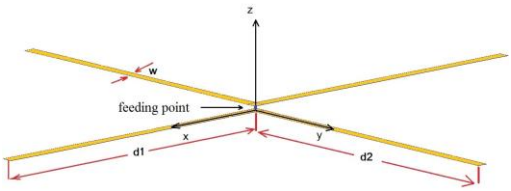

Fig. 1. Simple crossed dipole antenna.

The modal analysis of this structure is performed by the software for electromagnetic simulations (FEKO) [15] using characteristic modes request.

The core of the program FEKO is based on the method of moments (MoM). The MoM is a full wave solution of Maxwell's integral equations in the frequency domain. The FEKO solver supports RWG (Rao-Wilton-Glisson) [16] and higher order hierarchical basis functions. The procedure begins when the antenna surface is discretized using triangles. Then with the aid of the RWG method, the software extracts the Z impedance matrix.

This impedance matrix is used to calculate the eigenmodes and eigenvalues of the given antenna. This method is used stepwise at isolated frequency points through the predefined frequency range. The eigenvalues are the main parameters to calculate the additional modal parameters, e.g., modal significance and characteristic angle.

Figure 2 shows the variation of the modal significance and modal weighting coefficient with the frequency related to current modes (Jn) of the crossed dipole antenna.

It can be noticed that the modes 1 and 2 resonate around 2.4 GHz and mode 3 resonates at 2.6 GHz and other modes resonate at higher frequencies as indicated by their corresponding modal significance curves.

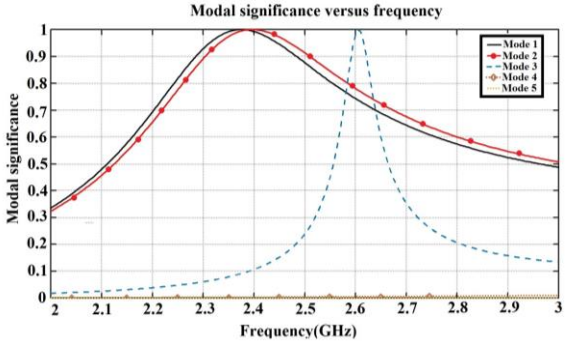

(a)

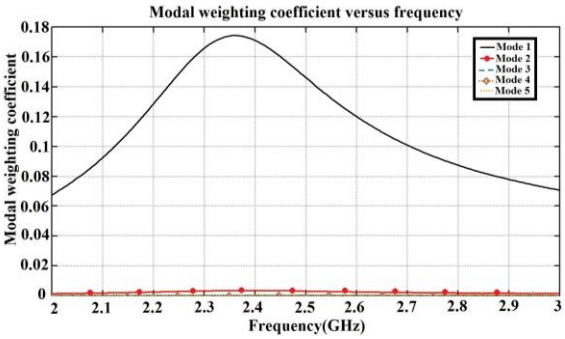

(b)

Fig. 2. Crossed dipole in linear mode: (a) modal significance, and (b) modal weighting coefficient.

Among these modes with feeding point in Fig. 1, only mode 1 radiates as seen in corresponding modal weighting coefficient curves, in other words, the antenna in Fig. 1 radiates in linear polarization mode.

Figure 3 shows the normalized electric field (En) at 2.4 GHz associated with the characteristic currents (Jn). It can be appreciated that far field produced by mode 1 is similar to the final far-field pattern of the antenna.

B. Circular polarization mode

It is a well-known fact that to get circular polarization, it is essential to combine two orthogonal and linearly polarized modes with the same current amplitude and with a phase difference of 90º.

This is simply achieved by combining modes 1 and 2. To produce the required phase shift of current the

length of d1 (for both arms) can be increased making d`1=d1+a, causing the resonance frequency of mode 1 which moves to lower values and simultaneously shortens the length of the d2 (for both arms) making d`2=d2-a causing the resonance frequency of mode 2 that moves to higher values as seen in the curves of modal significance of Fig. 4.

Figure 4 also shows what happens to the curves of the characteristic angle and modal weighting coefficient. It can be seen that the characteristic angle curves corresponding to modes 1 and 2 have a phase difference of 90º at the point that both modes have exactly the same amplitude of the normalized current.

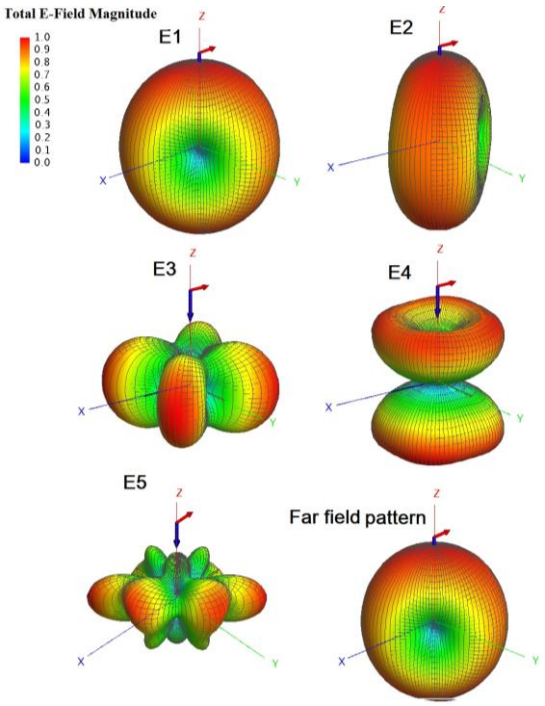

Fig. 3. Comparison of modal field and far-field pattern.

For a value of a = 2.5 mm the desired displacement between modes 1 and 2 is obtained. Moreover, as shown in Fig. 4, modal weighting coefficient curves (mode 1 and mode 2) have identical parts in final radiation power and other modes can be neglected in comparison to them. So there are two orthogonal modes that meet the required conditions for circular polarization.

Depending on which arms (increased or decreased), the polarization can be RHCP or LHCP.

Also, based on current distribution, we could assess this antenna. From Fig. 2 (b) and Fig. 4 (c), we learn that in linear mode, only mode one radiates although in circular mode, two modes (one and two) radiate simultaneously.

Figure 5 shows the current distribution in linear and circular modes. As we can see in linear mode, the current flow to all four antenna arms via antenna port, we get linear slant polarization.

In the circular mode, the current flow in two aligned arms in mode1, and other two arms in mode 2, with a phase difference of 90º, resulted in circular polarization [17-18].

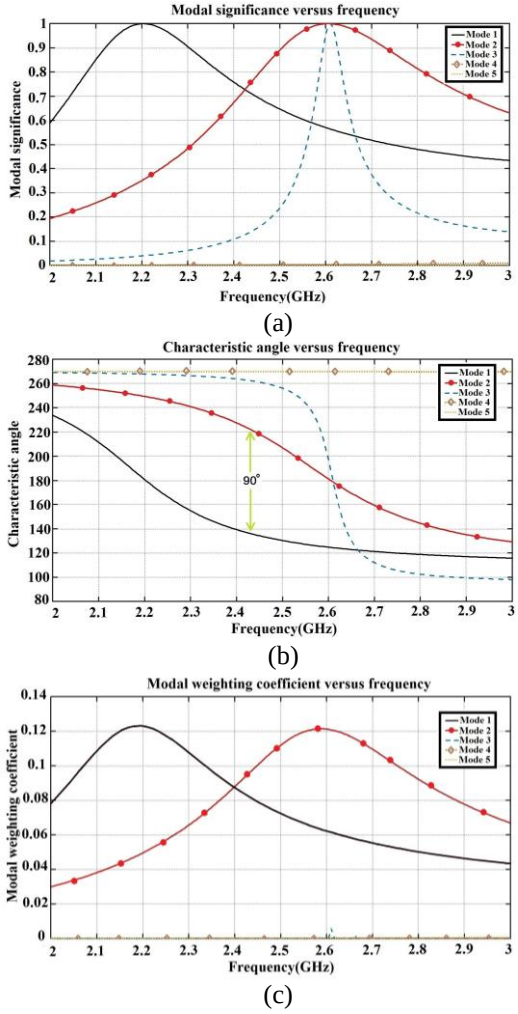

Fig. 4. Crossed dipole in circular mode: (a) modal significance, (b) characteristic angle, and (c) modal weighting coefficient.

C. Proposed antenna geometry

With the ideas explained in parts A and B, we propose the configuration of the antenna in Fig. 6. There are L-shape elements composed of two orthogonal arms on both sides of a dielectric substrate. On each arm, there is a narrow gap and a conductive metal tab or metal bridge as an ideal switch that can be inserted on each gap. A reflector is used for providing balanced feeding with a coaxial cable and a higher gain. The air gap between the ground-connected reflector and the crossed dipole is equal to $\lambda_0/4$.

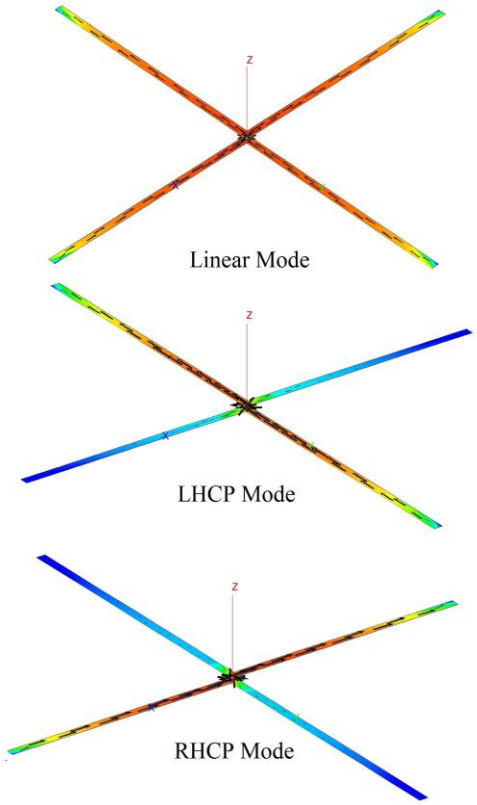

Fig. 5. Crossed dipole current distribution for linear mode in comparison to circular modes.

The states of the switches and the antenna polarization are summarized in Table 1.

Table 1: Antenna polarization corresponding to states of switches

Switch	D1	D2	D3	D4	Polarization
State 1	On	Off	On	Off	LHCP
State 2	Off	On	Off	On	RHCP
State 3	On	On	On	On	Linear Pol.

When D1and D3 are on and D2 and D4 are off, the antenna radiates on a left-hand CP (LHCP) mode and the opposite states of the diodes generate the radiation on a right-hand CP (RHCP) mode. When all switches are on, the antenna radiates on a linear polarization mode.

The proposed antenna is implemented on a substrate with a relative permittivity of 4.4 (FR4) and a thickness of 0.508 mm. Figure 8 shows the photo of an RHCP antenna.

Ideal switches that are on, in Fig. 6, are represented by conductive metal tabs on the gaps while those that are off are represented by leaving the gap unchanged. It has been shown that these simplified implementations of switches, provide acceptable representations for the actual switches [19-22].

The parameters of the crossed dipole shown in Fig. 6 are L_1 = 20.4 mm, L_2 = 3.1 mm, L_3 = 30 mm, G = 1.1 mm, W_1 = 1 mm, r_1 = 0.8 mm, r_2 = 1.5 mm, r_3 = 1.9 mm, and $\alpha = 45°$.There are two vias each with a diameter of 0.2 mm. The antenna is center-fed by a 50 Ω coaxial cable and is placed at a quarter-wavelength above a square reflector to obtain a directional CP or linear radiation pattern.

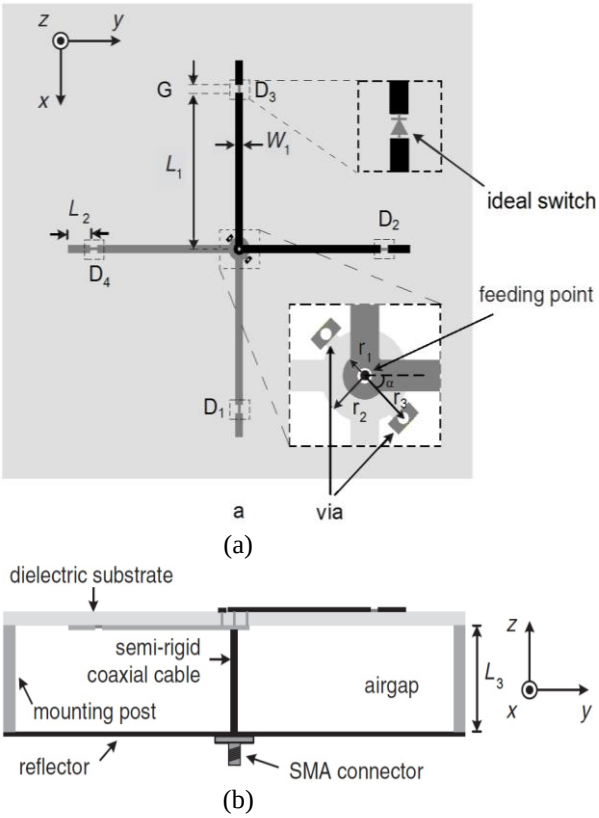

Fig. 6. The configuration of the proposed antenna: (a) top view, and (b) side view.

The antenna has one port for both linear and circular polarization. For isolation between linear mode and circular mode, we can consider the axial ratio. The axial ratio in the circular antenna (LHCP or RHCP) is about 3 dB and in the linear antenna is greater than 30 dB in the desired bandwidth.

HFSS computes the polarization ratio circular LHCP and polarization ratio circular RHCP at each selected aspect angle, so if the polarization ratio circular RHCP is high it means that we have RHCP antenna and vice versa. So the difference between the two graphs in each figure indicates the isolation between the two circular polarization in the antenna. Polarization ratio for RHCP antenna and LHCP antenna are shown in Fig. 7 so as we see in the figure there is proper isolation between RHCP and LHCP mode.

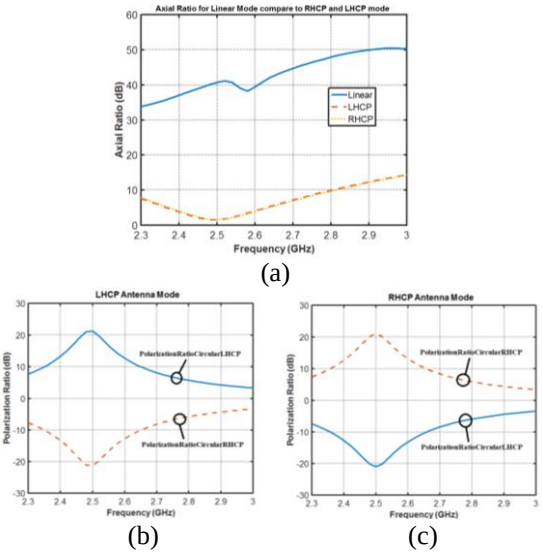

Fig. 7. (a) Axial ratio for linear mode compare to circular modes, (b) polarization ratio in LHCP antenna mode, (c) polarization ratio in RHCP antenna mode.

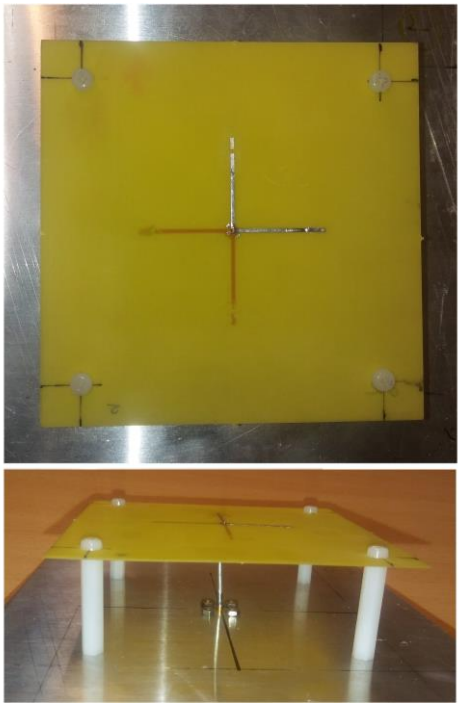

Fig. 8. Photos of RHCP crossed dipole antenna.

IV. RESULTS

The proposed antenna has been analyzed and optimized with the aid of the Ansoft HFSS and a prototype of the proposed design with the operating frequency at about 2500 MHz has been constructed and studied.

Figure 9 shows the simulated and measured return losses in three states based on Table 1. The measured data in general, agree with the simulated results.

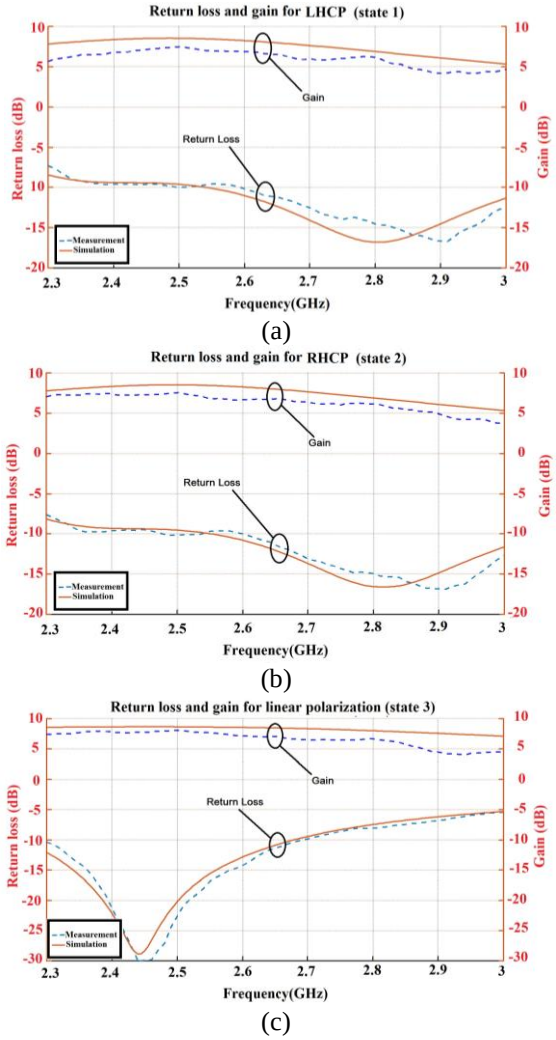

Fig. 9. Return loss and gain: (a) LHCP, (b) RHCP, (c) Linear Polarization.

Figure 10 shows the simulated and measured axial ratio for circular polarization mode. The obtained 3-dB axial ratio bandwidth reaches 140 MHz (2500-2640 MHz) with a center frequency of 2570 MHz that is slightly shifted in respect to the center frequency at 2500 MHz at which a minimum axial ratio is expected. From the measured return loss shown in Fig. 9, it is evident that the return loss for circular polarization is about 10 dB and for linear polarization is better than 12 dB in 3-dB axial ratio bandwidth. Figure 9 also presents the measured antenna gain and the average antenna gain level is about 7 dBi in 3-dB axial ratio bandwidth.

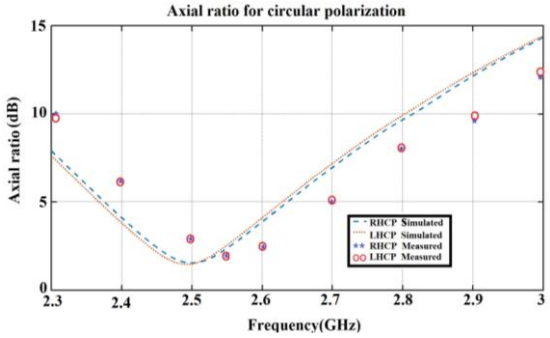

Fig. 10. Axial ratio for circular polarization.

Figures 11 and 12 show the simulated and measured radiation pattern in linear and circular polarization modes respectively. The radiation patterns have been measured in XZ-plane (Φ = 0°) and YZ-plane (Φ = 90°). It is also noted that the antenna has a slant polarization in linear mode.

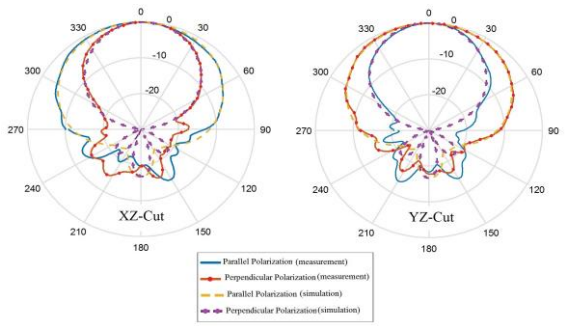

Fig. 11. Normalized radiation pattern in linear polarization mode.

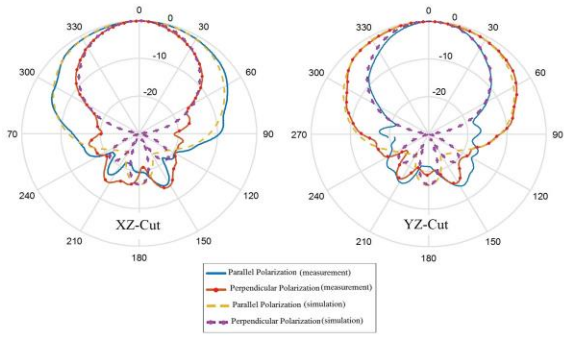

Fig. 12. Normalized radiation pattern in left-hand circular polarization mode.

A comparison of the performances of the proposed antenna and other crossed dipole antennas [8, 14] is shown in Table 2. According to this table, the proposed antenna can produce three polarizations including linear polarization, LHCP, RHCP and possesses better return loss in 3-dB axial ratio bandwidth.

V. CONCLUSION

This paper demonstrates a crossed dipole antenna by employing the theory of characteristic modes in a single coaxial feed. It has been shown that CM theory provides valuable information for mode excitation without any design complexity. The design in this paper illustrates that with changing lengths of antenna arms, we can excite desired modes and polarizations. The proposed reconfigurable antenna can produce LHCP and RHCP and linear polarization. It is expected that by applying this procedure on other CP antennas, we can achieve new design for polarization reconfigurable antennas.

Table 2: Comparison of the performances of crossed dipole antennas

Antenna Structure	Size of Antenna (Without Biasing Circuit)	3-dB Axial Ratio Bandwidth	Return Loss in 3-dB Axial Ratio BW	Number of Polarizations
Proposed antenna	$0.422\lambda_0 \times 0.422\lambda_0$ (at 2.57 GHz)	(2500-2640 MHz) 4.3%	10 dB (average)	Three (Linear Pol.-LHCP-RHCP)
Ref. [8]	$0.37\lambda_0 \times 0.37\lambda_0$ (at 2.16 GHz)	(2050-2270 MHz) 10.2%	7.4 dB (average)	Two (LHCP-RHCP)
Ref. [14]	$0.516\lambda_0 \times 0.448\lambda_0$ (at 289.25 MHz)	(296-282.5 MHz) 4.7%	-----	Two (LHCP-RHCP)

REFERENCES

[1] G. Brown, "The turnstile," *Electron.*, vol. 9, pp. 4–17, Apr. 1936.

[2] M. F. Bolster, "A new type of circular polarizer using crossed dipoles," *IRE Trans. Microwave Theory Tech.*, vol. 9, no. 5, pp. 385-388, Sept. 1961.

[3] J. W. Baik, K.-J. Lee, W.-S. Yoon, T.-H. Lee, and Y.-S. Kim, "Circularly polarized printed crossed dipole antennas with broadband axial ratio," *Electron. Lett.*, vol. 44, no. 13, pp. 785-786, June 2008.

[4] J.-W. Baik, T.-H. Lee, S. Pyo, S.-M. Han, J. Jeong, and Y.-S. Kim, "Broadband circularly polarized crossed dipole with parasitic loop resonators and its arrays," *IEEE Trans. Antennas Propag.*, vol. 59, no. 1, pp. 80-88, Jan. 2011.

[5] Y. He, W. He, and H. Wong, "A wideband

circularly polarized cross-dipole antenna," *IEEE Antennas Wireless Propag. Lett.*, vol. 13, pp. 67-70, Jan. 2014.

[6] S. X. Ta, H. Choo, and I. Park, "Planar, lightweight, circularly polarized crossed dipole antenna for handheld UHF RFID reader," *Microw. Opt. Technol. Lett.*, vol. 55, no. 8, pp. 1874-1878, Aug. 2013.

[7] F. S. Chang, K. L. Wong, and T. W. Chiou, "Low-cost broadband circularly polarized patch antenna," *IEEE Transactions on Antennas and Propagation*, AP-51, 10, pp. 3006-3009, Oct. 2003.

[8] W.-S. Yoon, S.-M. Han, J.-W. Baik, S. Pyo, J. Lee, and Y.-S. Kim, "Crossed dipole antenna with switchable circular polarization sense," *Electron. Lett.*, vol. 45, no. 14, pp. 717-718, July 2009.

[9] Y. Chen and C.-F. Wang, "Characteristic-mode-based improvement of circularly polarized U-slot and E-shaped patch antennas," *IEEE Antennas Wirel. Propag. Lett.*, vol. 11, pp. 1474-1477, 2012.

[10] E. Antonino-Daviu, M. Cabedo-Fabres, M. Gallo, M. Ferrando-Bataller, "Design of a multimode MIMO antenna using characteristic modes," *3rd European Conference on Antennas and Propagation, EuCAP*, pp. 1840-1844, 2009.

[11] R. J. Garbacz, "A generalized expansion for radiated and scattered fields," *Ph.D. dissertation*, Ohio State University, Columbus, 1968.

[12] R. F. Harrington and J. R. Mautz, "Theory of characteristic modes for conducting bodies," *IEEE Trans. Antennas Propagat*., vol. AP-19, no. 5, pp. 622-628, Sept. 1971.

[13] R. F. Harrington and J. R. Mautz, "Computation of characteristic modes for conducting bodies," *IEEE Trans. Antennas Propagat.*, vol. AP-19, no. 5, pp. 629-639, Sept. 1971.

[14] J. P. Ciafardini, et al., "Analysis of crossed dipole to obtain circular polarization applying Characteristic Modes techniques," *Biennial Congress of Argentina (ARGENCON)*, *IEEE*, 2016.

[15] EM Software & Systems - S.A. (Pty) Ltd - FEKO (www.feko.info) EM Software & Systems - S.A. (Pty) Ltd Address: PO Box 1354, Stellenbosch, 7599, South Africa.

[16] S. M. Rao, D. R. Wilton, and A. W. Glisson, "Electromagnetic scattering by surfaces of arbitrary shape," *IEEE Trans. Ant. Propa*., vol. AP-30, no. 3, pp. 409-418, May 1982.

[17] J. Wang, L. Zhao, Z. C. Hao, and J. M. Jin, "A wideband dual-polarized omnidirectional antenna for base station/WLAN," *IEEE Transactions on Antennas and Propagation*, vol. 66, no. 1, pp. 81-87, 2017.

[18] J. Wang, Z. Shen, and L. Zhao, "Wideband dual-polarized antenna for spectrum monitoring systems," *IEEE Antennas and Wireless Propagation Letters*, vol. 16, pp. 2236-2239, 2017.

[19] F. Yang and Y. Rahmat-Samii, "Patch antenna with switchable slot (PASS): Dual frequency operation," *Microwave Opt. Technol. Lett*., vol. 31, no. 3, pp. 165-168, Nov. 2001.

[20] W. Li and Q. Ye, "A reconfigurable triple notch band antenna integrated with defected microstrip structure band-stop filter for ultra-wideband cognitive radio applications," *International Journal of Antennas and Propagation*, no. 472645, pp. 1-13, 2013.

[21] W. Li, W. Yu, and Y. Li, "A switchable UWB slot antenna using SIS-HSIR and SIS-SIR for multi-mode wireless communications applications," *Applied Computational Electromagnetics Society Journal*, vol. 27, no. 4, pp. 340-351, 2012.

[22] W. Li and R. Mittra, "A CPW-fed wide-slot antenna with reconfigurable notch bands for UWB and multi-band communication applications," *Microwave and Optical Technology Letters*, vol. 55, no. 11, pp. 2777-2782, Nov. 2013.

Amirreza Nikfal was born in Tehran, Iran, in 1970. He received his B.Sc. degree from Sharif University of Technology and M.Sc. degree from Iran University of Science & Technology, Tehran, Iran, respectively in 1994 and 1998, both in Electrical Engineering. Currently, he is a Ph.D. student at Islamic Azad University - Science and Research Branch.

Gholamreza Dadashzadeh was born in Urmia, Iran, in 1964. He received the B.Sc. degree in Communication Engineering from Shiraz University, Shiraz, Iran, in 1992 and M.Sc. and Ph.D. degrees in Communication Rngineering from Tarbiat Modarres University, Tehran, Iran, in 1996 and 2002, respectively. He is currently an assistant professor with the department of electrical engineering, Shahed University, Tehran.

Broadband Microwave Absorber based on End-loading Folded-Dipole Array

Yumei Chang [1] and Yung L. Chow [2]

[1] College of Electronic and Optical Engineering
Nanjing University of Posts & Telecommunications, 210023 Nanjing, China
changym@njupt.edu.cn

[2] Department of Electrical and Computer Engineering, University of Waterloo, Waterloo, ON, Canada N2L3G1
ylchow@maxwell.uwaterloo.ca

Abstract ─ Microwave absorbers have been widely used in electromagnetic compatibility, radar absorbing material and cloaking etc., and therefore attract much attention in recent years. In this work, a microwave absorber based on an array of receiving folded-dipoles with a grounded air spacer is proposed. The cell of the absorber can be seen as a three resonators in tandem formed by dipole-mode and stub-modes of the receiving folded dipole and the grounded spacer with thickness of $\lambda/4$, i.e., an equivalent three-pole filter. Based on the equivalent circuit, the impedance matching during a wide frequency range can be achieved. Moreover, to verify the proposed technique, a prototype of dual-polarized absorber is fabricated and measured. A little variation between the simulation and measurement results are observed, however, the relative bandwidth can still reach up to 105%. In addition, compared with other absorbers constructed with metal and lumped elements, the proposed absorber has a high ratio of *bandwidth/thickness*, which is around 8.5 and be with dual-polarizations.

Index Terms ─ Electromagnetic shielding, equivalent circuit, folded dipole array, microwave absorber.

I. INTRODUCTION

Electromagnetic absorber have been used in many areas, such as Radar Absorbing Material (RAM) for improving the radar performance (by reducing interfering reflections from other objects) or radar camouflages [1], measurements of electromagnetic compatibility (EMC) and measurements of antenna radiation pattern in anechoic chambers etc.

The classical Salisbury screen invented by Salisbury in 1952 is one type of well-known absorbers, which is constructed with a resistive sheet of 377 Ω /sq. and a backing ground plane at $\lambda/4$ away [2]; and gives a perfectly zero reflection at the resonance. Others like Dallenbach layers loaded with high impedance surfaces, circuit analogue RAMs, magnetic absorbers, and lossy frequency selective surfaces has been investigated [3] - [7]; however, most of their relative bandwidths are not wide – substantially less than 100%.

Usually, to furtherly enhance the bandwidth, multi-layer structure is the primary choice. A capacitive circuit absorber with three layers in [8], which replaces the band-stop resonating frequency selective surfaces (FSS) with low-pass capacitive circuit analog absorber (CA absorber) that gives a very wide bandwidth of 4 GHz to 24 GHz. Some other examples use optimization method like Genetic Algorithm (GA) to find the optimal layer thickness so as to achieve a maximum bandwidth [9]. Unfortunately, although the bandwidth can be made very wide, the absorber is bulky, difficult to fine adjust on the layers and therefore expensive. In [10], double square loop and dipole with lumped resistors are used to form the absorber, which can achieve better performance at the absorption band; but the bandwidth is not very wide. Other structures like 3-D periodic absorber invented by Shen's group [11]. In their work, a periodic structure of 3-D geometry with lump elements is introduced between the ground plane and the top resistive/capacitive layer. A microwave absorber of 100% bandwidth was achieved and the performance of absorption under oblique incidence were stable at the range of $\theta = 0^{o}$~30^{o}. However, it is some kind of difficult to assemble for its 3-D geometry and the amount of soldering work involved.

Generally, in most publications, absorbers based on periodic cells are considered as independent microwave circuits or an extensive application of FSS. However, in our previous work [12-13], the design of an absorber starts with a *receiving antenna*. The most difference from the absorber and the traditional receiving antenna is that the incident wave received by the former ones is mostly dissipated, while by the latter ones is transmitted to the next level. Therefore, the absorber based on periodic cells can be seen as a special application of receiving antenna array. In [14], Lin etc. also proposed a broadband absorber of single-polarization with the receiving antenna concept.

Submitted On: May 16, 2018
Accepted On: May 12, 2019

In this work, a novel broadband absorber constructed with a top-loading folded-dipole array is proposed. The measured results show a small deviation from the simulations, that the measured relative bandwidth is 105% approximately, which is less than our expectation. The reasons might be the wide band has reached the frequency limit of the measuring system. Besides, the parasitic effects of the surface mounted resistor also contribute to the frequency deviation. For further demonstration, we compare the performances of this absorber with others in the literatures above, and find that the proposed absorber can achieve wide bandwidth but with small thickness.

II. EQUIVALENT CIRCUITS & DESIGNS

A. Equivalent circuit of the absorber cell based on folded dipole

As mentioned above, an absorber is more like a receiving antenna array, while the receiving EM wave dissipated other than transmitted to the receiver, as shown in [12]. In this work, the folded dipole array receive the incident wave and then dissipate on the load at the center and end of the dipole. Each cell of the absorber is equivalent to a square waveguide (with electric or magnetic walls) loaded across with a folded-dipole with resistor R_L, and followed by a $\lambda/4$ spacer to a ground plane. Figure 1 gives the corresponding equivalent circuit , while the upper R_u of the stub mode comes from the optional loading R_s at the end of each stub of the ($\lambda/4$) folded dipole, with $R_u = Z_0^2/R_s$; the lower R_d is similar to R_u. The equivalent circuit is composed of three resonators, i.e., a parallel-circuit resonator (of the stub mode of the folding), a series-circuit resonator (of the mode of a standard dipole) and then a parallel-circuit resonator (of the unit cell stub of spacer and ground below the folded-dipole). The resonators in tandem, parallel to series to parallel, perform as standard filter.

Nevertheless, the equivalent circuit of the unit cell in Fig. 1 does not precisely describe the characteristics of folded-dipole absorber; this is because a) the fringe fields have been neglected, e.g., the field effect of the short end of the folded-dipole. More importantly, b) the Z_M from the mutual impedances of all adjacent folded-dipoles outside the unit cell is tedious to derive analytically. Therefore, based on the equivalent circuit, one can move S_{11} loops in Smith chart analytically, such as *up*, *down*, *left*, *right*, and *changing loop sizes*. The goal of the moves above is to fit the multi-loop locus of S_{11} within the -10 dB circle at the center of the Smith chart as long a length as possible; and therefore make the bandwidth as wide as possible.

Table 1 lists the links of the physical parameters to the impedance and reflections of the absorber surface; following these links, a regular folded dipole with initial settings of $D = 4a_r$, $a_l = a_r = 0.15$ mm, $l_u = l_d = l = 25$mm and $R_A = 600$ ohm can be improved to have a wide bandwidth of 99.1%.

Table 1 Parameter adjustments and its theoretical basis

Parameter Adjustments	Theoretical Basis and Dffects
$D\uparrow$	$C_r\uparrow$and $L_r\uparrow$, then $Q\downarrow$, and then wider bandwidth
a_r	To achieve wide bandwidth, it is better to have $\frac{dX_T}{df} + \frac{dB_t}{df} = 0$ in a wide band.
K	When D is fixed, a proper value of a_r and K can be found.
$l_u<l$ & $l_d<l$	Off-tuning the resonances, to get a maximum length of frequency locus running within the -10 dB circle
R_A	To suppresses the high current and therefore the lowers the reflections S11 of the spurious resonances to below -10 dB over a wide band.

B. A practical wideband dual-polarized absorber

A dual-polarized folded dipole array for practical use is a little more complicated than a singly polarized one. Therefore, for the dual polarized folded dipole array as a practically wideband absorber, three further adjustments may be needed and given below.

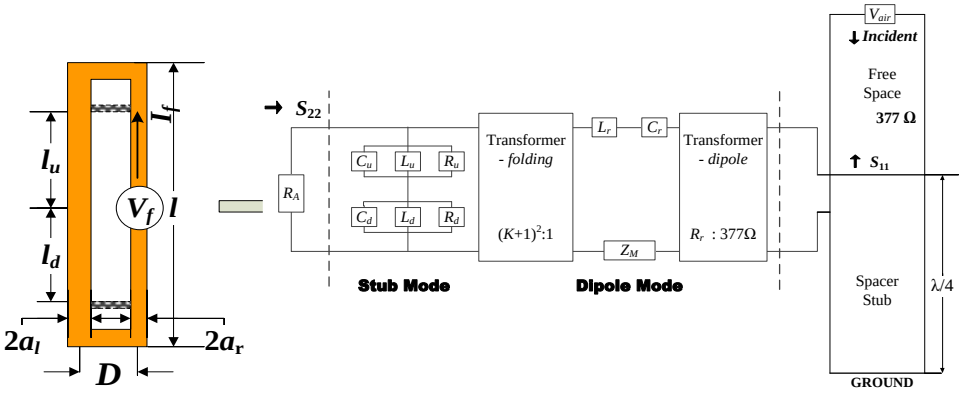

Fig. 1. Equivalent circuit of a unit cell on a folded-dipole array absorber.

(a) Increasing the dipole length to get off-tuning

By *top-loading* the dipole with triangles at the sides of each end of the dipole as shown in Fig. 2, the dipole length l is effectively made longer but still within the unit cell. Obviously, the length $2l_u$ twin-strip stubs is shorter than the dipole l, and with a suitable *off tuning* between the stub and dipole modes, one can get a wider band, as listed in Table 1.

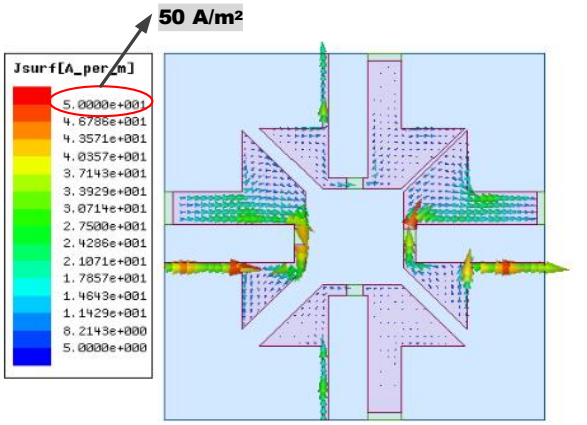

(a) R_s = 60 ohm, J_{max} = 50 A/m

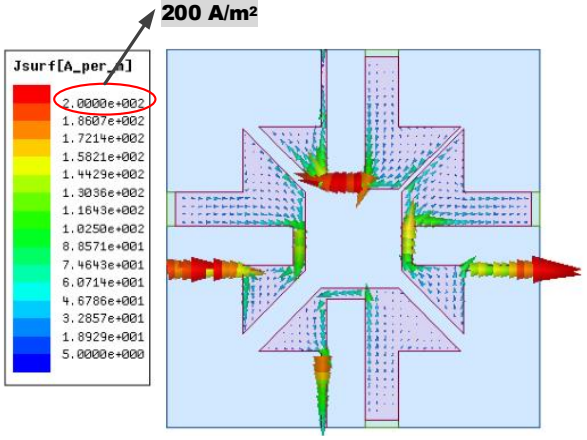

(b) R_s = 0, J_{max} = 200 A/m

Fig. 2. Current distributions at f = 7.2 GHz for the two cases.

(b) Adding Rs to each end of the folded dipole to suppress spurious mode

The closeness of the dipole ends means high capacitance between them, which might produce an extraneous mode of narrow band of high S_{11}. The extraneous mode can bring strong current flowing across the short circuits of the opposite folded dipoles as bridges from the left to the right. However, the strong current can be suppressed by inserting a resistor of the R_s. Figure 2 also shows the actual current flow of suppression before and after the insertion of R_s. Figures 3 (a) and 3 (b) show the corresponding elimination of the spurious S_{11}, in the Smith chart and in linear plots. Meanwhile, R_s is about 60 Ω, which is substantially smaller than the characteristic Z_0 of the twin-strip at about 200 Ω; as a result, the presence R_s does not significantly affect the characteristic of the open circuit resonator.

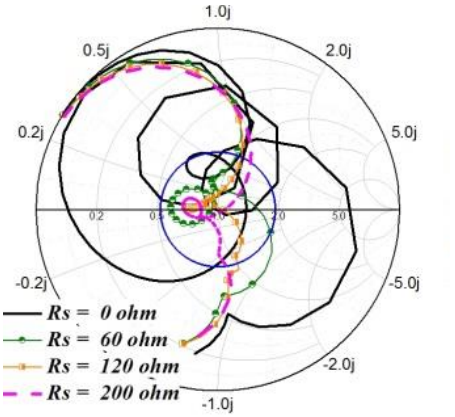

(a) S_{11} in Smith chart

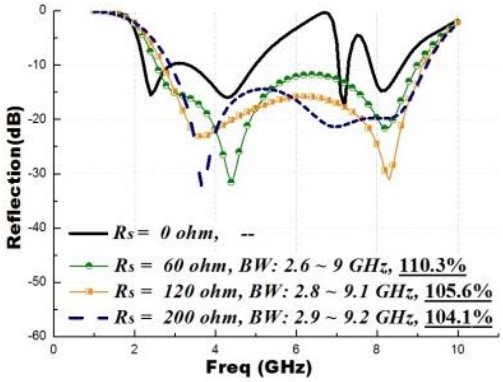

(b) Linear S_{11} vs. f

Fig. 3. Adding *Rs* to illuminate the spurious mode.

(c) Flipping thin dielectric slab on top of the air spacer

Generally, the folded dipole is usually printed on the top of the dielectric slab; however, to protect the metal parts of the absorber, one can flip the normal dielectric slab, and so that the folded dipoles are printed at the bottom of the dielectric slab as shown in Fig. 2. The flipping of the thin Teflon slab change the mutual couplings a little between the dipole ends, and therefore changes the excitation of the spurious mode as well. This means that the resistance R_s at the end of the folded dipole may be adjusted slightly to get the best suppression of the spurious mode and the final optimized bandwidth of the absorber. When t = 0.5 mm, Fig. 4 then shows the final S_{11} and bandwidths of the absorber, at the flipped case and the normal cases. Although the bandwidth improvement is not very significant, the flipping moves the printed folded dipoles behind the dielectric slab; and the move does provide some mechanical protect to the folded dipoles against possible mechanical damages,

e.g., scratches causing an open circuit to a folded dipole in the array. Additionally, the move can also protect the metal parts from oxidation and other chemical damages in some extent. Most importantly, the final bandwidth of the flipped case can reach up to 120%, i.e., a ratio of 4:1 between the upper and lower frequency limits.

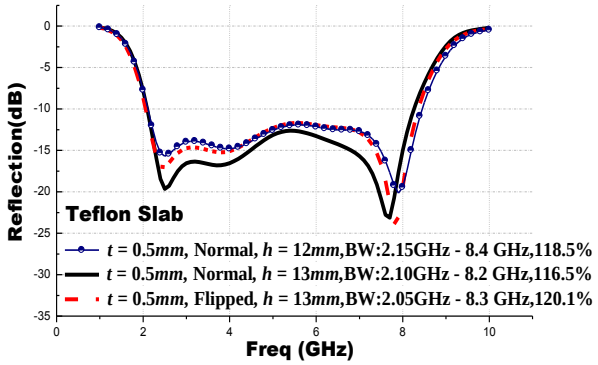

Fig. 4. Comparison of reflections of the absorber surface with optimized parameters in different cases, while a_l =0.2mm, a_r = 1.2mm, D = 4.2mm, b_f = 4.5mm, l_t = 20mm, a_e = 0.4mm, R_A = 300 ohm and R_s = 80 ohm.

III. RESULTS AND DISCUSSIONS

A. Experimental validation and discussions

To validate the final designs at Fig. 4 of the folded dipole absorber with flipped and normal slabs, we fabricated two prototypes with same array size (300mm * 300mm) but with different total thicknesses h. They both consist of 11*10 folded dipole elements as in Fig. 5. By using plastic screws via the slab to the ground, one can easily adjust the distance between them, which is also the thickness of the spacer. For practical engineering, however, the foam spacer may still be necessary because of its mechanical stability. The measurement setup is composed of two wideband horn antennas positioned on an arch support, with operating range of the horns from 2 GHz to 18 GHz.

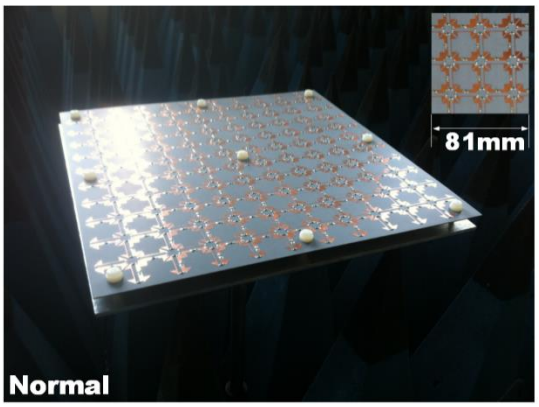

(a) Folded dipoles in Normal position

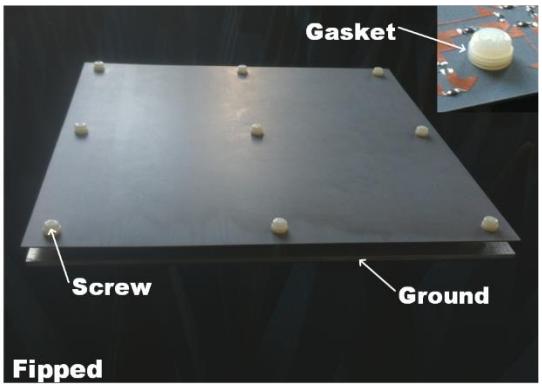

(b) Flipped folded dipole array

Fig. 5. Prototype of the absorber surface made of top-triangle-loaded folded dipole.

Figure 6 then shows the measured and simulated reflection coefficients of the four absorbers with similar physical parameters, except that the position and the thicknesses of the slab.

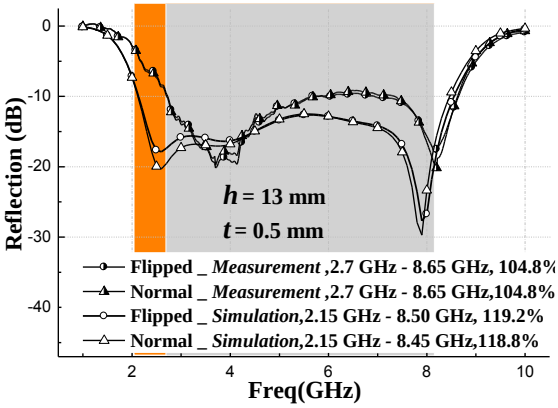

(a) t = 0.5 mm

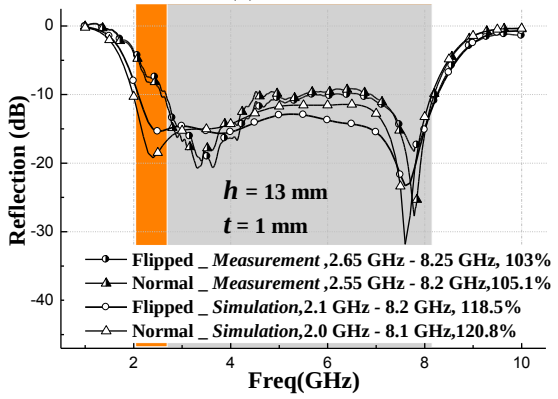

(b) t = 1 mm

Fig. 6. Comparison of the reflections between simulation and measurement for the cases of slab with different, while a_l = 0.2 mm, a_r = 1.2 mm, D = 4.2mm, b_f = 4.5 mm, l_t = 20 mm, a_e = 0.4 mm, R_A = 310 ohm and R_s = 82 ohm.

From Fig. 6, one can find that the measured result has a small deviation from the simulated ones at the lower frequency part, which the lower limit of the frequency band moves from 2 GHz to 2.6 GHz, and therefore leads to a decrease of the relative bandwidth, i.e., from 120% to 104%. The reasons could be as the follows: 1) the simulated bandwidth of the dipole is from 2 GHz to 8.3 GHz, in which the lower bounder is reaching the measurement limit of the horn antenna. This means that the feeding horn is operating at the right to its frequency limit, and minor error would happen at the limit; 2) the parasitic effects appeared on the Surface-mount resistor. The prototype measured in this work contains 11*10 cells, and each cell has eight resistors. For the consideration of cost, we apply normal surface-mount resistors to the cell, which might bring parasitic inductive reluctance at higher frequencies, and lead to a frequency deviation to the right. Actually, to decrease the parasitic effects, the author tried to lower the center frequency of the absorber, but still bound to the measurement system. However, if we did not consider too much on the cost, the results would agree well with the simulation results.

Figure 6 also indicates that the differences in S_{11} between absorbers made of normal slab and flipped ones is little. One can see that, the bandwidths for both cases are almost same, which means that the effects of flipping is very less. However, in practical engineering, the flipped structure of Fig. 5 (b) might be better in preventing from the unexpected mechanical damages to the printed folded dipoles.

B. S_{11} of the dual-polarized surface under oblique incidences of TE and TM Modes

Figures 7 (a) and 7 (b) give the calculated S_{11} vs. f for the case of (slab thickness) t = 1 mm, in the TE and TM incidence directions respectively. Figures 7 (a) and 7 (b) also show the angular stability of S_{11} vs. f curves of the dual-polarization absorber surface of the folded dipole array. Angular stability represents the effects of the oblique incident waves on the bandwidth of the absorber. For instance, when the direction of the incident wave θ is under 30° (from the normal direction of the absorber), the -10 dB bandwidth can be above 100% for both the TE and TM waves; the angular stability may be said to be good. As the angle θ becomes 45°, the reflections become larger but can still be under -7dB (absorption of 80%) during a wide band, one can still consider the angular stability as reasonably good.

C. *Discussions*

Table 2 lists the comparisons between our work and others published in recent years. Note that the that the *fractional bandwidth* of the absorber usually refers to $FB=(f_h-f_l)/f_0$, while f_h and f_l denote the upper and lower frequency limits of $|S_{11}|\leqslant$-10dB (the absorption A = (1-$|S_{11}|^2$)*100%, -10dB of $|S_{11}|$can get an absorption of 90%, which is good enough for most applications). From Table 2, one can find that, with the techniques of lossy FSS or metal FSS with lumped elements, the widest bandwidth is 117% in Ref. [7], but the thickness is larger and then lead to a lower value of Q, which is only five. In our work, the relative bandwidth of our proposed folded-dipole absorber can reach up to 120% in simulation, and 105% in measurement. Besides, by comparing the value of Q of each absorber in Table 2, one can also find that, the proposed absorber in this work has shown a good performance.

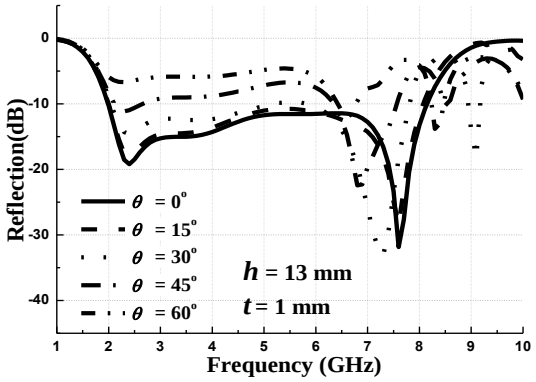

(a) TE wave

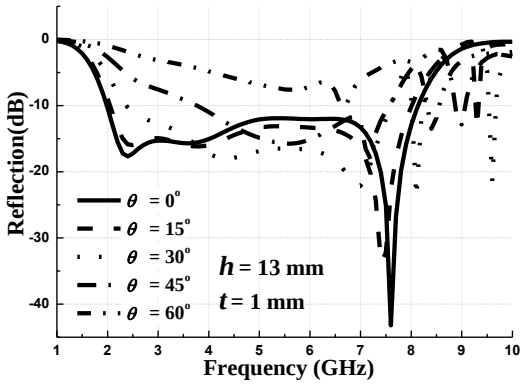

(b) TM wave

Fig. 7. S_{11} of the absorber surface under oblique incident waves, while the oblique angle is ranging from 0° to 60°.

Table 2: Comparison of numerical results of different absorber surfaces in the literature

Absorbing Surface Type	Type	Spacers	Total Thickness (d)	$f_L \sim f_H$ (GHz) ($BW = \frac{2(f_H - f_L)}{f_H + f_L} \times 100\%$)	$Q = \Delta\lambda/d$ ($\Delta\lambda = \lambda_{max} - \lambda_{min}$)	Good Angular Stability
Ref. [4]	Shaped resistive sheet	Air	5.0 mm ($0.25\ \lambda_0^*$)	7 ~ 22 (BW=103.5%)	5.84	$0^o \sim 45^o$
Ref. [7]	Salisbury screen with resistive loading	Air	9.0 mm ($0.33\ \lambda_0$)	4.5 ~ 17.5 (BW=117%)	5.5	$0^o \sim 40^o$
Ref. [9]	Metal with lump resistors	FR4 substrate $\varepsilon_r = 4.4$	3.18 mm ($0.138\ \lambda_0$)	8 ~ 18 (BW=77%)	6.55	-
Ref. [10]	3-D geometry	$\varepsilon_r = 3$	20.0 mm ($0.22\ \lambda_0$)	1.5 ~ 5 (BW=107%)	7	$0^o \sim 30^o$
Our work	Metal with lump resistors	Teflon substrate ($\varepsilon_{r1} = 2.65$, $h_1 = 1$ mm) and foam ($\varepsilon_{r2} = 1.06$, $h_2 = 10$ mm)	11.0 mm ($0.19\ \lambda_0$)	2.05 ~ 8.3 (BW=120%)	10.02 (simulation)	$0^o \sim 45^o$

VI. CONCLUSION

A practical dual-polarized absorber surface with high ratio of *bandwidth/thickness* is proposed in this work, which is constructed in the form of a folded dipole array with a grounded spacer. Unlike the traditional understanding of the absorber made of lossy FSS, the proposed absorber surface in this work is considered as a receiving dipole array but dissipating the incident wave other than transmitting it to the receiver. To verify our proposal, we fabricated and measured two prototypes of the dual-polarized absorber with different thickness of the slab. The hardware experiments show that the bandwidth only reaches 105%, a small decrease from the simulation results, which is likely due to an error of the measuring system being pushed to its frequency limits, and the parasitic effects occurs at the surface-mounted resistors. However, the absorber in this work shows a quite good performance in $Q = \Delta\lambda/d$, which can be around 8.5.

In this work, all simulations are carried out through HFSS or CST; however, with the manipulations of the Smith chart guided by the equivalent circuit, the amount of computation might be quite small. This is in contrast with the amount of computation needed when optimization of the absorber surface is done solely by numerical means and over the whole structure in a one-off solution. It is reasonable to expect the computation and optimization of a device would speed up by making use of prior knowledge; to achieve this, the space mapping approach uses coarse segmentation; this paper uses equivalent circuit and Smith chart manipulations, and thus provides a good physical insight.

ACKNOWLEDGMENT

This work was financial supported by Natural Science Foundation of Jiangsu Province for Youth (Grant No. BK20160912), Natural Science Foundation of China for Youth (Grant No. 61701256) and NUPTSF (Grant No. NY215038).

REFERENCES

[1] W. H. Emerson, "Electromagnetic wave absorbers and anechoic chambers through the years," *IEEE Trans. Antennas Propagation*, vol. 23, no. 4, pp. 484-490, 1973.

[2] W. W. Salisbury, "Absorbent Body for Electromagnetic Waves," U.S. Patent 2-599-944, 10, 1952.

[3] B. Chambers and A. Tennant, "Active Dallenbach radar absorber," *IEEE Antennas and Propagation Society International Symposium*, pp. 381-384, 2006.

[4] F. Costa, A. Monorchia, and G. Manara, "Analysis and design of ultra-thin electromagnetic absorbers comprising resistively loaded high impedance surfaces," *IEEE Transaction on Antennas and Propagation*, vol. 58, no. 5, pp. 1551-1558, May 2010.

[5] C.-X. Yuan, Z.-X. Zhou, J. W. Zhang, X.-L. Xiang, Y. Feng, and H.-G. Sun, "Properties of propagation of electromagnetic wave in a multilayer radar-absorbing structure with plasma- and radar-absorbing material," *IEEE Transactions on Plasma Science*, vol. 39, no. 9, pp. 1768-1775, 2011.

[6] F. C. Seman, R. Cahill, V. F. Fusco, and G. Goussetis, "Design of a Salisbury screen absorber using frequency selective surfaces to improve bandwidth and angular stability performance," *IET Microwaves, Antennas & Propagation*, vol. 5, no. 2, pp. 149-156, 2011.

[7] H.-Y. Chen, H.-B. Zhang, and L.-J. Deng, "Design of an ultra-thin magnetic-type radar absorber embedded with FSS," *IEEE Antennas and Wireless Propagation Letters*, vol. 9, pp. 899-901, 2010.

[8] A. K. Zadeh and A. Karlsson, "Capacitive circuit method of fast and efficient design of wideband

radar absorbers," *IEEE Trans on Antennas and Propagation*, vol. 57, no. 8, pp. 2307-2314, 2009.
[9] B. Chambers and A. Tennant, "Optimized design of Jaumann radar absorbing materials using a genetic algorithm," *IEE Proceedings on Radar, Sonar and Navigation*, vol. 143, no. 1, pp. 23-30, 1996.
[10] J. Yang and Z. Shen, "A thin and broadband absorber using double-square loops," *IEEE Antennas and Wireless Propagation Letters*, vol. 6, pp. 388-391, 2007.
[11] A. K. Rashid, Z. Shen, and S. Aditya, "Wideband microwave absorber based on a two-dimensional periodic array of microstrip lines," *IEEE Transactions on Antennas and Propagation*, vol. 58, no. 12, pp. 3913-3922, 2010.
[12] Y. Chang, W. Che, and Y. L. Chow, "Dipole array absorbing surface made thin and wideband with inductive ground," *IEEE Asia Pacific Microwave Conference*, pp. 927-930, 2011.
[13] Y. Chang, W. Che, and Y. L. Chow, "Broadband dual-polarization microwave absorber based on broadside-folded dipole array with triangle-lattice cells," *IEEE Antennas and Wireless Propagation Letters*, vol. 13, pp. 1084-1087, 2014.
[14] X. Q. Lin, P. Mei, P. C. Zhang, et al., "Development of a resistor-loaded ultra-wideband absorber with antenna reciprocity," *IEEE Transactions on Antennas and Propagation*, vol. 64, no. 11, pp. 4910-4913, 2016.

Yumei Chang received the M.Sc. and Ph.D. degrees from the Nanjing University of Science and Technology (NUST), Nanjing, China, in 2009 and 2014. She is currently a Lecturer in Nanjing University of Posts and Telecommunications.

From September 2012 to February 2013, she was a Visiting Scholar in the Department of Electronic and Computer Engineering at University of Waterloo, Canada. She has authored or coauthored over 30 journal and conference papers. Her research interests include microwave absorbers, FSS and microwave/millimeter-wave devices.

Yung L. Chow received the Ph.D. degree from the University of Toronto, Toronto, ON, Canada, in 1965. From 1964 to 1966, he was with the National Radio Astronomy Observatory, where he designed the array configuration of the VLA of 27 25-m dishes of Socorro, NM. In 1966, he was with the University of Waterloo (UW), Waterloo, ON, Canada, where he was involved with numerical methods and simplification of electromagnetic theory for monolithic microwave integrated circuit (MMIC) designs. In 1996, he retired from UW and became a Professor with the City University of Hong Kong (CITYU), Hong Kong. In 2002, he returned to UW as Professor Emeritus. He has authored or coauthored over 320 journal and conference papers. He holds seven U.S. and Canadian patents.

Three-bit Unit-cell with Low Profile for X-Band Linearly Polarized Transmitarrays

Binh Duong Nguyen and Minh Thien Nguyen

School of Electrical Engineering
International University, Ho Chi Minh City, 700000, Vietnam
nbduong@hcmiu.edu.vn, nmthien@hcmiu.edu.vn

Abstract ─ In this paper, we present a three-bit phase resolution and low profile unit-cell structure for X-band passive transmitarrays. The unit-cell is implemented using four metallic layers printed on two substrates separated by an air gap. The phase shift is achieved by a combination between current flow modification on middle layers and the variation of the size of path elements. Eight unit-cells are optimized to provide eight phase states with a step of 45°. Experimental results are conducted by using WR-90 waveguide to validate the design. These eight unit-cells cover a wide -3 dB transmission bandwidth of 15% and exhibit a low thickness of $0.18\lambda_0$.

Index Terms ─ Cut-ring patch, reflectarray, ring slot, transmitarray, unit-cell design.

I. INTRODUCTION

Microstrip transmitarray antenna is currently received many attentions for applications which require high gain antennas such as point-to-point wireless communications, satellite communications and radar applications. The microstrip transmitarray antenna offers many advantages over classic lens antenna in terms of light weight, low profile and low cost. A typical microstrip transmitarray antenna consists of a feeding source placed at the focal point and an array of transmitarray unit-cells. The operating principle of a transmitarray is based on the phase compensation. Each unit-cell is designed to provide a required phase shift in order to collimate the incident power from the source into a desired direction. To compensate for any required phase, the unit-cell should have a phase range of at least 360° while maintaining low transmission loss to maximize the efficiency.

Currently, unit-cell structures based on multi-layer frequency selective surfaces (FSS) are widely applied in transmitarray antennas [1-5]. The advantages of these structures are simple manufacturing process and low transmission loss. However, they are usually bulky due to large number of dielectric layers separated by an air gap of $\lambda_0/4$ between layers. As presented in [8], a maximum phase range for a single layer is 90° for -3dB transmission coefficient. To achieve a full 360° phase range, the unit-cells using four-layer structure have been proposed in [1-2]. The spacing between two layers of $\lambda_0/4$ makes the total thickness of these unit-cells to $3\lambda_0/4$. Different efforts have been devoted to reduce the profile of transmitarray unit-cells by reducing the number of layers to three [3-5]. Although the number of layers is reduced, the phase range of these proposed unit-cells cannot achieve 360° for -3 dB transmission coefficient. A transmitarray unit-cell based on a combination of C-patches and a ring slots loaded with rectangular gap was investigated [6]. The unit-cell was designed by using two substrates with only one air gap. This helps reduce the unit-cell complexity and the cost to precisely align multiple layers. Simulation results showed that the unit-cell can provide a large phase range and a low thickness.

In this paper, experimental validation for the transmitarray unit-cell structure using C-patch and ring slot loaded with rectangular gap is presented. We demonstrate that a low profile unit-cell structure can provide a large transmission phase range, wide -3 dB transmission bandwidth. A set of eight unit-cells are optimized for providing eight phase states with a step of 45° at 11.5 GHz. Prototypes of the eight unit-cells have been fabricated to validate the performance of the proposed unit-cell structure.

II. TRANSMITARRAY UNIT-CELL

A. Transmitarray unit-cell structure

The unit-cell structure is shown in Fig. 1. It is fabricated using two identical substrates which are Roger 5870 with a thickness of 1.575 mm and ε_r = 2.33. The two substrates are placed in cascade and separated by 1.6 mm of air. For each substrate, a C-patch is printed on the top while a ring slot loaded by rectangular gap is printed on the bottom. The structure operates with a linear polarization. In this case, the orientation of E-field is perpendicular to the gap of the C-patch, as shown in Fig. 1.

Submitted On: May 22, 2019
Accepted On: September 2, 2019

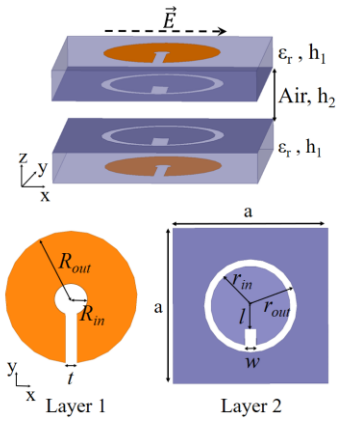

Fig. 1. Geometry of the proposed transmitarray unit-cell structure.

For a unit-cell using FSS, a full 360° phase range cannot be obtained with a single layer. An approach to increase the phase range is to increase number of layers of relatively wideband patch elements. As demonstrated in [8], the maximum transmission phase range for -1dB transmission coefficient, applying for a separation between layers of $\lambda_0/4$ are 54°, 170°, 308°, and full 360° for single, double, triple, and quad-layer FSS, respectively. In our design, the unit-cell is also made of a four-layer structure, we optimize it to achieve a low thickness while maintaining a large phase range. The method to vary the transmission phase is based on the variation of dimension of patch elements, combining with the modification of the current flow on two middle layers. The modification of the current flow on two middle layers causes a modification of the current on C-patches, which leads to a modification of the transmission phase of the transmission wave. Modifying the current on middle layers is carried out through modifying the rectangular gap length of the ring slots, as shown in [7]. In this work, eight unit-cells are optimized to provide eight phase states with a phase step of 45° at 11.5 GHz. These eight unit-cells can be divided into two groups. The first group comprises three unit-cells (cell No.1, No.2 and No.3) in which the rectangular gap is terminated at the centre of the ring slot, while the rectangular gap of the unit-cells in the second group is terminated at a distance l of about 1.75 mm from the centre of the ring slot. The distance (l) of 1.75 mm is chosen so that the current directions on the C-patch when l = 1.75 mm is opposite to that when l = 0 mm. The opposite of the current directions leads to a large difference of transmission phase between two cases. The variation of the transmission phase of unit-cells in each group is obtained by varying the dimension of C-patches and ring slots. Table 1 shows detailed dimension of the eight unit-cells. Total thickness of a unit-cell is 4.75 mm corresponding to $0.18\lambda_0$ and the cell size equals $0.54\lambda_0$, where λ_0 is the wavelength in free-space.

Table 1: Dimensions of the eight unit-cells

Unit Cell	Cut-ring Patch (mm)	Ring Slot (mm)	Normalized Phase (°) at 11.5 GHz
No.1	R_{out}=5.4, R_{in}=1.3, t=1	r_{out}=6, r_{in}=5.1, w=0.3, l=0	0°
No.2	R_{out}=5.5, R_{in}=0.7, t=0.5	r_{out}=6, r_{in}=5.4, w=0.3, l=0	-45°
No.3	R_{out}=5.7, R_{in}=0.7, t=0.5	r_{out}=6, r_{in}=5.6, w=0.3, l=0	-90°
No.4	R_{out}=5.1, R_{in}=1.5, t=1	r_{out}=5.7, r_{in}=4.6, w=1, l=1.8	-135°
No.5	R_{out}=5.3, R_{in}=1.5, t=1.2	r_{out}=6, r_{in}=4.7, w=1, l=1.75	-180°
No.6	R_{out}=5.4, R_{in}=1.5, t=1	r_{out} =6, r_{in}=4.8, w=1, l=1.75	-225°
No.7	R_{out}=5.6, R_{in}=1, t=1	r_{out}=6, r_{in}=4.9, w=1, l=1.8	-270°
No.8	R_{out}=5.7, R_{in}=1.3, t=1.2	r_{out}=6, r_{in}=4.9, w=1.2, l=1.75	-315°
	Substrate: h_1 = 1.575 mm, ε_r = 2.33, tanδ = tanδ = 0.0012, a = 14 mm, h_2 = 1.6 mm		

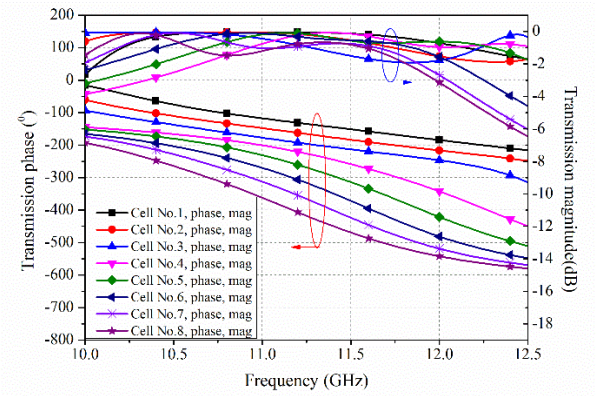

Fig. 2. Simulated transmission coefficients of eight unit-cells.

Parametric analysis and optimization have been performed by using ANSYS HFSS software, version 15. Eight unit-cells are simulated under array environment by using Floquet ports and Master-Slave boundaries, with a normal incident wave (incident angle of 0°). The simulated transmission phase and magnitude of eight unit-cells are shown in Fig. 2. As can be seen, two adjacent phase curves have a distance of 45° at 11.5 GHz. The phase variation of the unit-cells in group 1 is more linear than that of the unit-cells in group 2. Due to the non-linearity of the phase curves, the difference of 45° between two adjacent phase curves are not maintained at the frequencies far from 11.5 GHz. The eight unit-cells cover a large common -3 dB transmission bandwidth, from 10.3 GHz to 12.0 GHz, corresponding to 14.8%. The transmission magnitude is better than -1.5 dB at 11.5 GHz.

B. Equivalent circuit model

To better understand the operation principle of the proposed structure, it would be helpful to represent the structure in the form of the equivalent circuit. In order to simplify the circuit, we assume that the circuit has no ohmic loss, the equivalent circuit contains only capacitors and inductors. The C-patches on the top of two substrates are modeled as two series LC circuits which are placed in parallel (C_{S1}, L_{S1}, C_{S2}, L_{S2}). The modified ring slot loaded with a rectangular gap can be represented as a series LC circuit in parallel with a LC tank (C_{P1}, L_{P1}, C_{P2}, L_{P2}). The substrates are represented by a transmission lines with a length of h_1 and a characteristic impedance of $Z_1 = Z_0/\sqrt{\varepsilon_r}$, where ε_r is the relative permittivity of the substrate and $Z_0 = 377\ \Omega$ is the free space impedance. The equivalent circuit model of our proposed unit-cell is shown in Fig. 3.

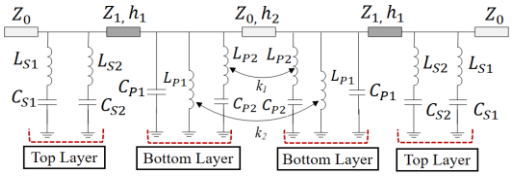

Fig. 3. Equivalent circuit model of our proposed unit-cell.

The equivalent circuit model of each element of the unit-cell structure is derived by using the retrieval method. The first step of this method is the full-wave analysis of the reflection coefficients of the C-patch and ring slot elements by assuming that the reflection coefficients obtained from full-wave simulation are exact. Since the number of capacitors and inductors is proportional to the number of resonances, the resonant behavior of the reflection coefficient suggests us the number of inductors and capacitors and their arrangement. The value of each component of the equivalent circuit can be determined by solving an iterative matching procedure. For this procedure, we compute the value of capacitors and inductors based on the poles and zeros of the reflection coefficient curves. We are first interested in the reflection coefficient of the C-patch and ring slot elements in the free space. In this case, the dielectric permittivity of the substrate is assumed to be 1. From [9], the reflection coefficient of a freestanding FSS is given by:

$$\Gamma_{element} = \frac{-1}{1 + 2Z_{element}/Z_0}, \qquad (1)$$

where $\Gamma_{element}$ is the reflection coefficient, $Z_{element}$ is the impedance of the element and Z_0 is the free-space impedance.

Once the value of lumped components of the equivalent circuit of the freestanding C-patch and ring slot is determined, we compute the value of the lumped components when the substrates are presented. The capacitance can be derived by using $C = (\varepsilon_{eff}+1).C_0/2$ for the case when a dielectric slab is present on one side of the element, where C_0 is the capacitance of a freestanding FSS. The approximated effective permittivity for the case when a dielectric slab is present on one side of the element is given by the equation 2, [9]:

$$\varepsilon_{eff} = \varepsilon_r + (\varepsilon_r - 1)\left(\frac{-1}{e^N(x)}\right), \qquad (2)$$

where $x=10*h/D$, h is the thickness of dielectric slab, D is the cell spacing and N is an exponential factor that takes into account the slope of the curve [10]. For the C-patch and ring slot, we select N=1.8.

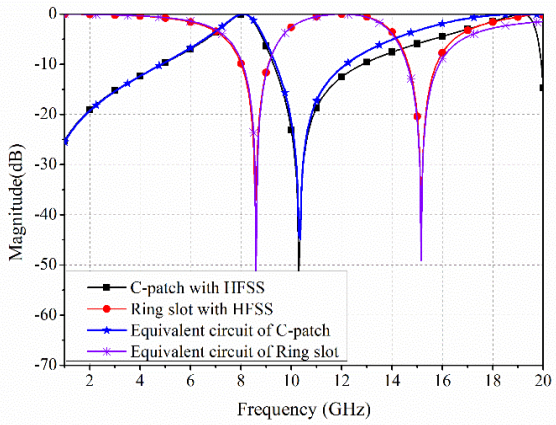

Fig. 4. Reflection magnitude of the C-patch and ring slot of the unit-cell No.1 in free space, obtained by HFSS and by equivalent circuit model (C_{S1}=0.021 pF; L_{S1}=18.42 nH; C_{S2}=0.024 pF; L_{S2}=2.92 nH; C_{P1}=0.135 pF; L_{P1}=1.595 nH; C_{P2}=0.039 pF; L_{P2}=4.52 nH).

Figure 4 shows the reflection coefficients of the freestanding C-patch and ring-slot of the unit-cell No.1, obtained from the full-wave EM simulations using ANSYS HFSS and the reflection coefficients of the equivalent circuit model simulated using Advanced Design System (ADS), version 2011 from Keysight Technologies, Inc. Figure 5 shows the transmission magnitude of the unit-cell No.1, obtained from HFSS and the transmission magnitude of the equivalent circuit model. As it can be seen, the results obtained from equivalent circuit models agree well with that from the full-wave EM simulations. However, there is a difference at high frequency. The difference is due to higher modes of the structure. We note that the equivalent circuit model using the above procedure is an approximate circuit. Although the equivalent circuit model does not totally match with the full-wave simulations, it is a useful tool for understanding the operation of our structure.

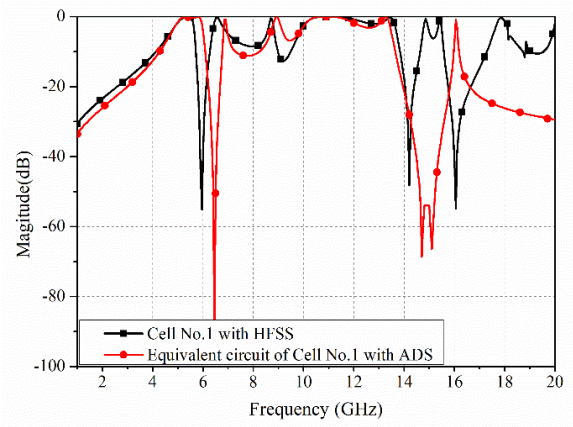

Fig. 5. Transmission magnitude of the unit-cell No.1 obtained by HFSS and by equivalent circuit model (C_{S1}=0.033 pF; L_{S1}=18.42 nH; C_{S2}=0.036 pF; L_{S2}=2.92 nH; C_{P1}=0.22 pF; L_{P1}=1.595 nH; C_{P2}=0.064 pF; L_{P2}=4.52 nH, coupling coefficient k_1=0.14, k_2=0.14).

For a transmitarray using multi-layer FSS structure, to achieve a large phase range, multi-resonant FSS structures are employed [1-2]. For our proposed unit-cell structure, the C-patch and ring-lot loaded with a rectangular gap create multiple resonances. For the ring slot loaded with a rectangular gap, the presence of the rectangular gap creates a second resonance at high frequency. The second resonance frequency is a function of the length of the rectangular gap. When the length of the rectangular gap is reduced the second resonant frequency is shifted towards to the higher frequency. The variation of the second resonance of the ring slot leads to a variation of the transmission phase of the unit-cell. Therefore, in this work, we combine the variation of the size of C-patch, ring slot and the length of the rectangular gap on the ring slot to vary the transmission phase.

III. VALIDATION OF UNIT-CELLS USING THE WAVEGUIDE SIMULATOR

Eight unit-cells have been fabricated to validate the simulation results. To get the transmission phase and magnitude of the unit-cells, a technique is to use the waveguide simulator. In our validation, the WR-90 standard waveguide was used as a waveguide simulator. The measurement system consists of two WR-90 waveguides and two rectangular-to-square transitions, as shown in Fig. 6. The rectangular-to-square transition is used to connect the square unit-cell to rectangular WR-90 waveguide. It has a square aperture of 17x17 mm^2, a rectangular aperture of 22.86x10.16 mm^2, and a thickness of 3 mm. The measurement system was calibrated using Through-Reflect-Line (TRL) calibration procedure. The reference plane is at the open-end of two WR-90 waveguides (it does not include the two rectangular-to-square transitions).

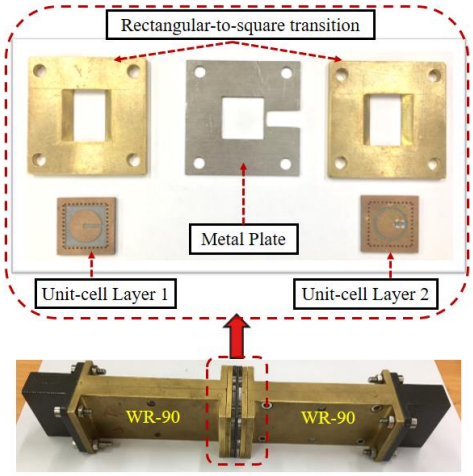

Fig. 6. Photo of the measurement system.

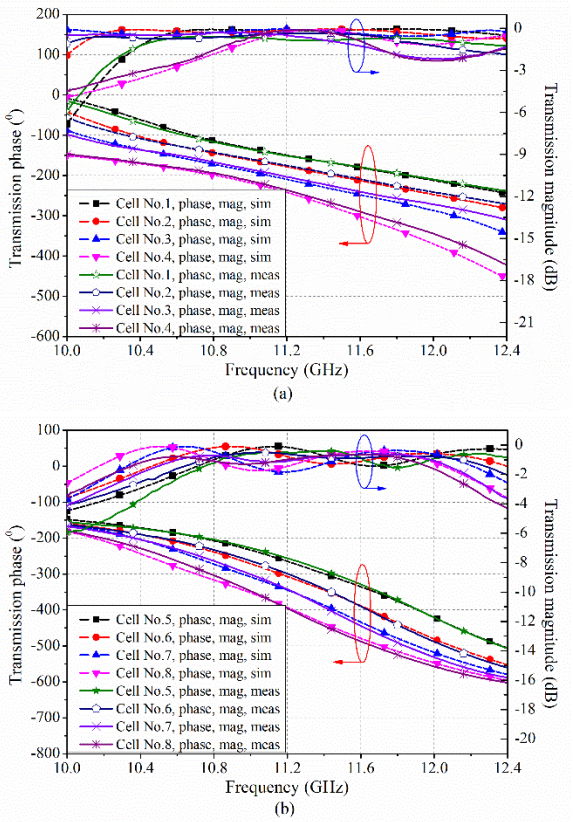

Fig. 7. Measured and simulated transmission coefficients of eight unit-cells in waveguide. (a) Unit-cells No.1, No.2, No.3, and No.4; (b) unit-cells No.5, No.6, No.7, and No.8.

The measured and simulated transmission coefficients of eight unit-cell in WR-90 waveguides are shown in Fig. 7. Measured results show that the transmission phase of eight unit-cells changes with a step of about 45° at 11.5 GHz. The transmission magnitude is

better than -1.5 dB at 11.5 GHz. The -3 dB transmission bandwidth is 1.75 GHz from 10.5 GHz to 12.25 GHz, corresponding 15%. A good agreement between simulation and measurement can be observed. Compared to the simulated results shown in Fig. 2; Fig. 7 has a lager phase range of 40°. The difference may due to the oblique angle of incident wave. We note that using the WR-90 waveguide to measure the transmission coefficients, the unit-cells are illuminated by a plane wave with an incident angle of 35° at 11.5 GHz. For the results in Fig. 2, unit-cells are simulated with a normal incident wave (incident angle of 0°).

The radiation patterns of one of unit-cell prototypes have been measured at different frequencies. The co- and cross-polarizations are shown in Fig. 8. In this case, we use a WR-90 waveguide combining with a rectangular-to-square transition to feed the unit-cell prototype that was placed at the open-end of the rectangular-to-square transition. As it can be seen, the co-polarizations in E-plane and H-plane are almost identical. Low side-lobe and good isolation of -15 dB between co-polarizations and cross-polarizations are obtained at 11.5 GHz. The gain of the unit-cell is determined based on the comparison method where the gain of a standard horn is used as the reference. The gain of the measured unit-cell is about 6.9 dBi at 11.5 GHz.

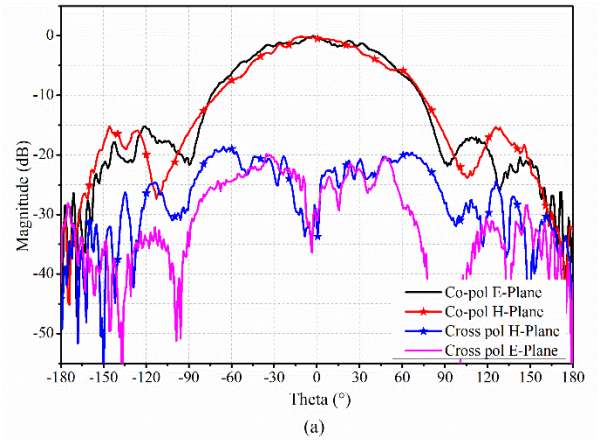

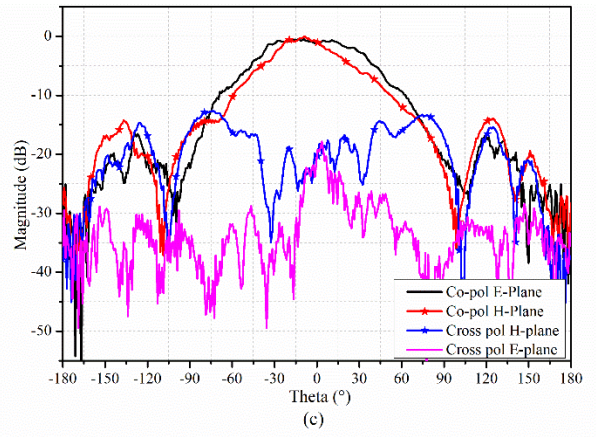

Fig. 8. Measured radiation pattern of a unit-cell at different frequencies: (a) 10.5 GHz, (b) 11.5 GHz, and (c) 12.4 GHz.

IV. CONCLUSION

A wide phase range and low profile unit-cell structure for X-band transmitarray antennas has been proposed and validated. The structure is made of C-patches and ring slots load rectangular gap printed on two substrates. Eight unit-cells provide eight phase states with a phase step of 45° at 11.5 GHz and a large -3 dB transmission bandwidth of 15%.

ACKNOWLEDGMENT

This research is funded by the Vietnam National Foundation for Science and Technology Development (NAFOSTED) under grant number 102.01-2016.35.

REFERENCES

[1] C. G. M. Ryan, M. R. Chaharmir, J. Shaker, J. R. Bray, Y. M. M. Antar, and A. Ittipiboon, "A wideband transmitarray using dual-resonant double square rings," *IEEE Trans. Antennas Propag*., vol. 58, no. 5, pp. 1486-1493, 2010.

[2] G. Liu, H. J. Wang, J. S. Jiang, F. Xue, and M. Yi, "A high-efficiency transmitarray antenna using double split ring slot elements," *IEEE Antennas Wirel. Propag. Lett.*, vol. 14, pp. 1415-1418, 2015.

[3] T. Chao, J. Yong-Chang, Z. Gang, and Hao Wang, "A wideband transmitarray using triple-layer elements combined with cross slots and double square rings," *IEEE Antennas Wirel. Propag. Lett.*, vol. 16, pp. 1561-1564, 2017.

[4] B. Rahmati and H. R. Hassani, "High-efficient wideband slot transmitarray antenna," *IEEE Trans. on Antennas Propag.*, vol. 63, no. 11, pp. 5149-5155, 2015.

[5] A. H. Abdelrahman, A. Z. Elsherbeni, and F. Yang, "High-gain and broadband transmit-array antenna using triple-layer spiral dipole element," *IEEE*

Antennas Wirel. Propag. Lett., vol. 13, pp. 1288-1291, 2014.

[6] M. T. Nguyen and B. D. Nguyen, "Wideband unit-cell design for X-band transmitarray," *18th International Symposium on Antenna Technology and Applied Electromagnetics (ANTEM)*, Aug. 2018.

[7] B. D. Nguyen and C. Phichot, "Unit-cell loaded with PIN diodes for 1-bit linearly polarized reconfigurable transmitarrays," *IEEE Antennas Wirel. Propag. Lett.*, vol. 18, pp. 98-102, 2018.

[8] H. Abdelrahman, A. Z. Elsherbeni, and F. Yang, "Transmission phase limit of multilayer frequency-selective surfaces for transmitarray designs," *IEEE Trans. Antennas Propag.*, vol. 62, no. 2, pp. 690-697, 2014.

[9] F. Costa, A. Monorchio, and G. Manara, "An overview of equivalent circuit modeling techniques of frequency selective surfaces and metasurfaces," *ACES Journal*, vol. 29, no. 12, pp. 960-976, 2014.

[10] F. Costa, A. Monorchio, and G. Manara, "Efficient analysis of frequency selective surfaces by a simple equivalent circuit model," *IEEE Antennas and Propagation Magazine*, vol. 54, no. 4, pp. 35-48, 2012.

Binh Duong Nguyen was born in Vietnam in 1976. He received the B.S. degree in Electronic and Electrical Eengineering from Ho Chi Minh University of Technologies, Ho Chi Minh, Vietnam, in 2000 and the M.S. and Ph.D. degrees in Electronic Engineering from the University of Nice-Sophia Antipolis, France, in 2001 and 2006 respectively. From 2001 to 2006, he was as a Researcher at the Laboratoire d'Electronique d'Antennes et Telecommunication, University of Nice-Sophia Antipolis, France. Currently, he is working at the International University, VNU-HCM. His research interests focus on millimeter antenna, reflector, reflect-array, transmitarray and FSS.

Minh Thien Nguyen was born in Vietnam in 1995. He received his Bachelor of Engineering in Electrical Engineering from the International University, Ho Chi Minh City in 2017. He is currently a Research Assistant for the School of Electrical Engineering, International University. His research interests mainly focus on design high gain antenna array, unit-cell design for passive reflect-array, transmitarrays, electronically reconfigurable transmitarray.

Circularly Polarized Circular Slit Planar Antenna for Vehicular Satellite Applications

Ebenezer Abishek B. [1], Arun Raaza [1], S. Ramesh [2], S. Jerritta [1], and V. Rajendran [1]

[1] Department of Electronics and Communication Engineering
Vels Institute of Science, Technology & Advanced Studies (VISTAS), Chennai, 600117, Tamil Nadu, India
abishek.se@velsuniv.ac.in, director.card@velsuniv.ac.in, jerritta.se@velsuniv.ac.in, director.ece@velsuniv.ac.in

[2] Department of Electronics and Communication Engineering
SRM Valliammai Engineering College, Chennai, 603203, Tamil Nadu, India
rameshs.ece@valliammai.co.in

Abstract ― A compact, ultra light weight and efficient asymmetric circular slit circularly polarized patch antenna is proposed for vehicular satellite communications. The circular slit in the corners of the patch is utilized for achieving circular polarization and an edge-fed through a microstrip feed line incorporates a quarter-wave transformer for impedance matching. Simulation results indicate an improvement in cross polarization isolation. The proposed antenna is fabricated using RT/DUROID 5880 material which is lighter, flexible and less expensive compared to the commercially existing ceramic corner curtailed patch antennas. The measured results indicate a reflection coefficient of -24.1 dB at resonant frequency, impedance bandwidth of 490 MHz ranging from 11.03 GHz to 11.52 GHz, axial ratio bandwidth of 180 MHz ranging from 11.16 GHz to 11.34 GHz and constant gain through the operating bandwidth with an apprehended peak gain of 5.6 dB. Experimentations affirmed that measured radiation results of the suggested antenna are similar to the simulation results and can be utilized as vehicle roof mounted antennas for diverse satellite communication applications.

Index Terms ― Asymmetric circular slit, circular polarization, patch antenna, vehicular satellite communication.

I. INTRODUCTION

The rapid growth in satellite communication attributes to the numerous services such as navigation, weather prediction, remote sensing, mobile communication, vehicular communication and so on [1]–[4]. Vehicular communication has recently become very important to carry out a good roadway management. The road accidents and burglary have increased in the urban areas to a level which is alarming. The accidents cause loss of human life which can be avoided if the accident victim is rescued at the earliest and given the necessary treatment. Similarly the thief can be caught at the earliest, if information of his vehicle is immediately sent to the corresponding authorities. Vehicular communication becomes inefficient due to the problem of losing vital information due to missed clusters [5], [6]. The only option to overcome this disadvantage is by utilizing satellites for vehicular communication called as vehicular satellite communication. Satellites have a larger footprint and provide communication even to the region where there are no communication systems [7]–[9]. In particular, vehicular satellite applications in the X band are widespread and are found to be robust across a variety of moving vehicles such as land vehicles, aero planes and even ships [10]–[12]. Parabolic Reflector antennas are conventionally used as X band satellite antennas which are generally large and hefty like a viable dish antenna or a reflector which has a diameter of 50 cm [13]. Such antennas degrade the radiation characteristics due to aerodynamic drag at high speed and are not best suited to be mounted on the roof of fast movable automobiles [14]. Applications utilizing satellite in automobiles and other moving vehicles will need a low-cost, light weight and high performance roof mountable antenna. In addition, circular polarized antennas are needed for satellite systems because the circularly polarized antennas are more immune to faradays rotation effect caused in ionosphere, reduction in degradation of signals due to fading or multipath interferences and orientation of transmitting and reception antenna need not be the same. Cross polarization isolation for these mobile satellite systems also require improvement for efficient communication [15].

To obtain miniaturization of an antenna for communication devices fitted in automobiles, investigators have also considered utilizing ceramic patch antennas but these antennas have reduced gain,

Submitted On: December 27, 2018
Accepted On: July 29, 2019

increased weight and increased cost; making it less affordable for day to day users [16].

Efforts have been made by researchers to design the circularly polarized (CP) patch antennas which are low cost, easy to fabricate and with good radiation characteristics like wide angle axial ratio bandwidth and improved cross polarization isolation. Apart from patch antennas, CP antenna can be constructed utilizing other antennas like helical antennas, spiral antennas, magneto-electric dipoles or slot antennas [17]–[20]. In microstrip patch antenna, the circular polarization can be achieved in any feed structure. Single feed is preferred because of its simpler feed structure. A recognized method of obtaining circular polarization in a single-feed patch antenna is by marginally perturbing the patch utilizing stubs, slits, notches, slots and curtailed corners[21], [22].

In this research, a circular shaped asymmetric slit edge feed microstrip patch antenna is proposed for CP radiation with a compact antenna size. The design was arrived by studying and analyzing different circularly polarized microstrip antennas. The slit circumference plays an important role in reduction of patch dimension and hence obtains the desired compact size. The performance of the antenna was compared with the conventional CP microstrip antenna with truncated corners using Ansys HFSS Electromagnetic simulation. The overall antenna dimensions were optimized and fixed to enhance and achieve the desired radiation characteristics. The proposed antenna has good cross polarization isolation compared to the conventional CP microstrip antenna with truncated comers. The proposed design was fabricated easily and inexpensively. The information of the proposed antenna design, simulated radiation results, fabrication and measured results are given in the following sections.

II. ANTENNA DESIGN METHODOLOGY

Figure 1 depicts the geometry of the proposed antenna and the optimized dimensions are listed in Table 1. The proposed antenna is printed on RT/DUROID 5880 substrate with thickness of 0.79 mm. The relative permittivity of this substrate is 2.2. The dimensions were calculated for the quarter wave transformer edge fed rectangular microstrip patch antenna using the design equations [23]. To achieve circular polarization, the rectangular patch is converted to a square patch by changing the dimensions and the inclusion of perturbation elements. A pair of symmetric perturbation elements in the form of circular slits in the main diagonal corners is inserted on the square patch as shown in Fig. 1. Another pair of circular slits in the corners of secondary diagonals are also inserted with a smaller radius when compared with the circular slits in the main diagonal corners. The corner slit structure in the patch radiator is asymmetric due to the difference in circumference of the two pairs of circular slits. The four circular slits are connected to the corresponding corners of the patch through a slit gap Sgl x Sg as shown in Fig. 1 given below.

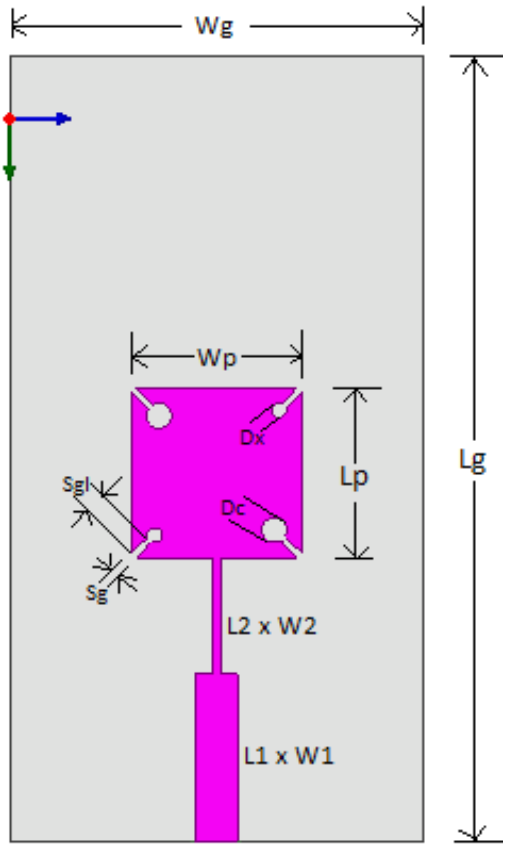

Fig. 1. Structure of the CP asymmetric slit patch antenna.

Table 1: Optimum parametric values of the proposed antenna

Parameters	Values (mm)
Lg	37.18
Wg	19.6
Lp	8
Wp	8
Dc	1.2
Dx	0.69
L1	7.8
W1	2
L2	5.6
W2	0.4
Sg	0.28
Sgl	1.1
Substrate thickness	0.79

The presented antenna is edge fed by quarter wave transformer. Circular slits in the main diagonal direction of the patch acts as a perturbation to the microstrip patch which excites two modes which are orthogonal and has

a 90° phase shift, thus causing CP radiation. Two modes Ex and Ey are excited from the corner slits which has larger radius. This excitation of the two modes causes vector rotation of current to achieve left handed circular polarization. The corner slits in secondary diagonal corners suppresses cross polarization. This improves the cross polarization isolation of the antenna. When the two pairs of the corner slits in main diagonal and secondary diagonal are swapped- right handed circular polarization is achieved.

Variation of the diameter of the circular slits on the main and secondary diagonal direction of the proposed antenna causes variation in the resonance frequency of the antenna [24]. The optimal dimensions of the antenna are obtained by Ansys HFSS Electromagnetic simulation.

III. RESULTS AND DISCUSSION

A. Simulation of proposed asymmetric circular slit circularly polarized patch antenna

The simulation results of the proposed CP patch antenna are shown Figs. 2, 3, 4 and 5. Figure 2 shows the reflection coefficient (S_{11}) simulated over a frequency range of 9 GHz to 13 GHz and it's seen that S11 values for the frequency range of 11.02 GHz to 11.52 GHz is less than -10 which is the industrial standard for measuring impedance bandwidth. Thus the impedance bandwidth of 500MHz is achieved.

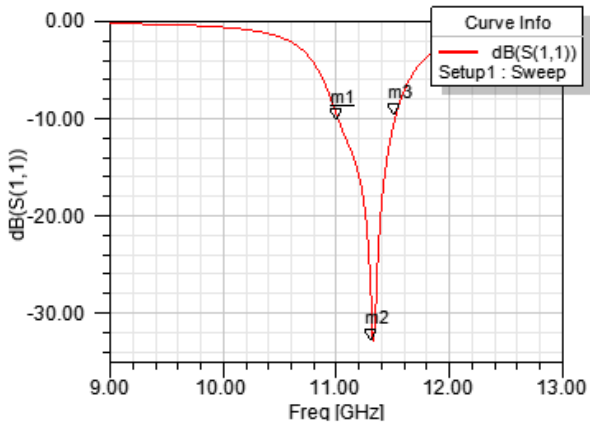

Fig. 2. Reflection coefficient (S11) of the proposed antenna.

The simulated result of axial ratio is shown in Fig. 3. The axial ratio values are simulated over the frequency range of 11.00 GHz to 11.5 GHz with the step size of 0.02 GHz and the angle Phi=90deg is kept constant for selecting the electric field component. Its seen that the axial ratio for the frequency range of 11.16 GHz to 11.34 GHz is less than 3 which is the industrial standard required for circular polarized antennas. The axial ratio bandwidth is 180MHz.

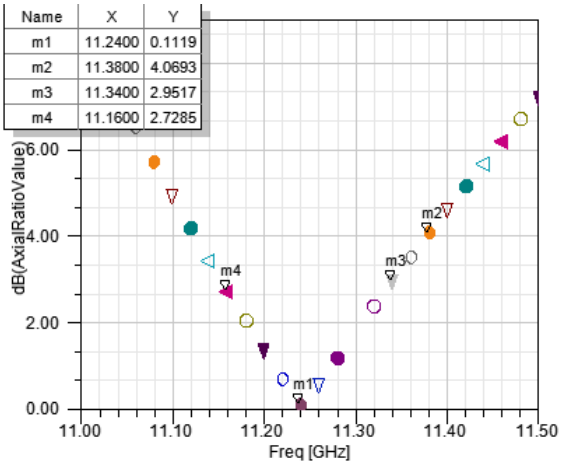

Fig. 3. Axial ratio of the proposed antenna.

The peak gain is found to be 6.6985dB in simulation. Figure 4 and Fig. 5 given below shows the radiation pattern of the proposed antenna and conventional truncated corner patch antenna respectively.

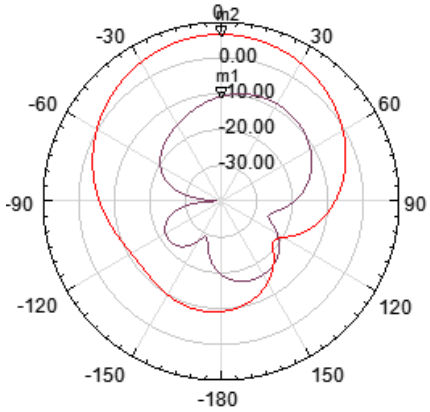

Fig. 4. Radiation pattern of the proposed antenna.

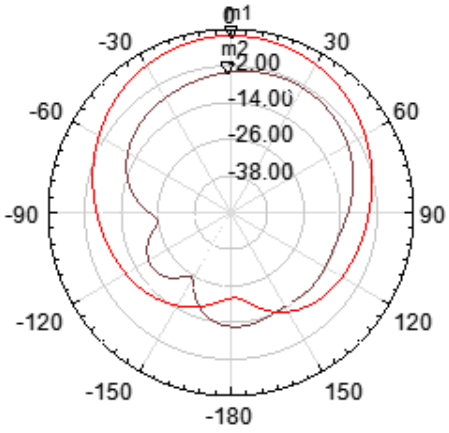

Fig. 5. Radiation pattern of the conventional corner truncated antenna.

The red colour trace in Fig. 4 and Fig. 5 indicates the co-polarization plot which is left-handed circular polarization plot. Similarly, the lavender colour trace in both the figures indicate the cross-polarization plot which is right handed circular polarization plot. The cross polarization isolation is the difference between the co-polarization and cross-polarization at 0 dB. The radiation pattern proposed single element circularly polarized microstrip patch antenna and conventional corner truncated circularly polarized patch antenna is shown in Fig. 4 and Fig. 5 respectively. These results indicate a significant improvement of cross polarization isolation by 4dB in the proposed single element circularly polarized microstrip patch antenna which will be very useful in enhancing the efficiency of the mobile satellite communication systems [15]. This enhancement in cross polarization isolation is due to the smaller slits in the secondary diagonal that suppresses the cross polarization.

B. Fabrication, testing and validation of the proposed asymmetric circular slit circularly polarized patch antenna

The optimized antenna design was fabricated on a RT/DUROID 5880 substrate. The fabricated circularly polarized asymmetric slit patch antenna is shown in Fig. 6. The external dimensions are 37.18 mm × 19.6mm × 0.79mm. All the dimension values including patch, feed etc are specified in Table 1.

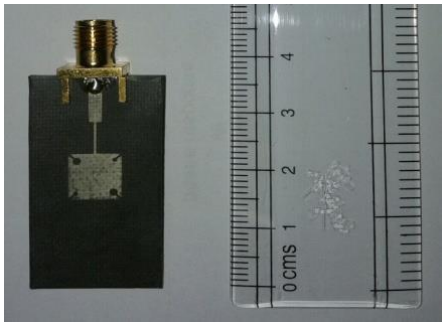

Fig. 6. Fabricated circularly polarized asymmetric slit patch antenna.

This circularly polarized asymmetric slit patch antenna is designed to operate at the centre frequency of 11.3 GHz for vehicular satellite communication applications. Agilent N9917A vector network analyzer was utilized to measure the reflection coefficient. Figure 7 shows the comparison plot of measured and simulated reflection coefficient of the proposed antenna. The simulated -10dB impedance bandwidth was 500 MHz (11.02 to 11.52 GHz) and the measured impedance bandwidth was 490 MHz (10.9 to 11.39 GHz). The Fig. 7 also shows a small shift in the resonant frequency due to manufacturing errors.

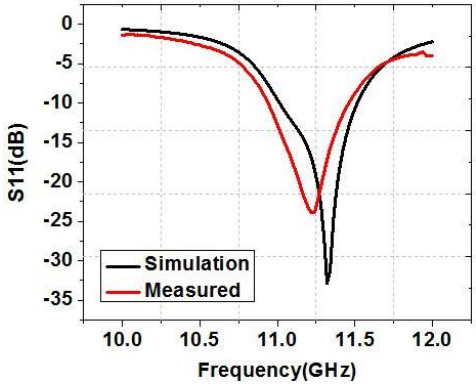

Fig. 7. Reflection coefficient of proposed antenna.

The radiation patterns were measured in a test setup which consists of an anechoic chamber with a Verdant JR12 horn antenna as the transmitting antenna of the measurement system for validation of the proposed antenna design.

The measured Vs. simulation radiation patterns of proposed antenna at the resonant frequency of 11.3 GHz in E and H principal planes is shown in Fig. 8 and Fig. 9 respectively. These figures show left-handed circularly polarized broadside radiation pattern with maximum directivity along 0deg. The axial ratio is found to be less than 3-dB across a 100° beamwidth over the axial-ratio bandwidth frequency range in both the principal planes and the side lobe level of this proposed antenna is measured as -14.9 dB. The test setup comprising of anechoic chamber and JR12 transmitting horn antenna was used to measure the radiation pattern. The direct measurement of gain was not possible utilizing this test setup. Therefore, the gain of the proposed antenna was determined manually using Friss's transmission formula by applying the measured received power obtained by the test setup. There is a slight reduction in gain which occurs due to losses in the connector. But still the simulated results are in good agreement with the measured results and the radiation patterns of simulated and measured results are similar.

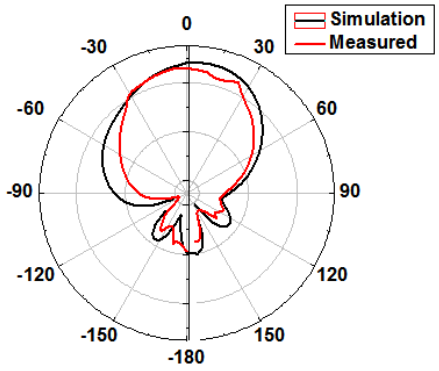

Fig. 8. E-plane pattern of the proposed antenna.

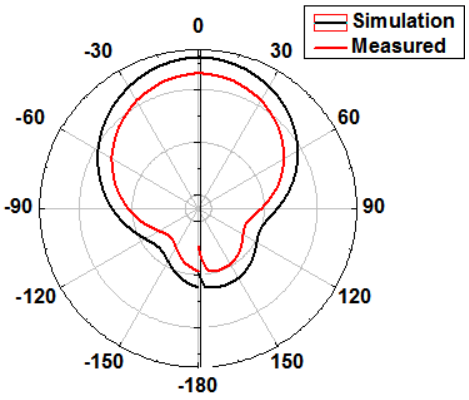

Fig. 9. H-plane pattern of the proposed antenna.

The simulated vs. measured results of the proposed antenna discussed in this section is consolidated and given in Table 2 shown below.

Table 2: Optimum parametric values of the proposed antenna

Parameters	Simulated	Measured
Axial ratio bandwidth	180 MHz	170 MHz
Impedance bandwidth	500 MHz	490 MHz
Peak Gain	6.6985 dB	5.6 dB

IV. CONCLUSION

The compact circularly polarized asymmetric slit patch antennas have been presented on low loss RT/DUROID 5880 substrate. The antenna has a 3-dB axial ratio bandwidth of 180 MHz and impedance bandwidth of 490 MHz. The proposed antenna has improved cross polarization isolation when compared to the conventional corner truncated patch antenna. The measured gain 5.6 dB was lower by 1dB for the antenna when compared with simulation results on the RT/DUROID 5880 substrate. The largest possible slit without changing the required characteristics enabled size reduction to get a compact structure. The proposed antenna because of its improved cross polarization isolation besides the good radiation characteristics is best suited for vehicular satellite applications.

REFERENCES

[1] W. Lin and H. Wong, "Circularly polarized conical-beam antenna with wide bandwidth and low profile," *IEEE Trans. Antennas Propag.*, vol. 62, no. 12, pp. 5974-5982, 2014.

[2] Q. X. Chu, W. Lin, W. X. Lin, and Z. K. Pan, "Assembled dual-band broadband quadrifilar helix antennas with compact power divider networks for CNSS application," *IEEE Trans. Antennas Propag.*, vol. 61, no. 2, pp. 516-523, 2013.

[3] A. R. Weily and Y. J. Guo, "Circularly polarized ellipse-loaded circular slot array for millimeter-wave WPAN applications," *IEEE Trans. Antennas Propag.*, vol. 57, no. 10 PART 1, pp. 2862-2870, 2009.

[4] S. I. Jeon, Y. W. Kim, and D. G. Oh, "A new active phased array antenna for mobile direct broad-casting satellite reception," *IEEE Trans. Broadcast.*, vol. 46, no. 1, pp. 34-40, 2000.

[5] J. Chen, G. Mao, C. Li, W. Liang, and D. G. Zhang, "Capacity of cooperative vehicular networks with infrastructure support: Multiuser case," *IEEE Trans. Veh. Technol.*, vol. 67, no. 2, pp. 1546-1560, 2018.

[6] Y. A. Shah, H. A. Habib, F. Aadil, M. F. Khan, M. Maqsood, and T. Nawaz, "CAMONET: Moth-flame optimization (MFO) based clustering algorithm for VANETs," *IEEE Access*, vol. 6, pp. 48611-48624, 2018.

[7] R. De Gaudenzi, S. Member, and F. Giannetti, "DS-CDMA satellite diversity reception for personal satellite communication: Satellite-to-mobile link performance analysis," vol. 47, no. 2, pp. 658-672, 1998.

[8] M. Buck et al., "An advanced satellite UMTS testbed for laboratory and over-the-air experiments of third-generation mobile services: Part I - System design aspects," vol. 57, no. 1, pp. 169-179, 2008.

[9] K. Kaneko, "Construction of a flexibility analysis model for flexible high-throughput satellite communication systems with a digital channelizer," vol. 67, no. 3, pp. 2097-2107, 2018.

[10] J. Huang, et al., "A new compact and high gain circularly-polarized slot antenna array for ku-band mobile satellite TV reception," *IEEE Access*, vol. 5, pp. 6707-6714, 2017.

[11] M. T. Zhang et al., "Design of novel reconfigurable reflect arrays with single-bit phase resolution for ku-band satellite antenna applications," *IEEE Trans. Antennas Propag.*, vol. 64, no. 5, pp. 1634-1641, 2016.

[12] S. Ye, et al., "High-Gain planar antenna arrays for mobile satellite communications," *IEEE Antennas Propag. Mag.*, vol. 54, no. 6, pp.256-268, 2012.

[13] A. K. Kundu, M. T. Hossain Khan, W.Sharmin, M. O. Goni, and K. A. Barket, "Design and performance analysis of a dual band parabolic reflector antenna with waveguide dipole feed and link budget optimization," *Proc. 2013 2nd Int. Conf. Adv. Electr. Eng. ICAEE 2013*, pp. 309-312, 2013.

[14] A. Liu, Q. Yang, X. Zhang, and W. Deng, "Collision avoidance radar system for the bullet train: Implementation and first results," *IEEE Aerosp. Electron. Syst. Mag.*, vol. 32, no. 5, pp.4-17, 2017.

[15] R. Touzi, P. W. Vachon, and J. Wolfe, "Requirement on antenna cross-polarization isolation for the operational use of C-band SAR

constellations in maritime surveillance," *IEEE Geosci. Remote Sens. Lett.*, vol. 7, no. 4, pp.861-865, 2010.

[16] X. Tang, H. Wong, Y. Long, Q. Xue, and K. L. Lau, "Circularly polarized shorted patch antenna on high permittivity substrate with wideband," *IEEE Trans. Antennas Propag*., vol. 60, no. 3, pp. 1588-1592, 2012.

[17] Q. Zhu, K. B. Ng, and C. H. Chan, "Printed circularly polarized open loop antenna array for millimeter-wave applications," *2017 IEEE Antennas Propag. Soc. Int. Symp. Proc.*, vol. 2017-Janua, no. 2, pp. 2561-2562, 2017.

[18] Y. Li and K. M. Luk, "A 60-GHz Wideband circularly polarized aperture-coupled magneto-electric dipole antenna array," *IEEE Trans. Antennas Propag*., vol. 64, no. 4, pp. 1325-1333, 2016.

[19] J. Wu, Y. J. Cheng, and Y. Fan, "Millimeter-wave wideband high-efficiency circularly polarized planar array antenna," *IEEE Trans. Antennas Propag*., vol. 64, no. 2, pp. 535-542, 2016.

[20] H. W. Lai, D. Xue, H. Wong, K. K. So, and X. Y. Zhang, "Broadband circularly polarized patch antenna arrays with multiple-layers structure," *IEEE Antennas Wirel. Propag. Lett*., vol. 16, pp. 525-528, 2017.

[21] Y. F. Lin, C. H. Lee, S. C. Pan, and H. M. Chen, "Proximity-fed circularly polarized slotted patch antenna for RFID handheld reader," *IEEE Trans. Antennas Propag*., vol. 61, no. 10, pp. 5283-5286, 2013.

[22] Nasimuddin, Z. N. Chen, and X. Qing, "A compact circularly polarized cross-shaped slotted microstrip antenna*," IEEE Trans. Antennas Propag*., vol. 60, no. 3, pp. 1584-1588, 2012.

[23] C. A. Balanis, *Antenna Theory*, 3rd ed., John Wiley & Sons, Inc., 1997.

[24] Nasimuddin, X. Qing, and Z. N. Chen, "Compact asymmetric-slit microstrip antennas for circular polarization," *IEEE Trans. Antennas Propag*., vol. 59, no. 1, pp. 285-288, 2011.

Ebenezer Abishek B. received his B.E. in Electronics and Communication Engineering from Anna University, M.E. in VLSI Design from Anna University, Chennai and Ph.D. in Electronics and Communication Engineering from VISTAS in 2010, 2012 and 2019 respectively. He is currently, working as an Assistant Professor in the department of Electronics and Communication Engineering, VISTAS, Chennai with teaching experience of 6 years. His area of interest includes Antennas & Propagation and Electromagnetic Applications. His ORCiD is 0000-0003-2908-7069.

Arun Raaza holds a Master of Research degree from Institute of Advanced Telecommunications, Swansea University, UK and Ph.D. – ECE at VISTAS, Chennai. His research work in Antennas include the completion of the CABS/DRDO funded project titled "Design and Simulation study of Low profile Ku band airborne SATCOM antenna unit for early warning system" in 2017. He has contributed towards 6 Govt. of India projects (2 for DAE, 2 for DSIR, 2 for DRDO), several Industry funded projects, 30+ National patents, 2 International patents and 8 Transfer of Technologies.

S. Ramesh received his B.E. in Electronics and Communication Engineering from University of Madras, M.Tech. in Communication Engineering from VIT University, Vellore and received his Ph.D. degree on from SRM University, Chennai, in 2001, 2004 and 2015 respectively. He is currently working as an Associate Professor in the Department of Electronics and Communication Engineering, SRM Valliammai Engineering College, Chennai. He is a senior member (S'10-M'17-SM'18) of IEEE Antennas & Propagation Society. His ORCiD is 0000-0002-2946-5296.

Jerritta Selvaraj is an Associate Professor in the Department of ECE at VISTAS, Chennai, India. She holds a Ph.D. degree in Biomedical Electronics Engineering from University Perlis Malaysia (UniMAP). Her research focuses on electromagnetic applications.

V. Rajendran received his M.Tech. from Indian Institute of Science (IISc), Bangalore, India and received his Ph.D. degree from Chiba University, Japan in 1981 and 1993 respectively. He is currently, Professor and Director of the Department of ECE in VISTAS, Chennai.

High Impedance Surface Application to Dipole Antenna Design

Samir Berkani [1], Youssef Lamhene [1], Mustapha Hadj-Sadok [1], and Henri Baudrand [2]

[1] Laboratoire d'Instrumentation, FEI, Université USTHB, Alger
sam-30@live.fr, lamhene.y@gmail.com, mustaphahadjsadok@gmail.com

[2] Laboratoire RCEM, Toulouse, France
henri.baudrand@yahoo.fr

Abstract — in this paper, HIS (High Impedance Surface) are used, in order to verify their utilities; we have considered two different structures as a ground. The first is mushroom EBG (Electromagnetic Band Gap) structure which is composed of several patches with a ground connecting via, where the second is 2D metamaterial structure with resonant rings. Both the structures are investigated by simulation and compared at the frequency 12 GHz. The metamaterials proprieties are successfully verified around the resonant frequency.

Index Terms — Digital capacitance, EBG structures, metamaterials, negative index materials, wire antenna.

I. INTRODUCTION

The antennas manufacture requires a big precision in realization, because the dimensions of these circuits are of the same order of magnitude as the wave length. Considering imprecision factors due to the manufacture constraint, surface waves will be engendered; consequently, antenna performance will be influenced.

A special material is used to block surface waves known as metamaterial, it enhances significantly the antenna performance which is characterized by simultaneously negative values of the permeability and the permittivity [1]; it doesn't exist in natural state.

Metamaterials enhance significantly the antenna performance. They have interesting proprieties [2], it consists in stopping surface waves to propagate along the surface, there is no phase delay to be introduced to the progressive wave and the evanescent wave is amplified. Hence, we can say that both propagating and evanescent waves contribute to the resolution of the system and circuit's spatial frequency is restored. Therefore the wave behaves as there is no physical obstacle [3-4].

II. METAMATERIAL TRANSMISSION LINE THEORY

Figure 1 [5] shows a cell of metamaterial transmission line which is a combination of Right-Handed Transmission Line (RHTL) and Left-Handed Transmission Line (LHTL). By applying the Kirchhoff law, it results:

$$\begin{cases} \dfrac{\partial v(x,t)}{\partial x} = Zi(x,t) = j\left(L_R.\omega - \dfrac{1}{\omega.C_L}\right)i(x,t), & (1) \\ \dfrac{\partial i(x,t)}{\partial x} = Yv(x,t) = j\left(C_R.\omega - \dfrac{1}{\omega.L_L}\right)v(x,t). & (2) \end{cases}$$

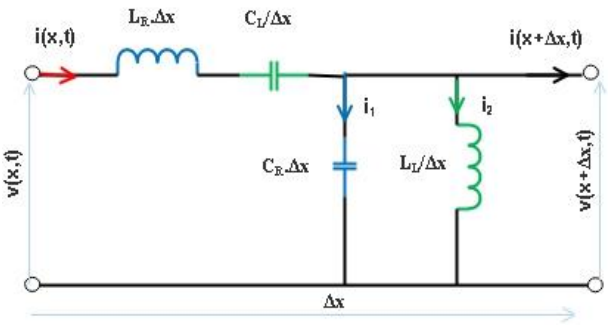

Fig. 1. Metamaterial transmission line cell model.

We solve simultaneously (1) and (2), we obtain the wave equations, for Voltage wave V:

$$\partial^2 v(x,t)/\partial x^2 = -Z\,Y v(x,t) = -\gamma^2 v(x,t). \quad (3)$$

Where:

$$\gamma = \sqrt{Z\,Y} = \alpha + j\beta = \sqrt{-\omega^2\left(L_R C_R + \frac{1}{\left(\omega^2\sqrt{L_L C_L}\right)^2} - \frac{L_R C_L + L_L C_R}{\left(\omega\sqrt{L_L C_L}\right)^2}\right)}\,. \quad (4)$$

We can introduce the RH resonant frequency: $\omega_R = \frac{1}{\sqrt{L_R C_R}}$. And LH resonant frequency $\omega_L = \frac{1}{\sqrt{L_L C_L}}$, it results:

$$\gamma = j\sqrt{(\omega/\omega_R)^2 + (\omega_L/\omega)^2 - k\omega_L^2}\,. \quad (5)$$

Equation (5) describes all the behaviors of the metamaterial transmission line.

Figure 2 shows the graph of the complex propagation constant. Where A = max($\boldsymbol{\omega_s}, \boldsymbol{\omega_P}$), B = min($\boldsymbol{\omega_s}, \boldsymbol{\omega_P}$) and C = ω_F, ω_s, ω_P and ω_F are respectively the series, shunt resonance frequencies and maximum attenuation frequency [5].

Submitted On: March 10, 2018
Accepted On: April 3, 2019

We consider Fig. 2, if $\omega < \min(\boldsymbol{\omega_s}, \boldsymbol{\omega_P})$, the phase velocity (slope of the line segment from origin to curve) and group velocity (slope of the curve) have opposite sign (they are antiparallel) which means that the transmission line is left-handed and that β is therefore negative.

If we apply Maxwell equations and use (1) and (2), it results:

$$\begin{cases} \mu(\omega) = L_R - \dfrac{1}{\omega^2 C_L}, & (6) \\ \varepsilon(\omega) = C_R - \dfrac{1}{\omega^2 L_L}. & (7) \end{cases}$$

When $\omega << \min(\boldsymbol{\omega_s}, \boldsymbol{\omega_P})$, (6) and (7) become:

$\begin{cases} \mu(\omega) = -1/\omega^2 C_L < 0 \\ \varepsilon(\omega) = -1/\omega^2 L_L < 0 \end{cases}$ Left-Handed Transmission Line.

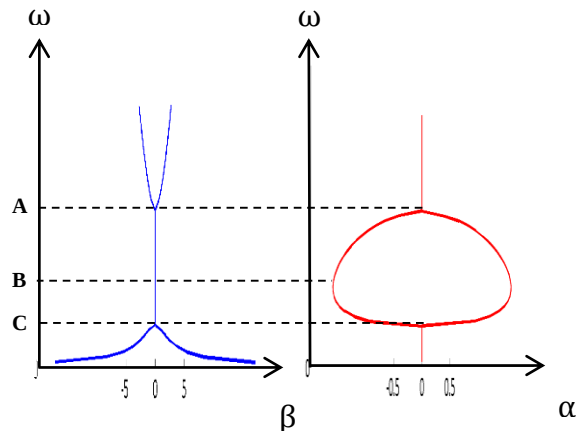

Fig. 2. Complex propagation constant vs. frequency

III. SIMPLE DIPOLE ANTENNA RESPONSE

Figure 3 shows the radiation pattern of dipole antenna in free space. In horizontal plane (3.B), when viewed from above, the pattern exhibits two lobes which represent the omnidirectional characteristic of the dipole antenna (bidirectional radiation).

When a dipole antenna is installed close to the earth's surface, the pattern radiation is attenuated because of the reflection from the surface [6]. In the ideal case, the gain of the dipole antenna doesn't exceed 3 dB as shown on Fig. 4.

IV. MODELS AND DIMENSIONS

In order to investigate the performance of the dipole antenna, it will be installed close to different surfaces and each structure will be also optimized in order to seek the best results.

A. Dipole above a perfect electric conductor (PEC)

The most simple structure is a ground plane placed under the dipole antenna (27.5X27.5 mm) of distance h_{dist} = 1.925 mm functions as reflector as shown on Fig. 5.

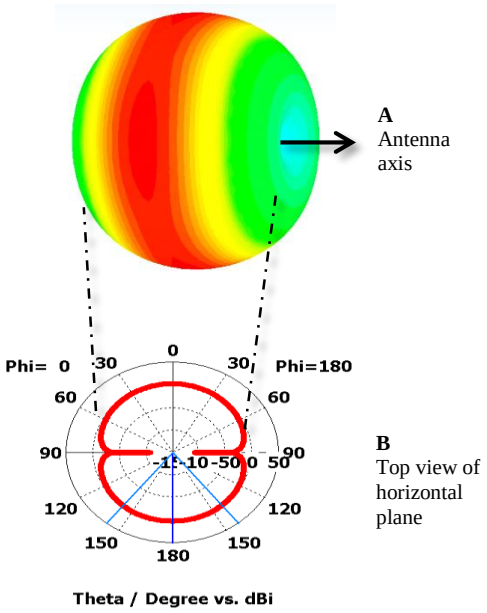

Fig. 3. Idealized dipole radiation pattern.

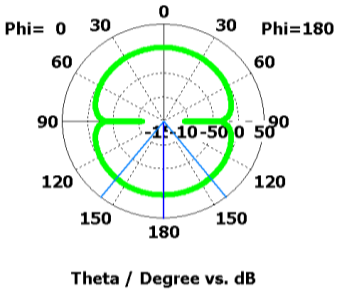

Fig. 4. Dipole radiation diagram of the gain at 12 GHz.

Fig. 5. Dipole antenna above a reflector.

B. Dipole above EBG substrate (mushroom)

The second model is the dipole antenna placed above EBG substrate of distance h_{dip} = 0.02λ. It is composed of several patches of side width w = 0.12λ, gap width g = 0.02 λ, substrate thickness h = 0.04 λ and via hole of ray r = 0.005λ.

We have considered the following parameters as: dipole length L = 0.452λ and dielectric constant ε_r = 2.17 for the frequency 12 GHz (red graph in Fig. 10), the dipole length L = 0.457λ and dielectric constant ε_r = 2.2 for the frequency 12.228 GHz (green graph in Fig. 10). Figure 6 illustrates the model.

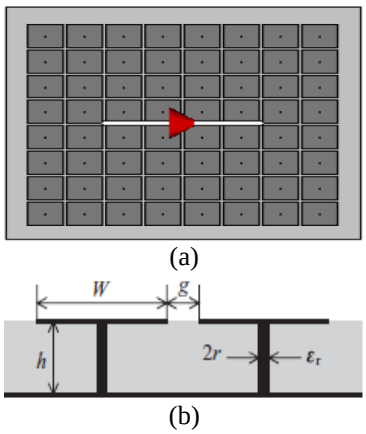

Fig. 6. (a) Dipole antenna above mushroom structure, and (b) parameters of mushroom cells.

C. Dipole antenna above 2D structure substrate with digital capacitors and rings

The third model is the dipole antenna placed above substrate of distance h_{dip} = 0.02λ, permittivity ε_r = 2.2 and thickness h = 1.25 mm. It is composed of several patches of width w_{patch} = 0.084λ, seven digits digital capacitors of parameters w_{digit} = 0.0084λ and rings with parameters: r_{ring} = 0.08λ [7], a = 0.007λ, the space between rings g = 0.02 λ and via hole of ray r = 0.005λ.

We have considered the digit length of the digital capacitor (L_{digit}) and the dipole length (L) as follows:

$$L_{digit} = \lambda/4 \quad \text{and} \quad L = 0.41\lambda;$$

for the frequency 12 GHz (red graph in Fig. 12):

$$L_{digit} = \lambda/5 \quad \text{and} \quad L = 0.42\lambda;$$

for the frequency 11.772 GHz (green graph in Fig. 12).

Figure 8 illustrates the model, where the digital capacitor as shown on Fig. 7 can be calculated by the following formula [8]:

$$C\left(^{pF}/_{\mu m}\right) = (\varepsilon_r + 1)l[(N-3)A_1 + A_2]. \quad (8)$$

Such as:

$$A_1 = 4.409 \tanh\left[0.55(^{h}/_{W})^{0.45}\right]10^{-6}, \quad (9.a)$$

$$A_2 = 9.92 \tanh\left[0.52(^{h}/_{W})^{0.5}\right]10^{-6}. \quad (9.b)$$

Where W = S = S', N is the number of digits.

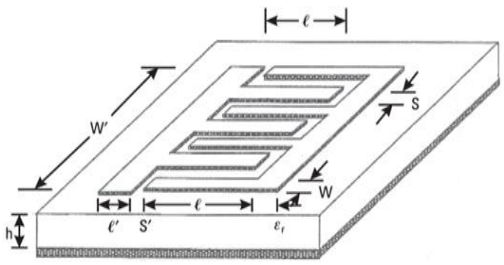

Fig. 7. Seven digits of the digital capacitor.

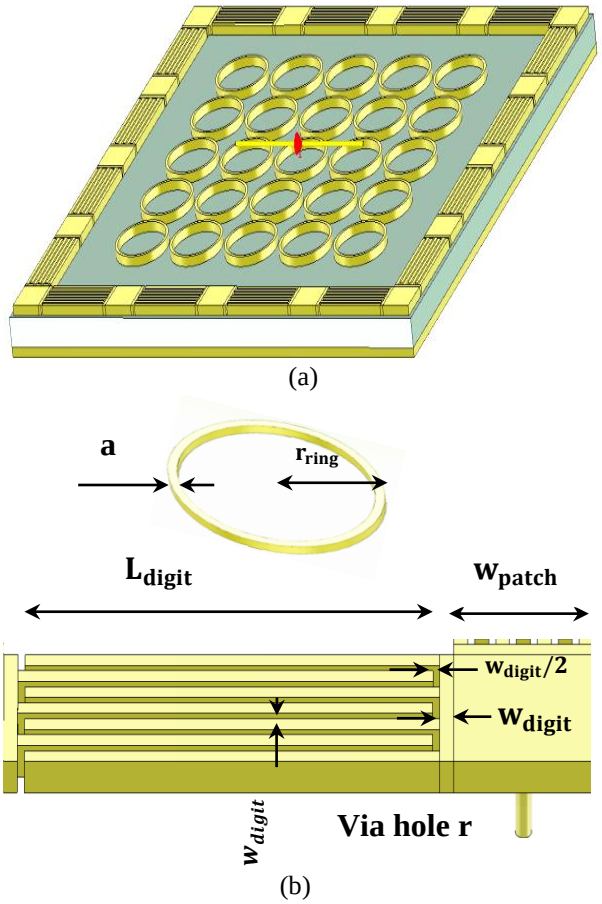

Fig. 8. 2D structure with digital capacitor and rings: (a) structure and (b) parameters.

V. RESULTS

The return loss of the first model as shown on Fig. 9 below doesn't satisfy the minimum attenuation, it can't be used as a ground.

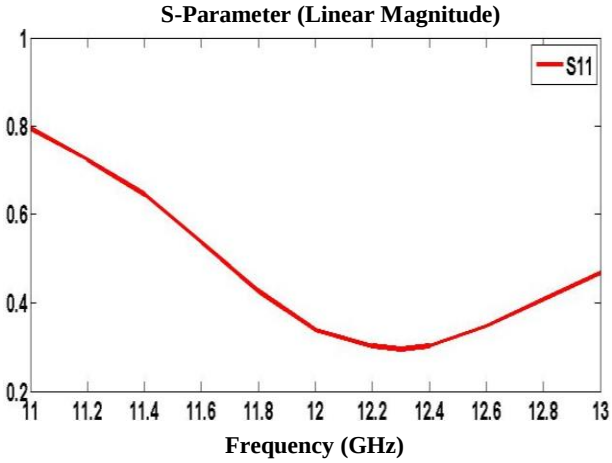

Fig. 9. Return loss vs. frequency of the dipole above PEC ground.

Figure 10 shows the graph of the reflection coefficient dipole antenna above mushroom structure. Two different graphs appear: we have considered the dipole length L = 0.452λ and ε_r = 2.17 for the red graph, the dipole length L = 0.457λ and ε_r = 2.2 for the green graph.

From the curve it's clear that the antenna at 12.228 GHz reaches a perfect resonance, it has the minimum value of the reflection coefficient -41.39 dB compared to 12 GHz operating frequency which has less reflection -26.45 dB.

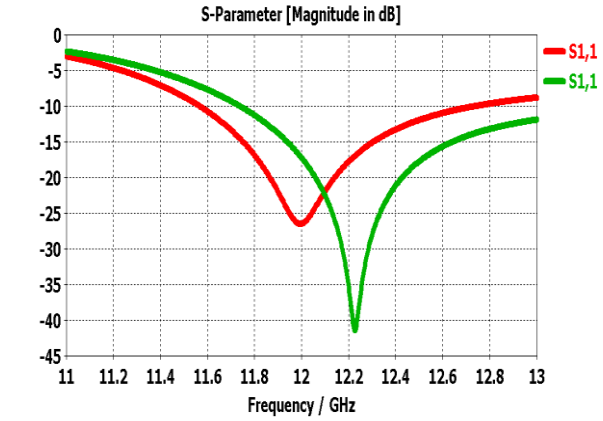

(a)

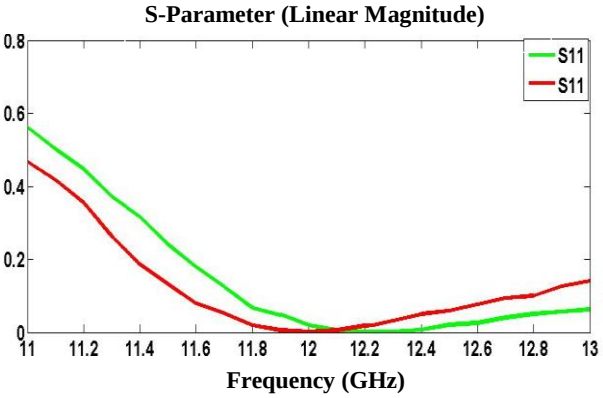

(b)

Fig. 10. Dipole mushroom return loss for 12 GHz operating frequency and around: (a) magnitude in dB and (b) linear magnitude.

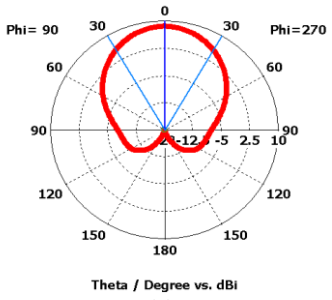

(a)

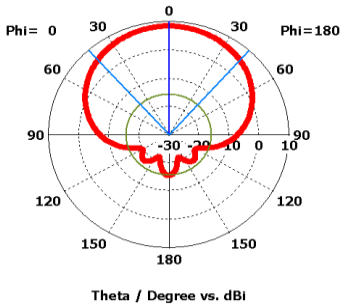

(b)

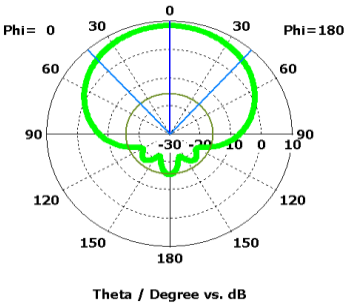

(c)

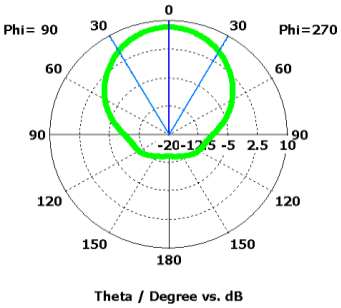

(d)

Fig. 11. Dipole mushroom parameters: (a) directivity at 12.228 GHz, (b) directivity at 12 GHz, (c) gain at 12 GHz, and (d) gain at 12.228 GHz.

Figure 11 shows the different parameters of the dipole mushroom structure, the graphs show that the gains are closely similar at 12 GHz and 12.228 GHz, they reach 8.3 dB, but the structure is more directive at 12.228 GHz, 59.8 deg. compared to 83.5 deg. at 12 GHz.

Figure 12 shows the graph of the reflection coefficient dipole antenna above 2D structure with digital capacitors and rings. Two different graphs appear: we have considered L_{digit} = λ/4 and the dipole length L = 0.41λ for the red graph, L_{digit} = λ/5 and the dipole length L = 0.42λ for the green graph.

Compared to the mushroom structure, we have more reflection at 12 GHz and also around the resonant frequency: -30 dB at 12 GHz and -45 dB at 11.772 GHz.

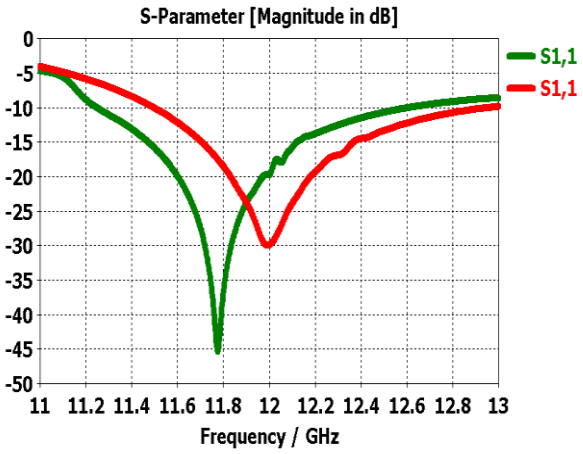

(a)

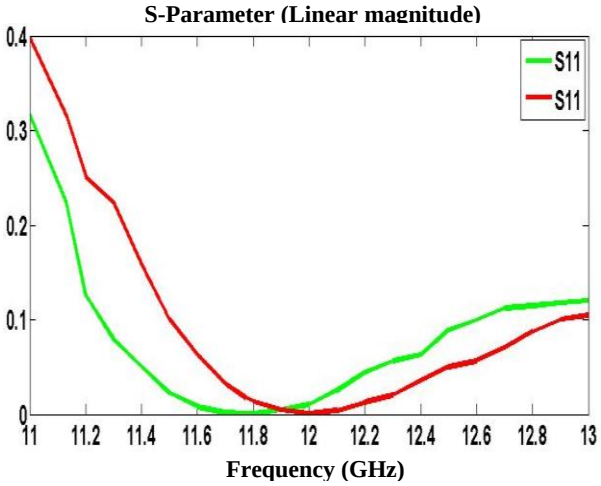

(b)

Fig. 12. Dipole above 2D structure with digital capacitors and rings: return loss for 12 GHz operating frequency and around.

Furthermore, the gain is increased by 1 dB at 12 GHz and close to 2 dB around the resonant frequency as shown on Fig. 13. As for the directivity, we obtain 59.4 deg. at 12 GHz and 56 deg. around the resonant frequency as shown on Fig. 14.

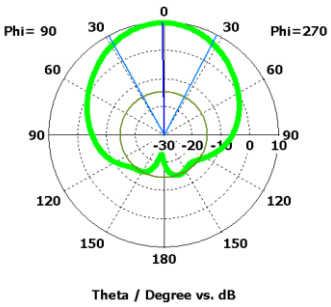

(a)

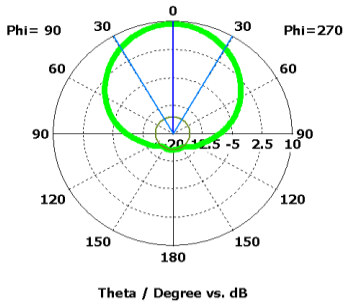

(b)

Fig. 13. Dipole above 2D structure with digital capacitors and rings: (a) gain at 11.772 GHz and (b) gain at 12 GHz.

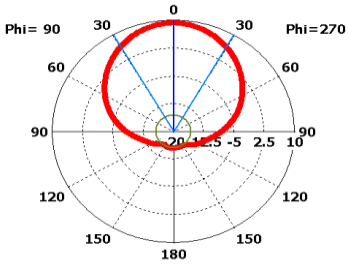

(a)

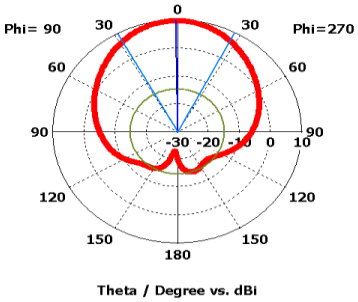

(b)

Fig. 14. Dipole above structure with digital capacitors: (a) directivity at 12 GHz and (b) directivity at 11.772 GHz.

VI. CONCLUSION

Two HIS structures have been simulated and compared to prove the application utility of the metamaterials and verify theirs proprieties. Both the structures considered have successfully enhanced the performance of the dipole antenna, whereas the simple dipole is an omnidirectional antenna, the antennas considered in this article become directives with a much higher gain, close to 10 dB compared to the gain of 2 dB of the simple dipole antenna. These structures have successfully contributed to block surface waves.

We have used the digital capacitor because it allows a greater capacity value than the gap capacitor and

combined resonators with 2D metamaterial make the circuit original compared to the classical mushroom.

The results are obtained by using CST which is based on one of the most popular numerical method for the solution of electromagnetic problems (FDTD) [9].

REFERENCES

[1] V. G. Veselago, "The Electronics of Substances with Simultaneously Negative Values of ε and μ," *P. N. Lebedev Physics Institute*, Academy of Science, USSR, Jan.-Feb. 1968.

[2] A. Ben, "Metamaterials Critique and Alternatives," *The Ohio State University*, ed., Wiley.

[3] J. B. Pendry, "Negative Refraction Makes a Perfect Lens, Condensed Matter Theory Group," *The Blackett Laboratory, Imperial College*, London SW7 2BZ, United Kingdom, 30 Oct. 2000.

[4] S. J. Orfanidis, *Electromagnetic Waves and Antennas*, Copyright ©1999-2008.

[5] C. Caloz and T. Itoh, "Electromagnetic Metamaterials: Transmission Line Theory and Microwave Applications: The Engineering Approach," *Ecole Polytechnique de Montréal, University of California at Los Angeles*, ed., Wiley 2006.

[6] J. J. Carr, *Practical Antenna Handbook*, ed., McGraw-Hill, 2001.

[7] I. Tomeo-Reyes and E. Rajo-Iglesias, "Comparative Study on Different HIS as Ground Planes and Its Application to Low Profile Wire Antennas Design," *University Carlos III of Madrid*, Spain, 2011.

[8] I. Bahl, *Lumped Elements for RF and Microwave Circuits*, ed., Artech House, Inc., 2003.

[9] J. B. Schneider, "Understanding the Finite-Difference Time-Domain Method," Jan. 2, 2011.

Samir Berkani is a Ph.D. student in Telecommunication and Microwave at the FEI (Faculté d'Electronique et d'Informatique) and LINS Laboratory (Laboratoire d'Instrumentation), USTHB (Université des Sciences et Technologies Houari Boumediene), he received the diploma of Electronics Dngineer from Saad Dahlab University Blida, Algeria, Faculty of Telecommunications, in 1998, and Magister in rayonment and microwave in USTHB, FEI, Bab ezzouar Algeria, in 2013.

He is working actually on metamaterials applied in antennas design interesting in enhancing gain and directivity, under the supervision of Dr. Y. Lamhene.

Youssef Lamhene received bachelor's degree then master's degree in Electronic, Electrotechnic and Automatic (EEA), in 1978 and 1980 from Lille University in France, and later on, in the same place, the DEA diploma in 1982 and the third cycle Doctorate diploma in Biotechnology domain in 1984. He is also, since 2009, state Doctor of the Houari Boumediène University of Sciences and Technology. He teaches graduate level courses in applied electronic, microwave and antenna theory at the sciences and technology university of Algiers. His research interests are in the area of electromagnetic simulations of microwave and millimeter-wave passive components.

Hadj Sadok Mustapha is a Ph.D. student in Electronique Instrumentation and Optronic Systems at the FEI (Faculty of Electronics and Data processing), in 2014 he received the master's degree from USTHB (University of Science and Technology Houari Boumediene), Algeria, He is working actually on metamaterials applied in antennas design interesting in enhancing gain and directivity, at LINS (Instrumentation Laboratory), under the supervision of Dr. Y. Lamhene.

Henri Baudrand is Emeritus Professor at ENSEEIHT, Toulouse, France. He specializes in modeling passive and active circuits and antennas. He is the author and co-author of three books at Cepadues edition. He has co-authored over 100 publications in journals and 250 contributions to international conferences. He is a Fellow Member of IEEE Society, a Member of "Electromagnetism Academy" and a Senior Member of IEE Society. He was the President of URSI, France Commission B for six years (1993 to 1999) and the President of the IEEE-MTT-ED French Chapter. He was awarded "Officier des Palmes Académiques", and Director Honoris causa of Lasi University.

On the Design of a Novel Fractal Antenna for Spectrum Sensing in Cognitive Radio

Monika Aggarwal and Amar Partap Singh Pharwaha

Department of Electronics & Communication Engineering
Sant Longowal Institute of Engineering and Technology, Longowal, Sangrur (Punjab), India
monika_pec1201@sliet.ac.in, apsingh@sliet.ac.in

Abstract ─ The present paper reports on the development of a novel compact fractal microstrip patch antenna for spectrum sensing in cognitive radio. The geometrical design of the proposed fractal antenna is optimized using nature inspired Moth Flame Optimization (MFO) method. The optimized antenna is having broadband characteristic within two bands (6.206 - 7.864 GHz, 23.56%) and (14.95 - 20 GHz, 28.89%), which are specified for IEEE C-band, Ku-band and K-band applications respectively. The proposed fractal antenna is also having high peak gain of 7.26 dBi at 18.04 GHz and omnidirectional radiation pattern at all frequencies. The performance of the proposed antenna is also validated experimentally by having a comparison of simulated results with the measured results. The proposed design offers 45.54% reduction in antenna physical size (copper required) as compare to a rectangular patch antenna of same size.

Index Terms ─ Cognitive radio, CPW feed, fractals, IFS, method of moment, microstrip patch antenna, moth flame optimization.

I. INTRODUCTION

Microstrip antenna is made up of a metallic patch printed at upper surface of a substrate having a ground plane incorporated on its lower surface. These antennas are inexpensive, low profile, simple, compact, conformal and easy to fabricate [1]. Microstrip antennas have a number of applications in the field of modern wireless communication including radar systems, satellite communication, telemetry, telemedicine, consumer and military applications [2]. In today's world of wireless communication, the most elementary constraint is to have wideband as well as compact antenna systems. Size of a microstrip antenna can be further reduced by using fractal geometry [3-4] in its design. Also, introduction of fractal geometry leads to multiband behavior [4-7]. Further, the concept of soft computing possesses its own position to optimize the parameters of antenna for enhancing its performance [8]. A variety of optimization techniques can be applied on the patch antenna to get better performance [9-10]. Basically, two antennas are required for cognitive radios, i.e., spectrum sensing antenna which searches the spectrum holes and communicating antenna which communicate in these holes [11-12]. Wideband antenna with omnidirectional radiation pattern is mandatory for spectrum sensing [13]. An antenna with very large bandwidth (1.35 - 30 GHz) is designed for spectrum sensing [14], but non-omni-directionality in H-plane is observed in the same. In [15], an ultrawideband slotted disc antenna for 0.7 - 11.23 GHz is presented but quasi-omnidirectional radiation pattern is observed. A multiband fractal antenna for spectrum sensing in cognitive radios is presented [16], but in this case, S_{11} is not improved significantly and only simulated results are presented. Again in [17] a multiband Sierpinski triangular antenna for cognitive radios is reported but with simulated results only. In [18], Sierpinski gasket antenna is presented for cognitive radios which resonates at 1.89 GHz, 4.01 GHz 7.89 GHz, 15.3 GHz frequency but the value of S_{11} is not much improved. In order to address these issues, in the present work, a novel fractal antenna is designed for spectrum sensing which is further miniaturized and optimized by a recently introduced heuristic nature inspired optimization technique, Moth Flame optimization proposed in [19]. This algorithm was applied on unimodal, multi-modal and composite functions, and observed that this algorithm explore and exploit the search space properly. In this paper, MFO algorithm is applied to optimize the dimensions of patch and ground plane to optimize S_{11}. In order to achieve this, polynomial curve fitting method in the MATLAB environment is applied to model input-output response of the proposed antenna. The performance of the Moth Flame optimization is further examined by optimizing the geometrical dimensions of the proposed fractal antenna and its comparison is done with other two highly explored and universally accepted optimization techniques including Genetic algorithm (GA) and Powell optimization.

II. PROPOSED FRACTAL ANTENNA DESIGN

A. Geometrical description of the proposed antenna

The proposed fractal antenna is designed on the architecture of having repeated geometry of isosceles

Submitted On: July 10, 2018
Accepted On: April 6, 2019

triangle. Scaling is applied on the angle. In 1st iteration, isosceles triangles are cut on the opposite sides of the rectangle of basic iteration. For next iteration, these sides of triangle are taken as base to make other isosceles triangles. In 2nd iteration, isosceles triangles with 0.5 scaling factor is introduced on each side of the triangle of 1st iteration. This course of action is repeated up to 3rd iteration. The geometrical description of the proposed architecture used to arrive at final geometrical shape of the proposed fractal antenna is illustrated in Fig. 1. Here, ABDC is a rectangle having AB = CD and AC = BD as well as ΔBOD is an isosceles triangle with angle ∠OBD = α, whereas, ΔOEB is also an isosceles triangle with ∠OBE=β. Again, using the same criteria, ΔOFE is drawn with ∠OEF = γ, where:

$$\gamma = \beta/2 = \alpha/4. \tag{1}$$

Same process of mathematical modelling is applied in all the quadrants. Figure 1 and Table 1 represent various dimensions of the proposed antenna geometry. The basic iteration is a CPW fed rectangle of 10 mm x 20 mm. Feed width is 2.6 mm and length is 15 mm. The gap, g, between patch and ground plane is 6 mm and that between feed & ground is 0.9 mm. Width of the ground plane is 4.8 mm and length is 9 mm. Overall dimensions are 25 mm x 20 mm. Various iterations of the proposed antenna is presented in Fig. 2. Basic geometry is fabricated with RT Duroid material having ε_r = 2.2, h = 1.6 and δ = 0.02. Antenna is fed by a 50 Ω CPW feed. Copper conductor with thickness of 35 μm is used. The proposed antenna geometry is mathematically presented by an Iterative Function System (IFS). An IFS is a method to create fractals. A series of affine transformations W is applied on the basic shape, defined by [3,20]:

$$W\begin{bmatrix} x \\ y \end{bmatrix} = \begin{bmatrix} a & b \\ c & d \end{bmatrix}\begin{bmatrix} x \\ y \end{bmatrix} + \begin{bmatrix} e \\ f \end{bmatrix}, \tag{2}$$

where matrix,

$$\begin{bmatrix} a & b \\ c & d \end{bmatrix} = \begin{bmatrix} (1/s)\cos\theta & -(1/s)\sin\theta \\ (1/s)\sin\theta & (1/s)\cos\theta \end{bmatrix}, \tag{3}$$

and a, b, c, d, e & f are real numbers in which rotation and scaling is controlled by a, b, c & d, whereas linear translation is controlled by e & f. IFS generator equations for the proposed geometry are given as:

$$w_1(x,y) = \left(\frac{1}{s}\cos\theta.x - \frac{1}{s}\sin\theta.y, \frac{1}{s}\sin\theta.x + \frac{1}{s}\cos\theta.y\right). \tag{4}$$

$$w_2(x,y) = \left(\frac{1}{s}\cos\theta.x + \frac{1}{s}\sin\theta.y + \frac{1}{2}, -\frac{1}{s}\sin\theta.x + \frac{1}{s}\cos\theta.y + \frac{1}{2}\tan\theta\right), \tag{5}$$

where, $\theta = \frac{44^0}{2^n}$, $s = \frac{1}{2\cos\theta}$, $n = \begin{bmatrix} 0 \text{ for } 1^{st} \text{ iteration} \\ 1 \text{ for } 2^{nd} \text{ iteration} \\ 2 \text{ for } 3^{rd} \text{ iteration} \end{bmatrix}$.

IE3D software which is based on method of moment (MOM) is used for the design and simulation of the proposed fractal antenna. It is an integrated full-wave electromagnetic simulation and optimization package used for the design and analysis of 3D and planar microwave circuits, MMIC, RFIC, RFID and antennas. Present results demonstrated in Fig. 3, illustrates that as the number of iterations goes on increasing, the lower cut off frequency of band I goes on reducing up to 2nd iteration. The lower cut off frequency in basic shape is at 6.884 GHz with S_{11} at –10.2 dB. In 1st iteration it has been shifted to 6.206 GHz with -10.35 dB S_{11}. In the 2nd iteration, it is further shifted to 6.055 GHz with S_{11} at -10.11 dB. In the 3rd iteration the lower cut off is 6.055 GHz with -10.29 dB.

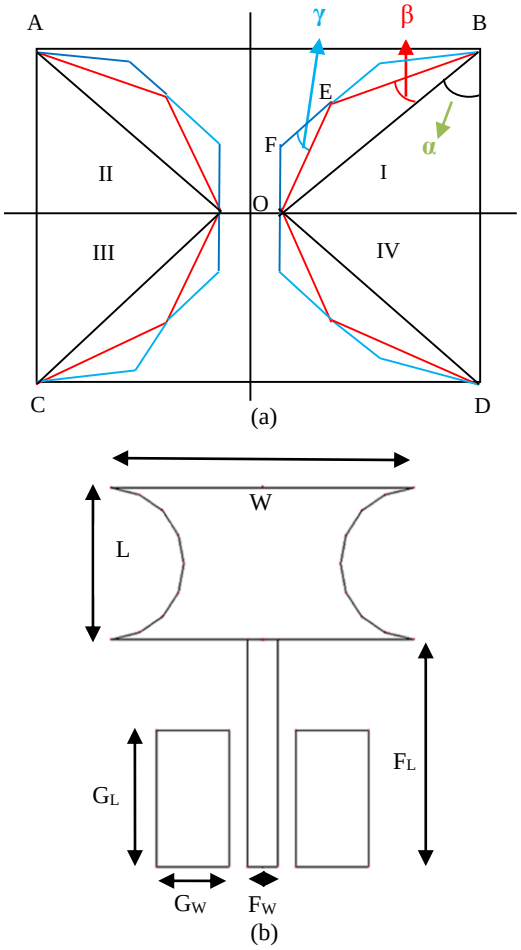

Fig. 1. Geometrical description of the proposed design.

Table 1: Dimensional parameters of proposed shape

Dimension	Value (in mm)
W	20
L	10
G_L	9
G_W	4.8
F_W	2.6
F_L	15

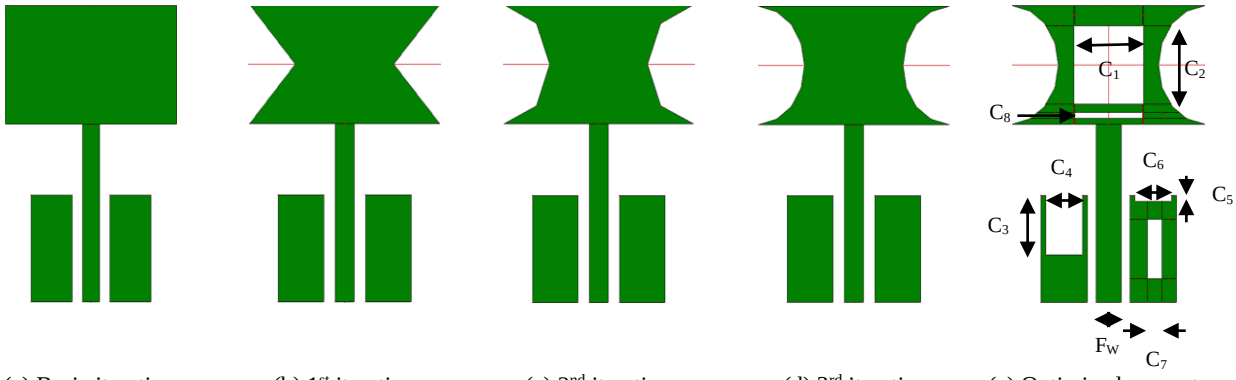

(a) Basic iteration (b) 1st iteration (c) 2nd iteration (d) 3rd iteration (e) Optimized geometry

Fig. 2. Multiple iterations of the proposed design.

B. Optimization of proposed fractal antenna

Three optimization methods namely Powell, Genetic and Moth Flame optimization are applied on the proposed design in the present work to achieve best results in terms of S_{11}. Comparative evaluation of these three techniques established the effectiveness of the proposed Moth Flame optimization method. Powell Optimization method is used to find out local minima of a function when derivative is not available. A set of directions is iteratively updated to reach at the desired direction [21]. The method is used to find out local minima of a continuous but simple functions but it is really very difficult to find optimal solutions for complex multi-objective problems with desired accuracy. Moreover, the function should be real-valued with a fixed number of real-valued inputs. Genetic algorithm is a heuristic search and optimization algorithm, based on the process of natural selection. These are computational models inspired by process of evolution [22]. The method is used extensively for the optimization of microstrip patch antennas. Hence, the same has been included in the present work so as to establish the effectiveness of the MFO. In MFO, the moths are actual search managers that travel around the search space and flames are their best positions [19]. Each moth search around a flame and bring up to date itself to find a best solution intended for the proposed design as defined in Table 2, with search agents, 1000 and iterations, 200. MFO is executed in MATLAB environment in which first of all, a random matrix (M) of moths is created. Then, an array of moth fitness (OM) is computed. In the next step, a matrix of flames is calculated. Ultimately, the location of the moth (M) with respect to flame is updated using following expression:

$$M_i = S(M_i, F_j),$$

where S is logarithmic spiral function and is given by the following expressions:

$$S(M_i, F_j) = D_i . e^{bt} . \cos(2\pi t) + F_j,$$

$D_i = | F_j - M_i |$, i.e., distance of i^{th} moth for j^{th} flame.

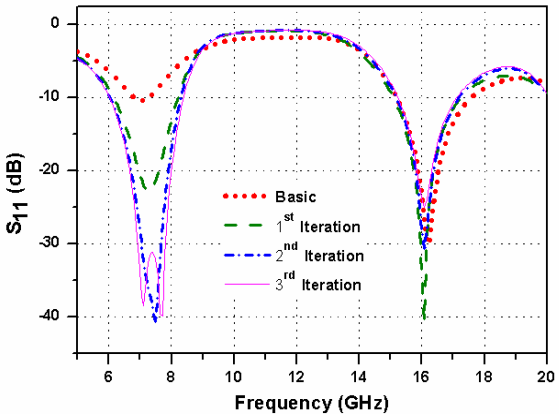

Fig. 3. Simulated S_{11} of proposed antenna in various iterations.

Table 2: Input/Output parameters for MFO with fixed C_8 (0.5 mm x 7 mm)

Parameter (in mm)	Lower Limit	Upper Limit	Optimized Value
Width, C_1	0.25	4.5	3.6
Length, C_2	0.25	4.75	3.3
Length, C_3	2	6.5	5
Width, C_4	0.8	3.8	3.8
Length, C_5	0.5	8.5	0.5
Width, C_6	0.5	3.8	3.8
Feed width, F_W	1	3.4	2.6
Width, C_7	0.5	3.5	1.5

Curve fitting tool in MATLAB is used to calculate the objective functions which are several order equations. Optimum value of the S_{11} is realized by optimizing a range of dimensions of the design. Various curve fitting equations to accomplish the task are shown in Table 3 with objective function described by:

Objective function = min *f(z)*,

$$where\ z = \begin{Bmatrix} z_1 \\ z_2 \\ . \\ . \\ z_8 \end{Bmatrix}.$$

Genetic, Powell and MFO have been applied on the design. From Fig. 4, it reveals that the end result obtained from moth flame optimization is best in terms of S_{11}, which must be least.

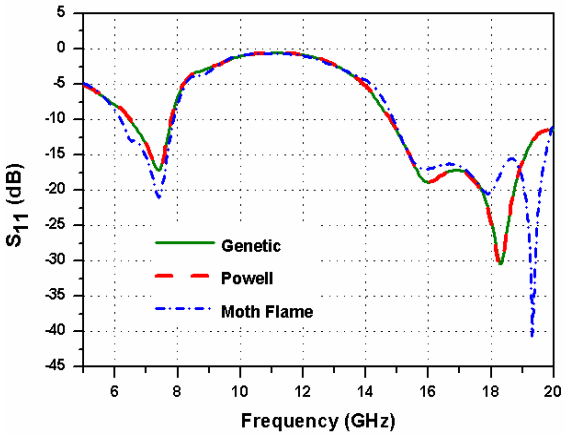

Fig. 4. Simulated S_{11} of proposed antenna with different optimization algorithms.

C. Proposed fabricated fractal antenna

In order to validate the performance of the proposed fractal antenna, the same is fabricated using printed circuit technology by making the use of single side RT Duroid copper clad board material as shown in Fig. 5. The measurements on the fabricated antenna were carried out by coupling it to the Vector Network Analyzer (ANRITSU MS46322A) through 50 ohm SMA connector. The simulated results are compared with measured results. The S_{11} is measured at different frequencies of its operation covering specified bands completely. The results are presented in next section.

III. RESULTS & DISCUSSION

A. Simulated and measured S_{11}

Experimental validation of the proposed fractal antenna is carried out by having a comparison of simulated and measured S_{11} from fabricated antenna. The graph obtained in Fig. 6 reveals that there is a good matching in simulated and measured results pertaining to S_{11}. A slight discrepancy is observed in band II which is due to fabrication tolerances as well as experimental errors. Such type of small deviation is always expected in the experimental investigations of the fabricated antenna in real time measurements.

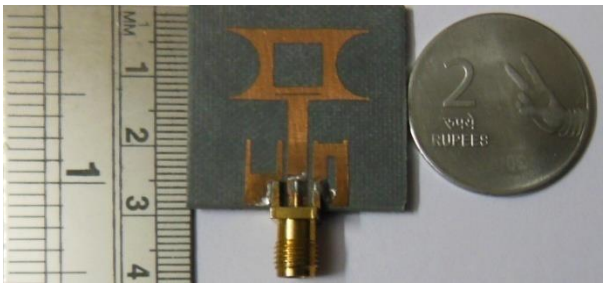

Fig. 5. Proposed fabricated fractal antenna.

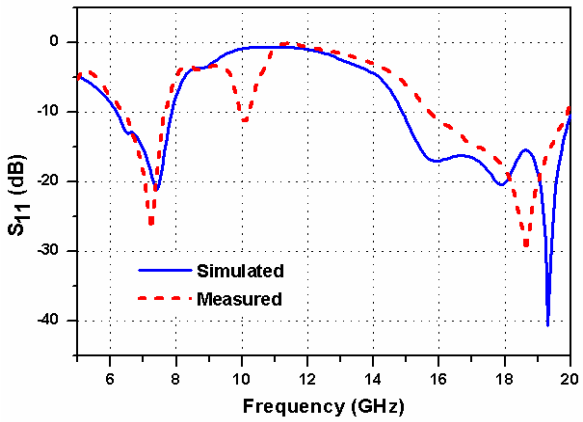

Fig. 6. Simulated and measured S_{11} of the proposed design.

Table 3: Curve fitting equations for MFO

Implemented Cut in Patch, Ground Plane	Subsequent Equation for Input-Output Response of Various Cut in Proposed Antenna
Width, C_1	$z_1 = -0.69x^6 + 10.56x^5 - 61.36x^4 + 172.2x^3 - 243.46x^2 + 160.58x - 53.58$
Length, C_2	$z_2 = 0.006x^6 - 0.08x^5 + 0.51x^4 - 1.428x^3 + 2.06x^2 - 2.57x - 9.37$
Length, C_3	$z_3 = -0.44x^6 + 10.006x^5 - 90.20x^4 + 413.97x^3 - 1021.2x^2 + 1285.1x - 664.82$
Width, C_4	$z_4 = -1.5x^3 + 9.5x^2 - 23x - 9.8$
Length, C_5	$z_5 = 0.02x^5 - 0.53x^4 + 4.406x^3 - 15.78x^2 + 27.33x - 47.26$
Width, C_6	$z_6 = 0.08x^3 - 0.64x^2 + 0.42x - 19.27$
Feed width, F_W	$z_7 = -5.65x^5 + 60.67x^4 - 246x^3 + 470.77x^2 - 432.92x + 147.07$
Width, C_7	$z_8 = -0.34x^3 + 2.93x^2 - 6.91x - 14.27$

B. Current distribution

Current distribution of the optimized geometry for two resonating frequencies is presented in Fig. 7. At lower resonant frequency, the current density is mainly due to the edges of the patch and feed, but at higher resonating frequency it is strongly confined at the edges of the cut because cylindrical cut is having more curvature than planar surface.

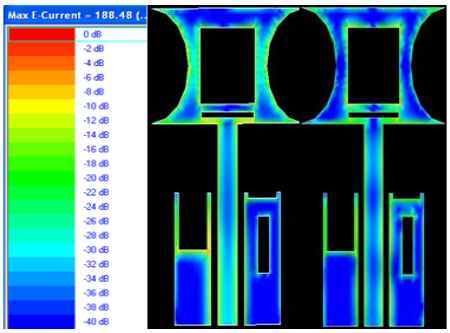

Fig. 7. Simulated current distribution at: (a) 7.412 GHz and (b) 19.32 GHz.

C. Gain versus frequency

Figure 8 reveals that gain of the proposed optimized design is positive for all frequencies of band I and band II. A significant value of gain 7.26 dBi at 18.04 GHz in band II has been achieved. Gain of the antenna is a factor which illustrates the capability of antenna to focus energy in a given direction, which is revealed by radiation pattern. Gain of the antenna should be positive.

D. Efficiency versus frequency

Figure 9 depicts the efficiency of the proposed design is more than 80% for numerous frequencies in both bands. High value of radiating efficiency is a sign of power delivered by the antenna is more and conduction-dielectric losses are less.

E. Radiation pattern

Figures 10 & 11 depict the radiation pattern of the proposed antenna for 7.03 GHz, 7.18 GHz, 7.26 GHz frequencies of band I and 18.04 GHz of band II. It may be noticed that radiation pattern is directional in elevation plane and non-directional in azimuth plane which means its radiation pattern is omnidirectional, which is the fundamental requirement of cognitive radio.

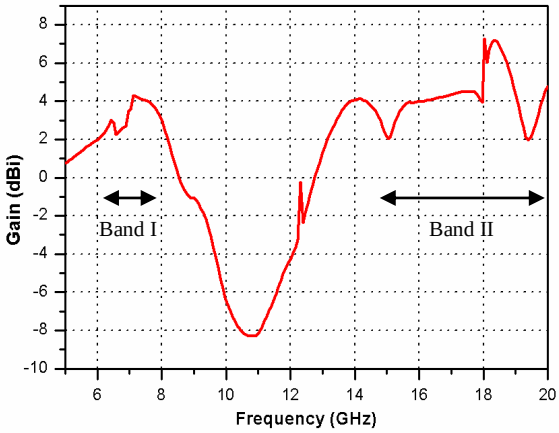

Fig. 8. Simulated peak gain vs. frequency of the proposed design.

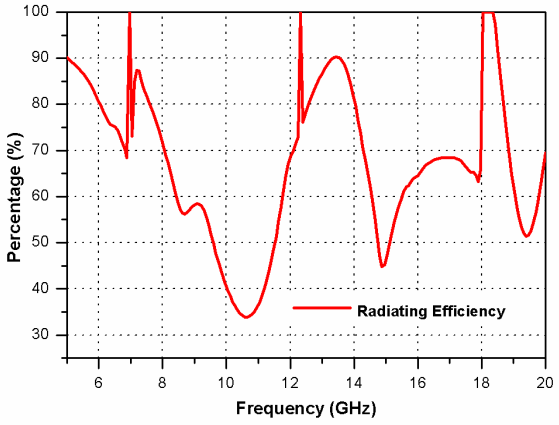

Fig. 9. Simulated efficiency of the proposed design.

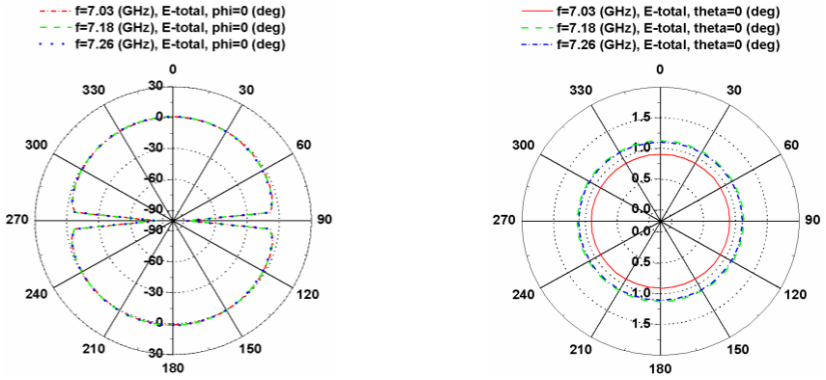

(a) (b)

Fig. 10. Radiation pattern for Band I in: (a) elevation plane and (b) azimuth plane.

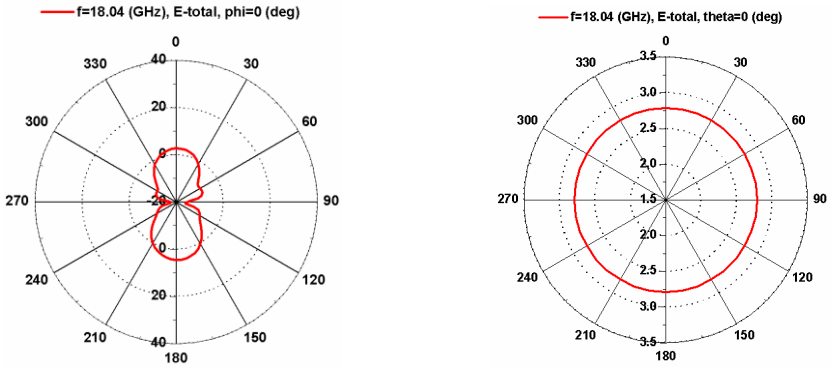

(a) (b)

Fig. 11. Radiation pattern for Band II in: (a) elevation plane and (b) azimuth plane.

IV. CONCLUSION

The results obtained illustrate that the antenna exhibits broadband characteristic within two bands (6.206 - 7.864 GHz, 23.56%) and (14.95 - 20 GHz, 28.89%) specified for IEEE C-band, Ku-band and K-band applications respectively by International telecommunication union and having very high peak gain (7.26 dBi at 18.04 GHz) and high radiation efficiency in these two bands. This antenna is also having omnidirectional radiation pattern and good impedance matching at all frequencies in both the bands thus making it a capable design for spectrum sensing in cognitive radios. From comparative evaluation, it is revealed that Moth Flame optimization technique outperforms in an attempt to achieve optimal S_{11} at most of the frequencies in the specified bands. Moreover, it is also found that very few parameters are required to be adjusted for the execution of this technique. The present study revealed that Moth flame optimization technique is an effective alternative for the optimization of microstrip fractal antennas.

REFERENCES

[1] C. A. Balanis, *Antenna Theory*, John Wiley & Sons, Inc., 1997.

[2] G. Kumar and K. P. Ray, *Broadband Microstrip Antennas*, Artech House, 2003.

[3] D. H. Werner and S. Ganguly, "An overview of fractal antenna engineering research," *IEEE Antennas and Propagation Magazine*, vol. 45, no. 1, pp. 38-57, Feb. 2003.

[4] L. F. V. T. Da Costa, A. G. D'Assunção, and C. Peixeiro, "Simulation and design of multiband Koch fractal CPS antennas," *International Applied Computational Electromagnetics Society (ACES) Symposium*, Denver, 2018.

[5] M. A. Dorostkar, R. Azim, M. T. Islam, and Z. H. Firouzeh, "Wideband hexagonal fractal antenna on epoxy reinforced woven glass material," *ACES Journal*, vol. 30, no. 6, pp. 645-652, June 2015.

[6] C. Puente Baliarda, J. Romeu, and A. Cardama, "The Koch monopole: A small fractal antenna," *IEEE Transactions on Antennas and Propagation*, vol. 48, no. 11, pp. 1773-1781, Nov. 2000.

[7] X. Bai, J.-W. Zhang, L.-J. Xu, and B.-H. Zhao, "A broadband CPW fractal antenna for RF energy harvesting," *ACES Journal*, vol. 33, no. 5, pp. 482-487, May 2018.

[8] B. Choudhury, S. Manickam, and R. M. Jha, "Soft computing techniques for mutual coupling reduction in metamaterial antenna array," *Journal of Optimization*, Hindawi Publishing Corporation, pp. 1-7, vol. 2013.

[9] Y. K. Choukiker and S. K. Behera, "Design of microstrip radiator using particle swarm optimization technique," *ICTACT Journal on Communication Technology*, vol. 2, iss. 3, pp. 382-386, 2011.

[10] S. Rani and A. P. Singh, "A novel design of hybrid fractal antenna using BFO," *Journal of Intelligent and Fuzzy Systems, IOS Press*, vol. 27, no. 3, pp. 1233-1241, 2014.

[11] Z. Jelacic, H. Balasko, and M. Grgic, "Cognitive radio and UHF spectrum revitalization," *International Symposium ELMAR-2009*, Zadar Croatia, 2009.

[12] I. F. Akyildiz, W.-Y. Lee, M. C. Vuran, and S. Mohanty, *Next Generation/Dynamic Spectrum Access/Cognitive Radio Wireless Networks: A Survey*, Elsevier, Computer Networks 50, pp. 2127-2159, 2006.

[13] Y. Tawk and C. G. Christodoulou, "A new reconfigurable antenna design for cognitive radio," *IEEE Antennas and Wireless Propagation Letters*, vol. 8, pp. 1378-1381, 2009.

[14] R. Narayan, C. Caradec, S. Ataman, and M. Manthian, "An ultra wideband planar monopole antenna for spectrum sensing applications," *IEEE International Conference on Communication Systems (ICCS)*, 2012.

[15] E. Gomez-Nunez, H. Jardon-Aguilar, J. A. Tirado-Mendez, and R. Flores-Leal, "Ultra-wideband slotted disc antenna compatible with cognitive radio applications," *Progress in Electromagnetics Research Letters*, vol. 34, pp. 53-63, 2012.

[16] P. B. Nayak, S. Verma, and P. Kumar, "Multiband fractal antenna design for cognitive radio applications," *IEEE International Conference on Signal Processing and Communication (ICSC)*, pp. 115-120, 2013.

[17] S. S. S. Pandian and C. D. Suriyakala, "A novel multiband Sierpinski triangular fractal antenna for cognitive radio," *International Conference on Circuits Power and Computing Technologies*, 2013.

[18] M. K. C. Durbhakula and V. K. R. Nalam, "Fractal antenna structures for cognitive radio applications," *International Journal of Latest Trends in Engineering and Technology*, vol. 6, iss. 4, pp. 464-468, 2016.

[19] S. Mirjalili, "Moth flame optimization algorithm: A novel nature inspired heuristic paradigm," *Elsevier Knowledge-Based Systems*, pp. 228-249, 2015.

[20] A. M. Abdul-Letif, M. A. Z. Habeeb, and H. S. Jaafer, "Performance characteristics of Minkowski curve fractal antenna," *Journal of Engineering and Applied Sciences*, vol. 1, iss. 4, pp. 323-328, 2006.

[21] S. S. Rao, *Engineering Optimization: Theory and Practice*, 2009.

[22] M. Mitchell, *An Introduction to Genetic Algorithms*, 1996.

Monika Aggarwal received her B.Tech and M.Tech in Electronics & Communication Engineering from Punjab Technical University, Jalandhar. She is currently pursuing Ph.D. in Fractal Antennas for Cognitive Radio from SLIET, Longowal. Since 2000, she had taught many courses like Digital Signal Processing, VLSI design, Microwave and Radar. She had published more than 30 papers in various International journal/conferences and national conferences.

A. P. Singh received his B.Tech in ECE from GNDU, Amritsar in1990. He had done his M.Tech degree from REC, Kurukshetra in 1994 and Ph.D. degree in 2005. At present, he is Professor of ECE at SLIET, Longowal. He has professional experience of more than 25 years. He has guided seven Ph.D. theses and six more students are pursuing their Ph.D. degrees under his supervision. He has published more than 180 research papers in various national and international journals/conferences and received various awards including IETE Students Journal Award-2006 by IETE, New Delhi, Certificate of Merit in 2006, KF Antia Award in 2009, Sir Thomas Award for the year 2010, and again KF Antia Award in 2014 by the Institution of Engineers (India).

Compact and Coding Expandable Chipless RFID Tag with Bending Arms

Hua Zhu [1,2], Xiuping Li [1,2], and Song Jia [1,2]

[1] School of Electronic Engineering
Beijing University of Posts and Telecommunications, Beijing, 100876, China

[2] Beijing Key Laboratory of Work Safety Intelligent Monitoring
Beijing University of Posts and Telecommunications, Beijing, 100876, China
judy-cool@163.com, xpli@bupt.edu.cn, 951684999@qq.com, xiaojun19861986@163.com

Abstract ─ In order to construct a compact chipless RFID tag with scalable coding capacity, a design is proposed that includes bending arms along both sides of the microstrip transmission line. Each bending arm produces a resonant frequency, which indicates one bit. And the bending structure can effectively reduce the coupling between units. A 12-bit chipless RFID tag with dimensions of 37×17.7mm^2 is designed with a frequency band from 5GHz to 6.05GHz. And a 40-bit chipless RFID tag is proposed with a frequency band from 2.95GHz to 5.65GHz. Both amplitude and Group Delay responses of the proposed tag are measured and analyzed. The measurement results are in good agreement with the simulation results. The measured results achieve stability and high capacity the coded information.

Index Terms ─ Chipless RFID tag, multi-stop band filter, resonant units.

I. INTRODUCTION

In recent years, the applications of radio frequency identification (RFID) are expanding exponentially in warehousing, supplied chain management and other automation processes due to penetrating ability and higher data transmission rate [1]. Although the traditional RFID systems based on the use of silicon RFID chips are very common and largely exploited in practice, some of their limitations, such as cost and robustness, are driving many researches towards alternative solutions, namely chipless RFID tag [2-3]. The most promising way for chipless RFID development is to directly print on product or package [4].

In general, a chipless RFID tag that utilizes frequency signature encoding consists of a vertically polarized UWB transmitting antenna, a horizontally polarized UWB receiving antenna and multi-resonant units, as shown in Figure 1. The cross-polarized antennas minimize cross talk between transmitting and receiving signal [5]. Overall, the receiving antenna is illuminated by the electromagnetic wave from the reader, and the signal from the receiving antenna is transmitted to the multi-resonant units to obtain multi-stopband or multi-passband filtering. The frequency band of operation is divided by N sections, corresponding to N bits. The presence and absence of resonance at each section of the frequency band is associated with bits '1' and '0', respectively. Research on chipless RFID tags can be broadly classified into two main categories: time domain reflectometry (TDR)-based chipless RFID tag [6-8], spectral signature-based chipless RFID tag [9-12] and amplitude/ phase backscatter modulation-based chipless RFID tag [13].

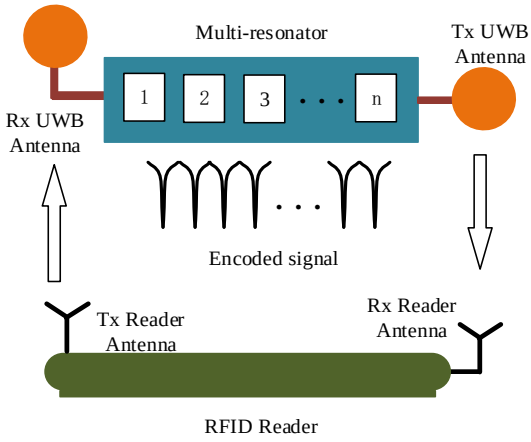

Fig. 1. Physical concept of the chipless RFID system.

Frequency-signature-based chipless RFID tag has a relatively high storage performance, which is an important feature in tag research. In [9], a 35-bit chipless RFID tag is designed with spiral resonance units. The tag operates between 3.1-7GHz. In [10], an 8-bit chipless RFID tag with eight E shape resonator units is proposed. The E shape resonators efficiently reduce coupling between units. However, the tag has low encoding density and the large dimension. In [11], an 8-bit chipless

Submitted On: June 28, 2018
Accepted On: May 12, 2019

RFID tag uses a split ring resonator unit that enhances the encoding capacity at a specific resonance frequency. In [12], 8-bit data encoded tag is proposed using multiple microstrip open stub resonators. In these researches, not only should the designed tag incorporate large amount of data, but should also be designed as compactly as possible. However, by increasing the number of bits on the tag, the couplings between the resonances are increased. Hence, the independence of the resonance frequency is reduced.

To overcome these problems, a 12-bit chipless RFID tag and a 40-bit chipless RFID tag with expandable coding capacity are designed and analyzed respectively in this paper. The chipless RFID tag consists of different bending arm units which are adopted to realize miniaturization and reduce the coupling between adjacent units.

II. DESIGN OF BENDING ARM ELEMENT

A. The resonant performance of the bending arm

To encode data within a frequency band, the design of a chipless RFID tag is combined with coupling filter technology, which is filtered through multiple resonant circuit units exited by a 50Ω microstrip transmission line. In this paper, the bending arms are loaded on both sides of the 50Ω microstrip transmission line to produce the multiple resonances and miniaturization, as shown in Fig. 2 (a). The yellow indicates metal and blue indicates the dielectric substrate. The bending arm consists of bends and lines, which is modeled by an equivalent T-network, as shown in Fig. 2 (b). Figure 2 (c) shows the simplified equivalent circuit which can be taken as a parallel circuit magnetically coupled to the main transmission line. Since the resonator unit is meandered, its equivalent inductance is increased, while the equivalent capacitance is slightly decreased [14]. This design assumes that the effective resistance of the bending arms can be ignored. The operating frequency f0 of the stop-band satisfies the following formula [13]:

$$f_0 = \frac{1}{2\pi} \frac{1}{\sqrt{\varepsilon_r \varepsilon_0 C_{Cs} (L_{Nm} + L_{T1} + M) \| L_{Ns}}}, \qquad (1)$$

where M is the mutual inductance of L_{Nm} and L_{T1}.

The gap is a main parameter that affects M. When the value of gap is reduced, the mutual inductance M increases, and as a result the resonance frequency f_0 decreases judging by the equation (1). C_{Ns} is mainly generated by the value of h_1, which is the sum of the capacitance of the bending arm unit. L_{Ns} is the sum of the inductance value produced by a bending arm unit, which is affect by w_1. When the effective length of the bending arm element (w_1) is decreased, and then the L_{Ns} and C_{Ns} becomes smaller that results in the resonant frequency f_0 increases. When the parameter h_1 is decreased, the equivalent C_{Ns} decreases leading to the resonant frequency f_0 increases.

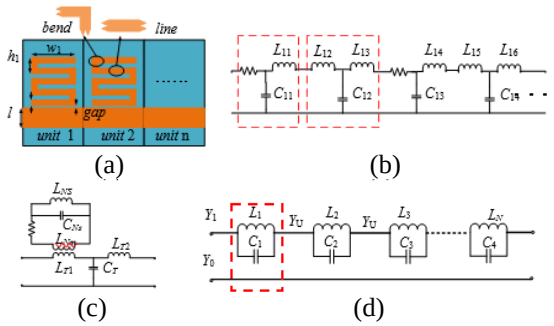

Fig. 2. The proposed chipless RFID structure and the equivalent circuit: (a) the proposed chipless RFID, (b) equivalent circuit of discrete element, (c) simplified equivalent circuit of bending arm unit, and (d) series parallel-resonant branches of N-bit chipless RFID tag.

Seen from the Fig. 3 (a), the center frequency of the bending arm unit is 5.07GHz with suitable band-stop filter characteristics. There is a significant in-band rejection using only 70MHz. The key parameters (w_1, h_1, *gap*) are simulated and analyzed, as shown in Figs. 2 (a-d). When the w_1 increases from 4mm to 6mm, the resonant frequency changes from 4.87GHz to 5.25GHz, as shown in Fig. 3 (b). Similarly, when the h_1 increases from 1.6mm to 2mm, the resonant frequency will shift from 5.55GHz to 4.63GHz in Fig. 3 (c). When the gap changes from 0.2mm to 0.5mm, the resonant frequency shifts from 5.02GHz to 5.12GHz, and the curve depth changes from -18.42dB to -11.04dB.

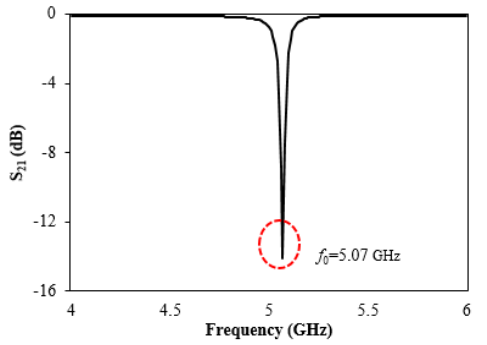

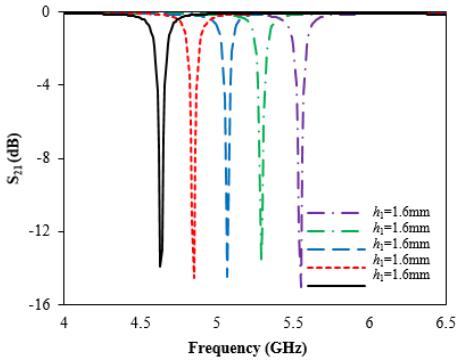

(c)

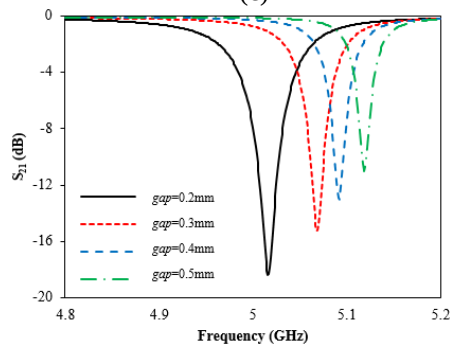

(d)

Fig. 3. Analysis of key parameters: (a) S_{21} of a single resonator, (b) S_{21} versus w_1, (c) S_{21} versus h_1, and (d) S_{21} versus *gap*.

B. The narrowband characteristic of the bending arm

In order to increase the number of codes at same bandwidth, the narrowband characteristic of the bending arm is required. The equivalent circuits for the multi-resonators of Fig. 2 (a) can be obtained as depicted in Fig. 2 (d), where Y_0 denote the terminating impedance and admittance. Consider a two-port network with a single series branch of $Y=j\omega C+1/j\omega L$, where L and C are the sum of inductance and the sum of capacitance.

The equation $\omega=\omega_0+\nabla\omega$, $\omega_0=1/\sqrt{LC}$, $b=\omega_0 C$ is substituted into the equation of Y:

$$\begin{aligned} Y &= j(\omega_0+\nabla\omega)\times C+\frac{1}{j(\omega_0+\nabla\omega)\times L} \\ &= j\omega_0 C+j\nabla\omega C+\frac{1}{j(\omega_0+\nabla\omega)}\times\omega_0^2 C \\ &= j\omega_0 C(1+\frac{\nabla\omega}{\omega_0}-\frac{\omega_0+\nabla\omega-\nabla\omega}{\omega_0+\nabla\omega}) \\ &\approx j\omega_0 C(1+\frac{\nabla\omega}{\omega_0}-1+\frac{\nabla\omega}{\omega_0}) \\ &= j\omega_0 C\times\frac{2\nabla\omega}{\omega_0} \end{aligned} \quad . \tag{2}$$

The transmission parameter with Y_0 is given by:

$$S_{21}=\frac{1}{1+\frac{Y_0}{2Y}}. \tag{3}$$

The equation (2) is substituted into the equation (3), and the S_{21} can be calculated as:

$$S_{21}=\frac{1}{1+\frac{Y_0}{2jb\frac{2\nabla\omega}{\omega_0}}}=\frac{1}{1-j\frac{Y_0}{4b\frac{\nabla\omega}{\omega_0}}}=\frac{1}{1-j\frac{1}{4\frac{b}{Y_0}}}\frac{\omega_0}{\nabla\omega}. \tag{4}$$

The amplitude of S_{21} can be calculated as:

$$|S_{21}|=\frac{1}{\sqrt{1+\left[\frac{\omega_0}{4(b/Y_0)\nabla\omega}\right]^2}}, \tag{5}$$

where a susceptance slope parameter $b=\omega_0 C=\frac{1}{\omega_0 L}$ and we can define the $|S_{21}|=m$dB .When the frequency shifts such as:

$$\frac{1}{4(b/Y_0)}\frac{\omega_0}{\nabla\omega_{\pm}}=\pm\sqrt{10^{\frac{m}{10}}-1}=\pm A, \tag{6}$$

the value of S_{21} will reach to $-m$dB. The mdB bandwidth can be defined by:

$$\nabla\omega_{mdB}=\nabla\omega_{+}-\nabla\omega_{-}=\frac{\omega_0}{4A(b/Y_0)}. \tag{7}$$

Therefore, we have:

$$\left(\frac{b}{Y_0}\right)=\frac{\omega_0}{4A\nabla\omega_{mdB}}=\frac{f_0}{4A\Delta f_{mdB}}, \tag{8}$$

$$\Delta f_{mdB}=\frac{Y_0}{8A\pi C}. \tag{9}$$

In conjunction with the preceding analysis, when the value of h_1 increases, the equivalent capacitance C increases leading to the bandwidth Δf_{mdB} decreases as shown in Fig. 3 (b). The performance of the designed chipless tag is simulated using the simulation tool HFSS. When the h_1 increases from 1.7mm to 2mm, the Δf_{3dB} shifts from 65.4MHz to 52.1MHz, and the Δf_{10dB} shifts from 20.4MHz to 14.6MHz. Similarly, when the *gap* increases, the equivalent capacitance C increases slightly, and the bandwidth Δf_{mdB} is decreased by equation (9), assuming that the frequency is constant. In Fig. 3 (d), when the *gap* increases from 0.2mm to 0.5mm, the Δf_{3dB} shifts from 76.5MHz to 29.4MHz, and the Δf_{10dB} shifts from 23.7MHz to 4.8MHz.

C. The coding independence of the bending arms

Furthermore, this is an efficient approach to encoding independently by reducing the coupling between the resonators. Figure 4 (a) shows the current distribution at 5.1GHz. The current is distributed mainly in the bending arm element along the x axis, while the current along the y axis is weak. Compared with the spiral structure [8], there is a strong current distribution along the direction of the x axis and y axis. When multiple units are arranged along with the transmission line, the coupling between adjacent units is reduced to achieve encoding independently. And the units' distance of proposed bending arm structure is 1mm for miniaturization,

compared the one of spiral structure (3mm). To sum up, the bending arm element provides the advantage of fully utilizing the frequency band without overlapping the resonant dips, and thus it prevents mutual coupling.

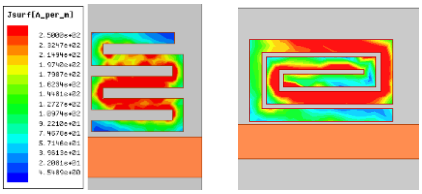

(a) (b)

Fig. 4. The current distribution at 5.1GHz: (a) bending arm structure, and (b) the spiral resonant units.

III. DESIGN OF CHIPLESS RFID TAG WITH BRNING ARMS

A. Design of the 12-bit chipless RFID tag

In the proposed chipless RFID tag, multi-resonance is achieved by adopting cascaded bending arm coupling to a 50Ω transmission microstrip line as shown in Fig. 5. The prototype is fabricated on a TXL-8 substrate (ε_r=2.55, h=0.787 mm, tanδ=0.0017) with dimensions of 37×17.7mm^2. The cascaded bending arms are distributed on both sides of 50Ω transmission line. The parameter for a 12-bit chipless RFID tag is shown in Table 1.

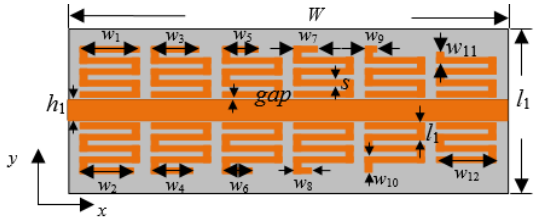

Fig. 5. Detail parameters of 12-bit chipless RFID tag.

Table 1: The optimal dimensions of the proposed 12-bit chipless RFID tag (Unit: mm)

Parameters	Value	Parameters	Value
L	17.7	w_5	3
W	37	w_6	2.5
h_1	2.2	w_7	2
s	0.6	w_8	1.5
l_1	1.8	w_9	1
w_0	5	w_{10}	1.7
w_1	5	w_{11}	1.2
w_2	4.5	w_{12}	0.7
w_3	4	gap	0.3
w_4	3.5	gap_1	1

The bending arm unit represents a logic state ‘1’ when interrogated with an incident wave. The logic state is changed to ‘0’ when the bending arm structure is removed or shortened. Each bending arm element with a different length contributes to a specific frequency. The removed bending arm unit will show no resonance in our desired band, and thus absence of a resonance dip corresponds to a 0-bit at the respective resonance frequency. Incorporating this concept, numerous tag IDs can be generated by removing or keeping different units, as shown in Fig. 6.

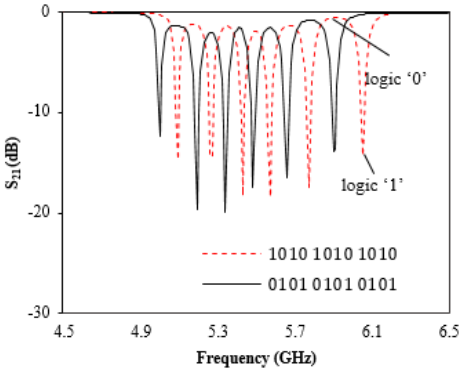

Fig. 6. The simulated result of bit combination ‘1010 1010 1010’ and ‘0101 0101 0101’.

Therefore, a unique ID can be allocated to each tag which results in avoiding the collision of data in any network. There is a code for ‘0101 0101 0101’ when the six resonant units above the transmission line is removed. Similarly, the six bending resonant units loaded below the transmission line are removed, and the code of ‘1010 1010 1010’ is achieved. Comparing the two sets of codes, it can be seen that two cases of coding frequency points are interspersed with each other, generating the code of ‘1111 1111 1111’. The coding works in the bandwidth of 5-6.04GHz, and each code occupies 88MHz.

Figure 7 shows surface current at 5.00GHz, 5.10GHz, 5.44GHz, and 5.91GHz. When the operating frequency is 5GHz, it implies the current distribution of the first bending arm element is strongest. And so as the other frequencies.

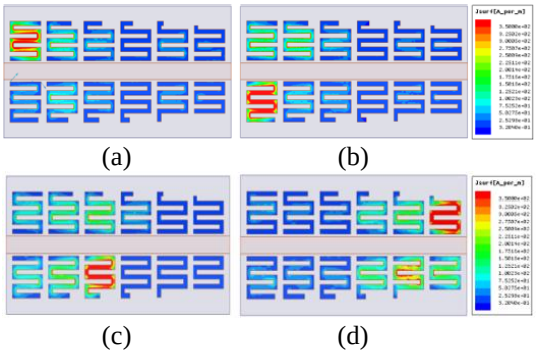

(a) (b)

(c) (d)

Fig. 7. Surface current distributions: (a) 5.00GHz, (b) 5.10GHz, (c) 5.44GHz, and (d) 5.91GHz.

B. Design of the 40-bit chipless RFID tag

To expand the coding capacity, a 40-bit chipless tag, which can reserve 240 data, is proposed. The 40-bit chipless RFID tag consists of 40 bending resonators and a transmission line, with dimension of 146.8×29.7mm^2, as shown in Fig. 8. In addition, each bending arm element responds to a specific resonant frequency.

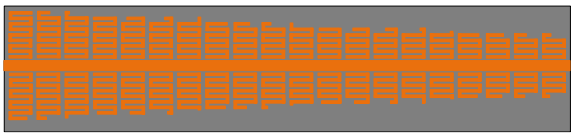

Fig. 8. A 40-bit chipless RFID tag.

Figure 9 shows the results of transmission coefficient and Group Delay for the 40-bit chipless RFID tag, which operates between 2.95GHz and 5.65GHz, occupying just 67.5MHz for each bit. Keeping the bending arm units above or below the transmission line respectively, the two kinds of codes are interspersed into each other, as shown in Fig. 10.

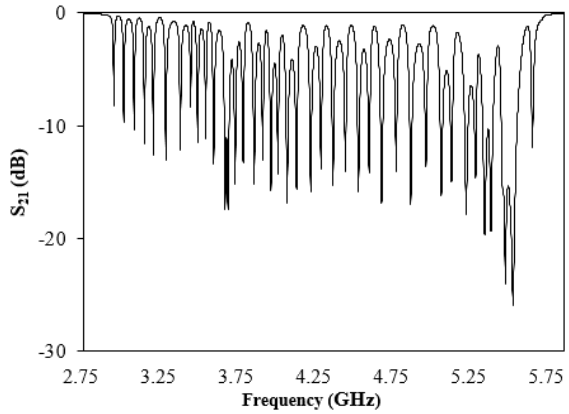

(a)

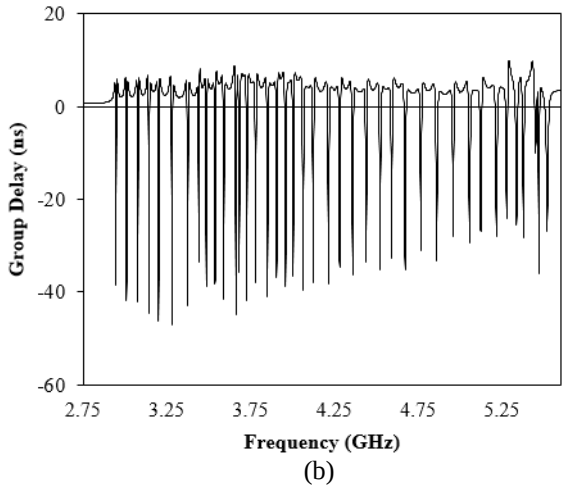

(b)

Fig. 9. Simulated results for 40-bit chipless RFID tag: (a) transmission characters, and (b) group delay.

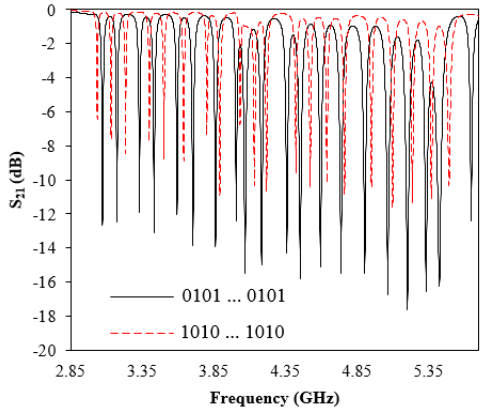

(a)

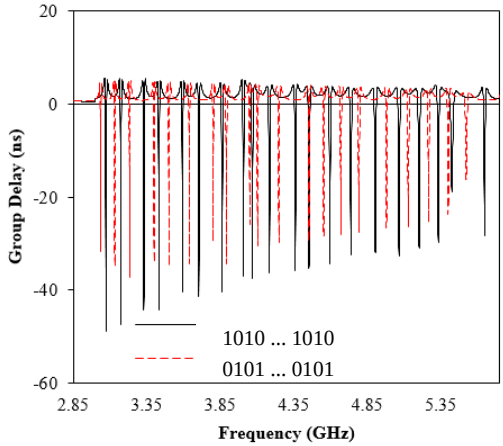

(b)

Fig. 10. Simulated results for 40-bit chipless RFID tag with different data: (a) transmission character, and (b) group delay.

IV. FABRICATION AND RESULTS

Figure 11 (a) shows photograph of the designed 12 bending arm units. The S_{21} and group delay is measured by vector network analyzer (VNA) connected to both ends of proposed 12-bit chipless RFID tag, as shown in Fig. 11 (b). Each bending arm unit has a 1:1 correspondence with a data bit (12 units=12 bits).

As shown in Fig. 12, the simulated bandwidth of the proposed 12-bit chipless RFID tag is from 5GHz to 6.05GHz, while the measured one is from 4.99GHz to 6.04GHz. And each of the bits occupies 87.5 MHz on average. Moreover, the measured data points show close correspondence with the simulated results with twelve different resonance points operating at the frequencies of 5.00GHz, 5.08GHz, 5.18GHz, 5.30GHz, 5.38GHz, 5.44GHz, 5.53GHz, 5.60GHz, 5.69GHz, 5.71GHz, 5.79GHz, 5.91GHz and 6.03GHz. It is clear that there is a small shift in the resonant frequency due to mutual coupling effect between the resonators. The band notches are well defined and for the worst case the magnitude of the dip is better than 5 dB.

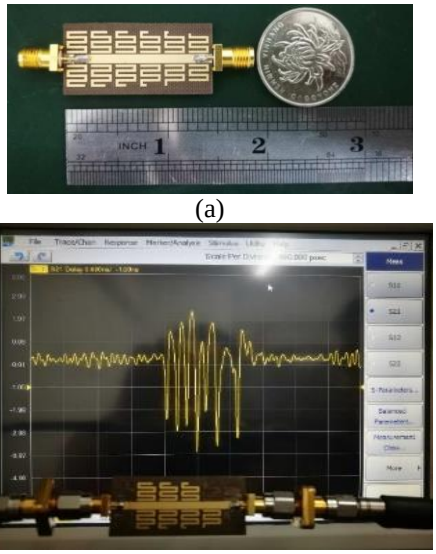

(a)

(b)

Fig. 11. Photo of the measurement environment: (a) fabrication of the 12-bit chipless RFID tag, and (b) experimental set up for bistatic measurement.

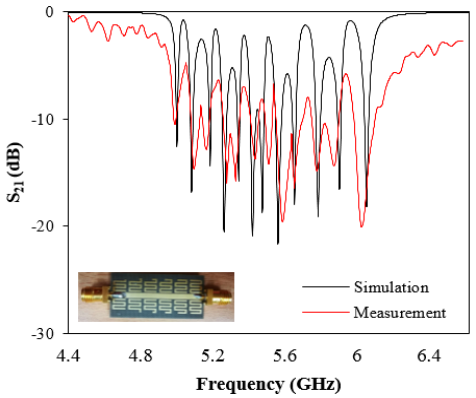

(a)

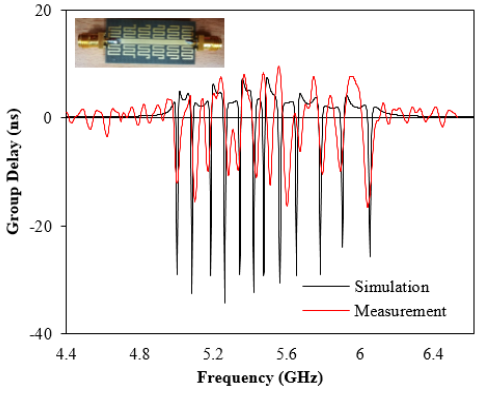

(b)

Fig. 12. Measured and simulated S_{21} results of proposed chipless RFID tag: (a) S_{21} result of the bit '1111 1111 1111', and (b) group delay result of the bit '1111 1111 1111'.

The performance comparison of the proposed and other reported chipless RFID tags are listed in Table 2. The proposed chipless tag with bending arms in this article has higher coding density and narrower inter-code bandwidth.

Table 2: Performance comparison of the proposed RFID chipless tags and references

	Dimensions (mm^3)	**Frequency (GHz)**	**Bandwidth/bit (MHz)**	**Capacity (bit)**
Work 1	37×17.7	1.09 (5.0-6.05)	87.5	12
Work 2	146.8×29.7	2.7 (2.95-5.65)	67.5	40
[9]	88×65	3.9 (3.1-7.0)	111.4	35
[10]	59×30	0.65 (3.12-3.77)	81.25	8
[11]	25×50	4 (3.4-7.4)	500	8
[12]	50×30	2.6 (1.9-4.5)	420	8

V. CONCLUSION

In this paper, a novel chipless RFID tag with bending arm units is presented. Each bending arm unit produces a resonant frequency that indicates one bit. The proposed tag not only enhanced the data capacity within the minimum frequency area, but also improved the isolation and density. A 12-bit RFID chipless tag is simulated and measured. A 40-bit chipless tag is simulated and analyzed. The simulated and measured results agree well.

ACKNOWLEDGMENT

This work is supported by the Fundamental Research Funds for the Central Universities.

REFERENCES

[1] X. Li, H. Zhu, D. Zhang, Z. Sun, Y. Yuan, and D. Yu, "Two-dimensional scanning antenna array for UHF radio frequency identification system application," *IET Microwaves, Antennas & Propagation*, vol. 8, no. 14, pp. 1250-1258, 2014.

[2] M. M. Khan, F. A. Tahir, M. F. Farooqui, A. Shamim, and H. M. Cheema, "3.56-bits/cm^2 compact inkjet printed and application specific chipless RFID tag," *IEEE Antennas and Wireless Propagation Letters*, vol. 15, pp. 1109-1112, 2016.

[3] Md. A. Islam and N. C. Karmakar, "A 4×4 dual polarized mm-wave ACMPA array for a universal mm-wave chipless RFID tag reader," *IEEE Transactions on Antennas and Propagation*, vol. 63, no. 4, pp. 1633-1640, 2015.

[4] A. Vena, E. Perret, and S. Tedjini, "A fully printable chipless RFID tag with detuning

correction technique," *IEEE Microwave and Wireless Components Letters*, vol. 22, no. 4, pp. 209-211, 2012.

[5] S. Preradovic and N. C. Karmakar, "Design of fully printable planar chipless RFID transponder with 35-bit data capacity," *Proceedings of the 39th European Microwave Conference*.

[6] A. Ramos, A. Lazaro, D. Girbau, et al., "Time-domain measurement of time-coded UWB chipless RFID tags," *Progress in Electromagnetics Research*, vol. 116, no. 8, pp. 313-331, 2011.

[7] M. Pöpperl, A. Parr, C. Mandel, R. Jakoby, and M. Vossiek, "Potential and practical limits of time-domain reflectometry chipless RFID," *IEEE Transactions on Microwave Theory & Techniques*, pp. 1-9, 2016.

[8] D. Girbau, Á. Ramos, A. Lazaro, and R. Villarino, "Passive wireless temperature sensor based on time-coded UWB chipless RFID tags," *IEEE Transactions on Microwave Theory & Techniques*, vol. 60, no. 11, pp. 3623-3632, 2012.

[9] S. Preradovic, I. Balbin, N. C. Karmakar, and G. F. Swiegers, "Multiresonator-based chipless RFID system for low-cost item tracking," *IEEE Transactions on Microwave Theory and Technique*, vol. 57, no. 5, pp. 1411-1419, 2009.

[10] M. Sumi, R. Dinesh, C. M. Nijas, S. Mridula, and P. Mohanan, "High bit encoding chipless RFID tag using multiple E-shaped microstrip resonators," *Progress In Electromagnetics Research B*, vol. 61, pp. 185-196, 2014.

[11] M. E. Jalil, M. K. A. Rahim, N. A. Samsuri, and R. Dewan, "Flexible printed chipless RFID tag using metamaterial-split ring resonator," *Applied Physics A*, pp. 122:348, 2016.

[12] C. M. Nijas, R. Dinesh, U. Deepak, A. Rasheed, S. Mridula, K. Vasudevan, and P. Mohanan, "Chipless RFID tag using multiple microstrip open stub resonators," *IEEE Transactions on Antennas and Propagation*, vol. 60, no. 9, pp. 4429-4432, Sept. 2012.

[13] E. Md. Amin, Md. S. Bhuiyan, N. C. Karmakar, and B. Winther-Jensen, "Development of a low cost printable chipless RFID humidity sensor," *IEEE Sensors Journal*, vol. 14, no. 1, pp. 140-149, 2014.

[14] C. M. Nijas, U. Deepak, P. V. Vinesh, and R. Sujith, "Low-cost multiple-bit encoded chipless RFID tag using stepped impedance resonator," *IEEE Transactions on Antennas and Propagation*, vol. 62, no. 9, pp. 4762-4770, 2014.

Hua Zhu received the M. S. degree from Guilin University of Electronic Technology, P. R. China, in 2010, and the Ph.D. degree from Beijing Institute of Technology, Beijing, P. R. China, in 2015. She has been a postdoc at Beijing University of Posts and Telecommunications, P. R. China.

Her research interests include UHF RFID beam scanning antenna array design in complex environment and millimeter wave/ Terahertz antenna design.

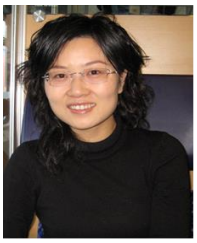

Xiuping Li received the B. S. degree from Shandong University, Jinan, Shandong, P. R. China, in 1996, and the Ph.D. degree from Beijing Institute of Technology, Beijing, P. R. China, in 2001. She has been a professor at Beijing University of Posts and Telecommunications, P. R. China.

Her research interests include microwave devices for communications, antennas, and microwave circuit design for millimeter wave/ Terahertz applications.

Jia Song received the B.S. degree from Chongqing University of Posts and Telecommunications, P. R. China, in 2013, and the M.S. degree from Beijing University of Posts and Telecommunications, P. R. China, in 2016.

Her research interests include chipless RFID techniques.

Miniaturized Elliptical Slot Based Chipless RFID Tag for Moisture Sensing

Iqra Jabeen [1], Asma Ejaz [1], Muhammad Ali Riaz [1], Muhammad Jamil Khan [1], Adeel Akram [1], Yasar Amin [1,2], and Hannu Tenhunen [2]

[1] ACTSENA Research Group
University of Engineering and Technology (UET), Taxila, 47050, Pakistan
iqra.jabeen@students.uettaxila.edu.pk, asma.ejaz@uettaxila.edu.pk, ali.riaz@uettaxila.edu.pk, muhammad.jamil@uettaxila.edu.pk, adeel.akram@uettaxila.edu.pk, yasar.amin@uettaxila.edu.pk

[2] TUCS, Department of Information Technology
University of Turku, Turku, 20520, Finland
hannu@kth.se

Abstract ─ This paper presents a compact 10-bit chipless radio frequency identification (RFID) sensor tag. The proposed structure has overall size of 22.8 mm×16 mm and possesses the capability of identification of data as well as moisture sensing of the tagged objects. The resonating structure comprises of elliptically shaped slots in a nested loop manner, investigated for three substrates that are Rogers RT/duroid®/5880, Taconic (TLX-0) and Rogers RT/duroid ®/5870. The prototype is fabricated by using Rogers RT/duroid®/5880, and moisture sensing is realized by deploying heat-resistant sheet of Kapton®HN (DuPontTM) on the smallest slot considered as sensing slot over the aspired frequency spectrum of 3.5 GHz-15.5 GHz. The proposed tag is quite suitable for cost effective applications and can be deployed on the conformal surfaces for identification and sensing purposes.

Index Terms ─ Chipless tag, moisture sensor, Radio Frequency Identification (RFID).

I. INTRODUCTION

The chipless RFID as contactless identification technique plays a vital role in RF sensing of low-cost item-level tagging along with identification. In the literature, different smart materials have been explored for temperature, moisture, strain and gas sensing in various chipless RFID tags [1]. Chip based RFID tags require silicon chip or integrated circuit for operation which makes the tag economically less viable [2]. In contrast with conventional RFID systems, chipless tags require neither an integrated chip, battery or power source nor a complex mechanism needed for interrogation of binary data between transmitter and receiver. Various flexible substrates such as paper and printing techniques like flexography have been analyzed to make the tag robust and less expensive [3]. Data-dense, compact and humidity sensor tag incorporating moisture absorbing polyvinyl-alcohol is used to monitor real-time humidity in the environment of tagged objects [4]. In the modern technological era, ceaseless development of internet of things (IoT) [5-6] facilitates the task automation by inclusion of wireless sensors and efficient home monitoring system using different internet protocols [7]. Application specific RFID tag fabricated on a low-cost paper substrate for efficient frequency band allocation and applications focusing on time and data identification using frequency shift encoding technique has been reported in [8]. Deposition of various moisture sensitive materials on the resonators/slots to make the tag capable of monitoring humidity has also been explored in recent works. Fully passive chipless RFID tag can be deployed on curved surfaces by using organic and flexible substrates such as paper-based tags [9-10].

Inductor-capacitor based humidity sensor tag provides a less expensive solution for tagging of millions of objects [11]. Multi-resonator chipless RFID tag optimized using Taconic substrate within the small size can be used for many industrial and IoT based applications [12]. The change in permittivity of the superstrate above the substrate using backscattering phenomenon is another approach to investigate the humidity sensing in chipless tags [13-14]. The reliable system of measurement is designed to monitor the read range of tag and humidity sensing behavior presented in [15]. The parameters of interest while designing the resonant element include shape, dimensions, and structure like ring-shaped tag structure using paper substrate [16], FSS based square shaped concentric loop tag design [17] and C-shaped chipless RFID tag [18]. Researchers are focused on achieving high data capacity and compactness in smart tags by introducing novel structures capable to perform sensing.

This research work presents a symmetric, moisture

Submitted On: October 26, 2018
Accepted On: May 7, 2019

sensitive and data-dense fully passive chipless RFID tag. A novel elliptically shaped slot resonator is designed to store massive data within a small size of 3.648 cm^2. While maintaining the bit density of 2.74 bits/cm^2, the proposed structure is geometrically optimized and comparatively investigated for three distinct substrates. Using Rogers RT/duroid®/5880 as a substrate, flexibility is accomplished over the operational RF band of 3.5 GHz-15.5 GHz. Furthermore, the most attractive feature of the presented tag is moisture sensor integration using Kapton® HN tape on the smallest slot along with being compact and flexible, in comparison with the recently published research work.

II. OPERATION MECHANISM

The proposed chipless RFID tag works on backscattering technique. The backscattering principle works with RFID reader (transceiver with antenna) and the chipless tag. The two main components of the RFID measurement system which play a vital role in the generation and reception of a signal from the chipless tag are VNA (vector network analyzer) and antenna subsystem. The function of VNA is to analyze the transmitted signals impinged on the tag and the backscattered signals that are reflected towards the reader. The antenna subsystem is responsible for transmission and reception of signals.

Incident plane EM waves are used to energize the RFID tag when placed in the vicinity of the reader. The chipless RFID tag absorbs electromagnetic waves transmitted by the reader. These EM waves when impinged on the tag, stimulate the current on the conductive layer of the resonating structure. In response to this, the modulated backscattered signals are returned towards the reader. This technique is called "backscattering" in which encoded data from the tag containing the exclusive tag IDs are used for tracking of tagged objects as illustrated in Fig. 1.

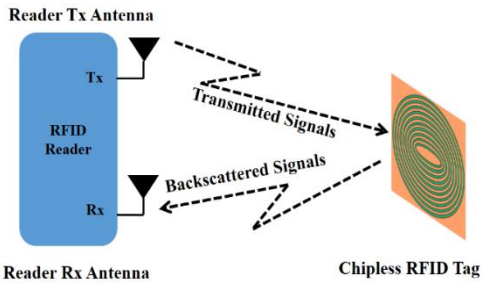

Fig. 1. Backscattering mechanism.

The proposed chipless tag design presented in this research article consists of elliptical slotted structures in a nested loop manner. The realized tag is placed at far field distance for the efficient measurement of RCS response. The Fraunhofer distance can be precisely calculated from (1):

$$R = 2D^2/\lambda, \quad (1)$$

here R represents far field distance, D signifies the longest dimension of the tag and λ denotes wavelength. There is an inverse relation of frequency with the wavelength. Hence, wavelength can be found from (2):

$$\lambda = c/f, \quad (2)$$

where, c indicates speed of light and its value is 3×10^8 m/s and f symbolizes centre frequency.

III. CHIPLESS TAG DESIGN

The design and analysis of chipless RFID tag is highly focused on maximizing the bit capacity to size ratio. The in-depth analysis of areas consumed by different shapes helped us to reach a compact structure. The proposed elliptic tag provides enhanced performance in comparison with conventional circular slot-based tag and Fig. 2 is provided to signify the choice of the structure. The resonance frequency of a particular slot can be calculated using (3):

$$f_r = \frac{c}{2A}\sqrt{\frac{2}{\epsilon_r + 1}}, \quad (3)$$

here, c represents speed of light, A symbolizes the dimension of the largest slot and ϵ_r is the relative permittivity. As per this equation, the larger slot produces resonance at smaller frequency. It is worth noticeable in Fig. 2 that the elliptical slot consumes less area and is able to produce resonance at smaller frequency in comparison with the circular configuration. This can be explained by carefully evaluating the design parameters of circle and ellipse. The area of circle is defined by only one parameter, i.e., radius. The overall area of the ellipse is controlled by major and minor axis. The two design parameters provide space for further optimization and hence, prove the elliptical structure a finest choice for the tag design.

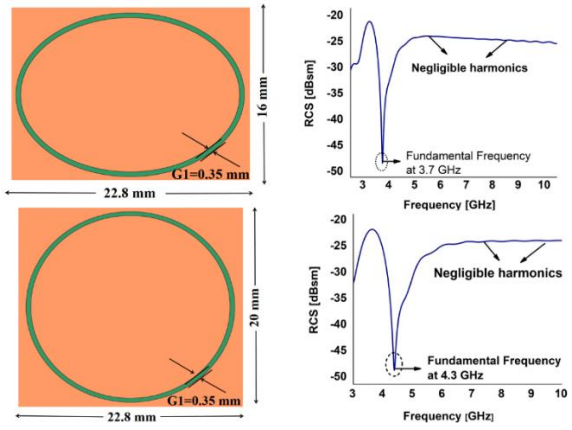

Fig. 2. Comparison between circular and elliptical slot.

A compact, miniaturized and passive chipless RFID tag structure loaded with slots in nested loop fashion with its geometric parameters is shown in Fig. 3. Rogers

RT/ duroid®/5880 having thickness of 0.508 mm, Rogers RT/duroid®/5870 with the thickness of 0.787 mm, and Taconic TLX-0 having thickness 0.635 mm are three substrates used for tag optimization. The area consumed by the compact tag design in all cases is 22.8 mm×16 mm. The length of minor axis is labelled as *M1*=11 mm, while the length of the major axis from the origin is represented as *M2*=7 mm. Slots are etched out from copper cladding with the thickness of 35µm. There are ten slots corresponding to ten bits generating 2^{10}=1024 multiple unique tag IDs. The tag is optimized in such a way that sharp resonances are produced at different frequencies in RF band of 3.5 GHz-15.5 GHz. The uniform width of slot *G1* is 0.35 mm, while the space between two neighboring slots is denoted by *G2* = 0.4 mm. The length of the minor axis of the innermost slot *E* and the height of the outer most ellipse *A* are 1.1 mm and 15.4 mm, respectively. Furthermore, *S2*=0.4 mm and *S1*=0.3 mm are the perpendicular and horizontal distances of the tag from the outermost slot, respectively. Incident plane wave is used for exciting the RFID tag and the presence of slot produces logic state "1" while a shorted slot generates logic state "0" which results in absence of that particular resonance in the RCS curve. After the successful optimization and analysis of single elliptical slot, additional number of resonators are added in the structure in a similar way. The proposed design is simulated, geometrically analyzed and optimized using CST Microwave Studio Suit®.

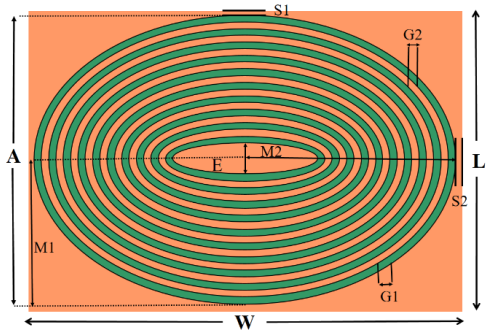

Fig. 3. Layout of proposed chipless RFID tag.

IV. RESULTS AND DISCUSSION

This section demonstrates the measured and computed RCS response of the proposed flexible, robust and ten-bit chipless RIFD tag. The presented tag design is examined for three dissimilar substrates, Rogers RT/duroid®/5880, Taconic TLX-0 and Rogers RT/duroid®/5870. The results are recorded in terms of different data encoding combinations for identification of tagged objects. It is observed from the results that changing the electrical properties of the substrate shifts the RCS graph on the frequency axis. The comparative analysis of the tag examined using different substrates is also discussed in this section and given in Table 1. The experimental arrangement consists of transmitting and receiving antennas and vector network analyzer (VNA) model R&S ZVL-13 for testing the fabricated sample of the proposed tag in the standard environment. The tag is positioned at the far-field distance of 32 mm to observe the RCS response. The fabricated prototype of the proposed chipless tag in comparison with euro coin is presented in Fig. 4.

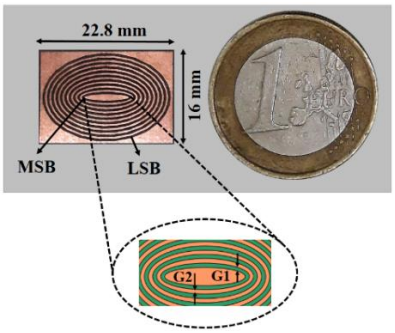

Fig. 4. Fabricated prototype of chipless tag.

A. Rogers RT/duroid®/5880 substrate

The frequency signatures of the articulated tag in terms of computed and measured RCS response with flexible laminate Rogers RT/duroid®/5880 is illustrated in Fig. 5 (a). The RFID tag design covers the operational RF spectrum from 3.5 GHz to 15.5 GHz and yields ten bits with unique tag ID: 1111111111. Sharp and clear resonances are observed, and every single resonance corresponds to one data bit. Figure 5(b) illustrates the arbitrary data encoding sequences that can be accomplished by adding and subtracting slots in the proposed structure generating two unique tag IDs: 0101111111 and 0000000000. Here "0" represents shorted slot and omission of a dip in the RCS graph. The proposed tag demonstrates acceptable agreement with measured and computed results.

Table 1: Comparison of proposed tag with various substrates

Characteristics	Rogers RT/duroid®/5870	Taconic TLX-0	Rogers RT/duroid®/5880
Thickness (mm)	0.787	0.635	0.508
Loss Tangent	0.0009	0.0019	0.0009
Permittivity	2.2	2.45	2.2
Radiator	Copper	Copper	Copper
Flexibility	×	×	✓
Freq. Band (GHz)	3.7-15	3.5-14.9	3.5-15.5

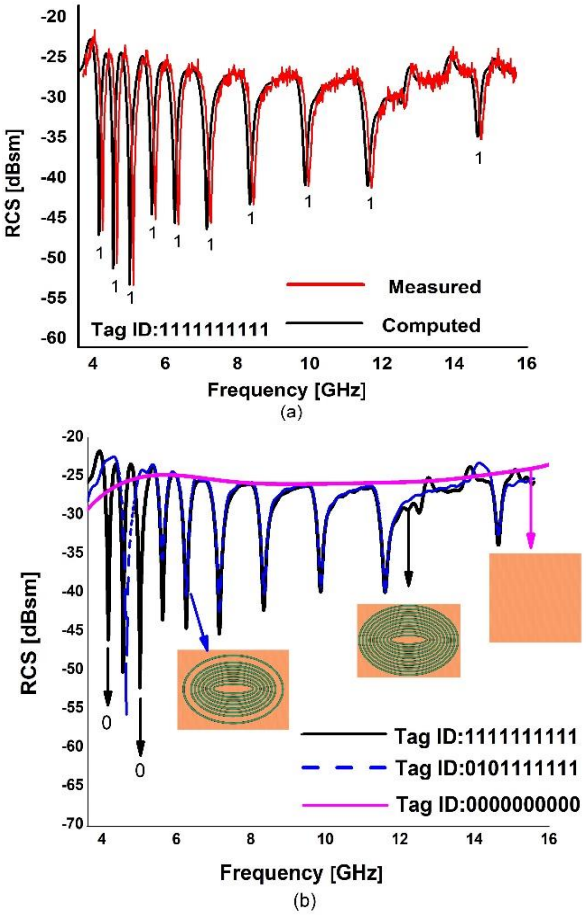

Fig. 5. (a) Simulated and measured results, and (b) RCS response with different bit sequences.

B. Taconic TLX-0 substrate

The optimized tag design by using the Taconic TLX-0 substrate with thickness 0.635 mm (∈r = 2.45) has ten bits as shown in Fig. 6. The RCS response of the tag illustrates ten resonance dips and covers the bandwidth of 11.4 GHz. It is observed from results that the most significant bit appears at 3.5 GHz, and the least significant bit is produced at 14.9 GHz.

C. Rogers RT/duroid®/ 5870 substrate

The proposed symmetric geometric structure is analyzed for Rogers RT/duroid®/5870 with the thickness 0.787 mm and loss tangent tan δ=0.0009. Figure 6 depicts the RCS magnitude response of the proposed structure in the squeezed frequency spectrum of 3.7 GHz -15 GHz.

The surface current distribution of the formulated slotted structure by using Rogers RT/duroid®/5880 laminate at the lowest frequency of 3.5 GHz is presented in Fig. 7 (a). The metallic portion acts as capacitive part while the non-metallic part behaves as an inductive element. The maximum concentration of current represents the inductive effects. The low intensity of the current indicates the capacitive effects. Figure 7 (b) indicates the surface current intensity at the highest frequency of 15.5 GHz.

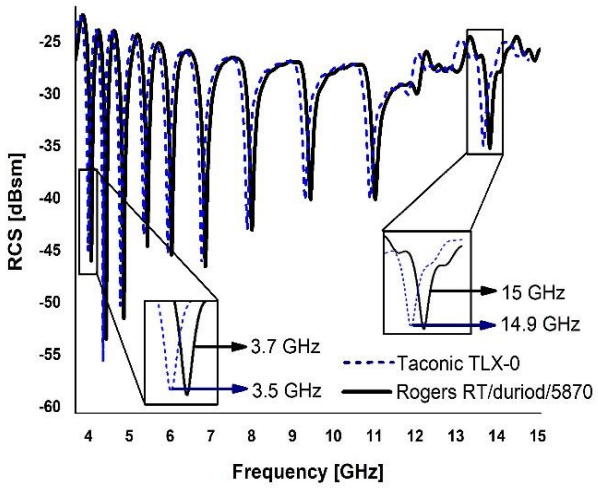

Fig. 6. RCS response with various substrates.

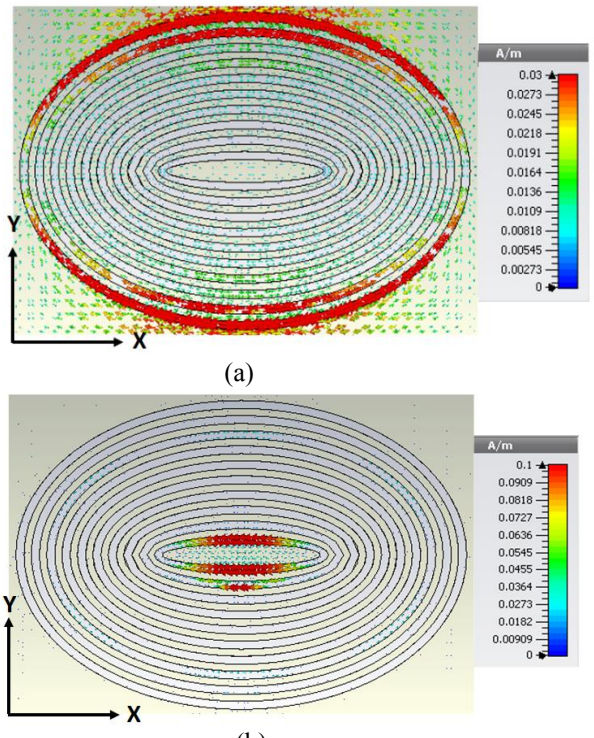

Fig. 7. (a) Current density at minimum frequency, and (b) current density at maximum frequency.

V. MOISTURE SENSOR

The proposed RFID tag holds an additional feature of moisture sensing when the heat-resistant polyamide sheet of Kapton® HN is incorporated into the structure. For this purpose, multiple steps are performed for the

proposed symmetric tag. We use Rogers RT/duroid®/5880 as substrate, and place thin sheet of the Kapton® HN with the thickness of 0.125 mm on the smallest slot. Here, Kapton HN tape is used for sensing purpose and absorbs moisture from the surroundings. This feature of Kapton enhances its usage for the moisture sensitive applications such as the food industry (cold storage eatables) and drug storage [14].

The change in the percentage of relative humidity level will alter the permittivity ($\epsilon r = 3.5$) of Kapton film which results in the shifting of resonances associated with sensing slot towards the left side in the RCS curve [11]. The linear change in permittivity level with relative humidity [20-21] of Kapton® HN is demonstrated in (4):

$$\epsilon_r = 3.05 + 0.008 \times RH. \quad (4)$$

To experimentally analyze the moisture sensing performance of proposed chipless tag, climatic chamber by Weiss Technik WK11-180 is used to investigate the sensor response of the tag for numerous humidity levels. As shown in Fig. 8, every 20% increase in moisture level shifts the resonance frequency of the sensing slot towards the lower side.

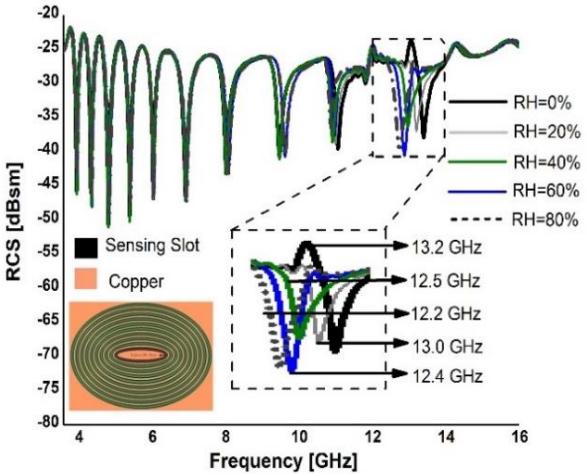

Fig. 8. RCS response for moisture sensing.

It is observed that when the % RH increments from 20% to 80%, the overall response of the tag shifts and the resonance frequency of sensing slot starts drifting from 13.2 GHz to 12.2 GHz. Thus, the integration of moisture sensing in proposed chipless RFID tag makes it novel as no external circuit is required for sensing purpose and it can be easily deployed for various smart sensing applications. The formulated tag provides the additional advantages of compactness, symmetry, flexible nature, low-cost, robustness, and moisture sensing.

The comparative analysis of the elliptically shaped tag with previously published research articles is demonstrated in Table 2.

Table 2 illustrates that proposed tag design has the ability to encode 10-bits over the miniaturized footprint of 3.648 cm^2. In contrast with other tag designs, the presented tag yields a high bit density of 2.74 bits/cm^2 with the additional feature of humidity sensing using flexible laminates.

VI. CONCLUSION

A novel, compact, robust and flexible 10-bit moisture sensing chipless RFID tag over the miniaturized dimensions of 22.8 mm × 16 mm is presented in this research article. The RCS response of the elliptically shaped tag design is optimized and investigated for three distinct substrates, i.e., rigid Rogers RT/duroid®/5870, flexible Rogers RT/duroid®/5880 and Taconic TLX-0. The proposed structure has the capacity to generate 2^{10}= 1024 exclusive IDs with the additional functionality of moisture sensing. Kapton®HN tape is used as moisture sensitive material on the shortest slot within a squeezed frequency band from 3.5 GHz to 15.5 GHz, and a shift in resonant frequency is observed by increasing the moisture level. Flexible nature of the realized chipless tag by using Rogers RT/duroid®/5880 substrate enhances its attractiveness for its deployment on bendable surfaces. Hence, the presented symmetrical geometric structure is a potential candidate for data encoding and various low-cost moisture sensitive applications.

Table 2: Comparison with already published work

Parameters	L-shape [10]	Rectangle [12]	Square [17]	E-shaped [19]	Ellipse Shape
Size [cm^2]	7.14	3.387	20.25	17.7	3.648
Tran. Bits	8	6	3	8	10
Bit density [Bits/cm^2]	1.120	1.771	0.14	0.45	2.74
Flexibility	✓	×	✓	×	✓
Sensing	✓	×	✓	×	✓

ACKNOWLEDGMENTS

We thank Higher Education Commission Pakistan for Technology Development Fund (HEC/TDF-067) for financial support of this work via ACTSENA research group funding.

REFERENCES

[1] E. M. Amin, J. Kumar, S. Nemai, and N. C. Karmakar, "Smart sensing materials for low-cost chipless RFID sensor," *IEEE Sensors*., vol. 14, pp. 2198-2207, 2014.

[2] F. Costa, S. Genovesi, and A. Monorchio, "A chipless RFID based on multiresonant high-impedance surfaces," *IEEE Transection on Microwave Theory and Techniques*, vol. 61, no. 1, pp. 146-153, 2013.

[3] A. Vena, E. Perret, S. Tedjini, G. E. P. Tourtollet, A. Delattre, F. Garet, and Y. Boutant, "Design of chipless RFID tags printed on paper by flexography," *IEEE Trans. Antennas Propag*., vol. 61, pp. 5868-5877, 2013.

[4] E. M. Amin, Md. S. Bhuiyan, N. C. Karmakar, and B. W. Jensen, "Development of low cost printable chipless RFID humidity sensor", *IEEE Sensors*., vol. 14, pp. 140-149, 2012.

[5] G. Dong, Y. Shen, H. He, J. Virkki, and S. Hu, "Chipless graphene tag and dual cp reader for internet of things," *2017 International Applied Computational Electromagnetics Society Symposium (ACES)*, pp. 1-2, 2017.

[6] F. Nekoogar and F. Dowla, "Passive RFID for IoT using UWB/UHF hybrid signaling," *2016 IEEE/ACES International Conference on Wireless Information Technology and Systems (ICWITS) and Applied Computational Electromagnetics (ACES)*, pp. 1-2, 2016.

[7] S. D. T. Kelly, N. K. Suryadevara, and S. C. Mukhopadhyay, "Towards implementation of IOT for envoirmental condition monitoring in homes," *IEEE Sensors*, vol. 13, pp. 3846-3853, 2013.

[8] M. M. Khan, F. A. Tahir, M. F. Farooqui, A. Shamim, and H. M. Cheema, "3.56 bits/cm^2 compact inkjet printed and application specific chipless RFID tag," *IEEE Antennas and Wireless Propag. Lett.*, vol. 15, pp. 1109-1112, 2016.

[9] A. Vena, E. Perret, D. Kaddour, and T. Baron, "Towards reliable chipless RFID humidity sensor tag based on silicon nanowires," *IEEE Trans. Microw. Theory. Tech*., vol. 64, pp. 2977-2985, 2016.

[10] A. Habib, R. Asif, M. Fawwad, Y. Amin, J. Loo, and H. Tenhunen, "Directly printable compact chipless RFID for humidity sensing," *IEIC Electron. Express*, vol. 14, pp. 20170169-20170169, 2017.

[11] Y. Feng, L. Xie, Q. Cheng, and L. R. Zheng, "Low cost printed chipless RFID humidity sensor tag for intelligent packaging," *IEEE. Sensors*, vol. 15, pp. 3201-3208, 2015.

[12] W. M. Adbulkawi and A. F. A. Sheta, "Printable chipless RFID tags for IOT applications," *IEEE Int. Conf. on Computer App. and Info Security (ICCAIS)*, pp. 1-4, 2018.

[13] S. Genovesi, F. Costa, M. Borgese, S. Tedjini, and T. Perret, "Enhanced chipless RFID tags for sensors," *IEEE. Int. Symposium on Antennas and Propag. (APSURSI)*, pp. 1275-1276, 2016.

[14] A. Ali, S. I. Jafri, A. Habib, Y. Amin, and H. Tenhunen, "RFID humidity sensor tag for low cost applications," *ACES*, vol. 32, pp. 1083-1088, 2017.

[15] J. Salmeron, A. Albrecht, S. Kaffah, M. Becherer, P. Lugli, and A. Rivadeneyra, "Wireless chipless systems for humidity sensing," *Sensors*, vol. 18, pp. 2275-2275, 2018.

[16] A. Habib, Y. Amin, M. A. Azam, J. Loo, and H. Tenhunen, "Frequency signature directly printable humidity sensing tag using organic electronics," *IEIC. Electron. Express*, vol. 14, pp. 201610181-201610181, 2016.

[17] M. Borgese, F. A. Dicandia, F. Costa, S. Genovesi, and G. Manara, "An inkjet printed chipless RFID sensor for wireless humidity monitoring," *IEEE Sensors*, vol. 17, pp. 4699-4707, 2017.

[18] M. Mumtaz, S. F. Amber, A. Ejaz, A. Habib, S. I. Jafri, and Y. Amin, "Design and analysis of C shaped chipless RFID tag," *2017 Int. Symposium. on Wireless Systems and Networks (ISWSN)*, pp. 1-5, 2017.

[19] M. Sumi, R. Dinesh, C. M. Nijas, S. Mridula, and P. Mohanan, "High bit encoding chipless RFID tag using multiple E shaped microstrip resonators," *Progress in Electromagnetics Research B*, vol. 61, pp. 185-196, 2014.

[20] J. Virtanen, L. Ukkonen, T. Bjorninen, A. Z. Elsherbeni, and L. Sydanheimo, "Inkjet-printed humidity sensor for passive UHF RFID systems," *IEEE Transection on Instrumentation and Measurement*, vol. 60, pp. 2768-2777, 2011.

[21] J. Virtanen, L. Ukkonen, T. Bjorninen, and L. Sydanheimo, "Printed humidity sensor for UHF RFID systems," *2010 IEEE Sensors Applications Symposium (SAS)*, pp. 269-272, 2010.

Iqra Jabeen did her B.Sc. degree in Telecommunication Engineering from University of Engineering and Technology Taxila, Pakistan in 2017. In the same year, she has joined ACTSENA Research Group and currently working there as a research scholar. She is a student member of Applied Computational Electromagnetics Society (ACES).

Asma Ejaz received her B.Sc. and M.Sc. degree in Telecommunication Engineering from University of Engineering and Technology Taxila, Pakistan in 2013 and 2015 respectively. At present, she is an Instructor and a Ph.D research scholar in the same institute, working under

ACTSENA Research Group focused on passive chipless RFID tags and advancements in antenna design techniques. She is member of IEEE and ACES.

Muhammad Ali Riaz received his M.S. and B.S. degree in Electrical Engineering from Iowa State University, USA in 2010 and 2009 respectively. Afterwards, he joined the Department of Electrical and Computer Engineering, Iowa State University, USA as a Research Assistant. He is currently serving as Assistant Professor associated with ACTSENA research group at University of Engineering and Technology, Taxila. Ali is working towards the design and implementation of chipless RFID tags based on electromagnetic signature and their signal processing applications. He also serves as the Director of Electronics and Measurements Laboratory at his department. His research work has been featured in a number of ISI-indexed journals.

Muhammad Jamil Khan received the B.Sc. Engineering degree in Computer Engineering, the M.Sc. degree in Telecommunication Engineering, and the Ph.D. degree in Computer Engineering from University of Engineering and Technology, Taxila, Pakistan, in 2005, 2009 and 2016 respectively. He is currently Assistant Professor and Director of Embedded Systems and Digital Signal Processing Laboratory in the same University. He is also the Founder of Virtual Reality Simulation Laboratory at the University. He has authored or co-authored numerous technical articles in well-known international journals and conferences. His current research interests include multimedia content analysis, RF identification and machine learning.

Adeel Akram is Dean and Professor of Telecommunication Engineering Department University of Engineering and Technology Taxila, Pakistan. He received his B.S degree in Electrical Engineering from University of Engineering and Technology Lahore, Pakistan in 1995. He received his M.S degree in Computer Engineering from National University of Sciences and Technology (NUST), Pakistan and his Ph.D in Electrical Engineering from University of Engineering and Technology Taxila, Pakistan, in 2000 and 2007 respectively. His research interests include microwave and communication systems and is leading a 5G wireless communication group at UET Taxila, Pakistan.

Yasar Amin received the B.Sc. degree in Electrical Engineering with specialization in Telecommunication and MBA in Innovation and Growth from Turku School of Economics, University of Turku, Finland. His M.Sc. is in Electrical Engineering with specialization in System on Chip Design, and also Ph.D. is in Electronic and Computer Systems from Royal Institute of Technology (KTH), Sweden, with the research focus on printable green RFID antennas for embedded sensors. He is currently an Associate Professor and Chairman of Telecommunication Engineering Department, University of Engineering and Technology Taxila, Pakistan. He is the Founder of ACTSENA (Agile Creative Technologies for Smart Electromagnetic Novel Applications) research group. He has authored or co-authored more than 100 international technical papers in conferences and journals. He is a member of more than a dozen international professional societies and the fellow of PAE.

Hannu Tenhunen is Chair Professor of Electronic Systems at Royal Institute of Technology (KTH), Stockholm, Sweden. He has been Full Professor, Invited Professor or Visiting Honorary Professor in Finland (TUT, UTU), Sweden (KTH), USA (Cornel U), France (INPG), China (Fudan and Beijing Jiaotong Universities), and Hong Kong (Chinese University of Hong Kong), and has an honorary doctorate from Tallinn Technical University. He has been the Director of multiple national large-scale research programs or being an initiator and director of national or European graduate schools. He has actively contributed to VLSI and SoC design in Finland and Sweden via creating new educational programs and research directions. He has authored or co-authored more than 900 international technical papers in conferences and journals. He has been granted 9 foreign patents and he is a member of Academy of Engineering Science of Finland.

Design of High Order Cross-Coupled Constant Absolute Bandwidth Frequency-Agile Bandpass Filters

Dengyao Tian, Quanyuan Feng, and Qianyin Xiang

School of Information Science and Technology
Southwest Jiaotong University, Chengdu, Sichuan, 611756, China
ty198826@126.com, fengquanyuan@163.com, qyxiang@swjtu.edu.cn

Abstract ─ Novel high order constant absolute bandwidth (ABW) cross-coupled electrical tunable bandpass filters (BPFs) are proposed. Microstrip cross-coupled tunable resonators are designed and investigated to meet the coupling requirement of the tunable BPF with constant ABW. A thorough theoretical analysis is derived to determine the performance of the proposed filter and verify the initial values of design parameters. To verify the design concept, two prototypes are fabricated and measured. The measurements show that the proposed four-order filter has a -3 dB ABW of 119.5±2.5 MHz with 1.31~1.98 GHz tuning frequency. And the proposed six-order filter has a -3 dB ABW of 102±6 MHz with 1.39~2.07 GHz tuning frequency. High selectivity has been achieved in the proposed filter by TZs (transmission zeros) beside the passband, good agreement between simulated and measured results has been demonstrated.

Index Terms ─ Bandpass filter, filter, four-order, six-order, source-load coupling.

I. INTRODUCTION

In recent years, people pay more and more attention to the research of filter [1-4]. Specifically, constant bandwidth BPF and high order BPF with high selectivity are a longstanding concern for wireless communication systems [5-9]. Up to now, many planar tunable filters have been proposed, but most of them focus on the design of two-order tunable filters [5-8]. Only a few numbers of high order (more than two poles) tunable filters have been reported to meet the high selectivity requirement. For example, in [9-12], the direct coupling topology was applicable to the varactor-loaded λ/2, λ/4 or LC resonators resulting in the simple-tunable filters. In [13], a four-order tunable BPF with cross-coupled stepped-impedance resonator (SIR) is designed, however, the passband and TZs are distorted, and the bandwidth is not constant due to the uncontrollable coupling coefficients. In order to introduce the TZs and enhance the selectivity of the tunable response, the cross-coupling or extra cross coupling structures were added to the conventional high order tunable filters [14]–[18]. Many different methods have been introduced and reported to design constant bandwidth BPFs. A magnetic-dominated mixed coupling method is proposed based on quarter wavelength resonator loaded with tunable capacitor at its open termination [5]. Since the coupling structure is magnetic-dominated, the whole hybrid coupling can be pre-designed while the tunable capacitance increasing. This method has been widely used in constant bandwidth tunable filters design [6-10]. Another method is built on electric coupling coefficient control. Constant bandwidth tunable filters based on microstrip LC resonators with electric coupling compensation capacitor network are provided in [9].

The above techniques are able to achieve the high order tunable filters. However, most of them are very complex, because a lot of varactors or pin diodes (more than the resonators) are utilized, and deteriorate the insertion loss. Besides, the selectivity of the reported filters needs to be further improved. Similar to the frequency-fixed filter design, the tunable filter with the fully canonical response is preferable. Only [14] reported a four-order tunable filter with the fully canonical response, but which needs a mass of controllable capacitor and bias to stabilize the passband, and the constant ABW was not achieved. To best of our knowledge, there is hardly any reported four-order or six-order cross-coupled tunable BPF with constant ABW (where there is no need to employ extra varactors to control the coupling between resonators).

This paper focuses on the novel high order cross-coupled tunable filter topology with constant ABW. The basic theories [19-20] are used in designing the proposed filters. This filter has four or six resonators. Cross-coupled tunable resonators and simple tuning method are designed to deal with multiple coupling coefficient curves requirement of tunable BPF with constant ABW.

II. DESIGN OF FOUR-ORDER SOURCE-LOAD BPF

Figure 1 shows the proposed four-order source-load BPF. The resonators are represented by the number 1 to 4. The source or load is represented by S or L, and

Submitted On: December 17, 2018
Accepted On: April 6, 2019

electric or magnetic coupling is represented by E or M, respectively. In order to devise this BPF, the coupling coefficient between the resonators must be obtained based on the prototype of the filter. In this paper, the design index: RL (Return Loss)=20dB, the normalized zero position is ±2 and ±4, and the N+2 coupling matrix is obtained by the method of reference [19]. The calculated normalized coupling coefficients are M_{S1}=1.0217, M_{SL}=0.0115, M_{12}=-0.8664, M_{23}=0.77286, M_{14}=-0.19728. The other coefficients in the matrix are the same as these five coefficients, or 0. When ABW=120MHz, the resonant frequency f_0=1.2~2GHz, then the desired non-normalized coupling coefficient k and Qe can be obtained from the following:

$$k_{ij} = FBW \cdot M_{ij}(i, j = S,1,2..L), \tag{1}$$

$$Qe = \frac{1}{FBW \cdot M_{S1}{}^2}, \tag{2}$$

where FBW is fractional bandwidth and FBW=ABW/f_0. When the resonant frequency and ABW are settled to 1.6 GHz and 120MHz, then FBW=7.6%. The non-unitary coupling matrix [k] and non-unitary Qe are calculated by (1) ~ (2):

$$[k] = \begin{bmatrix} 0 & -0.065 & 0 & -0.015 \\ -0.065 & 0 & 0.059 & 0 \\ 0 & 0.059 & 0 & -0.065 \\ -0.015 & 0 & -0.065 & 0 \end{bmatrix}, \tag{3}$$

$$Qe = 10.4, \tag{4}$$

$$k_{SL} = k_{LS} = 0.00087. \tag{5}$$

Once the coupling matrix [M] is determined, the filter frequency responses can be computed in terms of scattering parameters:

$$S_{21} = -2j[A]^{-1}_{n+2,1}, \tag{6}$$

$$S_{11} = 1 + 2j[A]^{-1}_{11}. \tag{7}$$

The matrix [A] is given by:

$$[A] = [M] + \Omega[U] - j[R], \tag{8}$$

in which [U] is similar to the (n+2) × (n+2) identity matrix, except that $[U]_{11} = [U]_{n+2,n+2} = 0$, [R] is the (n+2) × (n+2) matrix with all entries zeros, except for $[q]_{11} = [q]_{n+2,n+2} = 1$, and Ω is the frequency variable of lowpass prototype. The lowpass prototype response can be transformed to a bandpass response having a fractional bandwidth FBW at a center frequency f_0 using the well-known frequency transformation:

$$\Omega = \frac{1}{FBW}\left(\frac{f}{f_0} - \frac{f_0}{f}\right). \tag{9}$$

From equations (1) (2), In order to obtain constant ABW filter, the coupling coefficient needs to decrease with the increase of resonant frequency, while the external quality factor needs to increase with the increase of resonant frequency. For the coupling coefficient, the distance between two couplers and the position of the capacitance C_v need to be adjusted. In order to get an extra adjustment degree of freedom, the SIR structure is used in the regulation of k_{23} and k_{14} in this paper. For external quality factors, the length and width of the coupling lines and input capacitance C_{in} can be adjusted to achieve the purpose of constant ABW.

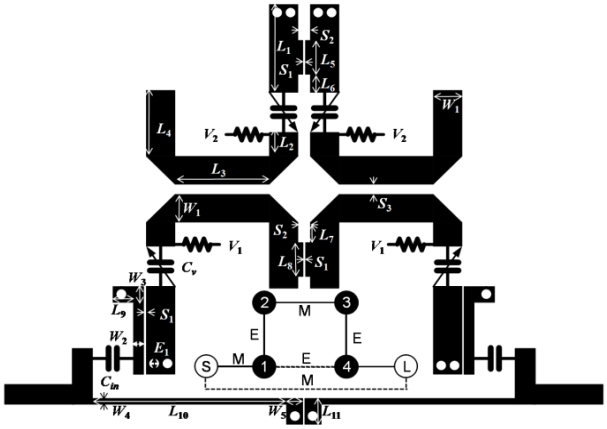

Fig. 1. The proposed four-order source-load BPF.

The simulated k and Qe can be got as [20]:

$$k = \frac{f_1^2 - f_2^2}{f_1^2 + f_2^2}, \tag{10}$$

$$Qe = \frac{2\pi f_0 \cdot \tau_{S_{11}}(f_0)}{4}, \tag{11}$$

where the f_1 and f_2 are characteristic frequencies when the input port is very weakly coupled to the coupled resonator structure, τ_{S11} is the group delay.

Consider an I/O structure that only involves the source-load coupling as shown in Fig. 2 (c). The simulated direct source-load coupling k_{SL} can be obtained as [20]:

$$k_{SL} = \frac{-1 - \sqrt{1 - |S_{21}|^2}}{|S_{21}|}, \tag{12}$$

where $0 \leqslant |S_{21}| \leqslant 1$ and $k_{SL} = 0$ for $|S_{21}| = 0$.

As shown in Fig. 2, the C_v of the resonator and the length of its coupling line are first selected by the desired adjustable range. Secondly, in the range of adjustable frequency, five coupling coefficients are required to be designed. For the coupling coefficient k_{12}, k_{23}, k_{14}, and Qe, can be varied by the position of the C_v, the coupling distance between the resonators, and the different positions of the SIR. After the initial adjustment of the four parameters, the k_{SL} was adjusted separately. Each coupler is then combined from the initialized BPF.

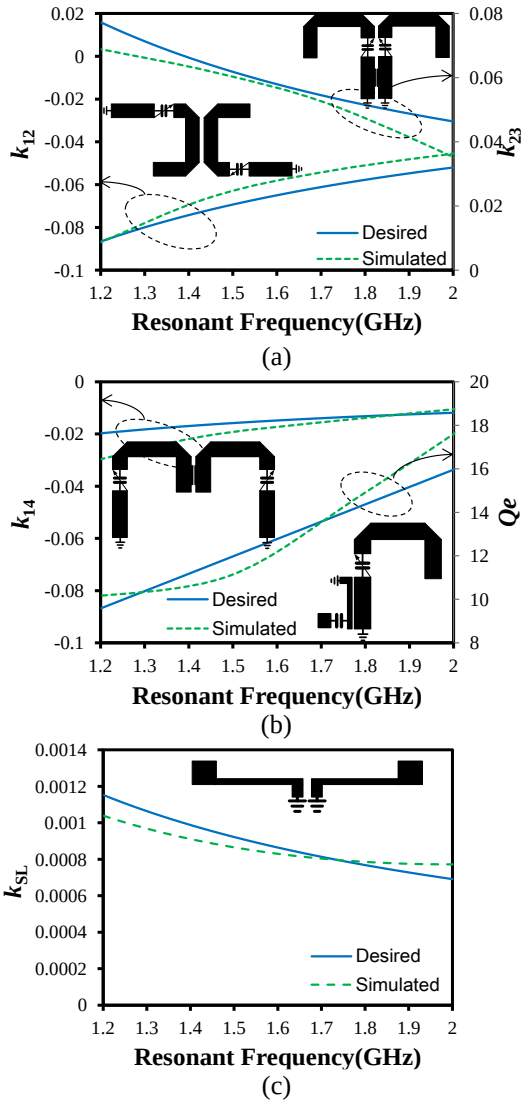

Fig. 2. Desired and simulated result: (a) coupling coefficient k_{12} and k_{23}, (b) coupling coefficient k_{14} and external quality factors Qe, and (c) source-load coupling coefficient k_{SL}.

Based on the tuning, the strength of magnetic-dominated coupling coefficient k_{23}, electric-dominated coupling coefficient k_{12} and k_{14} and source-load coupling coefficient k_{SL} decrease as the resonant frequency increase, and the external quality Qe increase as the resonant frequency increase, then the simulated slope of k_{12}, k_{23}, k_{14}, k_{SL} and Qe can be same with the desired. So these coupling structures can be used to build the cross-coupled tunable BPF with constant ABW.

III. DESIGN OF SIX-ORDER BPF

According to the above method and theory of designing four-order filter, the six-order filter is realized to have one pair of TZs on the normalized resonant frequency ±1.2 for high selectivity and maximum in-band return loss of the filter is 20dB. By using the synthesis technique [19], when the resonant frequency is 1.6GHz and the ABW is settled to 120MHz, the main design coupling coefficients are k_{12}=k_{56}=0.062 k_{23}=k_{45}=-0.040, k_{34}=-0.059, k_{25}=0.020 and external coupling factor Qe=13.6.

Figure 3 shows the proposed six-order BPF. Figure 4 is the comparison curve between simulated and desired after the adjustment of coupling coefficient. It can be seen that after a series of adjustments, the coupling coefficient curve has basically met the requirements. By using these initial values and further optimization, the purpose of designing a high-order constant ABW filter can be achieved.

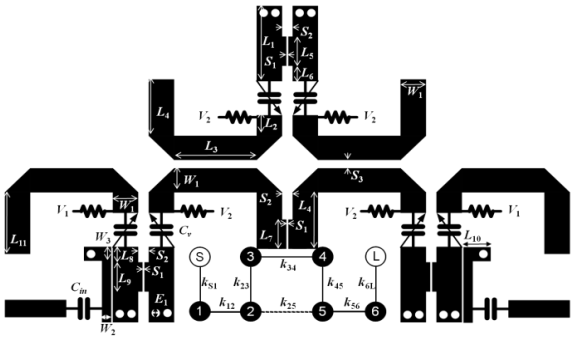

Fig. 3. The cross-coupled topology of the proposed six-order tunable bandpass filter.

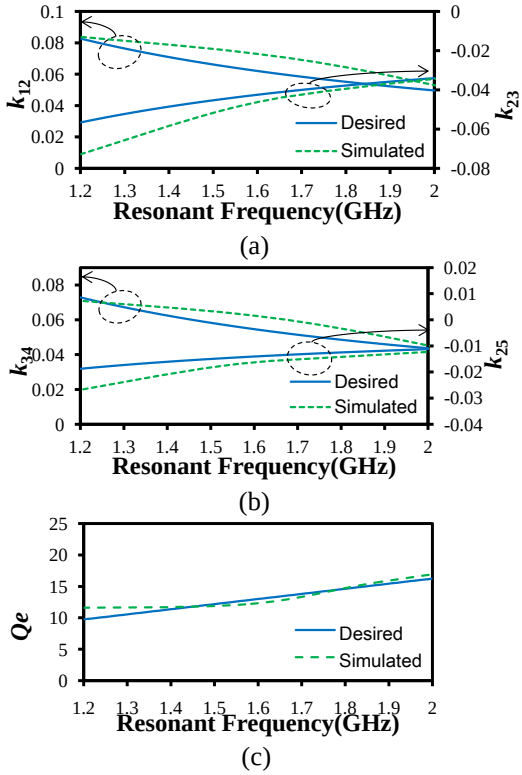

Fig. 4. The desired and simulated: (a) k_{12} and k_{23}; (b) k_{34} and k_{25}; (c) Qe.

IV. FABRICATION AND MEASUREMENT

Through the above analysis, combined with simulation software Sonnet and Agilent Advanced Design System for collaborative simulation, the four-order BPF with optimized geometry parameters (L_1=19.5, L_2=2.8, L_3=16.7, L_4=13.9, L_5=7.6, L_6=2.9, L_7=2, L_8=5.2, L_9=3.1, L_{10}=23.1, L_{11}=5.4, W_1=2.6, W_2=1, W_3=1.3, W_4=0.6, E_1=0.8, S_1=0.1, S_2=1.3, S_3=0.1, Unit: mm, *Cin*=2.2pF) has been obtained, and the six-order BPF filter with optimized geometry parameters (L_1=18.3, L_2=4, L_3=15.2, L_4=10.5, L_5=10.2, L_6=2.2, L_7=3, L_8=2.2, L_9=10.2, L_{10}=3.9, L_{11}=12, W_1=2.6, W_2=0.8, W_3=1.2, E_1=0.8, S_1=0.1, S_2=1.5, S_3=0.3, unit: mm *Cin*=2.4pF) has been obtained. The substrate is 0.8mm F4B-2 with a relative dielectric constant of 2.65 and a loss tangent of 0.001. SMV1405 varactors (C_v-0~30V, 0.63~2.67pF) is considered to be tuning elements. Since the input and output resonator are coupled to the feed in network, the designed filter needs to be synchronously tuned, and two different bias voltage V_1 and V_2 are used to tune the passband.

The fabricated four-order BPF with source-load is illustrated in Fig. 5. The core area is 80mm×82mm. The fabricated six-order BPF with source-load is illustrated in Fig. 7. The core area is 72mm×107mm. The S-parameters are measured by Agilent E5071C vector network analyzer. Figure 6 and Fig. 8 show the measured S-parameters, which is in good agreement with the simulation. The resonant frequency of four-order BPF can be continuously tuned from 1.31 GHz to 1.98 GHz, and four-TZs are generated beside the passband, leading to a sharp selectivity. The -3dB ABW is in the range of 119.5±2.5MHz. The insertion loss of the passband is 2.7 dB ~ 4.4 dB. The resonant frequency of six-order can be continuously tuned from 1.39 GHz to 2.07 GHz, and TZs are generated beside the passband, leading to a sharp selectivity. The -3 dB ABW is in the range of 102±6MHz. The insertion loss of the passband is 5.2 dB~6.8 dB. The return loss of two filters is better than 10 dB over the entire tuning range.

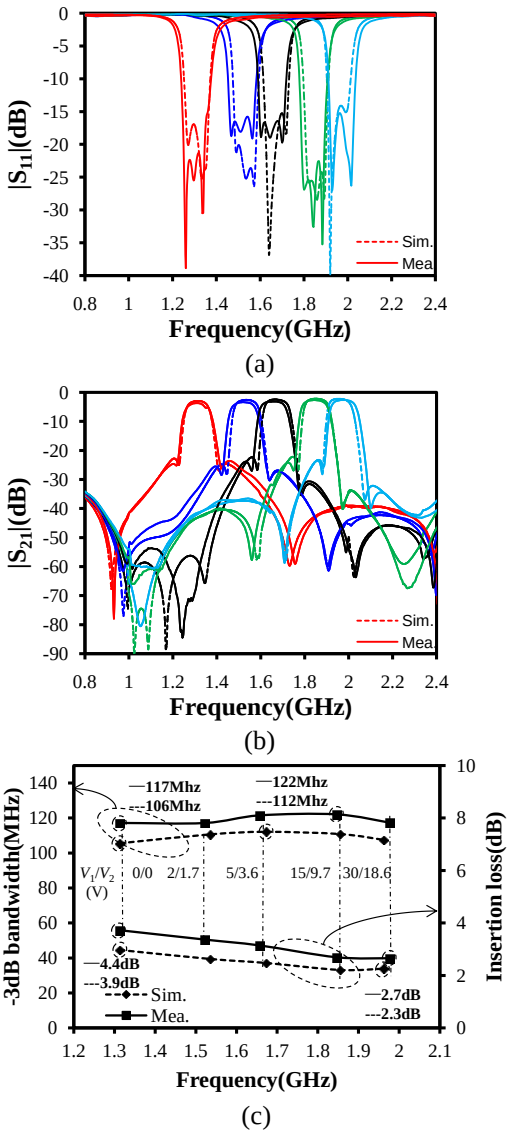

Fig. 6. Comparison between simulated and measured results of proposed four-order source-load BPF: (a) S_{11}, (b) S_{21}, and (c) -3dB bandwidth and insertion loss.

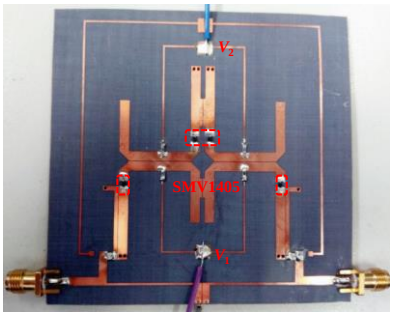

Fig. 5. Photograph of fabricated filter.

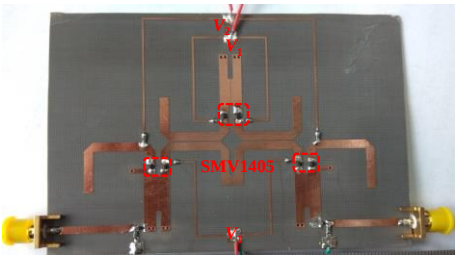

Fig. 7. Photograph of fabricated filter.

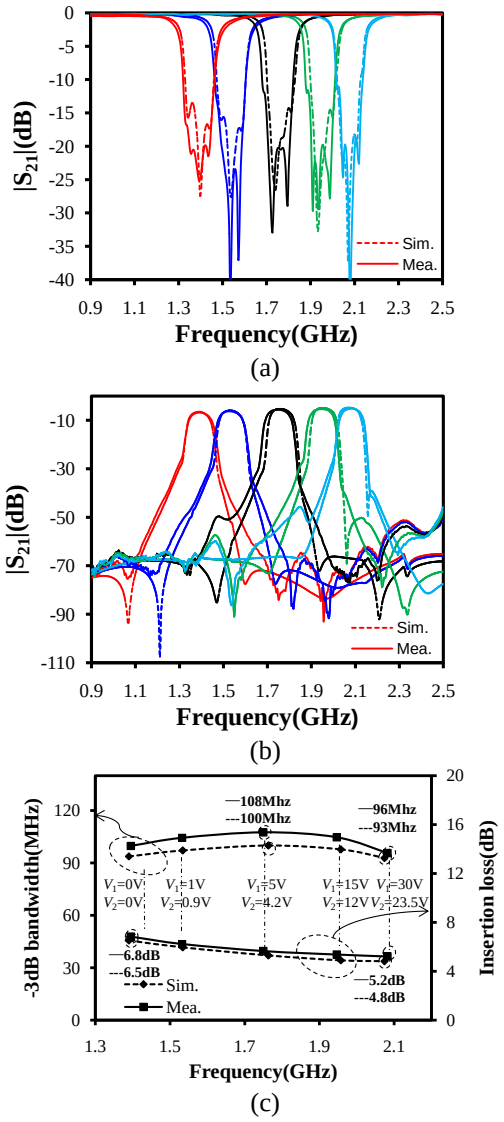

Fig. 8. Comparison between simulated and measured results of proposed six-order BPF: (a) S_{11}, (b) S_{21}, and (c) -3dB bandwidth and insertion loss.

It can be seen from the above measurements that the out-of-band suppression of the six-order filter is better than that of the four-order filter, but the insertion loss of the six-order filter is larger than that of the four-order filter, which also leads to the decrease of the overall bandwidth. How to reduce the insertion loss of high order tunable filters is also an important consideration. The two filters in this paper meet the design requirements.

V. CONCLUSION

The electric-dominated coupling structure and magnetic-dominated coupling structure is proposed, and two novel high order cross-coupled tunable BPF with constant ABW and four-TZs has been designed. The proposed coupling tuning method makes it easier to design high order BPF. Good agreement between simulated and measured responses of the filter is demonstrated. The proposed BPF with high selectivity will find its applications in RF front-end systems.

ACKNOWLEDGMENT

This work is supported by the National Natural Science Foundation of China under Grant 61771408, 61401375, 61531016, 61831017, and the Sichuan Provincial Science and Technology Important Projects under Grant 2018GZ0139, 2018GZDZX0001.

REFERENCES

[1] Q. Y. Xiang, Q. Y. Feng, and X. G. Huang, "Tunable bandstop filter based on split ring resonators loaded coplanar waveguide," *Applied Computational Electromagnetics Society Journal*, vol. 28, pp. 591-596, 2013.

[2] Q. Xiang, Q. Feng, X. Huang, and D. Jia, "Tunable bandstop filter with bandwidth compensation," *Applied Computational Electromagnetics Society Journal*, vol. 30, pp. 903-908, 2015.

[3] C. Zhao, W. Feng, Y. Li, and W. Che, "Ultra-wideband balanced bandpass filters based on transversal signal-interference concepts," *Applied Computational Electromagnetics Society Journal*, vol. 31, pp. 1232-1237, 2016.

[4] W. Yang, W. Feng, and W. Che, "Wideband filtering crossover based on ring resonator with sharp rejection," *Applied Computational Electromagnetics Society Journal*, vol. 32, pp. 924-928, 2017.

[5] S. Park and G. M. Rebeiz, "Low-loss two-pole tunable filters with three different predefined bandwidth characteristics," *IEEE Trans. Microw. Theory Techn.*, vol. 56, pp. 1137-1148, May 2008.

[6] D. Tian, Q. Feng, and Q. Xiang, "A constant absolute bandwidth tunable band-pass filter based on magnetic dominated mixed coupling and source-load electric coupling," *Journal of Electromagnetic Waves and Applications*, vol. 30, pp. 1953-1963, 2016.

[7] M. A. El-Tanani and G. M. Rebeiz, "A two-pole two-zero tunable filter with improved linearity," *IEEE Trans. Microw. Theory Techn.*, vol. 57, pp. 830-839, Apr. 2009.

[8] J. X. Chen, Y. Ma, J. Cai, L. H. Zhou, Z. H. Bao, and W. Che, "Novel frequency-agile bandpass filter with wide tuning range and spurious suppression," *IEEE Trans. Ind. Electron.*, vol. 62, no. 10, pp. 6428-6435, Oct. 2015.

[9] Q. Xiang, Q. Feng, X. Huang, and D. Jia, "Electrical tunable microstrip LC bandpass filters with constant bandwidth," *IEEE Trans. Microw. Theory Techn.*, vol. 61, pp. 1124-1130, Mar. 2013.

[10] B.-W. Kim and S.-W. Yun, "Varactor-tuned combline bandpass filter using step-impedance microstrip lines," *IEEE Trans. Microw. Theory Techn.*, vol. 52, no. 4, pp. 1279-1283, 2004.

[11] Z. Zhao, J. Chen, L. Yang, and K. Chen, "Three-pole tunable filters with constant bandwidth using mixed combline and split-ring resonators," *IEEE Microw. Wirel. Compon. Lett.*, vol. 24, no. 10, pp. 671-673, Oct. 2014.

[12] G. Suo, et al., "Four-pole narrowband superconducting tunable filter at VHF-band," *IEEE Trans. Appl. Supercond.*, vol. 24, no. 6, pp. 1-5, Dec. 2014.

[13] K. T. Park, Y. H. Cho, and S. W. Yun, "Low voltage tunable narrow bandpass filter using cross-coupled stepped-impedance resonator with active capacitance circuit," in *IEEE MTT-S International Microwave Symposium*, New York, pp. 1049-1052, 2009.

[14] H. M. Lee and G. M. Rebeiz, "A 640-1030 MHz four-pole tunable filter with improved stopband rejection and controllable bandwidth and transmission zeros," in *2013 IEEE MTT-S International Microwave Symposium Digest (MTT)*, pp. 1-3, 2013.

[15] S. Courreges, Y. Li, Z. Zhao, K. Choi, A. Hunt, and J. Papapolymerou,"A low loss X-band quasi-elliptic ferroelectric tunable filter," *IEEE Microw. Wirel. Compon. Lett.*, vol. 19, no. 4, pp. 203-205, Apr. 2009.

[16] S. Fouladi, F. Huang, W. D. Yan, and R. R. Mansour, "High-Q narrowband tunable combline bandpass filters using MEMS capacitor banks and piezomotors," *IEEE Trans. Microw. Theory Techn.*, vol. 61, no. 1, pp. 393-402, Jan. 2013.

[17] A. Anand and X. Liu, "Reconfigurable planar capacitive coupling in substrate-integrated coaxial-cavity filters," *IEEE Trans. Microw. Theory Techn.*, vol. 64, no. 8, pp. 2548-2560, Aug. 2016.

[18] B. Lee, S. Nam, T.-H. Lee, and J. Lee, "Third-order frequency-agile substrate-integrated waveguide filter with a pair of transmission zeros," *IEEE Microw. Wirel. Compon. Lett.*, 2017.

[19] R. J. Cameron, "Advanced coupling matrix synthesis techniques for microwave filters," *IEEE Trans. Microw. Theory Techn.*, vol. 51, pp. 1-10, 2003.

[20] J. S. Hong and M. J. Lancaster, *Microstrip Filter for RF/Microwave Applications*. New York: Wiley, 2001.

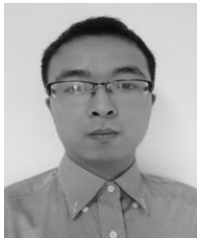

Dengyao Tian received the B.Eng. degree in Microelectronics from Southwest Jiaotong University, Chengdu, China, and is currently working toward the Ph.D. degree in Computer Science and Technology at the Institute of Microelectronics, Southwest Jiaotong University, Chengdu, China.

His research interests include circuit design, tunable filters, and antennas.

Quanyuan Feng received the M.S. degree in Microelectronics and Solid Electronics from the University of Electronic Science and Technology of China, Chengdu, China, in 1991, and the Ph.D. degree in EM Field and Microwave Technology from Southwest Jiaotong University, Chengdu, China, in 2000.

He is the Head of Institute of Microelectronics, Southwest Jiaotong University, Chengdu, China. He has been honored as the "Excellent Expert" and the "Leader of Science and Technology" of Sichuan Province because of his outstanding contribution. His research interests include RF and microwave circuits, antennas, EM compatibility, and environmental electromagnetic.

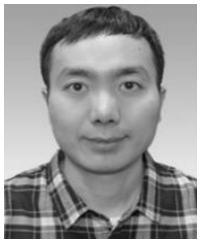

Qianyin Xiang received the Ph.D. degree in the Communication and Information Systems from Southwest Jiaotong University, Chengdu, China, in 2013.

He is currently with the Institute of Microelectronics, Southwest Jiaotong University. He has been the leader and researcher in many national research projects supported by the National Natural Science Foundation of China, and Chinese national 863 plan. In recent 5 years, he has published more than 30 research Journal papers on microwave circuits. He is also an active peer reviewer for IEEE Transactions on Microwave Theory and Techniques, IEEE Microwave and Wireless Components Letters, and so on. In 2015, he was awarded as the Young Scientist "Sishi Star" of SWJTU. His current research focuses on reconfigurable/tunable RF circuits, and MMIC design for broadband/high speed communications.

Miniaturized High Split Ratio Bailey Power Divider Based on Multi-Ring Split Ring Resonators

Omar J. Jibreel [1], Nihad I. Dib [1], and Khair A. Shamaileh [2]

[1] Department of Electrical Engineering
Jordan University of Science and Technology, Irbid, 22110, Jordan
omar.j.jibreel@hotmail.com, nihad@just.edu.jo

[2] Department of Electrical and Computer Engineering
Purdue University Northwest Hammond Campus, IN 46323, USA
kalshama@pnw.edu

Abstract ─ In this paper, a miniaturized microstrip-based Bailey power divider is proposed by incorporating split ring resonators. New analytical design equations are derived for predefined power split ratios. To validate the proposed design methodology, two miniaturized dividers with 5:1 and 20:1 split ratios at 600 MHz are simulated, fabricated and measured. Simulated and measured results agree very well and show input port matching better than -15 dB and -20 dB at the design frequency, for the 5:1 and 20:1 dividers, respectively. The desired high split ratios are achieved with transmission parameters, S_{21} and S_{31}, of -1.9 ± 0.1 dB and -8.9 ± 0.5 dB for the 5:1 divider, and -0.9 ± 0.1 dB and -13.9 ± 1.5 dB for the 20:1 divider, respectively. Furthermore, a size reduction better than 65% is achieved as compared to conventional footprints.

Index Terms ─ Bailey power divider, high split ratio power dividers, miniaturization, split ring resonators, slow wave effect.

I. INTRODUCTION

Power dividers find many applications in modern wireless communications systems, such as antenna feeders, radars, and amplifiers. Consequently, power dividers with enhanced electrical properties (e.g., high power-split ratio, multi-band operation) and physical characteristics (e.g., compact circuitry, ease of fabrication complexity/cost) are of utmost importance. To split power unequally at the output ports of a divider built with microstrip technology, a combination of printed circuit board (PCB) lines of high and low impedances are used. However, the design of high-split ratio dividers usually imposes microstrip lines with impractical widths. T-junctions, Wilkinson power dividers (WPDs), and Bagley power dividers (BPDs) are commonly utilized dividers for power division. A less known one, yet an attractive substitute, is the Bailey power divider [1].

The WPD uses lumped elements (i.e., resistors) to improve output ports isolation. Nevertheless, high-split ratio WPDs require narrow lines. In [2], a new design method of an unequal WPD using arbitrary resistor value was presented, where line impedances were evaluated after the resistor value was arbitrarily chosen. In [3], a dual-band 1:10 WPD was designed by replacing the impractical high impedance line in the conventional design with cascaded dual band T-section structures based on derived analytical equations.

The BPD, which is usually used for equal splitting, suffers from several drawbacks, such as its large size, inconvenient ports arrangement, and unmatched output ports. In [4], T- and π-shaped networks were utilized to design compact dual-band unequal-split BPDs.

Unlike other dividers, when high ratios of splitting are of interest, the Bailey power divider does not require lines with impractical high characteristic impedances. Unequal splitting with different ratios using this divider can be easily obtained by only varying the input port position according to an analytical design equation. The main drawback of this divider, however, is its large physical area. Recently, many miniaturization techniques have been introduced to overcome the large area occupied by transmission lines [5-9]. In [10], stepped impedance sections were used to minimize the length of the quarter-wave arms of a coupler, which is an integral part in the Bailey power divider. In [11], the low impedance line, with high width, was substituted by equivalent parallel high impedance lines, while avoiding the impractical thin lines. In [12], the reduction was achieved by using T- and π-sections.

Split ring resonators (SRRs) are widely used to reduce the size of microwave components. In [13], two rose-shaped resonators were etched under every line in a hybrid quadrature coupler, and an algorithm to modify the width of the lines to compensate the effect of these resonators was presented. In [14], a hybrid branch line coupler was miniaturized by loading its lines with

Submitted On: November 4, 2018
Accepted On: March 24, 2019

square-split ring resonators. In this work, the effect of etching multi-ring SRRs is studied, and applied to the transmission lines (TLs) forming the Bailey power divider to achieve miniaturization.

The rest of this paper is organized as follows: In Section 2, the Bailey power divider is presented. In Section 3, the effect of etching SRRs with different number of rings is studied and applied to a hybrid quadrature coupler. Measurements and simulation results of a Bailey power divider loaded with SRRs are introduced in Section 4. Finally, conclusions are given in Section 5.

II. BAILEY POWER DIVIDER

The unequal-split Bailey power divider is mainly a hybrid quadrature line coupler excited at its two input ports with equal amplitudes but different phases. At the output ports, the output signals are the superposition of two input signals fed to a hybrid coupler. The signals combine at the output ports such that the output amplitude ratio can be any desired value, while maintaining an in-phase relationship at the output [1]. To excite the two input ports of the hybrid coupler, a simple T-junction with unequal line lengths is connected to the inputs to produce the required phase difference, as illustrated in Fig. 1.

At the design frequency, $b = \lambda/4$, where λ is the wavelength. The power ratio at the output ports of the splitter is given as:

$$P_3 / P_2 = \tan^2(\pi a / 2b). \quad (1)$$

Therefore, the power split-ratio (at the design frequency) is simply determined by the position of the input port (i.e. the ratio a/b).

Figure 2 shows the layout of 600 MHz equal-split Bailey power divider (a/b = ½) using a 1.5 mm-thick FR-4 substrate with a dielectric constant of 4.4. As can be noticed, the divider occupies a very large area. A miniaturization technique, using SRRs will be discussed in the following section, and applied to reduce the Bailey power divider area.

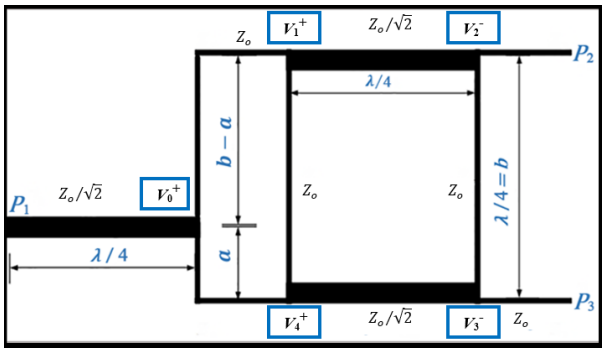

Fig. 1. Layout of the conventional Bailey power divider.

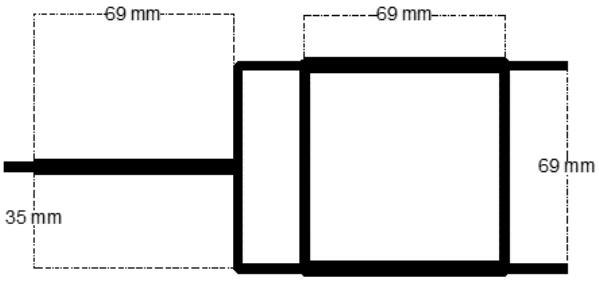

Fig. 2. Layout of 600 MHz equal-split Bailey power divider.

III. SPLIT RING RESONATORS

Meta-materials are synthesized materials, in which, electron oscillations over electrically small inclusions can result in new electromagnetic properties. SRRs are artificial magnetic metamaterials (AMMs). A conventional single split ring resonator cell has a pair of enclosed loops with splits at opposite ends. Etching an AMM in the ground plane under a microstrip TL generates a high magnetic coupling between the line and the rings. The SRR cell has a resonance (i.e., stopband) frequency that depends on its dimensions [15]. Loading a TL with an SRR causes a Slow Wave Effect, where the loaded TL has the properties of a longer one, which can be exploited to reduce the size of microwave components formed by these TLs.

A. Slow-wave effect

A schematic diagram of a microstrip TL loaded with an electrically small 2-ring resonator etched in the ground plane is presented in Fig. 3. The resonance frequency and the effect of this resonator on the TL depend on its dimensions and number of rings. Adding another cell with the same resonance frequency will increase the effect on the TL. As the radius of the etched resonator increases, its stopband frequency decreases. A fine tuning can be also obtained by changing the width of the rings and the gaps between them.

Fig. 3. Microstrip TL loaded with a two-ring SRR.

A 50 Ω microstrip TL is designed to exhibit a 90° phase shift at 600 MHz in the absence of the resonator. Different resonators with different stopband frequencies are loaded to the TL, and more rings are added inside

these resonators to study their effect on the line. Figure 4 illustrates a 4-ring SRR. The dimensions of the used SRRs are indicated in Table 1 considering the previously mentioned FR-4 substrate.

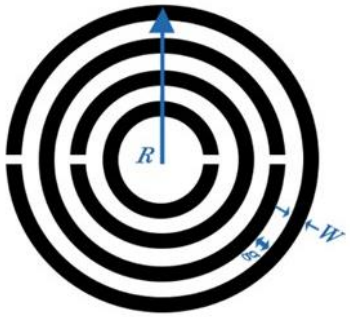

Fig. 4. 4-ring SRR.

Table 1: SRRs dimensions and their corresponding stopband frequencies

SRR	Rings	*R* (mm)	*W* (mm)	*g* (mm)	Stopband Frequency (GHz)
A	2	5.5	0.15	0.20	1.8
B	2	7.5	0.25	0.25	1.4
C	4	7.5	0.25	0.25	1.1
D	2	8.5	0.50	0.50	1.1
E	4	8.5	0.50	0.50	1.0
F	8	8.5	0.50	0.50	0.9

Table 1 shows the relation between the resonators dimensions and their stopband frequencies obtained through full-wave simulation. As the number of the rings increases, the resonance frequency decreases. SRRs *C* and *D* have the same resonance frequency, even though they have different dimensions. The extra rings and the narrow rings width in SRR *C* compensated the greater radius of SRR *D*. This fact can be taken into consideration to avoid the large area that may be occupied by the resonator when lower stopband frequencies are desired.

The slow-wave effect caused by these resonators can be determined by examining the transmission parameter phase [13]. Figure 5 (a) shows the phase of S_{21} for the microstrip lines with the resonators in Table 1 etched in the ground plane. For the unloaded TL, a 90° shift occurs at the design frequency 600 MHz. However, for the loaded lines, the 90° phase shift occurs at lower frequencies. This implies that the loaded line performs as a longer one and can be shortened. As the resonance frequency of the etched SRR decreases, the slow-wave effect on the loaded line increases, as shown in Fig. 5 (a).

For further shortening, two cells can be etched under the same line. The results of adding an extra cell are illustrated in Fig. 5 (b). The transmission parameter of the designed line has a phase of 90° at 0.46 GHz when two cells of SRR *F* are applied. In other words, the resulting line has the electrical parameters of a conventional 91 mm length line, while its actual length is 68 mm.

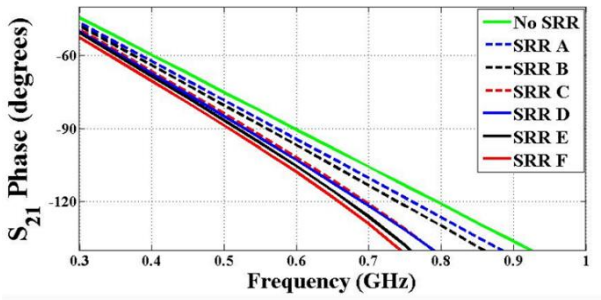

(a)

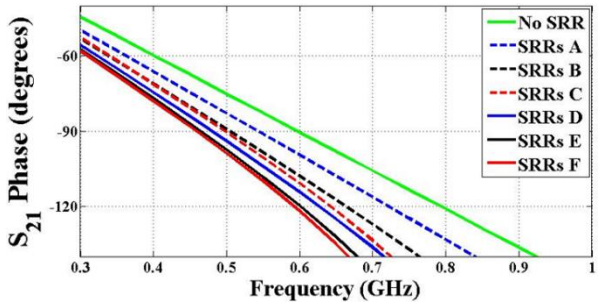

(b)

Fig. 5. The slow-wave effect using: (a) a single cell SRR, and (b) two cells SRRs.

The factor by which the line can be shortened is initially calculated by [13]:

$$F = -\phi / 90°, \tag{2}$$

where ϕ is the phase of S_{21} (in degrees) at the design frequency after loading the resonators. The length can be then tuned to achieve the desired transmission properties.

B. Hybrid coupler with SRRs

Firstly, SRRs are applied to a hybrid coupler with a design frequency of 600 MHz, as it is the main part of the Bailey power divider. Two 8-ring SRRs (with dimensions of SRR *F* in Table 1) are etched under each TL in the coupler, then, the line is shortened to obtain the same transmission properties of the original one. The layout of the loaded coupler is shown in Fig. 6.

The coupler in Figure 6 has an area of 17.5 cm^2 as compared to 47.6 cm^2 occupied by the conventional design. In Fig. 7, the simulated scattering parameters of the reduced size coupler show that it operates properly at the design frequency, with input port matching better than -35 dB and isolation parameters better than -20 dB. The transmission parameters, S_{21} and S_{31}, are in close proximity to -3 dB.

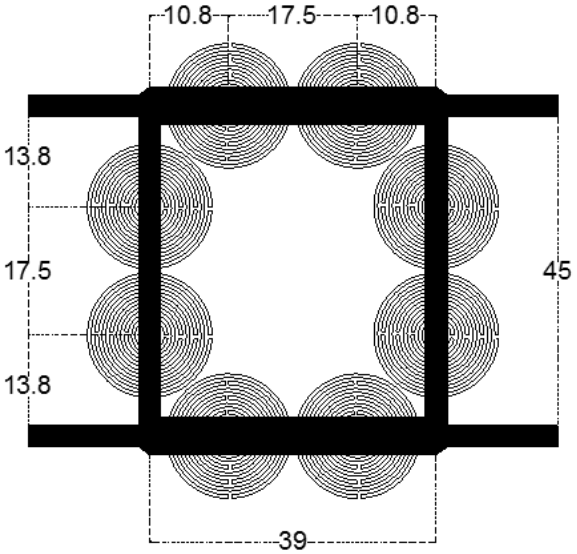

Fig. 6. Hybrid coupler loaded with 8-ring SRRs (dimensions in *mm*).

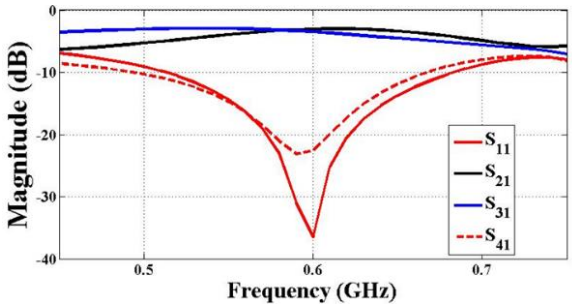

Fig. 7. Simulated *S*-parameters of the miniaturized coupler using SRRs.

IV. MINIATURIZED BAILEY POWER DIVIDER

A. New formulation

As the arms of the SRR-loaded coupler in the Bailey power divider are shortened, the expression in (1) cannot be used. In this subsection, a new formulation based on the miniaturized coupler is derived. Figure 8 represents the layout of a reduced size Bailey power divider.

The lengths x and y need to be calculated to achieve a specific splitting ratio. The design equation is derived based on transmission line theory. Referring to Fig. 8, at the design frequency, the incident voltage waves at the input ports of the coupler are given as follows:

$$V_1^+ = V_o^+ e^{-j\beta x}, \tag{3a}$$

$$V_4^+ = V_o^+ e^{-j\beta y}, \tag{3b}$$

where $\beta = 2\pi/\lambda$ at the design frequency. The scattered voltages at the output ports of the coupler can be calculated as the superposition of the response of a hybrid coupler to two input signals, as follows:

$$V_2^- = j\frac{V_1^+}{\sqrt{2}} + \frac{V_4^+}{\sqrt{2}}, \tag{4a}$$

$$V_3^- = j\frac{V_4^+}{\sqrt{2}} + \frac{V_1^+}{\sqrt{2}}. \tag{4b}$$

After some mathematical manipulations, one can derive the following expressions for the magnitudes of the output voltages:

$$\left|V_2^-\right| = \left|V_o^+\right|\left[1+\sin\beta(x-y)\right]^{1/2}, \tag{5a}$$

$$\left|V_3^-\right| = \left|V_o^+\right|\left[1-\sin\beta(x-y)\right]^{1/2}. \tag{5b}$$

The power at the output ports can be written as follows:

$$P_2^- = \frac{\left|V_2^-\right|^2}{2Z_o} = \frac{\left|V_o^+\right|^2}{2Z_o}\left[1+\sin\beta(x-y)\right], \tag{6a}$$

$$P_3^- = \frac{\left|V_3^-\right|^2}{2Z_o} = \frac{\left|V_o^+\right|^2}{2Z_o}\left[1-\sin\beta(x-y)\right]. \tag{6b}$$

Thus, the design equation of the miniaturized Bailey power divider, with a split ratio of $R = P_3^-/P_2^-$ is:

$$R = \frac{\left[1+\sin\beta(x-y)\right]}{\left[1-\sin\beta(x-y)\right]}. \tag{7}$$

Equation (7) shows that the split ratio depends on the difference between the lengths of the two arms feeding the coupler input ports. It also applies to the conventional design where (1) is a special case when $x + y = \lambda/4$.

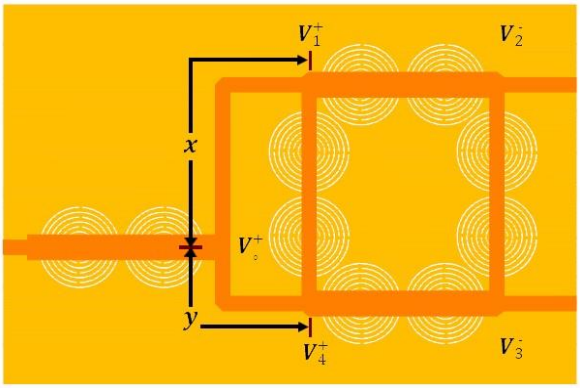

Fig. 8. Layout of the reduced size Bailey power divider.

B. Experimental results

Figure 9 shows the layout of a 5:1 ($P_2 : P_3 = 5 : 1$) SRR-loaded 600 MHz Bailey divider. Using equation (7), the difference between the two arms should be 0.116 λ at 600 MHz (33 mm), and tuned to be 34 mm. The input arm of the divider is also shortened by etching two 8-ring SRRs. The designed divider is fabricated on the previously mentioned FR-4 substrate. The *S*-parameters are measured using an E5071C ENA Keysight vector network analyzer and compared with the

simulated ones in Fig. 10, which shows measured input port matching better than -15 dB. The transmission parameters, S_{21} and S_{31}, are measured to be -1.9 dB and -8.3 dB, at the design frequency, respectively. Such values are close to the theoretical calculations, -0.8 dB and -7.8 dB, respectively.

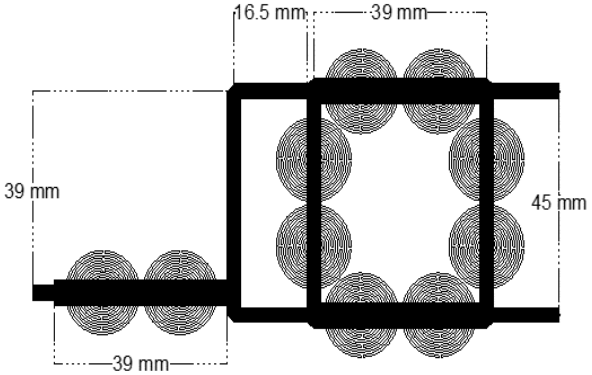

Fig. 9. Layout of the 5:1 miniaturized Bailey power divider.

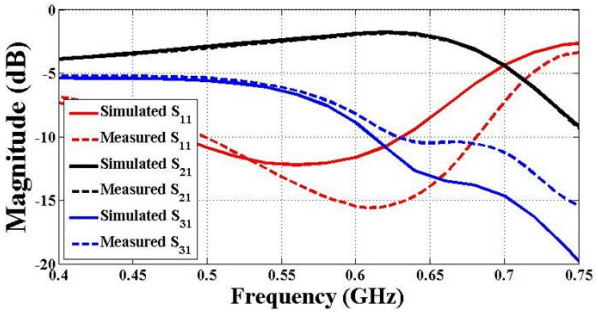

Fig. 10. Simulated and measured results of the miniaturized 5:1 Bailey power divider.

Instead of using SRRs at the input arm, it can be meandered as shown in Fig. 11. The input arm is positioned to obtain a 20:1 split ratio. The difference between the coupler feeders is 0.18 λ at 600 MHz (49.3 mm). Measured and simulated results are shown in Fig. 12. The measured input port matching is better than -20 dB at the design frequency. Simulated transmission parameters, S_{21} and S_{31}, are -0.9 dB and -13.9 dB, respectively, which are in a good agreement with the theoretical values, -0.2 dB and -13.2 dB, respectively. The small discrepancies between the simulated and measured results are thought to be due to conductor losses, and the soldering of the connectors to the lines.

A photograph of one of the fabricated dividers is illustrated in Fig. 13. The SRRs are etched in the ground plane exactly under the coupler TLs. The fabricated divider has an area of around 35% of the one occupied by the conventional divider.

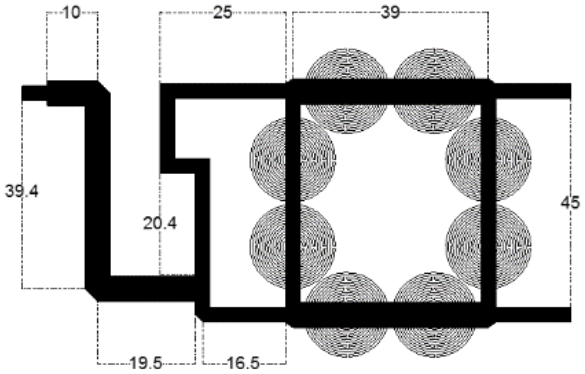

Fig. 11. The fabricated 20:1 miniaturized Bailey power divider (dimensions in *mm*).

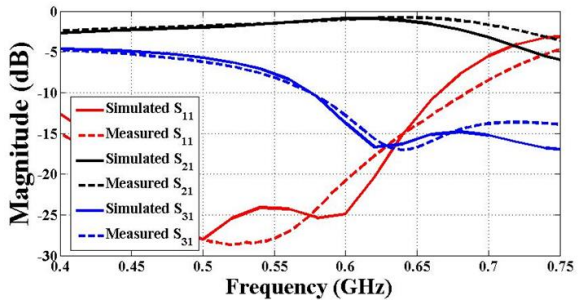

Fig. 12. Simulated and measured results of the miniaturized 20:1 Bailey power divider.

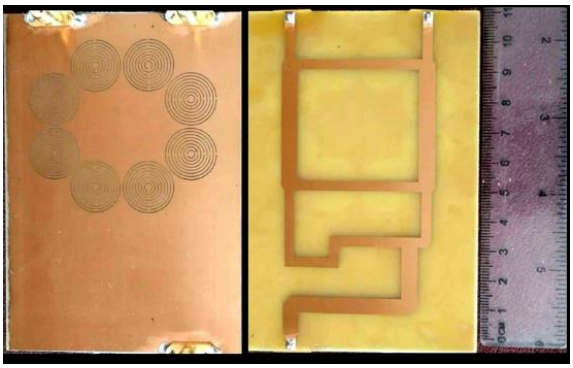

Fig. 13. Photograph of the fabricated 20:1 Bailey power divider with SRRs.

V. CONCLUSION

In this paper, the Bailey power divider was presented as a high split ratio divider which tackles the problem of the high impedance thin lines problem. A size reduction technique based on SRRs was studied, where the slow-wave effect resulting by these resonators was utilized to shorten the microstrip transmission lines. Adding more rings inside the resonators increased the slow-wave effect allowing for further size reduction. The

miniaturization technique was applied to reduce the large size of the Bailey power divider. Two prototypes of the miniaturized divider were fabricated and tested. High splitting ratios of 5:1 and 20:1 were achieved. The fabricated dividers have an area of less than 35% of the one occupied by the conventional 600 MHz Bailey power divider.

ACKNOWLEDGMENT

The authors acknowledge the financial support of the Deanship of Scientific Research at the Jordan University of Science and Technology under research grant number 2017/331.

REFERENCES

[1] M. C. Bailey, "A simple stripline design for uneven power split," *NASA Technical Memorandum* (81870), 1980.

[2] D. Lee, H. Doo, Y. Jang, H. Kim, S. Han, J. Lim, K. Choi, and D. Ahn, "A new design method of the unequal Wilkinson power divider using an arbitrary resistor value," *Microwave and Optical Technology Letters*, vol. 58, no. 10, pp. 2450-2452, 2016.

[3] K. Al-Shamaileh, N. Dib, and S. Abushamleh, "A dual-band 1:10 Wilkinson power divider based on multi-T-section characterization of high-impedance transmission lines," *IEEE Microwave and Wireless Components Letters*, vol. 27, no. 10, pp. 897-899, 2017.

[4] O. Abu-Al-Nadi, *Analysis and design of compact multi-frequency Bagley power dividers (Master's thesis)*, Department of Electrical Engineering, Jordan University of Science and Technology, Jordan, Irbid, 2012.

[5] K. Al-Shamaileh, N. Dib, and A. Sheta, "Design of miniaturized unequal split Wilkinson power divider with harmonics suppression using non-uniform transmission lines," *Applied Computational Electromagnetics Society (ACES) Journal*, vol. 26, no. 6, pp. 530-538, June 2011.

[6] M. Hayati, S. Roshani, and S. Roshani, "Miniaturized Wilkinson power divider with nth harmonic suppression using front coupled tapered CMRC," *Applied Computational Electromagnetics Society (ACES) Journal*, vol. 28, no. 3, pp. 221-227, Mar. 2013.

[7] D. Hawatmeh, K. Al-Shamaileh, and N. Dib, "Design and analysis of multi-frequency unequal-split Wilkinson power divider using non-uniform transmission lines," *Applied Computational Electromagnetics Society (ACES) Journal*, vol. 27, no. 3, pp. 248-255, Mar. 2012.

[8] G. Wu, G. Wang, L. Hu, Y. Wang, and C. Liu, "A miniaturized triple-band branch line coupler based on simplified dual-composite right/left-handed transmission line," *Progress in Electromagnetics Research C*, vol. 39, pp. 1-10, 2013.

[9] D. Ji, B. Wu, X. Ma, and J. Chen, "A compact dual-band planar branch-line coupler," *Progress in Electromagnetics Research C*, vol. 32, pp. 43-52, 2012.

[10] C. Hsu, C. Chang, and J. Kuo, "Design of dual-band microstrip rat race coupler with circuit miniaturization," *IEEE/MTT-S International Microwave Symposium*, Honolulu, HI, pp. 177-180, July 2007.

[11] S. Karthikeyan and R. Kshetrimayum, "Extremely unequal Wilkinson power divider with dual transmission lines," *Electronic Letters*, vol. 46, no. 1, pp. 90-91, 2010.

[12] M. Alkanhal and A. Mohra, "Dual-band ring couplers using T and Pi sections," *International Journal of Microwave and Optical Technology*, vol. 3, no. 4, pp. 460-466, 2008.

[13] B. Savitri, V. Fono, B. Alavikia, L. Talbi, and K. Hettak, "Novel approach in design of miniaturized passive microwave circuit components using metamaterials," *Microwave and Optical Technology Letters*, vol. 59, no. 6, pp. 1341-1347, 2017.

[14] L. Al-Khateeb, "Miniaturized hybrid branch line couplers based on square-split resonator loading technique," *Progress in Electromagnetics Research Letters*, vol. 40, pp. 153-162, 2013.

[15] J. Pendry, A. Holden, D. Ribbins, and W. Stewart, "Magnetism from conductors and enhanced non-linear phenomena," *IEEE Trans. Microwave Theory Tech.*, vol. 47, no. 11, pp. 2075-2084, 1999.

A General Mutual Inductance Formula for Parallel Non-coaxial Circular Coils

Kai-Hong Song*, Jian Feng, Ran Zhao, and Xian-Liang Wu

Key Laboratory of Intelligent Computing and Signal Processing, Ministry of Education
Anhui University, Hefei Anhui 230039, China
khsong@ahu.edu.cn

Abstract ─ In this paper, we present a complete derivation of a new formula for calculating the mutual inductance between two parallel non-coaxial circular coils by using the magnetic vector potential. Although this problem has been studied by Kim et al, their formula is wrong when the two parallel circulars are non-coaxial. The newly derived formula can not only clarifies the origin of the error introduced in Kim's work, but also can be reduced to the well-known F. W. Grover formula. Different from the Grove's formula that has various cases of the singularities, the new formula enables to simplify all the singular cases into single situation. The singularity in our formula has the clearly geometrical significance, i.e., the point located in one projected circular coil overlapped with the center of another one, which can be easily tackled by the principal value integrals. In order to check the validity of our formula, we have investigated the mutual inductance of the circular coil of the rectangular cross section, and the results demonstrate the correctness of our formula as compared with the other approaches, such as the Neumann's formula, Grover's formula and other published data. In addition, our formula is capable of handling the topics involving the circular coils such as the coils of the rectangular cross section, wall solenoids, disk coils and circular filamentary coils etc. In conclusion, our newly derived formula is of great importance for the electromagnetic applications concerning the calculation of the mutual inductance of the two parallel non-coaxial circular coils.

Index Terms ─ Filament method, Grover's formula, Kim's formula, magnetic vector potential, mutual inductance, Neumann's formula, non-coaxial coils.

I. INTRODUCTION

Circular coils are widely used in various electromagnetic applications such as metal detector [1], inductive coupled contactless energy transfer (CET) system [2], radio frequency identification (RFID) [3], biomedical engineering [4] and the magnetic force etc. [5-7]. The mutual inductance between the primary and secondary coils is an important parameter which determinates the current and electromotive force induced in the secondary windings [8], when the machines are of the induction type. If the machine is such that its secondary is not supported by any means, the axis of the secondary windings may not be the same as that of the primary coils. The mutual inductance between the coaxial circular filaments has been quite thoroughly calculated by a number of authors since the time of Maxwell, and the accuracy of these calculations meets the requirements in practice [9-11]. Many works were based on the Neumann's formula and Biot-Savart law [12-14]. Formula for circular loops with parallel axes has been derived by Butterworth [15] and Snow [16]. Unfortunately, these formulae were slowly convergent and not usable with a wide range of parameters. Using Butterworth's formula, Grover developed a general method to calculate the mutual inductance between circular coils located at any position with respect to each other [10, 11].

Nowadays, with the availability of the powerful numerical methods, such as the boundary element method (BEM) and the finite element method (FEM), it is convenient to obtain the mutual inductance for almost practical electromagnetic applications. However, it is still an interesting topic to discuss this problem by using analytical and semi-analytical methods in many circumstances, as it considerably simplifies the mathematical procedures, and often leads to a significant reduction of the simulation effort.

In this paper, we derived a new formula to calculate the mutual inductance between two non-coaxial circular coils with parallel axes by using the magnetic vector potential, which has been studied for the first time in [17]. First, our formula is not the same as those obtained by Kim et al. Second, the equation (12) in Kim's work is not correct, as pointed out in reference [18], but the reason for that mistake has never been discussed. Third, our formula reduces to the well-known F. W. Grover formula which is expressed in terms of the general Neumann integral, instead of the magnetic vector potential approach. Two numerical experiments are provided in Section 5 to show the validity of our derivations and arguments.

Submitted On: October 10, 2018
Accepted On: April 6, 2019

II. REVIEW OF BASIC EXPRESSION

Let's consider two circular coils as shown in Fig. 1. The center of the primary coil with radius R_p corresponds to the origin O(0,0,0) of plane *XOY* , and the circle's axis corresponds to the *Z* axis. The secondary coil with radius R_S is located in $X'O'Y'$ plane, and the *Z* and Z' axes are parallel with each other. The distance between the planes of the both coils is *c*, and the distance between the two corresponding axes is *d*. The mutual inductance between two closed circular loop l_1 and l_2 is given by the double integral Neumann formula:

$$M_{21}=\frac{\mu_0}{4\pi}\int_0^{2\pi}\int_0^{2\pi}\frac{R_pR_s\cos(\varphi_1-\varphi_2)d\varphi_1d\varphi_2}{R}, \qquad (1)$$

here *R* is the distance between point *P* and *Q*, which is given by:

$$R=[R_p^2+R_s^2+c^2+d^2-2R_pR_s\cos(\varphi_1-\varphi_2)$$
$$-2R_pd\cos\varphi_1+2R_sd\cos\varphi_2]^{\frac{1}{2}},$$

and $\mu_0=4\pi\times10^{-7}H/m$ is the magnetic permeability of free space.

In Ref. [11], Grover presented the formula for the mutual inductance between the two coils with parallel axes in terms of the Neumann integral, and in Ref. [18], Babic derived the Grover's formula by using the approach of the magnetic vector potential. The Grover's formula for the mutual inductance is given as follows:

$$M_{21}=\frac{2\mu_0\sqrt{R_sR_p}}{\pi}\int_0^{\pi}\frac{1-\frac{d}{R_s}\cos\varphi}{k\sqrt{V^3}}\Psi(k)d\varphi, \qquad (2)$$

where

$$a=\frac{R_s}{R_p},\quad b=\frac{c}{R_p},\quad V=\sqrt{1+\frac{d^2}{R_s^2}-2\frac{d}{R_s}\cos\varphi},$$

$$k^2=\frac{4aV}{(1+aV)^2+b^2},\ \Psi(k)=(1-\frac{k^2}{2})F(k)-E(k).$$

In the above equations, $F(k)$ and $E(k)$ are the complete elliptic integrals of the first and second kinds, respectively [19]:

$$F(k)=\int_0^{\frac{\pi}{2}}\frac{d\theta}{(1-k^2\sin^2\theta)^{1/2}},$$

$$E(k)=\int_0^{\frac{\pi}{2}}(1-k^2\sin^2\theta)^{1/2}d\theta.$$

Based on the approach of the magnetic vector potential, another solution to this problem has been proposed by Kim et al. [17], their expression for the mutual inductance can be expressed as:

$$M_{21}=\frac{\mu_0R_s}{2\pi}\int_0^{2\pi}\frac{[(R_p+r)^2+c^2)^{1/2}}{r}\Psi(k)d\varphi_2,$$

$$=\frac{2\mu_0R_s}{\pi}\int_0^{\pi}\frac{1}{k}(\frac{R_p}{r})^{1/2}\Psi(k)d\varphi_2, \qquad (3)$$

here *r* is the distance between the point *P* and *Z* axes, which is given by:

$$r=[(d+R_s\cos\varphi_2)^2+(R_s\sin\varphi_2)^2]^{\frac{1}{2}},$$

and

$$k^2=\frac{4R_pr}{(R_p+r)^2+c^2},\ \Psi(k)=(1-\frac{k^2}{2})F(k)-E(k).$$

As expected, the formula obtained by Kim et al. [17] should be equivalent to Grover's formula because both formulae are derived from the magnetic vector potential. However, in many examples, the numerical results based on equation (2) and (3) are not consistent with each other, which evidently indicate that at least one of them must be incorrect. In order to clarify this, we re-calculate the mutual inductance between two non-coaxial circular coils with parallel axes by using the approach of the magnetic vector potential, as done by Kim et al. The formula obtained in this work is not the same as Kim's work. However, our formula could reduce to the well-known F. W. Grover formula, which strongly supports that our formula is correct. All the details of our derivation and check for the validation of our formula are provided in section 3.

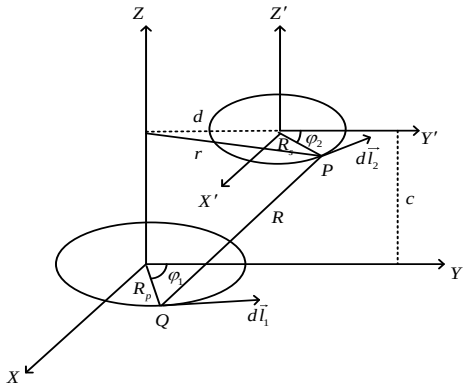

Fig. 1. Configuration of the primary coil and the secondary coil.

III. DERIVATION OF NEW FORMULA

In the following, based on the method of the magnetic vector potential, we will re-calculate the mutual inductance between the two non-coaxial circular coils with parallel axes as shown in Fig. 1. The magnetic vector potential at point *P* on the secondary coil produced by the primary coil carrying the current I_1 has a tangential component only, and it can be expressed as following:

$$A_\varphi=\frac{\mu_0I_1}{2\pi}\int_0^{\pi}\frac{R_p\cos\varphi_1}{R}d\varphi_1. \qquad (4)$$

Figures 1 and 2 show the dimensions and parameters for calculating the magnetic flux and the mutual inductance between two non-coaxial circular coils. *R* can be written as follows:

$$R = (R_p^2 + r^2 + c^2 - 2R_p r\cos\varphi_1)^{\frac{1}{2}}. \quad (5)$$

Letting $\varphi_1 = \pi + 2\theta$, so that,

$$\cos\varphi_1 = \cos(\pi + 2\theta) = -\cos 2\theta = 2\sin^2\theta - 1,$$

and $d\varphi_1 = 2d\theta$, then,

$$A_\varphi = \frac{\mu_0 I_1 R_p}{\pi}\int_0^{\frac{\pi}{2}} \frac{(2\sin^2\theta - 1)}{[(R_p + r)^2 + c^2 - 4R_p r\sin^2\theta)^{1/2}} d\theta \vec{e}_{\varphi 1}. \quad (6)$$

Substituting the modulus,

$$k^2 = \frac{4R_p r}{(R_p + r)^2 + c^2},$$

into equation (6), we can rearrange the integrand to get the following expression for the magnetic vector potential:

$$A_\varphi = \frac{\mu_0 I_1}{\pi k}\left(\frac{R_p}{r}\right)^{\frac{1}{2}}\left[\left(1 - \frac{k^2}{2}\right)\int_0^{\frac{\pi}{2}} \frac{d\theta}{(1 - k^2\sin^2\theta)^{1/2}}\right.$$

$$\left. - \int_0^{\frac{\pi}{2}} (1 - k^2\sin^2\theta)^{1/2} d\theta\right]$$

$$= \frac{\mu_0 I_1}{\pi k}\left(\frac{R_p}{r}\right)^{\frac{1}{2}}\left[\left(1 - \frac{k^2}{2}\right)F(k) - E(k)\right]. \quad (7)$$

Using Stokes' theorem, the magnetic flux through the secondary coil due to a current in the primary coil is:

$$\psi_{21} = \int_{s_2} \mathbf{B}_{21}\cdot d\mathbf{s}_2 = \int_{s_2} \nabla\times\mathbf{A}_{21}\cdot d\mathbf{s}_2$$

$$= \oint_{l_2} \mathbf{A}_{21}\cdot d\mathbf{l}_2, \quad (8)$$

where s_2 and l_2 are the cross section and the perimeter of the secondary circular coil, respectively.

By definition, the mutual inductance between the primary and secondary coils is given by:

$$M_{21} = \frac{\psi_{21}}{I_1}. \quad (9)$$

From (7) - (9), we obtain:

$$M_{21} = \frac{\int_0^{2\pi} A_\varphi \mathbf{e}_{\varphi 1}\cdot\mathbf{e}_{\varphi 2} R_s d\varphi_2}{I_1} =$$

$$\frac{\mu_0 R_s}{\pi}\int_0^{2\pi}\frac{1}{k}\left(\frac{R_p}{r}\right)^{\frac{1}{2}}\left[\left(1 - \frac{k^2}{2}\right)F(k) - E(k)\right]\mathbf{e}_{\varphi 1}\cdot\mathbf{e}_{\varphi 2} d\varphi_2$$

$$= \frac{2\mu_0 R_s}{\pi}\int_0^{\pi}\frac{1}{k}\left(\frac{R_p}{r}\right)^{\frac{1}{2}}\Psi(k)\cos\alpha d\varphi_2. \quad (10)$$

Obviously, equation (3) and equation (10) are not the same, because $\cos\alpha$ is not equal to 1 in general. Equation (3) is just coincident with equation (10) if and only if two coil axis coincide with each other.

The kernel function of equation (2) is singular in the case $V = 0$. For the case $c \neq 0$ and $d = R_s$, a modified Grover's formula can be adopted, and the Bessel function can be used to solve the singularity case for $c = 0$, $d = R_s = R_p$ and $c = 0$, $d = 2R_s = 2R_p$. However, the kernel function of equation (10) is singular in the case $r = 0$. The principle value integrals of Gaussian numerical integration are adopted for all the singularity case at $r = 0$.

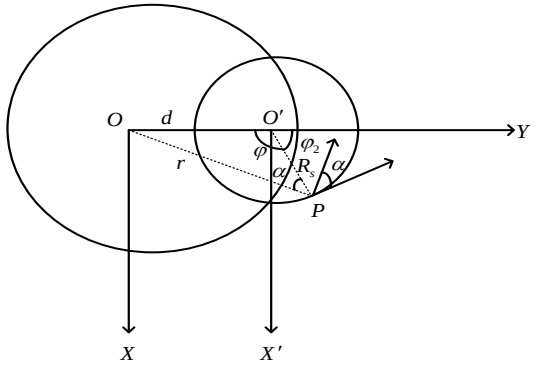

Fig. 2. Top view of the two circular coils.

Let's consider the two circular coils as shown in Fig. 1. The top view of the two circular coils is shown in Fig. 2. Using cosine theorem in triangle $\Delta OO'P$, we obtain:

$$d^2 = r^2 + R_s^2 - 2R_s r\cos\alpha, \quad (11)$$

$$r^2 = d^2 + R_s^2 - 2R_s d\cos\varphi. \quad (12)$$

Substituting equation (11) into equation (10), the mutual inductance between the primary and secondary coils is given by:

$$M_{21} = \frac{2\mu_0 R_s}{\pi}\int_0^{\pi}\frac{1}{k}\left(\frac{R_p}{r}\right)^{\frac{1}{2}}\psi(k)\frac{r^2 + R_s^2 - d^2}{2R_s r} d\varphi_2. \quad (13)$$

Substituting equation (12) into equation (13), and using $\varphi_2 = \pi - \varphi$ transforms, the mutual inductance can be re-written as:

$$M_{21} = \frac{2\mu_0 R_s}{\pi}\int_0^{\pi}\frac{1}{k}\left(\frac{R_p}{r}\right)^{\frac{1}{2}}\psi(k)\frac{r^2 + R_s^2 - d^2}{2R_s r} d\varphi_2. \quad (14)$$

Introducing additional dimensionless variable:

$$V = \sqrt{1 + \frac{d^2}{R_s^2} - 2\frac{d}{R_s}\cos\varphi} = \sqrt{\frac{R_s^2 + d^2 - 2dR_s\cos\varphi}{R_s^2}}$$

$$= \sqrt{\frac{r^2}{R_s^2}} = \frac{r}{R_s}. \quad (15)$$

Finally, equation (14) indeed reduces to well-known Grover formula (2):

$$M_{21} = \frac{2\mu_0\sqrt{R_p R_s}}{\pi}\int_0^{\pi}\frac{1 - \frac{d}{R_s}\cos\varphi}{k\sqrt{V^3}}\psi(k) d\varphi, \quad (16)$$

where

$$a=\frac{R_s}{R_p},\ \ b=\frac{c}{R_p},\ \ k^2=\frac{4aV}{(1+aV)^2+b^2},$$

$$\Psi(k)=(1-\frac{k^2}{2})F(k)-E(k),$$

which is the desired proof.

IV. FILAMENT METHOD

In order to verify the accuracy and the computational cost of the expressions for the mutual inductance obtained by using the Neumann formula of equation (1), Grover formula of equation (2), the formula in Kim et al. (also see equation (3)) and our new formula of equation (10), we will present an efficient filament method to calculate the mutual inductance of two circular coils with rectangular cross section.

In order to account for the finite dimensions of the coils, the primary and secondary coils are considered to be subdivided into meshes of filamentary cells as shown in Fig. 3. The cross sectional area of the primary coil is divided into $(2K+1)$ by $(2N+1)$ cells, and that the secondary coil into $(2m+1)$ by $(2n+1)$ cells. Each cell in each coil contains one filament, and the current density in the coil cross section is assumed to be uniform, so that the filament currents are equal. This means that it is possible to apply equations (1)-(3) and (10) to the pairs of the filament in two coils.

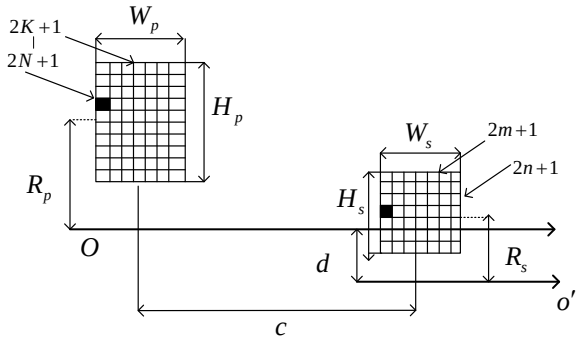

Fig. 3. Configuration of mesh coils.

Using the same procedure given in [17] the mutual inductance can be expressed in the following form:

$$M=\frac{N_pN_s}{(2K+1)(2N+1)(2m+1)(2n+1)}*$$

$$\sum_{g=-K}^{K}\sum_{h=-N}^{N}\sum_{p=-m}^{m}\sum_{l=-n}^{n}M_{ji}(g,h,p,l),\qquad(17)$$

where i and j are the corresponding thin coils of the first and second coil, respectively. M_{ji} is the mutual inductance between i and j filamentary coils. The number of turns in the primary coil is N_p, and that in the secondary coil is N_s:

$$R_p(h)=R_p+\frac{H_p}{(2N+1)}h,\qquad h=-N,\ldots,0,\ldots,N,$$

$$R_s(l)=R_s+\frac{H_s}{(2n+1)}l,\qquad l=-n,\cdots,0,\cdots n,$$

$$z(g,p)=c-\frac{W_p}{(2K+1)}g+\frac{W_s}{(2m+1)}p,$$

$$g=-K,\ldots,0,\ldots,K;\ p=-m,\ldots,0,\ldots,m,$$

$$\Psi(k)=(1-\frac{k^2}{2})F(k)-E(k).$$

V. NUMERICAL EXAMPLES

Example 1: Two circular coils of rectangular cross section with parallel axes

To validate our formula, we compare the results obtained by Neumann's formula, Grover's formula, the formula in Kim's work and our formula for a given application case. The problem consists of the two circular coils of rectangular cross section with the following dimensions:

(1) Primary coil:

$R_p=42.5mm$, $W_p=10mm$, $H_p=10mm$, $N_p=150$.

(2) Secondary coil:

$R_s=20mm$, $W_s=4mm$, $H_s=4mm$, $N_s=50$.

The number of subdivisions was $K=N=2$, $m=n=1$.

The mutual inductance between the two circular coils of rectangular cross section with lateral misalignment and parallel axes are calculated and shown in Fig. 4. The mutual inductance as a function of off-center distance d for c=0 is plotted. For the off-center distance d varied from 0.0 to 0.3 m, all the results obtained by Neumann's formula, Grover's formula and our formula are in an excellent agreement. The results by the formula in Kim's work are correct if and only if two coil axis coincidence. However, the results of Kim's formula are wrong when there is a slight misalignment of the two coil's center axes. The value of mutual inductance obtained by equations (1), (2) and (10) all presents a sign reversal (i.e., the sign of the value changes from positive to negative as shown in Fig. 4) when the secondary coil moves far away from the primary coil. There is a negative maximum at d = 0.06 m and the value of the mutual inductance approaches to zero for the large misalignment "d". The characteristics can be explained by the electromagnetic theory; the detailed reason is that the magnetic flux linked by the secondary coil change their orientation outside the primary coil. On the other hand, the mutual inductance obtained by equation (3) slowly approaches zero when the secondary coil is outside the primary coil, and never reach negative values, which is not correct according to electromagnetic theory. Thus, this proves that equation (3) is erroneous for non-coaxial circular coils. Actually, it is exact only when the coils' axes are in coaxial position. In addition, we have

compared the calculation time of these approaches, the calculation times of our formula and Grove's formula are 0.37 seconds and 0.32 seconds, respectively, which are comparable and considerably smaller than that of the Neuman's formula (70.08 seconds).

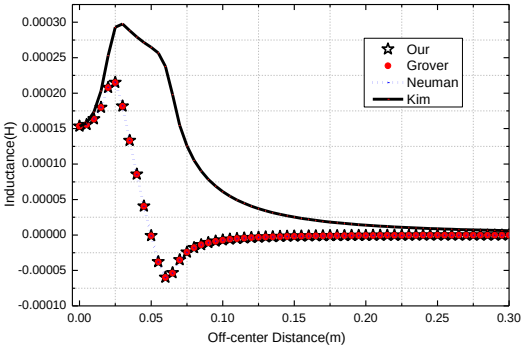

Fig. 4. Mutual inductance as a function of the off-axis displacement d, with axial distance c=0.

Example 2: Two circular coils of rectangular cross section with parallel axes

We further investigate the two reactance coils of rectangular cross section with parallel axes. The coils' dimensions and the number of turns are set as follows: R_p = 7.832*cm*, R_s = 11.7729*cm*, W_p = 14.2748*cm*, W_s = 2.413*cm*, H_p = 1.397*cm*, H_s = 4.1529*cm*, N_p = 1142, N_s = 516, d = 30.988*cm*, c = 7.366*cm*, and the number of subdivisions was $K = N = m = n = 12$. Table 1 lists the calculated results by analytical expression and Maxwell software.

From Table 1, one can see that our results agree well with the results obtained by equations (1), (2), the data from experiment and the Maxwell software, which also prove the formula of Kim's work are invalid for non-coaxial circular coils. Importantly, our formula is much easier to handle the singularity as compared to the Grove's formula. In addition, under the same accuracy, our approach only costs 4.524 seconds, which is comparable to Grove's formula (4.712 seconds) and faster than the Neumann's formula (489.047 seconds), Maxwell software (1486 seconds).

Besides, we have also investigated the other examples involving the circular coils such as the coils of rectangular cross section, wall solenoids, disk coils and circular filamentary coils etc. All the results reveal the correctness and effectiveness of our newly derived formula. The calculations of equations (1), (2), (3) and (10) were taken on a personal computer with Intel(R) core (TM) i7-4790 3.6 GHz processor with FORTRAN programming.

Table 1: Mutual inductance of two circular coils of rectangular cross section

Method	Measured [21]	Neumann's	Kim et al.	Grover's	This Work	Maxwell
M (mH)	-1.47	-1.4705	9.1398	-1.4743	-1.4625	-1.4772
Time (s)		489.047	4.377	4.712	4.524	1486

VI. CONCLUSION

In this paper, we re-derive the mutual inductance between two non-coaxial circular coils with parallel axes. The validity of our formula has been verified by comparing with the Neumann's formula, Grover's formula and previously published data. It should be noted that we only need a simple approach to deal with the singularity of the new formula. In singular situation, the Gaussian numerical integration is recommended. In all the cases, our formula is proved to be successful, therefore we can claim that the new formula (10) is the most general formula for the non-coaxial circular coils with parallel axes. The new formula is more intuitive than Grover's formula (2). The new formula can be easily applied to practical engineering applications, which can be served as an alternative tool as compared to the numerical method that requires a lot of memory and CPU time. In conclusion, we have proposed the new formula of the mutual inductance that can be efficiently calculated with only a personal computer, which is particularly useful to large-scale applications.

ACKNOWLEDGMENT

This work was supported in part by Natural Science Foundation of China (No. 61801002), Natural Science Foundation of Anhui Province (No. 1808085QF183) and Key Natural Science Project of Anhui Provincial Education Department No. KJ2018A0015.

REFERENCES

[1] M. Brighton and M. J. English, "Calculation of optimum spacing for a three coil axially symmetric metal detector," *Electronics Letters*, vol. 29, no. 10, pp. 838-839, 1993.

[2] J. Acero, C. Carretero, I. Lope, et al., "Analysis of the mutual inductance of planar-lumped inductive power transfer systems," *IEEE Trans. Power Electron.*, vol. 60, no. 1, pp. 410-420, 2013.

[3] M. Grzeskowiak, A. M. Diet, P. S. Diao, et al., "Pebbles tracking thanks to RFID LF multi-loops inductively coupled reader," *Progress in Electromagnetics Research C*, 55, pp. 129-137, 2014.

[4] M. Catrysse, B. Hermans, and R. Puers, "An induc-

tive power system with integrated bi-directional data-transmission," *Sensors & Actuators A Physical*, vol. 115, no. 2, pp. 221-229, 2004.

[5] Y. Ren, F. Wang, G. Kuang, et al., "Mutual inductance and force calculations between coaxial bitter coils and superconducting coils with rectangular cross section," *J. Supercond. Novel Magn.*, vol. 24, no. 5, pp. 1687-1691, 2011.

[6] Y. Ren, G. Kuang, and W. Chen, "Inductance of bitter coil with rectangular cross-section," *J. Supercond. Novel Magn.*, vol. 26, no. 6, pp. 2159-2163, 2013.

[7] L. Yao, "An accurate high-speed method for mutual inductance calculations of coplanar disk coils using generalized hypergeometric function," *IET Electric Power Applications*, vol. 31, no. 4, pp. 366-372, 2016.

[8] K. B. Kim, Z. Zabar, E. Levi, et al., "In-bore projectile dynamics in the linear induction launcher (LIL) - Part 1: Oscillations, *IEEE Trans. Mag.*, vol. 31, no. 1, pp. 484-488, 1995.

[9] J. C. Maxwell, *A Treatise on Electricity and Magnetism*. Dover Publications Inc., New York, 1954 (reprint from the original from 1873).

[10] F. W. Grover, "The calculation of the mutual inductance of circular filaments in any desired positions," *Proceedings of the IRE*, vol. 32, no. 10, 620-629, 1944.

[11] F. W. Grover, *Inductance Calculations*. Dover, New York, 1964.

[12] J. T. Conway, "Inductance calculations for non-coaxial coils using bessel functions," *IEEE Trans. Mag.*, vol. 43, no. 3, pp. 1023-1034, 2007.

[13] J. T. Conway, "Noncoaxial inductance calculations without the vector for axisymmetric coils and planar coils," *IEEE Trans. Mag.*, vol. 44, no. 4, 453-462, 2008.

[14] C. Akyel, S. I. Babic, and M. M. Mahmoudi, "Mutual inductance calculation for non-coaxial circular air coils with parallel axes," *Progress in Electromagnetics Research*, vol. 91, no. 4, pp. 287-301, 2009.

[15] S. Butterworth, "On the coefficients of mutual induction of eccentric coils," *Phil. Mag*., Ser. 6, 31, pp. 443-454, 1916.

[16] C. Snow, "Formulas for Computing Capacitance and Inductance," *National Bureau of Standards Circular 544*, Washington DC, Dec. 1954.

[17] K. B. Kim, E. Levi, Z. Zabar, et al., "Mutual inductance of noncoaxial circular coils with constant current density," *IEEE Trans. Mag.*, vol. 33, no. 5, pp. 4303-4309, 1997.

[18] S. I. Babic, F. Sirois, and C. Akyel, "Validity check of mutual inductance formulas for circular filaments with lateral and angular misaligments," *Progress In Electromagnetics Research M*, 8, pp. 15-26, 2009.

[19] W. R. Smythe, *Static and Dynamic Electricity*. McGraw-Hill, New York, 1950.

[20] S. I. Babic, F. Sirois, C. Akyel, et al., "New formulas for mutual inductance and axial magnetic force between a thin wall solenoid and a thick circular coil of rectangular cross-section," *IEEE Trans. Magn.*, vol. 47, no. 8, pp. 2034-2044, 2011.

[21] H. B. Dwight, *Electrical Coils and Conductors*. McGraw-Hill, New York, 1945.

HMSIW Cavity Filters Employing Various Complementary Split-Ring Resonators for Microwave Remote Sensing Applications

Lijun Wang [1,2,3], Zhengwei He [1], Yong Mao Huang [4], Shuai Ding [4], and Maurizio Bozzi [5]

[1] State Key Laboratory of Geohazard Prevention and Geoenvironment Protection
Chengdu University of Technology, Chengdu 610059, Sichuan, China
hzw@cdut.edu.cn

[2] College of Geophysics
Chengdu University of Technology, Chengdu 610059, Sichuan, China

[3] Chengdu College
University of Electronic Science and Technology of China, Chengdu 610051, Sichuan, China

[4] School of Physics
University of Electronic Science and Technology of China, Chengdu 611731, China
ymhuang128@gmail.com, uestcding@uestc.edu.cn

[5] Department of Electrical, Computers and Biomedical Engineering
University of Pavia, Pavia 27100, Italy
maurizio.bozzi@unipv.it.

Abstract ─ In this work, bandpass filters employing half-mode substrate integrated waveguide (HMSIW) cavities and various modified complementary split-ring resonators (CSRRs) are presented. The two modified CSRRs, which are called as Type-I and Type-II CSRRs, can exhibit larger effective inductance and capacitance, and eventually to contribute to the size miniaturization of the resonators. Thereafter, as the two CSRRs are independently loaded into HMSIW cavities, the newly-formed HMSIW-CSRR cavity resonators can achieve more size reduction as compared with the HMSIW cavity with the conventional CSRR. To demonstrate the proposed concept, two HMSIW cavity bandpass filters independently loaded with the proposed Type-I and Type-II CSRRs are implemented. Experimental results shows that measurements of the proposed filters agree with their corresponding simulations well. Meanwhile, as compared with some similar works, the two proposed filters achieve size reduction of 76.8% and 78.6%, respectively, as well as good selectivity, illustrating their suitability for the system integration application in microwave remote sensing and radar systems.

Index Terms ─ Bandpass filter, complementary split-ring resonator (CSRR), remote sensing system, substrate integrated waveguide (SIW).

I. INTRODUCTION

In contemporary wireless applications such as microwave remote sensing, mobile communications and radar systems, the radio frequency (RF) front-end is a fundamentally essential constituent for transmitting and receiving wireless signals. Generally, in a typical RF front-end of the microwave remote sensing system, bandpass filters are key components for frequency selection, which enable the remote sensing system to separate different channels or signals, and eventually realize sensing, detecting and controlling of different targets. More recently, with the rapid development of wireless technologies, many different operation modes and functions have been integrated in a single module. Nevertheless, integrating multiple functions together generally leads to larger physical size of the circuitry, which is inconvenient for practical applications. Under such situation, there is an increasing demand on the system integration that simultaneously focuses on the integration of circuit functions and the miniaturization of physical size.

On the other hand, substrate integrated waveguide (SIW) has captured plenty of attention in the past few years since it implements the planarization of the high-performance rectangular waveguide. Thanks to its quasi-closed form, SIW is with many merits like low loss, high

Submitted On: December 16, 2018
Accepted On: April 6, 2019

quality factor, and easy integration. Therefore, a large number of microwave components, including filters, have been developed [1]. Most reported SIW filters utilized the resonator-coupling scheme, that is, their typical unit cells are SIW cavity resonators, whose lengths and widths are generally about half guided-wavelength of the dominant mode in SIW. Thus, as operating at the same frequency, the conventional SIW cavity filters are usually larger than their corresponding microstrip counterparts in term of physical size, which consequently results in the SIW cavity filters being unsuitable for practical applications.

To improve the practicability of SIW cavity filters, various approaches for size miniaturization have been developed. The half-mode SIW (HMSIW) structure can help to reduce the size of SIW cavity by half or so [2]. The quarter-mode SIW (QMSIW) is an intrinsic resonant cavity and can get further size reduction of 50% on the basis of HMSIW cavity [3]. In [4], the defected ground structure (DGS) is etched on the surface of SIW to miniaturize the cavity size, and loading the SIW cavity with complementary split-ring resonator (CSRR) can even acquire more size reduction [5-7]. Another work introduces CSRR into QMSIW to achieve extra size miniaturization of 40% [8]. In [9], the C-shaped slots and microstrip stubs are simultaneously loaded into the circular SIW cavity to reduce its size by 80%. Recently, the stepped-impedance CSRR (SICSRR) has been proposed and utilized with HMSIW cavity for compact single- and dual-band filter applications [10, 11]. Additionally, the multilayered structure is utilized incorporating with the QMSIW and CSRRs for further size miniaturization [12]. However, the modification of CSRR hasn't been further investigated and applied deeply.

In this work, two different CSRRs, namely, Type-I and Type-II CSRRs, are developed and combined with HMSIW cavities to realize size-miniaturized bandpass filters. As compared with the conventional CSRR, the Type-I and Type-II CSRRs can exhibit larger effective inductance and capacitance, which makes them more preferred in size reduction applications. This work is organized as followed: Section II and III respectively investigate working principles of the two CSRRs and their application to size-miniaturized HMSIW cavity filters in detail. Experimental results of the two proposed filters, as well as their comparison with some similar state-of-art works, are briefly discussed in Section IV. Finally, a conclusion is given.

II. PROPOSED CSRRS AND HMSIW-CSRR CAVITIES

Figure 1 shows geometries and equivalent-circuit models of the conventional, Type-I and Type-II CSRRs. Here, L_r and C_r respectively stand for the equivalent inductance and capacitance of the conventional CSRR. L_1 and C_1 separately represent the extra equivalent inductance and capacitance contributed from the inner slots in Type-I CSRR. Similarly, in Type-II CSRR, L_2 and C_2 denote the incremental equivalent inductance and capacitance introduced by its inner-lengthened split, respectively. More exactly, equivalent-circuit models of the two proposed CSRRs can be clearly comprehended from their dual structures by applying duality. As is known, the dual structure of the conventional CSRR is the split-ring resonator (SRR) [13]. Hence, it can be simply obtained that the corresponding dual structures of the proposed Type-I and Type-II CSRRs are Type-I and Type-II SRRs, which have been given in Fig. 1 as well. By applying duality, the equivalent inductance and capacitance of the conventional CSRR can be derived from the equivalent capacitance and inductance of SRR. Specifically, as shown in Fig. 1 (a), the interrelation between the conventional single ring CSRR and SRR can be expressed as:

$$C_r = 4\varepsilon_0 L_{ro}/\mu_0, \tag{1}$$

$$L_r = \mu_0 C_{ro}/(4\varepsilon_0), \tag{2}$$

where L_{ro} and C_{ro} are the equivalent inductance and capacitance of the conventional SRR, respectively. μ_0 and ε_0 are the permeability and permittivity in free space.

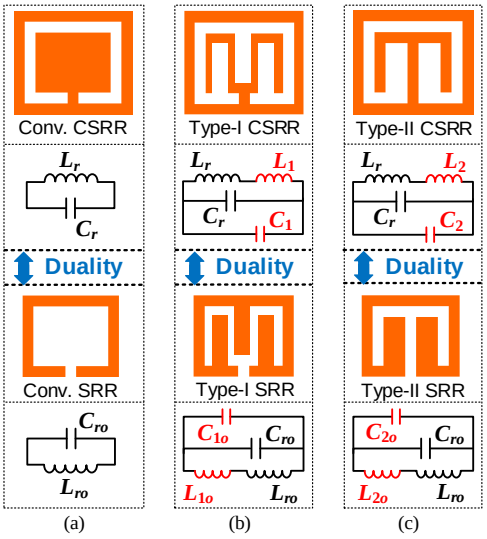

Fig. 1. Geometries and equivalent-circuit models of: (a) The conventional, (b) Type-I, and (c) Type-II CSRR.

Therefore, by using the duality theorem similarly, the equivalent inductance and capacitance of the Type-I and Type-II CSRRs can be derived from the equivalent capacitance and inductance of the Type-I and Type-II SRRs as well. For the proposed Type-I CSRR and its corresponding Type-I SRRs in Fig. 1 (b):

$$(C_1 + C_r) = 4\varepsilon_0 (L_{1o} + L_{ro})/\mu_0, \tag{3}$$

$$(L_1 + L_r) = \mu_0 (C_{1o} + C_{ro})/(4\varepsilon_0), \tag{4}$$

where L_{1o} and C_{1o} are the incremental equivalent

inductance and capacitance of Type-I SRR, respectively.

Similarly, for the proposed Type-II CSRR and its corresponding Type-II SRR in Fig. 1 (c):

$$(C_2 + C_r) = 4\varepsilon_0(L_{2o} + L_{ro})/\mu_0, \quad (5)$$

$$(L_2 + L_r) = \mu_0(C_{2o} + C_{ro})/(4\varepsilon_0), \quad (6)$$

where L_{2o} and C_{2o} are the incremental equivalent inductance and capacitance of Type-II SRR, respectively.

Then, resonant frequencies of the conventional, Type-I and Type-II CSRRs are respectively calculated as:

$$f_{\text{CSRR}} = 1\Big/\left(2\pi\cdot\sqrt{L_r\cdot C_r}\right), \quad (7)$$

$$f_{\text{T-I}} = 1\Big/\left[2\pi\cdot\sqrt{(C_r + C_1)\cdot(L_r + L_1)}\right], \quad (8)$$

$$f_{\text{T-II}} = 1\Big/\left[2\pi\cdot\sqrt{(C_r + C_2)\cdot(L_r + L_2)}\right]. \quad (9)$$

For the conventional, Type-I and Type-II SRRs, there are relations as: $(C_{1o}+C_{ro}) > C_{ro}$, $(L_{1o}+L_{ro}) > L_{ro}$, $(C_{2o}+C_{ro}) > C_{ro}$, and $(L_{2o}+L_{ro}) > L_{ro}$. Considering these relations with (4), (5) and (6) together, it can be captured that $(L_1+L_r) > L_r$, $(C_1+C_r) > C_r$, $(L_2+L_r) > L_r$, and $(C_2+C_r) > C_r$. Hence, as the conventional and proposed CSRRs are with the same outer physical size, dominate resonant frequencies of the proposed CSRRs will be lower than that of the conventional one. In other words, once the conventional, Type-I and Type-II CSRRs work at the same dominant frequency, outer sizes of the proposed ones will be smaller than that of the conventional one, which means physical size miniaturization is able to be expected. That is, the proposed CSRRs are electrically smaller than the conventional one as they operate at the same frequency. In addition, according to the geometry of Type-I SRR in Fig. 1 (b), the capacitance from inner stubs C_{1o} are dominant, while the inductance L_{1o} is smaller or even negative (a negative L_{1o} typically means L_{ro} and L_{1o} are parallel connected), which is mainly influenced by the specific geometrical dimensions. Therefore, for the Type-I CSRR, it can be deduced with the duality theorem that the inductance L_1 from the inner slots is dominant, while the capacitance C_1 is smaller or even negative (a negative C_1 typically means C_1 and C_r are series connected). On the other hand, according to the geometry of Type-II SRR in Fig. 1 (c), L_{2o} is mainly contributed from the inner-lengthening of the metal ring, and C_{2o} is mainly attributed from the widening of the split, which is originated from the lengthening of the metal ring. Hence, for the Type-II CSRR, it can be deduced with (9) that both C_2 and L_2 will have notable influence on the resonant frequency.

Subsequently, by etching the proposed CSRRs on the top metal cover of the HMSIW cavity, the Type-I and Type-II HMSIW-CSRR cavity resonators are formed, with their configurations listed in Fig. 2. With such defected electromagnetic structure being loaded on the top metal cover, the HMSIW cavity and the defected electromagnetic structure will interact with each other and further change distributions of the electromagnetic energy in the cavity. As a result, the evanescent mode resonance can be generated and size reduction of the HMSIW cavity will be eventually achieved [8].

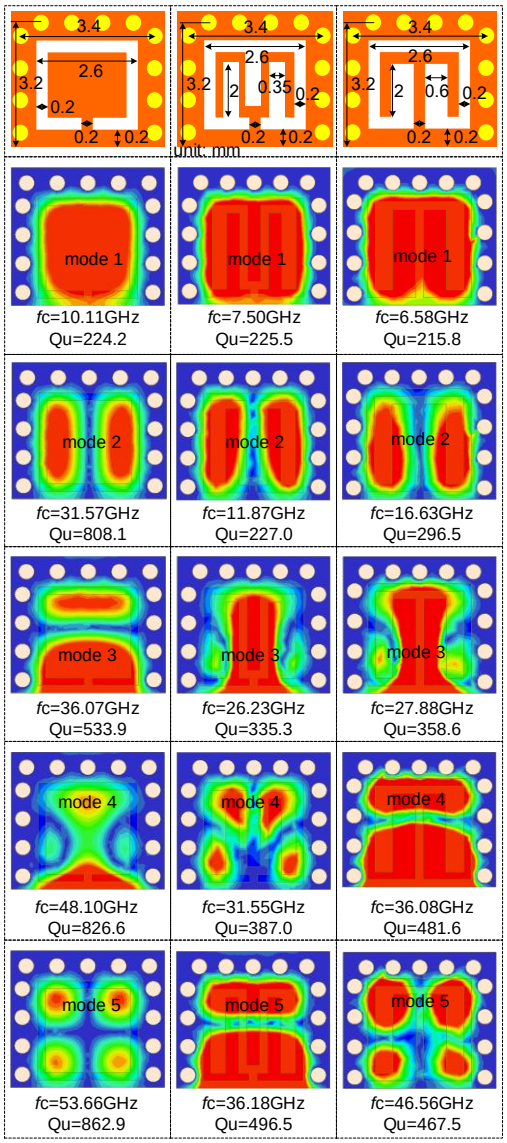

Fig. 2. Comparison of the simulated electric field distributions of the conventional, Type-I and Type-II HMSIW-CSRR cavity resonators.

Furthermore, since the proposed Type-I and Type-II CSRRs are more electrically compact than their corresponding conventional counterparts, they can help to acquire extra size reduction for the HMSIW cavity on the basis of the conventional CSRR [10,11]. In order to show the improvement in size reduction of the proposed Type-I and Type-II HMSIW-CSRR cavity resonators over the conventional one, some numerical simulations have been systematically carried out by using a commercial three-dimensional (3D) full-wave electromagnetic simulator. In order to study properties of these three cavities

conveniently and reasonably, all simulations are setup on a substrate with a relative permittivity of 2.94, a loss tangent of 0.0012, a thickness of 0.508mm, and a 0.035mm-thick conductor surface. For the full-wave electromagnetic simulator mentioned above, the PEC in its material library is with a conductivity of 1×10^{30}S/m, a relative permittivity of 1, and a relative permeability of 1, whereas the copper is with a default conductivity of 5.8×10^{7}S/m, a relative permeability of 0.999991, and a relative permittivity of 1. Hence, the PEC will contribute to better current conduction performance in the simulation, namely the simulated results with these two materials will be different, particularly on the conductor loss. Therefore, in the modeling setup, both the conductor surface and metallized vias are set as copper, instead of the perfect electric conductor (PEC), which is more accurate and realistic. Figure 2 shows comparison of the simulated electric field distributions of the conventional and the two proposed HMSIW-CSRR cavities, as well as their corresponding geometrical dimensions. It is clear that all the three HMSIW-CSRR cavities are with the same cavity size and slot-ring size, with the only difference on their splits. As shown in Fig. 2, the dominant resonant mode of the conventional HMSIW-CSRR cavity operates at 10.22GHz, while the proposed ones work at 7.5GHz and 6.58GHz, respectively. Hence, once the two proposed cavities are both set to operate at 10.22GHz, their physical sizes are supposed to be miniaturized. Meanwhile, the conventional HMSIW-CSRR cavity is with an unloaded quality factor (Q_u) of 224.2, whereas the proposed ones are with Q_u of 225.5 and 215.8, which means the three cavities in Fig. 2 are not with notable difference in term of the total loss. Actually, for these HMSIW-CSRR cavities, the radiation loss is dominate in the total loss.

Meanwhile, the lowest four higher-order modes in the conventional, Type-I and Type-II cavities are listed in Fig. 2 as well. Obviously, their first higher-order modes are the same one, mainly controlled by the CSRRs. On the other hand, their other three higher-order modes are much different with each other. For the conventional HMSIW-CSRR cavity, the operation frequency of its first higher-order mode is 31.57GHz, about three times of it's dominate resonant frequency. Whereas for the proposed cases, working frequencies of their first higher-order modes are 11.87GHz and 16.63GHz, respectively, about 1.58 and 2.53 times of their dominate operation frequencies. Moreover, resonate frequencies of the second, third and fourth higher-order modes of the proposed HMSIW-CSRR cavities are also much lower than the corresponding counterparts of the conventional one. It is clear that such difference is mainly caused by the difference between the conventional and proposed CSRRs.

III. HMSIW-CSRR CAVITIES FILTERS

To verify the aforementioned idea, two bandpass filters made of the proposed HMSIW-CSRR cavity resonators in Fig. 2 are developed. Figure 3 gives detailed configuration of the proposed Type-I HMSIW-CSRR cavity filter. It is designed with a central frequency (f_c) of 8.5GHz, a fractional bandwidth (FBW) of 8%, and a ripple of in-band insertion loss of 0.1dB. Hence, the initiated inner coupling coefficients (k_i) and external quality factor (Q_e) of the proposed Type-I HMSIW-CSRR cavity filter can be calculated by using the elements of the Chebyshev lowpass prototype filter. For this case, the coupling coefficients matrix k and Q_e are:

$$k=\begin{bmatrix} 0 & 0.0735 & 0 \\ 0.0735 & 0 & 0.0735 \\ 0 & 0.0735 & 0 \end{bmatrix}, \tag{10}$$

$$Q_e = 12.893. \tag{11}$$

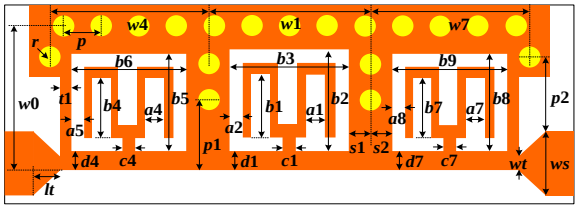

Fig. 3. Detailed configuration of the proposed Type-I HMSIW-CSRR cavity filter.

Afterwards, k_i and Q_e in the proposed Type-I HMSIW-CSRR cavity filter are numerically studied. These numerical simulations are carried out by using the same simulator mentioned above. Figure 4 sketches relation of the coupling window size between two adjacent Type-I HMSIW-CSRR cavity (px) and their k_i, with the scaled simulation model given in the inset. Figure 4 also shows the relation between width of the open port (pe) and Q_e, as well as the corresponding geometrical dimensions. Then, by taking Fig. 4 with (9) and (10) into consideration, the initiated geometrical parameters of the proposed Type-I filter can be selected. Finally, the entire filter in Fig. 3 is simulated and optimized by using the same full-wave simulator mentioned above.

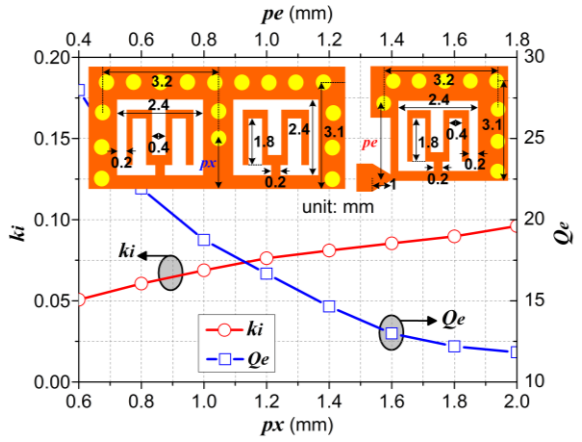

Fig. 4. Simulated k_i and Q_e in the proposed Type-I HMSIW-CSRR cavity filter.

Generally, there are two different strategies for the full-wave simulation and optimization. One is using the auto-optimization tool in the simulator, which can run optimizing procedures automatically. However, the auto-optimization typically cost too much time and not efficient in practical design. The second strategy is using the artificial tuning method. Firstly, setting initial values of geometrical parameters captured from the Eigenmode and coupling analyses as intermediate values. Then, choose two values for each geometrical parameter. For the two values, one is larger and the other is smaller than the intermediate one. Thirdly, by simulating the proposed filter respectively with geometrical dimensions of the larger, intermediate and smaller values, different results will be captured. Later, interrelation between the geometrical values and the transmission properties can be summarized by comparing these results. With the interrelation, it will be much faster to obtain the optimized values of the geometrical parameters of the proposed filter. For this case, some key geometrical parameters, including sizes of the cavities, widths of the coupling windows, and sizes of the feeding lines, are supposed to be tuned and simulated firstly, so that the optimization can be more efficiently. The optimized geometrical parameters are: lt=0.50, wt=0.25, ws=1.25, $w0$=3.10, $w1$=3.25, $w4$=$w7$=3.20, $s1$=$s2$=0.40, $t1$=0.20, r=0.20, p=0.70, $p1$=1.30, $p2$=1.55, $a1$=0.30, $a2$=0.20, b1=1.60, $b2$=$b3$=2.40, $c1$=0.20, $d1$=0.20, $a4$=0.30, $a5$=0.20, $b4$=1.60, b5=b6=2.40, $c4$=0.20, $d4$=0.20, $a7$=0.30, $a8$=0.20, b7=1.60, $b8$=$b9$=2.40, $c7$=0.20, $d7$=0.20 (unit: mm).

Later, for the proposed Type-II HMSIW-CSRR cavity filter in Fig. 5, it also contains three basic resonators and designed with the same specifications as the Type-I one. Naturally, same design procedures mentioned above are utilized to the Type-II filter as well. Figure 6 shows relation between width of the coupling window (px) and k_i of two adjacent Type-II HMSIW-CSRR cavities, and relation between width of the open port (pe) and Q_e, with the scaled simulation model simultaneously shown in the inset. Finally, the proposed Type-II HMSIW-CSRR cavity filter is simulated, with the optimized geometrical parameters as below: lt=0.50, wt=0.25, ws=1.25, $w0$=2.80, $w1$=3.00, $w4$=$w7$=2.95, $s1$=$s2$=0.40, $t1$=0.20, r=0.20, p=0.70, $p1$=1.20, $p2$=1.45, $a1$=0.50, $a2$=0.20, $b1$=1.29, $b2$=$b3$=2.20, $c1$=0.20, $d1$=0.20, $a4$=0.40, $a5$=0.20, $b4$=1.35, $b5$=$b6$=2.15, $c4$=0.20, $d4$=0.20, $a7$=0.40, $a8$=0.20, $b7$=1.35, $b8$=$b9$=2.15, $c7$=0.20, $d7$=0.20 (unit: mm). And the artificial tuning method is utilized again in the simulation and optimization as well.

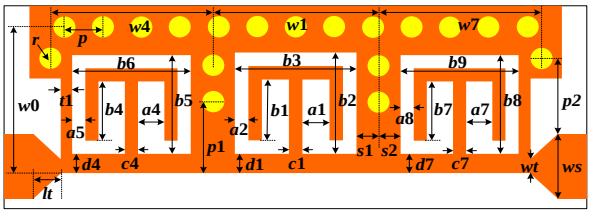

Fig. 5. Detailed configuration of the proposed Type-II HMSIW-CSRR cavity filter.

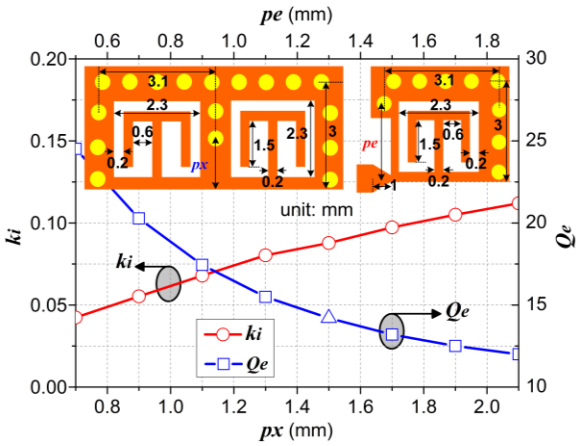

Fig. 6. Simulated k_i and Q_e in the proposed Type-II HMSIW-CSRR cavity filter.

IV. EXPERIMENTAL RESULTS

Prototypes of the proposed Type-I and Type-II HMSIW-CSRR cavity filters are fabricated by using the standard printed circuit board (PCB) process on a Rogers RT/Duriod 6002 substrate, with a thickness of 0.508mm, a relative permittivity of 2.2±0.02, a loss tangent of 0.0012. In the fabrication, the surface copper is grown with extra thickness of 0.011mm on the basis of the original copper of 0.024mm. Moreover, the metallized via-holes and the defected surface copper are dealt with separately: The via-holes are drilled firstly, with the mask corrosion and surface gold metal electroplating subsequently. Finally, all the via-holes are metallized by

wet electroplating. Photograph of the two fabricated HMSIW-CSRR cavity filter is given in the inset of Fig. 7 and Fig. 8, respectively. It can be easily captured that the functional part of the fabricated Type-I HMSIW-CSRR cavity filter is with a size of 3.9mm×10.0mm, while the value is 3.8mm×9.5mm for the Type-II case.

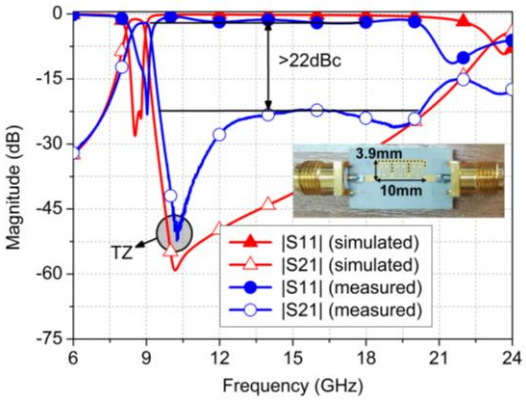

Fig. 7. Simulated and measured |S21| and |S11| of the fabricated Type-I HMSIW-CSRR cavity filter.

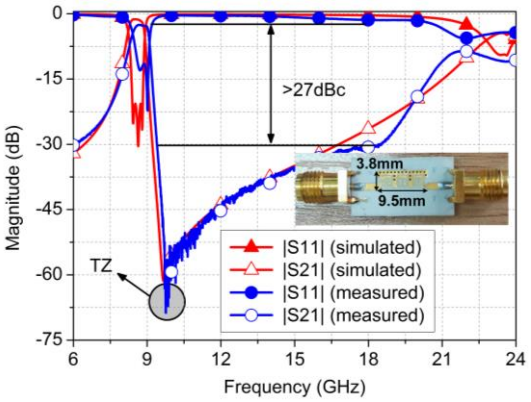

Fig. 8. Simulated and measured |S21| and |S11| of the fabricated Type-II HMSIW-CSRR cavity filter.

The fabricated HMSIW-CSRR cavity filters are measured by using a Keysight vector network analyzer N5242A, with the default SOLT calibration being used. Figure 7 shows measured and simulated magnitude of the transmission coefficient (|S21|) and input reflection coefficient (|S11|) of the fabricated Type-I filter. The fabricated Type-I filter achieves an f_c of 8.56GHz, a FBW of 7.8%, an in-band insertion loss of 1.62dB, and an in-band return loss better than 15dB. A transmission zero (TZ) located at 10.3GHz is able to provide suppression over 50dB, with the stopband up to 20GHz with rejection over 22dBc. On the other hand, measured and simulated results of the fabricated Type-II filter are given in Fig. 8. It can be obtained that the fabricated Type-II filter can exhibit an f_c of 8.60GHz, a FBW of 7.1%, an in-band insertion loss of 2.05dB, and an in-band return loss better than 13dB. Moreover, a TZ is captured at 9.7GHz with the rejection over 70dB, and the relative out-of-band suppression is larger than 27dBc from 9.2GHz to 18GHz.

In addition, Table 1 lists the comparison between the proposed HMSIW-CSRR cavity filters and some reported state-of-art works in similar technologies. Here, ε_r denotes the relative permittivity of the substrate. According to Table 1, as compared with the filter using QMSIW cavity and coplanar waveguide (CPW) resonator in [3], the filter employing SIW cavity and DGS in [6], and the filter utilizing SIW, C-shaped slots and microstrip stubs in [9], the proposed HMSIW-CSRR cavity filters are with much smaller electrical size. Particularly, as compared with the filter in [7], the proposed Type-I and Type-II filters separately achieve size reduction over 76.8% and 78.6%. Therefore, the two proposed HMSIW-CSRR cavity filters have the smallest size, as well as good performance.

Table 1: Comparison between some similar SIW cavity filters and the proposed HMSIW-CSRR cavity filters

Ref.	Poles	Topology	f_c (GHz), FBW	Elec. Size ($\lambda_0^2/\varepsilon_r$)
[3]	3	QMSIW+CPW	4.00, 16%	0.431
[6]	3	SIW cavity+DGS	4.90, 9.2%	0.406
[9]	3	SIW+slot+stub	5.20, 6.3%	0.410
I	3	HMSIW cavity+ Type-I CSRR	8.56, 7.8%	0.094
II	3	HMSIW cavity+ Type-II CSRR	8.60, 7.1%	0.087

V. CONCLUSION

In this work, bandpass cavity filters based on the proposed Type-I and Type-II HMSIW-CSRR cavity resonators are designed, fabricated and measured. Compared with some reported similar works, the proposed HMSIW-CSRR cavity filters achieve notable size-reduction, both with amount over 76%, as well as good selectivity performance, which demonstrates that they are applicable for the system integration and packaging of microwave remote sensing systems.

ACKNOWLEDGMENT

This work was supported in part by the State Key Laboratory of Geohazard Prevention and Geoenvironment Protection Independent Research Project under Grant SKLGP2017Z005 and the Sichuan Science and Technology Program under Grant 2018GZ0518.

REFERENCES

[1] M. Bozzi, A. Georgiadis, and K. Wu, "Review of substrate-integrated waveguide circuits and antennas," *IET Microw. Antennas Propag.*, vol. 5,

no. 8, pp. 909-920, July 2011.

[2] Y. Wang, W. Hong, Y. Dong, B. Liu, H. J. Tang, J. Chen, X. Yin, and K. Wu, "Half mode substrate integrated waveguide (HMSIW) bandpass filter," *IEEE Microw. Wireless Compon. Lett.*, vol. 17, no. 4, pp. 265-267, Apr. 2007.

[3] S. Moscato, C. Tomassoni, M. Bozzi, and L. Perregrini, "Quarter-mode cavity filters in substrate integrated waveguide technology," *IEEE Trans. Microw. Theory Tech.*, vol. 64, no. 8, pp. 2538-2547, Aug. 2016.

[4] Y. L. Zhang, W. Hong, K. Wu , J. Chen, and H. J. Tang, "Novel substrate integrated waveguide cavity filter with defected ground structure," *IEEE Trans. Microw. Theory Tech.*, vol. 53, no. 4, pp. 1280-1287, Apr. 2005.

[5] Q. L. Zhang, W. Y. Yin, S. He, and L.-S. Wu, "Compact substrate integrated waveguide (SIW) bandpass filter with complementary split-ring resonators (CSRRs)," *IEEE Microw. Wireless Compon. Lett.*, vol. 20, no. 8, pp. 426-428, Aug. 2010.

[6] W. Shen, W. Y. Yin, and X. W. Sun, "Compact substrate integrated waveguide (SIW) filter with defected ground structure," *IEEE Microw. Wireless Compon. Lett.*, vol. 21, no. 2, pp. 83-85, Feb. 2011.

[7] W. Jiang, W. Shen, L. Zhou, and W. Y. Yin, "Miniaturized and high-selectivity substrate integrated waveguide (SIW) bandpass filter loaded by complementary split-ring resonators (CSRRs)," *J. Electromagn. Waves Appl.*, vol. 26, no. 11-12, pp. 1448-1459, Dec. 2012.

[8] D. E. Senior, A. Rahimi, and Y. K. Yoon, "A surface micromachined broadband millimeter-wave filter using quarter-mode substrate integrated waveguide loaded with complementary split-ring resonator," *IEEE MTT-S Int. Microw. Symp. Dig.*, Tampa, USA, pp. 1-4, May 2014.

[9] L. Riaz, U. Naeem, and M. F. Shafique, "Miniaturization of SIW cavity filters through stub loading," *IEEE Microw. Wireless Compon. Lett.*, vol. 26, no. 12, pp. 981-983, Dec. 2016.

[10] Y. M. Huang, Z. Shao, W. Jiang, T. Huang, and G. Wang, "Half-mode substrate integrated waveguide bandpass filter loaded with horizontal-asymmetrical stepped-impedance complementary split-ring resonators," *Electron. Lett.*, vol. 52, no. 12, pp. 1034-1036, June. 2016.

[11] Y. M. Huang, Y. Peng, Y. Zhou, H. Jin, S. Leng, and G. Wang, "Size-reduced dual-band HMSIW cavity filters loaded with double-sided SICSRRs," *Electron. Lett.*, vol. 53, no. 10, pp. 689-691, May 2017.

[12] Y. Z. Zhu, W. X. Xie, X. Deng, and Y. F. Zhang, "Compact modified quarter mode substrate integrated waveguide resonator and its application to filters design," *ACES Journal*, vol. 32, no. 2, pp. 163-166, Feb. 2018

[13] F. Martin, *Artificial Transmission Lines for RF and Microwave Applications*. Hoboken: Wiley, USA, 2015.

Lijun Wang is currently pursuing the Ph.D. degree at Chengdu University of Technology, Chengdu, China, and is also a Lecturer at Chengdu College of University of Electronic Science and Technology of China, Chengdu, China. Her research interests including data analysis and system implementation for remote sensing.

Zhengwei He received the Ph.D. degree from Chengdu University of Technology in 1998, where he is now a Professor and Dean of Institute of Geological Survey. His research interests including remote sensing, geographic information system and urban planning. He has authored and coauthored over 220 referred papers.

Yong Mao Huang received the Ph.D. degree from University of Electronic Science and Technology of China, Chengdu, China, in 2017. He has been an Assistant Professor with the Department of Information Engineering, Xihua University, Chengdu, China, from 2018. His research interests including substrate integrated circuits. He has authored and coauthored about 50 referred papers.

Shuai Ding received the Ph.D. degree from University of Electronic Science and Technology of China, Chengdu, China, in 2013, where he is now an Associate Professor. His research interests including the microwave circuits and computational electromagnetics. He has authored and coauthored over 80 referred papers.

Maurizio Bozzi received the Ph.D. degree from the University of Pavia (Italy) in 2000, where he is now an Associate Professor. His current research interests concern substrate integrated waveguide technology, computational electromagnetics and novel material for microwave circuit applications. He is a Fellow of the IEEE. He is an Elected Member of the Ad-Com of the IEEE Microwave Theory and Techniques Society. He has authored and coauthored over 400 referred papers.

Super Wide Band Tunable Microstrip BPF Using Stub Loaded MMR

Aditi Sengupta [1], Somdotta R. Choudhury [2], and Santanu Das [1]

[1] Department of Electronics & Telecommunication Engineering
Indian Institute of Engineering Science & Technology, Shibpur, Howrah-711 103, India
itsmeaaditi@gmail.com, santanumdas@yahoo.com

[2] Department of Electronics & Telecommunication Engineering
Ramarao Adik Institute of Technology, D. Y. Patil University Campus, Navi Mumbai-400 706, India
somdottaroychoudhury@gmail.com

Abstract ─ A simpler structure of super wide band (SWB) tunable microstrip band pass filter (BPF) using stub loaded multimode resonator (MMR) is presented here. The MMR is formed by loading a single open-ended shunt stub at the center with a simple stepped impedance resonator. By incorporating this MMR with two interdigital parallel coupled feed lines, a novel SWB tunable BPF is formed. The BPF is fabricated using FR-4 substrate of 1.6 mm thickness with dielectric constant of 4.4 and simulated using high frequency structure simulator (HFSS) software. The simulated and measured results are in good agreement with each other, with a wide fractional bandwidth (FBW) of 179%. The measured insertion loss is less than -0.9 dB throughout the pass band of 3.1 GHz-15.4 GHz with the return loss higher than 11.5 dB. The group delay of the filter is relatively constant and less than 0.3 ns over the desired pass band.

Index Terms ─ Band Pass Filter (BPF), Multimode Resonator (MMR), Super Wide Band (SWB), Ultra Wide Band (UWB).

I. INTRODUCTION

Since 2002, the ultra-wideband (UWB) system was approved for civilian-use, by the US Federal Communications Commission (FCC) for both academic and industrial fields [1]. It provides high data rate transmission, low power assumption and low cost for the wireless communication system. Filter is an essential component in the UWB communication system. The challenge to design an UWB BPF is that the fractional bandwidth must exceed 110%. The parallel-coupled microstrip lines are one of the most commonly used RF/microwave circuits due to their design simplicity, planar structure, and relatively wide bandwidth [2]. Multiple coupled transmission line structure implementations have been increased to develop multiple-mode resonator (MMR) filters with wideband passband [3-9]. An UWB passband with five transmission poles was achieved by forming MMR and introducing quarter-wavelength parallel coupled lines in the input and output ports [10]. An improved microstrip line UWB BPF is proposed, designed, and implemented based on the stub-loaded MMR [11]. An equivalent circuit was used to derive filtering transfer function and the mathematical formulation was used to calculate characteristic impedance of filter [12]. Wideband BPF with high passband selectivity and deep stopband rejection performances, have been proposed based on various structures, e.g., ring resonators with open stubs [13], stub-loaded multimode resonators (MMRs) [14], harmonic-suppressed dual-transmission lines [15]. A highly selective triple band notch UWB (3.3 GHz-10.7 GHz) filter was presented where the UWB pass band characteristics were achieved by two coupled multi-mode resonators [16].

In this paper, a simpler structure of SWB tunable microstrip BPF is developed to cover the frequency range from 3.1 GHz-15.4 GHz. Therefore, the designed filter has a wide band passband to cover C-band (4 GHz-8 GHz), X-band (8 GHz-12 GHz), and some part of Ku-band (12 GHz-18 GHz) frequency range. This feature can also be used for the Cable Television Relay Service (CARS) stations with frequency range from 12.7 GHz-13.20 GHz. The CARS stations are point-to-point or point-to-multipoint microwave systems used by cable and other multichannel video programming distributor (MVPD) operators. The proposed filter is designed based on MMR, which is constructed by properly loading a stepped-impedance resonator with a single open-ended stub at the center. This SWB BPF with excellent passband selectivity is designed, analyzed and fabricated with FBW of 179%, insertion loss is less than -0.9 dB, return loss higher than 11.5 dB and group delay is relatively constant and less than 0.3 ns at the pass band.

Submitted On: November 5, 2018
Accepted On: April 6, 2019

II. UWB FILTER DESIGN AND ANALYSIS

A. Design of MMR and allocating UWB passband

Figure 1 (a) illustrates the schematic of designed UWB microstrip filter. The MMR is constructed with two sections of three coupled lines separated by a stub-loaded resonator. The stub-loaded resonator is formed by attaching one open-circuited stub with two high-impedance microstrip lines at its center. The first three resonant modes of the MMR can be evenly allocated within the 3 GHz-10.8 GHz passband with FBW of 113% by properly adjusting the length and width of the stub as shown in Fig. 1 (b). Two interdigital coupled line (ICL) sections are placed at two sides of the resonator to provide tight coupling with 50 Ω microstrip feed lines. These coupled line sections also provide the desired coupling for the passband. The length of the coupled lines is quarter wavelength ($\lambda_g/4$) at the center frequency. The effects of varying coupled line lengths of the filter structure are analyzed on parameter basis. The capacitively coupled gap and the quarter wavelength open stubs are adopted to generate transmission zeros at the edges of the desired passband to improve the selectivity of the parallel coupled BPF.

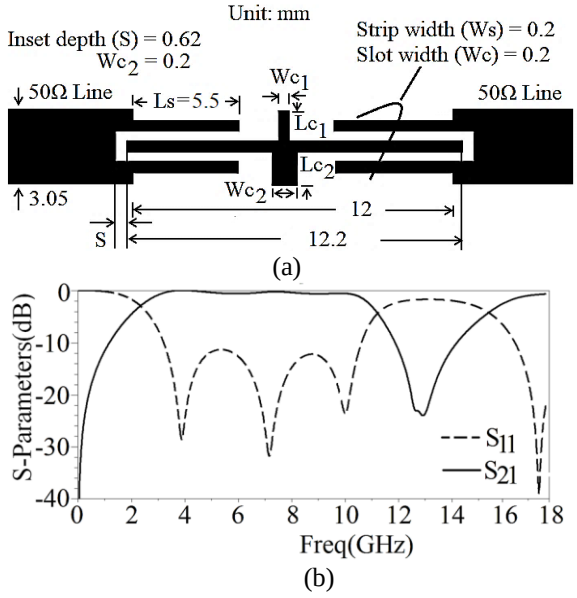

Fig. 1. (a) Schematic diagram, and (b) simulated S parameters performance of UWB BPF.

B. Equivalent transmission line network of the UWB BPF

Figure 2 gives an equivalent transmission line network of Fig. 1 (a), in which the pair of stubs can be perceived as an equivalent frequency dependent capacitance C_s (ω). The ICL section is characterized as a J-inverter susceptance (J) and two electrical lengths (θ/2), which represents the series capacitive coupling and equivalent phase shifts respectively [17]. On the other hand, the central line can be perceived as an additional phase factor (ϕ/2), so that the total electrical length φ should be made up of three separate parts, i.e. Φ = θ/2+ ϕ/2+ θ/2. For a symmetric two port network,

$$\bar{J} = \frac{\tan(\theta/2) + \bar{B}_{11}}{\bar{B}_{11}\tan(\theta/2)}, \tag{1}$$

$$\theta = -\tan^{-1}\left\{\frac{2\bar{B}_1}{1-\bar{B}_{11}^2+\bar{B}_{12}^2}\right\}, \tag{2}$$

where $\bar{J} = J/Y_0, \bar{B}_{11} = B_{11}/Y_0 = B_{22}/Y_0, \bar{B}_{12} = B_{12}/Y_0 = B_{21}/Y_0$ and Y_0 is the characteristic admittance of the microstrip line. On the basis of transmission line theorem, the normalized input admittance ($\bar{Y}_{in} = Y_{in}/Y_0$) at one termination (#1), looking into opposite termination (#1'), can be easily deducted and expressed as a function of $\bar{J}$ and Φ such that,

$$\bar{Y}_{in} = \frac{\bar{J}^2\left(1 + j\bar{J}^2\tan\Phi\right)}{\bar{J}^2 + j\tan\Phi}. \tag{3}$$

Accordingly, the reflection coefficient (S_{11}) at #1 can be expressed as:

$$S_{11} = \frac{j\left(1-\bar{J}^4\right)\tan(\Phi)}{2\bar{J}^2 + j\left(1+\bar{J}^4\right)\tan(\Phi)}. \tag{4}$$

The stub-loaded resonator section of the circuit is responsible for the stopbands at two edges of the UWB bandpass filter.

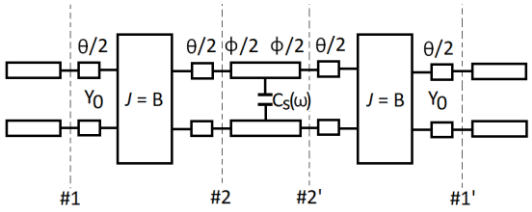

Fig. 2. Equivalent transmission line network of the proposed UWB BPF.

To analyze this section, odd and even mode methods are implemented along this AA' line as shown in the following Figs. 3 (a-e). This AA' line subdivided the above section into two symmetric portions. For odd and even mode analysis, equivalent circuits are shown in Figs. 3 (b) and 3 (c) respectively. The input impedance expressions for odd mode and two even modes are given by equation (5) to equation (7):

$$Z_{in,odd} = jZ_1\tan\theta_1, \tag{5}$$

$$Z_{in,even1} = jZ_1\frac{\left(Z_1\tan\theta_1 - Z_2\cot\theta_2\right)}{Z_1 + Z_2\tan\theta_1\cot\theta_2}, \tag{6}$$

$$Z_{in,even2} = jZ_1\frac{\left(Z_1\tan\theta_1 - Z_3\cot\theta_3\right)}{Z_1 + Z_3\tan\theta_1\cot\theta_3}. \tag{7}$$

For the resonance condition, to achieve stopbands at the two UWB response,

$$Z_{in,even1} = Z_{in,even2} = 0, \quad (8)$$

and,

$$Z_{in,odd} = \infty. \quad (9)$$

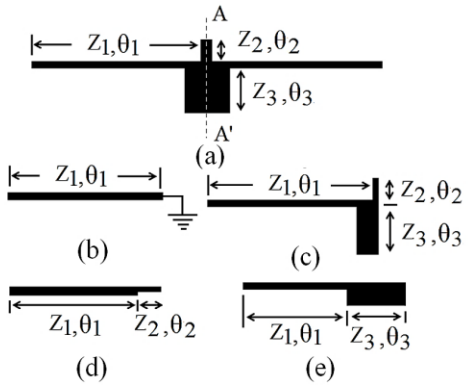

Fig. 3. (a) Circuit layout for, (b) odd, and (c) even mode analysis; (d) & (e) decomposed parts of even mode.

III. MODIFIED UWB FILTER DESIGN AND ALLOCATING SWB PASSBAND

A. Modified design of MMR and allocating SWB passband

The proposed structure is modified according to the consideration of inset feed and infinite ground plane. The simulated S parameters performance of SWB BPF is shown in Fig. 4.

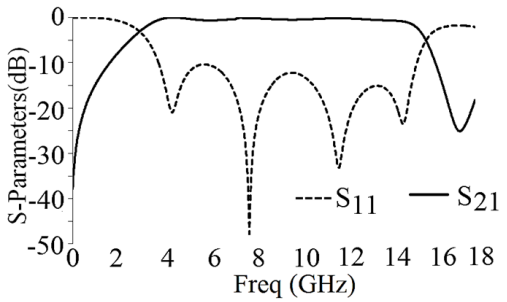

Fig. 4. Simulated S parameters performance of proposed SWB BPF.

The first four resonant modes of the MMR can be evenly allocated within 3.1 GHz-15.4 GHz passband by decreasing the coupling line lengths and stub width, where S_{11} < -11.5 dB and thus SWB passband is achieved. The slot width between the parallel coupled strip lines and strip width are defined by W_c and W_s respectively. The Inset depth is taken as S, length of coupled lines is defined by L_s, and the width and length of the open-ended stub are described by W_{c1}, W_{c2}, L_{c1}, and L_{c2} respectively. From this comparison the optimized dimensions of the wideband BPF are fabricated and the final design dimensions are: L_s = 4 mm, L_{c1} = 0.25 mm, W_{c1} = 0.2mm, W_{c2} = L_{c2} = 0.76 mm, W_s = W_c = 0.2 mm, and S = 0.62 mm as labeled in Fig. 1 (a). The overall length of this filter is approximately equal to one full wavelength at 6.85 GHz, which is much smaller than those reported in literatures. Finally, the bandwidth is increased with FBW of 179%. Increase of the slot width (W_c) reduces the bandwidth of the desired passband and vice versa. So, the pass band is controlled by the slot width. The performance of the BPF is improved by changing the coupling strip line lengths and stub width, to cover the SWB frequency range from UWB passband.

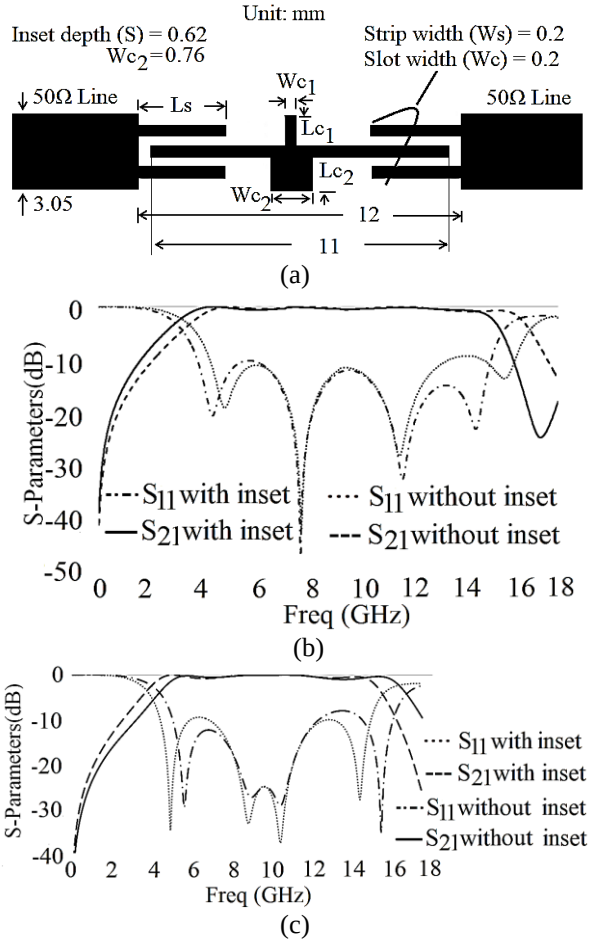

Fig. 5. (a) Schematic diagram of modified SWB BPF, (b) simulated S-parameters performance, with and without inset feed of SWB BPF for infinite ground, and (c) finite ground.

B. Effect of infinite and finite ground plane with inset and without inset feed line

Here the frequency re-configurability can be achieved with a change in the induced current distribution by varying the size of the ground plane and inset feed. Better impedance matching is achieved

by giving the inset feed. The schematic diagram of modified SWB microstrip BPF is shown in Fig. 5 (a). In this design no inset feeding is provided, and the ground plane is finite. It is seen that the lower frequency and higher frequency shifted from 3.1 GHz to 5.4 GHz and 15.4 GHz to 15.8 GHz respectively due to the finite plane and without inset feeding. So, the size of ground plane has a significant effect on the frequency shifting.

Figures 5 (b-c) show the simulated S parameters performance, with and without inset feed of proposed and modified SWB BPF for infinite and finite ground respectively. The performance comparison of SWB and modified SWB BPF is shown in Table 1.

Table 1: Performance comparison of SWB and modified SWB BPF

Figure No.	Ground Plane	Feeding	Bandwidth (GHz)
Fig. 5 (b)	Infinite	Without Inset	3.6-15.8
		With Inset	3.1-15.4
Fig. 5 (c)	Finite	Without Inset	5.4-15.8
		With Inset	4.3-15.4

Figure 6 shows the comparison of ground plane size with inset feed. And it confirms that the infinite ground plane with inset feed give the best results. The current density of the proposed filter at the center frequency of 6.85 GHz of the pass band is shown in Fig. 7.

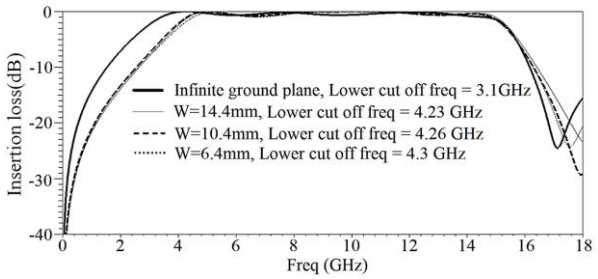

Fig. 6. S_{21} performance for different widths of ground plane with inset feed.

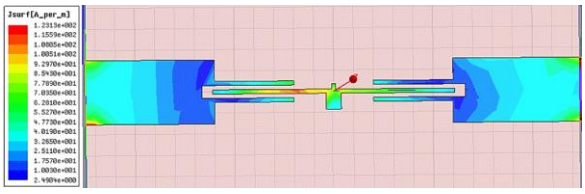

Fig. 7. Current density of the proposed SWB BPF.

Here the stub loaded resonator with high impedance line resonates with a much higher density at the center frequency.

IV. FABRICATION AND MEASUREMENTS

A prototype of the proposed SWB microstrip BPF with MMR is fabricated as shown in Fig. 8. It is also measured by vector network analyzer (VNA). The fabricated filter occupies a small size of 12.2 mm × 1.01 mm which amounts to 0.279 λ_0 × 0.023 λ_0, where λ_0 is the free-space wavelength of the operating frequency. For the measurement, a 6.4 mm long 50 Ω microstrip feed line is added at both input and output. The simulated and measured results are in good agreement with each other over the wide frequency range of 500 MHz-18 GHz. In the measurement, the lower and higher cut-off frequencies of the SWB pass band are equal to 3.1 GHz and 15.4 GHz respectively, as observed in Fig. 9. This indicates that the relevant fractional bandwidth about 179% is achieved. The measured insertion loss is found as -0.9 dB at the centre frequency of 6.85 GHz. The return loss in simulation and measurement are both higher than -11 dB with four transmission poles over the passband.

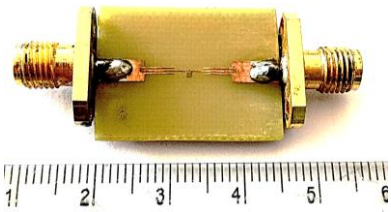

Fig. 8. The photograph of the fabricated SWB BPF.

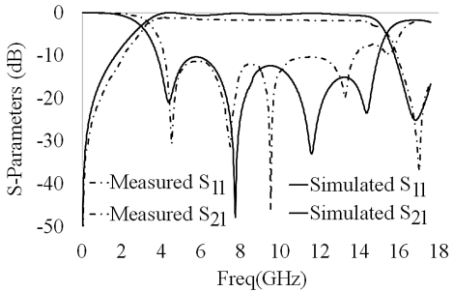

Fig. 9. The measured and simulated SWB BPF S parameters performance.

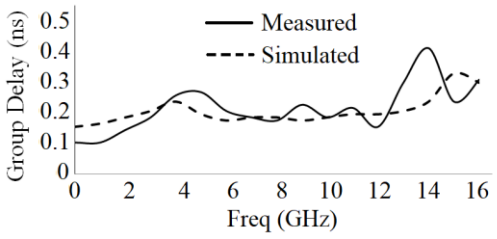

Fig. 10. Simulated and measured group delay of proposed SWB BPF.

The proposed SWB BPF group delay is obtained from the simulated as well as measured results as shown in Fig. 10. It is clear that the variations in the group delay are around 0.3 ns for the frequency band of 3.1 GHz-15.4 GHz.

V. PERFORMANCE SUMMARY OF SOME PUBLISHED WIDEBAND BPFs

The SWB filter here shows two transmission zeros at the lower and upper edges of the desired passband and four attenuation poles inside the passband which enhanced the performance of the filter. Taking λ_0 is the free-space wavelength of the operating frequency, the resonator size is compared. It can be easily found that the overall length of this proposed SWB BPF is smaller and simpler than the existing publications as shown in Table 2. At the center of 6.85 GHz, the insertion loss and return loss results are better as compared with some referred journals [5-11].

Table 2: Comparison with other topologies

Reference	Center Frequency (GHz)	FBW	$\|S_{21}\|\ dB$	$\|S_{11}\|\ dB$	Physical Dimension (mm)	Dielectric Constant/Height (mm)
[5]	6.85	119%	≤ 1.1	≥10	9.44 x 7.09	10.8/0.635
[6]	6.85	117%	≤ 2.0	≥7.0	22.3 x 13.64	2.55/0.8
[7]	6.85	117%	≤ 1.4	≥12.5	22.3 x 16.18	10.5/0.635
[8]	6.85	116%	≤ 1.4	≥11.0	31.92 x 15.3	2.55/0.8
[9]	6.85	120%	≤ 1.6	≥12.5	10.1 x 6.99	10.5/0.635
[10]	6.85	113%	≤0.55	≥10	15.65 x 1.049	10.8/1.27
[11]	6.85	114%	≤0.8	≥14.3	13.77 x 2.711	10.8/1.27
Proposed work	6.85	179%	≤0.9	≥11.5	12.2 x 1.01	4.4/1.6

VI. CONCLUSION

The MMR is constructed of two sections of three coupled lines separated by a stub-loaded resonator. The stub-loaded resonator is formed by attaching one open-circuited stub with two high-impedance microstrip lines at its center. The MMR structure is analyzed, and the corresponding transmission line equivalent model is given. The coupling space of the input/output interdigital coupled line sections are largely taken to realize a good SWB pass band performance. All the predicted parameters, i.e., insertion loss, return loss, group delay are experimentally verified. It can be seen that, a SWB passband can be achieved from a UWB BPF, by decreasing the coupled line length and width of stub. When the ground plane is finite, resonator length is decreasing and the structure is without inset feeding, this leads to shift of the overall passband frequency to higher value. By giving the inset feed, better impedance matching is achieved and the SWB passband is realized. So, the pass band is tuned by the size of resonator length, coupling line length, stub width, ground plane and inset feed. The SWB BPF is fabricated using FR-4 substrate. The filter is simulated using HFSS software and realized using photolithographic technique. The outcome of FBW about 179% of this smaller and simpler structure is the achievement of the design. Here the insertion loss ≤ -0.9 dB and the variations in the group delay are around 0.3 ns throughout the pass band of 3.1 GHz-15.4 GHz and has a wide -30 dB rejection in the upper stop band. The simulated results are in good agreement with the measured ones and a sharp selectivity is achieved.

REFERENCES

[1] Federal Communications Commission, "Revision of part 15 of the commission's rules regarding ultra-wideband transmission systems," *Tech. Rep., ET-Docket 98-153*, FCC02-48, Apr. 2002.

[2] G. L. Matthaei, L. Young, and E. M. T. Jones, *Microwave Filters, Impedance-Matching Network, and Coupling Structures*, Norwood, MA: Artech House, 1980.

[3] S. Wong and L. Zhu, "Quadruple-mode UWB bandpass filter with improved out-of-band rejection," *IEEE Microw. Wireless Compon. Lett.*, vol. 19, no. 3, pp. 152-154, Mar. 2009.

[4] R. K. Mongia, M. Bahl, P. Bhartia, and B. Hong, *RF and Microwave Coupled-Line Circuits*, Norwood, Artech House, 2007.

[5] R. E. Collin, *Foundations for Microwave Engineering*, Wiley, 2001.

[6] Q.-X. Chu, X.-H. Wu, and X.-K. Tian, "Novel UWB bandpass filter using stub-loaded multiple-mode resonator," *IEEE Microw. Wireless Compon. Lett.*, vol. 21, no. 8, pp. 403-405, Aug. 2011.

[7] X.-H. Wu, Q.-X. Chu, X.-K. Tian, and X. Ouyang, "Quintuple-mode UWB bandpass filter with sharp roll-off and super-wide upper

stopband," *IEEE Microw. Wireless Compon. Lett.*, vol. 21, no. 12, pp. 661-663, Dec. 2011.

[8] Q.-X. Chu and X.-K. Tian, "Design of UWB bandpass filter using stepped-impedance stub-loaded resonator," *IEEE Microw. Wireless Compon. Lett.*, vol. 20, no. 9, pp. 501-503, Sep. 2010.

[9] H.-W. Deng, Y.-J. Zhao, L. Zhang, X.-S. Zhang, and S.-P. Gao, "Compact quintuple-mode stub-loaded resonator and UWB filter," *IEEE Microw. Wireless Compon. Lett.*, vol. 20, no. 8, pp. 438-440, Aug. 2010.

[10] L. Zhu, S. Sun, and W. Menzel, "Ultra-wideband (UWB) bandpass filters using multiple-mode resonator," *IEEE Microwave and Wireless Components Lett.*, vol. 15, no. 11, pp. 796-798, 2005.

[11] R. Li and L. Zhu, "Compact UWB bandpass filter using sub-loaded multiple-mode resonator," *IEEE Microwave and Wireless Components Lett*., vol. 17, pp. 40-42, 2007.

[12] S. Khalid, W. P. Wen, and L. Y. Cheong, "Synthesis and design of four pole ultra-wide band (UWB) bandpass filter (BPF) employing multi-mode resonators (MMR)," *IEEE/MTT-S International Microwave Symposium Digest*, Montreal, QC, pp. 1-3, 2012.

[13] W. Feng, X. Gao, W. Che, and Q. Xue, "Bandpass filter loaded with open stubs using dual-mode ring resonator," *IEEE Microw. Wireless Compon. Lett.*, vol. 25, no. 5, pp. 295-297, May 2015.

[14] B. Zhang, S. S. Li, and J.-M. Huang, "Wideband bandpass filter with wide stopband based on stub-loaded resonator," in *Proc. Asia-Pacific Microw. Conf. (APMC)*, pp. 922-924, Nov. 2014.

[15] B. Zhang, Y. Wu, C. Yu, and Y. Liu, "Miniaturised wideband bandpass filter based on harmonic suppressed dual transmission lines," *Electron. Lett.*, vol. 52, no. 9, pp. 734-736, Apr. 2016.

[16] A. Kamma, R. Das, D. Bhatt, and J. Mukherjee, "Multi-mode resonators based triple band notch UWB filter," *IEEE Microwave and Wireless Components Letters*, vol. 27, no. 2, Feb. 2017.

[17] L. Zhu, H. Bu, and K. Wu, "Broadband and compact multi-pole microstrip bandpass filters using ground plane aperture technique," *IEE Proc.-Microw. Antennas Propag.*, vol. 149, no. 1, pp. 71-77, Feb. 2002.

Aditi Sengupta was born in 1984. She received her B.Tech and M.Tech degree from West Bengal University of Technology, India in 2007 and 2011 respectively. Her field of interest includes microwave circuits, antennas and EMI/EMC. She is a member of IEEE and Life Member of Society of EMC Engineers (India).

Somdotta Roy Choudhury was born in 1982. She received her B.Tech degree in Electronics and Communication Engineering from West Bengal University of Technology, India in 2007 and M.E. degree in 2009 from Bengal Engineering and Science University, Shibpur. She obtained the Ph.D. degree in 2017 from Indian Institute of Engineering Science & Technology, Shibpur. Her research interests include the planar circuits, antenna elements and metamaterial structures etc.

Santanu Das was born in 1968. He received the B.E. degree in Electronics and Telecommunication Engineering from Bengal Engineering College of Calcutta University and M.E. degree from Jadavpur University, Calcutta, in 1989 and 1992 respectively. He obtained Ph.D. degree from Jadavpur University in 1998. He is a Professor in the Dept. of Electronics and Telecommunication Engineering in Indian Institute of Engineering Science & Technology. His research interests include microstrip circuits, FSS, antenna elements and arrays. He is a Life Member of the Institution of Engineers, India (IE).

A Compact Rejection Filter based on Spoof Surface Plasmon Polartions and Folded Split-Ring Resonators with Controllable Rejection Bandwidth

Luping Li, Peng Chen, Pengfei Zhu, and Kai Yang

School of Aeronautics and Astronautics
University of Electronic Science and Technology of China, Chengdu, 611731, P. R. China
lplees@outlook.com, chenp@uestc.edu.cn, uestc_zpf@163.com, kyang@uestc.edu.cn

Abstract ─ A novel rejection filter composed of the single comb-shaped spoof surface plasmon polariton (SSPP) and the folded split-ring resonators (FSRR) is proposed in this letter. By embedding the FSRRs into grooves of the low-pass SSPP filter, the compact rejection filter with the same size as the low-pass filter is consequently realized. Compared with traditional ones, the proposed filter provides simpler structure, more compact size, lower insertion loss, higher frequency and controllable rejection bandwidth. The dispersion interprets the transmission modes of the rejection SSPP unit. And the approaches of controlling the rejection band prove the fine controllability in the filter. The fabricated filter has a size of $3.23\lambda_g \times 0.24\lambda_g$, a central rejection frequency of 18.43 GHz, a fractional rejection bandwidth of 7.8%, maximum rejection depth of 42 dB, and an average passband insertion loss of 2.5 dB. The simulated rejection bandwidth controllable range is 4.0%~6.8%. Improved performances confirm the advantages of the proposed filter.

Index Terms ─ Compact rejection filter, controllable rejection bandwidth, folded split-ring resonator, spoof surface plasmon polariton.

I. INTRODUCTION

The surface plasmon polariton (SPP) is a kind of surface wave transmitting on the interface of substrate and dielectric in the infrared and optical band [1]. Owing to its ability to constrain the field to the subwavelength range from the interface, it has been applied to achieve a variety of optical devices. The SSPP is a manmade periodical array to imitate the subwavelength confine ability of the SPP in lower frequency bands and it has been applied into various microwave devices [2]-[4]. Due to its different design methods and ultra-wide passband characteristic than common filters, the SSPP filters are popular among microwave engineering [5]-[6].

The rejection filters loading rejection bands on passbands to reject unwanted signals in the passbands are indispensable devices for today's wideband communication systems. Since the SSPP just performs the wide passband frequency characteristic, it was attempted to achieve a rejection filter when the planar SSPP was first proposed [7]. Only one year later, Ref. [8] introduced some resonators to the side or back of the low-pass SSPP transmission line, where a rejection band was generated on the low-pass band and a rejection filter was realized. Reference [9] also achieved a similar rejection filter by etching resonators on the low-pass SSPP transmission line, where width of the SSPP transmission line was reduced. However, because the signal feeds of both filters are implemented through the coplanar waveguide, the filters still take wide areas. Reference [10] embeds the resonators into grooves of the SSPP transmission line and the signal feeding was achieved by the microstrip, where a more compact filter with much reduced width was presented. The dispersion of the rejection SSPP unit was also illustrated in Ref. [10], explaining the transmission modes of the rejection filter. However, the resonators in the mentioned filters all are double-ring ones, whose structures are relative complex and they are worth simplifying. In addition, none of these filters consider the control of the rejection bandwidth through the structural parameters.

This letter replaces the double-ring resonators of Ref. [10] with single-ring ones to achieve a simpler rejection filter with controllable rejection bandwidth. The dispersion of the rejection SSPP unit is also analyzed to illustrates the transmission modes of the rejection filter. Moreover, approaches of controlling the rejection frequency, the rejection depth, the rejection bandwidth and the filter's cutoff frequency through structural parameters all are detailed. The fabricated filter is also compared with traditional ones, which proves that the proposed one provides more compact filter size, higher rejection frequency, smaller insertion loss and controllable rejection bandwidth.

II. DISPERSION ANALYSIS

Schematic of the novel SSPPs unit is presented in Fig. 1 (a) and its structural parameters are listed in Table 1. The proposed SSPP unit embeds a folded split-ring resonator (FSRR) into groove of the single comb-shaped (SCS) SSPP unit. The SCS unit is a representative planar

Submitted On: September 15, 2018
Accepted On: May 12, 2019

SSPP unit and its fundamental dispersion mode is a low-pass one [7]. The schematic is designed on the substrate RT/duroid 5880 whose permittivity and thickness are 2.2 and 0.508 mm, respectively.

Dispersion of the SSPP unit is simulated in CST Microwave Studio and corresponding results are displayed in Fig. 1 (b). In the figure, the *Light Line* is the dispersion of the light transmitting in the vacuum. *Mode 0* and *Mode 1* are transmitting modes of the proposed SSPP unit. The yellow and blue regions are passbands of the SSPP unit and the gray one is a rejection band. Consequently, dispersion of the SSPP unit has a frequency characteristic of pass-reject-pass and the introduction of the FSRR inserts a rejection band on the passband of the SCS unit. Passbands of mode 0 and 1 are DC~17.86 GHz and 18.67~27.72 GHz, respectively. Accordingly, central frequency and bandwidth of the rejection band are 18.27 GHz and 0.81 GHz, respectively.

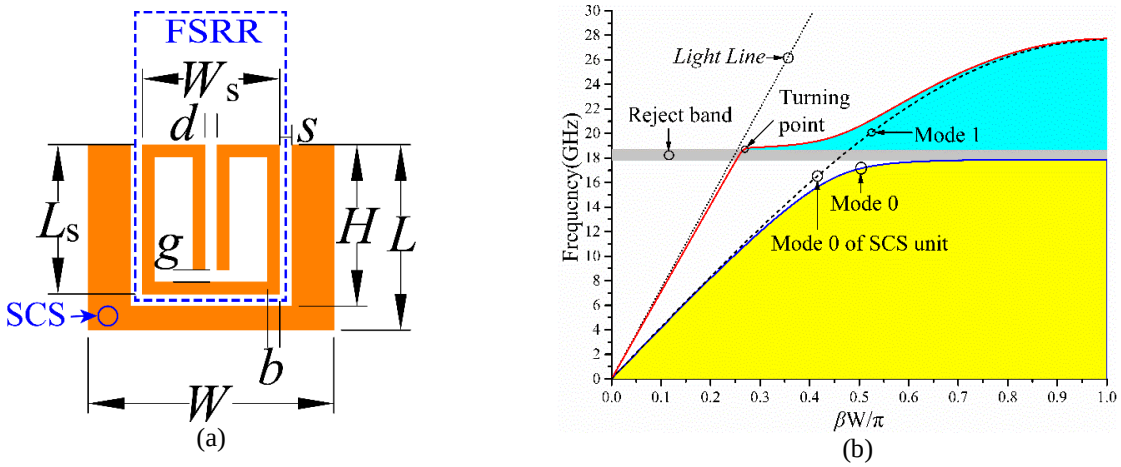

Fig. 1. Schematic and dispersion of the proposed SSPP unit: (a) the unit schematic and (b) the simulation dispersion.

Fig. 2. Schematic of the proposed rejection filter.

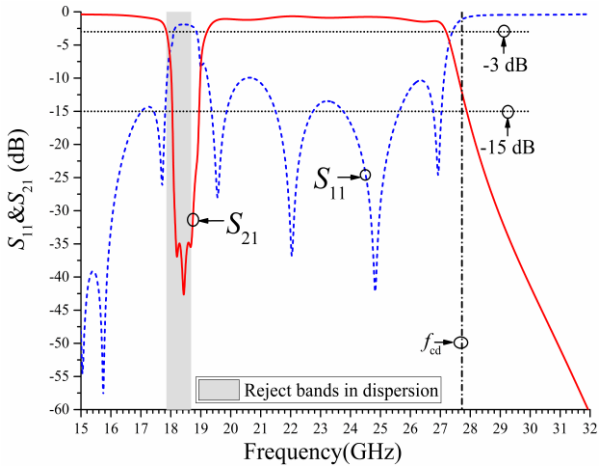

Fig. 3. Simulated S parameters of the proposed filter.

Table 1: Structural parameters of Fig. 1 (a)

Name	*L*	*W*	*Ls*	*Ws*
Value	1.54	2.04	1.24	1.14
Name	*H*	*d*	*s*	*g*
Value	1.34	0.1	0.1	0.1

III. FILTER SIMULATION

Due to the reject-pass-reject characteristic of the proposed SSPP unit, it is applied to achieve the proposed rejection filter in Fig. 2, where the SSPP part contains five periodical SSPP units and it determines the filter's frequency characteristics. The mode conversion parts transform the transmission modes of the microstrip and the SSPP bidirectionally and they are beneficial to the filter's performance. The microstrip is used for connecting with other microwave devices, width of which matches with 50 Ω characteristic impedance and it is 1.54 mm.

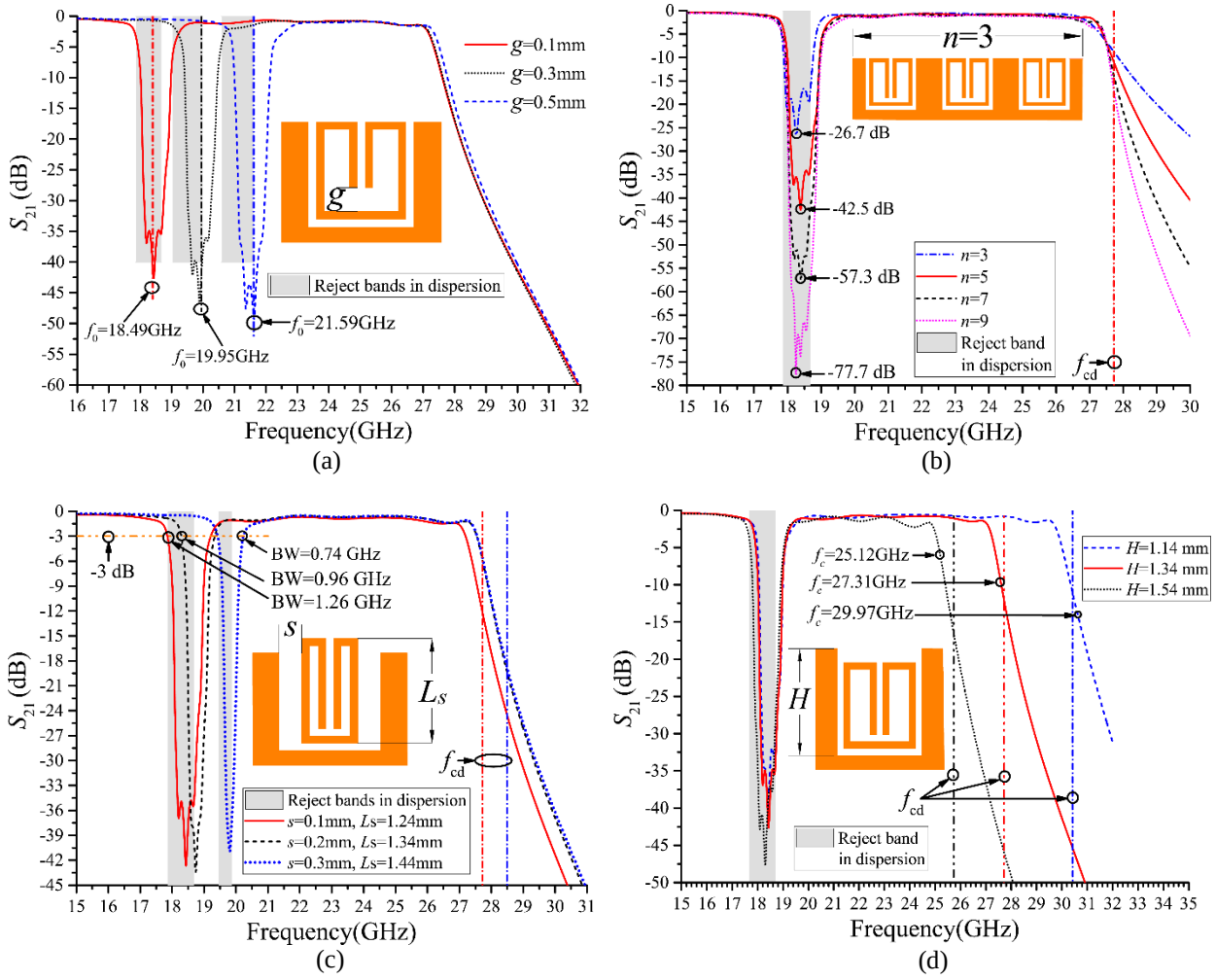

Fig. 4. Influence of the SSPP units on the frequency characteristics of the filter. (a) The influence of the FSRR length on the central rejection frequency; (b) the influence of the SSPP unit number on the rejection depth; (c) the influence of the structural parameter on the rejection bandwidth; (d) the influence of the groove depth on the filter's cutoff frequency.

The filter is simulated in CST Microwave Studio and simulation S parameters are displayed in Fig. 3, where the filter behaves one rejection band and two passbands. Central frequency and -3dB rejection bandwidth of the rejection band are 18.49 GHz and 1.26 GHz (6.8%), respectively. The -20dB rejection bandwidth and the maximal rejection depth are 0.84 GHz and 40.1dB, respectively. Moreover, the filter's cutoff frequency is 27.31 GHz and the average insertion losses in the passbands are 0.29 dB and 0.78 dB, respectively. Therefore, the filter provides a wide and deep rejection band.

The gray band in Fig. 3 is the rejection band of the dispersion, and f_{cd} is the cutoff frequency of *Mode 1*. According to the figure, the cutoff frequencies of the dispersion are closed to which of the filter, and the rejection bands of the dispersion are also entirely contained by which of the filter. This shows that frequency characteristics of the dispersion agree with those of the filter and the dispersion indicates the transmission modes of the SSPP units.

IV. FREQUENCY CHARACTERISTICS CONTROLLABILITY

To meet more demands in engineering applications, the methods of controlling the filter's S parameters through the structural parameters are discussed in this section.

A. Control on the central rejection frequency

In the proposed filter, the central frequency of the rejection band depends on the total length of the FSRR.

Accordingly, changing the length of the FSRR can alter the central frequency. The simulation results of three rejection filters with different *g* are illustrated in Fig. 4 (a) where the central frequency of the rejection band is increased by about 1.5 GHz when *g* increases by 0.1 mm, meanwhile the rejection bandwidth and the filter's cutoff frequency are roughly unchanged. The simulation result demonstrates that changing length of the FSRR can effectively control the central rejection frequency and make few impacts on other performances of the filter.

B. Control on the rejection depth

The effect of SSPP unit number on the rejection depth is shown in Fig. 4 (b), where the rejection depth is increased by about 16 dB as the SSPP unit number *n* increases by 2, and the central rejection frequency is maintained. In addition, the roll-off factor of the filter's cut-off band is also increased with the increasing of the SSPP unit number. Notably, dispersion of the SSPP unit remains unchanged in the whole process. The results indicate that number of the SSPP units can control the rejection depth and the roll-off factor. Meanwhile does not make influences on the central frequency of the rejection band.

C. Control on the rejection bandwidth

The influence of structural parameters on the rejection band is shown in Fig. 4 (c) where diverse *s* and *Ls* are set in different filters. According to the figure, the rejection band is decreased 0.52 GHz (2.8%) when *s* and *Ls* are increased 0.2 mm simultaneously, and the central frequency also shifts 1.31 GHz. Notably, total length of the FSRR in not changed in the processing, but the shape of the FSRR has been changed from a short and wide one into a high and thin one. It can be seen that the shape variation leads to changes in the rejection bandwidth and the central frequency. Besides, since the impact on the central frequency can be compensated by adjusting the FSRR's length, the rejection bandwidth control approach can be applied in engineering applications.

D. Control on the cutoff frequency

Groove depth *H* in low-pass comb-shaped SSPP filters almost decides their cutoff frequencies and it is usually used to control the cutoff frequencies. This approach is also applicable in the proposed rejection filter. Simulated S_{21} of three rejection filters with different *H* are illustrated in Fig. 4 (d), where the cutoff frequency is reduced by about 2.6 GHz as the groove depth increases by 0.2 mm, meanwhile the rejection band is nearly not affected. Two conclusions can be drawn from the simulation result. Firstly, the groove depth can effectively control cutoff frequency of the rejection filter. Secondly, frequency characteristics of the rejection band and the cutoff band are mutually independent and they can be independently controlled.

In conclusion, the approaches of controlling the central frequency, the rejection depth, the rejection bandwidth and the cutoff frequency are detailed in this section. The illustrated simulation results prove the fine frequency characteristics controllabilities of the proposed rejection filter and these controllabilities can be combined to meet different demands in practical designs. The application range of the filter is broadened by these controllabilities, especially the controllable rejection bandwidth contributes more to the broadening.

V. FABRICATION AND MEASUREMENT

Fabricated filter and microstrip are displayed in Fig. 5, where the microstrip is used for evaluating the additional loss from the welding, the substrate and the connectors. The filter and microstrip are put in the aluminum box to be measured by the vector network analyzer. Size of the filter is 40.0 mm×3.0 mm ($3.57\lambda_g \times 0.29\lambda_g$), where λ_g is the guided wavelength of the central rejection frequency. Substrate and length of the microstrip are same as the filter, where the characteristic impedance and length are 50 Ω and 40.0 mm, respectively.

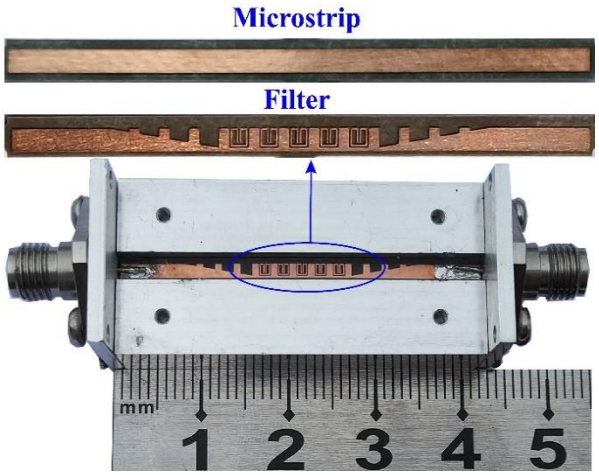

Fig. 5. Photograph of the fabricated filter and microstrip.

In the measurement, the microstrip is firstly measured and its S_{21} is normalized to 0 dB in the vector network analyzer before measuring the filter. Accordingly, measurement S_{21} of the filter has subtracted the loss of the microstrip. The measurement results are illustrated in Fig. 6, where the measurement S_{21} in Fig. 6 (b) is a result of taking away the measurement S_{21} in Fig. 6 (a). In the frequency band of 10-30 GHz of Fig. 6 (a), simulated and measured average insertion losses of the microstrip are 0.33 dB and 1.78 dB, respectively, hence the additional loss is about 1.45 dB.

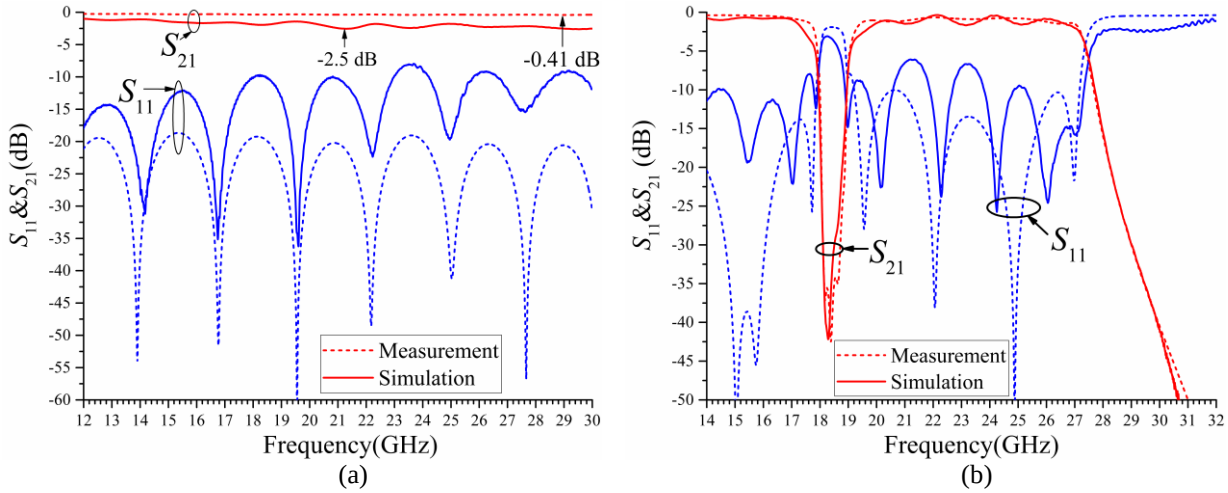

Fig. 6. Measurement S parameters of the fabricated filter and microstrip: (a) the microstrip and (b) the rejection filter.

Table 2: Comparison with SSPP rejection filters

Work	Size ($\lambda_g \times \lambda_g$)	f_0/GHz	*FBW* [1]/%	*IL*[2]/dB	Order	Depth	*RBC* [3]	Dispersion
[8]	5.64×1.40	6.75	1.9	4.6	8	-15	No	No
[8]	6.20×1.54	7.45	17.4	3.7	7	-42	No	No
[9]	13.4×3.18	8.15	5.8	5.5	5	-32	No	No
[9]	14.2×3.41	8.74	4.6	3.1	6	-33	No	No
[10]	5.85×0.15	14.47	14.7	4.3	5	-43	No	Yes
This work	3.23×0.24	18.43	7.8	2.5	5	-42	Yes	Yes

[1] *FBW* is the fractional rejection bandwidth;
[2] *IL* is the insertion loss of the passband;
[3] *RBC* is rejection bandwidth controllability.

As Fig. (b) demonstrates, central frequency and -3 dB bandwidth of the rejection band are 18.43 GHz and 1.45 GHz, respectively, thus the fractional rejection bandwidth is 7.9%. The -20dB rejection bandwidth is 0.84 GHz and the maximal rejection depth is 42.2 dB. The average insertion losses of two passbands are 0.58 dB and 1.02 dB, respectively. The filter's cutoff frequency is 27.32 GHz and the out-of-band rejection is greater than 60 dB. The measurement results agree well with the simulation, proving both the proposed filter and the design approach are available.

The comparison between traditional SSPP rejection filters and our filter is listed in Table 2, where the additional loss of our filter is taken into the total insertion loss. According to the table, the proposed filter provides more compact filter size, higher central frequency, middle rejection bandwidth and smaller insertion loss. In addition, the proposed filter gives the approach of controlling the rejection bandwidth for the first time. It can be concluded that the proposed filter has improved performances than traditional ones.

VI. CONCLUSION

By simplifying the structure of traditional SSPP units, a novel SSPP rejection filter with controllable rejection bandwidth is achieved in this letter. The dispersion is analyzed to explain the transmission mechanism of the rejection SSPP units. And the approaches of controlling the filter's S parameters through the structural parameters are also presented. The measured better performance than traditional filters proves that the proposed filter has an improvement from traditional ones.

ACKNOWLEDGMENT

This work was supported by the National Natural Science Foundation of China 61601088 and 61571093.

REFERENCES

[1] W. L. Barnes, A. Dereux, and T. W. Ebbesen, "Surface plasmon subwavelength optics," *Nature*, vol. 424, no. 6950, pp. 824-830, Aug. 2003.

[2] J. B. Pendry, "Mimicking surface plasmons with structured surfaces," *Science*, vol. 305, no. 5685, pp. 847-848, Aug. 2004.

[3] P.-S. Kildal, "Definition of artificially soft and hard surfaces for electromagnetic waves," *Electronics Letters*, vol. 24, no. 3, p. 168, 1988.

[4] P.-S. Kildal, "Artificially soft and hard surfaces in electromagnetics," *IEEE Transactions on Antennas*

and Propagation, vol. 38, no. 10, pp. 1537-1544, 1990.

[5] P. Chen, L. Li, K. Yang, and Q. Chen, "Hybrid spoof surface plasmon polariton and substrate integrated waveguide broadband bandpass filter with wide out-of-band rejection," *IEEE Microwave and Wireless Components Letters*, vol. 28, no. 11, pp. 984-986, Nov. 2018.

[6] J. Xu, et al., "Low-pass plasmonic filter and its miniaturization based on spoof surface plasmon polaritons," *Optics Communications*, vol. 372, pp. 155-159, Aug. 2016.

[7] X. Shen and T. Jun Cui, "Planar plasmonic metamaterial on a thin film with nearly zero thickness," *Applied Physics Letters*, vol. 102, no. 21, p. 211909, May 2013.

[8] B. C. Pan, Z. Liao, J. Zhao, and T. J. Cui, "Controlling rejections of spoof surface plasmon polaritons using metamaterial particles," *Optics Express*, vol. 22, no. 11, p. 13940, June 2014.

[9] Q. Zhang, H. C. Zhang, J. Y. Yin, B. C. Pan, and T. J. Cui, "A series of compact rejection filters based on the interaction between spoof SPPs and CSRRs," *Scientific Reports*, vol. 6, no. 1, p. 28256, Sep. 2016.

[10] S. Zhao, H. C. Zhang, J. Zhao, and W. X. Tang, "An ultra-compact rejection filter based on spoof surface plasmon polaritons," *Scientific Reports*, vol. 7, no. 1, p. 10576, Dec. 2017.

Luping Li received his Bachelor degree in Electronic Information Engineering from Chengdu University of Information Technology (CUIT) in 2016. Now he is studying his Master degree in University of Electronic Science and Technology of China (UESTC) since September 2016. His research interests are RF/microwave filters and metamaterials.

Peng Chen received Bachelor in Electronic Science and Technology and Ph.D. degree in Circuits and Systems from University of Electronic Science and Technology of China (UESTC) in 2009 and 2015, respectively, where he became a Lecturer in 2015. He was also a visiting scholar in Tohoku University, Sendai, Japan from November 2017 to November 2018. His main research interests are design and optimization RF and microwave devices and systems.

Pengfei Zhu received his Bachelor degree in Radio Wave Propagation and Antenna from University of Electronic Science and Technology of China (UESTC) in 2016, he is studying his Master degree at UESTC since September 2016. His research interests are RF/microwave circuits and systems.

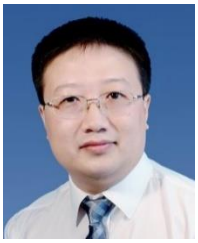

Kai Yang became an Associate Professor and a Professor of University of Electronic Science and Technology of China (UESTC) in 2001 and 2007, respectively. He became a Senior Member of Chinese Institution of Electronics in 2006. His research interests are RF/microwave circuits and systems, superconducting microwave components and circuit theory.

Non Destructive Testing of Cylindrical Ropes through the Parametric Transformer

Daniele Romano, Tommaso Scozzafava, and Giulio Antonini

UAq EMC Laboratory, Department of Industrial and Information Engineering and Economics
University of Study of L'Aquila, 67100 L'Aquila, Italy
giulio.antonini@univaq.it

Abstract – In order to ensure the safe operation of wire ropes, non-destructive testing methods are being applied to inspect wire ropes. Any geometrical discontinuity in magnetic permeability in the magnetized wire rope will impact the magnetic field conveyed by the rope, under a proper excitation. In this work, the electromagnetic device known as "parametric transformer" has is proposed for the non-destructive testing of ferromagnetic bodies having cylindrical symmetry, as tubes and ropes. The principle of its functioning is described by means of an equivalent magnetic network and a more rigorous approach using the Partial Element Equivalent Circuit (PEEC) method. Then, the proposed principle has been tested experimentally through the realization of a model which has confirmed the expected results.

Index Terms – Cylindrical ropes, non-destructive testing, parametric transformer.

I. INTRODUCTION

Steel wire ropes are the basic and important elements of loading, and, as such, they are widely employed in many fields, such as mining, architecture, transport, etc. Safe use of the wire ropes depends on their condition. Deterioration of a wire rope leads to a reduction of the wire rope safety factor. The manual inspection such as visual observing is often used to check wire ropes but it can only detect surface flaw, so this method is not that reliable. On the other hand, destructive inspection can only bring the information about tested part of rope and requires spare lengths of the rope be available for such test. Hence, non-destructive testing (NDT) for steel wire ropes has received increasing interest. The most popular NDT inspection methods include acoustic emission, electromagnetic methods [1, 2, 3], imaging methods. Among the electromagnetic methods, the most common technique applied in the NDT of ferromagnetic ropes are based on the magnetic inspection (MI) and in particular on the magnetic flux leakage (MFL) [4] making use of testing sensor, signal conditioning unit and computer system unit.

In this work a different approach is proposed. In particular, the parametric transformer is used to detect imperfections occurring in cylindrical ropes. Indeed, the principle is rather simple. Even small defects in the rope cause a magnetic flux to appear in the central limb of the transformer which is usually inactive in absence of defects. This flux causes an induced voltage on a sensing coil located on the same limb which can be easily measured by a voltage meter. The proposed method can be adopted in case of quite long ropes as those used in the elevators, cableways or skilifts when the length of the rope is in the range of tens, hundreds or even thousands of meters, to continuously monitor the state of the rope.

The paper is organized as follows. Section II briefly describes the parametric transformer (PT) and explains how it can be used for NDT purposes. The ideal model of the PT is presented in Section III and a simplified solution is proposed. In order to more accurately model the PT and give evidence to its capability to be used fo NDT purposes, the Partial Element Equivalent Circuit method is used. It is summarized in Section IV. The numerical results are presented in Section V confirming also numerically that the PT is effective in detecting small defects occurring in cylindrical ropes. The conclusions are drawn in Section VII.

II. THE PARAMETRIC TRANSFORMER

The parametric transformer (PT thereafter) is a "two ports" device based on any special symmetric magnetic circuits which couples an input coil with an output coil; this coupling is inactive until the above mentioned symmetry is guaranteed, and the mutual induction coefficient is zero. There are many types of PT with different shape of the magnetic circuit [5]; we chose the particular one shown in Fig. 1, in which

Submitted On: July 27, 2018
Accepted On: May 7, 2019

the magnetic circuit is completed by a sample of the material to be tested, so that any defect present in the sample breaks the magnetic symmetry, the mutual induction coefficient turns into a non-zero value and an output signal is obtained if the input port is powered.

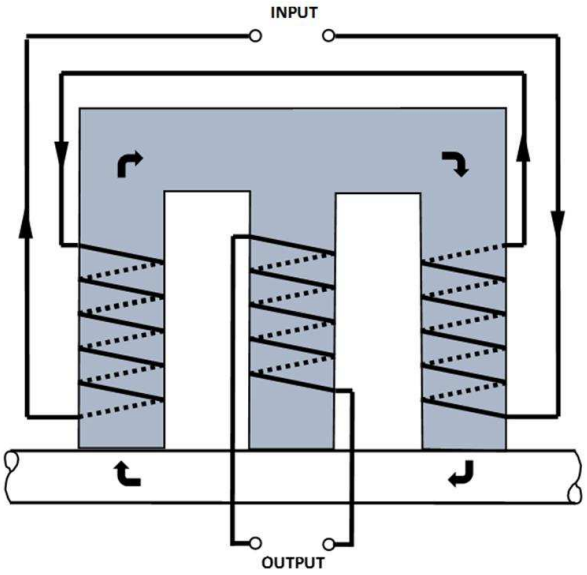

Fig. 1. Parametric transformer.

In Fig. 1, the coordinate directions of the currents and the magnetic fluxes are highlighted in order to clarify the functioning principle.

The equivalent magnetic network of this device is composed by:

- the left and right outer branches, including also their horizontal part, both of the same reluctance $\mathcal{R}$;
- the central branch of reluctance $\mathcal{R}_\mathcal{C}$;
- the sample of the material ferromagnetic to be tested, a part of which completes the magnetic mesh composed by the above mentioned outward branches; we set $\mathcal{R}_\mathcal{S} + \mathcal{R}_\mathcal{S} = 2\mathcal{R}_\mathcal{S}$ reluctance of this part if the sample is integer, but we set $2\mathcal{R}_\mathcal{S}+\mathcal{R}_\mathcal{D}$ if a defect of additional reluctance $\mathcal{R}_\mathcal{D}$ is present in its left or right part;
- two equal coils winding the two outward branches, powered by the same current, provides two equal exciting m.m.f. $\mathcal{F}$, having the same directions along the external magnetic mesh composed by the two outer branches and the portion of body under testing;
- a coil winding the central branch, providing an output signal if a variable magnetic flux ϕ appears in it.

In the first rough approach of the analysis of this device we assume:

- the magnetic fluxes are restricted inside the PT and inside the sample, namely no leakage flux exists;
- the behaviour of the PT and of the sample is linear.

III. IDEAL MODEL

If the aforesaid hypotheses are satisfied, we may draw the magnetic equivalent network of the Fig. 2. We assume the coils are powered by a steady state current; if the body to be tested may slide along (and in contact with) the three branches, a flux ϕ appears in the central branch when a defect of the sample is present; in Fig. 2 we suppose the existence of a defect in the right side.

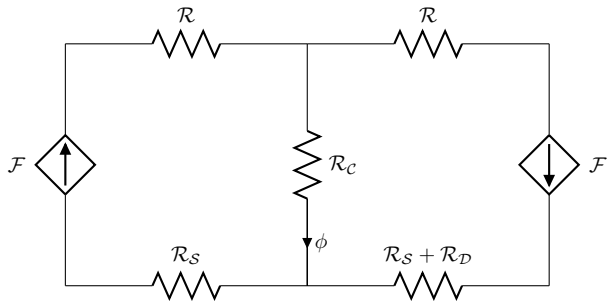

Fig. 2. Equivalent magnetic network.

If the sliding sample does not have any defect (that is if $\mathcal{R}_\mathcal{D} = 0$) a magnetic flux, whose value obviously equals $2\mathcal{F}/(2\mathcal{R}+2\mathcal{R}_\mathcal{S})$, is present only in the outer branches of the PT; consequently $\phi = 0$ and no output signal is present. If a defect occurs, the analysis (plain but cumbersome) of this network provides for the above flux the value:

$$\phi = \mathcal{F}\mathcal{R}_\mathcal{D}/[(\mathcal{R}+\mathcal{R}_\mathcal{C}+\mathcal{R}_\mathcal{S})(\mathcal{R}+\mathcal{R}_\mathcal{C}+\mathcal{R}_\mathcal{S}+\mathcal{R}_\mathcal{D})-\mathcal{R}_\mathcal{C}]. \quad (1)$$

Obviously the amplitude of the electrical output signal depends on the derivative of the flux ϕ and therefore on the flow rate of the sample, which may not be sufficient to obtain an adequate level; if, however, the feeding occurs in a sinusoidal regime, this limitation disappears and in addition there is the advantage of being able to perform the test even when stationary.

IV. BASIC PEEC FORMULATION

In order to verify the feasibility of the proposed methodology to detect defects in cylindrical ropes, the Partial Element Equivalent Circuit (PEEC) method [6] is used to model the parametric transformer and the rope. The PEEC method is based

on the volume equivalence principle of Maxwell's equations and use the electric field integral equation (EFIE) and the continuity equation. When conductors, dielectrics and magnetic materials are considered, the natural physical quantities which are usually adopted to express the magnetic vector potential are the electrical and polarization current densities and magnetization. Furthermore, the scalar electric potential is also used. Typically, rectangular basis functions are used to expand these quantities and to test the EFIE and continuity equation, based on the Galerkin's testing procedure. It results in the following set of equations:

$$\begin{bmatrix} j\omega\mathbf{P}^{-1} & -\mathbf{A}^T & \mathbf{0} \\ \mathbf{A} & \mathbf{Z}_s + j\omega\mathbf{L}_p & j\omega\mathbf{L}_m \\ \mathbf{0} & \mathbf{D} & \mathbf{T} \end{bmatrix} \cdot \begin{bmatrix} \mathbf{\Phi} \\ \mathbf{I} \\ \mathbf{M} \end{bmatrix} = \begin{bmatrix} \mathbf{I}_s \\ \mathbf{0} \\ \mathbf{GI}_s \end{bmatrix}, \tag{2}$$

where $\mathbf{P}$ accounts for the coefficients of potential, $\mathbf{L}_p$ is the partial inductance matrix, $\mathbf{L}_m$ represents the induced effects due to time varying magnetization, $\mathbf{D}$ and $\mathbf{T}$ matrices describe the constitutive relation of the magnetic field and $\mathbf{A}$ is the connectivity matrix. Matrix $\mathbf{Z}_s$ is diagonal with the self impedances of elementary volumes, which reduce to resistances for conductors [7] and the impedances of the excess capacitance [8] for dielectrics. Finally, $\mathbf{I}_s$ represents the independent current source which is assumed to drive the excitation coils. The term $\mathbf{GI}_s$ represents the magnetic flux density produced by the forced current. The derivation of (2) and the analytical formulas to fill matrices in (2) are detailed in [9, 10]. The time domain counterpart is straightforward to be obtained.

V. NUMERICAL TESTS

A 3D PEEC model of the parametric transformer has been set. It is shown in Fig. 3. The conductivity of the magnetic core is $\sigma = 10^6$ S/m and its relative magnetic permeability is $\mu_r = 400$ while the coils are made of copper ($\sigma = 5.8 \cdot 10^7$ S/m).

In addition a rope with a small defect (a hole with volume 1 cm^3) has been placed in the air-gap as shown in Fig. 3. The conductivity of the rope is $\sigma = 10^4$ S/m and its relative magnetic permeability is $\mu_r = 300$.

The geometrical parameters for the $x-y$ plane are given in Fig. 4. Respect to the z axis, both the rope and the magnetic core are 20 mm thick. The coils are 10 mm thick in all directions and the spacing between these and the magnetic core is 1 mm. Finally, the spacing between the rope and the magnetic core is 0.5 mm.

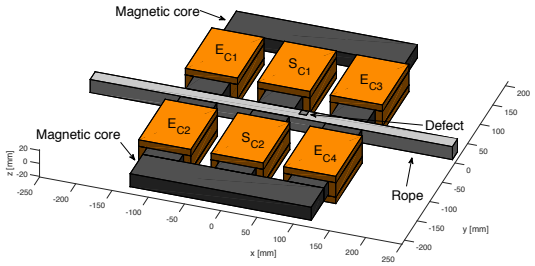

Fig. 3. 3D view of the PEEC model of the parametric transformer.

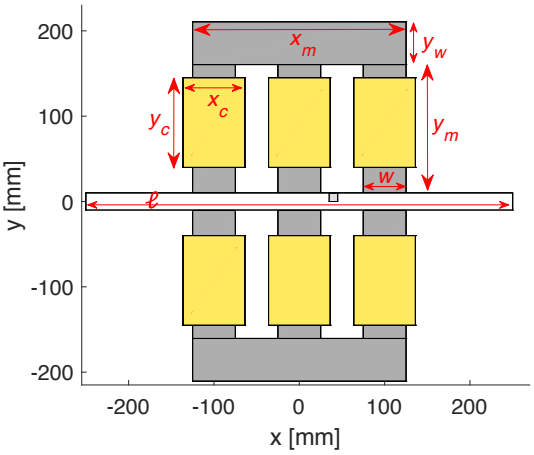

Fig. 4. Configuration of the parametric transformer, $x_m = 250$, $y_w = 50$, $y_m = 150$, $w = 50$, $x_c = 72$, $y_c = 105$ and $\ell = 500$ (all dimensions are in mm).

The excitation coils, namely $\mathrm{E_{C_1}}$, $\mathrm{E_{C_2}}$, $\mathrm{E_{C_3}}$ and $\mathrm{E_{C_4}}$, are driven by a 10 A sinusoidal current source (2.5 A for coil) varying at 50 Hz.

The analysis has been performed by using an uniform mesh resulting in by 9297 surface nodes, 29554 inductive branches and 3034 magnetic cells in the case of the absence of the defect for the rope while in the presence of the defect the mesh is constituted by 9297 nodes, 30304 inductive branches and 3180 magnetic cells.

The voltage revealed by the sensor coil $\mathrm{S_{C_1}}$ is reported in Figs. 5 and 6 for both the cases of absence and presence of the defect, respectively. As it is clearly seen, even a small defect, causes significant differences in the sensed voltage.

Finally, Figs. 7 and 8 show the z component ($|B_z|$) of the magnetic field for both the cases of absence and presence of the defect, respectively, at the time instant in which the excitation current is maximum (the surface in the x-y plane is located in the middle of the structure respect to the z axis). As before, a small defect causes significant differences also in the magnetic field.

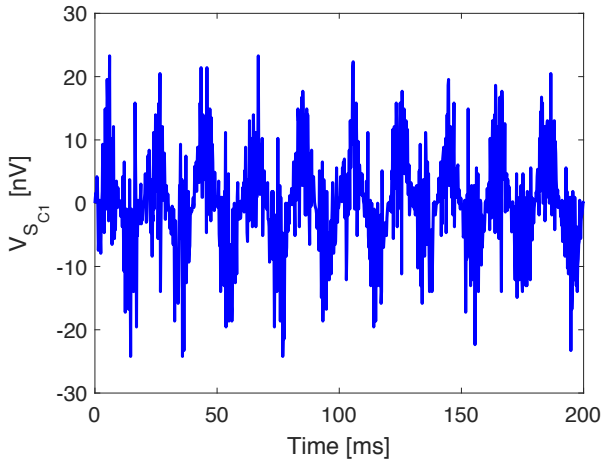

Fig. 5. S_{C_1} voltage without defect.

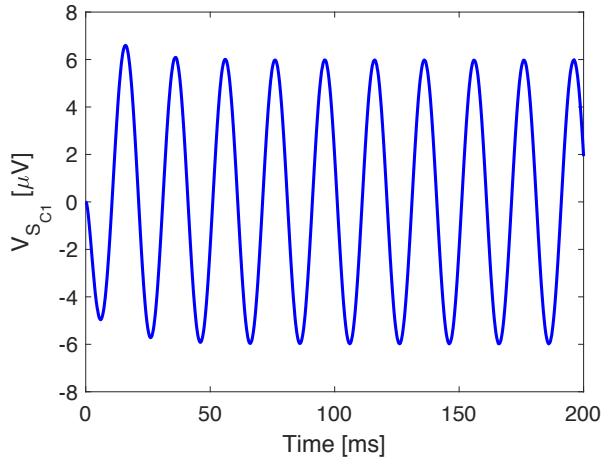

Fig. 6. S_{C_1} voltage in the presence of the defect.

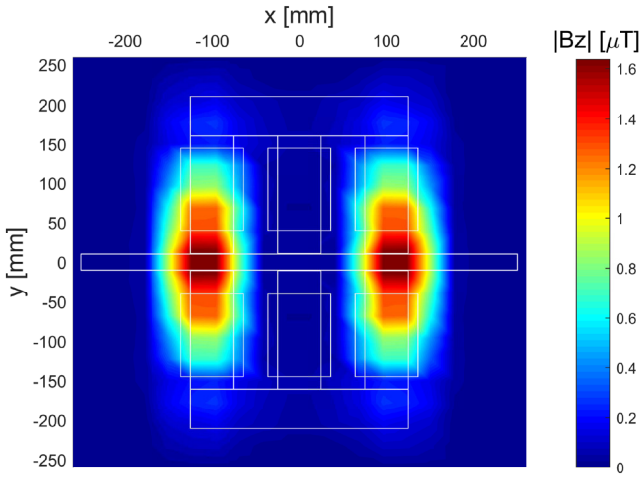

Fig. 7. $|B_z|$ without defect.

VI. EXPERIMENTAL SET-UP

Having described the operating principle, we describe now how we have realized the experimental

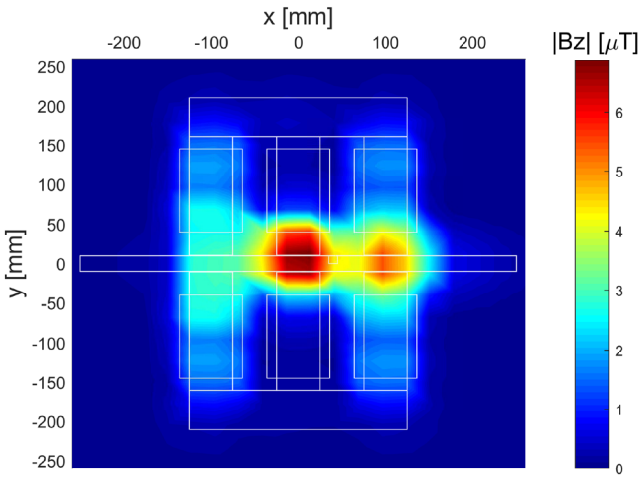

Fig. 8. $|B_z|$ in the presence of the defect.

fixture. We used for it the magnetic laminations of a common three-phase transformer; for a former prototype of this device it was chosen the arrangement shown in Fig. 1 [11]. In order to better identify the defects of the sample, the initial prototype has been developed as described in Fig. 1. Hence, it is constituted by two PTs mounted in opposite position; their outputs are connected in series, in order to obtain the sum of the two signals, with a significant improvement of the sensitivity.

The scheme of Fig. 2, which was used to clarify the operating principle, can no longer be used for quantitative evaluations, either because in the sinusoidal regime equation (1) should be recalculated in the complex field, and because it does not take into account the inevitable leakage flux that does not remain confined into the magnetic material under analysis. The estimation of this leakage flux is not easy. The rope sample has been modeled with a geometry composed of elementary parallelepipeds, in one of which an interruption has been introduced that simulates the defect. The permeability and resistivity values of the magnetic circuit are the normal values for a sheet from transformers, while for the cable we assumed the estimate of 400 as the average "iron-air" value of the relative permeability.

To evaluate the efficiency of the device, we carried out several series of measurements on a sample of parametric transformer, shown in Fig. 9. In the beginning, a piece of rope free of defects has been used. Since the operation must also take place with the rope in motion and this involves the existence of an air gap whose influence cannot be neglected, we have simulated its existence in the measurements (which were of the static type) by inserting two strips in cardboard 0.5 mm thick between the

Fig. 9. Experimental set-up.

sample and the surfaces of the pole pieces of the device. We fed the input with a 50 Hz sinusoidal generator at variable voltage, of which we measured the effective current and voltage values; of the signal at the output we measured the effective value in voltage. With the aforementioned sample, we have carried out a series of preliminary measurements that have served to highlight the inevitable constructional asymmetry of the apparatus, which produce a "bias" signal which must be taken into account in the results. Then the measurements were performed in the presence of defects that we simulated using the same integral sample to which we added a small piece of elementary wire at one of the two spaces between the poles.

Since the measurement is of the differential type, the equivalent of a lack of the same wire volume is obtained at the other space between the two poles. The results of the measurements were collected in Table 1, made up of 7 columns; in the first and in the second ones respectively, the effective values of the current C_{in} (in A) and of the voltage V_{in} (in V) at the input are indicated, having chosen to impose current values at constant intervals of 0.10 A; in the third column we have indicated the output voltage of "bias" (V_{bias}) detected with the rope sample intact; in the fourth and fifth columns we have indicated,

Table 1: Experimental results

C_{in}	V_{in}	V_{bias}	V_{outR}	V_{outL}	S_R	S_L
0.10	3.0	0.012	0.019	0.013	1.58	1.08
0.20	4.0	0.013	0.027	0.020	2.08	1.54
0.30	6.0	0.013	0.037	0.029	2.85	2.23
0.40	8.0	0.015	0.060	0.036	4.00	2.40
0.50	10.0	0.016	0.065	0.042	4.06	2.63
0.60	13.0	0.018	0.060	0.049	3.33	2.72
0.70	15.0	0.018	0.067	0.060	3.72	3.33
0.80	17.0	0.018	0.077	0.070	4.28	3.89
0.90	20.0	0.026	0.104	0.083	4.00	3.19
1.00	22.0	0.027	0.110	0.085	4.07	3.15
1.10	24.0	0.027	0.103	0.093	3.81	3.44
1.20	26.0	0.028	0.109	0.095	3.89	3.39
1.30	28.0	0.028	0.106	0.096	3.79	3.43
1.40	30.0	0.029	0.123	0.083	4.24	2.86
1.50	33.0	0.029	0.122	0.085	4.21	2.93
1.60	34.0	0.029	0.124	0.085	4.28	2.93
1.70	37.0	0.030	0.134	0.085	4.47	2.83
1.80	39.0	0.030	0.126	0.095	4.20	3.17
1.90	39.0	0.031	0.140	0.095	4.52	3.06
2.00	42.0	0.032	0.144	0.101	4.50	3.16
2.10	45.0	0.033	0.146	0.095	4.42	2.88
2.20	46.0	0.034	0.135	0.101	3.97	2.97
2.30	48.0	0.036	0.140	0.101	3.89	2.81
2.40	50.0	0.037	0.145	0.114	3.92	3.08
2.50	52.0	0.039	0.167	0.114	4.28	2.92

respectively, the output voltage with the fault positioned first on the right (as in Fig. 2) and then on the left of the central pole (V_{outR} and V_{outL}); in the sixth and seventh columns we have reported the respective useful signals (S_R and S_L) calculated as the ratio between the two aforementioned voltages and that of "bias"; S_R and S_L are obviously adimensional quantities. Figure 10 shows the measured voltages in presence of the defect at right (V_{outR}) and left (V_{outL}) of the central pole along with the bias voltage (V_{bias}).

A. Discussion

It can be seen how, while the input current increases with a constant pitch, the corresponding voltage does not increase with the same regularity; this is due to the fact that the rope, being composed of strands wound in a spiral, configures with the surfaces of the poles an average air gap that is variable and depends on the position assumed from time to time, when the defect is transferred from one part to the other of the sample. In other words, the reluctances $\mathcal{R}$ and $\mathcal{R}_{\mathcal{C}}$ of the scheme in Fig. 2 comprise the air gaps and are affected by their variability. It can also be noted that the state of the magnetic materials of the laminations and of the cable is always in the linearity zone, since the module of the

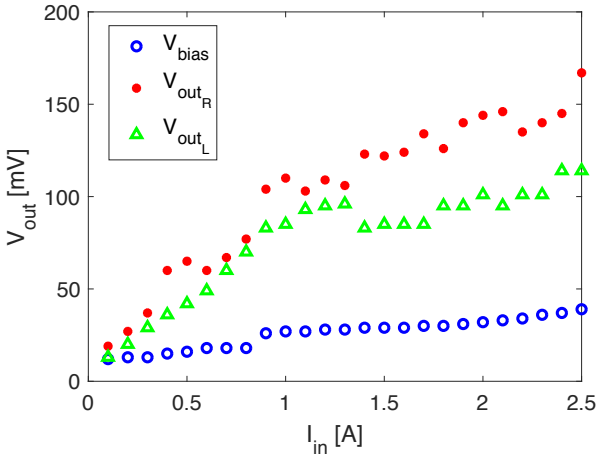

Fig. 10. Measured voltages in presence of the defect at right (V_{outR}) and left (V_{outL}) of the central pole and bias voltage (V_{bias}).

input impedance V_{in}/C_{in} has a very little variation between the minimum and maximum values of 20.0 Ω and 22.2 Ω (as is easy to verify) throughout the excitation current range between 0.10 A and 2.50 A. Its small variability is due to the not exact reproducibility of the air gaps during all the measurements. The magnitude of the fault signals (even these vary in an uncoordinated way, again due to the variability of the air gaps between one measurement and the other) seems sufficient to achieve the purpose for which the apparatus was designed, especially considering how the artificial failure has been achieved.

VII. CONCLUSIONS

The parametric transformer has been found effective in the detection of the defects present in a rope. A simple derivation has been presented along with a numerical simulation have given evidence to the theoretical claim. Furthermore, an experimental setup has been built and has confirmed the theoretical results, in spite of the complicated shape of the rope section which caused, owing to the variability of the air gap, little anomalies in the measurements. No doubt these anomalies disappear, if the material was a sample of a simple tube. In order to improve the output signal for the ropes, it is required a reduction of the air gap reluctances, achievable by an enlargement of the three poles along the axis of the sample. Despite these limitations, a satisfactory sensitivity has been achieved, confirming the possibility to use the parametric transformer as an effective device for non destructive testing of cylindrical ropes.

Acknowledgments

The authors acknowledge ELITAL s.r.l. of L'Aquila for having built and made available the parametric transformer.

REFERENCES

[1] M. Parise, "An exact series representation for the EM field from a circular loop antenna on a lossy half-space," *IEEE Antennas and Wireless Propagation Letters*, vol. 13, pp. 23–26, 2014.

[2] M. Parise, "On the surface fields of a small circular loop antenna placed on plane stratified earth," *International Journal of Antennas and Propagation*, vol. 2015, pp. 1–8, 2015.

[3] M. Parise, "Full-wave analytical explicit expressions for the surface fields of an electrically large horizontal circular loop antenna placed on a layered ground," *IET Microwaves, Antennas and Propagation*, vol. 11, pp. 929–934, 2017.

[4] C. Tomasz, P. Grzegorz, T. Takashi, and B. Bartosz, "Evaluation of fatigue-loaded steel samples using fusion of electromagnetic methods," *Journal of Magnetism and Magnetic Materials*, vol. 310, pp. 2737–2739, 2007.

[5] E. S. Tez and I. R. Smith, "The Parametric Transformer: A Power Conversion Device Demonstrating the Principles of Parametric Excitation," *IEEE Transactions on Education*, vol. E-27, no. 2, p. 9, 1984.

[6] A. E. Ruehli, G. Antonini, and L. Jiang, *Circuit Oriented Electromagnetic Modeling Using the PEEC Techniques*, Wiley-IEEE Press, 2017.

[7] A. E. Ruehli, "Equivalent circuit models for three dimensional multiconductor systems," *IEEE Transactions on Microwave Theory and Techniques*, vol. MTT-22, no. 3, pp. 216–221, Mar. 1974.

[8] A. E. Ruehli and H. Heeb, "Circuit models for three-dimensional geometries including dielectrics," *IEEE Transactions on Microwave Theory and Techniques*, vol. 40, no. 7, pp. 1507–1516, Jul. 1992.

[9] D. Romano and G. Antonini, "Quasi-Static Partial Element Equivalent Circuit Models of Linear Magnetic Materials," *IEEE Transactions on Magnetics*, vol. 51, no. 7, pp. 1–15, Jul. 2015.

[10] L. Lombardi, D. Romano, and G. Antonini, "Analytical Formula for the Magnetic-to-Electric Field Coupling of Magnetization in the Partial Element Equivalent Circuit Method," *IEEE Transactions on Magnetics*, vol. 54, no. 10, pp. 1–12, Oct. 2018.

[11] T. Scozzafava, "Differential magnetoscope," Italian Ministry of Industry, Italian Patent N.1182775, Oct. 1987.

Daniele Romano was born in Campobasso, Italy, in 1984. He received the Laurea degree in computer science and automation engineering in 2012 from the University of L'Aquila, L'Aquila, Italy. He received the Ph.D. degree in 2018. Since 2012 he has been with the UAq EMC Laboratory, University of L'Aquila, focusing on EMC modeling and analysis, algorithm engineering and speed-up techniques applied to EMC problems.

Tommaso Scozzafava received the Laurea degree (*cum laude*) in industrial electrical engineering from the University of Rome "La Sapienza", Italy, in 1960. Since 1971, he has been with the University of L'Aquila, where he has been an Associate Professor from 1982 until 2002. His scientific interests are in the field of electrical engineering and measurements.

Giulio Antonini received the Laurea degree (*cum laude*) in electrical engineering from the University of L'Aquila, L'Aquila, Italy, in 1994 and the Ph.D. degree in electrical engineering from University of Rome "La Sapienza" in 1998. Since 1998, he has been with the UAq EMC Laboratory, University of L'Aquila, where he is currently a Professor. He has coauthored the book "*Circuit Oriented Electromagnetic Modeling Using the PEEC Techniques*", (Wiley-IEEE Press, 2017). His scientific interests are in the field of computational electromagnetics.

Multilayer Half-Mode Substrate Integrated Waveguide Wideband Coupler with High Selectivity

Zhigang Zhang, Yong Fan, and Yonghong Zhang

Fundamental Science on Extreme High Frequency Key Laboratory
University of Electronic Science and Technology of China, Chengdu 611731, China
freemanzzg@163.com, yfan@uestc.edu.cn, zhangyhh@uestc.edu.cn

Abstract ─ A novel 3dB wideband coupler with enhanced selectivity has been proposed and developed in multilayer HMSIW topology. Periodic ginkgo leaf slots (GLS) are etched on top layer of HMSIW to realize a pass-band combining with high-pass characteristics of HMSIW. The novel GLS cells have stop-band characteristics aiming to improve the frequency selectivity and extend the upper stop-band. Moreover, the roll-off at the upper side is very sharper. A continuous coupling slot is etched in the conductor layer at the broadwall of HMSIW. Coupling takes place through the long, offset slot, which features a flexible design providing a wide coupling dynamic range with wideband characteristics. Detailed design process is introduced to synthesize a wideband filtering HMSIW coupler with better stop-band rejection. The novel coupler is showing a 34.9% coupling bandwidth at 8.87 GHz with good isolation, reflection and out-of-band rejection performances. Its stop band is from 13.8 to 17.6GHz with the rejection more than 40dB. Good agreement is obtained between the simulated and measured results of the proposed structure.

Index Terms ─ Electromagnetic band gap (EBG), Half-mode Substrate Integrated Waveguide (HMSIW), high selectivity, multilayer, wideband coupler.

I. INTRODUCTION

Directional couplers are essential components in transceivers for microwave communication systems. Because they have a great impact on the overall system performance, wideband, low insertion losses and high isolation are usually required in many applications. The substrate integrated waveguide (SIW) technology [1-17] is a promising candidate for modern wireless transceiver systems and has provided an excellent trade-off between waveguide and planar technologies [18-24] in terms of quality factor, volume, the losses, power handling and easy integration.

Nevertheless, the conventional SIW circuits are still too large for millimeter wave systems. Several solutions have been proposed to reduce the footprint of SIW structures, including the half-mode substrate integrated waveguide (HMSIW) [2-6] and the substrate integrated folded waveguide (SIFW) [7-8]. These two topologies allow the width of the SIW to be reduced by a factor of two. In [2], a 3-dB coupler is realized at Ku band using HMSIW, which keeps the good performance of the SIW coupler with nearly a half reduction in size. A ridged HMSIW was proposed in [5], which open side is capacitively loaded with a continuous ridge so as to lower the first-mode cutoff frequency. In [8], the proposed dual-band rat-race coupler was developed in the FSIW, consisting of two stacked layers of substrates.

Recently, miniaturization design is becoming one of the primary trends for many applications in transceivers. On one hand, the use of multilayered topologies [9-11] is known to provide more freedom to design coupling paths and control coupling levels between waveguided structures while preserving a compact circuit size. On the other hand, more and more attention has been paid to single devices integrated with different functionalities, such as a bandpass balun, bandpass coupler [12], and bandpass antenna [13]. A reduced size rat-race SIW coupler incorporating a bandpass frequency response characteristic was presented in [12].

The SIW has highpass performance and the periodic electromagnetic band gap (EBG) structures have slow-wave and stop-band characteristics [14-16]. As such, a periodic configuration is etched on the top layers of the HMSIW to realize the wideband filtering response. In [14], an EBG-loaded ridge substrate integrated waveguide (RSIW) ring coupler was presented. The periodic EBG structures are employed to increase the propagation constant to achieve further size reduction. In [16], a wideband directional coupler was proposed on the basis of the concept of slow-wave HMSIW to achieve compact size. Generally speaking, some problems faced by the above-mentioned structures are poor stopband suppression or narrower bandwidth. How to solve these two problems at the same time has been attracting increasing attention.

In this paper, to overcome the limitation of a conventional coupler, a novel wideband directional

Submitted On: November 19, 2018
Accepted On: March 3, 2019

filtering coupler with enhanced selectivity has been proposed and developed in multilayer HMSIW topology. Periodic ginkgo leaf slots (GLS) are etched on top layer of HMSIW to realize a pass-band combining with high-pass characteristics of HMSIW. The dimensions of the coupling slot and HMSIW are used to determine both the coupling ratio and the center frequency. Meanwhile, it is possible to control the bandwidth and the rejection level by adjusting the parameters of GLS. It's a good combination of multilayered topologies, HMSIW and EBG structures.

II. ANALYSIS AND DESIGN

A. Filtering coupler structure

As shown in Fig. 1 (a), Port 1 is the input port; Port 2 is the through port, whereas Ports 3 and 4 are coupling port and isolation port, respectively.

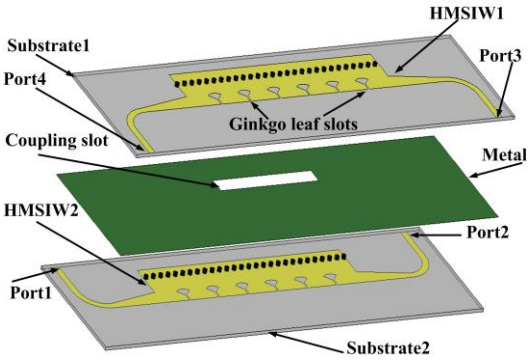

(a)

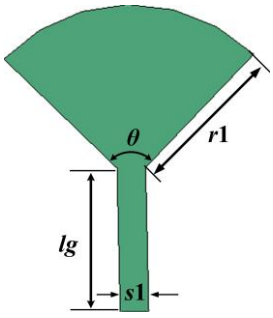

(b)

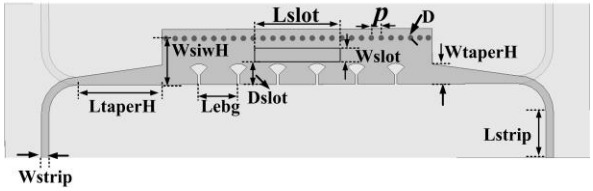

(c)

Fig. 1. The proposed HMSIW filtering coupler with GLS cells: (a) anatomy view, (b) geometries of ginkgo leaf slots (GLS), and (c) top view.

The multilayer E-plane HMSIW coupler consists of two parallel waveguides (HMSIW1 and 2) coupled together by means of a longitudinal slot etched in their common broad wall. The long coupling slot have variable lengths (Lslot), widths(Wslot) and offsets (Dslot), and are arranged with respect to the distribution of $TE_{0.5,0}$ mode. In the coupling region, the coupling slot is located on the metal plane between substrate 1 and 2. As depicted in Fig. 1 (b) and Fig. 1 (c), a periodic GLS configuration is etched on the top layer of the HMSIW1 and 2 to realize the wideband filtering response.

B. Analysis of coupler

As discussed above, the width of the HMSIW is half that of the SIW, so the width of an SIW properly operating in the same frequency range should be determined at first on the basis of the design considerations in [2-3]. The HMSIW has highpass performance and the electromagnetic band gap (EBG) structures have stop-band characteristics.

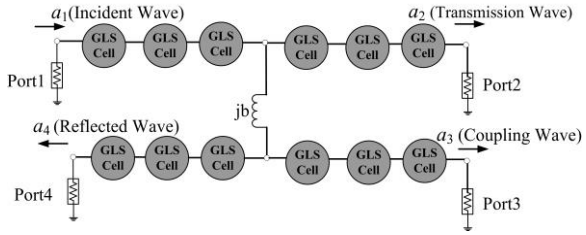

Fig. 2. Schematic of the filtering coupler with GLS.

Figure 2 illustrates the schematic of a four-port filtering coupler. As seen, the proposed structure integrates a bandpass filter and a directional coupler. There are three steps to design the proposed coupler. First, the cutoff frequency for the HMSIW can be determined by the following formulae:

$$a_{eff} = a_{siw} - \frac{D^2}{0.95 \cdot p}, \quad f_{c(TE10)} = \frac{c}{2a_{eff}\sqrt{\varepsilon_r}}. \tag{1}$$

Where, a_{eff} and a_{siw} are the equivalent and real width of SIW, respectively. a_{Hsiw} is the width of HMSIW (a_{siw}=2a_{Hsiw}). D and p are the diameter of metallized via-holes and center-to-center pitch between two adjacent via-holes. c is the light velocity in vacuum, and ε_{r} is the dielectric constant of substrate. Secondly, the dimensions of the coupling slot and the feed lines for transition between the HMSIW and the microstrip are determined to achieve equal coupling strength. Finally, the parameters of the GLS and the periodic separation can be determined by using electromagnetic simulation to obtain good out-of-band rejection.

As observed in Fig. 1 (a) and Fig. 3, the physical fields existing in the structure can always be expressed as the superposition of these two modes, i.e. even mode

and odd mode. When the ports 1 and 4 are excited with two signals of same amplitude and phase, only $TE_{0.5,\,0}$ mode (even mode) can be observed in the coupling region. However, when the two ports are excited by two signals with same amplitude but reverse phase, only TEM mode (odd mode) can be found. The electric field intensities of $TE_{0.5,\,0}$ mode and TEM mode are summed at ports 2 and 3, resulting in the power output at these two ports.

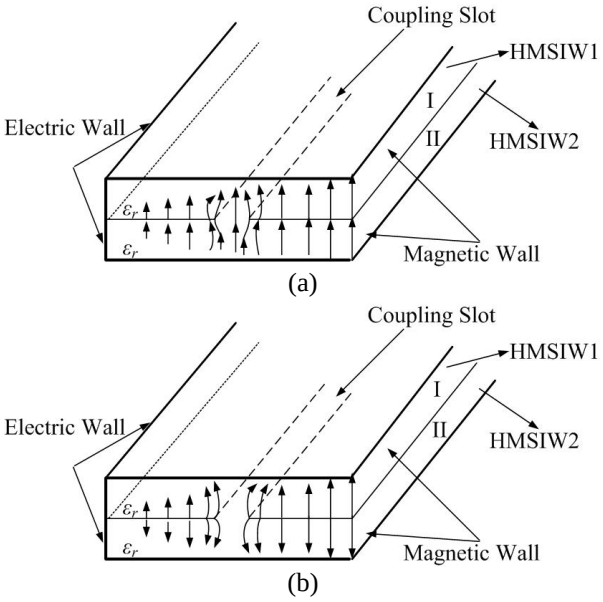

Fig. 3. Electric field distribution in coupling region: (a) even mode and (b) odd mode.

The superposition filed in the coupling slot satisfies [10]:

$$A_I(z) = a_1 e^{-j\beta z}\cos(Kz), \tag{2}$$

$$A_{II}(z) = j a_1 e^{-j\beta z}\sin(Kz), \tag{3}$$

$$K = \frac{1}{2}(\beta_e - \beta_o) = \frac{1}{2}\Delta\beta = \pi(1/\lambda_{0.5,0} - 1/\lambda_{TEM}), \tag{4}$$

where, β_e and β_o are the propagation constant of even mode and odd mode respectively. In this way, within the coupling region, there are two kinds of modes, namely $TE_{0.5,\,0}$ mode in HMSIW and *TEM* mode in stripline. Supposing the length of the coupling region as *L*, the wavelength of $TE_{0.5,\,0}$ mode in HMSIW as $\lambda_{0.5,0}$, whereas the wavelength of *TEM* mode as λ_{TEM}. The coupling ratio at port 3 can be controlled by changing the size of the coupling region, it can be defined as:

$$C = 20\times\lg\left|\frac{A_{II}(L)}{a_1}\right| = 20\times\lg\left|\sin(KL)\right| = 20\times\lg\left|\sin(\frac{\Delta\beta}{2}L)\right|. \tag{5}$$

For a 3-dB coupler(*C*=-3dB), we have,

$$\Delta\beta L = \pi/2 = (\beta_e - \beta_o)\,L. \tag{6}$$

According to reflection suppression condition of $TE_{0.5,\,0}$ mode at both ends of coupling region [25]:

$$1 + e^{-j2\beta_e L} = 0. \tag{7}$$

Based on (7), we have,

$$\sin(2\beta_e L)=0, \text{ and } \cos(2\beta_e L) = -1. \tag{8}$$

So that the relation between β_e and *L* is given by,

$$\beta_e L = (2n+1)\,\pi/2. \tag{9}$$

From (6) and (9), the propagation constant of the two modes is thus obtained:

$$\frac{\beta_o}{\beta_e} = \frac{2n}{2n+1}. \tag{10}$$

When the difference between the propagation constants increases the coupled length *L* decreases. Therefore, smaller value of n corresponding to shorter coupler slot. Hence,

$$\beta_o/\beta_e = 2/3 \ (n=1). \tag{11}$$

In the coupling region of coupler, the propagation constant for $TE_{0.5,0}$ mode is given below:

$$\beta_e(f) = \sqrt{\left(\frac{2\pi\sqrt{\varepsilon_r}f}{c}\right)^2 - \left(\frac{\pi}{a_{eff}}\right)^2}. \tag{12}$$

According to the theory of Bethe hole, there is an approach to obtaining flat coupling versus frequency. So, the initial location of the coupling slot is given by [26], [27]:

$$D_{slot} = a_{eff}/4. \tag{13}$$

At the center frequency *f*, the initial length of the coupling region (*L*) may be determined by using formula (6), (10), (11), and (12).

C. EBG design

EBG structures are periodic structures that produce variations in the refractive index of the medium to introduce both a slow-wave effect and a certain stopband in its frequency response. The following step is to identify the EBG dimensions to be used for realizing out-of-band rejection. In Fig. 1 (b), there are five parameters to determine the band-gap properties: the periodic separation Lebg between adjacent EBG cells, the radius *r*1, the angle θ, the length lg, and the width *s1* of the GLS cell. The radius of the GLS structures *r1* (the first parameter) was increased in steps to find out its influence on the bandwidth and rejection, as shown in Fig. 4 (a).

The simulated results in Fig. 4 (a) revealed that for increasing radius of GLS, the relative bandwidth of the coupler was also found to decrease correspondingly. The parameters of the EBG cells (*r*1, *s*1) as well as the relative bandwidth are summarized in Table 1.

The second parameter is the width *s*1 of the EBG cell. Fig. 4 (b) shows the relationship between relative bandwidth and *s*1. The coupling bandwidth increases when the width *s*1 of the EBG cell is increased. In addition, smaller *s*1 corresponds to narrower bandwidth and steeper rolloff slope in transition band.

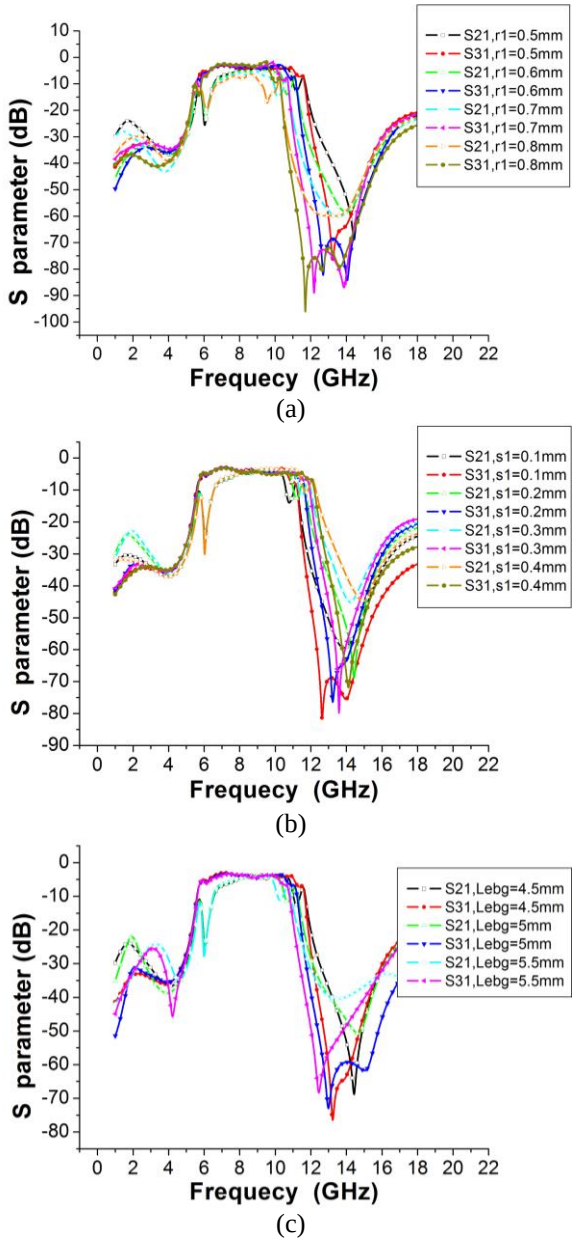

Fig. 4. Variation of frequency responses with respect to the parameters of the GLS cells: (a) the radius *r*1, (b) the width *s*1, and (c) the period Lebg.

Table 1: Relative bandwidth $\Delta f/f_0$ change with *r1* and *s*1

***r1* (mm)**	**$\Delta f/f_0$ (%)**	***s*1 (*mm*)**	**$\Delta f/f_0$ (%)**
0.5	38.16	0.1	34.18
0.6	33.42	0.2	38.16
0.7	27.44	0.3	42.04
0.8	23.16	0.4	45.19

The third parameter is the period Lebg of the structure, as it controls the center frequency of the stopband where Lebg=$\lambda_{gs}/2$ and λ_{gs} is the corresponding guided wavelength of the stopband center frequency. Lebg should be chosen such that, this stopband comes after the band of operation required.

The period (Lebg) of the EBG cells can be calculated by using HFSS. As shown in Fig. 4 (c), the center frequency of the stopband (f_s) reduces evidently with the distance between the EBG cells increased. Table 2 illustrates the period Lebg may affect the center frequency of the stopband and the corresponding guided wavelength.

Table 2: f_s and relative bandwidth change with *L*ebg

***L*ebg (*mm*)**	**f_s (GHz)**	**$\Delta f/f_0$ (%)**
4.5	15.85	38.16
5	15.79	35.79
5.5	15.17	32.56

The number of EBG structure controls the rejection whereas the bandwidth is determined by the size (which is controlled by the radius and width) of the EBG structure. Such configuration can be employed efficiently where wide-band stopband rejection is desired. Finally, the rest of the dimensions are estimated using HFSS simulation tool.

D. Coupling slot

As depicted in Fig. 1, the coupling slot is located on the metal plane between substrate 1 and 2. Moreover, the long coupling slot has variable lengths (Lslot), widths (Wslot) and offsets (Dslot), and the design parameters control the mutual coupling between two parallel waveguides.

From the formula (5), (6), and (12) we can see that the coupling ratio depends on the lengths (Lslot=L) of coupling slot. For a 3-dB coupler, $\Delta\beta$ decreases with increasing lengths (Lslot) of coupling slot. In addition, Lslot is also related to the center frequency of the coupler.

Table 3: Coupling ratio and f_0 change with Dslot

Dslot (mm)	**f_0 (GHz)**	**Coupling Ratio (dB)**
2.5	7.6370	-4.8276
3	8.6437	-4.1445
3.5	8.9273	-4.0869
4	9.0407	-3.9610
4.5	9.0832	-3.9045

But for a 6-dB coupler ($\Delta\beta L=\pi/3$), the length (Lslot=L) of coupling slot is shorter than the corresponding length of a 3-dB coupler. The other two parameters of the coupling slot have effects on both the coupling ratio and the center frequency.

According to the Table 3, both coupling ratio and the center frequency (**f_0**) of the coupler increase when the offset (Dslot) is increased.

Table 4: Coupling ratio and f_0 change with Wslot

Wslot (mm)	f_0 (GHz)	Coupling Ratio (dB)
2	8.9862	-3.9778
2.5	9.0430	-3.9611
3	9.2131	-3.9956
3.5	9.2273	-3.9917
4	9.2982	-4.0039

The simulated results in Table 4 revealed that for increasing widths (Wslot) of coupling slot, the center frequency of the coupler was also found to increase correspondingly. However, the change of coupling ratio is just the opposite. Moreover, it has to be noted that among all of the parameters of the slots, the offset distance (Dslot) has a critical effect. This is due to its direct impact on the field within the coupling slot as it causes a rapid variation for small offsets and slow variations for larger ones.

E. Deign example

In our design, the center frequency and relative bandwidth of the filtering coupler are 9 GHz and 36%, respectively. The used substrate is Taconic RF35 with relative permittivity (ε_r) of 3.5 and height of 0.508 mm.

Based on our knowledge, HMSIW structure has high-pass characteristics and can be used to realize lower sideband response of coupler. In addition, periodic ginkgo leaf slots (GLS) determine the center frequency of the stopband and can be used to form upper sideband response. As such, bandpass response of the coupler can be easily realized by combining above two characteristics. After the parameters of GLS cells have been properly adjusted, better out-of-band rejection in wideband may be achieved at the same time.

Therefore, the first step is to decide the dimensions of HMSIW structure. According to our specification, the cutoff frequency for the $TE_{0.5,0}$ dominant mode in HMSIW is estimated to 6.3GHz. By using (1), the initial values of width of HMSIW (a_{Hsiw}) should be 6.5 mm. There are six EBG cells in our design, as shown in Fig. 1. So, the length of the HMSIW should be at least more than five times of period of EBG cells. As such, the initial length of HMSIW can be determined as: L_{Hsiw}=8 *L*ebg.

The second step is to determine the parameters of GLS cells. As above discussion, the period of the GLS cells controls the center frequency of the stopband (f_{s0}) which can be calculated by using HFSS. According to Fig. 4 (c), Table 2, and our specification, the value ranges for the center frequency of the stopband are from 15.17 to 16GHz. Thus, the value ranges for period of EBG cells *L*ebg are from 4.5 to 6 mm.

The bandwidth and rolloff slope in the transition band are also affected by the radius *r1* and the width *s1* of the GLS structures. According to Table 1 and the specifications, the value ranges for the radius *r1* are from 0.5 to 0.6mm. Similarly, as observed in Table 1, the value ranges for the width *s*1 are from 0.1 to 0.3mm.

The third step is to calculate the length and location of coupling slot in HMSIW coupler. According to (6), (11), (12), and (13), the initial length (*L*slot) and location (*D*slot) of coupling slot should be 17.75mm and 3.38mm, respectively. Based on above considerations, the final optimal dimensions of the proposed coupler can be easily determined.

III. SIMULATED AND MEASURED RESULTS

After optimization implemented by HFSS, the geometry parameters of the proposed coupler are listed in Table 5. The proposed coupler was designed and fabricated on a substrate with thickness of 0.508 mm, relative dielectric constant of 3.5 and dielectric loss tangent 0.0018 (at 10 GHz). The simulated and measured results of S11, S21, S31 and S41 are presented in Fig. 5 (a).

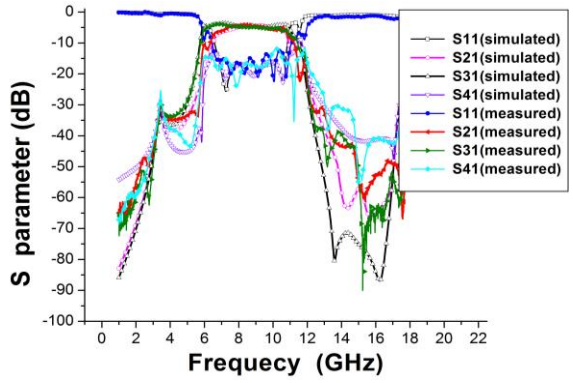

(a)

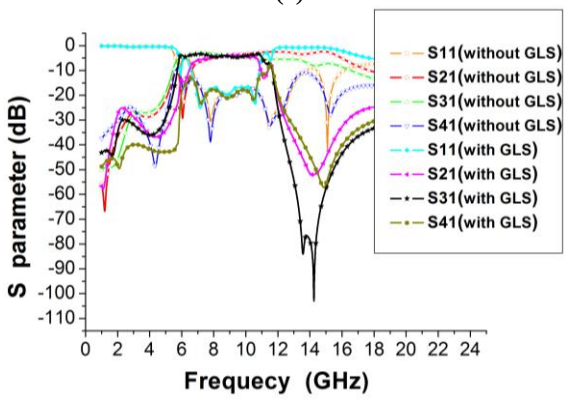

(b)

Fig. 5. Response of the coupler: (a) The proposed coupler with high selectivity, and (b) The coupler with and without GLS.

In the frequency range 6.6-10.7 GHz, the return loss (S11) is below -14.5dB. The isolation (S41) is above 15 dB in the range 6.1-10.5 GHz. With the acceptable

performance of S11 and S41, a measured power equality of -4.15±0.5 dB for S21 and S31 is achieved in the frequency range of 7.3-10.4GHz.

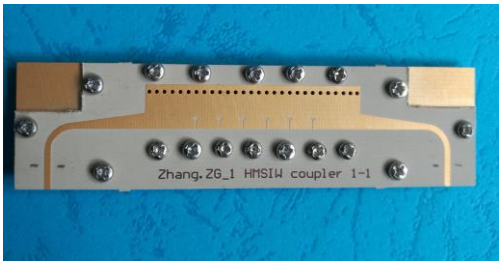

Fig. 6. Photograph of the fabricated coupler.

The insertion losses of the multilayer HMSIW filtering coupler are estimated to be nearly 1 dB in the frequency range 7.3-10.4 GHz. Its stop band is from 13.8 to 17.6GHz (Upper Sideband) with the rejection (S31) more than 40dB. In lower sideband (from 1 to 4.8GHz) the rejection is more than 25dB.

Table 5: Parameters of the fabricated coupler

***D* (mm)**	0.8	*W*strip (mm)	1.18
***p* (mm)**	1.5	Lstrip (mm)	11
ε_r	3.5	*W*siwH (mm)	6.5
***r1* (mm)**	0.5	*W*slot (mm)	2
***s1* (mm)**	0.2	*L*slot (mm)	16
θ (deg)	90	*D*slot (mm)	4
***L*ebg (mm)**	5	*lg* (mm)	3
LtaperH (mm)	13	*h* (mm)	0.508
WtaperH (mm)	3		

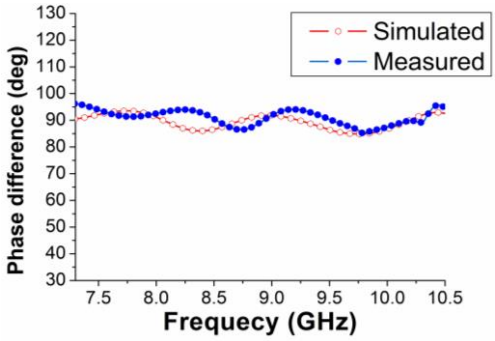

Fig. 7. Phase difference between Port 2 and Port 3.

As shown in Fig. 5 (b), the proposed coupler with GLS can realize high selectivity and improved coupling bandwidth. Compared with the coupler without GLS, the frequency selectivity and stopband suppression bandwidth of the proposed structure are improved evidently. In addition, the roll-off at the upper side is very sharper. The power equality points increased indicate that the coupling efficiency of the coupler is also improved. Figure 6 is the photograph of the fabricated HMSIW filtering coupler. The simulated phase difference is 90°±5° from 7.3 to 10.4GHz, as shown in Fig. 7.

Table 6: Performance comparison of SIW/HMSIW couplers

Ref.	**f_0 (GHz)/ FBW (%)**	**Size (λ_g^2)/ Isolation (dB)/ SFBW* (%)**	**Stopband Rejection (dB)/ Layers*/ε_r**
[2]	13/20	2.36/16/2.4	7/1/2.2
[5]	7/7	2.64/15/10.5	10/1/2.2
[12]	7.75/2.58	2.23/30/15.05	25/2/3.5
[14]	8/12.5	2.2/20/2.8	8/2/2.94
[15]	10.2/24.6	5.96/15/4	10/1/2.2
[16]	14.1/ 42	2.1/15/5.1	8/1/9.5
[28]	10.25/34	5.26/15/3.1	8/1/9.5
This work	8.87/34.9	2.2/15/24.64	40/2/3.5

Where λg is the guided wavelength on the substrate at the center frequency f_0, FBW represent the fractional bandwidth. Layers represent number of substrate layers. SFBW* represent the Stopband (Upper Sideband) fractional bandwidth.

A detailed performance comparison with SIW/ HMSIW couplers in recent years is shown in Table 6, which demonstrates the advantage of the proposed coupler clearly. Compared with the works in Table 6, the proposed structure has the better stop-band rejection and steeper transition band.

Its stop band is from 13.8 to 17.6GHz with the rejection more than 40dB. The stopband (Upper Sideband) fractional bandwidth is about 24.64%. Compared with the works in [2], [5], [12], [14], and [15], the presented coupler has featured wider bandwidths and lower loss.

IV. CONCLUSION

A novel multilayer 3dB filtering coupler with high selectivity has been proposed and developed in multilayer HMSIW topology. This modification allows HMSIW operation, resulting in significant size reduction using both multilayer and half-mode schemes simultaneously. Moreover, the novel GLS cells are etched on top layer of HMSIW to realize filtering coupler, which is a kind of multifunctional structure. Since the proposed structure integrates a bandpass filter and a directional coupler, it can contribute to the miniaturization of an RF transceiver. Compared with the coupler without GLS, the frequency selectivity and stopband suppression bandwidth of the proposed structure are improved evidently. It's a good combination of multilayered topologies, HMSIW and EBG structures. The proposed wideband coupler with GLS shows advantages of low cost, compact size, high selectivity and wide stopband

bandwidth, indicating it being a good candidate for wideband wireless communication applications.

ACKNOWLEDGMENT

This work was supported in part by the Ministry of Science and Technology of the People's Republic of China under grant 2013YQ200503 and in part by the National Natural Science Foundation of China (NSFC) under grant 61001028.

REFERENCES

[1] W. Hong, B. Liu, et al., "Integrated microwave and millimeter wave antennas based on SIW and HMSIW technology," *IEEE International Workshop on Antenna Technology (iWAT'2007*), Cambridge, UK, pp. 69-72, Mar. 2007.

[2] B. Liu, W. Hong, Y. Q. Wang, Q. H. Lai, and K. Wu, "Half mode substrate integrated waveguide (HMSIW) 3dB coupler," *IEEE Microw. Wireless Compon. Lett.*, vol. 17, no. 1, pp. 22-24, Jan. 2007.

[3] Y. J. Cheng, W. Hong, K. Wu, and Y. Fan, "A hybrid guided-wave structure of half mode substrate integrated waveguide and conductor-backed slotline and its application in directional couplers," *IEEE Microw. Wireless Compon. Lett*., vol. 21, no. 2, pp. 65-67, Feb. 2011.

[4] M. H. Ho and C. S. Li, "Novel balanced bandpass filters using substrate integrated half-mode waveguide," *IEEE Microw. Wireless Compon. Lett.*, vol. 23, no. 2, pp. 78-80, Feb. 2013.

[5] R. J. Thomas and M. Daneshmand, "The characterization of a ridged Half-Mode Substrate-Integrated Waveguide and its application in coupler design," *IEEE Trans. Microw. Theory Tech*., vol. 64, no. 11, pp. 3580-3591, Apr. 2016.

[6] W. Shao and J. L. Li, "Design of a half-mode SIW high-pass filter," *Appl. Comp. Electro. Society (ACES) Journal*, vol. 26, no. 5, pp. 447-451, May 2011.

[7] G. H. Zhai, W. Hong, K. Wu, J. X. Chen, P. Chen, and H. J. Tang, "Substrate integrated folded waveguide (SIFW) narrow-wall directional coupler," *International Conference on Microwave and Millimeter Wave Technology*, Nanjing, China, vol. 1, pp. 174-177, Apr. 2008.

[8] P. L. Chi and T. Y. Chen, "Dual-band ring coupler based on the composite right/left-handed folded substrate integrated waveguide," *IEEE Microwave and Wireless Components Letters*, vol. 24, no. 5, pp. 330-332, May 2014.

[9] J. R. Aitken, J. S. Hong, and Z. C. Hao, "Out-of-phase power divider based on two-layer SIW," *Electron Lett*., vol. 50, no. 14, pp. 1005-1007, July 2014.

[10] C. Wang, W. Q. Che, and P. Russer, "High-isolation multiway power dividing/combining network implemented by broadside-coupling SIW directional couplers," *International Journal of RF and Microwave Computer-Aided Engineering*, vol. 19, no. 5, pp. 577-582, Sep. 2009.

[11] Z.-G. Zhang, Y. Fan, and Y.-H. Zhang, "Compact 3-D multilayer substrate integrated circular and elliptic cavities (SICCs and SIECs) dual-mode filter with high selectivity," *Appl. Comp. Electro. Society (ACES) Journal*, vol. 28, no. 4, pp. 333-340, Apr. 2013.

[12] Y. J. Cheng and Y. Fan, "Compact substrate-integrated waveguide bandpass rat-race coupler and its microwave applications," *IET Microwaves, Antennas & Propagation*, vol. 6, no. 9, pp. 1000-1006, June 2012.

[13] O. A. Nova, J. C. Bohórquez, N. M. Peña, G. E. Bridges, L. Shafai, and C. Shafai, "Filter-antenna module using substrate integrated waveguide cavities," *IEEE Microw. Wireless Compon. Lett*., vol. 10, no. 1, pp. 59-62, June 2011.

[14] A. A. M. Ali, H. B. El-Shaarawy, and H. Aubert, "Miniaturized hybrid ring coupler using electromagnetic bandgap loaded ridge substrate integrated waveguide," *IEEE Microw. Wireless Compon. Lett.*, vol. 21, no. 9, pp. 471-473, Sep. 2011.

[15] X. Zou, C. M. Tong, C. Z. Li, and W. J. Pang, "Wideband hybrid ring coupler based on Half-Mode Substrate Integrated Waveguide," *IEEE Microwave and Wireless Components Letters*, vol. 24, no. 9, pp. 596-598, Sep. 2014.

[16] H. Y. Jin, Y. L. Zhou, Y. M. Huang, S. Ding, and K. Wu, "Miniaturized broadband coupler made of slow-wave half-Mode substrate integrated waveguide," *IEEE Microw. Wireless Compon. Lett.*, vol. 27, no. 2, pp. 132-134, Feb. 2017.

[17] R. Rezaiesarlak, M. Salehi, and E. Mehrshahi, "Hybrid of moment method and mode matching technique for full-wave analysis of SIW circuits," *Appl. Comp. Electro. Society (ACES) Journal*, vol. 26, no. 8, pp. 688-695, Aug. 2011.

[18] I. Bouchachi, J. Mateu, and M. L. Riabi, "Waveguide filter modeling and dimulation using mode-matching, fullwave network analysis and swarm optimization," *Appl. Comp. Electro. Society (ACES) Journal*, vol. 32, no. 2, pp. 169-177, Feb. 2017.

[19] Z. J. Zhu, L. Cao, and C. L. Wei, "Novel compact microstrip dual-Mode filters with two controllable transmission zeros," *Appl. Comp. Electro. Society (ACES) Journal*, vol. 33, no. 1, pp. 43-48, Jan. 2018.

[20] L. X. Zhou, S. J. Liu, J. Duan, and M. Xun, "A novel tunable combline bandpass filter based on external quality factor and internal coupling tunings," *Appl. Comp. Electro. Society (ACES) Journal*, vol. 33, no. 6, pp. 690-696, June 2018.

[21] Y. S. Li, W. X. Li, W. H. Yu, and C. Y. Liu, "A miniaturization band-pass filter with ultra-narrow multi-notch-band characteristic for ultra-wideband communication applications," *Appl. Comp. Electro. Society (ACES) Journal*, vol. 29, no. 4, pp. 289-300, Apr. 2014.

[22] W. J. Feng, M. L Hong, and W. Q. Che, "Narrow-band bandpass filters with improved upper stop-band using open/shorted coupled lines," *Appl. Comp. Electro. Society (ACES) Journal*, vol. 31, no. 2, pp. 152-158, Feb. 2016.

[23] L. X. Zhou, Y. Z. Yin, W. Hu, and X. Yang, "Compact bandpass filter with sharp out-of-band rejection and its application," *Appl. Comp. Electro. Society (ACES) Journal*, vol. 32, no. 3, pp. 249-255, Mar. 2017.

[24] Y. Li, W. Li, C. Liu, and Q. B. Ye, "A compact UWB band-pass filter with ultra-narrow tri-notch-band characteristic," *Appl. Comp. Electro. Society (ACES) Journal*, vol. 29, no. 2, pp. 170-177, Feb. 2014.

[25] S. I. Yamamoto, J. Hirokawa, and M. Ando, "Length reduction of a short-slot directional coupler in a single-layer dielectric substrate waveguide by removing dielectric near the side walls of the coupler," *IEEE Antennas and Propagation Society International Symposium*, Monterey, CA, vol. 8, pp. 2353-2456, June 2004.

[26] R. Levy, "Analysis and synthesis of waveguide multi-aperture directional couplers," *IEEE Trans. Microw. Theory Tech.*, vol. 16, no. 12, pp. 995-1006, Apr. 1968.

[27] A. A. Oliner, "Equivalent circuits for small symmetrical longitudinal apertures and obstacles," *IRE Trans. Microw. Theory Tech.*, vol. 8, no. 12, pp. 72-80, Jan. 1960.

[28] H. Jin, L. Jian, and G. Wen, "A novel coupler based on HMSIW," *IEICE Trans. Electron.*, vol. E93-C, no. 2, pp. 205-207, Feb. 2010.

Zhigang Zhang was born in Shanxi Province, China. He received the B.S. degree in Electronic Information Engineering and M.S. degree in Wireless Physics from Sichuan University and is currently working toward the Ph.D. degree in Electromagnetic Field and Microwave Technology from The University of Electronic Science and Technology of China (UESTC), Chengdu, Sichuan, China. His current research interests include SIW technology and its application, microwave and millimeter-wave filters, and couplers, electromagnetic theory.

Yong Fan received the B.E. degree from the Nanjing University of Science and Technology, Nanjing, Jiangsu, China, in 1985, and the M.S. degree from the University of Electronic Science and Technology of China (UESTC), Chengdu, Sichuan, China, in 1992.

He is currently with the School of Electronic Engineering, UESTC. He has authored or coauthored over 60 papers. From 1985 to 1989, he was interested in microwave integrated circuits. Since 1989, his research interests include millimeter-wave communication, electromagnetic theory, millimeter-wave technology, and millimeter-wave systems. Mr. Fan is a Senior Member of the Chinese Institute of Electronics (CIE).

Yonghong Zhang received the B.S., M.S., and Ph.D. degrees from the University of Electronic Science and Technology of China (UESTC), Chengdu, China, in 1992, 1995, and 2001, respectively. From 1995 to 2002, he was a Teacher with the UESTC. In 2002, he joined the Electronic Engineering Department, Tsinghua University, Beijing, China, as a Doctoral Fellow. In 2004, he rejoined the UESTC. His research interests are in the area of microwave and millimeter-wave technology and applications.

Design and Finite Element Analysis of a Novel Reverse Salient Pole Permanent Magnet Synchronous Motor

Xianming Deng, Shusheng Gong, Ran Li, and Junhong Zhou

Jiangsu Province Laboratory of Mining Electric and Automation
China University of Mining and Technology, Xuzhou, 221116, China
xmdengcumt@126.com, shushenggong@cumt.edu.cn

Abstract ─ Since traditional permanent magnet synchronous motor (PMSM) with salient pole effect has a lower d- than q-axis inductance, the maximum torque has a power angle higher than 90 degrees, which poses threat to demagnetization when the motor runs under load. To solve the problem, a novel PMSM with reverse salient pole is designed and optimized to realize the characteristic of $L_d > L_q$ in this paper. Firstly, the electromagnetic design of reverse salient pole PMSM is carried out, followed by finite element analysis (FEA) of traditional PMSM and reverse salient pole PMSM. The simulation results show that air-gap flux density and no-load back EMF of reverse salient pole PMSM is closer to sinusoidal wave compared with the traditional PMSM. The danger of permanent magnet demagnetization is reduced due to $L_d > L_q$. In addition, reverse salient pole PMSM improves the maximum torque and overload capacity and has less loss and higher efficiency in steady-state operation. Finally, the optimal design of reverse salient pole PMSM is carried out. From the comparison of the simulation results, the optimized structure is superior to reverse salient pole PMSM in these performances, which shows that the design is reasonable.

Index Terms ─ Finite element analysis (FEA), PMSM, reverse salient pole, the optimized reverse salient pole.

I. INTRODUCTION

Permanent magnet synchronous motor (PMSM) has been widely used and researched in the industrial field due to high efficiency and high power density. In the analysis and design of PMSM, researchers at home and abroad have done a lot of work and achieved stage results. A lot of work has been done on motor structure and parameter design, which laid the foundation for the design and research of PMSM [1]. A controllable flux PMSM with built-in hybrid rotor magnetic circuit structure was proposed to improve the air-gap flux density waveform, which provides ideas for improving the speed regulation performance of the motor [2]. Optimize the rotor structure by grooving the rotor surface of interior PMSM, reducing the cogging torque of the motor [3].

Recently, a new type of PM motor with the characteristic of $L_d > L_q$, often named a flux-intensifying interior PM (FIIPM) motor, has been proposed and investigated [4, 5]. In addition, Xiaoyong has also carried out a lot of simulations and experiments on permanent magnet Flux-Intensifying Motors [6, 7]. The most obvious characteristic is that the d-axis inductance L_d is greater than the q-axis inductance L_q by the modification of rotor topology. In this paper, reverse salient pole effect of $L_d > L_q$ is realized by changing the rotor structure on the basis of the traditional PMSM. This not only reduces the demagnetization risk of permanent magnets under load operation, but also reduces the saturation degree of rotor magnetic circuit. Next, FEA of traditional PMSM and reverse salient pole PMSM are carried out. The simulation results show that the air-gap flux density and no-load back EMF of reverse salient pole PMSM are closer to sinusoidal wave and have stronger overload capability. In addition, in the starting process, reverse salient pole PMSM can reach the stable operation state more quickly, with less loss and higher efficiency in the steady state. Furthermore, the reverse salient pole PMSM is optimized. The results of FEA show that the optimized structure is superior to the reverse salient pole motor in these performances, which proves the rationality of the structure design.

II. ELECTROMAGNETIC DESIGN OF THE REVERSE SALIENT POLE PMSM

A. Basic parameters design of motor

Basic parameters include the main size of motor, the size and working point of permanent magnet, slot and stator winding. If the slot type is not suitable or electric load is not satisfied, it is necessary to adjust the size of permanent magnet and its correspondence parameters to meet design requirements and technical and economic indicators.

The main dimensions of the motor are the inner and outer diameters of stator and rotor, the stator core length

Submitted On: December 21, 2018
Accepted On: April 6, 2019

and the effective length of air-gap, etc. The main dimensional relationship of the induction motor can be approximated by using to derive the main size relations of the motor. Selected main parameters of motors are shown in Table 1 below.

Table 1: Main parameters of the motor

Parameters	Value
Rated power/kW	20
Rated speed/rpm	1000
Rated line voltage/V	380
Frequency/Hz	50
Stator outer diameter/mm	400
Stator inner diameter/mm	285
Core length/mm	210
Number of poles	3
Stator slot number	72
Rotor slot number	54
Magnet type	NdFe35
Steel type	D23_50

B. Design of rotor structure

Rotor structure design mainly includes the selection of rotor slot shape, the determination of slot size, the determination of permanent magnet type and size, etc. The slots of PMSM rotor with traditional structure and reverse salient pole structure are trapezoidal slots with the same slot size.

$$L=\frac{\psi}{I}=\frac{N\Phi}{I}=\frac{NF}{I\Lambda}=\frac{N\cdot NI}{I\Lambda}=\frac{N^2}{\Lambda}. \quad (1)$$

In (1), ψ is the winding flux, N is the number of winding turns, F is the magnetic motive force, I is the current in the coil, and Λ is the magnetic reluctance.

Formula (1) shows that the inductance is proportional to magnetic permeability and inversely proportional to the magnetic reluctance when the number of coil turns is constant.

The traditional PMSM has a permanent magnet on the d-axis, whose permeability is close to that of air, which is equivalent to air-gap widening on the d-axis and makes the magnetic reluctance of the d-axis higher than q-axis. According to Formula (1), the q-axis reactance is greater than the d-axis reactance. The structure of traditional PMSM is shown in Fig. 1 (a). Realizing the characteristics of $L_d > L_q$ in PMSM means that the d-axis inductance is higher than q-axis inductance. It is necessary to increase the magnetic reluctance on the q-axis magnetic circuit, so trapezoidal ventilation holes should be set up at the q-axis position of the rotor. The structure of reverse salient pole PMSM is shown in Fig. 1 (b).

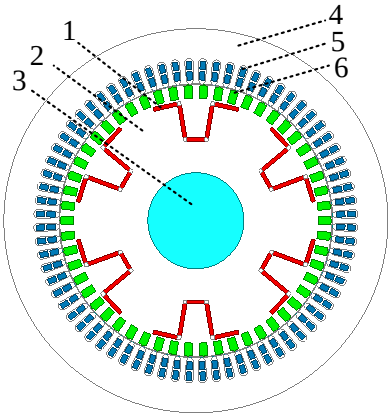

(a)

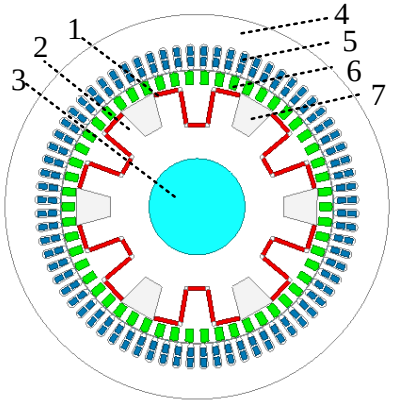

(b)

1-Permanent magnet, 2-Rotor core, 3-Shaft, 4-Stator core, 5-Stator winding, 6-Squirrel cage bar, 7-Ventilated slot

Fig. 1. (a) FEA model of the traditional PMSM, and (b) FEA model of reverse salient pole PMSM

The figures above show the structure of two kinds of motors. In order to accurately compare their performances, the outer and inner diameters of stator and rotor and the amount of permanent magnet are exactly the same. Different from the traditional PMSM, the trapezoidal ventilation holes are formed along the q-axis direction of reverse salient pole PMSM. This makes the flux leakage of the motor less than that of traditional PMSM. The degree of magnetic saturation of q-axis is alleviated and the distribution of magnetic density is more reasonable. As the saturation of magnetic circuit is greatly reduced, the iron loss is reduced and the efficiency of reverse salient pole PMSM is improved. Moreover, ventilation holes can facilitate the rotor heat dissipation, which reduces the rotor temperature and protects the permanent magnet.

III. FEA OF THE REVERSE SALIENT POLE PMSM

In this paper, the FEA software is used to establish the model of the traditional PMSM and the reverse salient pole PMSM. This paper obtains and analyses air-gap flux density waveform, no-load back EMF waveform, d-axis and q-axis inductance characteristics, power angle characteristics and rated load starting performance of the two motors with different structures.

A. Analysis of no-load back EMF and air-gap flux density

The FEA of the traditional PMSM and the reverse salient pole PMSM is carried out. The no-load back EMF and air-gap flux density of the two motors are solved by using the FEA software [8], and the Fourier analysis and the comparison of harmonic component are performed. The no-load back EMF and air-gap flux density waveforms of the two motors are shown in Figs. 2 and 4, respectively.

From Figs. 3 and 5, it can be seen that the fundamental components of no-load back EMF and air-gap flux density of reverse salient pole PMSM increase to a certain extent compared with the traditional PMSM. The fifth and seventh harmonics are also reduced, and the third and ninth harmonics can be suppressed by the Y-connection of the stator windings. Therefore, reverse salient pole PMSM effectively increases the fundamental component and reduces the harmonic component, making back EMF waveform and air-gap flux density waveform closer to sinusoidal wave.

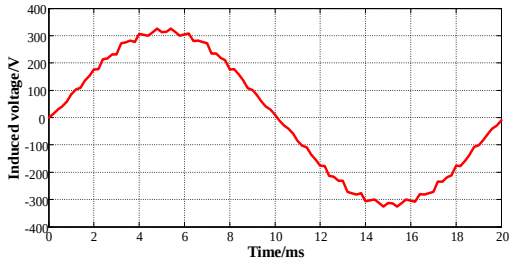

(a)

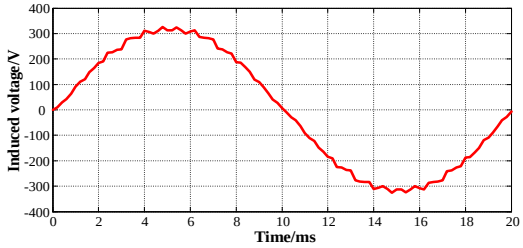

(b)

Fig. 2. (a) No-load back EMF waveform of the traditional PMSM, and (b) no-noad back EMF waveform of reverse salient pole PMSM.

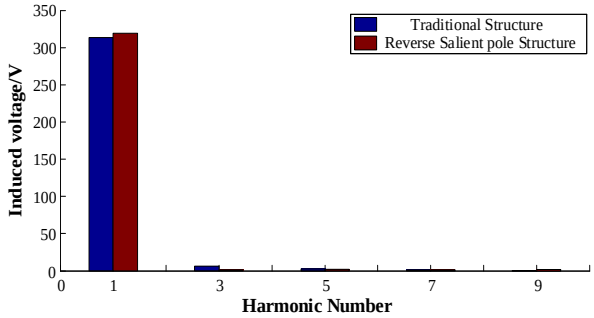

Fig. 3. Harmonic analysis results of no-load back EMF for two kinds of motors.

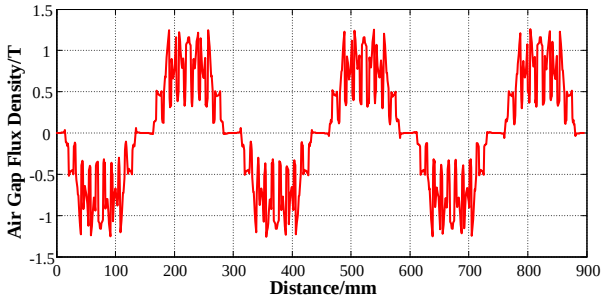

(a)

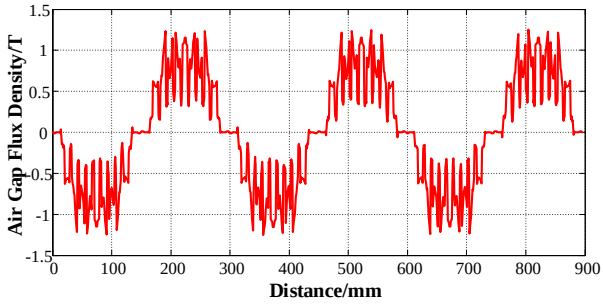

(b)

Fig. 4. (a) Air-gap flux density waveform of the traditional PMSM, and (b) air-gap flux density waveform of reverse salient pole PMSM.

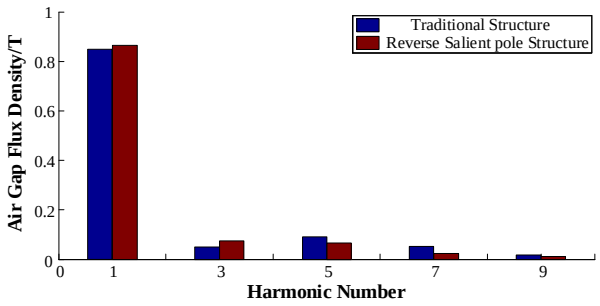

Fig. 5. Harmonic analysis results of air-gap flux density for two kinds of motors.

B. Analysis of inductance characteristics of d-axis and q-axis

The d-axis and q-axis inductances have great influence on the operation characteristics. The reverse salient pole effect of motor is expressed in terms of the parameter $L_d > L_q$. Therefore, it is very important to analyze the inductance characteristics. At present, most inductance calculation methods are based on magnetic circuit method. By introducing some optimum parameters and calculating them according to empirical formulas, the accuracy is not high. When the structure of magnetic circuit is complex, it is difficult to calculate by this method. In this paper, the FEA is used to calculate the reactance of PMSM.

The winding flux linkage of d-axis and q-axis are mutually vertical, but in the actual motor, d-axis and q-axis are not completely decoupled. So there is a strong cross-coupling between them. The expression of flux linkage considering cross-coupling is as follows [9]:

$$\lambda_d=\lambda_d(i_d, i_q)=L_d i_d+L_{dq} i_q+\lambda_f, \quad (2)$$

$$\lambda_q=\lambda_q(i_d, i_q)=L_q i_q+L_{dq} i_d. \quad (3)$$

In the formula, L_d and L_q are the self-inductance of d-axis and q-axis respectively; L_{dq}, L_{qd} are the d-axis and the q-axis mutual inductance; λ_f is the flux linkage of the permanent magnet.

According to the expression of flux linkage shown in formula (2), (3), Aimeng from North China Electric Power University has proposed and revised the calculation model of L_d and L_q considering cross-saturation of magnetic circuit:

$$L_d = \frac{\lambda_d(i_d,i_q)-\lambda_f(0,0)}{i_d}\Big|_{i_q=constant}, \quad (4)$$

$$L_q=\frac{\lambda_q(i_d,i_q)}{i_q}\Big|_{i_d=constant}. \quad (5)$$

The calculation model of inductance parameters shown in formula (4), the flux linkage of permanent magnet is obtained when the stator current is zero. Therefore, in solving the d-axis inductance, the flux that acts only on permanent magnet is subtracted, and the effect of q-axis current on d-axis magnetic circuit is fully considered. According to formulas (4), (5), the FEA method is used to analyze the calculation model of inductance parameters. When calculating d-axis inductance of two kinds of motors, q-axis current is set to the rated value, and d-axis current changes from 5A to 50A. Similarly, when calculating q-axis inductance, d-axis current is set to the rated value, and q-axis current changes from 5A to 50A [10]. Therefore, the inductance characteristics of two motors that fully consider the cross-saturation of the d-axis and q-axis magnetic circuit can be obtained, as is shown in Figures 6 (a) and 6 (b).

It can be seen from Fig. 6 (a) that the traditional PMSM expresses salient pole effect of $L_d > L_q$. Because of the high degree of magnetic saturation, the inductance of d-axis and q-axis decrease obviously with the increase of the current of their respective axis. Moreover, due to the existence of permanent magnets on the d-axis, the saturation degree of the d-axis is less than that of the q-axis, so reduction of the d-axis inductance is less obvious than that of the q-axis inductance. In Fig. 6 (b), due to the trapezoidal ventilation slot on the q-axis, reverse salient pole PMSM expresses the reverse salient pole effect of $L_d > L_q$. In addition, a trapezoidal ventilation slot is opened on the q-axis of the rotor for the motor, which greatly reduces degree of saturation. Thus, with the increase of current, inductance drop of d-axis and q-axis is less than that of the traditional PMSM.

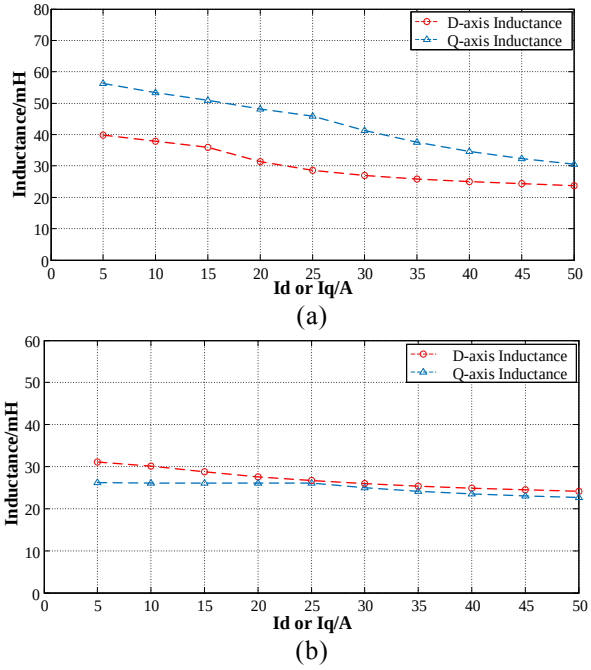

Fig. 6. (a) Inductance curve of the traditional PMSM, and (b) inductance curve of reverse salient pole PMSM.

C. Analysis of power angle characteristics

In order to obtain the power angle characteristics of PMSM, it is necessary to solve the torque. By setting different power angles in the FEA software, the torque values corresponding to different power angles are solved, and the power angle characteristics are obtained.

Generally, the stator winding resistance R_1 is small, neglecting its influence, the torque of the salient pole PMSM is as follows [11]:

$$T_{em}=m\frac{E_0 U}{X_d \Omega_s}\sin\delta+m\frac{U^2}{2\Omega_s}\left(\frac{1}{X_q}-\frac{1}{X_d}\right)\sin 2\delta. \quad (6)$$

In (6), m is phase number, E_0 is no-load EMF, U is power supply voltage, Ω_s is mechanical angular velocity, δ is power angle, X_d and X_q are d-axis and q-axis reactance, respectively.

It can be seen from (6) that the torque consists of two parts: basic electromagnetic torque by the interaction

between the rotor permanent magnet field and the stator magnetic field, which is called the permanent magnet torque; as well as the second one donating reluctance torque caused by the unequal reluctance of d-axis and q-axis. In the traditional PMSM, because the q-axis inductance is larger, the power angle corresponding to the maximum torque is over 90° [12]. In reverse salient pole PMSM, the d-axis inductance is higher, so the power angle corresponding to the maximum torque is less than 90°.The power angle characteristics of the two structural motors are obtained by FEA are shown in Fig. 7.

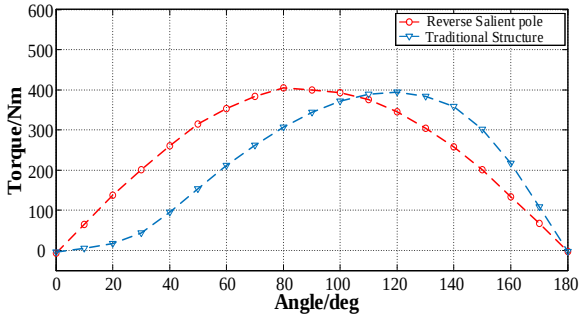

Fig. 7. Power angle characteristics of two kinds of motors.

As can be seen from Fig. 7, different from the power angle characteristic of the traditional PMSM, the maximum torque of reverse salient pole PMSM is at the position where the power angle is at 80 degrees. Therefore, it is known that the reluctance and torque component $T_{em2}=m\frac{U^2}{2\Omega_s}\left(\frac{1}{X_q}-\frac{1}{X_d}\right)sin2\delta$ of the motor is positive when the power angle is less than 90 degrees. It is also proved the reverse salient pole PMSM has reverse salient pole effect of $L_d > L_q$. When the motor operates under load, the magnetic field of the armature reaction in the same direction as the magnetic field of the rotor, which acts as a magnetizing aid. Moreover, compared with the traditional PMSM, the maximum torque of reverse salient pole PMSM increases under the same amount of permanent magnets. It not only improves the utilization ratio of permanent magnet, but also increases the overload capacity [13].

D. Starting performance analysis of rated load

Line-start permanent magnet synchronous motor (LSPMSM) can be regarded as placing permanent magnet in the rotor of three-phase induction motor, which can start by the asynchronous torque generated by the rotor cage winding [14]. The motor has the advantageous ability of self-starting. In this paper, three-phase rated voltage is loaded into three-phase stator windings of two motors by FEA method. In addition, they start at zero speed under rated load (T_N =200N.m). Starting performance of the two motors under rated load are obtained by simulation [15]. Corresponding speed and torque curves are obtained as shown in Figs. 8 and 9.

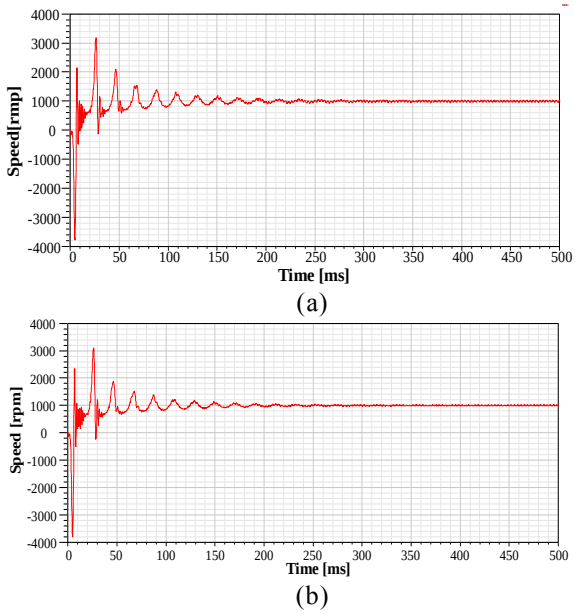

Fig. 8. (a) Starting speed curve of rated load for the traditional PMSM, and (b) starting speed curve of rated load for reverse salient pole PMSM.

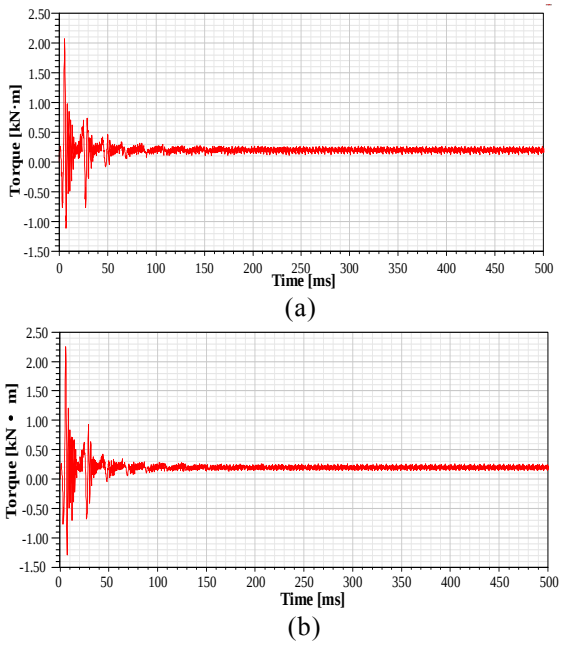

Fig. 9. (a) Starting torque curve of rated load for the traditional PMSM, and (b) starting torque curve of rated load for reverse salient pole PMSM.

Figures 8 and 9 show the speed and torque curves

of the two motors during starting with rated load, respectively. During the process of load starting, the torque is higher in low speed section, and the motor is accelerated close to synchronous speed. After a period of oscillation, it is pulled into synchronous operation. From the speed curve, it can be seen that the speed of the traditional PMSM stabilizes to synchronous speed close to 350*ms*. Speed of reverse salient pole PMSM stabilizes to synchronous speed around 300*ms*. In addition, it can be seen from Figs. 9 (a) and 9 (b) that the torque ripple of the traditional PMSM is more obvious than that of reverse salient pole PMSM in steady-state operation. It shows that the latter is better than the former in starting performance.

E. Efficiency analysis of rated load

Efficiency is an important performance index. When motor operates under load, loss inevitably exists. In this paper, the FEA method is used to obtain the iron loss, stator copper loss and rotor copper loss of two kinds of motors at steady-state operation [16]. As shown in Table 2 below.

Table 2: Efficiency of two kinds of motors under rated load

	The Traditional PMSM	The Teverse Salient Pole PMSM
Iron loss (W)	338.5	318
Stator copper loss (W)	285.7	226
Rotor copper loss (W)	366.6	287.3
Output power (W)	20947.9	20945.6
Efficiency	95.48%	96.18%

As can be seen from Table 2, the efficiency of the two kinds of motor is more than 95%, and the efficiency of reverse salient PMSM is higher than that of the traditional PMSM. The efficiency of the two motors fully meets the requirements of PMSM design. The results show that feasibility and reason of the proposed design.

IV. OPTIMAL DESIGN OF THE REVERSE SALIENT POLE PMSM

Improving fundamental component of air-gap magnetic field and restraining harmonic component are effective ways to improve motor performance. In this paper, a rotor structure with non-uniform teeth is proposed to improve the performance of motor. As shown in Fig. 10, the teeth distance of the rotor at the d-axis position is widened by two times as much as that of the conventional teeth, so that the magnetic reluctance on the d-axis direction decreases, the magnetic density and the fundamental component of the air-gap magnetic field increases.

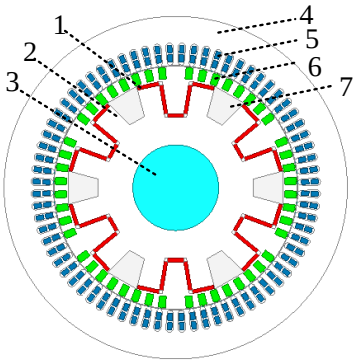

1-Permanent magnet, 2-Rotor core, 3-Shaft, 4-Stator core, 5-Stator winding, 6-Squirrel cage bar, 7-Ventilated slot

Fig. 10. The structure of the optimized reverse salient pole PMSM.

V. FEA OF THE OPTIMIZED REVERSE SALIENT POLE PMSM

In this paper, a model of the optimized reverse salient pole PMSM is established by using FEA software. The FEA simulation is used to obtain air-gap flux density waveform, no-load back EMF waveform, power angle characteristic and rated load starting performance, and then the reverse salient motor described earlier in these main performance is used to compare.

A. Analysis of no-load back EMF and air-gap flux density

The solution of no-load back EMF and air-gap flux density of the optimized reverse salient pole PMSM is carried out by using FEA software. The waveforms are shown in Figs. 11 (a) and 11 (b). At the same time, the no-load back EMF and air-gap flux density are analyzed by Fourier method, and compared with the reverse salient pole PMSM. The results are shown in Figs. 12 and 13.

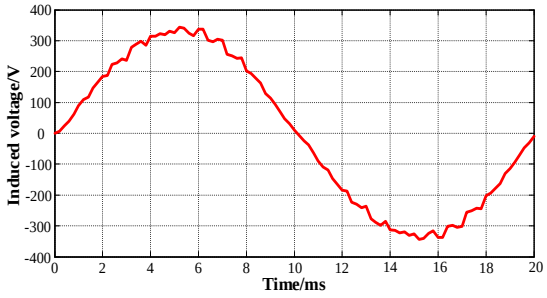

(a)

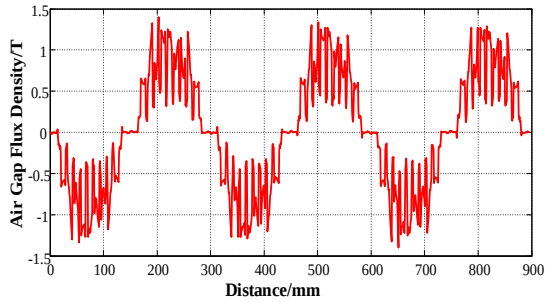

(b)

Fig. 11. (a) No-load back EMF waveform of the optimized reverse salient pole PMSM, and (b) air-gap flux density waveform of the optimized reverse salient pole PMSM.

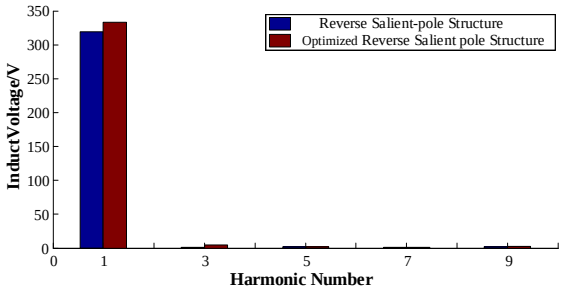

Fig. 12. Harmonic analysis results of no-load back EMF for two kinds of motors.

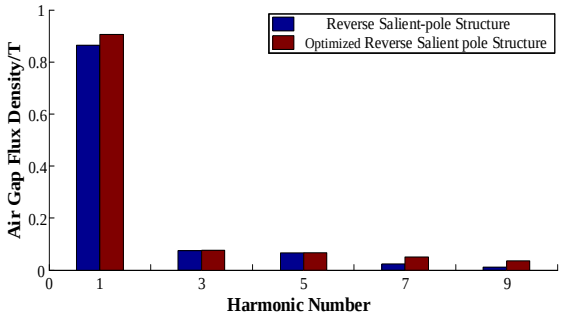

Fig. 13. Harmonic analysis results of air-gap flux density for two kinds of motors.

From Figs. 12 and 13, it can be seen that the fundamental components of no-load back EMF and air-gap flux density of the optimized reverse salient pole PMSM obviously increase compared with reverse salient pole PMSM. The fifth and seventh harmonics are roughly the same, while the third and ninth harmonics are also suppressed. Therefore, the optimized reverse salient pole PMSM effectively increases the fundamental component and reduces the proportion of harmonic components, making the back EMF waveform and air-gap flux density waveform are closer to sinusoidal wave.

B. Analysis of power angle characteristic for the optimized reverse salient pole PMSM

In this paper, the optimized reverse salient pole PMSM is set different power angles by FEA software, and the corresponding torque values are solved to obtain its power angle characteristics. Compared with the power angle characteristic of reverse salient pole PMSM, the results are shown in Fig. 14.

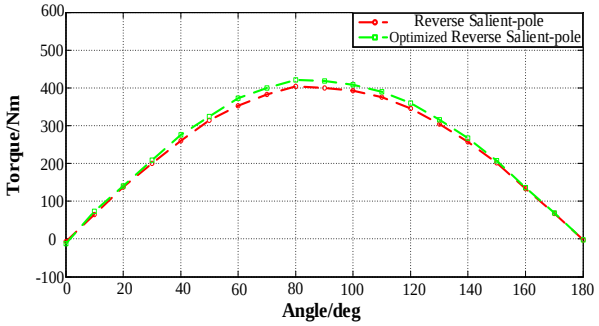

Fig. 14. Power angle characteristics of two kinds of motors.

As can be seen from Fig. 14, the trend of power angle characteristics of the optimized reverse salient pole PMSM are basically the same as that of reverse salient pole PMSM. Because the optimized reverse salient pole PMSM removes six squirrel cage bars on d-axis, which enlarges the width of the rotor teeth and increases the magnetic flux of the motor. Thus, in the case of the same amount of permanent magnets, the torque corresponding to each power angle of the optimized reverse salient pole PMSM will be greater than that of reverse salient pole PMSM, which improves the overload capacity of the motor. Therefore, it is shown that the optimized reverse salient pole PMSM has better performance in the torque.

C. Starting performance analysis of the optimized reverse salient pole PMSM

In this paper, three-phase rated voltage is loaded into three-phase stator windings of the optimized reverse salient pole PMSM. In addition, it also starts at zero speed under rated load (T_N=200N.m). The speed and torque curves of the motor during rated load are obtained by simulation, which is shown in Figs. 15 (a) and 15 (b) below.

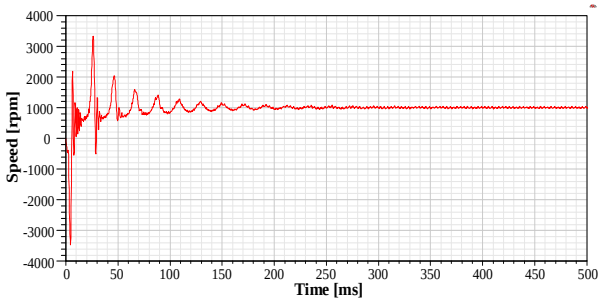

(a)

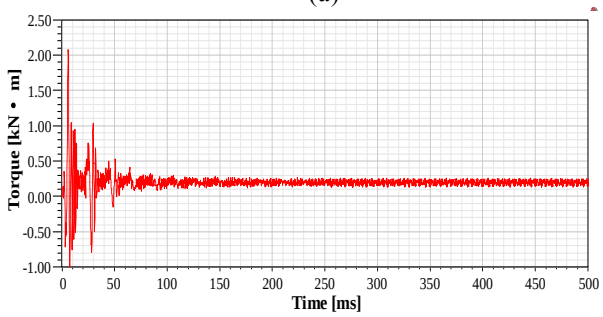

(b)

Fig. 15. (a) Starting speed curve of rated load for the optimized reverse salient pole PMSM, and (b) starting torque curve of rated load for the optimized reverse salient pole PMSM.

From the speed and torque curves, it can be seen that the optimized reverse salient pole PMSM has reached the synchronous speed near 300ms. After reducing six squirrel cage bars of the rotor starting winding, the starting performance of the motor is not affected, which shows the superiority of the starting performance of the optimized reverse salient pole PMSM.

D. Efficiency analysis of the rated load

In this paper, the FEA method is used to simulate the iron loss, stator copper loss and rotor copper loss of the optimized reverse salient pole PMSM during steady-state operation, and compare with reverse salient pole PMSM. The results are shown in Table 3 below.

Table 3: Efficiency of two kinds of motor under rated load

	The Optimized Reverse Salient Pole PMSM	The Reverse Salient Pole PMSM
Iron loss (W)	270.9	318
Stator copper loss (W)	267.7	226
Rotor copper loss (W)	279	287.3
Output power (W)	20949.2	20945.6
Efficiency	96.24%	96.18%

From Table 3, it can be seen that the efficiency of the two kinds of motors is over 96%. Moreover, the efficiency of the optimized reverse salient PMSM is slightly higher than that of the reverse salient PMSM which shows the superiority in efficiency and proves the rationality of the optimized design.

VI. CONCLUSION

In this paper, a novel reverse salient pole PMSM is proposed and optimized. Two-dimensional models of PMSM with three different rotor structures are established and simulated by FEA software. The results show that air-gap flux density and back EMF of reverse salient pole PMSM are closer to sinusoidal wave than those of the traditional PMSM. By opening trapezoidal slots on the q-axis of the rotor, it has reverse salient pole effect of $L_d > L_q$, reducing the risk of demagnetization and increasing operation stability. The reverse salient pole PMSM improves the maximum torque and the overload capacity of the motor. In addition, reverse salient pole PMSM has higher efficiency at rated load. Moreover, the optimized reverse salient pole PMSM in these performances will be better than reverse salient pole PMSM. It also proves the rationality of reverse salient pole PMSM and its optimal design.

ACKNOWLEDGMENT

This work has been supported by the Top-notch Academic Programs Project of Jiangsu Higher Education Institutions PPZY2015B132 and the National Natural Science Foundation of China (U1610113).

REFERENCES

[1] R. Y. Tang, *Modern Permanent Magnet Machines Theory and Design*. Beijing: China Machine Press, 1997, pp. 37-87.

[2] Y. G. Chen, W. G. Zhong, and Y. H. Shen, "Finite element analysis of interior composite-rotor controllable flux permanent magnet synchronous machine," *Proceedings of the CSEE*, vol. 29, no. 6, pp. 61-66, Feb. 2009.

[3] G. Kang, Y. Son, G. Kim, and J. Hur, "A novel cogging torque reduction method for interior-type permanent-magnet motor," *IEEE Transactions on Industry Applications*, vol. 45, no. 1, pp. 161-167, Jan.-Feb. 2009.

[4] N. Limsuwan, Y. Shibukawa, D. D. Reigosa, and R. D. Lorenz, "Novel design of flux-intensifying interior permanent magnet synchronous machine suitable for self-sensing control at very low speed and power conversion," *IEEE Transactions on Industry Applications*, vol. 47, no. 5, pp. 2004-2012, Sept.-Oct. 2011.

[5] N. Limsuwan, T. Kato, K. Akatsu, and R. D. Lorenz, "Design and evaluation of a variable-

flux flux-intensifying interior permanent-magnet machine," *IEEE Trans. Ind. Appl.*, vol. 50, no. 2, pp. 1015-1024, Mar./Apr. 2014.

[6] X. Zhu, S. Yang, Y. Du, Z. Xiang, and L. Xu, "Electromagnetic performance analysis and verification of a new flux-intensifying permanent magnet brushless motor with two-layer segmented permanent magnets," *IEEE Transactions on Magnetics*, vol. 52, no. 7, pp. 1-4, July 2016.

[7] X. Zhu, J. Huang, L. Quan, Z. Xiang, and B. Shi, "Comprehensive sensitivity analysis and multi-objective optimization research of permanent magnet flux-intensifying motors," *IEEE Transactions on Industrial Electronics*, vol. 66, no. 4, pp. 2613-2627, Apr. 2019.

[8] A. Mahmoudi, S. Kahourzade, A. A. Rahim, W. P. Hew, and M. N. Uddin, "Design, analysis, and prototyping of a novel structured solid rotor ringed line-start axial-flux permanent magnet motor," *IEEE Trans. Ind. Electron.*, vol. 61, no. 4, pp. 1722-1734, Apr. 2014.

[9] A. Hassanpour Isfahani and S. Vaez-Zadeh, "Effects of magnetizing inductance on start-up and synchronization of line-start permanent-magnet synchronous motors," *IEEE Transactions on Magnetics*, vol. 47, no. 4, pp. 823-829, Apr. 2011.

[10] D. Mingardi, M. Morandin, S. Bolognani, and N. Bianchi, "On the proprieties of the differential cross-saturation inductance in synchronous machines," *IEEE Transactions on Industry Applications*, vol. 53, no. 2, pp. 991-1000, Mar-Apr. 2017.

[11] D. Stoia, M. Cernat, A. A. Jimoh, and D. V. Nicolae, "Analytical design and analysis of line-start permanent magnet synchronous motors," *AFRICON 2009*, Nairobi, pp. 1-7, 2009.

[12] R. T. Ugale and B. N. Chaudhari, "A new rotor structure for line start permanent magnet synchronous motor," *2013 International Electric Machines & Drives Conference*, Chicago, IL, pp. 1436-1442, 2013,.

[13] L. Wang, X. Deng, J. Lu, K. Wang, and R. Wang, "Design and finite element analysis of permanent magnet synchronous motor with novel rotor type," *2010 Asia-Pacific Power and Energy Engineering Conference*, Chengdu, pp. 1-4, 2010.

[14] W. Fei, P. C. K. Luk, J. Ma, J. X. Shen, and G. Yang, "A high-performance line-start permanent magnet synchronous motor amended from a small industrial three-phase induction motor," *IEEE Transactions on Magnetics*, vol. 45, no. 10, pp. 4724-4727, Oct. 2009.

[15] R. T. Ugale and B. N. Chaudhari, "Rotor configurations for improved starting and synchronous performance of line start permanent-magnet synchronous motor," *IEEE Transactions on Industrial Electronics*, vol. 64, no. 1, pp. 138-148, Jan. 2017.

[16] M. J. Melfi, S. D. Umans, and J. E. Atem, "Viability of highly efficient multi-horsepower line-start permanent-magnet motors," *IEEE Transactions on Industry Applications*, vol. 51, no. 1, pp. 120-128, Jan.-Feb. 2015.

Xianming Deng was born in Sichuan, China. He received his B.S., M.S., and Ph.D. in Electrical Engineering from China University of Mining and Technology, Jiangsu, China. He is currently a Professor in the School of Electrical and Power Engineering of China University of Mining and Technology. His current research fields include power electronics and motor drive.

Shusheng Gong was born in Fujian, China. He received his B.S. in Electrical Engineering from Fujian Agriculture and Forestry University, Fujian, China. He is currently receiving a Master education at China University of Mining and Technology. His current research directions include motor design and motor control.

Ran Li was born in Shanxi, China. He received his B.S. in Electrical Engineering from Shandong University of Technology, Shandong, China. He is currently receiving a Master education at China University of Mining and Technology. His current research interests include power electronics and motor drive.

Junhong Zhou was born in Hunan, China. He received his B.S. in Information Engineering from China University of Mining and Technology, Jiangsu, China. He is currently receiving a Master education at China University of Mining and Technology. His current research interests include power electronics and motor drive.

Trajectory Tracking of Rotating Shaft with Active Magnetic Bearings under Different Reference Signals

Xudong Guan, Jin Zhou, Haitong Wu, and Yue Zhang

College of Mechanical and Electrical Engineering
Nanjing University of Aeronautics and Astronautics, Nanjing 210016, China
guanxd@nuaa.edu.cn, zhj@nuaa.edu.cn, wu_haitong@163.com, haianzy95@126.com

Abstract **–** Using magnetic levitation technology to implement a reference signal can avoid fluid mechanical surge and better control the movement of motorized spindle-mounted cutting tools. Magnetic levitation has the advantages of no friction, no mechanical wear, and high efficiency. In this paper, the performance of axial trajectory tracking control of active magnetic bearings with a classical proportional-integral-derivative (PID) controller is studied. First, the principles of trajectory tracking with an active magnetic bearing system are expounded, and the mechatronics models of such a system are established. Then, a PID controller is designed and trajectory tracking performance using different reference signals is verified by simulation and experiment. The results show that PID-based control of magnetic bearings can meet the requirements of tracking position control. In the experiments, the tracking errors were all within 18 μm in the rotating state.

Index Terms **–** Active magnetic bearings, machining movement, mechatronics modeling, reference signal, trajectory tracking.

I. INTRODUCTION

Magnetic levitation technology has been widely used in rotating machinery for its advantages of having no mechanical contact or wear, zero friction, long service life, no lubrication, high efficiency, and low noise [1]. In recent years, it has been applied to active magnetic bearings (AMBs) and maglev trains. It is also gradually being applied in trajectory tracking control, such as fluid mechanical surge suppression and the tracking of motorized spindle machining tools.

Tooltip tracking refers to the use of a reference signal as a guide for the machining of parts with complex geometries. In previous work, tooltip tracking has been implemented with ball screw mechanisms [2, 3] and actuators [4, 5]. In the present study [6], a synchronous tool tracking method for an AMB rigid rotor with invariant control is proposed. Wang [7] put forward a principle for machining noncircular piston pin-holes by controlling the trajectory of the spindle's axis to achieve high-frequency and radial micromotions. Smirnov [8] adopted tool tracking in AMB spindle and adjusted magnetic bearings through a PID control strategy, which enables the tool to reach a set position. Classical PID control methods are very practical due to their clear physical concepts and intuitive design processes. However, they require a high level of knowledge and insights in the fields of system dynamics and classical control [9]. Sanadgol [10] and Yoon [11] achieved surge control in a magnetic suspension centrifugal compressor by using the H_∞ robust control method, which mainly depends on the adjustment of the rotor's axial position; that is, axial trajectory tracking control of the rotor. Minihan [12] investigated the variation in electromagnetic forces at different levitation positions for large displacement tracking control of magnetic bearings and designed three kinds of nonlinear controllers to achieve position tracking control. Pesch [13] and others studied the rotor position tracking performance of radial magnetic bearings based on μ-synthesis. Reference [14] proposed an adaptive tracking method that ensures stable operation throughout the rotational speed range. Grochmal [15] introduced a nonlinear reduced-order disturbance observer and applied it to flatness-based tracking control. In reference [16], an adaptive control algorithm was applied to the suspension system of a single-degree-of-freedom magnetic bearing system. It proved valuable in the design and implementation of a precise positioning platform based on this magnetic bearing system. In summary, many scholars have studied the trajectory tracking control of AMBs, but few have studied tracking performance under different reference signals, which is also very important. Therefore, it is necessary to track the trajectory of AMBs under different reference signals. Furthermore, it is particularly important to ensure that a bearing rotor has good positional tracking performance under different reference signals in the process of axial position tracking control. In this process, the magnetic thrust bearings need to drive a rotor and change its axial position to meet the needs of different reference signals (part contours).7

Based on the above research, in this paper, a PID

Submitted On: November 28, 2018
Accepted On: April 6, 2019

controller is applied to a magnetic thrust bearing to study the positional tracking of AMBs. The main contribution of this paper is to study trajectory tracking control performance with AMBs under different reference signals based on axial variable reference positional control of the rotor, which is the basis of machining or fluid mechanical surge control. The implementation process of this study is as follows. First, the working principle of trajectory tracking about magnetic bearings is expounded. Then, an integrative electromechanical model of trajectory tracking is comprehensively described and mathematical models of a rotor-electromagnet, sensor, power amplifier, and controller time delay are analyzed. A simulation study based on trajectory tracking of magnetic thrust bearings is then carried out. In the simulation, a PID controller is used to realize trajectory tracking simulation analysis under different reference signals. Finally, the trajectory tracking control performance of different reference signals under static and rotational states is verified experimentally.

The rest of this paper is arranged as follows. Section 2 introduces the AMB trajectory tracking principle. Mechatronics modeling of trajectory tracking is presented in Section 3. Section 4 presents an analysis of the simulation. Section 5 presents the experimental results. Conclusions are drawn in the final section.

II. PRINCIPLE OF MAGNETIC SUSPENSION TRAJECTORY TRACKING

The principle of magnetic suspension trajectory tracking is graphically represented in Fig. 1, where C_0 is the unilateral air gap (C_0 = 0.75 mm), δ represents the offset relative to the middle position, I_0 is the bias current, and I_1 is the control current. The basic working principle is that both the bias current and control current enter the coil, which drives the electromagnet to generate an electromagnetic force. Thus, the value of δ is adjusted to implement trajectory tracking.

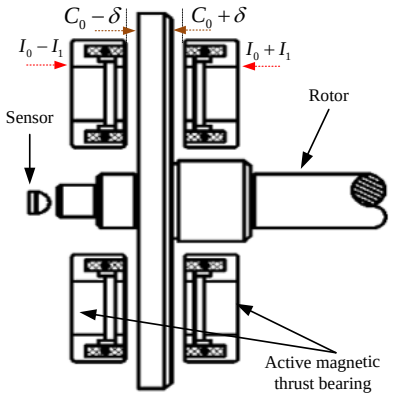

Fig. 1. Principle of magnetic suspension trajectory tracking.

According to Maxwell's principle, the electromagnetic force imposed on a suspended object (rotor) is given by [9]:

$$F_x = F_{x1} - F_{x2} = \frac{\mu_0 AN^2}{4}\left[\left(\frac{I_0+I_1+i_x}{C_0+\delta+x}\right)^2 - \left(\frac{I_0-I_1-i_x}{C_0-\delta-x}\right)^2\right], \quad (1)$$

where F_{x1} and F_{x2} are the electromagnetic forces imposed on the suspended object (rotor) on each side of the magnetic bearing, μ_0 is the permeability of the vacuum, A is the magnetic pole area, N is the number of coils turns, i_x is the current disturbance, and x is the displacement disturbance around the suspension position.

The function is expanded in Taylor's series when $i_x = 0$ and $x = 0$, and neglecting the higher-order term [9]:

$$\tilde{F}_x = \tilde{F}_0 + k_i \cdot i_x + k_x \cdot x, \quad (2)$$

where k_i and k_x indicate the force-current stiffness and force-displacement stiffness, respectively. The parameters in Eq. (2) are given as follows:

$$\tilde{F}_0 = \frac{\mu_0 AN^2}{4}\left[\left(\frac{I_0+I_1}{C_0+\delta}\right)^2 - \left(\frac{I_0-I_1}{C_0-\delta}\right)^2\right], \quad (3)$$

$$k_i = \frac{\mu_0 AN^2}{2}\left[\frac{(I_0+I_1)}{(C_0+\delta)^2} + \frac{(I_0-I_1)}{(C_0-\delta)^2}\right], \quad (4)$$

$$k_x = -\frac{\mu_0 AN^2}{2}\left[\frac{(I_0+I_1)^2}{(C_0+\delta)^3} + \frac{(I_0-I_1)^2}{(C_0-\delta)^3}\right]. \quad (5)$$

When the system is suspended stably, the current disturbance i_x and displacement disturbance x around the suspension position are both zero, and the system is force-balanced, that is:

$$\frac{\mu_0 AN^2}{4}\left[\left(\frac{I_0+I_1}{C_0+\delta}\right)^2 - \left(\frac{I_0-I_1}{C_0-\delta}\right)^2\right] = 0. \quad (6)$$

Finally, it can be deduced that $I_1 = \frac{\delta}{C_0} I_0$.

Both the force-current stiffness k_i and force-displacement stiffness k_x can be considered as nonlinear functions of the offset value relative to the middle position δ.

According to the parameters in Table 1, the relationships between the force-current stiffness k_i, the force-displacement stiffness k_x, and the offset relative to the middle position δ can be obtained, as shown in Fig. 2.

Variation in the electromagnetic force of the AMBs requires adjustment of the active controller. Thus, stable suspension and accurate trajectory tracking of the rotor

can be obtained. The control principle is depicted in Fig. 3. The error between the reference signal and feedback signal (that is, the trajectory tracking signal) is actively adjusted by the controller, with the target error being zero. If the error is not zero, the controller will keep actively adjusting the system. This adjustment process comprises the trajectory tracking of the AMBs.

Table 1: Major parameters of the magnetic thrust bearing

Parameter Name	Symbol	Value	Unit
Vacuum permeability	μ_0	$4\pi\times10^{-7}$	N/A^2
Magnetic pole area	A	7.69×10^{-4}	m^2
Coil turns	N	240	/
Single stage clearance of middle point	C_0	0.75×10^{-3}	m
Bias current	I_0	2.0	A

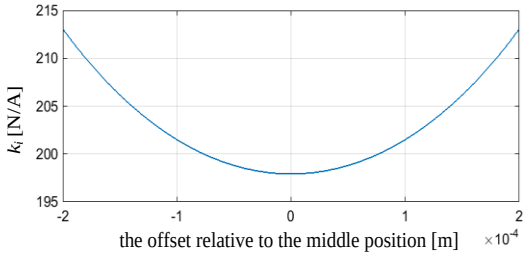

(a) Variation in force-current stiffness with suspension position

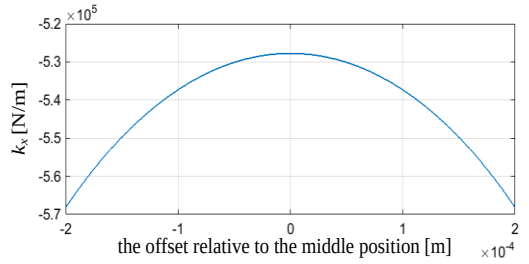

(b) Variation in force-displacement stiffness with suspension position

Fig. 2. Relationships of force-current stiffness k_i and force-displacement stiffness k_x.

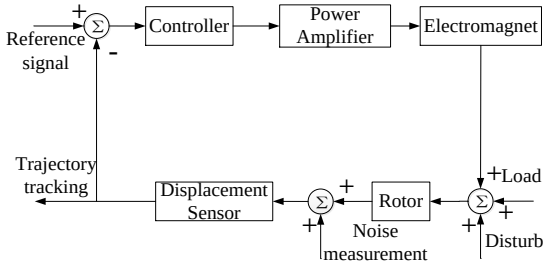

Fig. 3. Principle of trajectory tracking in AMBs.

Because variation in the suspension position can lead to changes in the force-current stiffness k_i and force-displacement stiffness k_x, it is necessary to determine whether the controller can ensure system stability and good tracking under changing values of k_i and k_x.

III. MODELING OF AMB TRAJECTORY TRACKING

The AMB trajectory tracking control model is depicted in Fig. 4. Displacement of the rotor relative to the reference position is detected by the sensor. The control signal is calculated by the controller according to the error signal. The control signal is sent to the power amplifier to be transformed into the control current, which will drive the electromagnet to generate the control force so that the rotor is suspended in a given position. In Fig. 4, C is the controller, K_a is the transfer function of the power amplifier, G_{AMB} is the transfer function of the electromagnet and rotor, and K_s is the gain of the sensor.

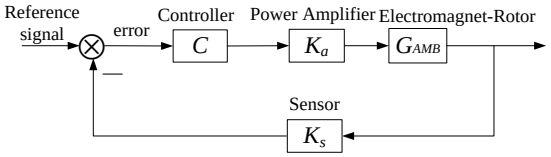

Fig. 4. Control model of trajectory tracking.

A. Electromagnet-rotor model

Around the stable working point of the magnetic bearing system, the transfer function of the electromagnet and rotor can be determined by small-scale linearization of force, displacement and current [9]:

$$G_{AMB} = \frac{k_i}{ms^2 + k_x}, \tag{7}$$

where m represents the rotor mass (m = 14.56 kg).

B. Displacement sensor model

The bandwidth of the eddy current displacement sensor is 5 kHz, which is much larger than the frequency of the axial tracking signal. Therefore, the displacement sensor can be considered as an ideal proportional system. The detection range of the axial displacement sensor is 0 to 0.9 mm and its output ranges from 0 to 5 V. The gain of the sensor is given by:

$$K_s = 50000/9 \ \text{(V/m)}. \tag{8}$$

C. Power amplifier model

The adopted power amplifier is a kind of voltage-current three-level PWM switching power amplifier. After obtaining the amplitude-frequency characteristics of the power amplifier by a frequency sweep test, the

transfer function can be identified by a third-order model:

$$K_a = \frac{0.04204s^3 + 3979s^2 + 8.737\times10^6 s + 1.505\times10^9}{s^3 + 9251s^2 + 6.451\times10^6 s + 1.098\times10^9}. \quad (9)$$

Figure 5 illustrates a comparison of the tested frequency response and the theoretical model of the power amplifier. The red solid line is the Bode diagram of the theoretical model, namely Eq. (9), and the blue dashed line is the Bode diagram of the experimental test. From this figure, it can be seen that the theoretical model accurately describes the characteristics of the power amplifier.

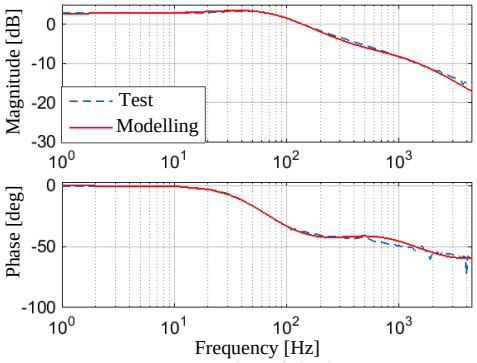

Fig. 5. Comparison between the tested frequency response and theoretical model of the power amplifier.

D. Modeling of the electrical part of the system

The digital control system was developed based on DSP. Its hardware included an anti-aliasing filter circuit added to the pre-processing circuit before the displacement input, and a smoothing filter was added to the post-processing circuit after the control signal. As for the DSP chip itself, A/D and D/A conversion were also added into the control system.

The transfer functions of the smooth filter link and partial voltage link were obtained by theoretical derivation, as follows:

$$G_{pp}(s) = \frac{0.6}{9.132\times10^{-10}s^2 + 4.22\times10^{-5}s + 1}. \quad (10)$$

The mathematical models of the DSP chip and D/A conversion module can be simplified to time delay transfer functions, and the mathematical model of the DSP chip and D/A transfer module can be obtained as:

$$G_D(s) = k_d e^{-sk_t T_s}. \quad (11)$$

In Eq. (11), k_t is the coefficient of lag time and k_d is the gain term. A more accurate mathematical model can be obtained by modifying k_t and k_d. In this paper, the approximate mathematical model can be obtained by adopting a second-order Pade approximation [17]. Taking k_t as 1.1, k_d as 3.35, and sampling time T_s as 0.0001, an approximate mathematical model of the time delay can be obtained as follows:

$$G_D(s) \approx k_d \frac{(0.3175T_s s - 1)^2}{(0.3175T_s s + 1)^2} = \frac{3.35(0.3175\times10^{-4}s - 1)^2}{(0.3175\times10^{-4}s + 1)^2}. \quad (12)$$

E. Reducing the order of the overall object model

After getting the model of each link in the trajectory tracking closed-loop, all links except the controller are incorporated into the controlled object, then the model of the controlled object is as follows.

$$G_s(s) = G_{AMB}(s)\bullet K_s(s)\bullet K_a(s)\bullet G_{pp}(s)\bullet G_D(s). \quad (13)$$

The order of the controlled object model is 10, and such high order number will make it difficult to adjust the controller parameters in the simulation. Thus, the control algorithm is hard to implement. Since the operating frequency range of the magnetic thrust bearing-rotor system mainly covers lower frequencies, the order of the controlled object model can be reduced if the accuracy of the system at low frequencies can be guaranteed. We used the hankelmr function to reduce the order of the model to 3. The model after reduction is given by:

$$G_s(s) = \frac{-11.47s^2 + 2.389\times10^4 s + 1.436\times10^8}{s^3 + 557.3s^2 - 1.101\times10^4 s - 2.501\times10^7}. \quad (14)$$

IV. SIMULATION OF TRAJECTORY TRACKING

The electromagnetic force of the magnetic suspension fluid mechanical rotor and the magnetic suspension machining tool will change nonlinearly with changes of the suspension position. In order to study the trajectory tracking performance of the magnetic bearing system, a PID controller was designed.

The structure of the PID controller is presented in Eq. (15), and its control parameters, obtained by trial-and-error, are illustrated in Table 2:

$$C(s) = K_p + \frac{K_i}{s} + K_d \frac{s}{\frac{1}{2\pi f}s + 1}. \quad (15)$$

Table 2: Control parameters of the PID controller in simulation

Control Parameter	Symbol	Value
Proportional coefficient	K_p	9
Integral coefficient	K_i	90
Differential coefficient	K_d	0.03
Cut-off frequency	f	1500

A reference signal is introduced into the sinusoidal signal with a frequency is 0.5 Hz and amplitudes of 0.2 V, 0.4 V, and 0.6 V, respectively. The obtained simulation of rotor position tracking is shown in Fig. 6. It can be seen from Fig. 6 that sinusoidal signals of different amplitudes have better tracking performance with a 0.5 Hz frequency. Moreover, the tracking error of the

sinusoidal signals with different amplitudes is almost the same, with a maximum value of about 0.58%.

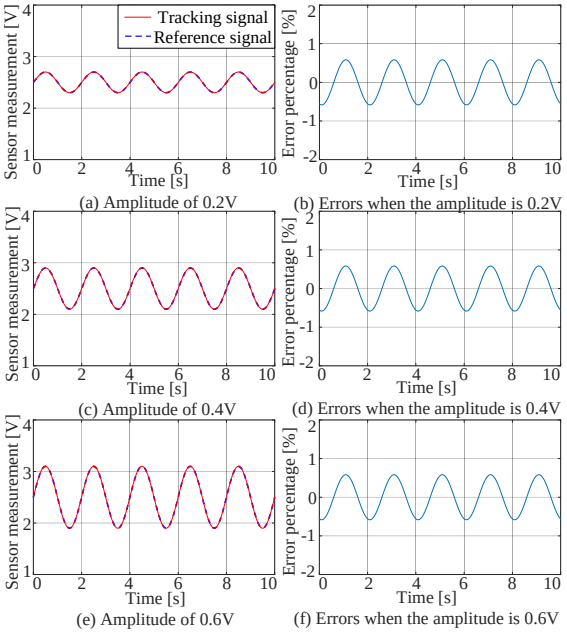

Fig. 6. Trajectory tracking of sinusoidal signals.

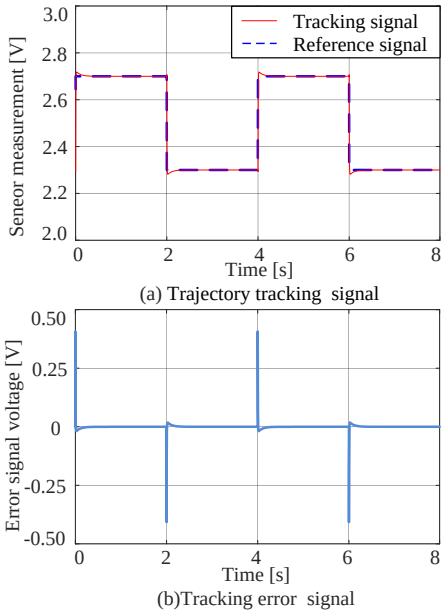

Fig. 7. Trajectory tracking of square wave signal.

The reference signal is superposed with a square wave signal with a frequency of 0.25 Hz and amplitude of 0.4 V so that a trajectory tracking simulation of the rotor can be obtained, as presented in Fig. 7. It can be seen from Fig. 7 that the square wave signal also has good tracking performance. The maximum tracking error occurs at the moment of sudden change in the signal. However, the error of the maximum amplitude relative to the equilibrium position is small, which is about 0.018V, and the adjustment time is about 0.32 seconds.

The reference signal is set to a continuous step form to achieve trajectory tracking simulation of the rotor, as illustrated in Fig. 8. From Fig. 8, we can see that the tracking effect is better with the continuous step signal. The maximum tracking error also occurs at the moment of sudden change in the reference signal. The error of the maximum amplitude relative to the equilibrium position is relatively small, which is 0.01 V. The adjustment time is only 0.19 seconds.

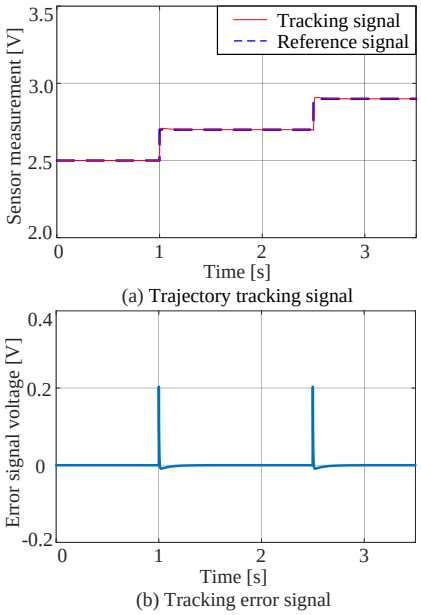

Fig. 8. Trajectory tracking of a continuous step signal.

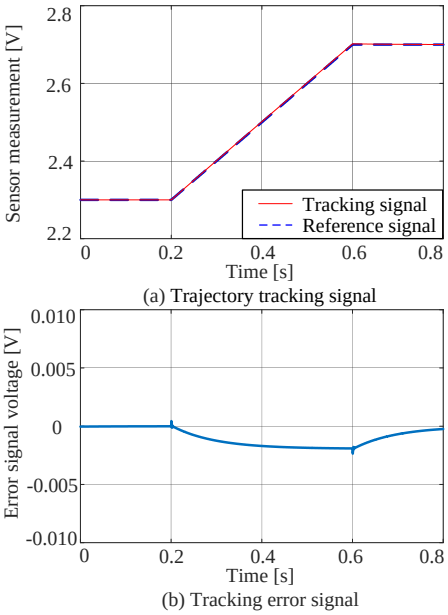

Fig. 9. Trajectory tracking of a ramp signal.

Figure 9 displays the tracking performance of a ramp signal. It can be concluded that since the variation amplitude of the signal transition is smaller than that of the square wave and step signals, the tracking error is relatively small, with a maximum tracking error of about 0.0024 V.

V. EXPERIMENTAL STUDY OF TRAJECTORY TRACKING PERFORMANCE

In this section, the tracking effect of different reference signals is verified by the axial trajectory tracking experiments under the static suspension and rotating states.

A. Trajectory tracking performance under a static suspension state

Figure 10 shows the test rig, whose main components were an AMB-rotor test bench, sensors and conditioning circuit, power amplifiers, digital controller, signal generator, PC, and so on. Table 3 lists the PID control parameters used in the experiment.

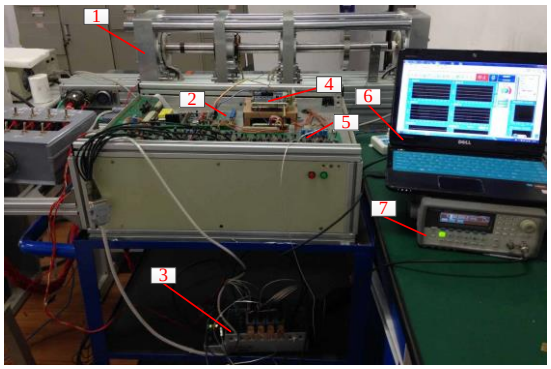

1.AMB-Rotor; 2.Sensors and conditioning circuit; 3.Data acquisition card; 4.Digital controller; 5.Power amplifier; 6. PC; 7.Signal Generator.

Fig. 10. Experimental equipment.

Table 3: PID controller parameters used in the experiment

Control Parameter	Symbol	Value
Proportional coefficient	K_p	7
Integral coefficient	K_i	70
Differential coefficient	K_d	0.0192
Cut-off frequency	f	1500

The signal generator generated sinusoidal signals with a frequency of 0.5 Hz and amplitudes of 0.2 V, 0.4 V, and 0.6 V. The signals were input to the digital controller of the magnetic bearing system as an axial position reference signal to obtain the axial position response of the rotor, as shown in Fig. 11.

From Fig. 11, it can be concluded that the positional tracking errors of the sinusoidal signals under PID control were small and meet the basic real-time tracking requirements. Due to the existence of high-frequency interference, the tracking errors were slightly larger than those of the simulation. The error was about 20% at an amplitude of 0.2 V and was within 15% at amplitudes of 0.4 V and 0.6 V. The larger error at the lower amplitude was also due to the existence of high-frequency interference, which increases the relative error at low amplitude.

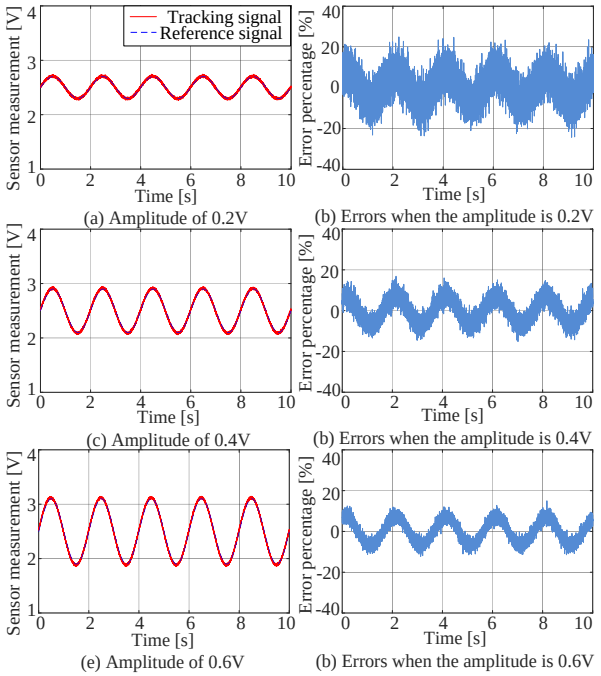

Fig.11. Trajectory tracking of sinusoidal signals (static suspension).

Figure 12 exhibits the tracking performance with a square wave reference signal. The reference signal was superimposed with a square wave signal with a frequency of 0.25 Hz and amplitude of 0.4 V. From Fig. 12, it is evident that the square wave signal also provided a good tracking effect in the experiment. The maximum tracking error occurred at the moment of abrupt change, but the error of the maximum amplitude relative to the equilibrium position was small, about 0.18 V, and the adjustment time was about 0.17 seconds.

The reference signal was set to a continuous step form, as illustrated in Fig. 13, and a rotor position tracking effect diagram was obtained. It can be observed from Fig. 13 that the continuous step signal had a good tracking effect. The maximum tracking error was at the moment of sudden change in the step signal. The errors of the maximum amplitude relative to the equilibrium position and adjustment time were small, about 0.12 V and 0.17 seconds, respectively.

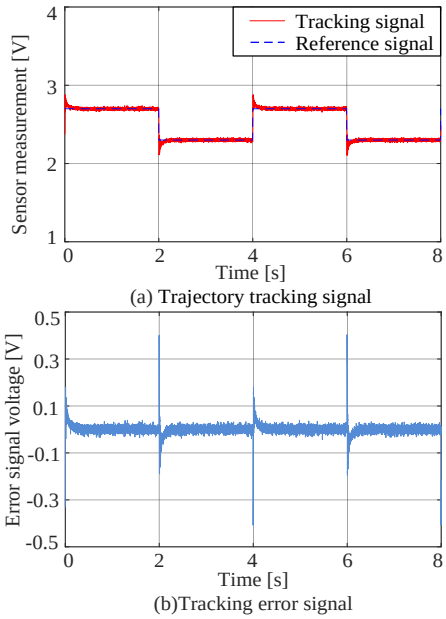

Fig. 12. Trajectory tracking of a square wave signal (static suspension).

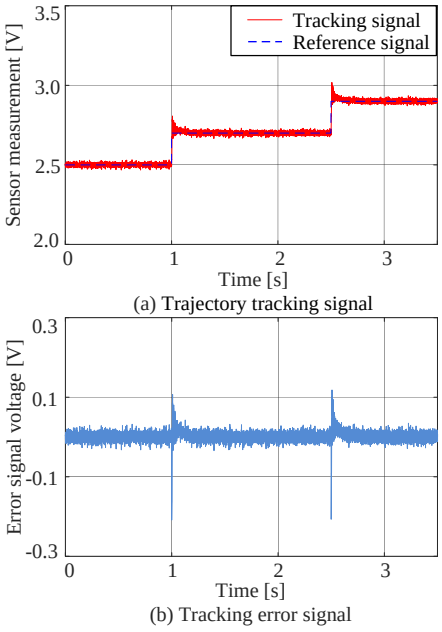

Fig. 13. Trajectory tracking by a continuous step signal (static suspension).

Fig. 14 shows a tracking effect diagram for a ramp reference signal. Similar to the simulation results, the error was smaller than with other mutation signals. The tracking effect meets the basic real-time tracking requirements.

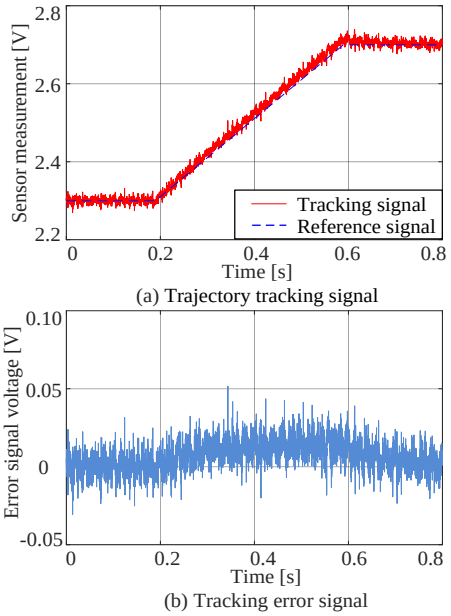

Fig. 14. Trajectory tracking by a ramp signal (static suspension).

The experimental results above indicate that the system had good axial position tracking performance under static suspension. However, the tracking performance in a rotating state still needs verification.

B. Trajectory tracking performance in a rotating state

The trajectory tracking accuracy of the magnetic bearing spindle system in the rotating state is directly related to the machining accuracy of the workpiece. And the magnetic suspended fluid mechanical surge control is also operated under the rotating state. So, it is particularly important to study the tracking accuracy in the rotating state. The tracking performance of sinusoidal signals at different rotational speeds is shown in Fig. 15. It can be indicated from Fig. 15 that the performance of the positional tracking of the magnetic bearing system was less affected by the rotational speed, with maximum errors of about 30% at the three speeds tested. The main reason for the larger error is that the amplitude of the sinusoidal reference signal was 0.2 V (too small for high-frequency noise) at the three speeds, and the final error was relatively large due to the existence of high-frequency noise.

To study the trajectory tracking performance of the magnetic bearing system while rotating, a speed of 3000 rpm was selected for the experiment. The tracking results with a sinusoidal signal with amplitudes of 0.4 V and 0.6 V are shown in Fig. 16. Compared with tracking during static suspension (Fig. 11), tracking while rotating was also good, with an error was less than 15% (Fig. 16).

Taking the sinusoidal signal with an amplitude of 0.6 V as an example, the tracking error was within 16.2 μm. It is also evident that the larger the amplitude of the sinusoidal signal, the smaller the tracking error. The reason is that the existence of high-frequency noise affects the tracking accuracy of low amplitude signals.

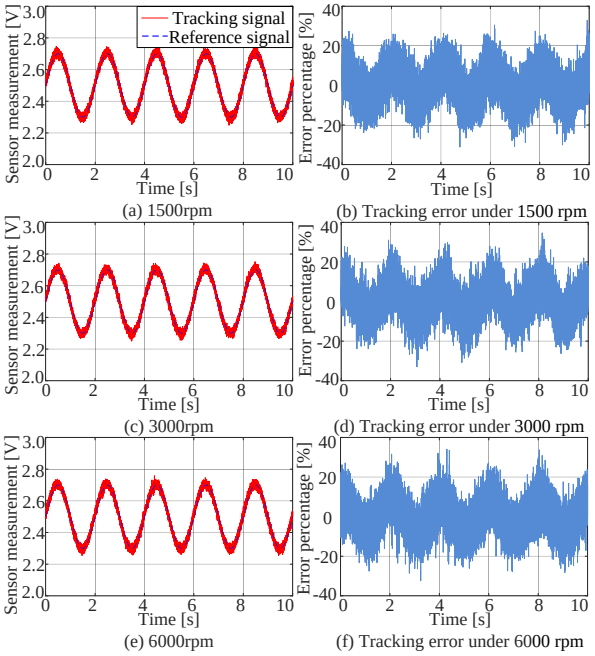

Fig. 15. Tracking by sinusoidal signals in a rotating state.

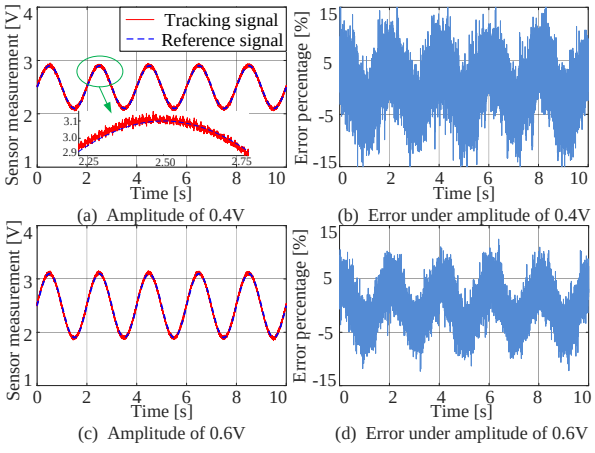

Fig. 16. Tracking by sinusoidal signals (3000 rpm).

Figure 17 displays the tracking performance with a square wave signal at a bearing speed of 3000 rpm. It shows that the tracking effect was better in the rotating state and the maximum error occurred at the position of signal mutation.

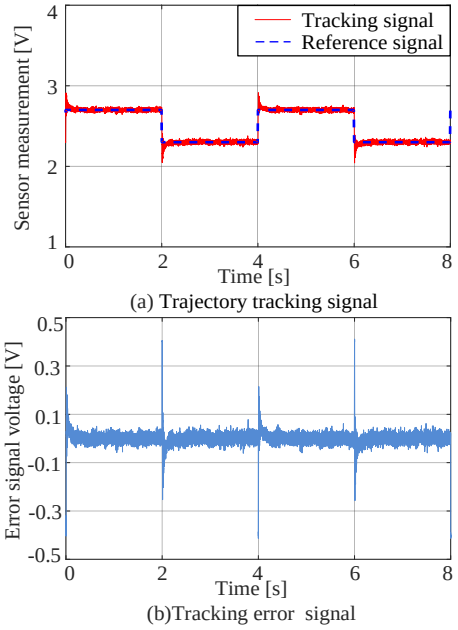

Fig. 17. Tracking by a square wave signal (3000 rpm).

The tracking performance with a continuous step signal at 3000 rpm is illustrated in Fig. 18. The tracking error was within ± 0.1 V, which is about 18 μm.

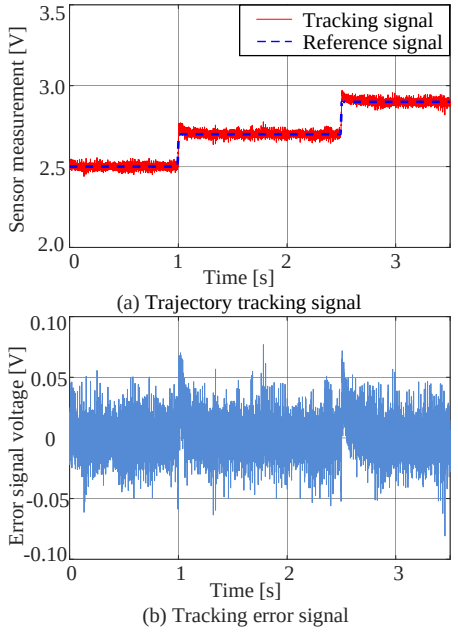

Fig. 18. Tracking by a continuous step signal (3000 rpm).

Figure 19 illustrates the tracking performance with a ramp signal at 3000 rpm. The tracking error was within ± 0.05 V, which is about 9 μm.

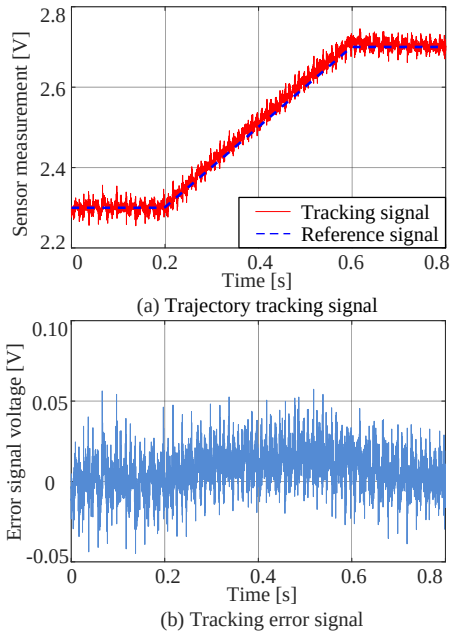

Fig. 19. Tracking by a ramp signal (3000rpm).

The results of the rotational tracking experiments demonstrate that axial position tracking was better, and all tracking errors were small with different machining contours.

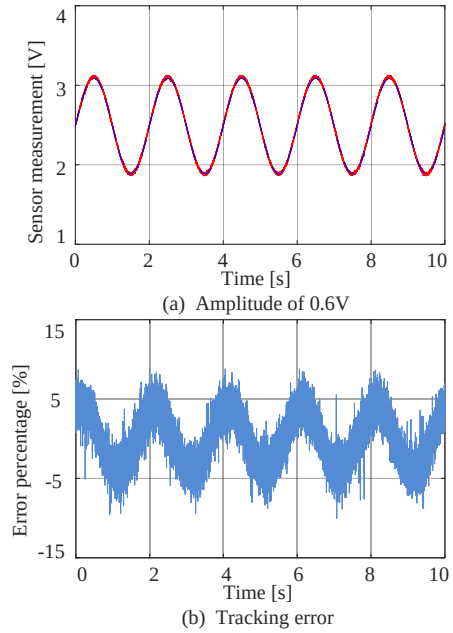

Fig. 20. Tracking by sinusoidal signals with a low-pass filter (3000 rpm).

In order to reduce the influence of sensor measurement noise, a displacement signal was input to the controller after it passed through the second-order low-pass filter with a cut-off frequency of 3 kHz, and then the corresponding control was performed. The transfer function of the low-pass filter was as follows:

$$G_s(s) = \frac{1}{1.1501\times10^{-9}s^2 + 6.7827\times10^{-5}s + 1}. \quad (16)$$

Taking the 0.6 V sinusoidal signal in Fig. 16 as an example, the tracking effect after introducing the low-pass filter is shown in Fig. 20. The comparison shows that the low-pass filter effectively reduced the high-frequency component of the displacement signal. At the same time, the error was reduced by about 2.3% compared with the original.

The lower the cut-off frequency, the lesser the influence of displacement signal noise on the controller, but an over-lowed cut-off frequency reduces the stability of the system. Therefore, an effective cut-off frequency should be obtained via repeated experiments.

VI. CONCLUSION

In this paper, we abstracted the machining curve into several different reference signals. Then, the trajectory tracking performance of the magnetic thrust bearing under these reference signals was studied. Simulations and experiments indicate that the PID controller can meet the performance requirements of axial position control, and the trajectory tracking errors are within the allowable range. All the different machining profiles tested in this paper can meet the requirements of positional control. The results obtained in this paper provide bases for the positional control of magnetic levitation motorized spindle tools and magnetic suspension fluid mechanical surge control. The conclusions are summarized as follows.

1) Both static and rotating states provide high trajectory tracking accuracy, but the accuracy is slightly lower in the rotating state.
2) Rotational speed has little effect on the accuracy of axial trajectory tracking.
3) High-frequency noise causes relatively large tracking errors with reference signals with small amplitudes.
4) Tracking accuracy based on sinusoidal signals is higher than that using other signals such as square waves.
5) Overall, under the experimental conditions, the tracking errors were all within 18 μm.
6) After the low-pass filter was introduced, the high-frequency component of the displacement signal could be significantly reduced.

In future work, we will study trajectory tracking with different interference signals and try to improve tracking accuracy by applying advanced algorithms. Reducing the influence of high-frequency noise on tracking accuracy is also worthy of further research.

ACKNOWLEDGMENT

This work has been supported by National Natural Science Foundation of China (51675261), Jiangsu Province Key R&D programs (BE2016180), Postgraduate Research & Practice Innovation Program of Jiangsu Province (KYCX17_0244).

REFERENCES

[1] M. Tang, J. Zhou, C. Jin, and Y. Xu, "Vibration isolation of magnetic suspended platform with double closed-loop PID control," *Applied Computational Electromagnetics Society Journal*, vol. 32, no. 8, pp. 712-719, 2017.

[2] K. Sato and G. J. Maeda, "A practical control method for precision motion-Improvement of NCTF control method for continuous motion control," *Precision Engineering*, vol. 33, no. 2, pp. 175-186, 2009.

[3] H. Shi, D. Zhang, J. Yang, C. Ma, and G. Gong, "Experiment-based thermal error modeling method for dual ball screw feed system of precision machine tool," *International Journal of Advanced Manufacturing Technology*, vol. 82, pp. 1693-1705, 2016.

[4] A. Woronko, J. Huang, and Y. Altintas, "Piezoelectric tool actuator for precision machining on conventional CNC turning centers," *Precision Engineering*, vol. 27, no. 4, pp. 335-345, 2003.

[5] Y. Tian, B. Shirinzadeh, and D. Zhang, "A flexure-based mechanism and control methodology for ultra-precision turning operation," *Precision Engineering*, vol. 33, no. 2, pp. 160-166, 2009.

[6] S. Eckhardt and J. Rudolph, "High precision synchronous tool path tracking with an AMB machine tool spindle," *The 9th International Symposium on Magnetic Bearings*, Lexington, KY, USA, 2004.

[7] H. Wang and D. Hu, "Machining principle for noncircular piston pin-hole based on magnetic levitated spindle," *Chinese Internal Combustion Engine Engineering*, vol. 27, no. 3, pp. 54-57, 2006.

[8] A. Smirnov, A. H. Pesch, O. Pyrhönen, and J. T. Sawicki, "High-precision cutting tool tracking with a magnetic bearing spindle," *Journal of Dynamic Systems Measurement & Control*, vol. 137, no. 5, pp. 1-8, 2015.

[9] G. Schweitzer and E. H. Maslen, *Magnetic Bearings*. Springer, Berlin, Germany, 2009.

[10] D. Sanadgol, "Active control of surge in centrifugal compressors using magnetic thrust bearing actuation," *Virginia: University of Virginia*, 2006.

[11] S. Y. Yoon, "Surge control of active magnetic bearing suspended centrifugal compressors," *Virginia: University of Virginia*, 2011.

[12] T. P. Minihan, S. Lei, G. Sun, A. Palazzolo, A. F. Kascak, and T. Calvert, "Large motion tracking control for thrust magnetic bearings with fuzzy logic, sliding mode, and direct linearization," *Journal of Sound and Vibration*, vol. 263, no. 3, pp. 549-567, 2003.

[13] A. H. Pesch, A. Smirnov, O. Pyrhönen, and J. T. Sawicki, "Magnetic bearing spindle tool tracking through μ-synthesis robust control," *IEEE/ASME Transactions on Mechatronics*, vol. 20, no. 3, pp. 1448-1457, 2015.

[14] S. Zheng, J. Yang, X. Song, and C. Ma, "Tracking compensation control for nutation mode of high-speed rotors with strong gyroscopic effects," *IEEE Transactions on Industrial Electronics*, vol. 65, no. 5, pp. 4156-4165, 2018.

[15] T. R. Grochmal and A. F. Lynch. "Precision tracking of a rotating shaft with magnetic bearings by nonlinear decoupled disturbance observers," *IEEE Transactions on Control Systems Technology*, vol. 15, no. 6, pp. 1112-1121, 2007.

[16] S. Basovich, S. Arogeti, and Z. Brand, "Adaptive output zero-bias tracking control of 1DOF AMB suspension system," *International Conference on Control Automation Robotics & Vision IEEE*, pp. 151-156, 2014.

[17] S. Skogestad and I. Postlethwaite, *Multivariable Feedback Control: Analysis and Design*. Wiley, New York, USA, 2005.

Uncertainty Problem as Illustrated by Magnetotherapy

Przemyslaw Syrek

Department of Electrical and Power Engineering
AGH University of Science and Technology, Krakow, Poland
syrekp@agh.edu.pl

Abstract ─ This article presents the impact of fixed tissue conductivities on the distribution of eddy currents in human body. Electrical conductivities characterising human tissues present in limbs have been collated based on various publications from the last 25 years. The article shows the extent to which simulation results are affected by changes to electrical conductivity of specific tissues. It has been demonstrated that the tissues taking the largest part of the studied domain have the greatest impact. The conclusions from these results suggest that it is very important to determine the electrical conductivity of tissues forming the human body with increasing precision, as it is an important factor affecting the accuracy of results. This factor seems much more significant than the growth in the precision of models resulting from increasing resolution of numerical models made available for research purposes.

Index Terms ─ Bioelectromagnetics, eddy currents, other dielectric or magnetic materials, magnetic devices, magnetic fields, uncertainty problem.

I. INTRODUCTION

Magnetotherapy is a method of treatment or stimulation of human body tissues the current is induced by means of a time-varying magnetic component (Magnetic Field–MF) of Electromagnetic Field (EMF) and used in the treatment of many diseases [1]. Unlike the stressful method involving electrodes, magnetotherapy relies on induction of electric currents in the tissue without physical contact and is used especially in regard to bones [2], [3]. Calculation of the distribution of magnetic field-induced eddy currents in limbs require relatively high computational complexity. However, as computers are becoming more powerful, and virtual human models that involve systems of hundreds of thousands of equations to be solved are becoming available, the time necessary to carry out relevant calculations can be less than an hour, even if we use computers available to the general public (at a reasonable price). The driver for research, including numerical computations, is multifaceted work related to transcranial magnetic stimulation (TMS). This is the area where solutions of very accurate models are being forced [4], which results in the necessity to solve systems of tens of millions of algebraic equations.

In addition to the tendency to increase the accuracy of calculations by compacting grids – resulting from the resolution of available models, sometimes it is necessary to use significantly simplified models, especially when devices are optimized, e.g., magnetic coils [5]. Then the field problem can be solved analytically or be reduced to calculate a curve integral [6] with a mathematical representation of a coil [7].

The growing accuracy of calculations, however, is still accompanied by some uncertainty. It is related to the electrical parameters of tissues, particularly their electrical conductivity. This article shows how significant for the analysis of eddy currents distribution is conductivity of specific tissues and how significantly it can impact the results. Based on the cited works, it has been shown that there are large discrepancies in tissue conductivity in computational models used in recent decades.

Although electrical parameters and publications on this subject have been appearing for several decades, in recent years, very high-resolution models of human body's structure have been developed. The article shows that, in contrast to the model's resolution, and three-dimensional mesh generation method, the tissues conductivities are very important, and may substantially affect the results – also those presented using statistical tools.

II. COMPUTATIONAL PROBLEM

A. Magnetotherapy background

Calculation of eddy currents distribution uses a model from Virtual Family [8], which is based on MRI scans of women (Ella): 26-year-old, 1.63 meters in height and over 58 kg in weight. The eddy currents distribution was evaluated in a 100 mm fragment of an upper limb (left arm), whose skeleton was shown in Fig. 1 in an X-Ray-like style. Calculations use a largely extended domain, i.e., nearly the entire arm from the humerus to the wrist. In the figure in question, three cross-sections (CS1, CS2, CS3) have been marked perpendicularly to both bones in this limb fragment.

Submitted On: July 10, 2018
Accepted On: December 25, 2018

Tissue distribution for these cross-sections have been shown in the subsequent illustrations: Figs. 2–4.

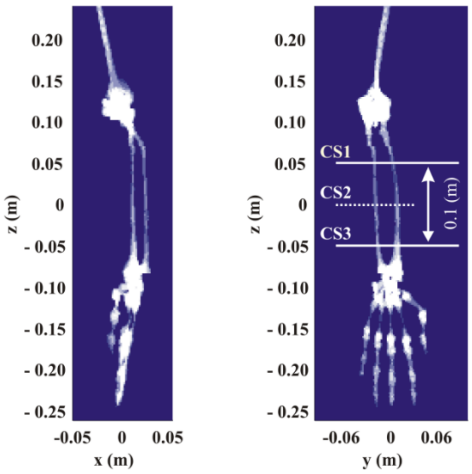

Fig. 1. The women's left hand. Cross sections (CS1, CS2, CS3) presented on next figures.

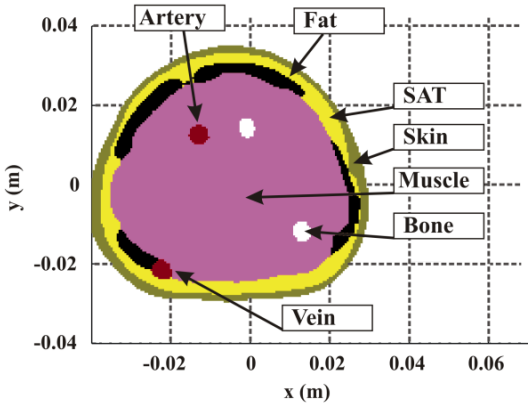

Fig. 2. Cross section CS1 and highlighted tissues. CS1 is an upper boundary of analysed domain.

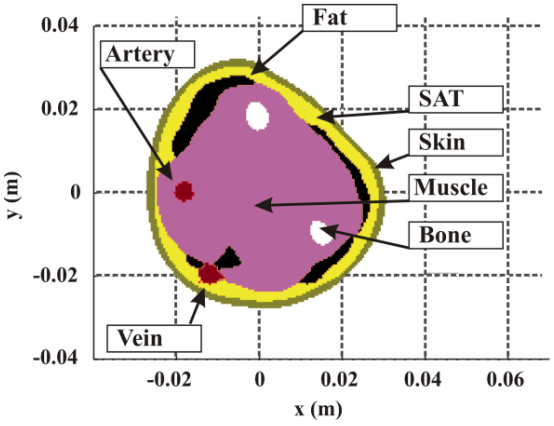

Fig. 3. Cross section CS2 and highlighted tissues.

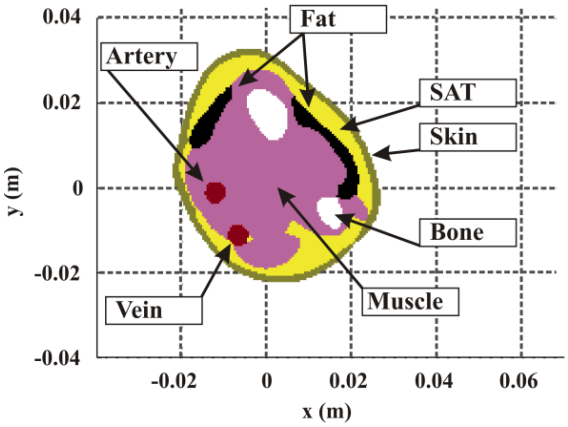

Fig. 4. Cross section CS3 and highlighted tissues. CS3 is a lower boundary of analysed domain.

This 100 (mm) limb fragment has the volume of nearly 276,000 cubic millimetres and is divided into sub-domains corresponding to 8 tissues present in them, which has been collated in Table 1. Data has been collated based on a model with the resolution of 1 mm. It also uses the Iso2mesh free library to overlay the tetrahedral mesh over the structural mesh [9] forming the border between both the arm and the air (insulator).

Table 1: Tissues in 100 mm part of the limb

Tissue	Volume (mm^3)	Percent of Total Volume (%)
All	275904	100.00
Muscle	168304	61.00
Subcutaneous adipose tissue (SAT)	45984	16.67
Skin	29608	10.73
Fat	22752	8.25
Bone	5072	1.84
Veins	2168	0.79
Arteries	1984	0.72
Marrow red	32	0.01

The simulations presented in the article use the coil with a multilayer solenoid (Fig. 5), 0.1 (m) in inner radius and 0.2 (m) in length (along the *z*–axis). The coil is powered with sinusoidal current whose RMS is equal to 1 (A). The axis of the main coil is parallel to and nearly coincides with the long bones of the upper limb, i.e. ulna and radius. Two bones positioned in such a way are extremely useful for this reflection, because a single long bone situated almost at the axis of symmetry of the domain in question could be located in such a manner, that eddy current paths would run around it regardless of its conductivity.

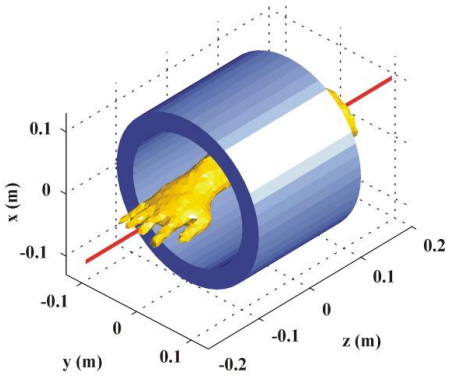

Fig. 5. Applicator, hand's model and *z*-axis.

The arm is exposed to a sinusoidal B-field of about 25 (mT) (RMS) at 50 (Hz). This coil is characterised by a relatively homogeneous B-field. The B-field distribution along the coil axis, is shown in Fig. 6.

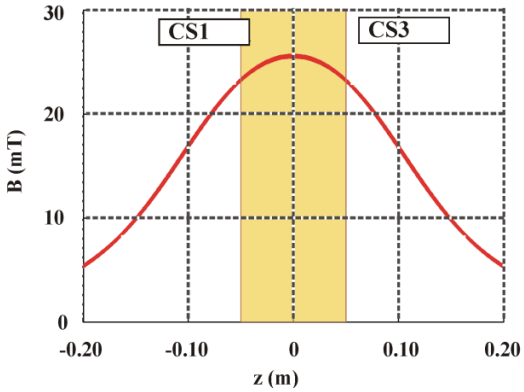

Fig. 6. Magnetic field with the x-axis.

B. Field model

Determining the current (here: eddy currents) density distribution using numerical methods requires the use of an appropriate model whose complexity depends on the type of problem being analysed. There is an assumption, that ferromagnetic materials are absent in the domain, and the entire domain is characterised by magnetic permeability equal to the magnetic constant. Due to the very low dielectric permittivity of human tissues and the air surrounding them, and due to the low frequency band, displacement current is neglected.

Human tissues are characterised by relatively low electrical conductivity as well, and in addition, the limb (body) is surrounded by air (an insulator of zero-conductivity). Hence, the eddy currents reach quite low values, and magnetic field induced by them (secondary magnetic field) it is insignificantly low in relation to the external field induced by the coil.

For this type of issues, the so-called AV model – a pair of: vector magnetic potential (A) and electrical potential (V) – is provided. Thus, the analysed domain is described by the Partial Differential Equation (PDE), which is replaced by a system of algebraic equations. In turn, the equation system and its dimension depend on accuracy (resolution) of model used. Both PDE and Boundary Conditions, which are unavoidable in this case, have been introduced in: [10]–[12].

Thanks to the properties of the domain presented above, the results are scalable, since the model is linear in the extremely low frequency band. Once the eddy current distribution is determined for a given spatial configuration of the limb and the coil, this gives the option of converting the result using a real coefficient. It is assumed that the source (current of coil and MF distribution) is scaled by this coefficient. This was used to standardize the results obtained for a collective presentation.

C. Numerical solution procedure

To obtain the results, proper partial differential equation has to be replaced by system of algebraic (here linear) equations. For this purpose, Finite Element Method (FEM) with cubic elements was used. This kind of spatial mesh is due to geometry of human body model, composed of voxels. The analyzed problem involves formulation and solution of over 338 thousand of equations. To obtain one solution of PDE on personal computer with clock rate of 3.30 GHz and 16 GB of RAM, about one hour is needed.

The total computational time consists of several stages. The first is creation of matrix corresponding to the left side of equation system. This matrix is rare, and its exact structure and values of entries depend on mutual location of individual elements of human body model and their electrical properties. Matrix formulation takes about 2600 seconds (it is almost 44 minutes).

Right-hand side of equation system is generated on the basis of magnetic vector potential's distribution within the border of subareas of different electrical conductivities. This stage lasts over 180 seconds, mainly because of integration related to a generation of MF. In turn, the very solution of equation system takes about 82 seconds.

The generation of a cubic structural mesh, unlike non-fixed structure meshes (e.g., tetrahedral mesh), is not characterized by high computational complexity. Meshing itself, however, is inseparable from computational solutions of partial differential equations.

However, as long as optimization is not carried out, but rather an evaluation of several or dozen of material properties' combinations, this total time seems to be satisfactory.

III. SOURCE OF UNCERTAINTY

The analysis of tissue conductivities made available in publications released over the last two decades and

parameters adopted by the authors lead to large discrepancies – this applies to both conductors [13] and low conductivity materials [14, 15]. Table 2 collates conductivities provided in various publications, which are discussed and commented on below. The percentage volume of tissue stems from a specific 0.1 m fragment of a limb. Chapter has been divided into 6 parts corresponding to respective columns of Table 2. Apart from the references to the literature, points below include some comments related to the more or less accurate characteristics of particular tissues.

1) Conductivity σ_1 collated in the table based on [16]; according to Scopus - database, this article was cited over 1900 times. The authors distinguish between two types of bone structure: cortical and cancellous. A number of articles cite results shown in that article, particularly for magnetotherapy simulation [17]. It is also worth noticing that electrical conductivity may to a smaller or greater extent vary with the frequency, also within a narrow band up to 1000 (Hz) [18]. Some tissues, such as muscle, also show anisotropy.

2) Conductivity σ_2 in the table was proposed on the basis of [19], which used the data from [20].

3) Article [21] sets together mean values of tissues conductivities on the basis of [22] – supplemented in the table as σ_3. [23] refers to the mean value from multiple references and bone tissue is adopted by them on the level of 0.010 (S/m).

4) The sinusoidal low frequency stimulation with varying magnetic component of EMF, at the frequency of 50 (Hz), is relatively compatible to models used in Transcranial Magnetic Stimulation (TMS) and Spinal Cord Stimulation, in relation to a tissue electrical conductivity. After the query of this topic, the table contains next column, due to conductivity values collected in [24], [25]. It is shown as σ_4.

5) In research [26] presents the σ_5 list of conductivities, clearly marking that the skin is treated as a composite tissue consisting of skin proper and subcutaneous fat (SAT). The above points show how complicated this problem is. Only some sources distinguish between skin and the subcutaneous adipose tissue (SAT).

6) In [27], authors collate data shown here as the σ_6 list. The article deals with calculation for an Extremely Low Frequency, namely 60 (Hz).

Further reflection is based on two different conductivity values for important tissues. The primary tissue chosen for the discussion is the muscular tissue, whose impact on the induction of eddy currents in a variable magnetic field is the greatest due to its large volume. Another significant conductivity is related to the bone tissue, due to the fact that magnetotherapy is used especially for bone injury treatment. Moreover, two conductivities were considered for subcutaneous adipose tissue (SAT), fat and skin tissue. Here, for the sake of the need to preserve transparency of the results, conductivities assigned to those tissues were identical in each variant, hence the subscripts (SFS) refer to data related to the three tissues. Fortunately, for the frequencies used in magneto therapy, dependencies between frequency and tissue conductivity do not exist in contrast to other form of therapy [28], and this factor may be omitted.

Without discussing the validity of the adopted tissue conductivities, the impact of specific parameters on the results will be shown with particular emphasis on currents induced in bones.

Table 2: Tissues electrical conductivities

Tissue	**σ_1 (S/m)**	**σ_2 (S/m)**	**σ_3 (S/m)**	**σ_4 (S/m)**	**σ_5 (S/m)**	**σ_6 (S/m)**
Muscle	0.241	0.202	0.150	0.160	0.350	0.233
SAT (subcutaneous adipose tissues)	–	0.012	–	0.078	–	–
Fat	0.020	0.012	0.078	0.078	0.040	–
Skin	0.0002	0.012	–	0.100	0.100	–
Veins and arteries	–	–	–	–	–	0.700
Blood vessel	0.264	0.700	0.600	0.600	0.700	–
Bone	–	0.020	–	0.015	0.020	0.050
Bone (cortical)	0.020	–	–	–	–	–
Bone (cancellous)	0.081	–	–	–	–	–
Bone (trabecular)	–	–	–	–	0.070	–

IV. RESULTS

A. Evaluation criteria

The maximum value in the analysed domain should be examined first. According to [29] and cited previously [11], the 99th percentile (A99) is used to avoid computational instabilities instead of maximum result from analysed domain. And the introduced A50 factor, corresponds to a median value of current within the analysed area. Other symbols for factors are formed by combining the first letter (or letters) of the name of the tissue and the percentile. These are: A – for all tissues considered together, M – for muscle tissue, B – for bone, SAT – for subcutaneous adipose tissue, Fat – for fat tissue and Skin – for skin. The 50th percentile (median)

and, in the case of the most important tissues, the 99th percentile are highlighted. It refers to a muscles, characterised by relatively high conductivity, and since the muscles take the most space within the examined domain. The second is bone tissue, and this results from the fact that this tissue is treated using magnetotherapy.

B. Exemplary results

For the coil in question, whose MF reaches 25 (mT) along the axis, and σ_{MUSCLE}=0.350 (S/m), σ_{SFS}=0.078 (S/m) (common conductivity for: subcutaneous adipose tissue (SAT), fat and skin), σ_{BONE}=0.050 (S/m), the results have been shown in Table 3.

Table 3: Exemplary results

Factor	J (mA/m^2)
A99	36.86
A50	12.94
M99	37.08
M50	20.06
B99	11.24
B50	6.56
SAT50	8.69
Fat50	8.73
Skin50	6.15

The results, particularly A99, lead to the conclusion that the MF and the assumed tissue conductivities (the highest ones among the considered values) do not produce results that might lead to a risk of bodily injury. As stated by [30], this level should not exceed 100 (mA/m^2).

Further reflection, involving various conductivities adopted for specific tissues, the results will be scaled to adjust the A99-factor to a value equal to 10 (mA/m^2) for the sake of greater clarity.

C. Impact of tissue properties on results

Table 4 shows the results for various tissue conductivities. In the fourth and fifth row of results, it can be seen that M50 is nearly equal to 60% of M99, unlike other cases, where it is merely 50%.

These two cases occur when combining lower conductivity for muscles with higher conductivity of SFS (SAT, fat, skin). This is confirmed by the fact, that the analysed domain, a set of tissues, jointly form eddy current paths, and the parameters of individual tissues do not directly translate into the results.

What can seem surprising is the fact, that the highest result for B50 (fifth row in Table 4) was achieved with low conductivity of muscles surrounding the bone. It is also worth stressing that lower conductivity of muscles, due to the fact that they form the majority of limb volume, significantly reduces A99 throughout the limb, which allows the MF to be set at a level not posing a risk to the tissues, and hence achieve much higher B50 levels. Furthermore, with the same fixed conductivities for muscles and SFS, B50 results preserve the proportion corresponding the ratio of the fixed conductivities for bone tissue itself (rows 1 and 2 and subsequent pairs of rows in the B50 column of Table 4). The change (by over three times) of the fixed bone conductivity in turn causes minimum fluctuations of results for all the remaining tissues, which results from the very low volume taken by bone tissue compared to the entire domain.

Table 4: Tissues electrical conductivities. Results for all combinations of selected tissue conductivities (A99 is 10 mA/m^2)

σ_{MUSCLE}	σ_{SFS}	σ_{BONE}	A50	M99	M50	B99	B50	SAT50	Fat50	Skin50
0.350	0.078	0.050	3.510	10.058	5.441	3.049	1.781	2.356	2.367	1.668
0.350	0.078	0.015	3.440	10.085	5.331	1.239	0.643	2.331	2.332	1.655
0.350	0.012	0.050	3.084	10.178	5.003	3.023	1.645	0.352	0.367	0.241
0.350	0.012	0.015	3.047	10.203	4.950	1.175	0.563	0.346	0.364	0.239
0.160	0.078	0.050	4.551	8.908	5.182	4.425	2.838	4.443	4.233	3.247
0.160	0.078	0.015	4.265	8.503	4.839	1.940	1.097	4.171	3.931	3.049
0.160	0.012	0.050	3.030	9.583	4.809	4.531	2.657	0.723	0.743	0.499
0.160	0.012	0.015	2.928	9.470	4.708	2.150	1.105	0.712	0.724	0.492

The mutual relations between conductivities of tissues significantly impact the possibility to achieve highest currents in bones undergoing treatment, as shown in Fig. 7 and Fig. 8. Eddy currents must always be concentrated in bone tissue with consideration to safe levels in other tissues.

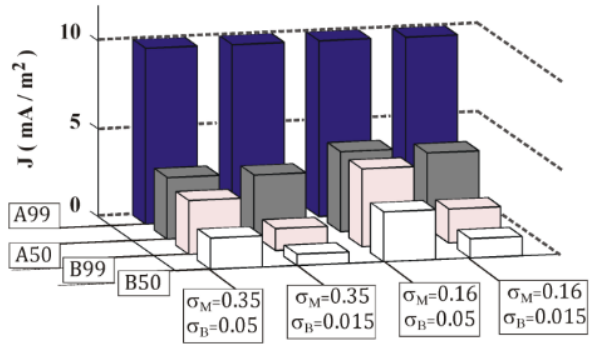

Fig. 7. Current densities factors (A99, A50, B99, B50) for σ_{SFS} = 0.078 (S/m).

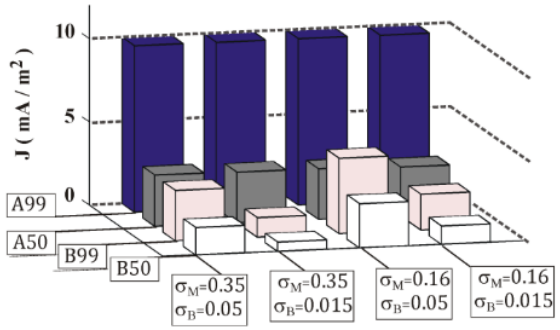

Fig. 8. Current densities factors (A99, A50, B99, B50) for σ_{SFS} = 0.012 (S/m).

V. CONCLUSIONS

Each organism might differ in size, which affects eddy current paths. Moreover, the percentage of specific tissues can vary depending on the fact content and other factors. As shown here, another factor contributing to the uncertainty of what human body tissues are exposed to, is the real conductivity characterising the tissues. While analysis the eddy current density distribution in human body, there is a need to decide what parameters should be assigned to specific tissues. As shown above, there are many options to choose from, and this decision can significantly influence the results achieved using the same device whose work is simulated in compliance with certain absolute allowed current levels. Virtual human models available for numerical investigations [31], [32] are becoming more numerous and more precise. Based on the results presented here, however, it can be observed, that despite the achievements of recent decades, it is very important to carry out further research to identify accurate and unambiguous parameters, particularly electrical conductivity of specific tissues.

REFERENCES

[1] D. Andritoi, V. David, and R. Ciorap, "Dynamics analysis of heart rate during magneto-therapy session," *2014 International Conference and Exposition on Electrical and Power Engineering (EPE)*, Iasi, pp. 514 517, 2014.

[2] S. M. Schwab, C. Androjna, E. I. Waldorff, J. T. Ryaby, L. R. Moore, R. J. Midura, and M. Zborowski, "Mechanical stress on suspended cortical bone sample by low frequency magnetic field," *IEEE Transactions on Magnetics*, vol. 52, no. 7, pp. 1-4, 2016.

[3] A. Miaskowski, A. Krawczyk, and Y. Ishihara, "A numerical evaluation of eddy currents distribution in the human knee with metallic implant," *COMPEL: The International Journal for Computation and Mathematics in Electrical and Electronic Engineering*, vol. 31, no. 5, pp. 1441 1447, 2010.

[4] P. I. Petrov, S. Mandija, I. Sommer, C. van den Berg, and S. Neggers, "How much detail is needed in modeling a transcranial magnetic stimulation figure-8 coil: Measurements and brain simulations," *PLoS ONE*, vol. 12, no. 6, pp. 1-20, 2017.

[5] B. Minnaert, L. De Strycker, and N. Stevens, "Design of a planar, concentric coil for the generation of a homogeneous vertical magnetic field distribution," *ACES Journal*, vol. 32, no. 12, pp. 1056-1063, 2017.

[6] G. M. Noetscher, S. N. Makarov, F. Sciré-Scappuzzo, and A. Pascual-Leone, "A simple absolute estimate of peak eddy currents induced by transcranial magnetic stimulation using the GR model," *IEEE Transactions on Magnetics*, vol. 49, no. 9, pp. 4999-5003, 2013.

[7] P. Syrek and R. Barbulescu, "Parametric curves to trace the TMS coils windings," *10th International Symposium on Advanced Topics in Electrical Engineering (ATEE)*, Bucharest, Romania, pp. 386-391, 2017.

[8] A. Christ, W. Kainz, E. G. Hahn, K. Honegger, M. Zefferer, E. Neufeld, W. Rascher, R. Janka, W. Bautz, J. Chen, B. Kiefer, P. Schmitt, H. P. Hollenbach, J. X. Shen, M. Oberle, D. Szczerba, A. Kam, J. W. Guag, and N. Kuster, "The virtual family – development of surface-based anatomical models of two adults and two children for dosimetric simulations," *Physics in Medicine and Biology*, vol. 55, no. 2, pp. 23 38, 2010.

[9] Q. Fang and D. Boas, "Tetrahedral mesh generation from volumetric binary and gray-scale images," *Proceedings of IEEE International Symposium on Biomedical Imaging*, pp. 1142-1145, 2009.

[10] G. M. Noetscher, S. N. Makarov, F. Sciré-Scappuzzo, and A. Pascual-Leone, "A simple absolute estimate of peak eddy currents induced by transcranial magnetic stimulation using the GR model," *IEEE Transactions on Magnetics*, vol. 49, no. 9, pp. 4999-5003, 2013.

[11] V. Guadagnin, M. Parazzini, S. Fiocchi, I. Liorni, and P. Ravazzani, "Deep transcranial magnetic stimulation: modeling of different coil configurations," *IEEE Transactions on Biomedical Engineering*, vol. 63, no. 7, pp. 1543-1550, 2016.

[12] S. N. Makarov, J. Yanamadala, M. W. Piazza, A. M. Helderman, N. S. Thang, E. H. Burnham, and A. Pascual-Leone, "Preliminary upper estimate of peak currents in transcranial magnetic stimulation at distant locations from a TMS coil," *IEEE Transactions on Biomedical Engineering*, vol. 63, no. 9, pp. 1944-1955, 2016.

[13] S. Lalléchère, "Advanced statistical 3D models of composite materials for microwave electromagnetic compatibility applications," *ACES Journal*, vol. 32, no. 12, pp. 1113-1116, 2017.

[14] G. Liu, "Time-domain electromagnetic inversion technique for biological tissues by reconstructing distributions of cole-cole model parameters," *ACES Journal*, vol. 32, no.1, pp. 8-14, 2017.

[15] P. Gas, "Optimization of multi-slot coaxial antennas for microwave thermotherapy based on the S11-parameter analysis," *Biocybernetics and Biomedical Engineering*, vol. 37, no.1, pp. 78-93, 2017.

[16] S. Gabriel, R. W. Lau, and C. Gabriel, "The dielectric properties of biological tissues: III. Parametric models for the dielectric spectrum of tissues," *Physics in Medicine & Biology*, vol. 41, no. 11, pp. 2271-2293, 1996.

[17] A. Miaskowski, A. Krawczyk, and Y. Ishihara, "Computer modelling of magnetotherapy in orthopedic treatments," *COMPEL: The International Journal for Computation and Mathematics in Electrical and Electronic Engineering*, vol. 29, no. 4, pp. 1015-1021, 2010.

[18] A. Bouazizi, G. Zaibi, M. Samet, and A. Kachouri, "Parametric study on the dielectric properties of biological tissues," *16th International Conference on Sciences and Techniques of Automatic Control and Computer Engineering (STA)*, Monastir, pp. 54-57, 2015.

[19] M. Parazzini, S. Fiocchi, I. Liorni, and P. Ravazzani, "Effect of the interindividual variability on computational modeling of transcranial direct current stimulation," *Computational Intelligence and Neuroscience*, vol. 2015, Article ID 963293, pp. 1-9, 2015.

[20] NRCaIfAP 2015, National Research Council and Institute for Applied Physics, "Nello Carrara", "An internet resource for the calculation of the dielectric properties of body tissues," *IFAC-CNR, Florence, Italy. http://niremf.ifac.cnr.it/tissprop/*, 2015.

[21] B. Sawicki and A. Krupa, "Experiments with models of variability for biological tissues," *Przeglad Elektrotechniczny*, vol. 92, no. 7, pp. 83 86, 2016.

[22] C. Gabriel, A. Peyman, and E. H. Grant, "Electrical conductivity of tissue at frequencies below 1 MHz," *Physics in Medicine & Biology*, vol. 54, no. 16, pp. 4863 4878, 2009.

[23] T. A. Wagner, M. Zahn, A. J. Grodzinsky, and A. Pascual-Leone, "Three-dimensional head model simulation of transcranial magnetic stimulation," *IEEE Transactions on Biomedical Engineering*, vol. 51, no. 9, pp. 1586 1598, 2004.

[24] M. Parazzini, S. Fiocchi, I. Liorni, E. Rossi, F. Cogiamanian, M. Vergari, A. Priori, and P. Ravazzani, "Modeling the current density generated by transcutaneous spinal direct current stimulation (tsDCS)," *Clinical Neurophysiology*, vol. 125, no. 11, pp. 2260-2270, 2014.

[25] M. Parazzini, S. Fiocchi, A. Cancelli, C. Cottone, I. Liorni, and P. Ravazzani, "A computational model of the electric field distribution due to regional personalized or nonpersonalized electrodes to select transcranial electric stimulation target," *IEEE Transactions on Biomedical Engineering*, vol. 64, no. 1, pp. 184-195, 2017.

[26] P. Dimbylow, "Development of the female voxel phantom, NAOMI, and its application to calculations of induced current densities and electric fields from applied low frequency magnetic and electric fields," *Physics in Medicine and Biology*, vol. 50, pp. 1047-1070, 2005.

[27] L. H. Hoang, R. Scorretti, N. Burais, and D. Voyer, "Numerical dosimetry of induced phenomena in the human body by a three-phase power line," *IEEE Transactions on Magnetics*, vol. 45, no. 3, pp. 1666-1669, 2009.

[28] P. Gas and A. Miaskowski, "SAR optimization for multi-dipole antenna array with regard to local hyperthermia," *Przeglad Elektrotechniczny*, vol. 95, no. 1, pp. 17-20, 2019.

[29] M. Parazzini, S. Fiocchi, and P. Ravazzani, "Electric field and current density distribution in an anatomical head model during transcranial direct current stimulation for tinnitus treatment," *Bioelectromagnetics*, vol. 33, no. 6, pp. 476-487, 2012.

[30] ICNIRP 2010, "Guidelines for limiting exposure to time-varying electric and magnetic fields (1 Hz–100 kHz)," *Health Physics*, vol. 99, no. 6, pp. 818-836, 2010.

[31] S. N. Makarov, G. M. Noetscher, J. Yanamadala, M. W. Piazza, S. Louie, A. Prokop, A. Nazarian, and A. Nummenmaa, "Virtual human models for electromagnetic studies and their applications," *IEEE Reviews in Biomedical Engineering*, vol. 10, pp. 95-121, 2017.

[32] P. C. Miranda, R. Salvador, C. Wenger, and S. R. Fernandes, "Computational models of non-invasive brain and spinal cord stimulation," *2016*

38th Annual International Conference of the IEEE Engineering in Medicine and Biology Society (EMBC), Orlando, FL, pp. 6457-6460, 2016.

Przemyslaw Syrek received his Master Degree in Electrical Engineering in 2005 and Ph.D. in the same area from AGH University of Science and Technology in Krakow, Poland (2011), where he has been working in Department of Electrical and Power Engineering. His major research interest is field theory, including biomedical applications of electromagnetic field.

Design of Low-Cost, Circularly Polarized, and Wideband U-Slot Microstrip Patch Antenna with Parasitic Elements for WiGig and WPAN Applications

Mourad S. Ibrahim [1,2]

[1] Department of Communications and Networks Engineering
College of Engineering, Prince Sultan University, Riyadh, 11586, KSA
mrizk@psu.edu.sa

[2] Department of Electrical Communication and Electronic Systems Engineering
College of Engineering, Modern Sciences and Arts University, 6th October, 12566, Egypt

Abstract ─ In this article, a well matched U-Slot Microstrip Patch Antenna (MPA) with two paratactic elements is designed and simulated. The antenna is designed to resonate at 60 GHz (V-band) and exhibits a wideband extend from 53.3 GHz to 60.8 GHz with more than 87% total efficiency. The presence of U-slot makes a current perturbation in the antenna which contributes to generate a Circular Polarization (CP). The 3-dB Axial Ratio (AR) is extended from 56 – 57.2 GHz (~ 1.2 GHz bandwidth). The analysis and optimization processes throughout this paper are carried out using Finite Element Method (FEM) and verified with Finite Integration Technique (FIT). Good agreement between the results by the two simulators is obtained. Hence, the performance of the proposed antenna makes it a good candidate for fifth generation applications at V-band like Wireless Gigabit Alliance (WiGig) and Wireless Personal Area Network (WPAN).

Index Terms ─ Circular Polarization, MPA, Parasitic elements, U – slot, V-band, WPAN, WiGig.

I. INTRODUCTION

This paper is an extension of work originally presented in EuCAP 2019 [1]. The unlicensed V-band at 60 GHz has motivated researchers to obtain a high data rate for short range communications within 10 meters [2]. The V-band has applications like WiGig and WPAN. Since the battery life is the main concern; the V-band has used to compensate between bandwidth efficiency and low power consumption [3]. The antennas at millimeter need to exhibit a high gain, wide bandwidth, and small size. MPAs are promising candidate for mm-wave applications, where the antenna is low-profile, can easily integrated with a Monolithic Microwave Integrated Circuit (MMIC), light in weight, and low fabrication cost. The main disadvantage of MPA is the narrow bandwidth [5]. Multilayer antenna structures using Low-Temperature Co-fired Ceramic (LTCC) technology in order to enhance the antenna bandwidth [6-8]. The complex fabrication processes of LTCC technology lead to a high manufacturing cost as well as high antenna volume. Parasitic elements [9], V – slot [10] and U – slot [11-12] also have used to enhance the antenna bandwidth. Due to the advantages of CP antennas over the linearly polarized (LP) antennas [13], CP is more preferable than LP. CP antennas are very prosperous in combating the multi path fading, eliminate the Inter – Symbol Interference (ISI), and they are vigorous to polarization mismatch [13-14]. The strength of the received signal is approximately same nevertheless of the CP antennas directions which make it likable for mm-wave applications.

In this article, the design of a CP matched wideband mm-wave antenna is developed. The simulation of the designed antennas was carried out using the FEM numerical method [15] and verified with the FIT numerical method [16]. The presence of parasitic elements enhances the antenna bandwidth. The U–slot allows current perturbation and the current take longer path. The U–slot dimensions are optimized to obtain a wide bandwidth. The proposed antenna exhibits a CP through the using of the two opposite square corners truncation as well as the U–slot. The truncation corners with U–slot work to generate two orthogonal filed components with equal amplitudes which are a necessary to obtain CP antennas. The proposed antenna is mounted on Netlec NH9338 ($\varepsilon_r = 3.38$) substrate with substrate thickness h = 0.2 mm and loss tangent $\tan\delta = 0.0025$.

In the following sections, the antenna structure and design of the CP wideband antenna is described, and then simulated results are presented and discussed.

II. ANTENNA STRUCTURE AND DESIGN

At the first, a single square MPA using λ/4 feeding network is designed to resonate at 60 GHz. The antenna mounted on substrate with dielectric constant (ε_r) of 3.38 and height (h) of 0.2 mm supported by conducting

Submitted On: November 8, 2018
Accepted On: July 1, 2019

ground plane. The patch length (L) dimension is calculated from the following equation [5]:

$$L = \frac{c}{2 f_r \sqrt{\frac{2}{\varepsilon_r + 1}}}, \quad (1)$$

where c is the speed of light, and f_r is the resonant frequency of the antenna.

The dimensions of a single element antenna are optimized to resonate at 60 GHz while exhibits a CP. The antenna structure and dimensions is illustrated in Fig. 1. The square patch with length (L) of 1.28 mm, ground plane dimensions are W_g by L_g with the same dimensions as the substrate. The 50Ω feed length L_f, and width W_f while the λ/4 section with length $L_{98\Omega}$ and width $W_{98\Omega}$ is used to match the 50Ω feed line with the patch antenna.

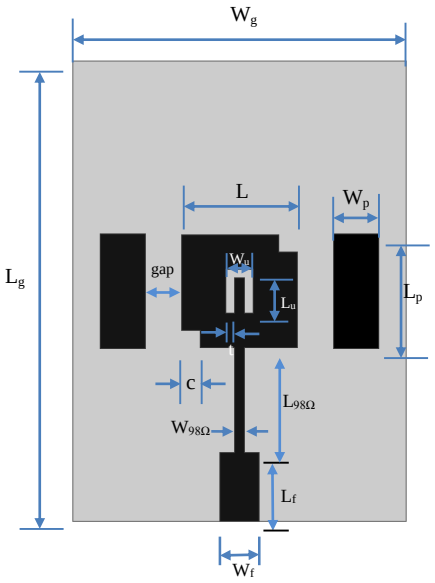

Fig. 1. The proposed corner-truncated square MPA antenna with two parasitic elements using λ/4 feeding network.

III. SIMULATION RESULTS AND DISCUSSION

A parametric study has been conducted in order to enhance the MPA bandwidth by varying the U – slot dimensions (L_u, W_u, and t) in addition to the parasitic elements dimensions and location (L_p, W_p, and gap). The square truncation area (c^2) is optimized in order to get a circularly polarized antenna. The optimized dimensions of the proposed antenna with U – slot, parasitic elements, and truncation area in order to obtain a wide bandwidth with CP are shown in Table 1.

Table 1: Optimized dimensions of the proposed antenna in mm

Parameter	Value	Parameter	Value
L	1.28	c	0.2
L_g	5.23	W_g	3.7
$L_{98\Omega}$	1.2	$W_{98\Omega}$	0.1
L_f	0.775	W_f	0.443
L_u	0.5	W_u	0.3
t	0.1	gap	0.4
L_p	1.3	W_p	0.5

Fig. 2 illustrates the effect of varying the parasitic elements dimensions (L_p, and W_p) with gap = 0.4 mm and the other parameters are fixed as indicated in Table 1. The effect of varying the U – slot dimensions (L_u, and W_u) with t = 0.1 mm is shown in Fig. 3.

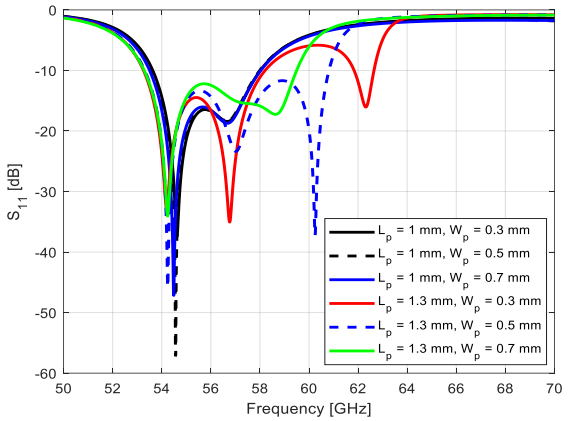

Fig. 2. S_{11} of the proposed antenna with varying parasitic elements' dimensions (L_P and W_P).

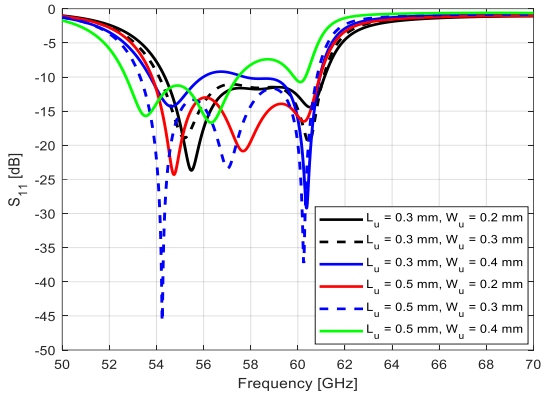

Fig. 3. S_{11} of the proposed antenna with varying U – slot dimensions (L_u and W_u).

Figure 4 illustrates the S_{11} using High Frequency Surface Structure commercial software (based on the FEM method) and CST Microwave Studio (based on FIT method) for the optimized dimensions indicated in Table 1. Small difference between the two simulated results is observed due to the different mesh sizes between the two simulators.

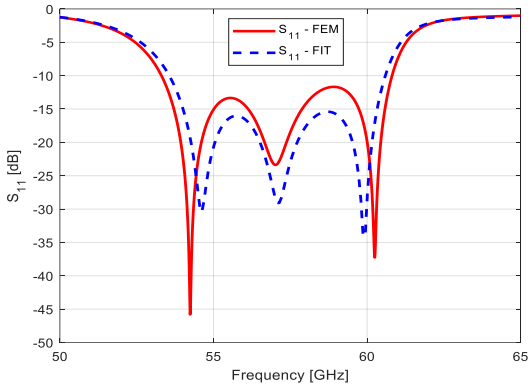

Fig. 4. S_{11} of the proposed antenna using FEM and FIT.

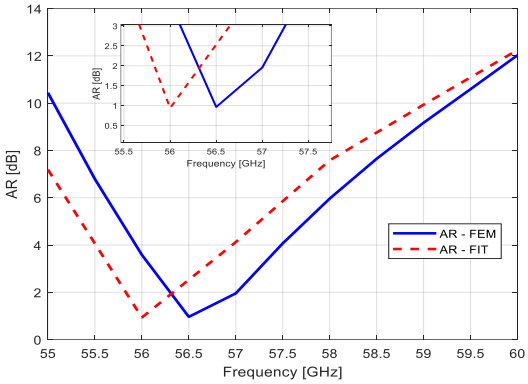

Fig. 5. AR versus the frequency using FEM and FIT.

The simulated bandwidths are 53.32 – 60.82 GHz (7.5 GHz), and 53.5 – 60.6 GHz (7.1 GHz) using FEM and FIT respectively. Figure 5 shows the AR with CP in the frequency bands of 56.1 – 57.2 GHz (1.1 GHz) and 55.64 – 56.74 (1.1 GHz) using FEM and FIT respectively. The radiation patterns in xz and yz planes using FEM and FIT at the resonant frequency (60 GHz) are illustrated in Fig. 6. Good agreement between results is obtained. The maximum realized gain is shown in Fig. 7 on the left y-axis with maximum values of 7.2 dB at 59.5 GHz and 7.63 dB at 58 GHz. Less than 1.3 dB and 0.43 dB gains variation along the antenna bandwidth using FEM and FIT respectively is obtained. The total efficiency using FIT along the entire antenna bandwidth is greater than 78% with maximum value of 92.6% at 57 GHz as illustrated in Fig. 7 on the right y-axis. The radiation efficiency is more than 87% along the antenna bandwidth using FEM and FIT. The surface current distributions of the proposed MPA with the two parasitic elements at 53 GHz, 55 GHz, and 60 GHz are shown in Fig. 8. It can be observed that the two parasitic elements act as two radiators and the presence of U – slot allows the current perturbation. It is clear that the peak current is focused around the patch element as well as the two parasitic elements.

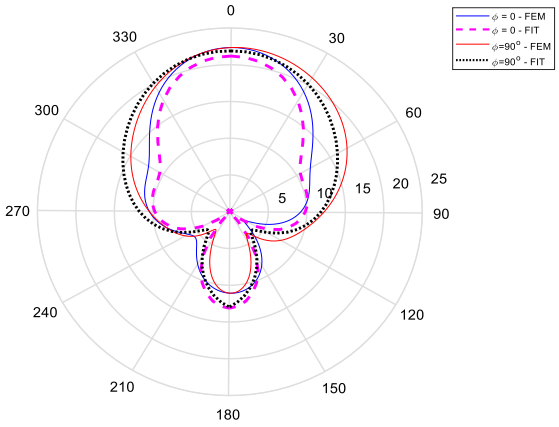

Fig. 6. Total gain of the antenna at xz– and yz–planes.

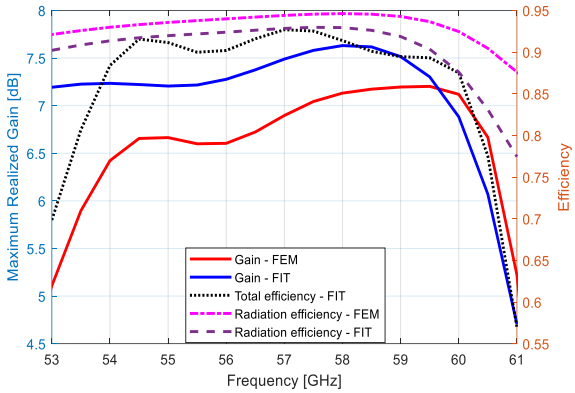

Fig. 7. Maximum realized gain and efficiencies against the frequency using FEM and FIT.

IV. CONCLUSION

Low–cost CP microstrip antenna with wide bandwidth for the 5G applications like WPAN and WiGig is provided. The proposed antenna with more than 7.1 GHz bandwidth (around 13%) is designed and simulated. The antenna matched by λ/4 matching network. The proposed antenna is mounted on a single layer which yields a low manufacturing cost. The proposed antenna exhibits a circular polarization within 1.1 GHz (around 1.94%) and a maximum gain of 7.2 dBi and 7.63 dBi at 60 GHz using FEM and FIT respectively. The total antenna efficiency is more than 78% along the entire antenna bandwidth. The gain-frequency variation is less than 1.3 dB over the antenna bandwidth which gives a stable antenna performance and makes the

antenna as a good candidate for the 5G applications.

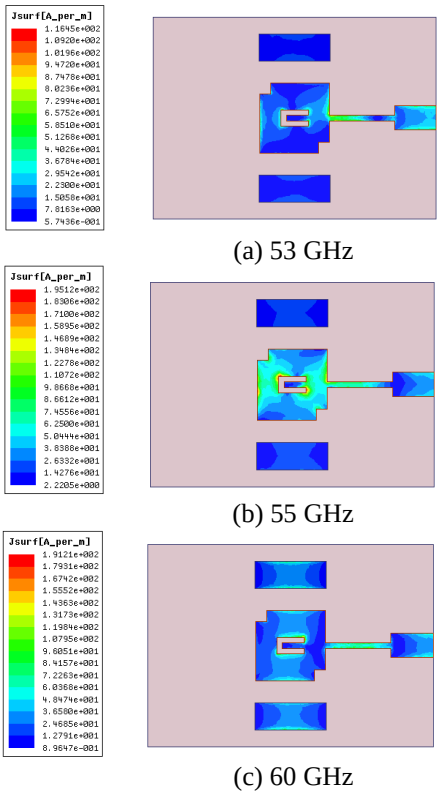

(a) 53 GHz

(b) 55 GHz

(c) 60 GHz

Fig. 8. The surface current distributions of the patch antenna with the two parasitic elements at (a) 53 GHz, (b) 55 GHz, and (c) 60 GHz.

REFERENCES

[1] M. S. Ibrahim, "Low-cost, circularly polarized, and wideband U-slot microstrip patch antenna with parasitic elements for WiGig and WPAN applications," 13th *Euro. Conf. on Ant. and Prop. (EuCAP 2019)*, Krakow, Poland, 31 Mar.-5 Apr. 2019.

[2] J. N. M. T. S. Rappaport and F. Gutierrez, "State of the art in 60-GHz integrated circuits and systems for wireless communications," *Proceedings of the IEEE*, vol. 99, pp. 1390-1436, 2011.

[3] R. Zhou, D. Liu, and H. Xin, "A wideband circularly polarized patch antenna for 60 GHz wireless communications," *Wireless Engineering and Technology*, vol. 3, no. 3, p. 4, 2012.

[4] B. Lee and Y. Yoon, "Low profile, low cost, broadband millimeter-wave antenna array for high data rate WPAN systems," vol. PP, 2017.

[5] C. A. Balanis, *Antenna Theory: Analysis and Design*. 4th ed., John Wiley & Sons, 2016.

[6] K.-S. Chin, E. S. Li, J. Huayan, et al., "60-GHz wideband LTCC microstrip patch antenna array with parasitic surrounding stacked patches," *IET Microwaves, Antennas & Propagation*, p. 8, 2018.

[7] L. Wang, Y. Guo, and W. Sheng, "Wideband high-gain 60-GHz LTCC L-probe patch antenna array with a soft surface," *IEEE Transactions on Antennas and Propagation*, vol. 61, pp. 1802-1809, 2013.

[8] H. Chu, Y. Guo, and Z. Wang, "60-GHz LTCC wideband vertical off-center dipole antenna and arrays," *IEEE Transactions on Antennas and Propagation*, vol. 61, pp. 153-161, 2013.

[9] A. A. Abdelaziz, "Bandwidth enhancement of microstrip antenna," *Progress In Electromagnetics Research, PIER*, vol. 63, pp. 311-317, 2006.

[10] K.-F. Lee, S. S. Yang, A. A. Kishk, and K.-M. Luk, "Design and study of wideband single feed circularly polarized microstrip antennas," *Prog. In Electromag. Res. C*, vol. 80, pp. 45-61, 2008.

[11] S. Wi, Y. Lee, and J. Yook, "Wideband microstrip patch antenna with U-shaped parasitic elements," *IEEE Transactions on Antennas and Propagation*, vol. 55, pp. 1196-1199, 2007.

[12] M. S. Ibrahim, "2 x 2 circularly polarized mimo antenna at ka-band for fifth generation applications," *Inter. Journal on Communications Antenna and Propagation (IRECAP)*, vol. 9, no. 2, 2019.

[13] F. A. Dicandia, S. Genovesi, and A. Monorchio, "Analysis of the performance enhancement of MIMO systems employing circular polarization," *IEEE Transactions on Antennas and Propagation*, vol. 65, pp. 4824-4835, 2017.

[14] J. Wang, Z. Lv, and X. Li, "Analysis of MIMO diversity improvement using circular polarized antenna," *International Journal of Antennas and Propagation*, vol. 2014, p. 9, 2014.

[15] *High Frequency Surface Structure (HFSS) (15 ed.)*. Available: http://www.ansys.com

[16] *CST Microwave Studio 2015*. Available: https://www.cst.com/products/cstmws

Mourad S. Ibrahim received the B.Sc and M.Sc degrees in Communications and Electronics Engineering from College of Engineering–Helwan University in 2002 and 2006 respectively. He did his Ph.D degree in Communications and Electronics Engineering from College of Engineering - Cairo University, Egypt 2011. He served as an Associate Director of Research and Translation Center (RTC), Prince Sultan University (PSU), KSA. He is currently an Assistant Professor at Communications and Networks Engineering department, PSU. His research interests at present includes Metamaterials, Millimeter wave Antennas, DRA, plasma antennas, optimization techniques, FDFD, and GPU.

Computational Analysis for the Combination of Inductive Coupled Wireless Coils and High Permittivity Materials to Improve B1 Field for Rhesus Monkey MRI

Daniel Hernandez and Kyoung-Nam Kim

Department of Biomedical Engineering
Gachon University, Incheon, Korea
theasdwmove@gmail.com, kn16.kim@gmail.com

Abstract ─ Magnetic resonance imaging (MRI) scanning of small animals such as non-human primates has been of interest in recent years. Imaging primates, such as rhesus monkeys, presents challenges due to the shape of their head. The shape and dimensions of the head can cause poor magnetic flux density ($|B_1|$) strength and penetration to specific regions of interest. In this study, we focus on the design of an eight-channel, helmet-style array coil for rhesus monkey brain imaging, and performed quantitative analysis by means of electromagnetic (EM) simulations and acquiring reception sensitivity ($|B_1^-|$)-fields to demonstrate that the use of combining inductively coupled wireless coils and high permittivity materials can improve the $|B_1^-|$-field sensitivity of a tradition phase array coil.

Index Terms ─ EM simulations, high permittivity materials, MRI RF coils, small animals, wireless coil.

I. INTRODUCTION

Rhesus monkey brain scanning with magnetic resonance imaging (MRI) is a useful method to study brain anatomy, functionality, and reactions to new drugs; these discoveries are intended to be transferable to human applications due to the similarities between primates [1]. Although anatomically and physiologically the brains of monkeys and humans share some similarities, imaging monkey brains requires dedicated hardware to accommodate the smaller size of their head and different structure of their body. Especial frames needs to be constructed to keep the monkey in an optimal and stationary position of the body and head inside the scanner during MR imaging. Given that the frontal facial area of the monkey is more pronounced than the human nose, it is necessary to tailor the dimensions of the radio-frequency (RF) coil. The use of traditional birdcage coils would fail to deliver a uniform field due to the different distances between the head and the coil in the upper and lower nasal areas. It has been reported that by using a birdcage coil positioned only around the upper area of the monkey's head it is possible to maintain a uniform field in the brain area [2]. However, this required a macaque monkey to be seated in a sphinx-like manner, with a frame used to restrain the monkey's movement, and performed while the monkey was sedated. A single transmit/receive (Tx/Rx) coil configuration was a standard approach taken to imaging conscious monkeys, since it is easy to setup and can be used with any size of monkey; however, in terms of imaging quality its performance was low. One study proposed a combination of a single 100 mm loop coil for transmission and a phase array coil of four channels for the reception coil [3]; this configuration was used to perform functional MRI (fMRI) and diffusion MRI on a monkey. Another novel proposal was the use of a traveling wave system as the Tx method by attaching a two-port patch antenna to the RF shield of the gradient system of the MRI scanner; the antenna produced a TE_{11} mode generating a circular polarized (CP) magnetic flux density ($|B_1|$)-distribution, while for reception a three-element phase array (PA) coil was used, but this configuration only covered the upper half of a cylinder around a monkey's brain [4]. The use of PA loop coils as receptors for MRI is common practice due to their simplicity and capacity to produce high sensitivity $|B_1|$-field, in addition to being able to perform parallel imaging (PI) [5], and thus reducing scan time. The use of helmet style PA loop array coils [6, 7] is common for its increase reception field sensitivity.

There is ongoing research into an optimal coil configuration and geometry that would produce a higher signal intensity and uniform $|B_1|$-field [8] for small animals such as rhesus monkeys. One potential coil configuration that has been proposed in recent years is the use of inductive coupled wireless (w_L) coils; these elements have been shown to enhance the imaging performance of standard PA coil by producing stronger and more uniform $|B_1|$-fields [9]. The operation of the w_L coils consists on generating a magnetic field from induced currents. The induced currents on the w_L come from pick up varying $|B_1|$-fields produced from the

Submitted On: June 11, 2019
Accepted On: September 7, 2019

standard PA coil with active current sources. In this coil configuration, the $|B_1|$-field intensity can be increased.

It has also been reported that the use of high-permittivity material (HPM) attachments can increase the magnetic field [10-12]. The HPM operate as a focusing material that will help increase the efficiency of the $|B_1|$-field, especially at high frequencies such as the ones used in high field MRI. Previous studies have shown that the use of HPM enhance the $|B_1|$-field strength, improving the signal-to-noise ratio (SNR) and the image quality overall. The HPM have been proposed as a simple and low-cost accessory to increase the performance of traditional PA coil.

In the present study we propose a receive only helmet-style PA coil for use with rhesus monkey brain imaging at 7T, by using a combination of wireless coils and HPM attachments, to enhance the sensitivity of the $|B_1^-|$-field produced by a traditional PA coil. We performed a quantitative analysis by using electromagnetic (EM) simulations to acquire $|B_1|$-field maps of the standard PA coil and the proposed combination with w_L coil and HPM attachments.

II. METHODS

A. Loop array coil design

The proposed receive only helmet-style PA coil is composed of eight loop coils that are distributed to fit around the shape of the head of a rhesus monkey. The PA coil array consists of two loop coils located at the front and back of the monkey head model, this coils will be referenced as anterior-posterior (AP) coils and two coils at each lateral side. The active coils (standard PA coil) are located close to the imaging object, as an inner layer, while the w_L array coils are located at the same position as the active coil but in an outer layer separated by 15 mm. Figure 1 shows the dimensions for each type of coil, the active and wireless coil for the AP and lateral locations in the array, in addition to the HPM materials corresponding to each set of coils.

Table 1 summarize the dimensions of each of the coils and the HPM. There is a slight curvature at top of each of the coils and HPM to cover the shape of the monkey head model. The AP active and w_L coils are smaller than the lateral coil, but their top and bottom width are same. The PA coils are placed near the monkey's head to receive a stronger $|B_1|$-field sensitivity, and in order to increase the sensitivity a w_L coil array was also attached as an outer layer to the active receive array.

In addition to the w_L coils, an arrangement of eight HPM attachments were inserted between the active and w_L coils. The HPM attachments had similar geometry to the coils shape, their dimensions are also listed in Table 1, and the geometry is show in Fig 1 (c).

Table 1: The dimensions of active and wireless coils and the HPM

	Height [mm]	Width [mm] Top/Bottom	Thickness [mm]
AP active coil (Fig. 1 (a))	40	20/30	0.5
AP w_L coil (Fig. 1 (a))	50	26/45	0.5
AP HPM (Fig. 1 (c))	40	23/35	5.0
Lat. Active coil (Fig. 1 (b))	80	20/30	0.5
Lat. w_L coil (Fig. 1 (b))	100	26/45	0.5
Lat. HPM (Fig. 1 (c))	90	23/35	5.0

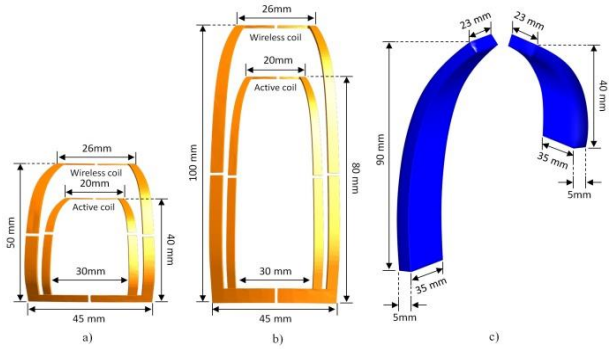

Fig. 1. Dimensions for the loop coils, with the active coils in the inner layer and the wireless coil in the outer layer, for (a) anterior and posterior (AP) coils, (b) lateral coils, and (c) the high permittivity material (HPM).

Figure 2 shows the combinations used in this study, as reference evaluation we will use the standard PA coil or active coil only (inner layer of coils), as can be visualized in Figs. 2 (a), (d) for the *xz*- and *xy*-plane views. The inner layer of eight loop coils was placed around a 33 mm radius circumference for the top of each coil. The first evaluation condition was the use of w_L coils as shown in Figs. 2 (a), (d), arranged in an outer layer of 42 mm of radius. The second evaluation condition was the use of the standard PA coil and the w_L with the HPM attachments (Figs. 2 (b), (e)). A model of a rhesus monkey is included with the array coil (Figs. 2 (c), (f)).

The three-dimensional (3D) model of a monkey head was computed by taking multiple coronal 2-D MRI images of a rhesus monkey head. The MR images were combined to form a 3D volume image. The voxeling was done with Photoshop (Adobe Inc, California 95110, USA) and it was rendered using Rhinoceros 3D modeling tools (McNeel, Seattle, WA, USA). The measured size

of the monkey was 86 × 125 × 105 mm, while the rhesus monkey head model has dimensions of 81.7 × 118.8 × 104.7 mm^3. Organ segmentation was excluded in modeling process, which makes the phantom solid, for this reason the electrical properties of the phantom were set to a continuous value.

The w_L coils were tuned to operate at the desired frequency of 300 MHz corresponding to a 7T MRI system, and matched to 50 Ohms. There was a frequency shift from the tuning condition when the HPM attachments were added, the frequency shift was on average 1.4 MHz between individual coils; for this reason, it was necessary to repeat the tuning of the w_L coil. The w_L coils are not connected with a current source as they operate with the currents induced by the active coils.

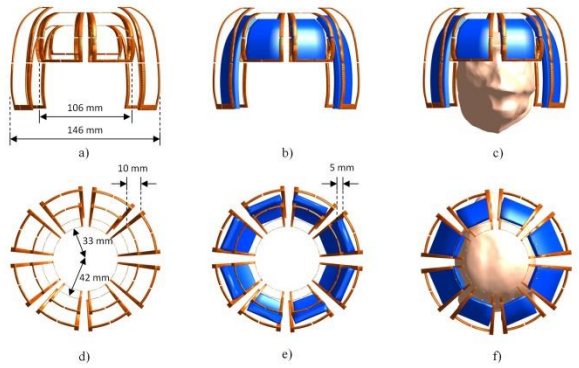

Fig. 2. View of the arrangement of the array coil, for the xz-plane (top) and the xy-plane (bottom). (a), (d): the active and wireless coils; (b), (e): the array with the high permittivity attachments; (c), (f): the array coil fitting the rhesus monkey phantom.

III. RESULTS

By means of electromagnetic (EM) simulations we designed and acquired reception sensitivity ($|B_1^-|$)-fields on a mimicked rhesus monkey phantom, with electrical properties of 0.413 S•m^{-1} and 43.77, conductivity and permittivity respectively. The electrical properties for the monkey phantom were selected to represent brain white matter, and the values were used as provided by the data base in the simulation software. The electrical values used in this work are similar to the human brain white matter, given that there's no information of the conductivity and permittivity of rhesus monkey brain at 300 MHz. however, these values fit well towards the goal of this work, which is to show the benefits of using wireless coils and HPM to increase the $|B_1^-|$-field. A dedicated study should be done such as [13] to compute the electrical properties of the rhesus monkey brain. In addition the focus of pre-clinical animal MRI research is to translate the technology to human applications, therefore the use of human brain electrical properties values are within our objective. The phantom model has an homogeneous filling because it was acquired by 3D scanning the surface of the monkey head, for this reason a single value of electrical properties were used. The HPM attachments were designed to emulate barium titanate ($BaTiO_3$), which has electrical properties of 300 permittivity and 0.5 S•m^{-1} conductivity [14, 15]. The simulations were performed using the commercial FDTD software, Sim4life (Zurich MedTech AG (ZMT)).

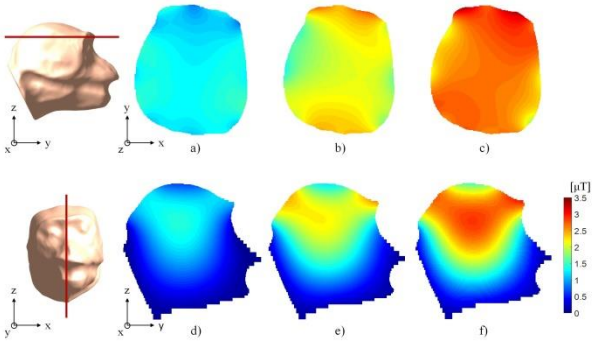

Fig. 3. The $|B_1^-|$-fields for two different slices from an axial view (top row) and sagittal view (bottom row). (a), (d): active array coil only; (b), (e): with the wireless coil; (c), (f): the combination of the wireless coil and HPM.

Figure 3 shows the $|B_1^-|$-field in the axial (*xy*)- and sagittal (*yz*)-slice for the reference active coil (Figs. 3 (a), (d)). The $|B_1^-|$-field resulting of the combination of the active and w_L coils are shown in Figs. 3 (b), (e), and the $|B_1^-|$-field from the combination of the active PA coil with w_L coils and the HPM attachments is shown in Figs. 3 (c), (f). The red arrows on the monkey's head model indicate the position of the slices taken for the figure. The average and normalized standard deviation values of each $|B_1^-|$-field for the whole slice are shown in Table 2.

Table 2: Statistical values for the $|B_1^-|$-field acquired using different coil configurations

	Average [µT]			**Standard Deviation [µT]**		
View	**Active**	**Active + w_L**	**Active +w_L +HPM**	**Active**	**Active + w_L**	**Active +w_L +HPM**
Slice #1	1.14	2.00	2.60	0.047	0.039	0.051
Slice # 2	0.96	1.90	2.50	0.100	0.065	0.061
Sagittal	0.56	1.02	2.32	0.152	0.240	0.300

Electrical ($|E|$)-fields were also acquired to understand the effect of the proposed combinations used in this study. Figures 4 (a), (d) show the $|E|$-field of the active coil for axial and sagittal slice. For the axial slice the average value was 51.09 and 2.91 V•m^{-1} of standard deviation. Figures 4 (b), (e) show the combination of the active coil and the w_L coil, with an average and standard deviation of 81.8 and 4.16 V•m^{-1} respectively, for the

axial slice. Lastly, the |E|-fields for the combination of the active PA coil with w_L coil and HPM attachments are show in Figs. 4 (c), (f), with average and standard deviation 102.1 and 4.58 V•m^{-1} respectively.

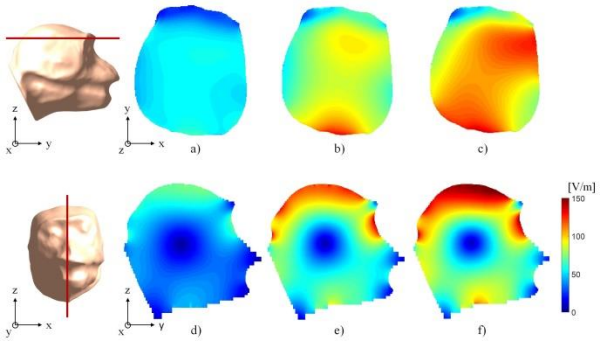

Fig. 4. The |E|-field for the axial view (top row) and sagittal view (bottom row) for (a), (d): only the active array coil; (b), (e): with the wireless coil; (c), (f): the combination of the wireless coil and HPM.

IV. CONCLUSION

The results from the simulation indicate the potential of the proposed combination of w_L coils and HPM attachments to improve the $|B_1^-|$-field of the traditional PA coil. On average, the $|B_1^-|$-field sensitivity was increased almost two times in comparison with the reference PA array coil only. The proposed receive only coil configuration could be a promising method for imaging small animals such as rhesus monkeys.

ACKNOWLEDGMENT

This research was supported by a grant (HO16C0004) from Osong Innovation Center, funded by the Ministry of Health & Welfare, the Republic of Korea.

REFERENCES

[1] S. Hofer, K. D. Merboldt, R. Tammer, and J. Frahm, "Rhesus monkey and human share a similar topography of the corpus callosum as revealed by diffusion tensor MRI in vivo," *Cerebral Cortex*, vol. 18, no. (5), pp. 1079-1084. 2007.

[2] C. A. Roopnariane, Y. C. Ryu, M. R. Tofighi, P. A. Miller, S. Oh, J. Wang, B. S. Park, L. Ansel, C. A. Lieu, T. Subramanian, and Q. X. Yang, "Quadrature RF coil for in Vivo brain MRI of a macaque monkey in a stereotaxic head frame," *Concepts Magn. Reson. Part B*, vol. 41, no. 1, pp. 22, 2012.

[3] M. H. Khachaturian, "A 4-channel 3 Tesla phased array receive coil for awake rhesus monkey fMRI and diffusion MRI experiments," *J. Biomed. Sci. Eng.*, vol. 3, no. 11, pp. 1085, 2010.

[4] T. Herrmann, J. Mallow, M. Plaumann, M. Luchtmann, J. Stadler, J. Mylius, M. Brosch, and J. Bernarding, "The travelling-wave primate system: A new solution for magnetic resonance imaging of macaque monkeys at 7 Tesla ultra-high field," *PloS One*, vol. 10, no. 6, 2015.

[5] M. A. Ohliger, and D. K. Sodickson, "An introduction to coil array design for parallel MRI," *NMR Biomed*., vol. 19, no. 3, pp. 300, 2006.

[6] M. Perez, D. Hernandez, E. Michel, M. H. Cho, and S. Y. Lee. "A tool box to evaluate the phased array coil performance using retrospective 3D coil modeling" *J. Korean Soc. Magn. Reson. Med.*, vol. 18, no. 2, pp. 107. 2014.

[7] B. Keil, J. N. Blau, S. Biber, P. Hoecht, V. Tountcheva, K. Setsompop, C. Triantafyllou, and L. L. Wald, "A 64- channel 3T array coil for accelerated brain MRI," *Magn. Reson. Med.*, vol. 70, pp. 248, 2013.

[8] J. R. Hadley, C. M. Furse, and D. Parker, "RF coil design for MRI using a genetic algorithm," *Applied Computational Electromagnetics Society Journal*, vol. 22, no. 2, pp. 277, 2007.

[9] M. Bilgen, "Inductively-overcoupled coil design for high resolution magnetic resonance imaging," *Biomedical Engineering Online*, vol. 5, no. 1, pp. 3, 2006.

[10] J. H. Seo, S. D. Han, and K. N. Kim, "Improvements in magnetic field intensity and uniformity for small-animal MRI through a high-permittivity material attachment," *Electron. Lett.*, vol. 52, no. 11, pp. 898, 2016.

[11] J. H. F. van Gemert, W. M. Brink, A. G. Webb, and R. F. Remis, "Designing high-permittivity pads for dielectric shimming in MRI using model order reduction and Gauss-Newton optimization," *ICEAA*, pp. 417. 2017.

[12] W. M. Teeuwisse, W. M. Brink, and A. G. Webb, "Quantitative assessment of the effects of high-permittivity pads in 7 Tesla MRI of the brain," *Magn. Reson. Med.*, vol. 67, no. 5, pp. 1285, 2012.

[13] L. Hao, L. Xu, B. Yang, and G. Li, "Image reconstruction based on the anatomical information for magnetic resonance electrical impedance tomography," *Applied Computational Electromagnetics Society Journal*, vol. 31, no. 6, 2016.

[14] N. S. Panwar and B. S. Semwal, "Study of electrical conductivity of barium titanate ceramics," *Ferroelectrics*, vol. 115, pp. 1, 1991.

[15] W. M. Teeuwisse, W. M. Brink, K. N. Haines, and A. G. Webb, "Simulations of high permittivity materials for 7 T neuroimaging and evaluation of a new barium titanate-based dielectric," *Magn. Reson. Med*., vol. 67, no. 4, pp. 912, 2012.